

**CONTENTS**

<b>Błażej Czajka</b> <i>Investigations into the Stability of Thin-Walled Composite Structures with Top-Hat Cross-Sections.....</i>	311
<b>Marcin Konarzewski, Michał Stankiewicz, Marcin Sarzyński, Marcin Wieczorek, Magdalena Czerwińska, Piotr Prasula, Robert Panowicz</b> <i>Properties of Rubber-Like Materials and Their Blends in Wide Range of Temperatures – Experimental and Numerical Study....</i>	317
<b>Adam Charchalis, Marcin Kneć, Daria Żuk, Norbert Abramczyk</b> <i>Use of 3D Optical Techniques in the Analysis of the Effect of Adding Rubber Recyclate to the Matrix On Selected Strength Parameters of Epoxy–Glass Composites .....</i>	333
<b>Djamel Ouzandja, Amina Tahar Berrabah</b> <i>Deterministic Seismic Damage Analysis for Concrete Gravity Dams: A Case Study of Oued Fodda Dam .....</i>	347
<b>Muhammad Amir, Jamil Abbas Haider, Jamshaid Ul Rahman, Asifa Ashraf</b> <i>Solutions of the Nonlinear Evolution Problems and their Applications .....</i>	357
<b>Natalia Morkun, Gerhard Fischerauer, Vitalii Tron, Alona Gaponenko</b> <i>Mineralogical Analysis of Iron Ore using Ultrasonic Wave Propagation Parameters .....</i>	364
<b>Mohamed Mohamed, Amjad Hamza, Tarig Elzaki, Mohamed Algom, Shiraz Elhussein</b> <i>Solution of Fractional Heat-Like and Fractional Wave-Like Equation by using Modern Strategy.....</i>	372
<b>Janusz T. Cieśliński, Paulina Boroń, Maciej Fabrykiewicz</b> <i>Stability Investigation of the PCM Nanocomposites .....</i>	381
<b>Heiko Meironke, Thomas Panten, Martin Hayduk, Frieder Strubel</b> <i>Development of a Test Rig for the Measurement of Small Wind Turbines in a Wind Tunnel.....</i>	390
<b>Nicol Daniela Jaramillo Rodríguez , Aline Luxa, Lars Jürgensen</b> <i>Adaptation and Application of a Polarisation Curve Test Protocol for a Commercial PEM Electrolyser on Cell and Stack Level..</i>	395
<b>Michel Zierow, Leon Lesemann</b> <i>Aerodynamic investigation on the artifact “Bird of Saqqara”.....</i>	405
<b>Vladimir Morkun, Natalia Morkun, Vitalii Tron, Oleksandra Serdiuk, Alona Haponenko, Iryna Haponenko</b> <i>Formation of Information Base for Controlling Settlement of Solid-Phase Ore Slurry Particles in a Thickener.....</i>	410
<b>Muhammad Amir, Jamil Abbas Haider, Shahbaz Ahmad, Sana Gul, Asifa Ashraf</b> <i>Approximate Solution of Painlevé Equation I by Natural Decomposition Method and Laplace Decomposition Method .....</i>	417
<b>Mohammad Reza Seifi, Reza Alimardani, Seyed Saeid Mohtasebi, Hossein Mobli, Maumoud Soltani Firouz</b> <i>A Supervisory Control System for Automation of Horizontal Form-Fill-Seal Packaging Plant Based on Modified Atmosphere Technology .....</i>	423
<b>Piotr Gierlak</b> <i>Neural Control of a Robotic Manipulator in Contact with a Flexible and Uncertain Environment .....</i>	435
<b>Damian Augustyn, Marek Fidali</b> <i>Method of Machining Centre Sliding System Fault Detection using Torque Signals and Autoencoder .....</i>	445
<b>Amina Tahar Berrabah, Amina Attia, Daoudi Mohammed Habib, Djamel Ouzandja</b> <i>Effect of Dam–Rock Foundation Interaction Modeling on the Modal Ratio-Related Quantity of Beni Behdel and `El Mefrouch Multi-Arch Dams.....</i>	452

<b>Amin Houari, Kouider Madani, Salah Amroune, leila Zouambi, Mohamed Elajrami</b> <i>Numerical Study of the Mechanical Behaviour and Damage of FGM Bent Pipes under Internal Pressure and Combined Bending Moment</i> .....	460
<b>Ewelina Ciba, Paweł Dymarski</b> <i>Modelling of the Viscosity Effect of Heave Plates for Floating Wind Turbines by Hydrodynamic Coefficients</i> .....	469
<b>Jagoda Kurowiak, Agnieszka Mackiewicz, Tomasz Klekiel, Romuald Będziński</b> <i>Material Characteristic of an Innovative Stent for the Treatment of Urethral Stenosis</i> .....	477
<i>Abstracts</i> .....	XXIII

## ABSTRACTS

**Błażej Czajka**

*Investigations into the Stability of Thin-Walled Composite Structures with Top-Hat Cross-Sections*

This paper presents a study of compressed thin-walled composite columns with an open cross-section. The tested specimens with a top-hat cross-section were made of CFRP material. Two arrangements of composite layers [0/-45/45/90]s and [90/0/90/0]s were compared. The paper focuses on the buckling phenomenon and the determination of the critical loads of the structure. It includes both numerical analyses using the finite element method (FEM) and validation on real specimens made using the autoclave technique. A comparison is made between the results obtained by both methods. The critical forces of the real specimens were determined using the P-wc3 approximation method. Both the evaluation of the buckling shape and the values of the critical forces showed a significant correlation between the experimental and numerical tests. This paper also compares the tested lay-ups.

**Marcin Konarzewski, Michał Stankiewicz, Marcin Sarzyński, Marcin Wieczorek, Magdalena Czerwińska, Piotr Prasula, Robert Panowicz**

*Properties of Rubber-Like Materials and Their Blends in Wide Range of Temperatures – Experimental and Numerical Study*

Elastomers are widely used in many industries. Their use requires thorough knowledge of their strength and stiffness parameters over a wide temperature range. However, determination of the parameters of such materials is still a challenge. Therefore, the paper presents research methodology allowing determination of the properties of rubber-like materials in a wide range of stretch and temperatures (from +50°C to -25°C) by using the example of styrene-butadiene rubber (SBR) and natural rubber (NR) elastomers. Additionally, two blends, chloroprene rubber/nitrile-butadiene rubber (CR/NBR) and NR/SBR blends, were also considered. Based on physical premises, a polynomial and Arruda–Boyce hyperelastic constitutive models parameters were determined using two different methods, namely curve-fitting and the successive response surface method.

**Adam Charchalis, Marcin Kneć, Daria Żuk, Norbert Abramczyk**

*Use of 3D Optical Techniques in the Analysis of the Effect of Adding Rubber Recyclate to the Matrix On Selected Strength Parameters of Epoxy-Glass Composites*

The article presents a method of modifying the strength properties of epoxy–glass composite by changing the percentage composition of the matrix by the addition of rubber recyclate. Taking into account environmental protection and economic conditions in the process of recycling and utilisation of waste, it is advisable to look for applications of non-degradable waste materials. Based on epoxy resin, a glass mat with a random direction of fibres and rubber recyclate, a test material with different percentage compositions was produced. Samples from the manufactured materials were subjected to a static tensile test on a ZwickRoell testing machine using the ARAMIS SRX measuring system. In addition, CT (computerized tomography) scans of the inside of the samples were made using a ZEISS METROTOM 6 Scout tomograph, and observations of the internal structures were made using a scanning electron microscope. The use of optical and microscopic techniques enabled the precise determination of strength parameters of the examined composites and the analysis of the behaviour of samples under load. The analysis of deformations over time in the examined samples showed a beneficial effect of the addition of rubber recyclate on the elastic properties of the examined composites.

**Djamel Ouzandja, Amina Tahar Berrabah**

*Deterministic Seismic Damage Analysis for Concrete Gravity Dams: A Case Study of Oued Fodda Dam*

One of the major dangers for seismic damage of concrete dams is the propagation of cracks in dam concrete. The present study undertakes a numerical investigation of the seismic damage for Oued Fodda concrete gravity dam, located in the northwest of Algeria, considering the impacts of properties of joints along the dam–foundation rock interface and cross-stream earthquake excitation. Three-dimensional transient analyses for coupled dam–foundation rock system are carried out using Ansys software. The hydrodynamic effect of reservoir fluid is modelled using the added mass approach. The smeared crack approach is utilised to present the seismic damage of dam concrete using the Willam and Warnke failure criterion. The dam–foundation rock interface joints are presented with two ways, adhesive joints and frictional joints. The Drucker–Prager model is considered for dam concrete in nonlinear analyses. Consideration of the study results indicates that the frictional joints model can reduce the seismic response and damage hazard of the dam body to a better extent compared with the adhesive joints model. Furthermore, the application of cross-stream earthquake excitation reveals the significant effect on cracking response of the dam in the two models of joints.

**Muhammad Amir, Jamil Abbas Haider, Jamshaid UI Rahman, Asifa Ashraf**
*Solutions of the Nonlinear Evolution Problems and their Applications*

In this article, a well-known technique, the variational iterative method with the Laplace transform, is used to solve nonlinear evolution problems of a simple pendulum and mass spring oscillator, which represents the duffing equation. In the variational iteration method (VIM), finding the Lagrange multiplier is an important step, and the variational theory is often used for this purpose. This paper shows how the Laplace transform can be used to find the multiplier in a simpler way. This method gives an easy approach for scientists and engineers who deal with a wide range of nonlinear problems. Duffing equation is solved by different analytic methods, but we tackle this for the first time to solve the duffing equation and the nonlinear oscillator by using the Laplace-based VIM. In the majority of cases, Laplace variational iteration method (LVIM) just needs one iteration to attain high accuracy of the answer for linearization and discretization, or intensive computational work is needed. The convergence criteria of this method are efficient as compared with the VIM. Comparing the analytical VIM by Laplace transform with MATLAB's built-in command Simulink that confirms the method's suitability for solving nonlinear evolution problems will be helpful. In future, we will be able to find the solution of highly nonlinear oscillators.

**Natalia Morkun, Gerhard Fischerauer, Vitalii Tron, Alona Gaponenko**
*Mineralogical Analysis of Iron Ore using Ultrasonic Wave Propagation Parameters*

Availability, relative simplicity and low cost, combined with ever-increasing capabilities, have led to a significant increase in the use of ultrasonic measurements of mining process variables in recent times. The scope of application varies from the study of the characteristics of raw materials and products of its processing to the operational assessment of the current parameters characterising the state of the process equipment. The purpose of this study is to develop methods for obtaining information about the characteristics of mineral raw materials as a result of ultrasonic logging of wells in a rock mass. The proposed approach makes it possible to improve the quality of information support for the management of technological processes of mining and processing of ore and thereby improve the quality of products supplied to the metallurgical stage and reduce overall production costs.

**Mohamed Mohamed, Amjad Hamza, Tarig Elzaki, Mohamed Algam, Shiraz Elhussein**
*Solution of Fractional Heat-Like and Fractional Wave-Like Equation by using Modern Strategy*

This paper introduces a novel form of the Adomian decomposition (ADM) method for solving fractional-order heat-like and wave-like equations with starting and boundary value problems. The derivations are provided in the sense of Caputo. In order to help understanding, the generalised formulation of the current approach is provided. Several numerical examples of fractional-order diffusion-wave equations (FDWEs) are solved using the suggested method in this context. In addition to examining the applicability of the suggested method to the solving of fractional-order heat-like and wave-like equations, a graphical depiction of the solutions to three instructive cases was constructed. Solution graphs were arrived at for integer and fractional-order problems. The derived and exact solutions to integer-order problems were found to be in excellent agreement. The subject of the present research endeavour is the convergence of fractional-order solutions. This strategy is considered to be the most successful way of addressing fractional-order initial-boundary value issues in science and engineering. This strategy is presented here.

**Janusz T. Cieśliński, Paulina Boroń, Maciej Fabrykiewicz**
*Stability Investigation of the PCM Nanocomposites*

Ensuring the stability is a key issue to be solved for the technical application of nanocomposites. In this work, fatty acid P1801 served as base phase change material (PCM) P1801, and its main ingredients are palmitic acid (58%) and stearic acid (38%). Titania (TiO<sub>2</sub>) and alumina (Al<sub>2</sub>O<sub>3</sub>) with mass concentrations of 1% and 5% were selected as nanoparticles, while polyvinylpyrrolidone (PVP) or oleic acid (OA) with mass concentrations of 5% were tested as surfactants. On the basis of the measured temperature distributions in the sample, which is subject to melting and solidification processes, it was determined which of the tested nanocomposites are stable and which are not. In addition, a thermal test was proposed to assess the stability of the produced nanoPCM, which consists in measuring the temperature distribution versus time according to a precisely given procedure.



**Heiko Meironke, Thomas Panten, Martin Hayduk, Frieder Strubel**

*Development of a Test Rig for the Measurement of Small Wind Turbines in a Wind Tunnel*

This paper describes the development, design and function of a test rig for the measurement of small wind turbines in a wind tunnel and presents the first exemplary measurements of the performance characteristics of various horizontal and vertical rotors. A central part of this test rig is the developed control system with an electronic load, which enables an automated recording of the measured values for the evaluation of the power coefficients ( $c_p$ ) and tip-speed ratio ( $\lambda$ ) values. Another challenge emerges owing to the known differences in the power spectrum, because the power coefficients of drag rotors (<20%) are different from those of buoyancy rotors (<40%). The system was adapted to the different ranges by means of a stepless switching using various resistors. The entire control and regulation unit was compactly implemented using a programmable logic controller (PLC) and dynamically linked to the operating parameters of the wind tunnel. This enables an automated operation of the wind tunnel during the determination of the performance parameters of the investigated wind turbines.

**Nicol Daniela Jaramillo Rodríguez , Aline Luxa, Lars Jürgensen**

*Adaptation and Application of a Polarisation Curve Test Protocol for a Commercial PEM Electrolyser on Cell and Stack Level*

The present study aims to develop a test protocol based on the literature for electrochemical characterisation of a polymer electrolyte membrane (PEM) electrolysis commercial stack using polarisation curves. For this, a 1-kW water electrolysis test stand with integrated temperature control and measurement systems was built around the stack. Afterwards, the stack performance was characterised under different operating pressure and temperature conditions by using polarisation curves. A measurement protocol was developed based on the literature. To ensure the reproducibility of the results, two rounds of experiments were performed. The experiments were carried out at temperatures between 20 and 60 °C and pressures up to 15 bar. The results show distinct regions in the polarisation curves related to the activation and ohmic overvoltage. The effect of temperature and pressure on the performance is shown and analysed. The performance of single cells in the stack is also measured. The stack polarisation curves are compared with those in the literature, which gives an understanding of the materials used in electrodes and types of membranes.

**Michel Zierow, Leon Lesemann**

*Aerodynamic investigation on the artifact "Bird of Saqqara"*

Lost, technical knowledge of ancient cultures is being rediscovered in modern times during archaeological excavations. A presumed example of the innovative power of ancient cultures is the artefact "Bird of Saqqara". In the context of this paper, the aerodynamic characteristics of the artefact are to be determined by a computational fluid simulation, in order to be able to make a statement about the actual flight suitability and to examine the theses of the pre-astronautics critically. Based on a 3D scan, a CAD model of the artefact is created and then a numerical flow simulation is performed. By varying the angle of attack, the dimensionless coefficients can be represented in corresponding polars. The results show that the artefact has a low maximum glide ratio and thus the glide properties are not sufficient for use as a handglider. The centre of gravity of the artefact is located at the trailing edge of the wing and behind the neutral point. The resulting longitudinal stability does not meet modern specifications. Asymmetric lift distribution in the spanwise direction results in uncontrolled roll. Consequently, the artefact cannot fly a straight path. Within the scope of this work, the connection between the "Bird of Saqqara" and an alleged knowledge of aerodynamics in ancient Egypt could not be confirmed.

**Vladimir Morkun, Natalia Morkun, Vitalii Tron, Oleksandra Serdiuk, Alona Haponenko, Iryna Haponenko**

*Formation of Information Base for Controlling Settlement of Solid-Phase Ore Slurry Particles in a Thickener*

Thickeners are process units that are often used at mining enterprises. There, they are involved in dehydration of mineral concentration products when water is removed from wet tailings containing metal concentrates. In mineral processing, large quantities of process water are used to separate different minerals from each other, so dehydration plays a major role in ore processing and preparation for concentration. This research aims to develop methods and tools of ultrasonic measurement of characteristics of settlement of solid-phase slurry particles and to assess their possible application to the automatic control system of the thickener to improve its efficiency.

**Muhammad Amir, Jamil Abbas Haider, Shahbaz Ahmad, Sana Gul, Asifa Ashraf**
*Approximate Solution of Painlevé Equation I by Natural Decomposition Method and Laplace Decomposition Method*

The Painlevé equations and their solutions occur in some areas of theoretical physics, pure and applied mathematics. This paper applies natural decomposition method (NDM) and Laplace decomposition method (LDM) to solve the second-order Painlevé equation. These methods are based on the Adomain polynomial to find the non-linear term in the differential equation. The approximate solution of Painlevé equations is determined in the series form, and recursive relation is used to calculate the remaining components. The results are compared with the existing numerical solutions in the literature to demonstrate the efficiency and validity of the proposed methods. Using these methods, we can properly handle a class of non-linear partial differential equations (NLPDEs) simply.

**Mohammad Reza Seifi, Reza Alimardani, Seyed Saeid Mohtasebi, Hossein Mobli, Maumoud Soltani Firouz**
*A Supervisory Control System for Automation of Horizontal Form-Fill-Seal Packaging Plant*
*Based on Modified Atmosphere Technology*

The packaging industry is one of the most important parts of agricultural products processing. A popular method of increasing the shelf life of agricultural products is modified atmosphere packaging (MAP). The main objective of this paper was to increase the adaptability and flexibility of the machines for packaging of different vegetables including lettuces, broccolis, cabbages, cauliflowers, etc. To achieve this goal, a supervisory control and data acquisition (SCADA)-based system was designed and developed for controlling and monitoring of MAP process of fresh vegetables. The system was divided into three physical layers: field devices, remote terminal unit (RTU) and master terminal unit (MTU). For packaging width adjuster system, the  $R^2$ , maximum error (ME), mean absolute error (MAE) and root mean square error (RMSE) were obtained as 0.999, 8 mm, 2.96 mm and 3.44 mm, respectively. For packaging height adjuster system, the  $R^2$ , ME, MAE and RMSE were obtained as 0.994, 10 mm, 3.53 mm and 4.57 mm, respectively. The SCADA system can be able to accurately adjust the speed of the conveyor and the temperature of the sealing jaws, based on the desired values. For gas injection unit, the value of 1.66 L/min, 0.557 L/min and 0.667 L/min were recorded for ME, MAE and RMSE, respectively. Four types of trends including temperature, speed, flow and digital parameter trends were designed. In addition to displaying screen alarms, the occurred alarms are stored, automatically as a text file for troubleshooting. Finally, the results showed that the designed system can be reliably used for MAP of various varieties of fresh vegetables.

**Piotr Gierlak**
*Neural Control of a Robotic Manipulator in Contact with a Flexible and Uncertain Environment*

This article presents the synthesis of a neural motion control system of a robot caused by disturbances of constraints limiting the movement, which are the result of flexibility and disturbances of the contact surface. A synthesis of the control law is presented, in which the knowledge of the robot's dynamics and the parameters of a susceptible environment is not required. Moreover, the stability of the system is guaranteed in the case of an inaccurately known surface of the environment. This was achieved by introducing an additional module to the control law in directions normal to the surface of the environment. This additional term can be interpreted as the virtual viscotic resistance and spring force acting on the robot. This approach ensured the self-regulation of the robot's interaction force with the compliant environment, limiting the impact of the geometrical inaccuracy of the environment.

**Damian Augustyn, Marek Fidali**
*Method of Machining Centre Sliding System Fault Detection using Torque Signals and Autoencoder*

The sliding system of machining centres often causes maintenance and process problems. Improper operation of the sliding system can result from wear of mechanical parts and drives faults. To detect the faulty operation of the sliding system, measurements of the torque of its servomotors can be used. Servomotor controllers can measure motor current, which can be used to calculate motor torque. For research purposes, the authors used a set of torque signals from the machining centre servomotors that were acquired over a long period. The signals were collected during a diagnostic test programmed in the machining centre controller and performed once per day. In this article, a method for detecting anomalies in torque signals was presented for the condition assessment of the machining centre sliding systems. During the research, an autoencoder was used to detect the anomaly, and the condition was assessed based on the value of the reconstruction error. The results indicate that the anomaly detection method using an autoencoder is an effective solution for detecting damage to the sliding system and can be easily used in a condition monitoring system.

**Amina Tahar Berrabah, Amina Attia, Daoudi Mohammed Habib, Djamel Ouzandja**
*Effect of Dam–Rock Foundation Interaction Modeling on the Modal Ratio-Related Quantity of Beni Behdel and 'El Mefrouch Multi-Arch Dams*

Using the Beni Behdel dam and the El Mefrouch dam as example studies, this paper intends to clearly demonstrate how modeling of the interactions between rock foundations and dams impacts the modal behavior of these two multi-arch dams. The uniqueness of this study is that the modal behavior of each dam is represented in terms of related parameters (period, participation factor, ratio, and effective mass), and more precisely in terms of ratio (defined as the ratio between the participation factor of the mode  $i$  and the maximum participation factor), as opposed to other works that have expressed this behavior in terms of frequency. In this article, stiff rock foundation, massless rock foundation, and massed rock foundation are the three methods used to simulate dynamic interactions. The investigated dams are three-dimensionally simulated using the ANSYS finite elements code. The modeling of the rock foundation–dam interaction has an effect on the fundamental mode value, its location, and the related parameters, according to the results. Furthermore, it is found that the upstream–downstream direction is not always the most important direction for dams and that interaction modeling influences the resonance bandwidth, which affects the forecast of the resonance phenomenon.

**Amin Houari, Kouider Madani, Salah Amroune, Leila Zouambi, Mohamed Elajrami**
*Numerical Study of the Mechanical Behaviour and Damage of FGM Bent Pipes under Internal Pressure and Combined Bending Moment*

The main objective of this work is the numerical prediction of the mechanical behaviour up to the damage of the bends of the functionally graded material (FGM) type ceramic/metal pipes. Firstly, the effective elastoplastic properties of bent FGM pipes were determined using the homogenisation law by the Mori–Tanaka models for the elastic part and TTO (Tamura-Tomota-Ozawa) for the plastic part based on a rule of mixtures per function in the form of a power law. Our work also aims at the use of a meshing method (UMM) to predict the behaviour of the FGM by finite element in the mesh of the model. The analysis was performed using the UMM technique for different loading cases and volume fraction distribution. Two stages are necessary for the analysis of the damage: the first is the model of initiation of the damage established by the criterion of maximum deformation named MAXPE and the second is criterion of the energy of the rupture according to the theory Hillerborg used to determine damage evolution. Both stages involve a 3D finite element method analysis. However, for damage, the XFEM technique was used in our UMM method to predict crack initiation and propagation in FGM pipe bends. The results of the numerical analysis concerning the mechanical behavior showed, that if the nature of the bent pipes is in FGM, a good reduction of the various stresses compared to those where the nature of the pipe is metallic material. The results were presented in the form of a force–displacement curve. The validation of the proposed numerical methodology is highlighted by comparisons of current results with results from the literature, which showed good agreement. The analysis took into account the effect of the main parameters in a bent FGM pipe under internal pressure and bending moment on the variation of the force–strain curves.

**Ewelina Ciba, Paweł Dymarski**
*Modelling of the Viscosity Effect of Heave Plates for Floating Wind Turbines by Hydrodynamic Coefficients*

One of the methods of modelling the movement of floating wind turbines is the use of the diffraction method. However, this method does not take into account the influence of viscosity; therefore, in many cases, it needs to be extended with a matrix of appropriate coefficients. The effect of viscosity causes both the added mass coefficient and the damping coefficient to increase. The determined coefficients were entered into the ANSYS AQWA program, and the calculation results of the transfer function determined with the use of linear and quadratic damping were presented. The results were compared with the results of the experiment, indicating greater convergence for the quadratic model.

**Jagoda Kurowiak, Agnieszka Mackiewicz, Tomasz Klekiel, Romuald Będziński**
*Material Characteristic of an Innovative Stent for the Treatment of Urethral Stenosis*

The appropriate development and customisation of the stent to the urethral tissues requires the determination of many factors such as strength and degradation. Given the distinctive conditions of urethral tissues, it is important that the design of the stent be properly developed. The selection of a stent material requires knowing its material characteristics and verifying that they are suitable for the future implantation site. In the present study, the development of a polydioxanone (PDO)-based stent was undertaken. The PDO material was fabricated using an additive technique – 3D printing. Then, in vitro tests were performed to determine the degradation time of the material under conditions simulating an aggressive urinary environment. The changes in the parameters of mechanical properties before and after the degradation period were determined, and the changes in the structure of the material before and after degradation were observed. Numerical analysis was performed for the proposed stent design. The results showed that PDO has good mechanical properties, but its degradation time is too short to be used in a urethral stent. Among the innovations of the studies conducted are bending strength tests, which is not a frequently considered aspect so far.

## INVESTIGATIONS INTO THE STABILITY OF THIN-WALLED COMPOSITE STRUCTURES WITH TOP-HAT CROSS-SECTIONS

Błażej CZAJKA\*

\*Faculty of Mechanical Engineering, Department of Machine Design and Mechatronics, Lublin University of Technology,  
ul. Nadbystrzycka 38D, 20-618 Lublin, Poland

[blazej.czajka@pollub.edu.pl](mailto:blazej.czajka@pollub.edu.pl)

*received 1 December 2022, revised 19 January 2023, accepted 7 February 2023*

**Abstract:** This paper presents a study of compressed thin-walled composite columns with an open cross-section. The tested specimens with a top-hat cross-section were made of CFRP material. Two arrangements of composite layers [0/-45/45/90]<sub>s</sub> and [90/0/90/0]<sub>s</sub> were compared. The paper focuses on the buckling phenomenon and the determination of the critical loads of the structure. It includes both numerical analyses using the finite element method (FEM) and validation on real specimens made using the autoclave technique. A comparison is made between the results obtained by both methods. The critical forces of the real specimens were determined using the P-wc3 approximation method. Both the evaluation of the buckling shape and the values of the critical forces showed a significant correlation between the experimental and numerical tests. This paper also compares the tested lay-ups.

**Key words:** buckling, post-buckling equilibrium paths, critical loads, thin-walled composite structures, finite element method, experimental tests

### 1. INTRODUCTION

Thin-walled structures are widely used in many industries such as civil engineering, automotive industry, aviation and aerospace. Many responsible components, for example, pads in sports, structural components for aircraft and helicopters [1, 2] and vehicle components [3] are made from these structures. Among these, structures made of composite materials are particularly important.

The use of thin-walled structures introduces the possibility of structural buckling. However, it is important to note that local buckling of a structure may not necessarily result in a loss of load-carrying capacity. Many structures show the ability to carry loads further in the post-buckling state. Nevertheless, for the safety design and subsequent behaviour of the structure, it is very important to determine the critical load and the behaviour in the post-buckling state.

Some of the first investigators dealing with the phenomenon of elastic stability were Koiter and Hutchinson [4], Byskov [5], Thompson and Hunt [6] and Goltermann and Mollman [7, 8]. Although the beginning of research into the phenomenon of buckling of structures dates to the 18th century, the subject is still relevant and further work is needed to design structures more and more confidently. This is confirmed, for example, by the fact that scientists such as Kubiak [9], Dębski [10] and Różyło [11] are continuously working on this topic. Many papers in recent years have been devoted to the study of the stability and buckling of structures constructed from various types of composites [12–16]. In addition, some of them deal precisely with columns with open cross-sections, which highlights the novelty and currency of the studied topic [10, 17, 18].

Due to the rapid evolution of computer hardware and engineering software, an increasing range of engineering problems may be solved using numerical simulations. Within these, finite element method (FEM) calculations are currently leading. These are used, for example, for thermal, modal and strength analyses. Numerical analysis also allows the determination of critical loads, which cause buckling of the structure. Critical loads may also be established through experimental investigations. Some of the approximation methods used to determine critical forces are the Koiter method [19, 20], P-wc2 and P-wc3 [21]. The use of the P-wc3 method, which is rarely used in the literature [21, 22, 23], brings a novelty to the paper and allows to expand the overall state of knowledge on the subject. The aforementioned methods are based on the post-buckling equilibrium paths recorded during experimental testing, which represents the dependence of the load on the deflection of the specimen.

In this study, the buckling tests were carried out using the numerical analysis in the Abaqus software and experimental tests on a universal testing machine. The interdisciplinary approach of the research made it possible to compare the results obtained from the computer simulations with the real samples. The influence of composite lay-up on the stability of the structure was also investigated. The presented research extends the state of knowledge regarding the stability and determination of critical loads of thin-walled composite columns with open cross-sections.

The research performed in this paper (on composite structures with top-hat sections) is a prelude to the research from project No. 2021/41/B/ST8/00148, National Science Centre (Poland), on composite profiles with closed sections.

**2. OBJECT OF RESEARCH**

The object of the study was thin-walled open-section columns made of CFRP (carbon fiber reinforced polymer) composite material. They had a top-hat cross-section of 60 mm × 30 mm × 15 mm and a height of 200 mm. A numerical model of the specimen with the marked dimensions is shown in Fig. 1. The test specimens consisted of eight laminate layers with a thickness of 0.105 mm per layer. The presented research focuses on the comparison of two lay-ups W1 – [0/-45/45/90]s and W2 – [90/0/90/0]s. Three samples from each layer arrangement were used in the experimental part of the study. These were made as long columns using the autoclave method and then cut to a dimension of 200 mm. In the numerical part of the study, the real specimens were represented by numerical models.

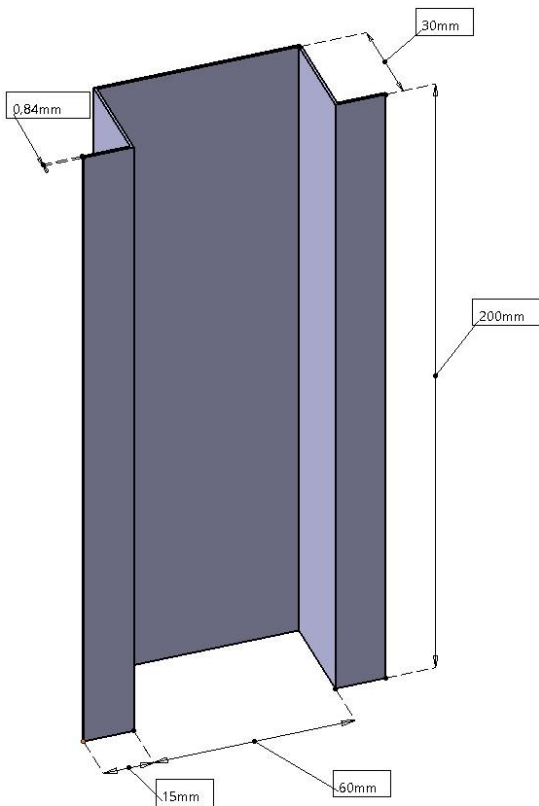


Fig. 1. Numerical model of the specimen with marked dimensions

The properties of the CFRP composite material were determined in compliance with ISO standards. The mechanical properties for a single laminate layer are shown in Tab. 1, where  $E_1$  is Young's modulus in the fibre alignment direction,  $E_2$  is Young's modulus in the direction perpendicular to the fibres,  $\nu_{12}$  is Poisson's ratio in the surface of the layer and  $G_{12}$  is Kirchoff's modulus in the surface of the layer.

Tab. 1. Mechanical properties of a single layer of CFRP material [24]

Symbol	Value	Unit
$E_1$	143,528.5	MPa
$E_2$	5,826.3	MPa
$\nu_{12}$	0.36	–
$G_{12}$	3,845.5	MPa

**3. NUMERICAL STUDIES**

Numerical analysis was carried out using the FEM in the Abaqus software. The paper is devoted entirely to the issue of linear buckling of structures. The linear stability analysis of the structure was conducted using a minimum potential energy criterion. The scope of the study included modelling the actual specimens and boundary conditions, discretising the models and solving the eigenproblem to determine the critical loads and buckling form of the columns.

The specimen models were made directly in Abaqus software using the lay-up ply modelling method. The layers were arranged in two configurations, W1 and W2, as described earlier, and the orthotropic properties were assigned to them as shown in Tab. 1. When discretising the models, shell-type finite elements with reduced integration and 4 nodes (S4R) were used. These are elements with 6 degrees of freedom at each node. The discretisation was performed using linear finite elements.

During the test, the models were placed between two non-deformable plates to represent the boundary conditions in the experimental test more precisely. The discretisation of the plates was performed using R3D4 elements. One of the plates (the bottom one) was completely restrained by removing the possibility of movement in each direction ( $U_x = 0, U_y = 0, U_z = 0, UR_x = 0, UR_y = 0, UR_z = 0$ ). The other plate (the top one) was allowed to move along the height of the column, and the other movements were blocked ( $U_x = 0, U_y = 0, UR_x = 0, UR_y = 0, UR_z = 0$ ). A compressive load was applied to the reference point on the top plate. The reference point is connected to the entire, non-deformable plate and move with all plate providing uniform load distribution. Contact interactions in the normal ('Hard' Contact) and tangential (frictional with friction coefficient = 1) directions were applied between the plates and the test columns. An overview of the whole model after discretisation, including the plates and the boundary conditions marked, is shown in Fig. 2. The whole model consisted of 2,153 nodes, 1,200 S4R elements and 800 R3D4 elements.

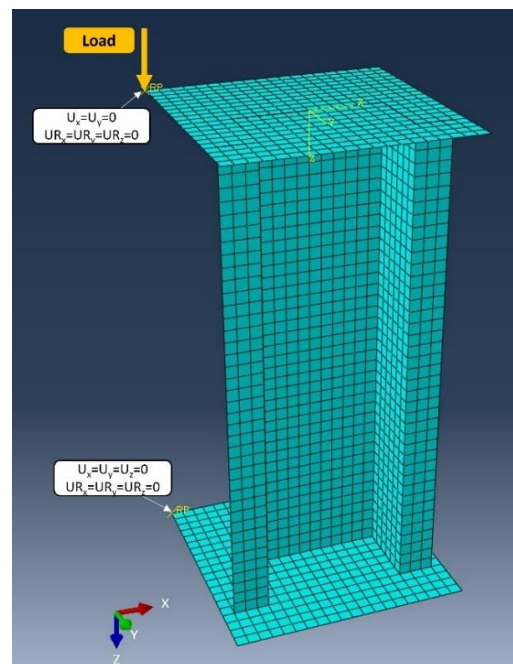


Fig. 2. Discrete model with boundary conditions



4. EXPERIMENTAL RESEARCH

The compression of the specimens was carried out on a Zwick Z100 universal testing machine. Room temperature was prevailing during the tests. The specimens were placed between two non-deformable, non-rotatable fixed plates. The lower one was fixed while the upper one compressed the specimens at a rate of 1 mm/min. The compression of the specimens was continued until the forces were about 30%–40% higher than the critical loads predicted by the numerical tests. This allowed a clear observation of the shape of the local buckling in the specimens. No signs of specimen failure were observed during or after the tests. During the test, pads made of soft material were placed between the specimens and the machine plates. These reduced the effect of non-ideal cutting of the specimens cross-sections on the uniformity of profile loading. The specimens were positioned precisely using special centring for the screw in the machine plate inserts. A general view of the test stand is shown in Fig. 3.

A laser sensor was used during the test to measure the deflection value at the point of maximum half-wave displacement. By plotting the deflection against the load, it was possible to approximate the value of the critical load in the experimental study. After a preliminary analysis of three approximation methods – the Koiter method,  $P-w_c^2$  and  $P-w_c^3$ , it was decided to use the  $P-w_c^3$  method due to the smallest discrepancies in critical loads between the various samples of a single configuration. The use of deflection instead of strain increment was possible due to the proportionality of these values [25]. The  $P-w_c^3$  method allows the critical force to be determined using a post-buckling equilibrium path for values of strain (or deflection due to proportionality) raised to the cube. The portion of the diagram occurring beyond the region of inflection is approximated by a straight line. The intersection of this straight

line with the vertical axis of the coordinate system determines the approximate value of the critical load. In this method, it is important to properly select the range of data that are approximated. The correlation coefficient  $R^2$  should take values not  $<0.95$  [23].  $R^2$  is the correlation coefficient indicating the matching quality between the approximation curve and the selected section of the experimental curve.



Fig. 3. A general view of the test stand

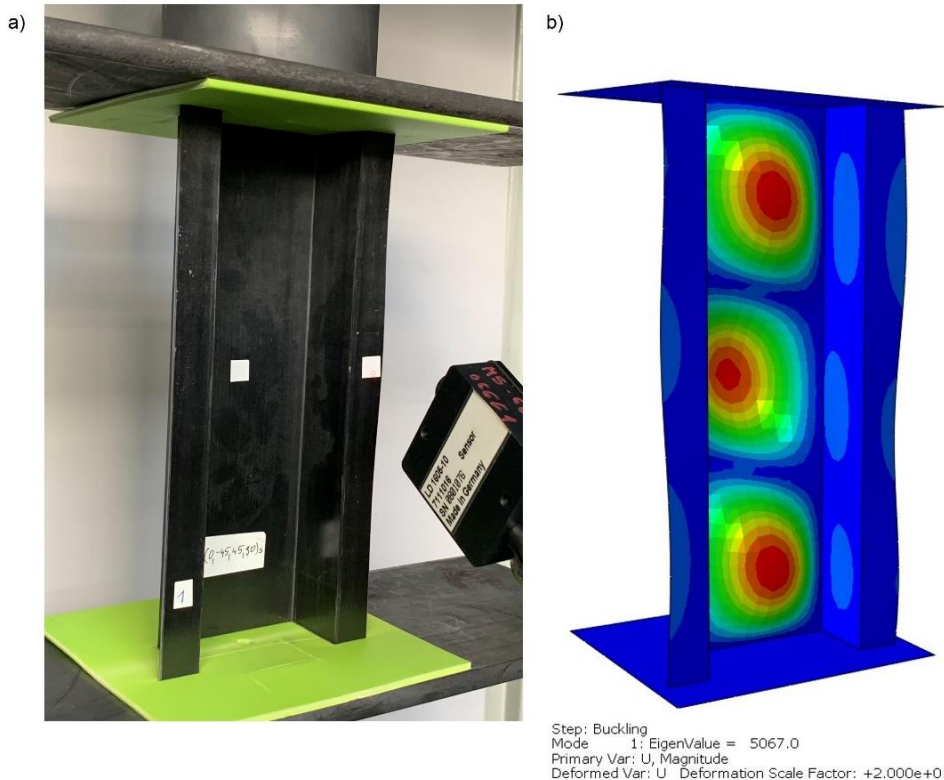


Fig. 4. Comparison of W1 configuration results: (a) experimental studies and (b) numerical analysis

**5. RESULTS**

The performed tests allowed verification of the similarity of critical loads determined by approximation methods through experimental tests and values obtained by numerical simulations. In addition, it was also possible to compare the shape of the local buckling occurring in real specimens and numerical models.

Both numerical and experimental studies have shown an iden-

tical arrangement of half-waves for the individual composite configurations. For the first one (W1 – [0/-45/45/90]s), three half-waves are visible, as shown in Fig. 4. For the experimental sample, the half-waves are best visible on the side shelf of the profile. For the W2 – [90/0/90/0]s configuration, five half-waves are observed, which are visible on both the numerical model and the actual sample (Fig. 5.) Similarly to the W1 configuration, the best visibility of the half-waves is at the same area of the column.

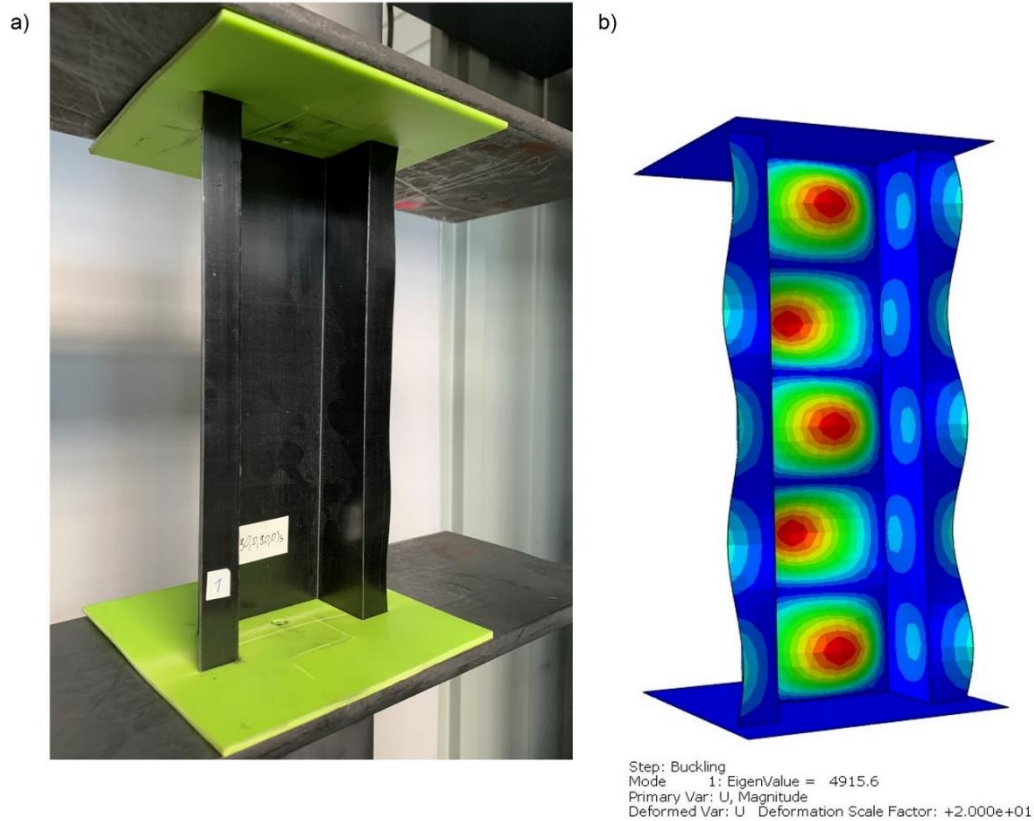


**Fig. 5.** Comparison of W2 configuration results: (a) experimental studies and (b) numerical analysis

The critical loads obtained from numerical and experimental studies also showed similar values. The average value of the critical load  $P_{cr,E}$  approximated by the  $P-w_c^3$  method for the W1 configuration was 5,224.7 N and for the W2 configuration was 4,387.1 N. In both cases, the standard deviation of the results obtained for the individual experimental samples was not >4%. The corresponding graphs used to approximate the critical force values are shown in Figs. 6 and 7 for the W1 and W2 configurations, respectively.

The critical load values achieved from the numerical simulations  $P_{cr,N}$  were 5,067.0 N for the W1 configuration and 4,915.6 N for the W2 configuration. The percentage error between the average values obtained from the experimental tests and the values from the numerical simulations was calculated according to the following Eq. (1):

$$\delta P_{cr} = \frac{|P_{cr,E} - P_{cr,N}|}{P_{cr,E}} \times 100\% \quad (1)$$

where  $P_{cr,E}$  is the average of the values approximated from the experimental tests and  $P_{cr,N}$  is the value obtained using FEM. A smaller error rate of only 3.0% was obtained for the composite in

the W1 configuration, while for the W2 configuration, it was 12.0%. The data discussed are shown in Tab. 2.

**Tab. 2.** Comparison of critical force values for experimental and numerical studies

Configuration	$P-w_c^3$ $P_{cr,E}$ [N]	FEM $P_{cr,N}$ [N]	$\delta P_{cr}$ [%]
W1 – [0/-45/45/90]s	5,224.7	5,067.0	3.0
W2 – [90/0/90/0]s	4,387.1	4,915.6	12.0

FEM, finite element method

For both experimental and numerical studies, the W1 configuration has a higher critical load value. However, this effect is more noticeable in the experimental studies, where the difference is about 837.6 N (>19% of the force value of W2). For the numerical analysis, the difference is only 151.4 N (about 3% of the force value of W2).

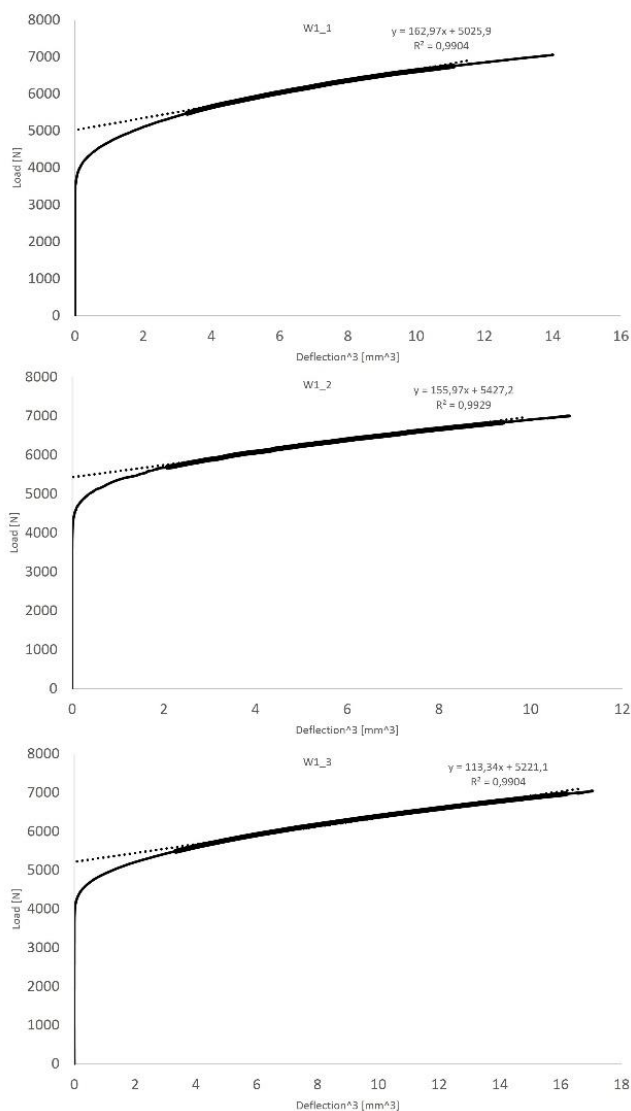


Fig. 6. Post-buckling equilibrium paths – configuration W1

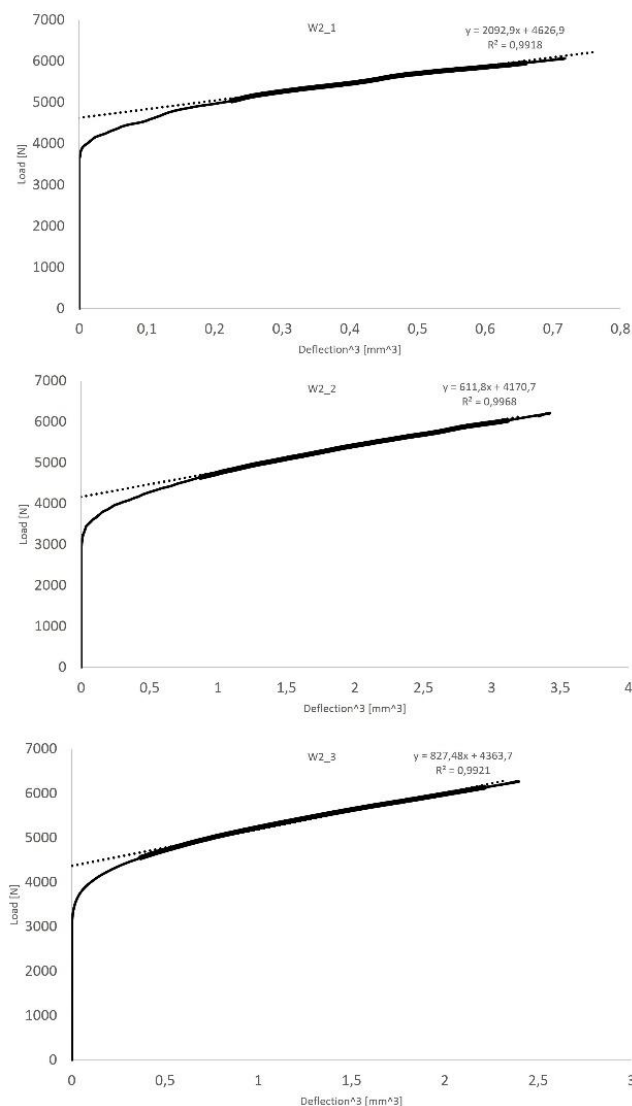


Fig. 7. Post-buckling equilibrium paths – configuration W2

## 6. CONCLUSIONS

The study carried out compares the critical state behaviour of composite columns with top-hat cross-sections in real conditions and numerical simulation. They show similar visual characteristics and identical half-wave quantities in experimental tests and FEM simulations. The critical load values obtained using the  $P-w_c^3$  approximation method are similar to those derived using numerical calculations. The difference between the methods does not exceed 12%.

The study also allowed the comparison of two composite layer configurations W1 – [0/-45/45/90]s and W2 – [90/0/90/0]s. Both methods ( $P-w_c^3$  approximation and eigenproblem solution using FEM) consistently show higher critical load values occurring for the W1 configuration.

Future studies of non-linear state behaviour and failure of structure analysis are planned. The acoustic emission method and microscopic observation will be used in this study.

## REFERENCES

1. Barkanov E, Ozoliņš O, Eglītis E, Almeida F, Bowering MC, Watson G. Optimal design of composite lateral wing upper covers. Part I: Linear buckling analysis, Aerospace Science and Technology. 2014;38: 1-8. <https://doi.org/10.1016/j.ast.2014.07.010>
2. Orifici AC, Thomson RS, Degenhardt R, Kling A, Rohwer K, Bayandor J. Degradation investigation in a postbuckling composite stiffened fuselage panel. Composite Structures. 2008;82(2): 217-224 <https://doi.org/10.1016/j.compstruct.2007.01.012>
3. Bambach MR. Fibre composite strengthening of thin-walled steel vehicle crush tubes for frontal collision energy absorption. Thin-Walled Structures. 2013;66: 15-22. <https://doi.org/10.1016/j.tws.2013.02.006>
4. Hutchinson JW, Koiter WT. Postbuckling theory. Applied Mechanics Reviews. 1970;12: 1353-1366.
5. Byskov E, Hutchinson JW. Mode interaction in axially stiffened cylindrical shells. AIAA. 1977;15(7):941-948. <https://doi.org/10.2514/3.7388>
6. Thompson JMT, Hunt GW. General theory of elastic stability. Wiley, New York; 1973.



7. Goltermann P, Møllmann H. Interactive buckling in thin-walled beams—II. Applications. *International Journal of Solids and Structures*. 1989;25(7): 729-749. [https://doi.org/10.1016/0020-7683\(89\)90010-3](https://doi.org/10.1016/0020-7683(89)90010-3)
8. Møllmann H, Goltermann P. Interactive buckling in thin-walled beams—I. Theory. *International Journal of Solids and Structures*. 1989;25(7): 715-728. [https://doi.org/10.1016/0020-7683\(89\)90009-7](https://doi.org/10.1016/0020-7683(89)90009-7)
9. Czapski P, Jakubczak P, Bieniaś J, Urbaniak M, Kubiak T. Influence of autoclaving process on the stability of thin-walled, composite columns with a square cross-section – Experimental and numerical studies. *Composite Structures*. 2020;250: 112594. <https://doi.org/10.1016/j.compstruct.2020.112594>
10. Rozylo P, Debski H. Stability and load-carrying capacity of short composite Z-profiles under eccentric compression. *Thin-Walled Structures*. 2020;157: 107019. <https://doi.org/10.1016/j.tws.2020.107019>
11. Rozylo P. Experimental-numerical study into the stability and failure of compressed thin-walled composite profiles using progressive failure analysis and cohesive zone model. *Composite Structures*. 2021;257: 113303. <https://doi.org/10.1016/j.compstruct.2020.113303>
12. Bohlooly-Fotovat M, Kubiak T, Perlikowski P. Mixed mode nonlinear response of rectangular plates under static and dynamic compression. *Thin-Walled Structures*. 2023;184: 110542. <https://doi.org/10.1016/j.tws.2023.110542>
13. Zhaochao L, Junxing Z. Nonlinear stability of the encased functionally graded porous cylinders reinforced by graphene nanofillers subjected to pressure loading under thermal effect. *Composite Structures*. 2020;233: 111584. <https://doi.org/10.1016/j.compstruct.2019.111584>
14. Zhaochao L, Qian Z, Hua S, Xinhui X, Haidong K, Junxing Z. Buckling performance of the encased functionally graded porous composite liner with polyhedral shapes reinforced by graphene platelets under external pressure. *Thin-Walled Structures*. 2023;183: 110370. <https://doi.org/10.1016/j.tws.2022.110370>
15. Guobin B, Zhihua O, Zhaochao L, Fangcheng L, Hui Z, Xingxing Z, Yonggui X. Static and buckling characteristics of the porous ring reinforced by graphene nanofillers. *Engineering Structures*. 2022;251: 113536. <https://doi.org/10.1016/j.engstruct.2021.113536>
16. Yan T, Fujian T, Junxing Z, Zhaochao L. In-plane asymmetric buckling of an FGM circular arch subjected to thermal and pressure fields. *Engineering Structures*. 2021;239: 112268. <https://doi.org/10.1016/j.engstruct.2021.112268>
17. Rozylo P. Failure phenomenon of compressed thin-walled composite columns with top-hat cross-section for three laminate lay-ups. *Composite Structures*. 2023;304: 116381. <https://doi.org/10.1016/j.compstruct.2022.116381>
18. Wysmulski P. Non-linear analysis of the postbuckling behaviour of eccentrically compressed composite channel-section columns. *Composite Structures*. 2023;305: 116446. <https://doi.org/10.1016/j.compstruct.2022.116446>
19. Koiter WT. Elastic stability and post-buckling behaviour. *Proceedings of the Symposium on Nonlinear Problems*. University of Wisconsin Press. Wisconsin; 1963.
20. Koiter WT. General theory of mode interaction in stiffened plate and shell structures. WTHD Report 590. Delft; 1976.
21. Zaras J, Krolak M, Kotelko M. Metody doświadczalne wyznaczania obciążeń krytycznych i analizy zachowania się elementów konstrukcji w stanie zakrytycznym. X Krajowa Konferencja Wytrzymałości Materiałów i Badania Materiałów. Kudowa-Zdrój; 20–22 wrzesień, 2006.
22. Rhodes J, Zaras J. Determination of critical loads by experimental methods, chapter. In: Kolakowski Z, Kowal-Michalska K, editors. *Statics, dynamics and stability of structural elements and systems*. Lodz: Lodz University of Technology, a series of monographs; 2012.
23. Rozylo P, Teter A, Debski H, Wysmulski P, Falkowicz K. Experimental and Numerical Study of the Buckling of Composite Profiles with Open Cross Section under Axial Compression. *Applied Composite Materials*. 2017;24: 1251-1264. <https://doi.org/10.1007/s10443-017-9583-y>
24. Debski H, Rozylo P, Wysmulski P. Stability and load-carrying capacity of short open-section composite columns under eccentric compression loading. *Composite Structures*. 2020;252: 112716. <https://doi.org/10.1016/j.compstruct.2020.112716>
25. Jones RM. *Mechanics of composite materials*. Taylor & Francis, Inc. Philadelphia; 1999.

Acknowledgements: The research was conducted under project no. 2021/41/B/ST8/ 00148 and financed by the National Science Centre, Poland.

Błażej Czajka:  <https://orcid.org/0000-0002-0870-5334>



This work is licensed under the Creative Commons BY-NC-ND 4.0 license.

## PROPERTIES OF RUBBER-LIKE MATERIALS AND THEIR BLENDS IN WIDE RANGE OF TEMPERATURES – EXPERIMENTAL AND NUMERICAL STUDY

Marcin KONARZEWSKI\*, Michał STANKIEWICZ\*, Marcin SARZYŃSKI\*\*, Marcin WIECZOREK\*,  
Magdalena CZERWIŃSKA\*\*\*, Piotr PRASUŁA, Robert PANOWICZ\*

\*Faculty of Mechanical Engineering, Military University of Technology, ul. gen. Sylwestra Kaliskiego 2, 00-908 Warszawa, Poland

\*\*Faculty of Mechatronics and Aeronautics, Military University of Technology, ul. gen. Sylwestra Kaliskiego 2, 00-908 Warszawa, Poland

\*\*\*Military Institute of Armament Technology, ul. Wszeźńskiego, 05-220 Zielonka, Poland

[marcin.konarzewski@wat.edu.pl](mailto:marcin.konarzewski@wat.edu.pl), [michal.stankiewicz@wat.edu.pl](mailto:michal.stankiewicz@wat.edu.pl), [marcin.sarzyński@wat.edu.pl](mailto:marcin.sarzyński@wat.edu.pl), [marcin.wieczorek@wat.edu.pl](mailto:marcin.wieczorek@wat.edu.pl),  
[czerwinskam@witu.mil.pl](mailto:czerwinskam@witu.mil.pl), [prasulap@witu.mil.pl](mailto:prasulap@witu.mil.pl), [robert.panowicz@wat.edu.pl](mailto:robert.panowicz@wat.edu.pl)

received 19 January 2023, revised 24 February 2023, accepted 13 March 2023

**Abstract:** Elastomers are widely used in many industries. Their use requires thorough knowledge of their strength and stiffness parameters over a wide temperature range. However, determination of the parameters of such materials is still a challenge. Therefore, the paper presents research methodology allowing determination of the properties of rubber-like materials in a wide range of stretch and temperatures (from +50°C to –25°C) by using the example of styrene-butadiene rubber (SBR) and natural rubber (NR) elastomers. Additionally, two blends, chloroprene rubber/nitrile-butadiene rubber (CR/NBR) and NR/SBR blends, were also considered. Based on physical premises, a polynomial and Arruda–Boyce hyperelastic constitutive models parameters were determined using two different methods, namely curve-fitting and the successive response surface method.

**Key words:** polymers, uniaxial tension, temperature effects, optimisation

### 1. INTRODUCTION

Elastomers are currently one of the most commonly used material groups in modern industry. Their usage extends from the automotive industry, where they are used mostly for car tires and suspension components, up to civil engineering, aviation and biomechanics.

The determination of the mechanical properties of such materials is crucial due to their wide usage in different industries. Especially, it is very important to take into account the influence of the operating temperature on the change of the mechanical properties [1]. The change of such parameters as tensile strength, stress or stiffness with the temperature change results from the internal structure of rubber-like materials in which polymer chains are joined by intermolecular bonds [2, 3]. The study of this influence is all the more important as, during the tensile tests of such materials, we observe an increase in displacement when the temperature is lowered and not when it is increased, contrary to what might intuitively be hypothesised to be the case [4, 5]. In the case of elastomers, we observe a rapid degradation of the polymer chains at elevated temperatures [6].

There is a whole range of elastomers differing significantly in their mechanical properties and, thus, their usage [7]. The presented article focuses on several commonly used materials and blends, namely styrene-butadiene rubber (SBR), natural rubber (NR), and NR/SBR and chloroprene rubber/nitrile-butadiene rubber (CR/NBR) blends.

SBR is a synthetic copolymer consisting of styrene and butadiene [8]. Due to its properties, it is widely used in the automotive tires industry and for various parts of car interiors [9]. Owing to the

addition of the styrene, the strength, abrasion resistance and blend properties of butadiene are improved [10]. On the other hand, the SBR is vulnerable to thermal and oxidative degradation due to the presence of double bonds in the polydiene backbone. This process manifests itself by an increase in stiffness of the material due to the cross-linking [11]. The typical operating temperature of SBR is in a range between –50°C and 100°C.

NR is one of the oldest materials known to man, but only the discovery of the vulcanisation process caused the rapid development of the rubber processing industry [12]. The main application of NR is in the truck tire industry, because of its high tear resistance, toughness and high tensile strength [13]. Additionally, NR is chemically stable, except for oils. However NR is also characterised by low thermal resistance and low organic solvent resistance, and thus various chemical modifications are required in some cases of usage [14].

Chloroprene rubber (CR) is a synthetic material created in the process of polymerisation of chloroprene [15]. This material is characterised by high resistance to weather conditions, to ozone and even to weak acids. Due to high chemical stability, it is relatively well resistant to aging [16].

Nitrile-butadiene rubber (NBR), which is a copolymer of acrylonitrile and butadiene, is characterised by an excellent resistance to a wide range of oils of mineral, animal and vegetable origin as well as to fuels and other chemicals [17]. It is an elastic material with a high tensile strength and a low compression deformation [18]. For this reason, it is frequently used in the automotive or aviation industry, to produce seals (for both hydraulic and pneumatic installations), vibration damping elements and self-sealing fuel tanks.

In order to improve the properties of rubber-like materials, the technology of polymer–polymer blends was extensively researched. Development of the multi-component systems allowed for enhancing the properties, especially mechanical, of polymeric materials [19]. One of the most commonly used materials is the above-mentioned rubber, which – due to its properties (especially high tensile strength) – is commonly blended with synthetic rubbers [19, 20]. In the case of the NR/SBR blends, the main advantage is improved oxidative stability [21], whereas in case of the CR/NBR blend, an increase in the mechanical properties is observed [22].

In the literature, a description of a series of constitutive material models that can be used to describe the behaviour of elastomers can be found. They include, among others, the Mooney–Rivlin model, neo-Hookean, Gent–Thomas, Yeoh, polynomial and Arruda–Boyce [23]. The greatest difficulty in their use is the need to have a set of appropriate material parameters. Since the mechanical properties of this type of materials are strongly influenced by e.g. the ambient temperature, one universal data set covering the entire temperature range is insufficient to correctly describe the material's behaviour under operating conditions. It is necessary to conduct experimental tests in the required temperature range, and then use the obtained data to determine the required parameters of the constitutive model. In order to determine the aforementioned parameters, usually a tensile or compression test is carried out. The stress–strain curve obtained as a result of the tests then forms the basis for determining the parameters using the curve-fitting technique. In this method, in subsequent iterations, the values of the parameters are being substituted, and then the resulting output curve is compared with the input curve. The iterations are repeated until the desired convergence is obtained, usually determined by the value of R-squared, which is a statistical metric used to evaluate the degree to which variations in the dependent variable, which is the target of the analysis, are accounted for by variations in the independent variables, which are the predictors. It is a ratio expressed as a value between 0 and 1, where a higher value indicates that the model explains a larger proportion of the variance in the dependent variable, and a value of 0 indicates that the model does not explain any of the variance.

The article aimed mainly to show the change in properties and to determine the constitutive models' parameters of various elastomers such as SBR and NR rubbers and their blends, NR/SBR and CR/NBR, in a wide range of temperatures. Both the experimental and numerical approach were utilised during the research. The experimental research allowed for determining the glass transition temperatures with use of the both dynamic mechanical analysis (DMA) and differential scanning calorimetry (DSC) methods. The tensile tests allowed for determination of the change in the stiffness and the fracture energy of the tested materials in conditions of both lowered and increased ambient temperatures (ranging from -25°C up to 50°C). The selected temperature range corresponds to the typical operating conditions of such materials. During the tests in the negative temperature, the crystallisation process was observed for NR material. Additionally, in the case of the NR/SBR blend, a crystallisation of the NR component can be witnessed at low temperatures, which indicates that this blend is characterised by a low miscibility.

The results of the experimental tests served as the basis on which, using the curve-fitting method, the material constants of two commonly used hyperelastic constitutive models – polynomial and Arruda–Boyce – were determined for the presented temperature range. The obtained values were also verified numerically

using the finite element method and the results were compared with the experimental tests. By means of application of the successive response surface method (SRS), the optimisation process of the previously obtained values was carried out. It was found that in most cases the true-strain vs. true-stress curve representing the polynomial model coincides with the average curve obtained from experimental tests, whereas for the Arruda–Boyce material model the discrepancies are greater. The average difference between the values obtained from the Arruda–Boyce model and experimental tests is about 16%, whereas for the polynomial model the difference is about 4%.

In practice, especially in numerical analysis, rubber materials are assumed to be practically incompressible. For this reason, a significant proportion of hyperelastic models are able to correctly predict the behaviour of the material in different deformation states (e.g. tensile, biaxial tension or compression). Therefore, only the tensile test curves were used for curve-fitting and parameter determination. It should be noted, however, that the use of the presented parameters in deformation states other than uniaxial stress may lead to slight inaccuracies.

Such a large database of parameters – covering both a wide range of different materials and taking into account the high variability of thermal conditions – gathered in one place is an extremely large help for all those interested in the most accurate numerical modelling of construction elements made of elastomers.

## 2. MATERIALS AND METHODS

### 2.1. Specimen preparation

In order to conduct the research, commercially available materials were selected, namely SBR and NR, and two additional blends, NR/SBR and CR/NBR. Materials were obtained from the manufacturer in the form of 300 mm × 300 mm and 2 mm thick sheets. Prior to preparing specimens, the hardness of the materials was measured using the Shore A scale at a temperature of 21°C. The values of the hardness are in the range from 61 to 64. Accordingly, all tested materials have a comparable hardness at ambient temperature and can be classified as rather hard rubbers. The exact composition of the tested materials and results of the hardness measurements are presented in Tab. 1.

The dimensions of the samples were determined based on the PN-ISO 37:2007 standard concerning the determination of the tensile properties of rubber (Fig. 1). The water jet cutting technique was used to prepare the test samples. In order to minimise deformation caused by the water jet cutting process, the material sheets were clamped between two steel plates during the cutting operation. Due to the low stiffness exhibited by all the tested materials, it was not feasible to perform machining on their surfaces to enhance their parallelism accuracy. An example of the prepared samples is presented in Fig. 2.

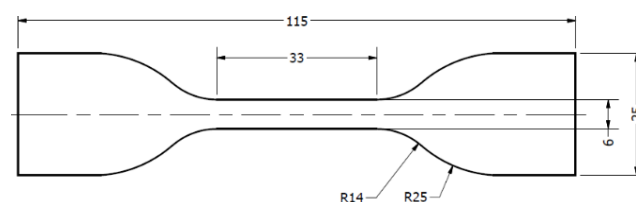


Fig. 1. Dimensions of the test samples according to the PN-ISO 37:2007 standard

Tab. 1. Composition of tested materials

Component (phr)	CR/NBR	NR	SBR	NR/SBR
NR (RSS I)	-	100	-	50
CR (Denka S-40)	50	-	-	-
Acrylonitrile-butadiene rubber (Perbunan 1847)	50	-	-	-
SBR (Ker 1500)	-	-	100	50
Carbon black (N-550)	83.3	40	50	45
Cross-linking complex (sulphur, ZnO and others)	-	20	13.8	19
Cross-linking complex (MgO, ZnO and others)	13.8	-	-	-
Softener (ADO or AN-68*)	27	7*	10*	12
Hardness Shore A (at 21°C)	64	62	61	64

\* AN-68 softener phr, weight parts per 100 parts of rubber.  
CR, chloroprene rubber; NBR, nitrile-butadiene rubber; NR, natural rubber; SBR, styrene-butadiene rubber.

White paint markers were applied on every sample in the measuring part. They were necessary to determine the deformations of the samples during the tensile test using a motion tracking method.

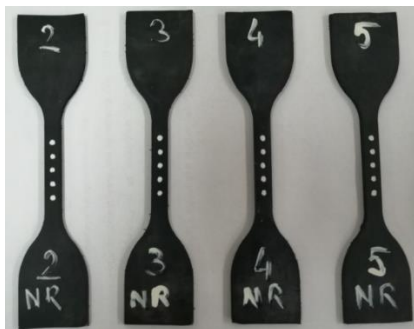


Fig. 2. Example of the test samples. NR, natural rubber

## 2.2. DMA

DMA is one of the most frequently used methods for determining the viscoelastic properties of materials. Generally, in this method, a sinusoidal force (stress) is applied to the sample, which results in a sinusoidal deformation (strain). In case of the viscoelastic materials, the shift in the corresponding stress and strain curves is observed. The phase difference between those curves is called phase angle or phase lag  $\delta$  [24].

From the DMA tests, several viscoelastic terms can be calculated [25]:

$$E' = (\sigma_0 / \varepsilon_0) * \cos \delta \quad (1)$$

$$E'' = (\sigma_0 / \varepsilon_0) * \sin \delta \quad (2)$$

$$\tan \delta = E'' / E' \quad (3)$$

where  $E'$  is the storage (elastic) modulus,  $E''$  is the loss (viscous) modulus,  $\tan \delta$  is an index of viscoelasticity (loss factor),  $\sigma_0$  is the maximum applied stress,  $\varepsilon_0$  is the maximum strain amplitude and

$\delta$  is the phase angle. The storage modulus is a measure of elastic energy stored in the material, the loss modulus measures the energy dissipation during each cycle of the loading and  $\tan \delta$  is a ratio of the two previously mentioned values.

DMA was performed by using TA Instruments' DMA Q800 analyser. Strips in dimensions of 55 mm  $\times$  10 mm  $\times$  3 mm (length  $\times$  width  $\times$  thickness) were used as samples. They were made in the same way as the tensile test specimens, using a water jet cutter. A dual cantilever clamp was used to examine the thermo-mechanical properties. The storage and loss modulus and  $\tan \delta$  were measured at a frequency of 1 Hz over a temperature range of  $-90^\circ\text{C}$  to  $50^\circ\text{C}$  at a heating rate of  $5^\circ\text{C}/\text{min}$ . The amplitude of test sample deformation was established at 20  $\mu\text{m}$ .

## 2.3. DSC

Another commonly used thermal test method is DSC [26]. The main principle of the method is to heat a sample of a known mass and track changes in its heat capacity as changes in the heat flow [27]. Typically, the test sample is enclosed in the pan and mounted inside the furnace on the thermoelectric disk. The empty reference pan is also present [24]. Throughout the test procedure, the temperature inside the furnace is changed at a constant rate, the temperature difference  $\Delta T$  between the samples is measured and recorded, and then the heat flow is determined based on the following expressions [28]:

$$q = \Delta T / R \quad (4)$$

$$q = c_p (dT/dt) + f(T, t) \quad (5)$$

where  $q$  is sample heat flow,  $\Delta T$  is the temperature difference between the samples,  $R$  is the resistance of the thermoelectric disk,  $c_p$  is sample-specific heat capacity,  $dT/dt$  is a heating rate and  $f(T, t)$  is kinetic response at a specific temperature and time.

A DSC Q250 calorimeter from TA Instruments with Refrigerated Cooling System RCS90 was used to perform the DSC analysis. Measurements were carried out in an inert gas atmosphere (nitrogen) at a heating rate of  $10^\circ\text{C}/\text{min}$ , in the range from  $-80^\circ\text{C}$  to  $70^\circ\text{C}$ , using non-hermetic aluminium pans. During the tests, the glass transition temperature was obtained.

## 2.4. Tensile test

In order to perform the tensile tests, an MTS Criterion Model 45 electromechanical universal test system was used. The system is characterised by a maximum displacement range of  $\pm 500$  mm and the maximum piston speed is 750 mm/min. Additionally, the ThermCraft temperature chamber was utilised to perform tests in both negative and positive temperatures.

The tensile test was carried out based on the PN-ISO 37:2007 standard with the speed of the traverse of 50 mm/min. The strain rate during the tests was constant and equal to  $3.3 \cdot 10^{-2} \cdot \text{s}^{-1}$ . The force and the position of the transverse were recorded with 50 Hz frequency. Additionally, the motion tracking method was used in order to determine the strain of the test samples. For this purpose, every test was recorded using a high-resolution camera (1,920  $\times$  1,080 pixels). In the next step, recordings were imported into TEMA software, which allowed for tracking the points painted on the samples and recording their position-change over time.



Recorded coordinates were the basis for calculation of the strain. The stress was calculated as the loading force related to the initial cross-section area of the tested sample. The effect of transverse deformations of the sample during the test was not taken into account.

The samples were tested in the following temperatures:  $-25^{\circ}\text{C}$ ,  $0^{\circ}\text{C}$ ,  $25^{\circ}\text{C}$  and  $50^{\circ}\text{C}$ . Prior to the tests, the samples were placed in the chamber for 1 h in the test temperature. After that, the samples were sequentially mounted in the clamps of the testing system and an additional 15 min was allowed to pass for the samples' settling and temperature-normalisation. The tests were performed when the control system was showing constant, set temperature. Temperature measurements were obtained using two K type thermocouples – one located within the working field of the chamber, and another inserted between two layers of the test material. To obtain the latter, two pieces of the test material were placed in contact, with the thermocouple inserted between them. The tests were carried out once the control system indicated a constant, predetermined temperature. The chamber specifications indicated that the temperature stabilisation accuracy was within  $\pm 1^{\circ}\text{C}$ , whereas the acceptable error range for the K type thermocouples was  $\pm 1.5^{\circ}\text{C}$ .

### 3. RESULTS AND DISCUSSION

#### 3.1. DMA

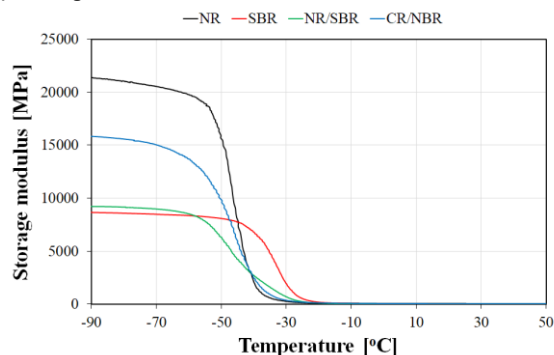
The DMA allowed us to investigate two-component rubber compounds and their interactions. The storage modulus value of the NR in the below- $T_g$  plateau region is considerably higher than for any other considered elastomer and equal to 21,310 MPa, whereas for SBR it is only 8,640 MPa (the lowest value of all considered samples) (Fig. 3a). The addition of the NR to SBR causes a slight increase in its value to 9,215 MPa and considerable widening of the glass transition by approximately 57% (onset at  $-56^{\circ}\text{C}$ , termination at  $-27^{\circ}\text{C}$ ). Additionally, the course of the storage modulus curve in the glass transition temperature is not linear, and a slight change in the slope can be observed at approximately  $-44^{\circ}\text{C}$ . It indicates the two-phase structure of the NR/SBR blend, and thus a low miscibility of the individual components. The glass transition temperature of the NR is equal to  $-51.7^{\circ}\text{C}$ , which is a similar value to that obtained for the CR/NBR blend, whereas in the case of the SBR it is  $-40.7^{\circ}\text{C}$ . The blend of those two components shows a slightly lower  $T_g$  of about  $-56.2^{\circ}\text{C}$ .

Analysing the storage modulus of the CR/NBR blend, we can observe that at  $-90^{\circ}\text{C}$ , its value attains 15,830 MPa and is 71% higher than that corresponding to the NR/SBR blend. The change in stiffness is more pronounced than in the NR/SBR blend. The onset of the glass transition is observed at a relatively low temperature of  $-80^{\circ}\text{C}$ , whereas termination at  $-30^{\circ}\text{C}$ . The glass transition temperature is  $-55.8^{\circ}\text{C}$ .

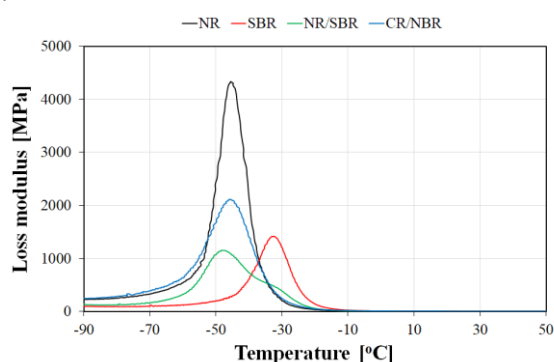
Concerning the cases of the NR, SBR and their blend, we can make the common observation that the peak value of the loss modulus of the NR (4,340 MPa at  $-45.5^{\circ}\text{C}$ ) is considerably higher compared with the corresponding values for other materials, due to its storage modulus having a high value (Fig. 3b). The SBR peak value is equal to 1,420 MPa at  $-32.3^{\circ}\text{C}$ . The NR/SBR blend is characterised by two clearly visible peak values in both loss

modulus and  $\tan \delta$  curves, corresponding to the values of the glass transition temperature of individual NR and SBR rubber. Such behaviour proves that individual components of the blend are rather immiscible.

#### (a) Storage modulus



#### (b) Loss modulus



#### (c) $\tan \delta$

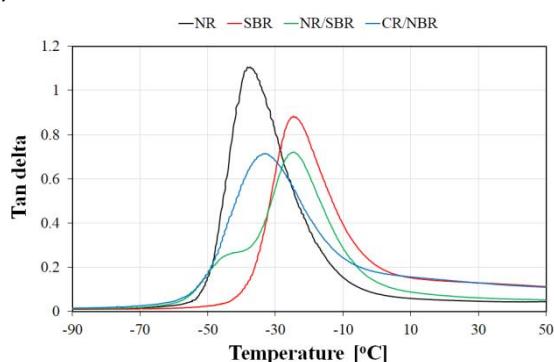


Fig. 3. Values of: a) storage modulus, b) loss modulus and c)  $\tan \delta$  modulus received by DMA. CR, chloroprene rubber; DMA, dynamic mechanical analysis; NBR, nitrile-butadiene rubber; NR, natural rubber; SBR, styrene-butadiene rubber.

In the case of the CR/NBR blend, the loss modulus peak value is equal to 2,115 MPa at a temperature of  $-45.7^{\circ}\text{C}$  (Fig. 3b). Additionally, only one peak is observed, which proves the good miscibility of the blend components. In the case of the  $\tan \delta$ , for the CR/NBR, the maximum value is equal to 0.71 at  $-33.1^{\circ}\text{C}$  (Fig. 3c). Analogically as in the loss modulus curve, only one peak is visible.

The values of the glass transition temperature ( $T_g$ ) of rubber were estimated based on the temperature DMA curves and are presented in Tab. 2.

Tab. 2. The glass transition temperatures of rubbers received by DMA

Glass transition temperature Tg (°C)			
	E'	E''	Tan δ
NR	-51.7	-45.5	-37.4
CR/NBR	-55.8	-45.7	-33.1
SBR	-40.7	-32.3	-24.7
NR/SBR	-56.2	-48.4	-32.7
			-24.5

CR, chloroprene rubber; DMA, dynamic mechanical analysis; NBR, nitrile-butadiene rubber; NR, natural rubber; SBR, styrene-butadiene rubber.

### 3.2. DSC

The thermograms for all considered materials are presented in Fig. 4. The obtained results allow the conclusion that for all samples except NR/SBR, the glass transition process was one-stage. In the case of sample NR/SBR, a two-stage incidence of the glass transition process was observed, due to the presence of two immiscible components with different glass transition temperatures. In the case of the CR/NBR blend, we can observe a single-stage thermal conversion, which can be an indication of the good miscibility of the blend components. The glass transition temperatures obtained by DSC are presented in Tab. 3.

The test results obtained by DSC confirm the results gained based on analysis performed by DMA, and thus the behaviour of CR/NBR and NR/SBR blends.

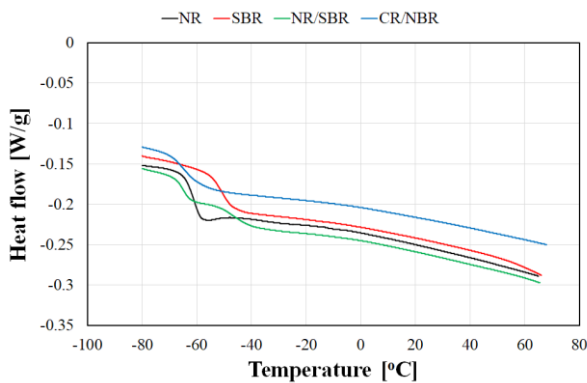


Fig. 4. DSC thermograms for considered rubbers. CR, chloroprene rubber; DSC, differential scanning calorimetry; NBR, nitrile-butadiene rubber; NR, natural rubber; SBR, styrene-butadiene rubber.

Tab. 3. The glass transition temperatures of rubbers received by DSC

Glass transition temperature Tg (°C)			
	T <sub>onset</sub> (°C)	T <sub>midpoint</sub> (°C)	T <sub>end</sub> (°C)
NR	-64.6	-61.4	-58.7
CR/NBR	-69.0	-64.2	-59.3
SBR	-54.5	-50.4	-46.1
NR/SBR	-67.9	-65.2	-62.4
	-51.3	-46.3	-41.4

CR, chloroprene rubber; DSC, differential scanning calorimetry; NBR, nitrile-butadiene rubber; NR, natural rubber; SBR, styrene-butadiene rubber.

### 3.3. Tensile tests

In Fig. 5, an example of the test sample during the tensile test in the elevated temperature is presented.



Fig. 5. Example of the specimen during the tensile test at 50°C

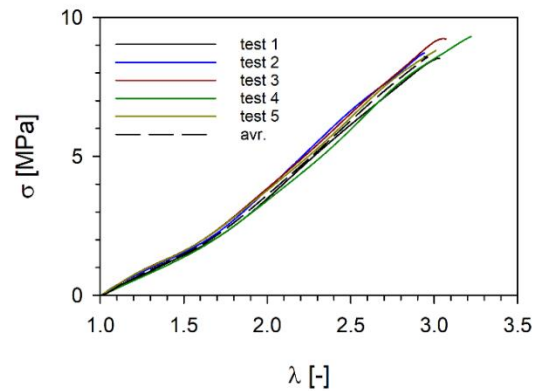
The stress ( $\sigma$ )-extension ratio ( $\lambda$ ) plots for all tested materials at the ambient temperature are presented in Fig. 6. Extension ratio is defined as:

$$\lambda = \varepsilon + 1 \quad (6)$$

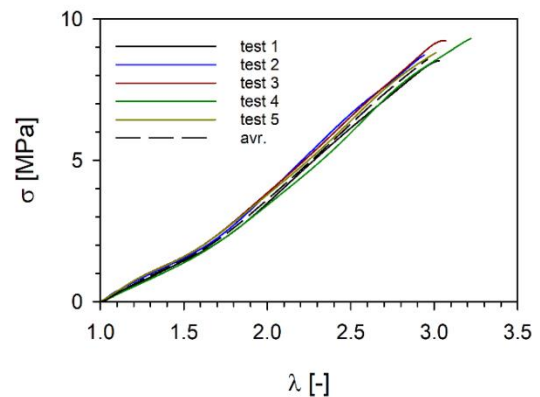
where  $\varepsilon$  is an engineering strain.

It can be observed that all the curves are located in a relatively narrow range in all considered cases. The standard deviation of maximum extension ratio at ambient temperature is 0.16 for CR/NBR, 0.23 for SBR, 0.41 for NR and 0.42 for NR/SBR.

(a) CR/NBR



(b) NR



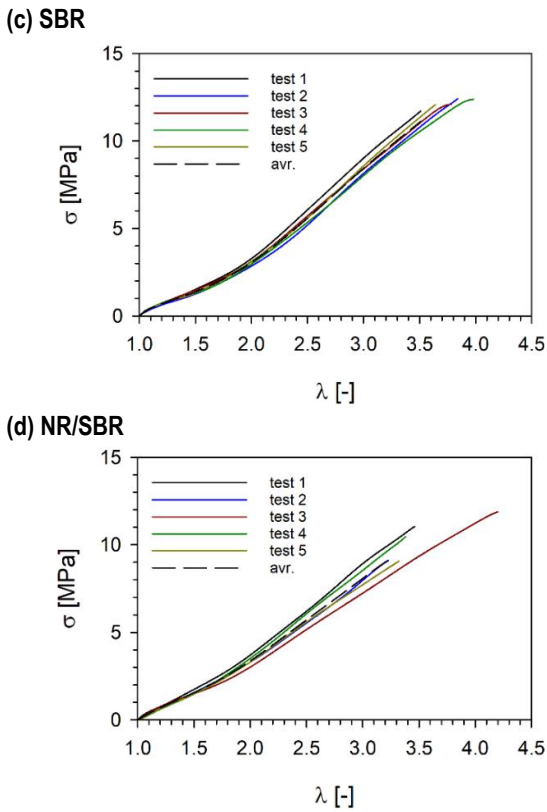


**Fig. 6.** Stress-extension ratio curves for tests at the ambient temperature: (a) CR/NBR, (b) NR, (c) SBR, (d) NR/SBR. CR, chloroprene rubber; NBR, nitrile-butadiene rubber; NR, natural rubber; SBR, styrene-butadiene rubber.

The averaged curves of stress-extension ratio for tests performed in the considered range of temperatures are presented in Fig. 7.

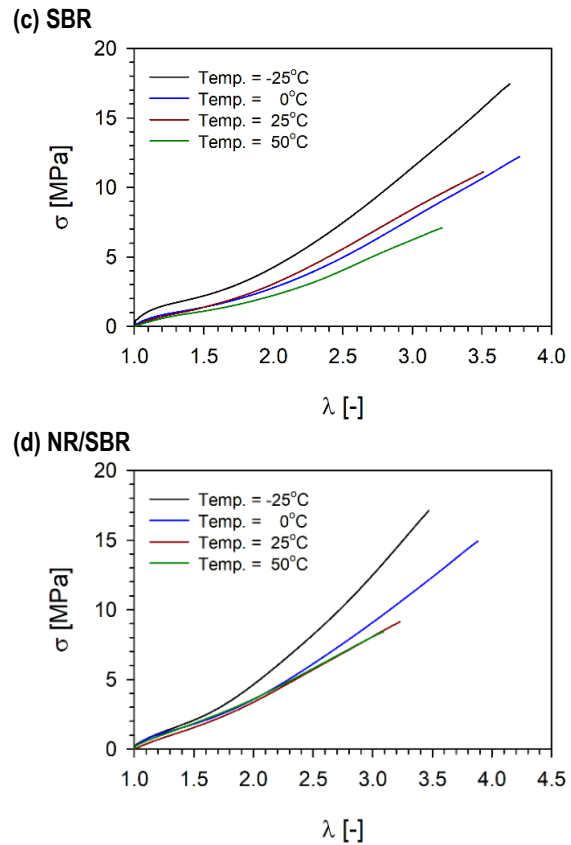
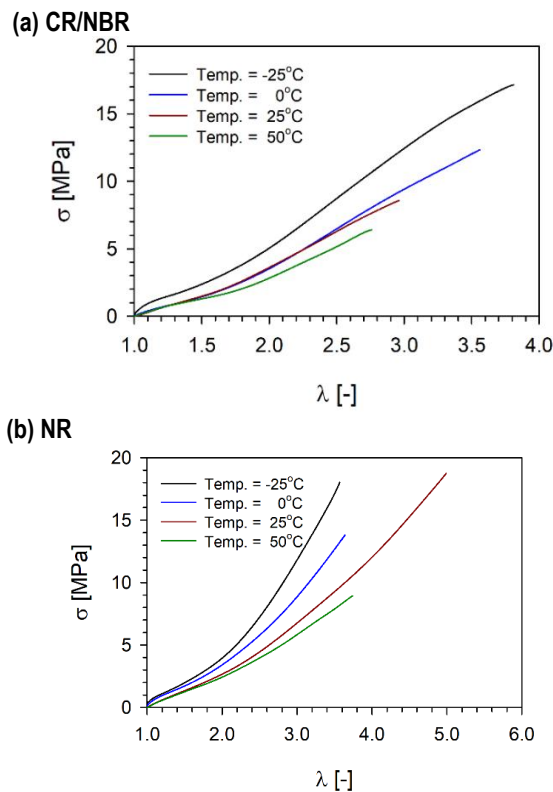


**Fig. 7.** Stress-extension ratio curves for a wide range of temperatures: (a) CR/NBR, (b) NR, (c) SBR, (d) NR/SBR. CR, chloroprene rubber; NBR, nitrile-butadiene rubber; NR, natural rubber; SBR, styrene-butadiene rubber.

In the case of the CR/NBR blend, the stiffness values at 0°C and 25°C are almost identical up to an extension ratio of 2.5 (Fig. 7a). Although both of the blend components are characterised by the upturn in the stress, no such behaviour is observed for the CR/NBR. The mechanical behaviour of the blend can somewhat be visualised as a mixture of the properties of its components, i.e. unlike in the NBR, there is no rapid change in the material stiffness at -25°C, whereas the maximum stress values are lower than those obtained for the CR. For the temperature of 50°C, the maximum stress value was equal to 6.5 MPa, whereas for -25°C it was higher and equal to 17 MPa.

In the case of NR, we can observe that curves for ambient temperature and 50°C coincide to the value of the extension ratio of 1.6, whereas other curves have different slopes (Fig. 7b). Two phenomena related to crystallisation can be observed. The first one is strain-induced crystallisation. High deformations result in a change of molecular orientation of its network, whereas the induced crystallites slow down the crack growth [29]. The second phenomenon is the ability to crystallise in the un-stretched state in the lowered temperatures, the so-called thermally induced crystallisation (TIC). As a previous research showed, the maximal crystallisation rate takes place at approximately -25°C [30]. These two behaviours are especially visible in the stress-extension ratio for -25°C when a rapid change in the slope is observed at  $\lambda = 2.2$ . Analogically as in other considered cases, the lowest value of stress (9 MPa) was obtained at 50°C.

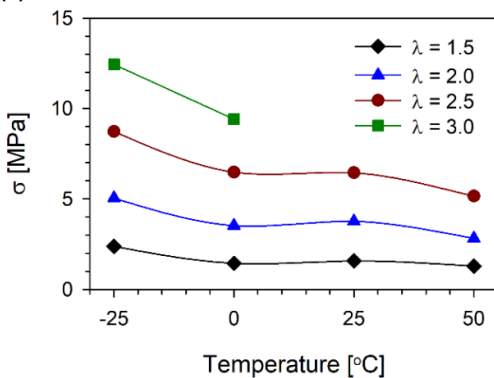
For the SBR material, we can observe that initially the curves in the temperature-range from 0°C to 50°C coincide, but com-

mencing from the extension ratio  $\lambda = 1.5$ , the slope of the 50°C curve changes (Fig. 7c). The curves for 0°C and 25°C continue to coincide until the extension ratio reaches the value of 1.75, but even after that, the value of stress in both cases remains at a very similar level. Analogically as in the case of the NBR, we can observe a change in the stiffness and strength of the SBR at -25°C; however, the maximum stress value is lower and equal to 17.5 MPa. The lowest value of 7 MPa was obtained at 50°C. A slight upturn in the stress is visible in the range from 50°C to 0°C, whereas for -25°C it is significantly more pronounced. As indicated in a previous research, when there is an absence of the crystallisation effect in the SBR rubbers, such behaviour can be explained by the limited extensibility of the network [31].

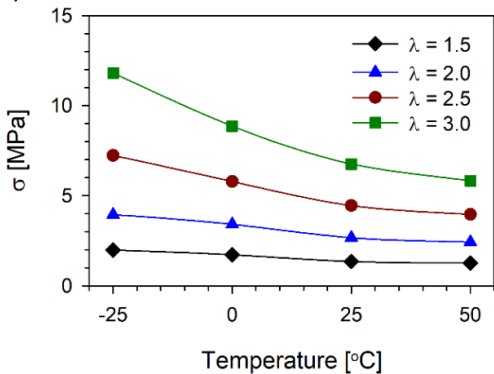
The NR/SBR blend is characterised by a stiffness that is almost identical at both 25°C and 50°C (Fig. 7d). Additionally, the curve for 0°C coincides with the curves for 25°C and 50°C up to an extension ratio of 2.3. The lowest value of the stress was obtained for 50°C (8.5 MPa), but it was only slightly lower than the stress for 25°C (9.2 MPa). The highest value of 17 MPa was obtained for 50°C. Particularly worth noting is the fact that for the temperature range from 0°C to 50°C, the curves have a single-phase nature, without the visible onset of the stress value. For -25°C, the two-stage characteristic is clearly visible. It is caused by the crystallisation process in the NR component of this low-miscible blend, due to the strain and low temperature.

The influence of the temperature on the material samples' stretching process is also presented in Fig. 8. It shows a relationship between the stress and the temperature for selected extension ratio values. The observed variation exhibits almost monotonic behaviour. In the case of CR/NBR and SBR, a deviation from this trend is evident at 25°C, resulting in an increase in stress values. Conversely, the NR/SBR blend demonstrates a slight increment in stress at 50°C.

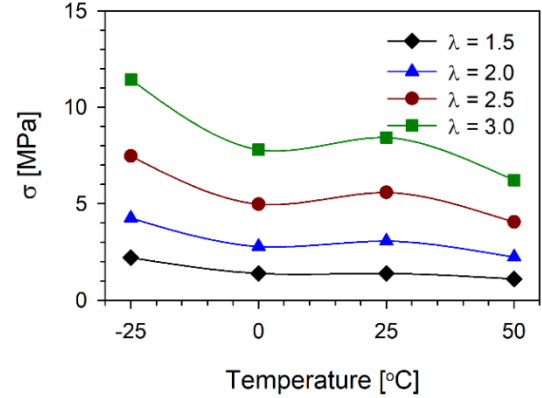
(a) CR/NBR



(b) NR



(c) SBR



(d) NR/SBR

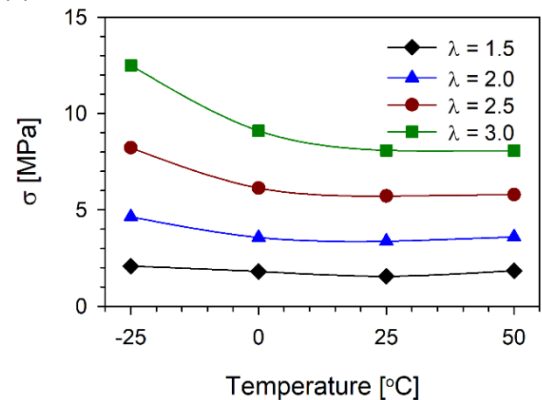


Fig. 8. The stress-temperature curve for different values of extension ratio: (a) CR/NBR, (b) NR, (c) SBR, (d) NR/SBR. CR, chloroprene rubber; NBR, nitrile-butadiene rubber; NR, natural rubber; SBR, styrene-butadiene rubber.

The change in fracture energy  $W_f$  is presented in Fig. 9. The fracture energy is calculated as the area below the stress-strain curve. For a given temperature and for a particular material, stress-strain curves obtained from the tensile test of multiple samples were consolidated into a single curve. Subsequently, the area beneath the consolidated curve was determined via a numerical integral algorithm and Excel. It can be observed that the decrease in its value is steady in the whole temperature range. Only in the case of the NR/SBR blend is a rapid decrease observed in the 0–25°C area.

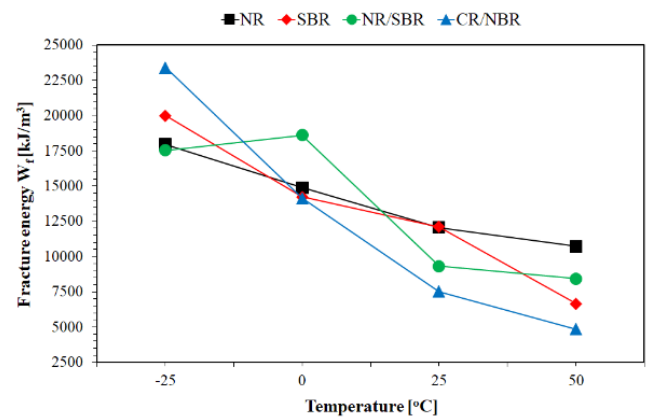


Fig. 9. Fracture energy at various temperatures. CR, chloroprene rubber; NR, natural rubber; NBR, nitrile-butadiene rubber; SBR, styrene-butadiene rubber



In order to better understand the tensile test method results, a so-called Mooney–Rivlin plot can be used [32]. The basis of this plot is the Mooney–Rivlin equation [33,34]:

$$\sigma = 2 \left( C_1 + \frac{C_2}{\lambda} \right) \left( \lambda - \frac{1}{\lambda^2} \right) \quad (7)$$

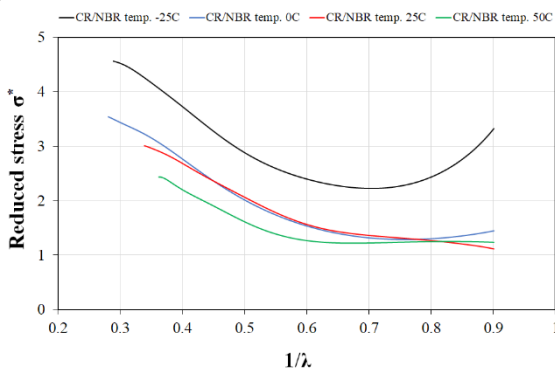
where  $C_1$  and  $C_2$  are material constants and  $\lambda$  is the extension ratio. These constants are associated with the intermolecular forces between the polymer chains and  $C_1$  is related to the crosslink density for elastomers without fillers [35]. Eq. (6) can be rewritten using the term of reduced stress  $\sigma^*$  [32]:

$$\sigma^* = \frac{\sigma}{\lambda - \frac{1}{\lambda^2}} \quad (8)$$

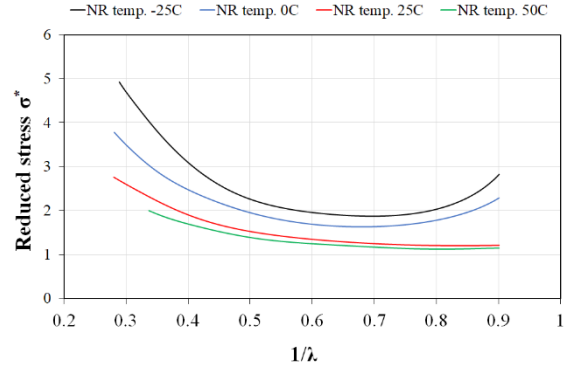
The Mooney–Rivlin plots were constructed by plotting the reduced stress  $\sigma^*$  against the inverse extension ratio  $1/\lambda$  and are presented in Fig. 10. Three regions of strain can be distinguished on the plots: low strain ( $1/\lambda > 0.8$ ), intermediate strain and high strain (generally  $1/\lambda < 0.4$ , but the border value may vary from material to material). Generally, at low strain, the reduced stress decreases up to a certain value, after which it starts to grow, which is associated with the limited chain extensibility between crosslinks (in the non-crystallisable rubbers) and strain-induced crystallisation [36]. Analysing those plots, we can clearly observe that practically in every considered case, the material is characterised by a linear curve in the intermediate strain range at 25°C and above. The only exception is CR/NBR blend, where such behaviour is observed only at 50°C. In the high strain, an upturn is visible in every material at every considered temperature. In the case of NR, the upturn is caused mainly by strain crystallisation. In the case of the non-crystallisable rubbers, the extensibility is reduced due to the presence of the filler (i.e. carbon black). As a result of the interactions between the rubber chains and the filler particles, a bound rubber is formed. The ‘tightly bounded rubber’ and ‘loosely bounded rubber’ can be distinguished. The tightly bounded rubber is characterised by low elasticity and high strength [37]. Additionally, some rubber chains are trapped in the filler aggregates and act as part of the filler, thus effectively increasing the volume of the filler and the high strain modulus [38]. In all cases, the reduced stress value increases with the temperature decrease.

In Fig. 11, the upturn strain values are presented. The upturn strain was defined as the strain corresponding to the minimum reduced stress. It is worth noting that in all considered materials, a rapid decrease in the upturn strain at 25°C is observed. At 50°C the value increases again.

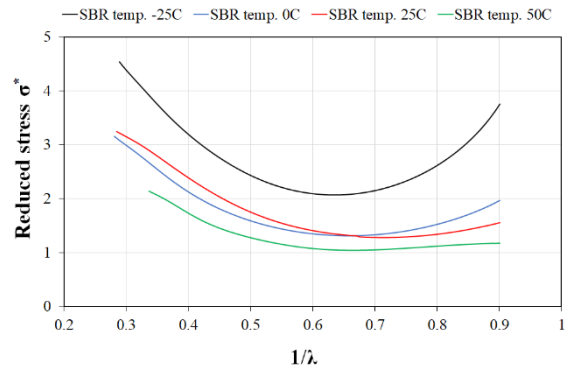
(a) CR/NBR



(b) NR



(c) SBR



(d) NR/SBR

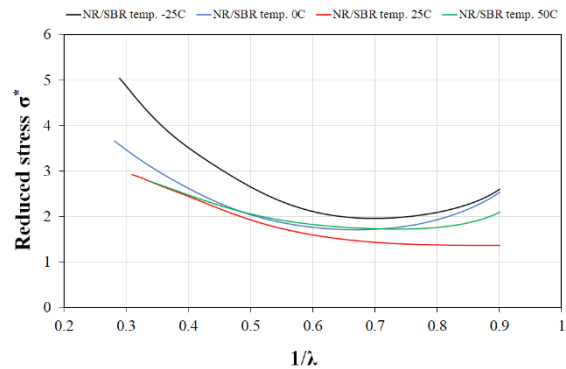


Fig. 10. Mooney–Rivlin plots for the considered materials: (a) CR/NBR, (b) NR, (c) SBR, (d) NR/SBR. CR, chloroprene rubber; NBR, nitrile-butadiene rubber; NR, natural rubber; SBR, styrene-butadiene rubber.

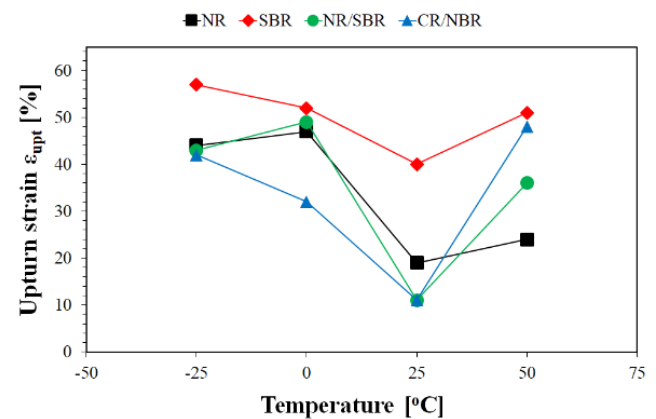


Fig. 11. Values of upturn strain at various temperatures. CR, chloroprene rubber; NBR, nitrile-butadiene rubber; NR, natural rubber; SBR, styrene-butadiene rubber

Similar effects are also seen in Fig. 12. Stress-extension ratio curves for 0°C and 25°C temperatures are presented for all tested materials. It can be observed that in the case of 25°C, all curves are located in a relatively narrow range. Additionally, the extension ratios of all materials in the ambient temperature are practically equal ( $\lambda = 3$ ), except the NR material, which is characterised by the highest extension ratio ( $\lambda = 5$ ).

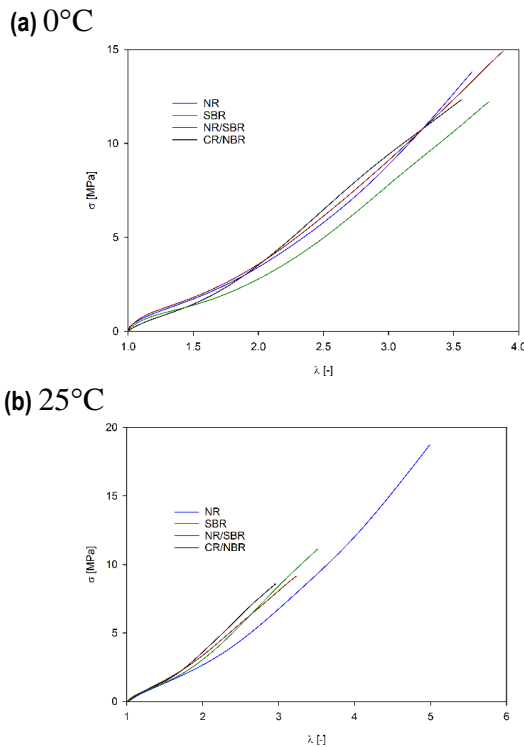


Fig. 12. Stress-extension ratio curves for (a) 0°C and (b) 25°C temperatures. CR, chloroprene rubber; NBR, nitrile-butadiene rubber; NR, natural rubber; SBR, natural rubber.

#### 4. NUMERICAL MODELLING

##### 4.1. Hyperelastic constitutive models

The behaviour of hyperelastic material, which is frequently assumed to be incompressible, is usually described through of the Cauchy stress tensor [39]:

$$\tilde{\sigma} = -p\tilde{I} + 2\left(\frac{\partial W}{\partial I_1} + I_1 \frac{\partial W}{\partial I_2}\right)\tilde{B} - 2\frac{\partial W}{\partial I_2}\tilde{B}^2 \quad (9)$$

where  $p$  is pressure,  $\tilde{B} = FF^T$  is the left Cauchy–Green tensor,  $F$  is a deformation gradient tensor,  $I_i$  ( $i = 1, 2, 3$ ) are strain invariants,  $W$  is a strain-energy function dependent on strain invariants  $W(I_1, I_2, I_3)$  and  $\tilde{I}$  is an identity tensor.

The left Cauchy–Green tensor is defined as:

$$\tilde{B} = FF^T \quad (10)$$

where  $F$  is the deformation gradient tensor.

The assumption of rubber incompressibility also limits the number of variables on which strain-energy functions depend ( $I_3 = 1$ , to  $W(I_1, I_2)$ ).

Strain-energy functions should allow reflecting the behaviour of hyperelastic material, including dependence on symmetry, thermodynamic, energetic and entropic considerations in the whole range of extension ratio variability. Functions should also meet certain conditions [40]:

- energy vanishes in the undeformed configuration:

$$W|_{I_1=3} = 0 \quad (11)$$

- strain-energy functions and stress tend to infinity at very large deformation:

$$\lim_{\lambda_i \rightarrow 0} W = +\infty, \lim_{\lambda_i \rightarrow 0} \frac{\partial W}{\partial \lambda_i} = -\infty, \quad (12)$$

$$\lim_{\lambda_i \rightarrow +\infty} W = +\infty, \lim_{\lambda_i \rightarrow +\infty} \frac{\partial W}{\partial \lambda_i} = +\infty, \quad (13)$$

- stress is equal to 0 in the undeformed configuration and strain-energy functions achieve a minimum:

$$\left. \frac{\partial W}{\partial \lambda_i} \right|_{\lambda_1=\lambda_2=\lambda_3=1} = 0,$$

$$\left. \frac{\partial^2 W}{\partial \lambda_i^2} \right|_{\lambda_1=\lambda_2=\lambda_3=1} > 0, \quad (14)$$

$$\det[H_{ij}] > 0,$$

where  $H_{ij}$  is a Hessian matrix and  $i, j = 1, 2, 3$  and  $\lambda_i$  is the principal stretch ratio.

Numerous articles are devoted to the problems associated with the definition of strain-energy functions. These articles present a phenomenological approach [39, 40], a theoretical approach using statistical mechanics of molecular chains network [41, 42] or a mixed approach.

Based on the kinetic theory of elasticity developed by Wall, Treloar defined the simplest form of strain-energy functions, commonly known as the neo-Hookean model [43]:

$$W = \frac{\mu}{2}(I_1 - 3) \quad (15)$$

where  $\mu$  is the shear modulus.

The value of the shear modulus is related to the temperature and chain density dependence [43]:

$$\mu = nkT \quad (16)$$

where  $k$  is the Boltzmann constant,  $T$  is temperature and  $n$  is chain density.

Arruda and Boyce [42], using a phenomenological approach, developed a model with other material constants dependent on temperature assuming their linear temperature dependence:

$$\lambda_{chain} = \sqrt{\frac{I_1}{3}} \quad (17)$$

$$\beta = L^{-1}\left(\frac{\lambda_{chain}}{\sqrt{n}}\right) \quad (18)$$

$$W = NkT\sqrt{n}\left[\beta\lambda_{chain} - \sqrt{n}\ln\left(\frac{\sinh\beta}{\beta}\right)\right] \quad (19)$$

where  $n$  is the number of chain segments,  $T$  is temperature,  $k$  is the Boltzmann constant,  $N$  is the number of chains in the network

of a cross-linked polymer,  $I_1$  is the first invariant of the left Cauchy–Green strain tensor and  $L^{-1}$  is the inverse Langevin function.

The Arruda–Boyce model can be expressed also in the following form, which is often implemented in the finite element method software [40]:

$$\begin{aligned}
 W = G & \left[ \frac{1}{2} (\bar{I}_1 - 3) + \frac{1}{20N} (\bar{I}_1^2 - 9) \right. \\
 & + \frac{11}{1050N^2} (\bar{I}_1^3 - 27) \\
 & + \frac{19}{7000N^3} (\bar{I}_1^4 - 81) \\
 & + \left. \frac{519}{673750N^4} (\bar{I}_1^5 - 243) \right] \\
 & + \frac{K}{2} (J - 1)^2
 \end{aligned} \quad (20)$$

where  $G$  is the shear modulus,  $N$  is the number of statistical links,  $J$  is relative volume and  $K$  is the bulk modulus.

This model also showed that the adopted model successfully reflects the behaviour of tire rubbers even at relatively high temperatures and under a moderate finite deformation.

The polynomial model was discussed in the study of Rivlin and Saunders [45] as the strain-energy function:

$$W = \sum_{p,q=0}^N C_{pq} (I_1 - 3)^p (I_2 - 3)^q \quad (21)$$

with  $C_{00} = 0$ , which is a generalisation of the Mooney–Rivlin and neo-Hookean strain-energy functions.

Note that the invariant based formulation is valid for isotropic materials. However, rubber-like materials are often isotropic, and thus this approach is valid.

## 4.2. Material model parameters identification

In the first stage of preparation of the numerical model of the studied phenomenon, it was necessary to properly determine the

**Tab. 4.** Polynomial model constants obtained through curve-fitting technique

	Temp. (°C)	$C_{10}$ (MPa)	$C_{01}$ (MPa)	$C_{11}$ (MPa)	$C_{20}$ (MPa)	$C_{02}$ (MPa)	$C_{30}$ (MPa)
CR/NBR	50	0.53698	0.01331	0.00007	0.07965	0.00058	0.00002
	25	0.66766	0.00002	0.06605	0.05914	0.00034	0.00001
	0	0.52132	0.00905	0.24118	0.00868	0.00006	0.00000
	–25	0.53088	0.00810	0.01617	0.04099	0.79866	0.00017
NR	50	0.70485	0.00042	0.00002	0.01733	0.00043	0.00070
	25	1.06824	0.00000	0.00088	0.01164	0.00003	0.00083
	0	1.16694	0.00046	0.00047	0.00803	0.01057	0.00231
	–25	0.92199	0.00995	0.00013	0.07905	0.00002	0.00244
SBR	50	0.50133	0.01044	0.02173	0.04461	0.00002	0.00020
	25	1.16859	0.01050	0.01124	0.00014	0.00000	0.00161
	0	0.25955	0.01184	0.17839	0.04629	0.00006	0.00088
	–25	1.12534	0.00126	0.03109	0.04438	0.00001	0.00200
NR/SBR	50	0.82210	0.00085	0.02343	0.04706	0.00391	0.00001
	25	1.08278	0.00058	0.00000	0.02202	0.00058	0.00000
	0	1.17437	0.00013	0.01408	0.00726	0.00055	0.00214
	–25	0.92199	0.00995	0.00013	0.07905	0.00002	0.00244

CR, chloroprene rubber; NBR, nitrile-butadiene rubber; NR, natural rubber; SBR, styrene-butadiene rubber.

material constants of the constitutive model, which can correctly describe the behaviour of the hyperelastic material. After reviewing the available models, two models that are commonly used in various types of analyses involving the use of the finite element method were selected, namely the polynomial and Arruda–Boyce models. To determine the values of both constitutive models, the curve-fitting technique was used. The principle underlying this method is the determination of the function describing the series of data in relation to which analyses are required – in this case, the strain and stress values obtained during the experimental tests – in the best possible way, concomitant with taking into account any predefined constraints.

In the case of the model described by Eq. (27), the values of all material constants ( $C_{10}$ ,  $C_{01}$ ,  $C_{11}$ ,  $C_{20}$ ,  $C_{02}$  and  $C_{30}$ ) were determined, with the proviso that all values must be greater than 0. Such a limitation was adopted because negative values of the constants, despite potentially very good curve fitting, may lead to instability during numerical analyses [46]. The determined constant values are presented in Tab. 4.

The Arruda–Boyce material model requires a much smaller number of constants. In practice only two, in addition to density and bulk modulus, are needed: the shear modulus ( $G$ ) and the number of statistical links ( $N$ ). The constraint was that both values should be greater than 0 and we assumed that the number of statistical links should be an integer. The values determined for this constitutive model are presented in Tab. 5.

After determining all the necessary constants, a finite element method numerical model was constructed, which allowed for the numerical validation of the material model constants' correctness and evaluation of the difference in the stress values between the experimental tests and numerical analyses. A geometrical model of the used tensile sample was created, which was then discretised using fully integrated solid elements. In order to replicate the real test, the application of the loading and boundary conditions is made as similar as possible to that relevant to the actual tensile experiment. Since the study is static, it was decided to use the implicit scheme of integrating the equations of motion implemented in the LS-Dyna solver.

**Tab. 5.** Arruda–Boyce constitutive material model constants obtained through curve-fitting technique

	Temp. (°C)	N (-)	G (MPa)
NR	50	7	1.33213
	25	12	1.92605
	0	6	1.66705
	-25	5	1.86775
CR/NBR	50	3	1.03194
	25	4	1.53908
	0	6	1.93717
	-25	9	2.90620
SBR	50	4	1.02686
	25	6	1.62532
	0	6	1.55613
	-25	6	2.18831
NR/SBR	50	5	1.58015
	25	5	1.61376
	0	7	1.99259
	-25	5	2.1981

CR, chlorprene rubber; NBR, nitrile-butadiene rubber; NR, natural rubber; SBR, styrene-butadiene rubber.

In total, a mesh of 6,080 elements is used for the analyses. The prepared numerical model is presented in Fig. 13. The constitutive model parameters are presented in Tabs. 4 and 5. The value of Poisson ratio was constant for every tested material and equal to 0.495.

The obtained results and comparison between the considered constitutive models are presented in Figs. 14a–d. To facilitate a comparison between the outcomes of the experimental tests and

numerical analyses, the engineering values were transformed into true values by utilising the following set of formulae:

$$\epsilon_{true} = \ln(1 + \epsilon_{eng}) \quad (22)$$

$$\sigma_{true} = \sigma_{eng} * e^{\epsilon_{true}} = \sigma_{eng} * (1 + \epsilon_{eng}) \quad (23)$$

where  $\epsilon_{true}$  represents true strain,  $\epsilon_{eng}$  engineering strain,  $\sigma_{true}$  true stress,  $\sigma_{eng}$  engineering stress and  $e$  Euler's number.

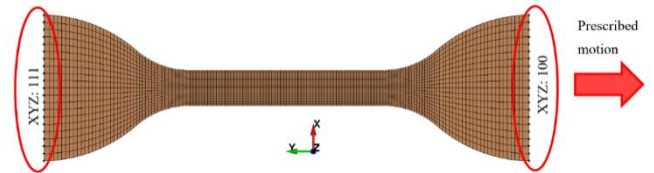
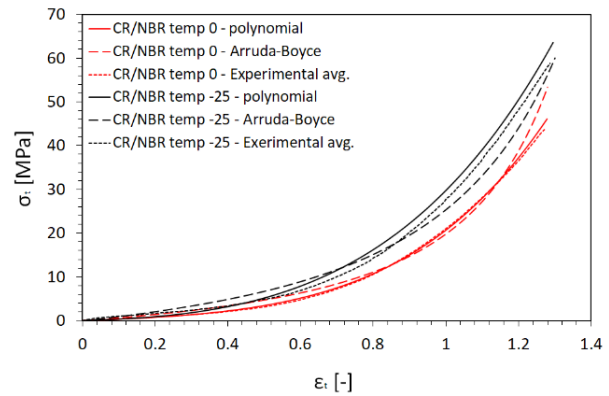
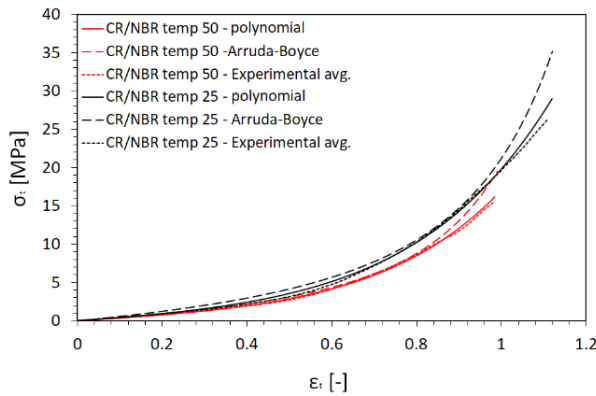


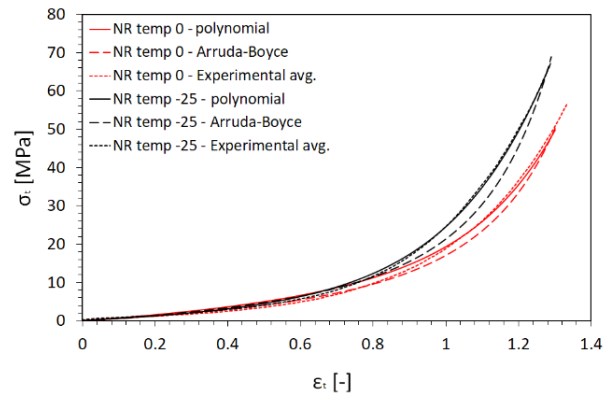
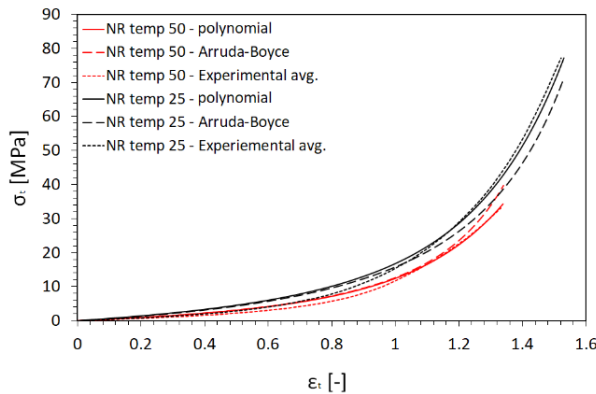
**Fig. 13.** Numerical model of the test sample with visible boundary conditions

When analysing the graphs in fig. 14, we can observe a high degree of agreement among the true-strain vs. true-stress curves representative of both constitutive models in the entire temperature range. Comparing them qualitatively, we can see that in most cases the curve representing the polynomial model coincides with the average curve obtained from the experimental test. The quantitative comparison of the obtained values of maximum true stress is presented in Tab. 6. Additionally, the difference between the experimental and numerical results is presented for both constitutive models. The average difference between the values obtained from the Arruda–Boyce model and experimental tests is about 16%, which is four times greater than from the polynomial model, where the difference is about 4%.

**(a) CR/NBR**



**(b) NR**



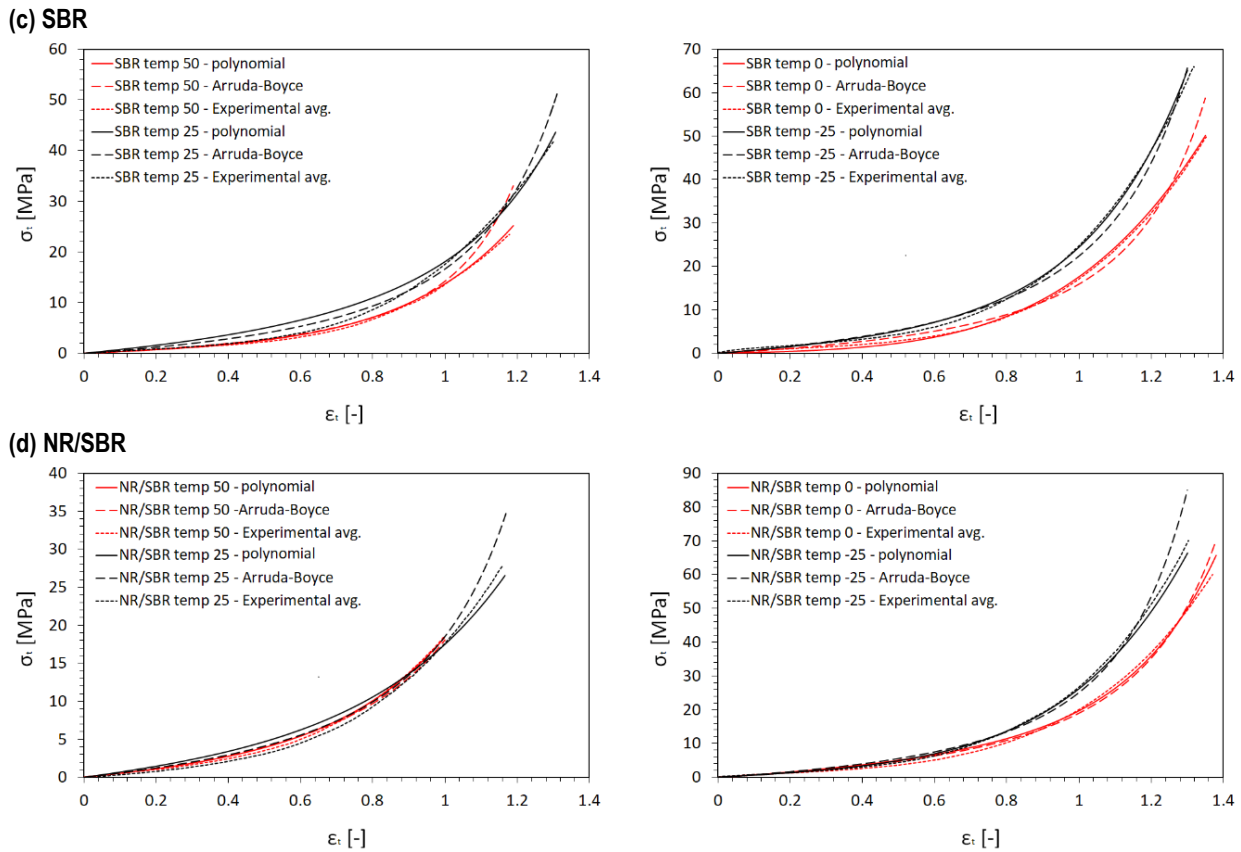


**Fig. 14.** True-strain vs. true-stress curves for polynomial and Arruda–Boyce material models in comparison with experimental results: a) CR/NBR, b) NR, c) SBR, d) NR/SBR. CR, chloroprene rubber; NBR, nitrile-butadiene rubber; NR, natural rubber; SBR, styrene-butadiene rubber.

**Tab. 6.** True stress obtained for constant true strain in every considered case

		True stress (MPa)				
		Exp. avg.	Polynomial	Arruda–Boyce	Polynomial diff. (%)	Arruda–Boyce diff. (%)
CR/NBR	50°C	15.42	16.15	19.55	4.73	26.78
	25°C	26.37	29.00	35.21	9.97	33.52
	0°C	43.69	46.08	53.40	5.47	22.22
	–25°C	58.85	63.57	60.06	8.02	2.06
NR	50°C	33.14	34.34	39.79	3.62	20.07
	25°C	77.08	77.18	71.06	0.13	7.81
	0°C	56.55	49.85	50.19	11.85	11.25
	–25°C	67.07	67.16	68.84	0.13	2.64
SBR	50°C	23.46	25.17	33.06	7.29	40.92
	25°C	41.77	43.97	51.16	5.27	22.48
	0°C	49.71	50.14	58.78	0.87	18.25
	–25°C	65.95	65.13	65.64	1.24	0.47
NR/SRB	50°C	18.56	18.33	18.05	1.24	2.75
	25°C	27.89	26.54	34.67	4.84	24.31
	0°C	59.96	65.66	69.93	9.51	16.63
	–25°C	70.08	66.39	85.04	5.27	21.35

### 4.3. Material model parameters calibration

The material model constants determined above served as a starting point for the optimisation process using the SRSM implemented in the LS-OPT software. SRSM is based on the response surface methodology (RSM), which is a statistical method for constructing approximations to the objective function in

the multi-dimensional parameter space. In this approach, a design space is defined, and variable sets are selected within it:

$$G = \frac{1}{K} \sum_{i=1}^K [F_{exp}(\epsilon_i) - F_{num}(\epsilon_i)]^2 \quad (24)$$

where G is an objective function and K is the number of sampling points.

In the optimisation process, both variables and constraints were normalised, following the classical, commonly used approach:

– variable:

$$\gamma_i = \frac{x_i - x_{i\min}}{x_{i\max} - x_{i\min}}; i = 1, 2, \dots \quad (25)$$

– constraints:

$$1 \geq \frac{g_j}{L_{\max}}; j = 1, 2, \dots \quad (26)$$

$$0 \leq g_j; j = 1, 2, \dots \quad (27)$$

The dynamic leapfrog method for constrained minimisation was used to solve the optimisation problem [47].

A series of finite element method analyses are performed for the variable combinations, the model response is calculated and polynomial functions are fitted to the previously selected variables [48]. In the SRSM, a sub-region is defined in the design space and the optimum is determined on the approximated response surface. In the subsequent step, a new region is defined in such a way that its centre is located on the previous successive optimum and its size is reduced [49].

The parameters obtained through optimisation process for both polynomial and Arruda–Boyce material models are presented in Tabs. 7 and 8.

The comparison between the true-strain and true-stress curves is depicted in Fig. 15. A significant degree of agreement is observed between the curves for the post-calibration models and the experimental curve. The polynomial model shows better

agreement with the experimental data at higher true-strain values, particularly above the value of 1.2. However, despite the calibration process, the Arruda–Boyce model exhibits an overestimation of the true-stress values and an underestimation of the true-strain values for large strain values.

Tab. 7. Optimised material parameters for Arruda–Boyce constitutive model

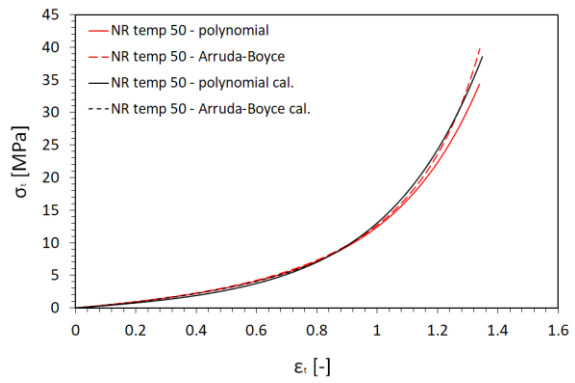
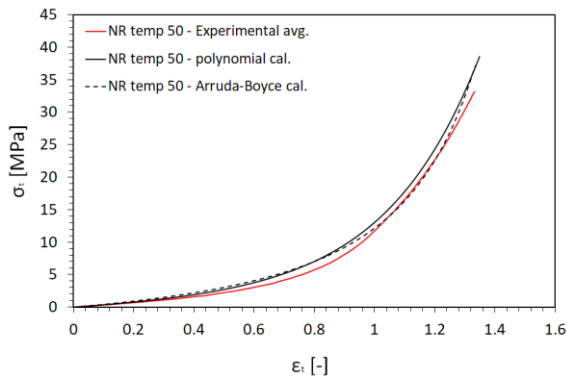
	Temp.(°C)	N (-)	G (MPa)
NR	50	7	1.27683
	25	6	1.38102
	0	5	1.50824
	-25	4	1.50441
CR/NBR	50	4	1.23285
	25	5	1.51941
	0	5	1.68370
	-25	5	1.87934
SBR	50	6	1.18632
	25	6	1.56921
	0	6	1.44424
	-25	5	1.67927
NR/SBR	50	6	1.58506
	25	5	1.46674
	0	4	1.49668
	-25	4	1.46575

CR, chloroprene rubber; NBR, nitrile-butadiene rubber; NR, natural rubber; SBR, styrene-butadiene rubber.

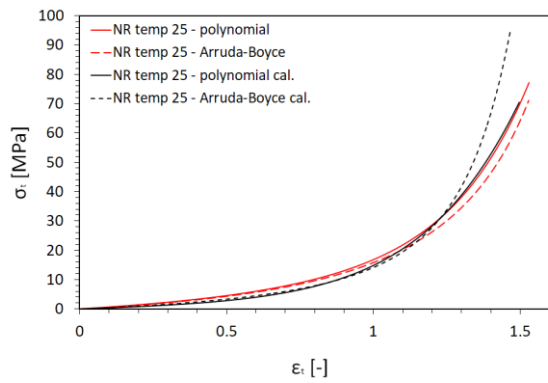
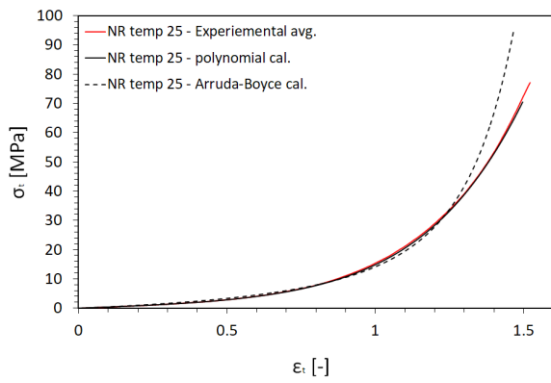
Tab. 8. Optimised material parameters for polynomial constitutive material model

	Temp. (°C)	C <sub>10</sub> (MPa)	C <sub>01</sub> (MPa)	C <sub>11</sub> (MPa)	C <sub>20</sub> (MPa)	C <sub>02</sub> (MPa)	C <sub>30</sub> (MPa)
CR/NBR	50	0.11474	0.00001	0.37600	0.10684	0.04652	0.00024
	25	0.06402	0.31676	0.39453	0.10772	0.01939	0.00000
	0	0.00563	0.03458	0.36411	0.30683	0.00288	0.00000
	-25	0.04090	0.36302	0.62358	0.10171	0.04711	0.00000
NR	50	0.06811	0.04967	0.50681	0.00408	0.03136	0.00050
	25	0.18600	0.01373	0.42619	0.05592	0.03299	0.00055
	0	0.08466	0.02086	0.55986	0.09241	0.02707	0.00202
	-25	0.11986	0.04841	0.52687	0.02299	0.08504	0.00406
SBR	50	0.02147	0.00000	0.37557	0.05590	0.04300	0.00023
	25	0.02460	0.04584	0.43551	0.10649	0.04947	0.00000
	0	0.07404	0.01176	0.44553	0.04083	0.05496	0.00103
	-25	0.20000	0.00000	0.56579	0.09205	0.07829	0.00072
NR/SBR	50	0.04796	0.03702	0.60932	0.15244	0.00246	0.00000
	25	0.02381	0.05043	0.53841	0.18494	0.00000	0.00000
	0	0.11481	0.08666	0.56767	0.01504	0.06928	0.00000
	-25	0.19999	0.05387	0.52350	0.14427	0.07685	0.00051

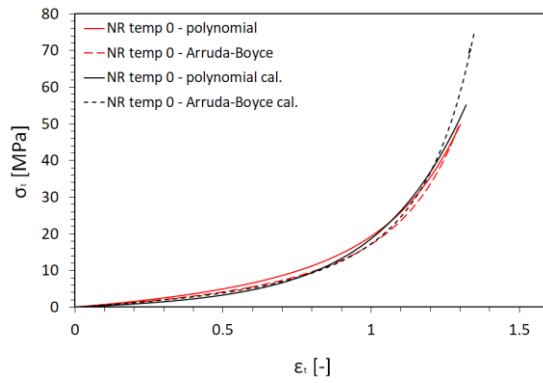
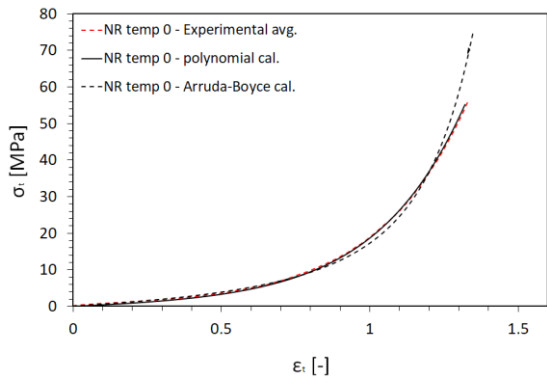
(a) NR 50 °C



(b) NR 25 °C



(c) NR 0 °C



(d) NR -25 °C

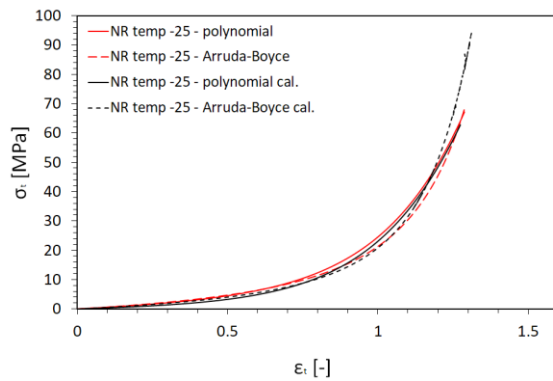
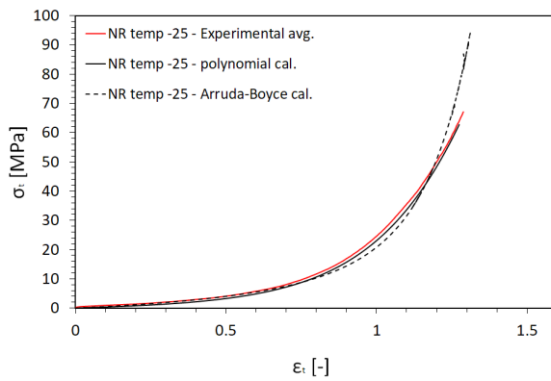


Fig. 15. Comparison of true-strain vs. true-stress curves for calibrated and non-calibrated polynomial and Arruda–Boyce models parameters for NR at temperatures: a) 50°C, b) 25°C, c) 0°C and d) -25°C. NR, natural rubber.



## 5. CONCLUSION

In conclusion, we report the change in the thermal and mechanical properties of several hyperelastic materials tested in the temperature ranging from  $-25^{\circ}\text{C}$  up to  $50^{\circ}\text{C}$ . The results of the experimental tests show a significant change in the materials' behaviour, especially in the lowered temperatures.

Such changes in the properties of hyperelastic materials clearly shows that, in order to perform a correct numerical analysis of components prepared with the use of these materials, a wide range of the material parameters is necessary. There are a number of a constitutive material models that can be used to describe the behaviour of rubber-like materials; however, we have focused on the two most commonly used: the Arruda–Boyce and polynomial models. A combination of the experimental tests and the finite element method, along with the curve fitting, allowed for the determination of a set of material constants for both models for the whole considered temperature range. The performed analyses showed that for true-strain values above 1, the hyperelastic polynomial model provides a better representation of the material behaviour than the Arruda–Boyce model.

We believe that the determined parameters would be a great help for anybody interested in numerical simulations of the components made from rubber-like materials.

## REFERENCES

- Li X, Dong Y, Li Z, Xia Y. Experimental study on the temperature dependence of hyperelastic behavior of tire rubbers under moderate finite deformation. *Rubber Chem Technol.* 2011 Jun 1;84(2):215–28.
- Gordon M. *The Physics of Rubber Elasticity (Third Edition)*. L. R. G. Treloar, Clarendon Press, Oxford. 1975 pp. xii + 370. *Br Polym J.* 1976 Mar;8(1):39–39.
- Bell CLM, Stinson D, Thomas AG. Measurement of Tensile Strength of Natural Rubber Vulcanizates at Elevated Temperature. *Rubber Chem Technol.* 1982 Mar 1;55(1):66–75.
- Stevenson A. The influence of low-temperature crystallization on the tensile elastic modulus of natural rubber. *J Polym Sci Polym Phys Ed.* 1983 Apr;21(4):553–72.
- D20 Committee. Test Method for Brittleness Temperature of Plastics and Elastomers by Impact [Internet]. ASTM International; [cited 2023 May 29]. <http://www.astm.org/cgi-bin/resolver.cgi?D746-20>
- Hussein M. Effects of strain rate and temperature on the mechanical behavior of carbon black reinforced elastomers based on butyl rubber and high molecular weight polyethylene. *Results Phys.* 2018 Jun;9:511–7.
- Barlow C, Jayasuriya S, Suan Tan C. *The World Rubber Industry* [Internet]. 0 ed. Routledge; 2014 [cited 2023 May 29]. <https://www.taylorfrancis.com/books/9781317829133>
- McKeen LW. Elastomers and Rubbers. In: *The Effect of UV Light and Weather on Plastics and Elastomers* [Internet]. Elsevier; 2019 [cited 2023 May 29]. p. 279–359. <https://linkinghub.elsevier.com/retrieve/pii/B9780128164570000101>
- Ramesan MT, Anil Kumar T. Preparation And Properties Of Different Functional Group Containing Styrene Butadiene Rubber. *J Chil Chem Soc* [Internet]. 2009 [cited 2023 May 29];54(1). [http://www.scielo.cl/scielo.php?script=sci\\_arttext&pid=S0717-97072009000100006&lng=en&nrm=iso&tlng=en](http://www.scielo.cl/scielo.php?script=sci_arttext&pid=S0717-97072009000100006&lng=en&nrm=iso&tlng=en)
- Chandrasekaran VC. Rubbers, Chemicals and Compounding for 'O' Rings and Seals. In: *Rubber Seals for Fluid and Hydraulic Systems* [Internet]. Elsevier; 2010 [cited 2023 May 29]. p. 57–69. <https://linkinghub.elsevier.com/retrieve/pii/B9780815520757100061>
- Guo L, Huang G, Zheng J, Li G. Thermal oxidative degradation of styrene-butadiene rubber (SBR) studied by 2D correlation analysis and kinetic analysis. *J Therm Anal Calorim.* 2014 Jan;115(1):647–57.
- Kurian T, Mathew NM. Natural Rubber: Production, Properties and Applications. In: Kalia S, Avérous L, editors. *Biopolymers* [Internet]. Hoboken, NJ, USA: John Wiley & Sons, Inc.; 2011 [cited 2023 May 29]. p. 403–36. <https://onlinelibrary.wiley.com/doi/10.1002/9781118164792.ch14>
- Kobayashi S, Müllen K, editors. *Encyclopedia of Polymeric Nanomaterials* [Internet]. Berlin, Heidelberg: Springer Berlin Heidelberg; 2015 [cited 2023 May 29]. <http://link.springer.com/10.1007/978-3-642-29648-2>
- P M, Te M. Natural Rubber and Reclaimed Rubber Composites—A Systematic Review. *Polym Sci* [Internet]. 2016 [cited 2023 May 29];2(1). <http://polymerscience.imedpub.com/natural-rubber-and-reclaimed-rubber-composites-a-systematic-review.php?aid=11066>
- Chandrasekaran C. *Anticorrosive rubber lining: a practical guide for plastics engineers*. Oxford: Elsevier; 2017. 266 p. (Plastics design library).
- Thomas S, editor. *Progress in rubber nanocomposites*. Amsterdam: Elsevier; 2017. 574 p. (Woodhead Publishing series in composites science and engineering).
- Huang Y, Li Y, Zhao H, Wen H. Research on constitutive models of hydrogenated nitrile butadiene rubber for packer at different temperatures. *J Mech Sci Technol.* 2020 Jan;34(1):155–64.
- Bauccio M, American Society for Metals, editors. *ASM metals reference book*. 3rd ed. Materials Park, Ohio: ASM International; 1993.
- Ismail MN, El-Sabbagh SH, Yehia AA. Fatigue and Mechanical Properties of NR/SBR and NR/NBR Blend Vulcanizates. *J Elastomers Plast.* 1999 Jul;31(3):255–70.
- Ward IM, Sweeney J. *Mechanical Properties of Solid Polymers: Third Edition* [Internet]. 1st ed. Wiley; 2012 [cited 2023 May 29]. <https://onlinelibrary.wiley.com/doi/book/10.1002/9781119967125>
- Copley BC. Tackification Studies of Natural Rubber/Styrene-Butadiene Rubber Blends. *Rubber Chem Technol.* 1982 May 1;55(2):416–27.
- Zeng X, Li G, Zhu J, Sain M, Jian R. NBR/CR-Based High-Damping Rubber Composites Containing Multiscale Structures for Tailoring Sound Insulation. *Macromol Mater Eng.* 2023 Feb;308(2):2200464.
- Tobajas R, Ibartz E, Gracia L. A comparative study of hyperelastic constitutive models to characterize the behavior of a polymer used in automotive engines. In: *Proceedings of 2nd International Electronic Conference on Materials* [Internet]. Sciforum.net: MDPI; 2016 [cited 2023 May 29]. p. A002. <http://sciforum.net/conference/ecm-2/paper/3398>
- Saha S, Bal S. Detailed study of dynamic mechanical analysis for nanocomposites. *Emerg Mater Res.* 2019 Sep 1;8(3):408–17.
- Jose Chirayil C, Abraham J, Kumar Mishra R, George SC, Thomas S. Instrumental Techniques for the Characterization of Nanoparticles. In: *Thermal and Rheological Measurement Techniques for Nanomaterials Characterization* [Internet]. Elsevier; 2017.. <https://linkinghub.elsevier.com/retrieve/pii/B9780323461399000013>
- Gill P, Moghadam TT, Ranjbar B. Differential scanning calorimetry techniques: applications in biology and nanoscience. *J Biomol Tech JBT.* 2010 Dec;21(4):167–93.
- Leyva-Porras C, Cruz-Alcantar P, Espinosa-Solis V, Martínez-Guerra E, Piñón-Balderrama CI, Compean Martínez I, et al. Application of Differential Scanning Calorimetry (DSC) and Modulated Differential Scanning Calorimetry (MDSC) in Food and Drug Industries. *Polymers.* 2019 Dec 18;12(1):5.
- Gallagher P. K., Brown M. E., Kemp R. B. *Handbook of Thermal Analysis and Calorimetry*. Amsterdam [Netherlands]; New York: Elsevier; 1998.
- Loos K, Aydogdu AB, Lion A, Johlitz M, Calipel J. Strain-induced crystallisation in natural rubber: a thermodynamically consistent model of the material behaviour using a serial connection of phases. *Contin Mech Thermodyn.* 2021 Jul;33(4):1107–40.



30. Wood L. A., Bekkedahl N. Crystallization of Unvulcanized Rubber at Different Temperatures. *Journal of Applied Physics* 17. 1946;362–75.
  31. Doherty WOS, Leè KL, Treloar LRG. Non-Gaussian effects in styrene-butadiene rubber: Non-Gaussian effects in styrene-butadiene rubber. *Br Polym J*. 1980 Mar;12(1):19–23.
  32. Schieppati J, Schritteser B, Wondracek A, Robin S, Holzner A, Pinter G. Temperature impact on the mechanical and fatigue behavior of a non-crystallizing rubber. *Int J Fatigue*. 2021 Mar;144:106050.
  33. Mooney M. A Theory of Large Elastic Deformation. *J Appl Phys*. 1940 Sep;11(9):582–92.
  34. Large elastic deformations of isotropic materials IV. further developments of the general theory. *Philos Trans R Soc Lond Ser Math Phys Sci*. 1948 Oct 5;241(835):379–97.
  35. Peddini SK, Bosnyak CP, Henderson NM, Ellison CJ, Paul DR. Nanocomposites from styrene-butadiene rubber (SBR) and multiwall carbon nanotubes (MWCNT) part 2: Mechanical properties. *Polymer*. 2015 Jan;56:443–51.
  36. Tzounis L, Debnath S, Roj S, Fischer D, Mäder E, Das A, et al. High performance natural rubber composites with a hierarchical reinforcement structure of carbon nanotube modified natural fibers. *Mater Des*. 2014 Jun;58:1–11.
  37. Kondyurin A, Eliseeva A, Svistkov A. Bound (“Glassy”) Rubber as a Free Radical Cross-linked Rubber Layer on a Carbon Black. *Materials*. 2018 Oct 16;11(10):1992.
  38. Fröhlich J, Niedermeier W, Luginsland HD. The effect of filler–filler and filler–elastomer interaction on rubber reinforcement. *Compos Part Appl Sci Manuf*. 2005 Apr;36(4):449–60.
  39. *Mechanics of Solid Polymers* [Internet]. Elsevier; 2015. <https://linkinghub.elsevier.com/retrieve/pii/C20130154931>
  40. Darijani H, Naghdabadi R, Kargarnovin MH. Hyperelastic materials modelling using a strain measure consistent with the strain energy postulates. *Proc Inst Mech Eng Part C J Mech Eng Sci*. 2010 Mar 1;224(3):591–602.
  41. Yeoh OH. Characterization of Elastic Properties of Carbon-Black-Filled Rubber Vulcanizates. *Rubber Chem Technol*. 1990 Nov 1;63(5):792–805.
  42. Arruda EM, Boyce MC. A three-dimensional constitutive model for the large stretch behavior of rubber elastic materials. *J Mech Phys Solids*. 1993 Feb;41(2):389–412.
  43. Treloar LRG. The elasticity of a network of long-chain molecules—II. *Trans Faraday Soc*. 1943;39(0):241–6.
  44. Zhang MG, Cao YP, Li GY, Feng XQ. Spherical indentation method for determining the constitutive parameters of hyperelastic soft materials. *Biomech Model Mechanobiol*. 2014 Jan;13(1):1–11.
  45. Large elastic deformations of isotropic materials VII. Experiments on the deformation of rubber. *Philos Trans R Soc Lond Ser Math Phys Sci*. 1951 Apr 24;243(865):251–88.
  46. Hallquist, J.O. *LS-Dyna. Material Manual*. 2005;
  47. Stander N, Craig K.J, Reichert R. Material identification in structural optimization using response surfaces. *Struct Multidiscip Optim*. 2005 Feb;29(2):93–102.
  48. Snyman JA. The LFOPC leap-frog algorithm for constrained optimization. *Comput Math Appl*. 2000 Oct;40(8–9):1085–96.
  49. Mullerschön H, Thiele M. Optimization of an Adaptive Restraint System Using LS-OPT and Visual Exploration of the Design Space Using D-SPEX. 2006;
- This research was funded under the Project of the Ministry of National Defense of the Republic of Poland Program – Research Grant (GBMON/13-999/2018/WAT), and the article was written as part of the implementation of the university research grant No. 22-874 of Military University of Technology.

Marcin Konarzewski:  <https://orcid.org/0000-0003-3352-8621>

Michał Stankiewicz:  <https://orcid.org/0000-0003-1925-5292>

Marcin Sarzyński:  <https://orcid.org/0000-0003-3561-6123>

Marcin Wieczorek:  <https://orcid.org/0000-0002-0297-535X>

Magdalena Czerwińska:  <https://orcid.org/0000-0002-7968-5019>

Piotr Prasula:  <https://orcid.org/0000-0001-5053-2046>

Robert Panowicz:  <https://orcid.org/0000-0002-0709-1369>



This work is licensed under the Creative Commons BY-NC-ND 4.0 license.

## USE OF 3D OPTICAL TECHNIQUES IN THE ANALYSIS OF THE EFFECT OF ADDING RUBBER RECYCLATE TO THE MATRIX ON SELECTED STRENGTH PARAMETERS OF EPOXY–GLASS COMPOSITES

Adam CHARCHALIS<sup>\*✉</sup>, Marcin KNEC<sup>\*\*✉</sup>, Daria ŻUK<sup>\*✉</sup>, Norbert ABRAMCZYK<sup>\*✉</sup>

\*Faculty of Mechanical Engineering, Gdynia Maritime University, ul. Morska 81-87, 81-225 Gdynia Poland

\*\*Construction Laboratory, Faculty of Civil Engineering and Architecture, Lublin University of Technology,  
ul. Nadbystrzycka 40, 20-618 Lublin, Poland

[a.charchalis@wm.umg.edu.pl](mailto:a.charchalis@wm.umg.edu.pl), [m.knec@pollub.pl](mailto:m.knec@pollub.pl), [d.zuk@wm.umg.edu.pl](mailto:d.zuk@wm.umg.edu.pl), [n.abramczyk@wm.umg.edu.pl](mailto:n.abramczyk@wm.umg.edu.pl)

*received 25 February 2023, revised 9 April 2023, accepted 19 April 2023*

**ABSTRACT:** The article presents a method of modifying the strength properties of epoxy–glass composite by changing the percentage composition of the matrix by the addition of rubber recyclate. Taking into account environmental protection and economic conditions in the process of recycling and utilisation of waste, it is advisable to look for applications of non-degradable waste materials. Based on epoxy resin, a glass mat with a random direction of fibres and rubber recyclate, a test material with different percentage compositions was produced. Samples from the manufactured materials were subjected to a static tensile test on a ZwickRoell testing machine using the ARAMIS SRX measuring system. In addition, CT (computerized tomography) scans of the inside of the samples were made using a ZEISS METROTOM 6 Scout tomograph, and observations of the internal structures were made using a scanning electron microscope. The use of optical and microscopic techniques enabled the precise determination of strength parameters of the examined composites and the analysis of the behaviour of samples under load. The analysis of deformations over time in the examined samples showed a beneficial effect of the addition of rubber recyclate on the elastic properties of the examined composites.

**Keywords:** epoxy–glass composites, ARAMIS SRX, static tensile test, rubber recyclate, 3D optical techniques

### 1. INTRODUCTION

Epoxy–glass composites are modern construction materials that have been used for years in many industries, i.e. construction, automotive, aviation or yacht industry [1–3]. These materials have a wide spectrum of possibilities for modification of their mechanical properties, obtained by changing their structure or using various types of additives and fillers [2, 4, 5].

As additives for composites with glass matt reinforcement, various types of materials of both inorganic and natural origin are used [6–8]. In most of the solutions used in composite materials, the addition of recyclate is aimed at using the maximum amount of rubber additive as a filler and flexible material with a limited range of strength parameters of finished elements [2, 23, 24]. In the latest scientific research, rubber recyclate obtained from car tires is used as an additive or filler for polymers [9–11]. However, there is a lack of research on the addition of rubber recyclate to epoxy–glass composites.

The use of rubber recyclate as a component of new epoxy–glass composite materials is very important from the perspective of environmental protection because it reduces the amount of harmful waste. Using rubber recyclate allows obtaining a new composite material with unknown properties that can be verified through strength tests.

The use of 3D optical techniques enables measurements and analyses of deformations both in large and in small samples of materials [8–10]. Digital image correlation (DIC) measurements

using optical methods are particularly useful in composite materials for which numerical analysis in programs based on the finite element method is difficult due to their anisotropy [11]. In the case of a composite with the addition of rubber recyclate, the creation of the FEM (Finite Element Method) numerical model is complicated and time-consuming. Observation of sample deformations using 3D optical techniques enables obtaining information on the behaviour of materials under load, as well as precise determination of their strength parameters. In the case of deformation analysis of composites with the addition of rubber recyclate, it is important to take into account the voids in the cross-section of the samples used in the static tensile test. These voids result in a change in the value of the cross-sectional area of the sample in the measuring part, which assumes the load during stretching. The determination of the actual stress values that appear in materials during the test as well as Young modulus is more precise and accurate using 3D optical techniques in the case of an anisotropic material, which is a composite with the addition of rubber recyclate. By scanning the samples with the ZEISS METROTOM 6 Scout tomograph, we can accurately determine the values of cross-sectional areas, and thus obtain information on the strength of materials closer to reality than that obtained from the software of the testing machine.

Systems of optical measurement techniques are often used in the analysis of the properties of composite materials. The article in Ref [12] presents the possibilities of using the ARAMIS system in the fatigue strength analysis of aircraft structures. In the study in Ref [13], examples of validation of meso-FE (meso-scale finite

element)models of carbon epoxy and glass/polypropylene composites were shown. DIC was used in these studies to record distortions in the full field. In the article in Ref [14], it was analysed based on measurements using the ARAMIS system, the mechanical and acoustic properties of starch–hemp composites, including the mechanism of cracking and sample damage. Working with optical systems, i.e. ARAMIS, also enables monitoring of composite damage; in the article in Ref [15], three techniques are combined to search for correlations during incremental cyclic tensile tests of glass fibre-reinforced polymers. In Ref [16], ARAMIS optical deformation analysis was used in direct tensile tests to observe crack propagation in SHCC (strain-hardening cement composite) materials. In article in Ref [17], using the ARAMIS optical deformation measurement system, the intensity of surface deformations at various load levels was analysed and used to indicate the location and geometrical characteristics of both external and internal damage. The research in Ref [18] indicated the great potential of the DIC technique in determining the fracture toughness of concrete composites with the addition of FA ( class F fly ash). In this study, based on data from the ARAMIS program, the values of fracture mechanics parameters were determined, which allowed observing the behaviour of the structural material precisely at the time of initial cracking.

We used optical measurement techniques to determine and analyse the strength properties of new epoxy–glass composites by the addition of rubber recyclate. The use of the ARAMIS SRX system, similar to studies in Ref [12, 13, 17], allows obtaining information on the properties and strength parameters of materials, while we additionally extended the scope of the present research by scanning using a ZEISS METROTOM 6 Scout tomograph to verify the actual Young E modulus values of new composite materials.

For an anisotropic material, the generalised Hooke law written in the summation convention is expressed as follows:

$$\epsilon_j = S_{jk} \sigma_k$$

where  $S_{jk}$  is the material compatibility matrix, and  $j, k = 1, 2, \dots, 6$  ( $j$  denotes stress directions and  $k$  denotes the direction of the corresponding deformation).

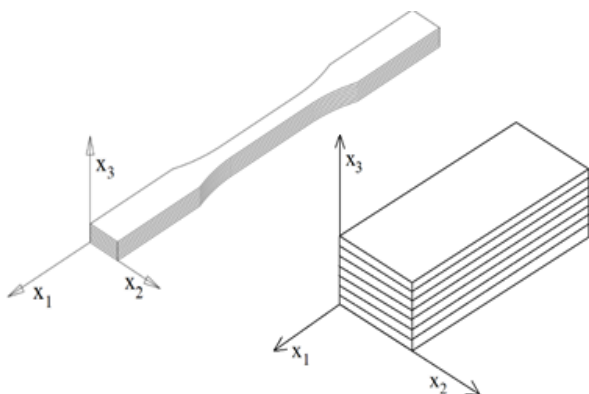


Fig. 1. Orientation in the coordinate system of the measuring part of the sample [19]

In the literature on the description of the properties of composites, the index designations 1, 2, and 3 are used, corresponding to the coordinate axis systems (Fig. 1). Only for orthotropic materials, the components of the compliance tensor can be represented by engineering constants in the form of a matrix using the

matrix described in Eq. (1). The numerical solution to such a problem leads to considerable difficulties. Using modern imaging tools that record the course of strength tests, the solution and determination of the sought values are much simpler.

$$S = \begin{bmatrix} \frac{1}{E_1} & -\frac{\nu_{21}}{E_2} & -\frac{\nu_{31}}{E_3} & 0 & 0 & 0 \\ -\frac{\nu_{12}}{E_1} & \frac{1}{E_2} & -\frac{\nu_{32}}{E_3} & 0 & 0 & 0 \\ -\frac{\nu_{13}}{E_1} & -\frac{\nu_{23}}{E_2} & \frac{1}{E_3} & 0 & 0 & 0 \\ 0 & 0 & 0 & \frac{1}{G_{32}} & 0 & 0 \\ 0 & 0 & 0 & 0 & \frac{1}{G_{13}} & 0 \\ 0 & 0 & 0 & 0 & 0 & \frac{1}{G_{12}} \end{bmatrix} \quad (1)$$

The measurements presented in the article using 3D optical techniques allowed verifying the values of the parameters obtained from a ZwickRoell stretching machine. The analysis of the obtained results showed differences in the measurements of significant values characterising the elastic and strength properties of the tested materials, which resulted from the accuracy of the measurement of stresses appearing in the cross-sections of the analysed variants of the samples.

## 2. DESCRIPTION OF THE TESTED MATERIAL AND RESEARCH METHODOLOGY

### 2.1. Properties of the used rubber recyclate

Recycling rubber products is a technologically complex process. In addition to rubber, a car tire contains steel reinforcement and fibres, while the rubber compound in addition to rubber includes components such as soot, silica, kaolin, chalk, lit stone, plasticisers, anti-ageing agents, flame retardants and vulcanising assembly (sulphuric or peroxide).

Rubber recyclate is obtained by processing used car tires. One of the most common methods of recycling rubber from car tires is mechanical shredding, which involves breaking tires into smaller fragments. They are then cleaned of metals and other foreign materials such as fabrics and wires. After cleaning, the rubber granules obtained from the crushed rubber can be used to produce new products. A diagram of the recycling process of rubber recyclate from car tyres is presented in Fig. 2.

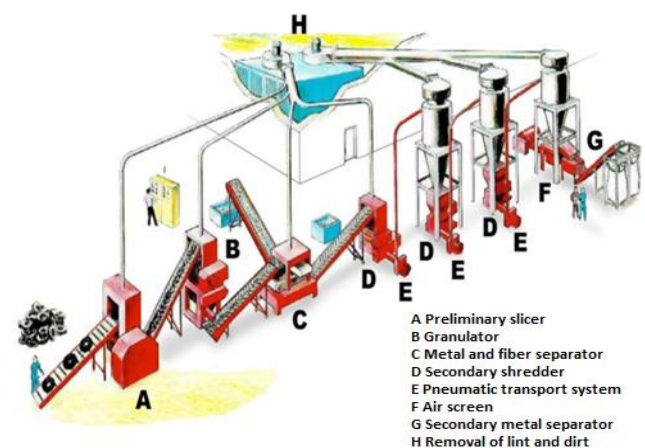


Fig. 2. Diagram of the process of obtaining rubber recyclate from car tyres [24]

Rubber recyclate derived from processed car tires with a grain size of 0–3 mm was used for this study. The recyclate was pre-sieved using a LAB 11-200 laboratory sieve shaker from EKOLAB (Fig. 3) to precisely separate its various fractions. As an addition to the matrix of composites, a recyclate fraction with a grain size from 0.5 mm to 1.5 mm was used. The percentage composition and physicochemical parameters of the rubber recyclate used in the tested materials are presented in Tabs 1 and 2. The chemical composition of the tyre tread does not differ from the chemical composition of the rubber granules obtained in the recycling process [25].

Tab. 1. Percentage composition of rubber recyclate [26]

Ingredient	Content (%)
Natural rubber	15
SBR	20
BR	10
IIR/XIIR (butyl and halogenated butyl rubber)	5
Silica	15
Soot	15
Sulphur	2
Resin	2
Mineral and vegetable oils	10
Other (zinc oxide, stearic acid)	6

BR, butadiene rubber; SBR, styrene-butadiene rubber.

Tab. 2. Physical and chemical properties of rubber recyclate used in materials [26]

Parameter	Value
Density	360–370 kg/m <sup>3</sup>
Flash point	>350 °C
Thermal decomposition	>180 °C

## 2.2. Creation of research materials

The test materials were manufactured based on an EM 1002/300/125 structural glass mat, with random fibre distribution and a mass of 350 g/m<sup>2</sup>. This mat was made of cut strands of glass fibre glued together with an emulsion binder. Epoxy resin Epidian® 6 with a Z-1 hardener was used as the matrix of the composite. The composition of the epoxy resin used is presented in **Błąd! Nieprawidłowy odsyłacz do zakładki: wskazuje na nią samą.** The components of the research materials are shown in Figs **Błąd! Nie można odnaleźć źródła odwołania.** and 4.

As the base material about which the results obtained from other variants of composites were compared, the K0 composite was used, which is a material without the addition of rubber recyclate. The K0 composite consisted of 12 layers of glass mat successively filtered with Epidian® 6 resin mixed in a predetermined proportion with the Z-1 hardener. In all made composites, a hardener in an amount of 13 g/100 g of warp was added. The weight share of the glass mat in the material K0 was 40%.

Based on these materials and a selected fraction of rubber recyclate with a grain size from 0.5 mm to 1.5 mm, four variants of research materials were produced: K0 – pure epoxy-glass com-

posite without the addition of recyclate, K3 – composite containing 3% rubber recyclate and variants K5 and K7 containing, respectively, 5% and 7% of the weight volume of the recyclate additive to the composite matrix.

Tab. 3. Epidian® 6 Epoxy resin characteristics

Parameter	Unit	Value
Epoxy number	[Mol/100 g]	0.510–0.540
Density at 25 °C	[g/cm <sup>3</sup> ]	1,17
Viscosity at 25 °C	[mPa*s]	1,000–1,500
Gel time of 100 g at 20 °C	[min]	20
Hardness time at 20 °C	[days]	7



Fig. 3. Components of manufactured research materials



Fig. 4. Sieve shaker LAB-11-200 with separated rubber recyclate fractions

Composite research plates were made by hand lamination with the use of constant double-sided pressure for all variants. For manual lamination, a rectangular steel mould with dimensions of 300 mm × 900 mm, brushes and rollers were used. Standardised test samples were produced from the prepared boards. Fig. 5 shows the geometry of the samples obtained after using the water-cutting method. The cut samples were subjected to a static tensile test on a ZwickRoell testing machine using the ARAMIS



SRX measuring system and scanning with a ZEISS METROTOM 6 Scout tomograph.

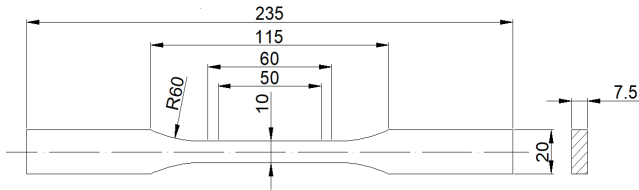


Fig. 5. Shape and dimensions of samples to be tested

Fig. 6 shows the process of manufacturing the K5 material by manual lamination. Fig. 7 shows samples of the K3 material prepared for the static tensile test. Tab. 4 shows the percentage composition of the manufactured variants of composite materials.



Fig. 6. Manufacture of materials by hand lamination



Fig. 7. Test samples cut by water cutting

Tab. 4. Mass content of the components of the epoxy–glass composite with the addition of rubber recyclate to the matrix, made by hand lamination

Material signification	Number of glass mat layers	Resin content (%)	Content of the glass mat (%)	Rubber recyclate content (%)
K0	12	60	40	0
K3	12	60	37	3
K5	12	60	35	5
K7	12	60	33	7

### 3. PLANNING AND CONDITIONS OF THE EXPERIMENT

The samples, before being fixed in the holders of the testing machine, were pre-prepared by coating them with white and black paints. This made it possible to carry out measurements using the ARAMIS SRX system during the static tensile test. During the test, two cameras of the ARAMIS SRX system recorded deformations occurring on the surfaces of the samples. Fig. 8 shows the K0 material composite samples prepared for testing, covered with paint, Fig. 9 shows the K0 sample mounted on the holders of the ZwickRoell testing machine, and the ARAMIS SRX measuring system recording the deformations appearing on the surface of the samples in real-time during the static tensile test. In addition, all samples were measured using a ZEISS METROTOM 6 Scout tomograph with a 3k X-ray detector. This detector has a 225 kV X-ray source and an X-ray detector with a resolution of  $3,008 \times 2,512$  pixels. Thanks to the CT scans of the analysed samples, it was possible to visualise the internal structures of the tested materials. Because a tomograph scan allows for the detection of material defects, pores and cavities in the material, it was possible to determine the actual cross-sectional areas of the tested samples and the actual stress values based on the obtained CT scans. For each of the tested composite samples, models were developed in GOM Suite software based on imaging using the ARAMIS SRX system and CT scans. The analyses allowed obtaining information about the exact values of the strength parameters of the tested materials.



Fig. 8. Samples prepared for measurements using the ARAMIS SRX system

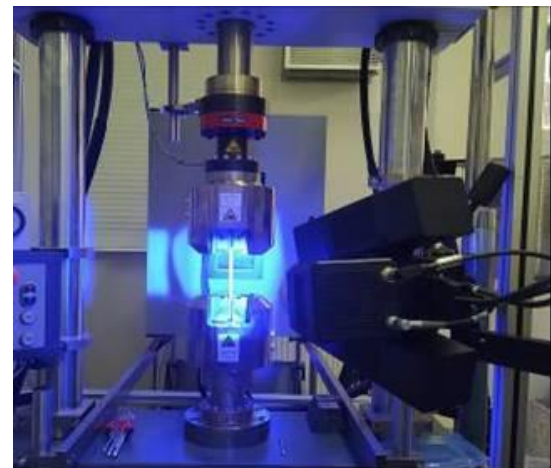


Fig. 9. Research using the ARAMIS SRX camera system



### 3.1. Measurements and analysis using electron microscopy SEM

A SEM (Scanning electron microscope) Zeiss EVO MA 15 was used to study the microstructures of the composites (Fig. 10). The device allows obtaining electron images of samples with a resolution of 3 nm at a voltage of 30 kV. The range of possible magnifications is from 5 to 1,000,000 times. The microscope allows the observation of samples weighing up to 500 g (with full mobility of the microscope table in XYZ directions) or up to 5 kg (then the movement of the table is limited to directions along the XY axis). The aim of the observation of microstructures of composite materials was to determine the influence of rubber recyclate content on the microstructure and thus on the mechanical properties. The research was carried out on cut pieces of samples from each composite. The cross-sectional surfaces were prepared using 320, 800 and 1,200 gradation abrasive papers, and then polished with a 3 μm diamond polishing slurry.

Figs 11–14 Fig. 14

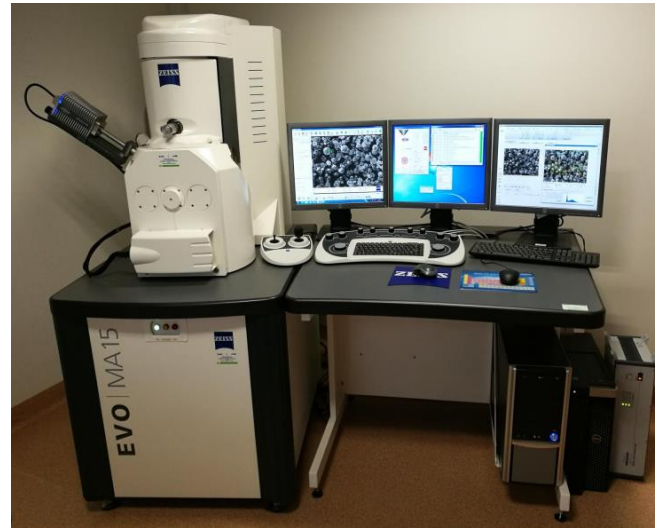


Fig. 10. Scanning electron microscope Zeiss EVO MA 15 used to observe the microstructure of the tested materials

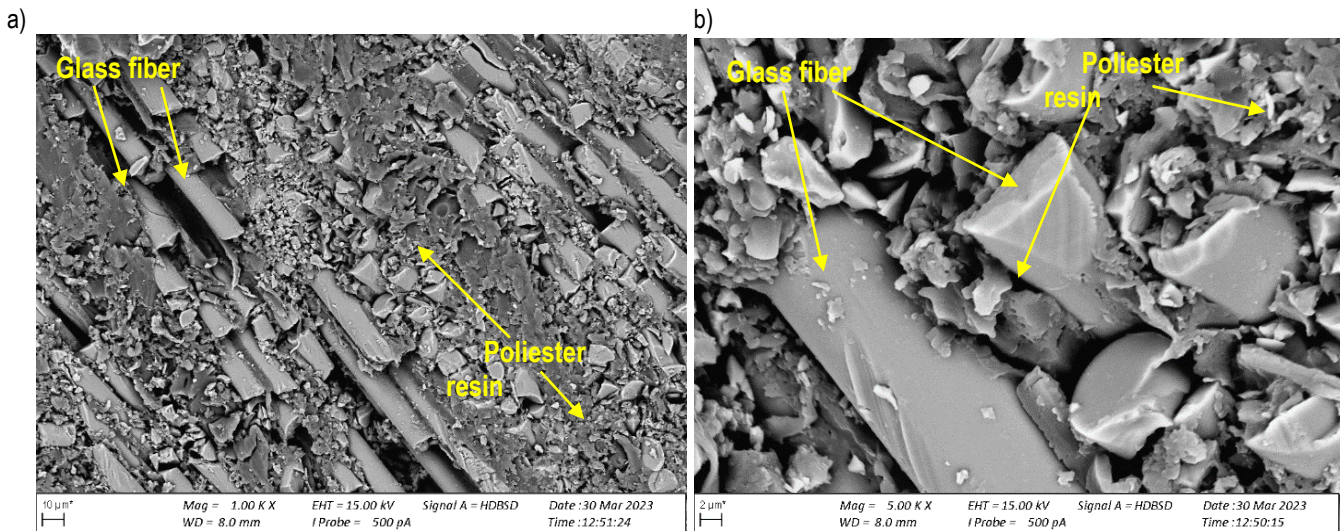


Fig. 11. Structures of composite materials: a) Composite K0, area 1000x; b) Composite K0, area 5000x

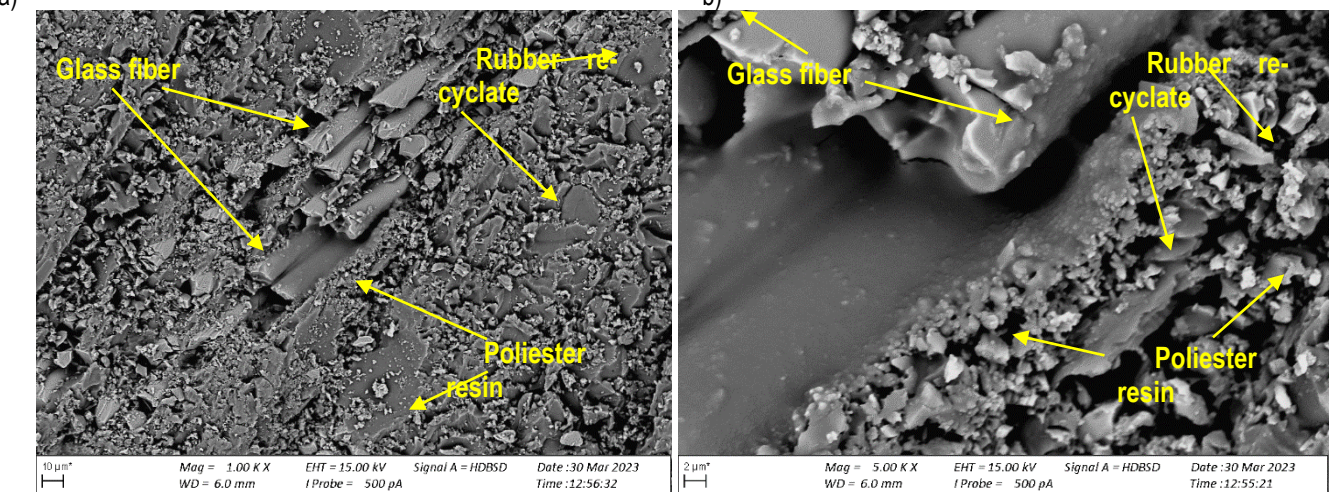


Fig. 12. Structures of composite materials :a) Composite K3, area 1000x; b) Composite K3, area 5000x



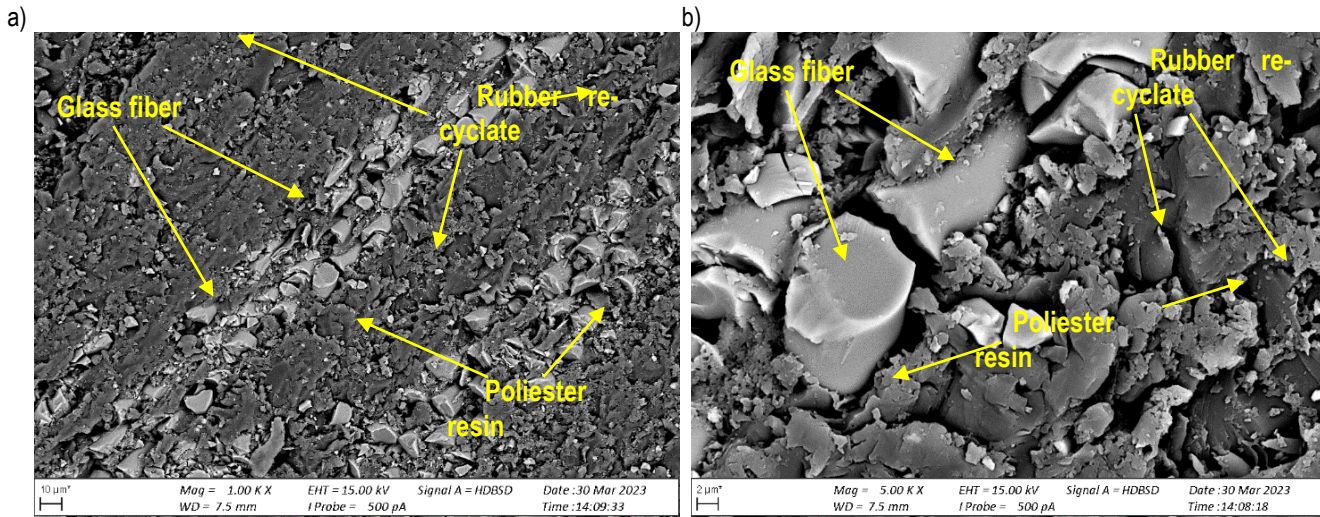


Fig. 13. Structures of composite materials: a) Composite K5, area 1000x; b) Composite K5, area 5000x

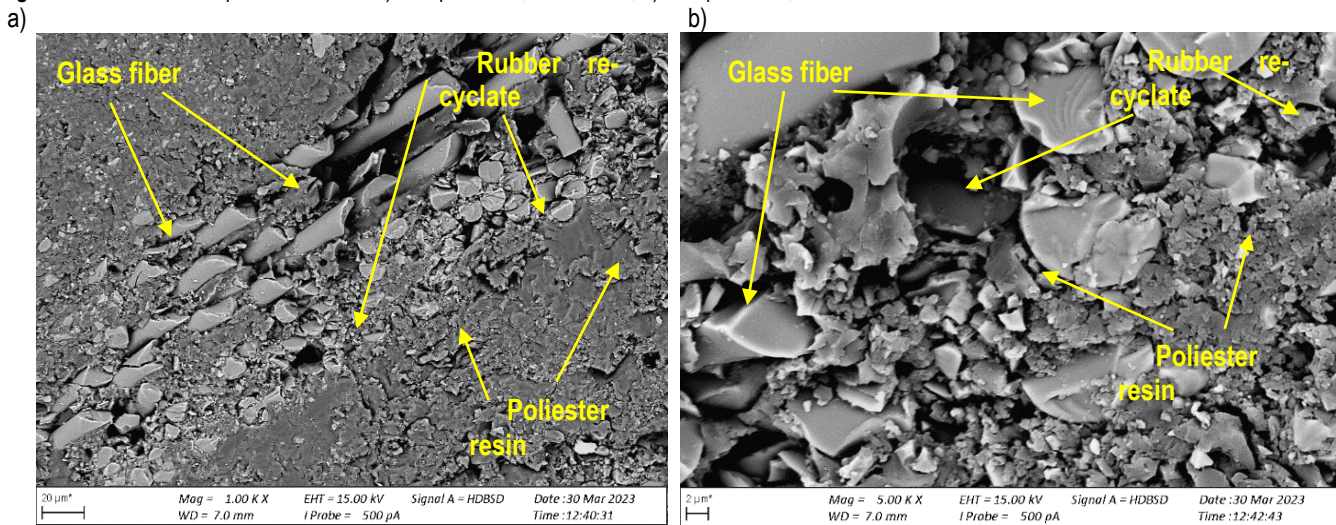


Fig. 14. Structures of composite materials: a) Composite K7, area 1000x; b) Composite K7, area 5000x

Based on the obtained images of structures, for a composite with 3%, 5% and 7% content of rubber recyclate, there is a difference in structure compared to K0 composites – without the addition of recyclate. In microstructures, the effect of rubber recyclate on the adhesion of the resin to glass fibres can be noticed. For the K3 material, the adhesion between the resin with rubber recyclate and reinforcement is greater than that in the case of K5 and K7 materials, although small air pores are visible. Comparing these materials with the K0 composite, the effect of recyclate on the structure between successive layers of reinforcement can be noticed. Microscopic observations showed that the addition of rubber recyclate has a significant impact on the structure of the examined materials. In Figs. 12–14, there are grains of recyclate, surrounded by the pores of the ventilation formed around them and at the interface of the glass mat resin. Air pores weaken the bond between the reinforcement and the resin, which may affect the strength parameters of K3, K5 and K7 composites.

#### 4. RESULTS OF EXPERIMENTAL RESEARCH AND THEIR ANALYSIS

The obtained test results made it possible to determine the effect of the addition of rubber recyclate to the composite matrix on changes in the strength properties of the samples. The strength

parameters were obtained from the ZwickRoell testing machine and GOM Suite 2021 software.

##### 4.1. Analysis of the results obtained from the TestXpert II software of the ZwickRoell testing machine

Fig. 15 shows a graph from the static tensile test of the tested composite samples obtained from TestXpert II software of the ZwickRoell testing machine. The list of parameters obtained for the tested composite materials from TestXpert II software is presented in Tab. 5.

Tab. 5. Strength parameters obtained from TestXpert software of the ZwickRoell machine for epoxy–glass composite materials based on Epidian® 6 resin with the addition of rubber recyclate, randomly, to the matrix

Material	$\sigma_m$ [MPa]	$\epsilon$ [%]	E [MPa]
K0	112.38	1.75	7,930
K3	96.46	2.09	5,978
K5	103.85	1.97	6,632
K7	94.92	2.14	5,874

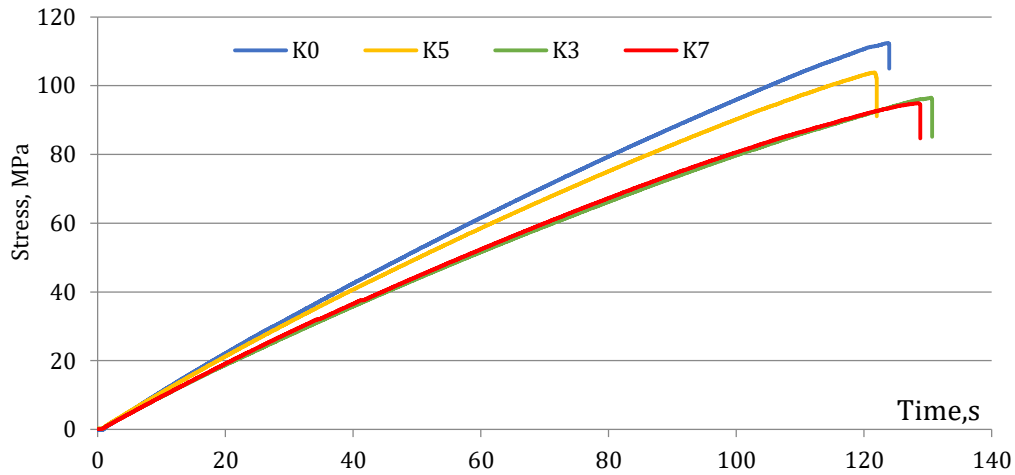


Fig. 15. Graph of the static tensile test of the tested composite materials obtained from the ZwickRoell testing machine

Analysing the results obtained from TestXpert II software, it was found that the highest strength parameters in comparison with a pure composite were obtained for the K5 material containing 5% of rubber recyclate. For this material, the Young modulus E value decreased by 16.4% compared to the E value of the K0 material. For the K3 and K7 materials, the values of the Young modulus E decreased by more than 25% compared to the E value of pure composite K0. It is worth noting the beneficial effect of adding rubber recyclate to the matrix of composites on their susceptibility to deformation, which is defined by the value of parameter  $\epsilon$ . The value of this parameter in all variants of the composite with the addition of rubber recyclate to the matrix increased. The highest increase in the value of the  $\epsilon$  parameter compared to the  $\epsilon$  value for the pure K0 composite was recorded for the K7 sample; this increase was of the order of 22.3%. The lowest increase was recorded for the K5 variant; in this case, the  $\epsilon$  value increased by 12.6% compared to the  $\epsilon$  value for the K0 composite. In the case of the analysis of the tensile strength  $\sigma_m$ , the variants of the composite with the addition of rubber recyclate reached lower values than those of the pure composite. The variant of the K5 material was the best because for it the decrease in the value of  $\sigma_m$  was only 7.6% compared to that of the pure K0 composite. Tab. 6 presents a list of percentage increases and decreases in strength parameters obtained from TestXpert II software for K3, K5 and K7 materials about the pure K0 epoxy-glass composite.

Tab. 6. Values of percentage changes in the strength parameters of composites with the addition of rubber recyclate about the K0 composite (Data from Test Xpert II software)

Material	$\sigma_m$ [MPa]	$\epsilon$ [%]	E [MPa]
K3	14.2	-19.4	24.6
K5	7.6	-12.6	16.4
K7	15.5	-22.3	25.9

#### 4.2. Analysis of the results obtained from GOM Suite 2021 software

During the static tensile test, the ARAMIS SRX system recorded the deformations appearing on the samples in a real-time test. From the obtained records, files were obtained, on which

GOM Suite 2021 software was based. The data obtained from GOM Suite 2021 software made it possible to read the values and graphically display the deformations appearing on the surface of the samples during the stretching process. An example of such imaging is shown in Fig. 16.

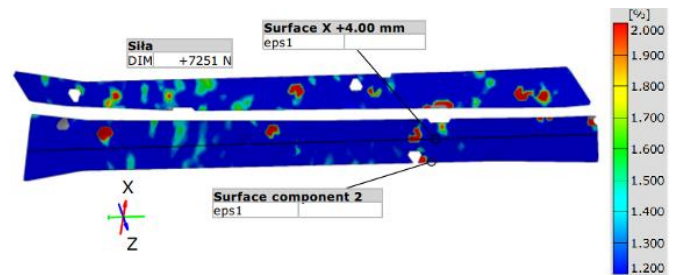


Fig. 16. Map of principal strains of the K3 sample subjected to a static tensile test obtained in the GOM Suite program

The analysis of the results obtained in GOM Suite software provided information on the mechanical properties of the tested materials and the behaviour of the samples under load conditions. After entering the data from the ZwickRoell machine on the tensile force and data on the geometry of the samples into GOM Suite software and performing a series of calculations, information on the values of strength parameters and changes in deformations occurring during the test were obtained for each sample. An example of parameter values obtained from GOM Suite software for the K7 sample is shown in Fig. 17.

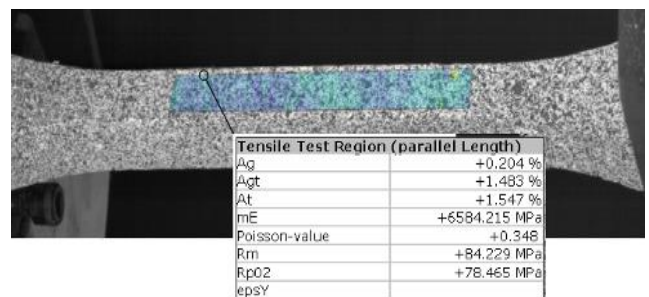


Fig. 17. Values of strength parameters obtained based on GOM Suite software for the K7 sample



Tab. 7 presents the values of strength parameters obtained during the static tensile test with the ARAMIS SRX system and GOM Suite software for the tested material variants.

**Tab. 7.** Values of strength parameters obtained during a static tensile test with the use of the ARAMIS SRX system (obtained from GOM Suite 2021)

Parameter	K0	K3	K5	K7
Ag [%]	0.317	0.204	0.320	0.204
E [MPa]	8,391	6,812	7,084	6,584
$\nu$ [-]	0.334	0.350	0.298	0.348
Rm [MPa]	118.57	84.47	92.93	84.23

During the analysis of the results obtained from GOM Suite software, it was found that the addition of rubber recyclate to the resin reduces the strength parameters of the epoxy–glass composite. The Young modulus decreased compared to the value of this modulus for the K0 material: in the case of the addition of 3% recyclate by about 19%, with the addition of 5% recyclate, the modulus decreased by about 16%, and in the case of the addition of 7% recyclate, it decreased by 21%. A similar trend was maintained for tensile strength values. This parameter has decreased for the variant K3 by 29% compared to the Rm value for the pure K0 composite, which decreased by 22% for the K5 variant, and by 29% for the K7 variant. At the same time, a beneficial effect of the addition of rubber recyclate on the elasticity and deformation method of the tested composite materials was observed. For each of the variants of the K3, K5 and K7 materials, the value of the Poisson number increased compared to that of the base material. These values increased by a maximum of 5% for the variant K3. Such a change in the elasticity of the material is caused by the impact of an additional component with elastic properties greater than that of the pure composite. The comparison of percentage decreases and increases of materials with the addition of rubber recyclate to the pure K0 composite based on data from GOM Suite software is presented in Tab. 8.

**Tab. 8.** Values of percentage changes in the strength parameters of composites with the addition of rubber recyclate about the K0 composite (Data from GOM Suite software)

Parameter	Percentage changes of strength parameters of samples K3, K5 and K7 about K0 material		
	K3	K5	K7
Ag [%]	-35.65	+0.95	-35.65
E [MPa]	-18.82	-15.58	-21.53
$\nu$ [-]	+4.79	-10.78	+4.19
Rm [MPa]	-28.76	-21.62	-28.96

**4.3. Analysis of the results obtained from scanning samples with the ZEISS METROTOM 6 Scout tomograph**

To precisely determine the strength parameters of the new composite materials, and in particular the values of the Young modulus *E*, the inside of the tested samples was X-rayed using a ZEISS METROTOM 6 Scout tomograph. Fig. 12 shows the image of the obtained CT scans of the samples made using a tomo-

graph. These measurements allowed for the analysis of the internal structure of the tested materials. Based on this, we can obtain information about the distribution of granulation inside the samples and to determine the size of the actual cross-sectional areas. The purpose of the analyses performed using CT scans was to find the smallest cross-section. This was carried out by creating several dozen cross-sections in 2-mm steps (black lines in Fig. 18b), and then by analysing the cross-sectional area (taking into account voids in the structure), the smallest cross-section was found (red lines in Fig. 18b). Using values of the actual cross-sectional areas obtained, thanks to the CT scans, we can determine the tensile strength of the tested samples after taking into account the voids in the internal space of the material caused by the presence of rubber recyclate grains.

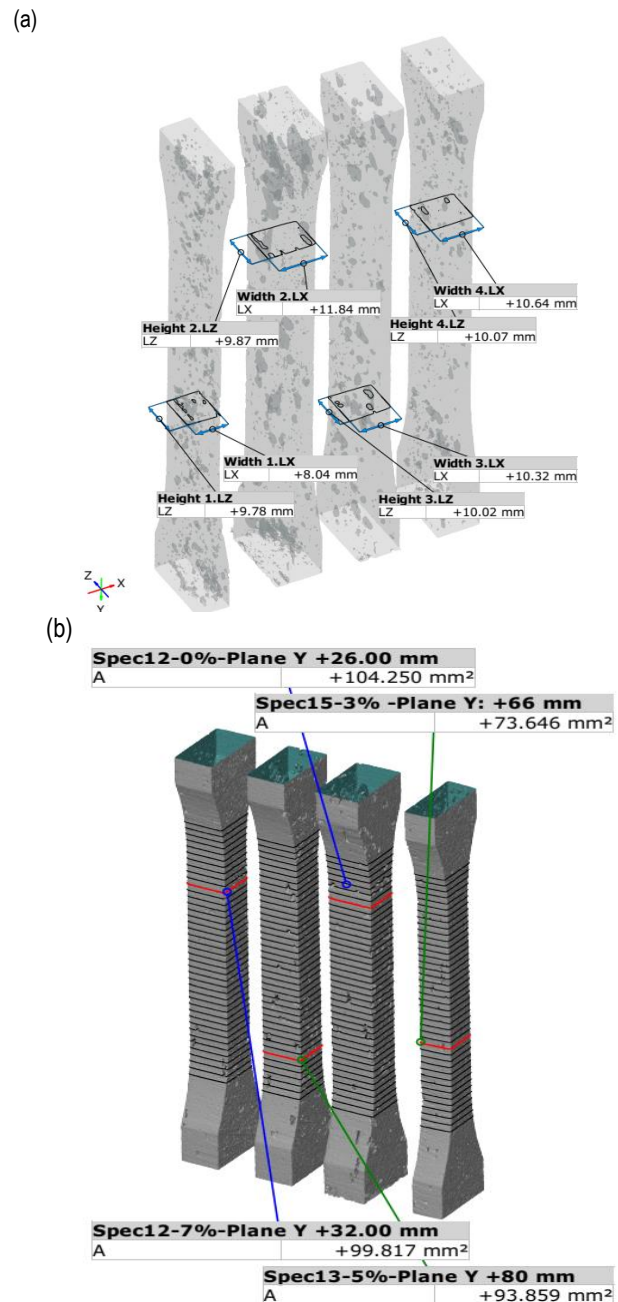


**Fig. 18.** (a) View of the external sections of the analysed samples obtained with the ZEISS METROTOM 6 Scout (GOM CT) tomograph; (b) Values of actual cross-sectional areas obtained with GOM Suite software

Fig. 19a–c and d present a summary of differences in the stress analysis for the tested samples about the actual cross-sectional area of the sample (from data based on CT scans after taking into account the recyclate in the cross-section). There are

three tensile curves in each graph, and the stress and  $\epsilon$  values obtained from TestXpert II and GOM Suite software (for files from the ARAMIS SRX system and CT scans) were compared.

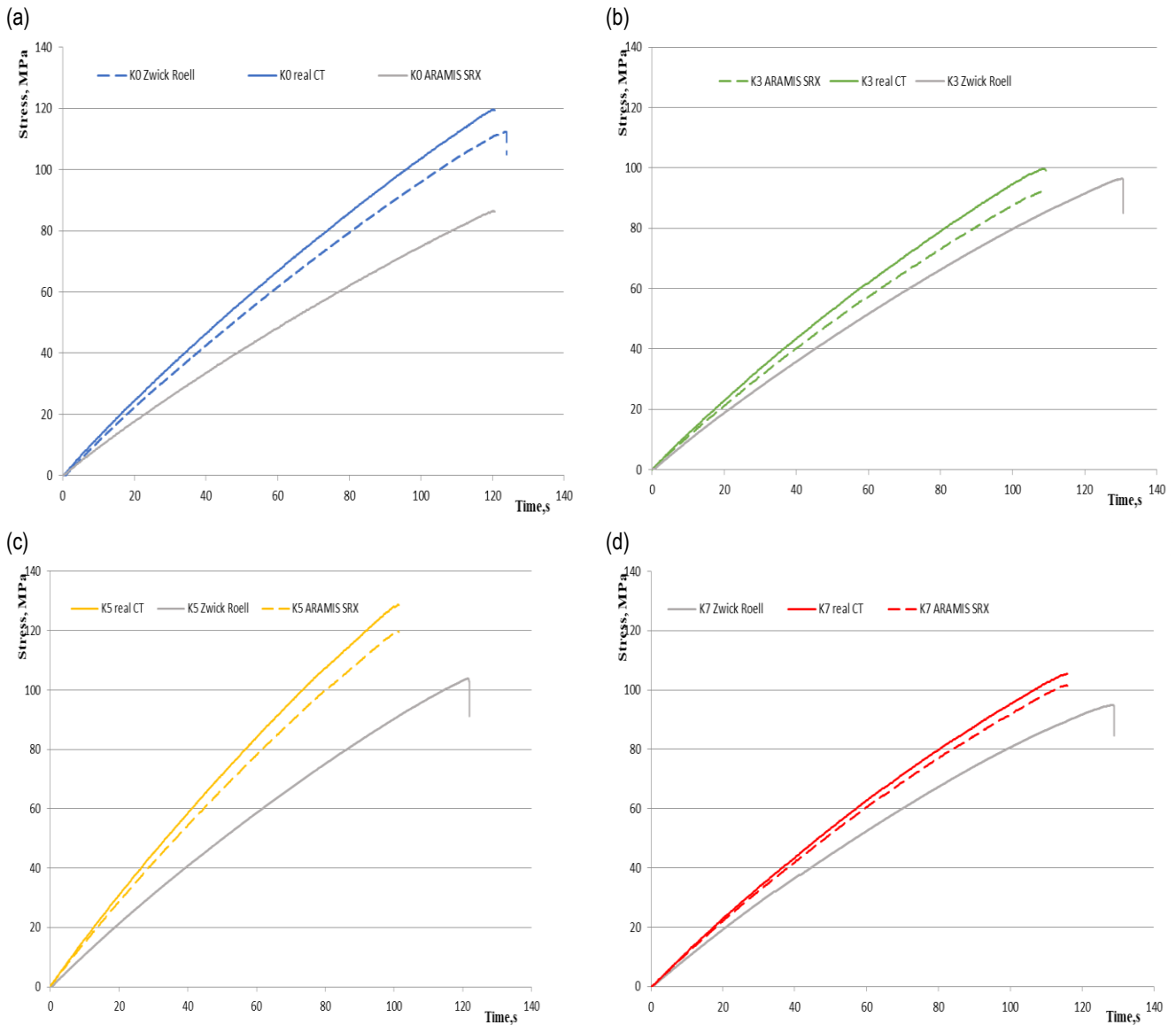


**Fig. 19.** Differences in the stress values in the samples after taking into account the actual cross-sectional areas, thanks to the CT scans made for the samples: a) without recyclate addition; b) with 3% recyclate addition; c) with 5% recyclate addition; d) with 7% recyclate addition

Fig. 20 presents a summary of the obtained test time–stress diagrams, taking into account the minimum real external cross-section, taking into account voids and without taking into account voids. Section Analyses with and without voids were performed by GOM Suite software based on measurements made with the ZEISS METROTOM 6 Scout. The diagram also shows the minimum cross-sections corresponding to the places of stress calculation.

The performed CT scans allowed illustrating the differences in the actual stress values that the analysed research materials can transfer. The new composite material, which is an epoxy–glass composite with the addition of rubber recyclate, is a unique combination of the strength properties of the resin with the elastic properties of the rubber recyclate.

Fig. 21 presents the lists of the obtained tensile strength values for the tested variants of materials, depending on the measurement method used. The presented values vary significantly. The essence of these differences is taking into account the actual cross-sectional areas of the tested samples in their measuring parts in the calculations.

As a result of the analysis of the  $R_m$  values obtained from Test Xpert II software of the testing machine and after the use of optical measurement techniques, it can be concluded that the addition of rubber recyclate significantly affects the strength parameters of the obtained composites. Rubber recyclate grains creating voids in cross-sections affect the reduction of stress values that the material can transfer. This reduction is only visible after CT scans. After taking into account the values of the actual

cross-sectional areas obtained from CT scans, a decrease in the Rm parameter of 24% was noted for the K5 material compared to the Rm value for the K5 material obtained after measurements using the ARAMIS SRX system, which were based on the external dimensions of the samples in their measuring parts. The summary of the obtained Rm values for the tested composite materials is presented in Tab. 9.

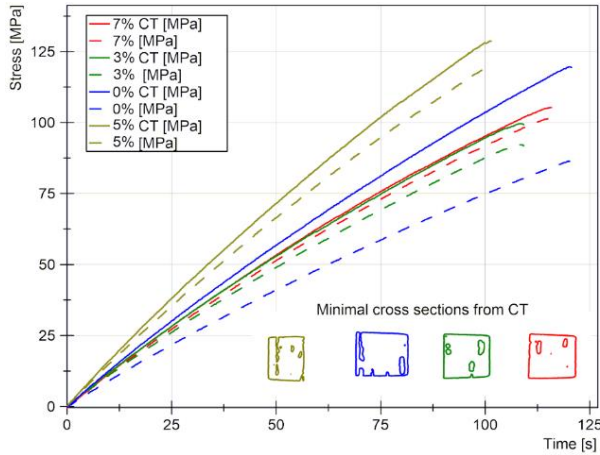


Fig. 20. Summary of differences in stress measurements in samples based on CT scans – after taking into account the recyclate in the cross-section

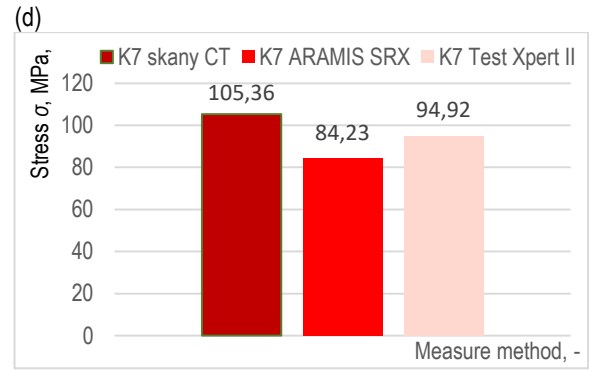


Fig. 21. Summary of the obtained tensile strength Rm values for the tested materials, taking into account the measurement method used for samples: a) K0; b) K3; c) K5; d) K7

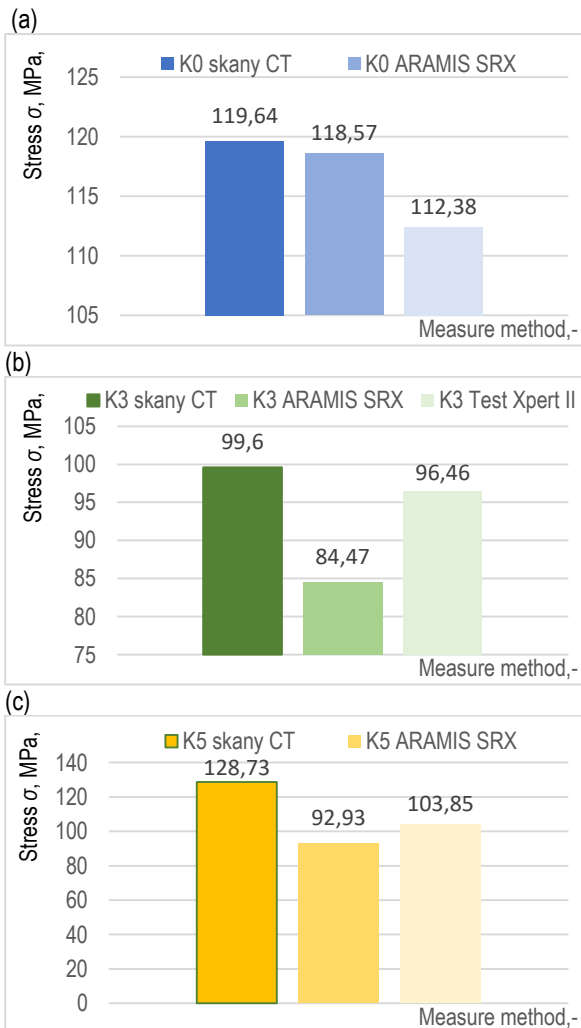
Tab. 9. Tensile strength values obtained from ARAMIS SRX data and CT scans

Material	Rm, MPa scans CT	Rm, MPa ARAMIS SRX	Percentage drop, %
K0	119.64	118.57	-0.9
K3	99.6	84.47	-3.3
K5	128.73	92.93	-24.0
K7	105.36	84.23	-11.0

Analyses made in GOM Suite 2021 software, taking into account the cross-sectional areas of the measuring parts of the samples, were used to determine material properties such as Young modulus E. Bearing in mind that the modulus E is the quotient of stress and strain, it can be concluded that for the same longitudinal strains measured by the ARAMIS SRX system on the surface of the samples depending on the method of calculating the cross-section, a different value of the E modulus was obtained. After taking into account the voids in the sections caused by the presence of rubber recyclate grains, these fields will be smaller. Reducing the cross-sectional area of the measuring part affects the value of the Young modulus E determined for each sample. Tab. 10 presents the differences in the values of the Young modulus for the tested variants of materials obtained as a result of verifying the values of the cross-sectional areas of the measuring parts of the samples, after analysing the CT scans.

Tab. 10. Young modulus values of K0, K3, K5 and K7 composites determined from the ZwickRoell machine and by using the ARAMIS SRX system and by using CT scans

Material	Young modulus E, MPa		
	Data obtained from TestXpert II software of the ZwickRoell testing machine	Data from the ARAMIS SRX system, based on external measurements of the sample geometry	Data obtained from CT scans, after accounting for voids in the cross-sections of the samples
K0	7,930	8,467	8,391
K3	5,978	8,032	6,812
K5	6,632	9,813	7,084
K7	5,874	8,236	6,584



The differences in Young modulus values for the tested variants of composite materials determined based on ARAMIS imaging and CT scans are significant. For the K0 variant, the discrepancy of the obtained  $E$  modulus values is almost 536 MPa, while for the K5 variant, this discrepancy is 3181 MPa. Such significant differences in measurements indicate a significant need to use modern measurement techniques to determine new composites' material constants. This is of particular importance when there are voids in the cross-section of the tested material, such as those caused by the presence of rubber recyclate grains in composite materials. The type of composite construction affects the strength properties, and taking into account voids in cross-sections is possible only after using the CT scanning technique; it makes allows predicting what load the tested material can take. After determining the actual cross-sectional areas of the tested samples, it turned out that the value of these loads must be lower than

that would result from the parameters determined during the static tensile test without the use of optical measuring techniques.

#### 4.4. Analysis of the course of deformations in the tested composite materials

During the tests, an analysis of the process of deformation in the samples during the static tensile test was performed for each of the analysed variants of the material. As the measurement threshold defines the occurrence of deformation that leads to the cracking of the sample, the value of 1.2% of the maximum deformation created in the sample during stretching was set. Such deformations were created in the sample and developed during the test until the material broke. An example of crack analysis carried out on the measuring length of the sample for samples K0 and K5 is shown in Figs 22–25.

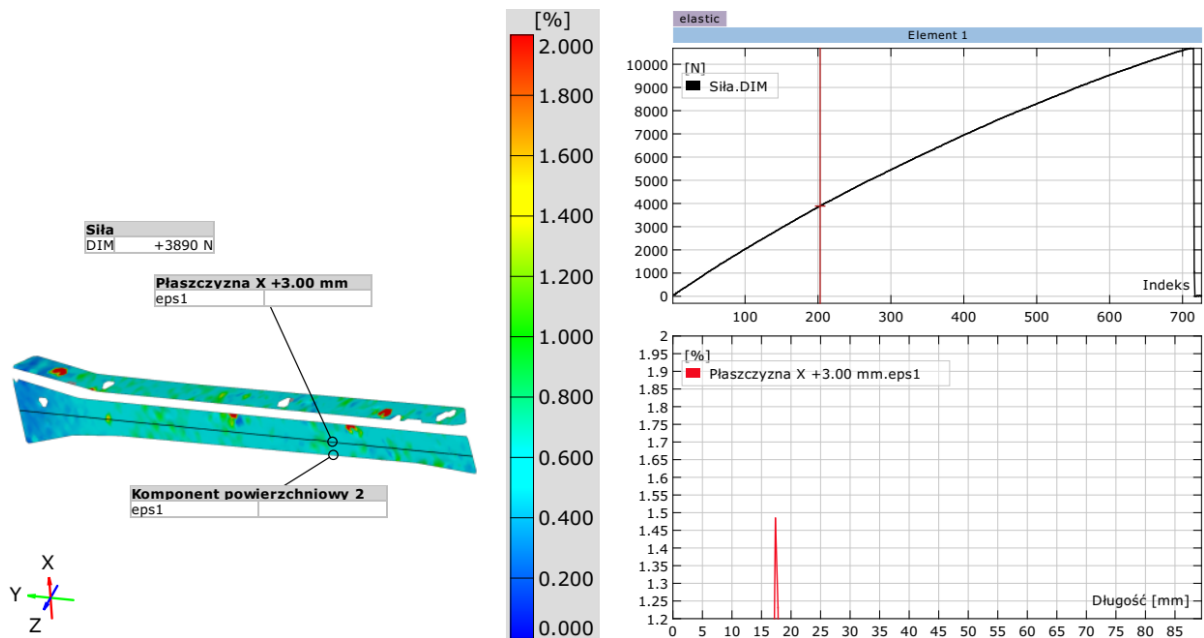


Fig. 22. Course of the main strains I in the longitudinal section of the K0 sample on the measuring part in the period of the first strains

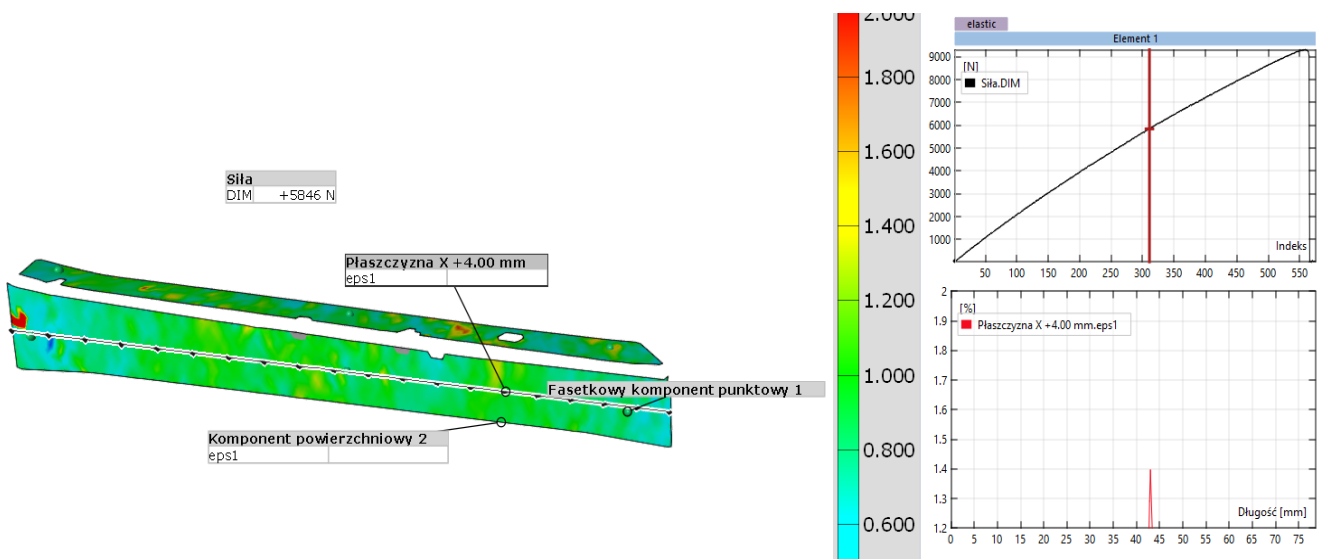


Fig. 23. Course of the main strains I in the longitudinal section of the K5 sample on the measuring part during the crack initiation period

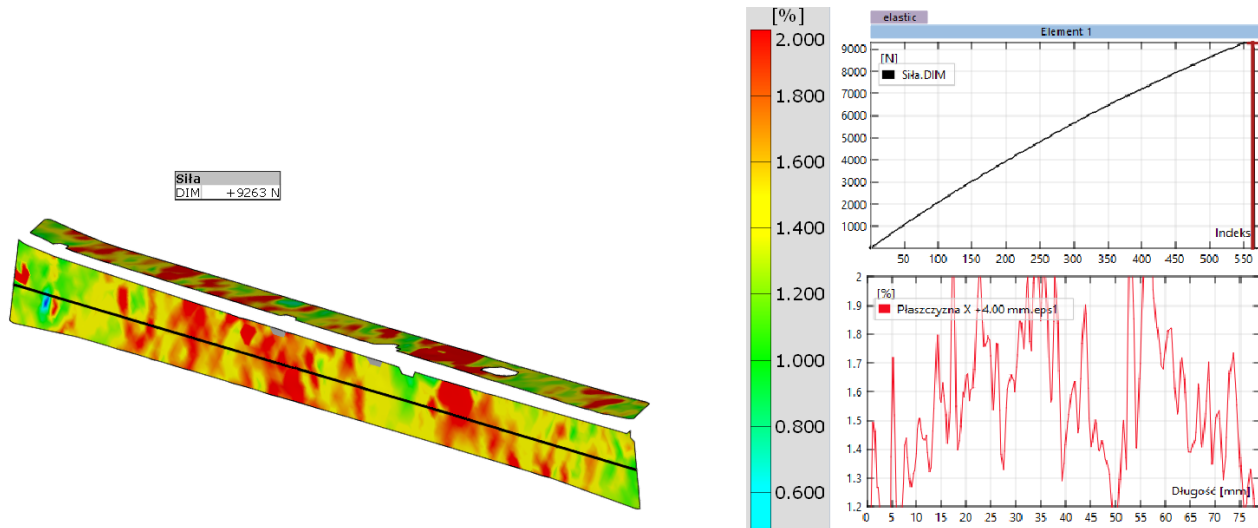


Fig. 24. Course of the main strains I in the longitudinal section of the K5 sample into parts in the period before the sample breaks

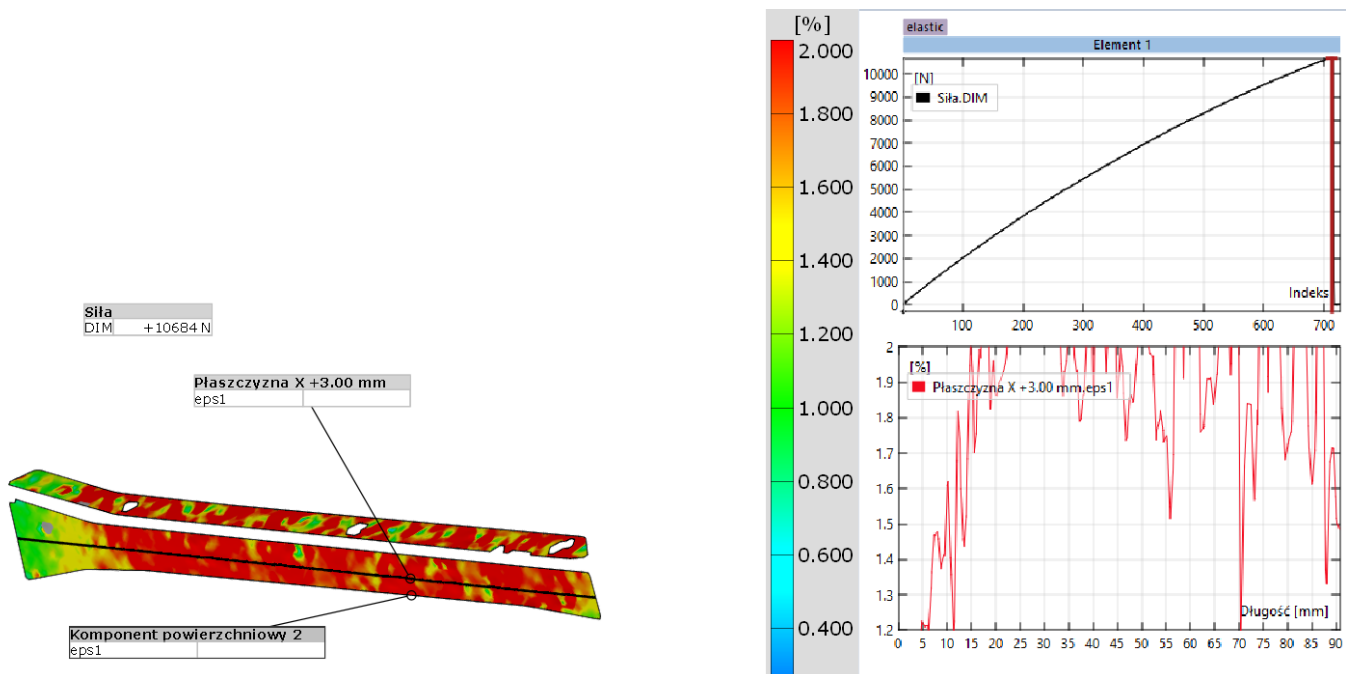


Fig. 25. Course of the main strains I in the longitudinal section of the K5 sample into parts in the period before the sample breaks

Tab. 11. Values of forces at which strains appear in the sample exceeding 1.2% of the maximum strains obtained in the sample during the static tensile test

Force / material	K0	K3	K5	K7
F [N]	3,890	7,251	7,846	7,826
$\sigma$ [%] of $\sigma_{MAX}$	1.45	1.5	1.4	1.42

The analysis of cracks in the tested samples confirms the beneficial effect of the rubber recyclate addition on the elastic properties of the tested composites. The addition of recyclate caused cracks in the samples to appear only after the tensile force was significantly exceeded in comparison with the pure composite. For the K0 sample, the value of the force beyond which deformations appear at the level of 1.2% propagating over time to the sample's fracture is about 3,890 N. For comparison, the value

of this force for the K7 composite is already 7,826 N. The list of forces at which they appear in the sample strains at the level of 1.2% of the maximum strains propagating with time until the sample breaks are shown in Tab. 11.

## 5. SUMMARY

The analysis of the obtained results showed that the addition of rubber recyclate to the resin reduces the strength parameters of the epoxy–glass composite in terms of percentage elongation, Young modulus and tensile strength. However, it is worth noting the beneficial effect of the rubber recyclate addition on the elasticity, as well as the deformation method of the tested composite materials. For each of the material variants, the value of the Poisson number increased in comparison with the base material K0.



In the case of the analysis of material properties for a new composite material, it is important to precisely determine the parameters characterising the strength of the new material. The studies and analyses carried out have shown that the use of modern optical measurement systems creates new possibilities in the analysis of the properties of composite materials. Of particular importance are such measurements for newly developed composite materials with high anisotropy, for which it is difficult to use traditional computational models or numerical analyses based on FEM software. The article's authors used the ARAMIS system's capabilities and GOM Suite software to test the strength parameters of newly manufactured epoxy-glass composites with the addition of recyclate derived from non-degradable rubber substances. The production of a new construction material is the beginning of the road, the next stage of which is always the analysis of mechanical and physicochemical properties. These analyses lead to finding an area where the newly produced material can be used. Crack analysis in the variants of composite materials presented in this study confirms the beneficial effect of the addition of rubber recyclate on the elastic properties of the tested composites. The addition of recyclate caused cracks in the samples to appear only after the tensile force was significantly exceeded in comparison with the pure composite.

Important for the research is the noticeable effect of the percentage amount of the additive on the parameters of the new composite. The most promising composite turned out to be the variant containing a 5% random addition of rubber recyclate to the composite matrix. At the same time, the influence of the rubber recyclate addition on the actual tensile strength properties of the tested materials should be noted. The analysis of CT scans showed that the new material can transfer fewer loads than it would result from the data determined by traditional methods. Research has shown that it is beneficial to use additives from environmentally friendly recycling processes in new materials while improving their specific mechanical and functional parameters. For certain manufacturing applications, such a significant improvement in elasticity can be an important factor in choosing this variant of the solution. Ease of access to this raw material and its low cost of acquisition have a positive effect on the producer's favourable economic balance.

## REFERENCES

1. Abtew MA, Boussu F, Bruniaux P, Loghin C, Cristian I. Ballistic impact mechanisms – A review on textiles and fibre-reinforced composites impact responses. *Composite Structures*. 1 wrzesień 2019;223:110966.
2. Sienkiewicz M. Kompozyty poliuretanowo-gumowe otrzymane przy udziale recyklatów gumowych jako sposób na zagospodarowanie użytkowych opon samochodowych. Politechnika Gdańska; 2010.
3. Łopacka J. Nanocząstki wykorzystywane w celu poprawy właściwości fizycznych kompozytów polimerowych stosowanych jako materiały opakowaniowe do żywności. *Polimery*. 2013;58(11–12):864–8.
4. Andrzej Wilczyński. *Polimerowe kompozyty włókniste*. Warszawa: Wydawnictwo Naukowo Techniczne; 1996.
5. Golewski P, Sadowski T. A novel application of alumina fiber mats as TBC protection for CFRP/epoxy laminates –Laboratory tests and numerical modeling. *Journal of the European Ceramic Society*. 2018;38(8):2920–7.
6. A.A. Nayeef , Z.K. Hamdan, Z.W. Metteb, F.A. Abdulla, N.A. Jebur. Natural filler based composite materials. 1 lipiec 2022;116(1):5–13.
7. Dębska B, Licholai L, Miąsik P. Assessment of the Applicability of Sustainable Epoxy Composites Containing Waste Rubber Aggregates in Buildings. *Buildings* [Internet]. 2019;9(2). Dostępne na: <https://www.mdpi.com/2075-5309/9/2/31>
8. Żuk D, Abramczyk N, Drowing S. Investigation of the influence of recycle content on Poisson number of composites. *Science and Engineering of Composite Materials*. 2021;28(1):668–75.
9. Marta Chojnacka. Zastosowanie kopolimerów blokowych i recyklatów gumowych do modyfikacji asfaltów. 2012;TOM 16.
10. Parasiewicz W., Pyskło L., Magryta J., *Recykling zużytych opon samochodowych*. Instytut Przemysłu Gumowego „STOMIL”, Piastów 2005.
11. Al-Shabllle M, Al-Waily M, Njim E. Analytical evaluation of the influence of adding rubber layers on free vibration of sandwich structure with presence of nano-reinforced composite skins. *Archives of Materials Science and Engineering*. 2022;116(2):57–70.
12. Jweeg M, Alazawi D, Jebur Q, Al-Waily M, Yasin N. Hyperelastic modelling of rubber with multi-walled carbon nanotubes subjected to tensile loading. 2021;108(2):75–85.
13. Valášek P, Žarnovský J, Müller M. Thermoset composite on basis of recycled rubber. W: *Advanced materials research*. Trans Tech Publ; 2013. s. 67–73.
14. Luo J, Dai CY, Wang Z, Liu K, Mao WG, Fang DN, i in. In-situ measurements of mechanical and volume change of LiCoO<sub>2</sub> lithium-ion batteries during repeated charge–discharge cycling by using digital image correlation. *Measurement*. 2016;94:759–70.
15. Gljušić M, Franulović M, Lanc D, Božić Ž. Digital image correlation of additively manufactured CFRTP composite systems in static tensile testing. *Procedia Structural Integrity*. 2021;31:116–21.
16. Kneč M, Sadowski T, Balawender T. Technological problems and experimental investigation of hybrid: clinched-adhesively bonded joint. *Archives of Metallurgy and Materials*. 2011;(2).
17. Nelson TM, Quiros KAM, Mariano CA, Sattari S, Ulu A, Dominguez EC, i in. Associating local strains to global pressure–volume mouse lung mechanics using digital image correlation. *Physiological Reports*. 2022;10(19):e15466.
18. Lusiak T, Kneč M. Use of ARAMIS for Fatigue Process Control in the Accelerated Test for Composites. *Transportation Research Procedia*. 2018;35:250–8.
19. Lomov SV, Ivanov DS, Verpoest I, Zako M, Kurashiki T, Nakai H, i in. Full-field strain measurements for validation of meso-FE analysis of textile composites. *Composites Part A: Applied Science and Manufacturing*. 2008;39(8):1218–31.
20. Le AT, Gacoin A, Li A, Mai TH, Wakil NE. Influence of various starch/hemp mixtures on mechanical and acoustical behavior of starch-hemp composite materials. *Composites Part B: Engineering*. 2015;75:201–11.
21. Nag-Chowdhury S, Belléou H, Pillin I, Castro M, Longrais P, Feller JF. Crossed investigation of damage in composites with embedded quantum resistive strain sensors (sQRS), acoustic emission (AE) and digital image correlation (DIC). *Composites Science and Technology*. 2018;160:79–85.
22. Paul SC, Pirsakawetz S, Zijl GPAG van, Schmidt W. Acoustic emission for characterising the crack propagation in strain-hardening cement-based composites (SHCC). *Cement and Concrete Research*. 2015;69:19–24.
23. Zhang Z, Richardson M. Structural integrity evaluation of impacted glass fibre reinforced polyester composites using Optical deformation and Strain Measurement system (ARAMIS). W: *ACMC/SAMPE Conference on Marine Composites*, Plymouth, 11-12 September 2003. University of Plymouth; 2003. s. 99–106.
24. Golewski GL. Estimation of the optimum content of fly ash in concrete composite based on the analysis of fracture toughness tests using various measuring systems. *Construction and Building Materials*. 2019;213:142–55.

25. Gryniewicz-Bylina B, Rakwicz B, Słomka-Słupik B. Tests of rubber granules used as artificial turf for football fields in terms of toxicity to human health and the environment. *Scientific Reports*. 23 kwiecień 2022;12(1):6683.
26. <https://orzelsa.com/wp-content/uploads/2020/10/Karta-techniczna-1-3-mm.pdf>.
27. Liang S, Gning PB, Guillaumat L. A comparative study of fatigue behaviour of flax/epoxy and glass/epoxy composites. *Composites Science and Technology*. t. 72, nr 5, s. 535–543, 2012, doi: <https://doi.org/10.1016/j.compscitech.2012.01.011>.
28. Koricho EG, Belingardi G, Beyene AT. Bending fatigue behavior of twill fabric E-glass/epoxy composite. *Composite Structures*. t. 111, s. 169–178, 2014, doi: <https://doi.org/10.1016/j.compstruct.2013.12.032>.
29. Bhatnagar A. *Lightweight Ballistic Composites: Military and Law-Enforcement Applications*. Elsevier Science, 2016. [Online]. Dostępne na: <https://books.google.pl/books?id=qZPBCQAAQBAJ>
30. Chatterjee VA, Verma SK, Bhattacharjee D, Biswas I, Neogi S. Enhancement of energy absorption by incorporation of shear thickening fluids in 3D-mat sandwich composite panels upon ballistic impact. *Composite Structures*. t. 225, s. 111148, 2019, doi: <https://doi.org/10.1016/j.compstruct.2019.111148>.
31. Abdel-Magid B, Ziaee S, Gass K, Schneider M. The combined effects of load, moisture and temperature on the properties of E-glass/epoxy composites. *Composite Structures*, t. 71, nr 3, s. 320–326, 2005, doi: <https://doi.org/10.1016/j.compstruct.2005.09.022>.

The authors of the article give special thanks to Paweł Szerszeń for preparing and taking measurements using the ARAMIS SRX system and to Karol Mateja for making 3D scans on ZEISS METROTOM 6 Scout (GOM CT).

Adam Charchalis:  <https://orcid.org/0000-0003-0750-9849>

Marcin Kneć:  <https://orcid.org/0000-0002-1974-7345>

Daria Żuk:  <https://orcid.org/0000-0002-0810-0626>

Norbert Abramczyk:  <https://orcid.org/0000-0003-4556-7994>



This work is licensed under the Creative Commons BY-NC-ND 4.0 license.



## DETERMINISTIC SEISMIC DAMAGE ANALYSIS FOR CONCRETE GRAVITY DAMS: A CASE STUDY OF OUED FODDA DAM

Djamel OUZANDJA\*, Amina TAHAR BERRABAH\*\*

\*Laboratory of Materials and Mechanics of Structures (LMMS), Department of Civil Engineering, Faculty of Technology,  
University of Msila, PB 166 M'sila 28000, Algeria

\*\*Smart Structures Laboratory, University of Ain Temouchent, Department of Civil Engineering,  
Route de Sidi Bel Abbes - BP 284, Ain Temouchent, Algeria

[djamel.ouzandja@univ-msila.dz](mailto:djamel.ouzandja@univ-msila.dz), [amina.taharberrabah@uiniv-temouchent.edu.dz](mailto:amina.taharberrabah@uiniv-temouchent.edu.dz)

*received 10 December 2022, revised 19 February 2023, accepted 13 March 2023*

**Abstract:** One of the major dangers for seismic damage of concrete dams is the propagation of cracks in dam concrete. The present study undertakes a numerical investigation of the seismic damage for Oued Fodda concrete gravity dam, located in the northwest of Algeria, considering the impacts of properties of joints along the dam-foundation rock interface and cross-stream earthquake excitation. Three-dimensional transient analyses for coupled dam-foundation rock system are carried out using Ansys software. The hydrodynamic effect of reservoir fluid is modelled using the added mass approach. The smeared crack approach is utilised to present the seismic damage of dam concrete using the Willam and Warnke failure criterion. The dam-foundation rock interface joints are presented with two ways, adhesive joints and frictional joints. The Drucker–Prager model is considered for dam concrete in nonlinear analyses. Consideration of the study results indicates that the frictional joints model can reduce the seismic response and damage hazard of the dam body to a better extent compared with the adhesive joints model. Furthermore, the application of cross-stream earthquake excitation reveals the significant effect on cracking response of the dam in the two models of joints.

**Key words:** concrete dam, seismic damage, adhesive joints, frictional joints, smeared crack approach

### 1. INTRODUCTION

One of the major hazards of concrete dams subjected to strong earthquakes is the damage and failure of the dam concrete [1]. The need for ensuring a suitable degree of earthquake safety of such structures has attracted great interest from researchers in the field of dam engineering, and has prompted them to carry out measures of innovation and development of numerical models that can predict and capture the cracks in the dam structure. These approaches are classified into two categories: the first, the family of continuum cracking approaches, includes the smeared crack approach [2–4] and the plastic-damage constitutive model [5–8]. The fracture mechanics approach [9,10] and the extended finite element method (XFEM) [11–14], which belong to the family of discrete crack approaches, constitute the second category. The continuum crack approaches can introduce an excellent framework to characterise the first damage phase and insert parameters of internal failure to depict the stiffness degradation of solid materials without varying the topology of finite element model. These approaches are better suited to resolving the complex problems of the engineering area [15].

The earthquake behaviour of the concrete dam is based on its connection joints to the foundation rock [16–21]. The impact of contraction joints on the earthquake performance of concrete dams was cited by many researchers utilising the three-dimensional (3D) response [22–25]. Many researchers demonstrated the impact of contraction joints on the earthquake performance of concrete dams utilising the three-dimensional (3D)

response. The nonlinear behaviour of concrete gravity (CG) dams was exposed by Wang et al. [26] considering the dynamic contact between dam blocks. Study results demonstrated that the dam's seismic performance depends upon the adhesion degree between the monoliths. Kartal [27] investigated the earthquake behaviour of roller-compacted concrete (RCC) dams considering the joints at dam-reservoir-foundation interface. Wang et al. [28] analysed the seismic response of concrete dam-reservoir-foundation system with effects of contraction joints and cracking of the dam concrete. Their analysis demonstrated that the dam failure mode depends upon the ground motion variation along the dam-foundation rock interface. Yilmazturk et al. [29] presented the nonlinear seismic analyses of an RCC dam using 2D and 3D models. The results showed that the 3D analysis of the dam is significantly different from that resulting from the 2D analysis. This comparative study revealed the necessity and importance of considering 3D analysis for gravity structures such as these constructed in relatively narrow canyons for seismic safety assessment. Ouzandja et al. [30] used the contact element to model the joints along the dam-reservoir interaction interface for the study of the effect of dynamic fluid-structure interaction on the response of CG dams. In their investigation, Omidi and Lotfi [31] analysed the seismic failure of concrete dams considering the impact of the joints between the concrete blocks. The analysis showed that the cracking increases in the area of middle cantilevers due to opening the joints. Wang et al. [7] investigated the influence of contraction joints on seismic damage behaviour of Guandi gravity dam using hard and soft contact models. The analyses revealed that the contraction joints had a significant effect on the dam cracking hazard. The seismic

fragility of concrete arch dams was studied by Liang et al. [32] considering the sliding failure mode along the dam-foundation rock interface employing cohesion and friction. The study indicated that the levels of damage can be different, and the residual cohesion decreases the slippage amplitude development and enhances the earthquake stability of the concrete dam-foundation system. Ftima et al. [33] used a new modelling approach of CG dams based on the grillage method employing no-tension link elements that represent the structural connection between the monoliths. The study pointed out that the proposed approach provides good results compared to those obtained in practice. Khassaf et al. [34] exhibited the impact of contraction joints on structural response of concrete dams. Their work indicated that the optimum picking of the disposition of these joints leads to improvement in the dam earthquake stability. In Daneshyar and Ghaemian's study [35], dynamic analysis of arch dams with adhesive and frictional joints was conducted. The analysis gave rise to the inference that, in comparison with the adhesive joints model, the frictional joints model can be considered to affect the distribution of maximum stresses to a farther extent.

The present study displays the effects of contact conditions in dam-foundation rock interface and transverse earthquake excitation on the damage seismic behaviour of Oued Fodda dam, constructed in a high seismic activity zone of Algeria. The dam-foundation rock interface joints are presented with two ways, adhesive joints and frictional joints. The frictional joints model is modelled by surface-to-surface contact elements based on Coulomb's friction, which provide friction contact at the interface. The smeared crack approaches used to predict the damage of dam concrete due to a multiaxial stress state using the Willam and Warnke failure criterion [36]. The added mass approach [37] is employed to model the reservoir fluid hydrodynamic effect on dam-fluid and foundation-fluid interfaces. The Drucker–Prager model [38] is used in nonlinear analyses for dam concrete. All transient analyses are realised using ANSYS software [39].

**2. FAILURE CRITERION OF CONCRETE**

The Willam and Warnke failure criterion [36], defined below by Eq.(1), is used to predict the concrete failure, for both cracking and crushing failure modes, due to a multiaxial stress state.

$$\frac{F}{f_c} - S \geq \tag{1}$$

Where:  $F$ : denotes a function of the principal stress state ( $\sigma_{xp}$ ,  $\sigma_{yp}$ , and  $\sigma_{zp}$ ).  $S$ : the failure surface expressed in terms of the principal stresses and material properties of concrete,  $f_c$ : the maximal compressive strength and  $\sigma_{xp}$ ,  $\sigma_{yp}$ , and  $\sigma_{zp}$ : the principal stresses in the principal directions.

If Eq. (1) is satisfied, the concrete element will crack or crush. Fig. 1 manifests the 3D failure surface projection for stress states that are biaxial or nearly biaxial. Both the function  $F$  and the failure surface  $S$  are expressed in terms of principal stresses denoted as  $\sigma_1$ ,  $\sigma_2$ , and  $\sigma_3$ , where:

$$\sigma_1 = \max(\sigma_{xp}, \sigma_{yp}, \sigma_{zp}) \tag{2}$$

$$\sigma_3 = \min(\sigma_{xp}, \sigma_{yp}, \sigma_{zp}) \tag{3}$$

The failure of concrete is divided into four domains according to different failure modes as:

1.  $0 \geq \sigma_1 \geq \sigma_2 \geq \sigma_3$

The concrete is presumed to be crushed provided the failure

criterion is satisfied.

2.  $\sigma_1 \geq 0 \geq \sigma_2 \geq \sigma_3$

If the failure criterion is satisfied, the cracking occurs in the plane perpendicular to principal stress  $\sigma_1$ .

3.  $\sigma_1 \geq \sigma_2 \geq 0 \geq \sigma_3$

If the failure criterion is satisfied, the cracking occurs in the plane perpendicular to principal stresses  $\sigma_1$ , and  $\sigma_2$ .

4.  $\sigma_1 \geq \sigma_2 \geq \sigma_3 \geq 0$

If the failure criterion is satisfied, the cracking occurs in the planes perpendicular to principal stresses  $\sigma_1$ ,  $\sigma_2$ , and  $\sigma_3$ .

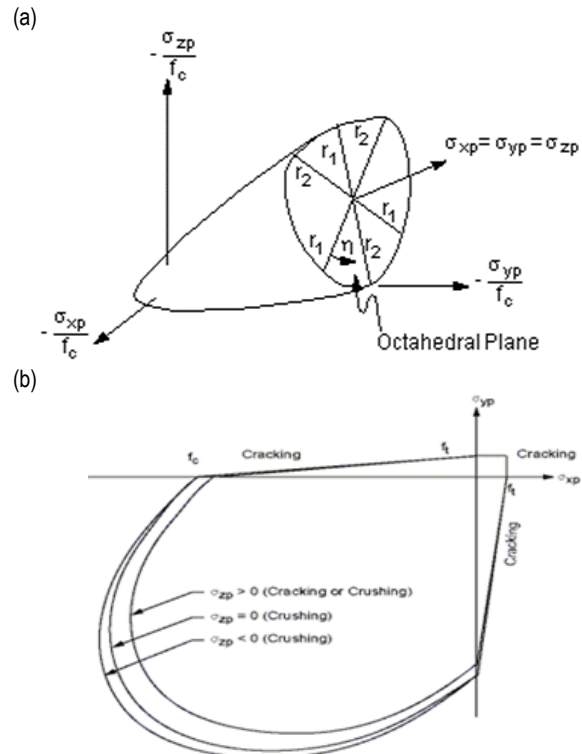


Fig. 1. Failure surface of concrete: (a) in principal stress space; and (b) in principal stress plane [39]

**3. CASE STUDY OF OUED FODDA DAM**

The selected model in this numerical application presents the Oued Fodda CG dam, located in Chlef at the northwest territory of Algeria, classified as falling under a high seismic activity zone according to the national seismic code. This region (El Asnam) suffers constantly from seismic activities. Four seismic events have shaken the region during the last century. The 1980 El Asnam earthquake (M7) is the most recent major earthquake, which destroyed more than 70% of the city. The geometry of Oued Fodda dam-foundation rock system is given in Fig. 2.

The material properties of the studied dam and its foundation rock are recapitulated in Table 1. Nonlinear response is based on the Drucker–Prager model [38], in which the cohesion and angle of internal friction of the dam concrete are 2.50 MPa and 35°, respectively. The dynamic tensile and compressive strengths of dam concrete are 2.3 MPa and 24 MPa, respectively.

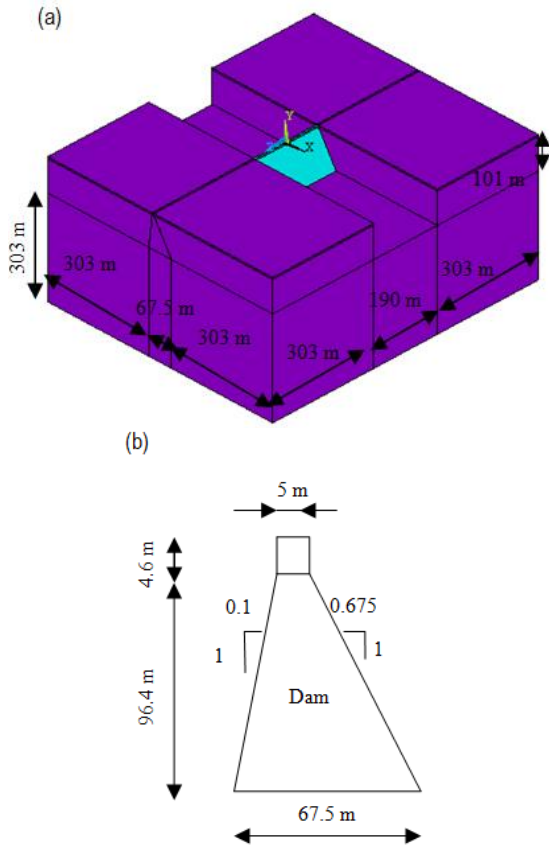


Fig. 2. Geometry of Oued Fodda dam-foundation rock system: (a) dam-foundation rock system; and (b) dam body

Tab. 1. Material properties of Oued Fodda dam-foundation rock system

Material	Material properties		
	Modulus of elasticity (MPa)	Poisson's ratio	Mass density (kg/m <sup>3</sup> )
Concrete dam	24600	0.20	2640
Foundation rock	20000	0.33	2000

### 3.1. Finite element discretization of dam-foundation rock system

The finite element modelling of dam-foundation rock system is shown in Fig. 3. The dam body is modelled by eight-node solid elements (Solid65); the model contains 2,700 elements and 2,850 nodes. The foundation rock domain is discretised using eight-node solid elements (Solid45); the model consists of 37,050 elements and 41,640 nodes. The hydrodynamic effect of reservoir fluid is modeled employing the Westergaard approach [37]. This technique, which is an approximate approach, replaces the fluid with equivalent mass distributed uniformly on dam-fluid and foundation-fluid interfaces; that is, the fluid is represented as added structural masses to that of the dam and foundation. 3D surface elements (Surf154) are considered in the modelling of the added mass approach in this study, resulting in 900 elements. Additionally, the contraction joints along dam-foundation rock interface are represented by 3D surface-to-surface contact elements based on Coulomb's friction, which take a target surface (Targe170) and a contact surface (Conta174) to make a contact pair, available in ANSYS code [39].

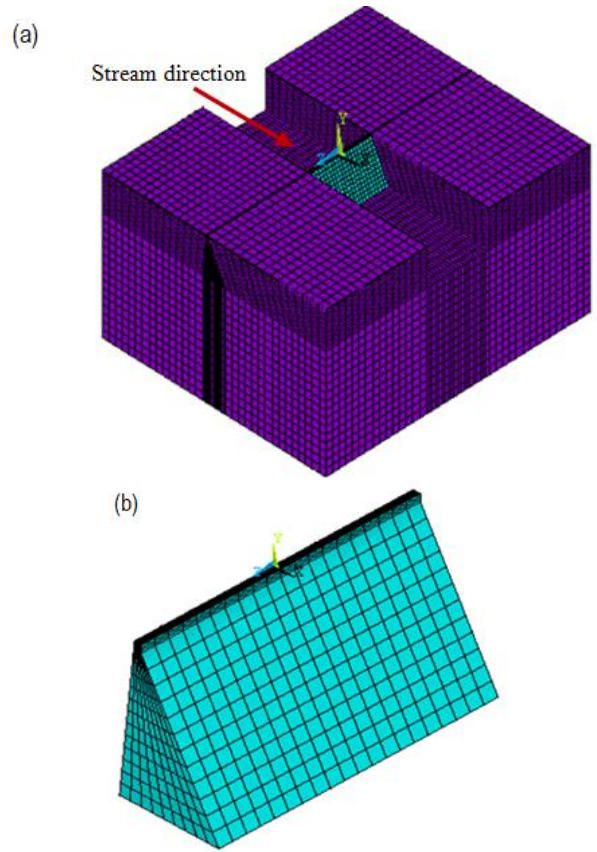


Fig. 3. 3D finite element modeling of Oued Fodda dam-foundation rock system: (a) dam-foundation rock system; and (b) dam body

### 3.2. Modelling of dam-foundation rock interface contraction joints

The dam-foundation rock interface behaviour plays a role as a significant factor in securing the earthquake stability of concrete dams due to the presence of contraction joints along the interface. The contraction joints are generally modelled by two formulations: adhesive joints and frictional joints. In effect, a concrete dam does not directly establish contact with the foundation rock. According to this reason, the use of contact elements, which represent the friction contact, in finite element analyses can provide more realistic results. The concrete dam may slip over its foundation rock by utilising these elements. These elements, which are defined between the surfaces of volumes, provide the friction behaviour by normal and tangential shear stiffness. During the course of the investigation, the presumption that the concrete dam and the foundation rock are independent deformable bodies is used when the frictional joints model is employed, and that they are dependent deformable bodies is used when the adhesive joints model is employed. 3D contact elements based on Coulomb's friction law are employed in this application.

The following are the joints properties of dam-foundation rock contact interface employed in this simulation: normal stiffness (Knn) equal to 240 GPa/m, and transverse shear stiffness (Ktt) equal to 24 GPa/m. Additionally, the 'no separation' contact model, which allows the sliding of surfaces, is considered in dam-foundation bottom interface. The 'standard' contact model, which allows the sliding and separation of surfaces, is used in dam-foundation side interface.



#### 4. NONLINEAR EARTHQUAKE ANALYSIS OF OUED FODDA DAM

The seismic damage response of the Oued Fodda dam is presented in this study. Nonlinear seismic analyses are performed for the Oued Fodda dam-reservoir-foundation rock system considering the impacts of contact conditions in dam-foundation rock interface and transverse earthquake excitation using 3D finite element models. The smeared crack model based on the Willam and Warnke failure criterion [36] is used to present seismic cracking of dam concrete. The stream direction is subjected to the horizontal component of the 1980 El Asnam seismic replica record with a peak ground acceleration (PGA) of 0.132 g scaled by a factor of 2.5 to obtain a PGA of 0.33 g (Fig. 4), equal roughly to an estimated PGA of the 1980 El Asnam earthquake (M7), which, unfortunately, was not registered.

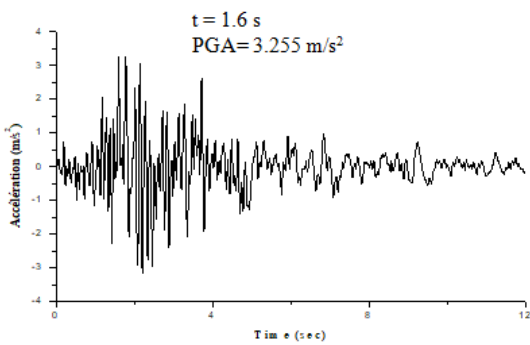


Fig. 4. Horizontal component of 1980 El Asnam earthquake replica record scaled by factor of 2.5

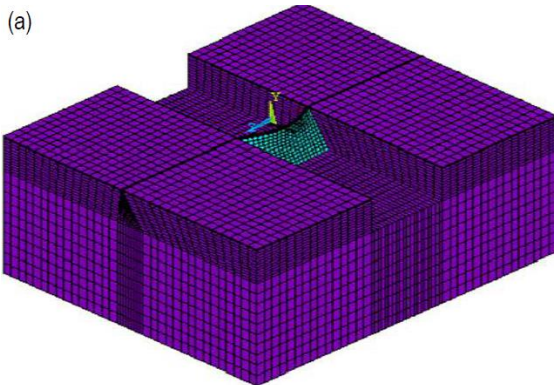
#### 4.1. Modal analysis

The modal analysis results of the first five natural frequencies of the dam-foundation rock system are recapitulated in Table 2 for the adhesive and frictional joints models. The natural frequency values are similar with an average difference of 5.25%, 2.50%, 0.81%, 3.48% and 1.45%, respectively. In general, the natural frequency of free vibration depends upon the mass and stiffness matrix of the dam-foundation rock system, but it is not related to contact conditions between the dam and its foundation.

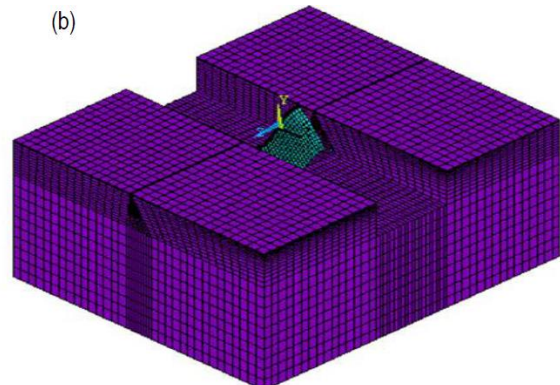
Tab. 2. First five natural frequencies of Oued Fodda dam-foundation rock system

Mode number	Adhesive joints model		Frictional joints model	
	Frequency (Hz)	Period (s)	Frequency (Hz)	Period (s)
1	2.5955	0.3853	2.4395	0.4099
2	2.7924	0.3581	2.7228	0.3673
3	2.8422	0.3518	2.8191	0.3547
4	3.0696	0.3258	2.9629	0.3375
5	3.0930	0.3233	3.0483	0.3281

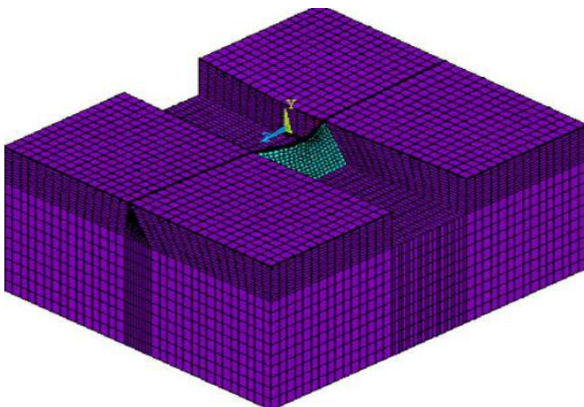
The first three mode shapes of the two studied models are plotted in Fig. 5. As may be seen, the dam can slide along the dam-foundation rock interface in the frictional joints model due to the presence of connection joints at the interface plane.



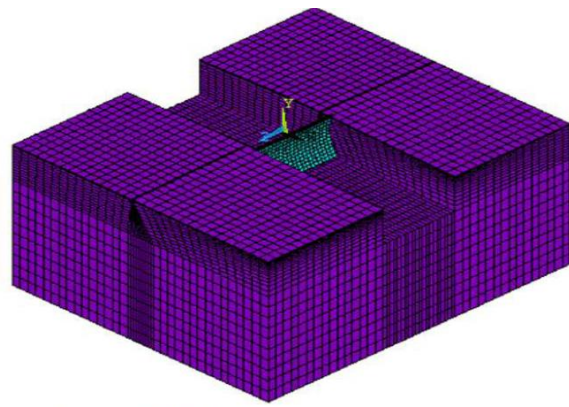
1<sup>st</sup> mode (f = 2.5955 Hz)



1<sup>st</sup> mode (f = 2.4395 Hz)



2<sup>nd</sup> mode (f = 2.7924 Hz)



2<sup>nd</sup> mode (f = 2.7228 Hz)

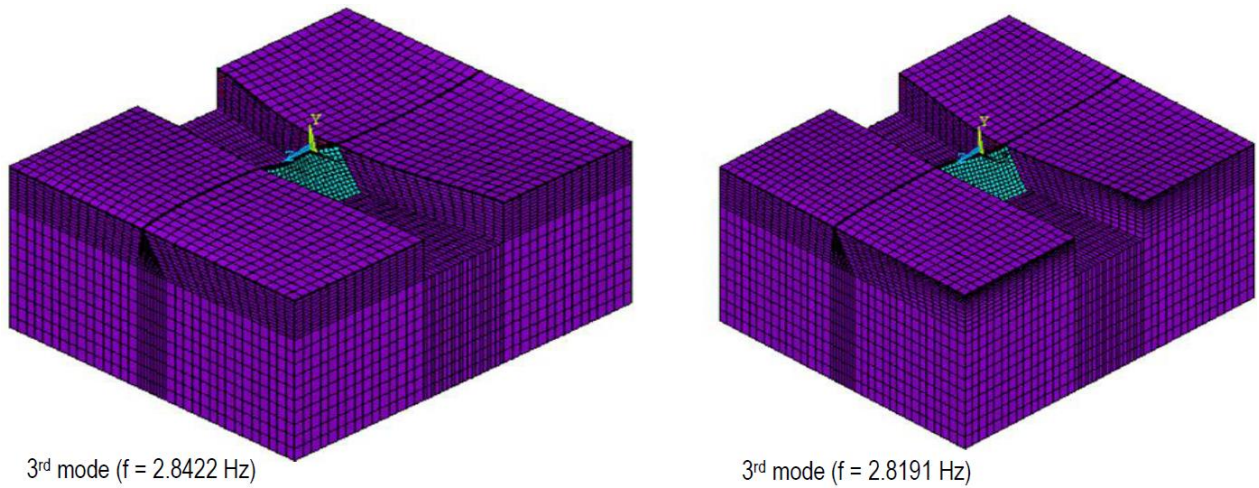


Fig. 5. First three mode shapes of Oued Fodda dam-foundation rock system: (a) adhesive joints model; and (b) frictional joints model

4.2. Dynamic analysis

The repartition of maximum horizontal displacements in the upstream face along the dam crest is presented in Fig. 6 for the adhesive and frictional joints models. As may be seen, the maximum displacements resulting from the frictional joints are smaller than those from the adhesive joints. This reduction in displacement response is due to the dissipation of energy into the interface zone for the frictional joints model when the dam is authorised to slide on its foundation rock. Fig. 7 shows the envelopes of maximum horizontal displacements of the dam during an earthquake for the adhesive and frictional joints models. As can be seen from Fig. 7(b), the dam structure tends to slide along the dam-foundation rock interface, which is known as sliding failure. In general, the sliding failure of a CG dam reduces the deformation response and affects the seismic performance of the dam.

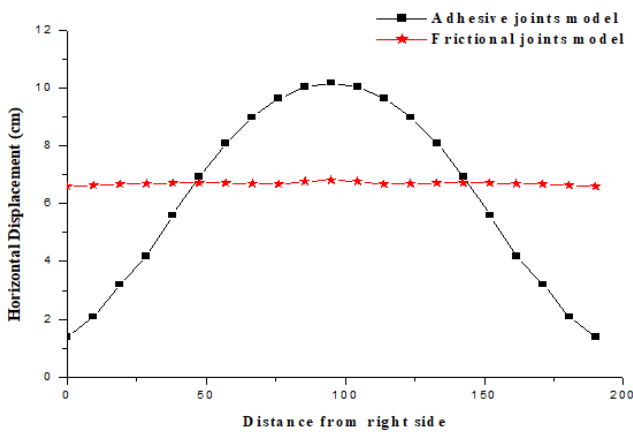


Fig. 6. Distribution of maximum horizontal displacements in upstream face along the dam crest

The time history of horizontal displacement at the upstream middle crest located along the dam central axis is illustrated in Fig. 8 for both of the two joints formulations, in which the maximum displacement at the crest reduces from 10.17 cm for the adhesive joints model to 6.82 cm for the frictional joints model. Fig. 9 represents the time history of horizontal and sliding displacements at the heel and toe located along dam symmetry central axis for the two models of joints.

It is obvious that the time histories of horizontal and sliding displacements for both the toe and heel of the dam are similar to each other, in that the maximum displacement at the heel (or toe) increases from 1.57 cm for the first model to 6.04 cm for the second model. This is explained by the presence of joints along the dam-foundation rock interface, which decrease the stiffness in interface zones, thus leading to sliding of the dam along the interface plane.

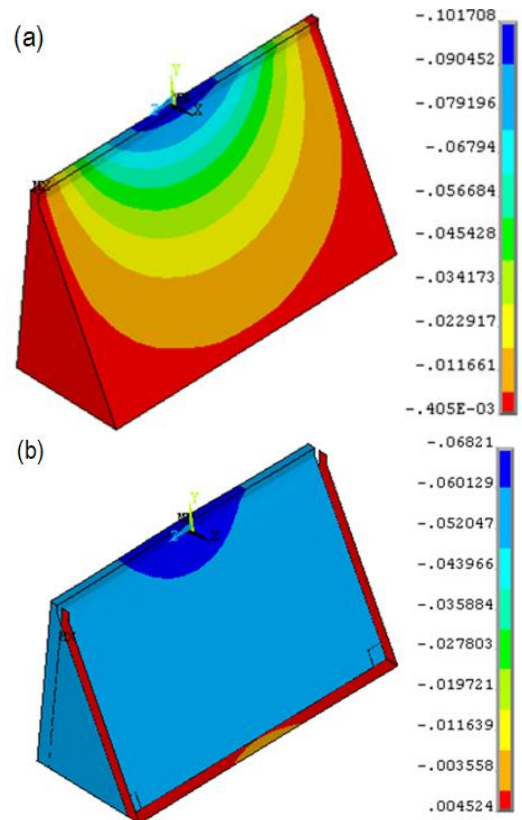
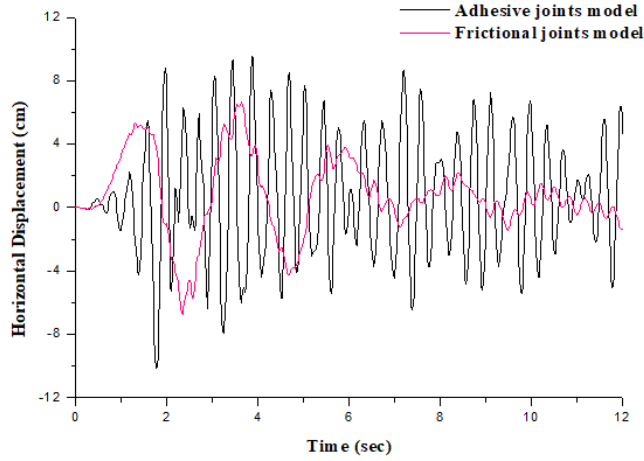


Fig. 7. Envelopes of maximum horizontal displacements for the dam: (a) adhesive joints model; and (b) frictional joints model (Unit: m)

The profiles of final damage in the upstream and downstream faces of the Oued Fodda dam are compared in Figs. 10 and 11, respectively, for the adhesive joints model and the frictional joints model. As can be seen, several damaged elements may appear

due to tension, particularly at right and left upper lateral extremities and middle bottom parts for both upstream and downstream faces in the first model, while a few of them at middle upper parts along dam central axis in the second model due to the sliding failure of the dam, which reduces the amount of maximum tensile stresses in the dam body.



**Fig. 8.** Time history of horizontal displacement at the dam crest for adhesive and frictional joints models

Figs. 12 and 13 depict the evolution process of crack propagation in both of the two faces of the dam under an earthquake. In the first model, the first cracks can appear at middle bottom parts. After that, the cracking occurs at right and left upper lateral extremities and it is observed that the damaged area expands more to grow at middle bottom parts. In the last step, cracks keep growing up at all these parts that the cracks touched. These fractures

may give rise to instability and failure of the dam structure. In the second model, the cracks start at middle upper parts located along dam central axis in both faces. With continuation as well as passage of time, the damaged elements become increasingly vulnerable to complete deterioration, which is definitively attributable to the fact that there is a progressive expansion in the cracked area.

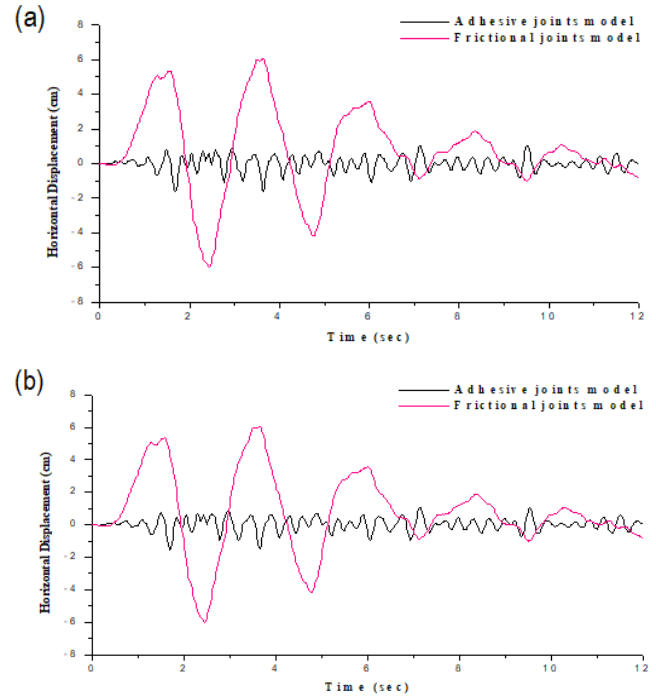


**Fig. 9.** Time history of horizontal and sliding displacements at: (a) heel; and (b) toe of the dam

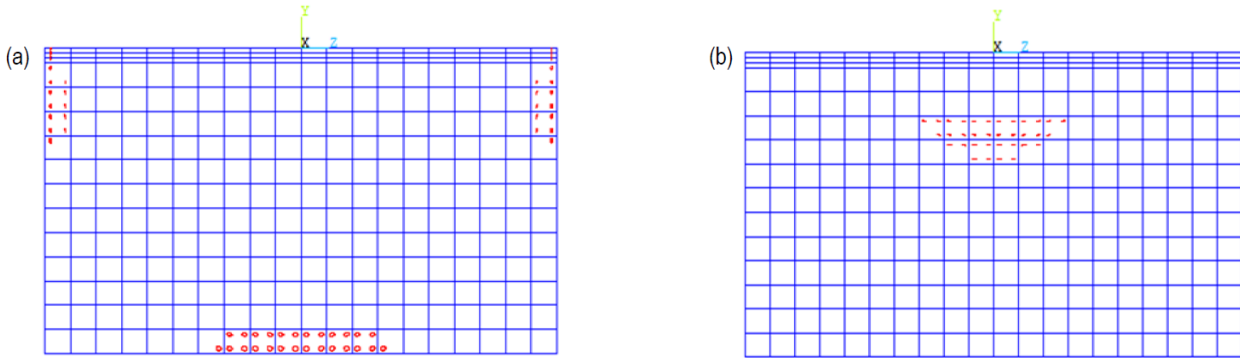


**Fig. 10.** Profiles of final damage in upstream face of Oued Fodda dam: (a) adhesive joints model; and (b) frictional joints model

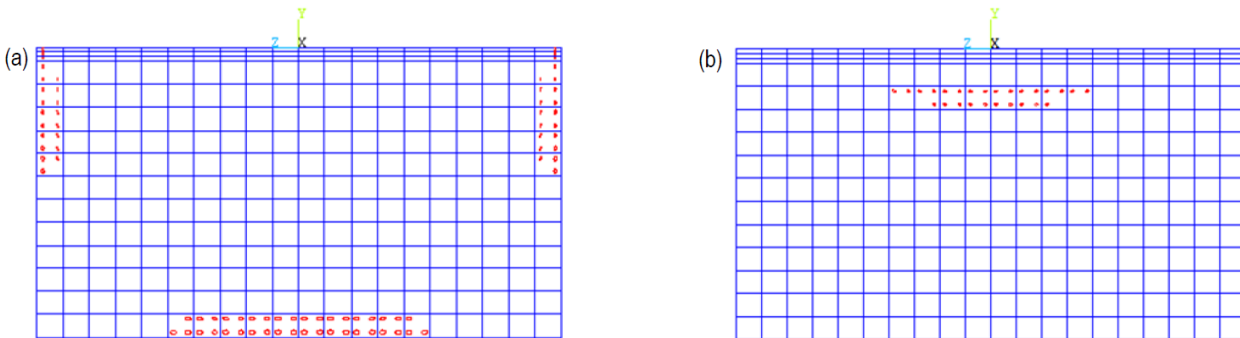


**Fig. 11.** Profiles of final damage in downstream face of Oued Fodda dam: (a) adhesive joints model; and (b) frictional joints model



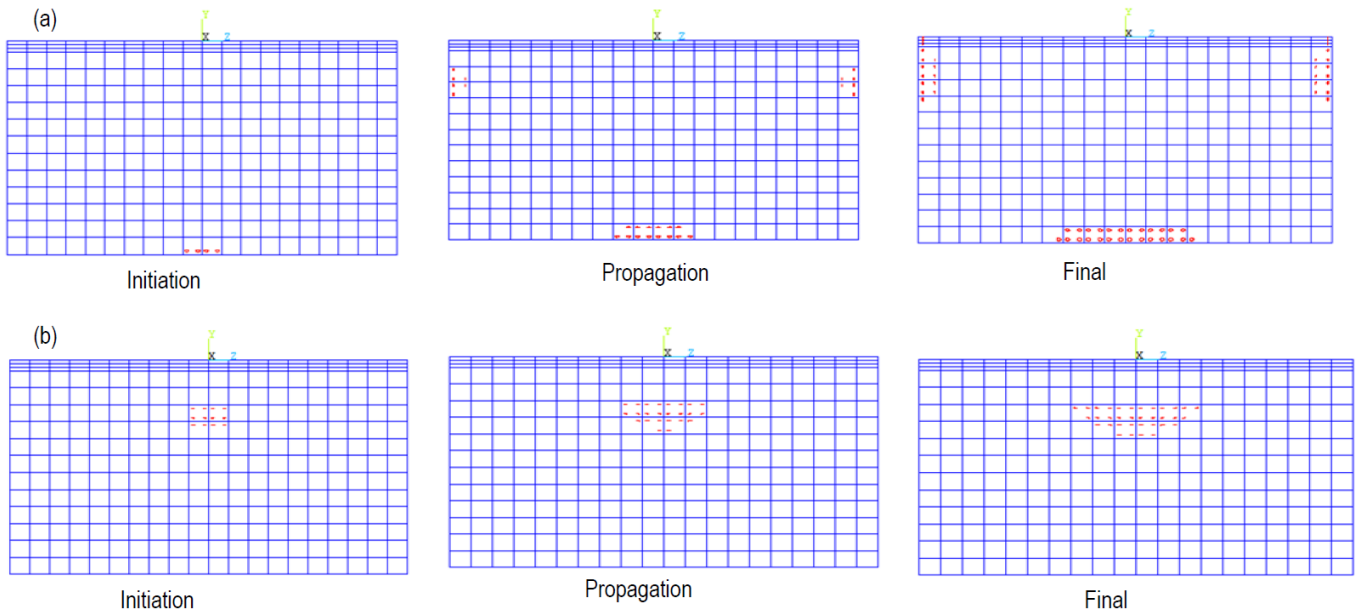


Fig. 12. Process of crack propagation in upstream face of Oued Fodda dam: (a) adhesive joints model; and (b) frictional joints mode

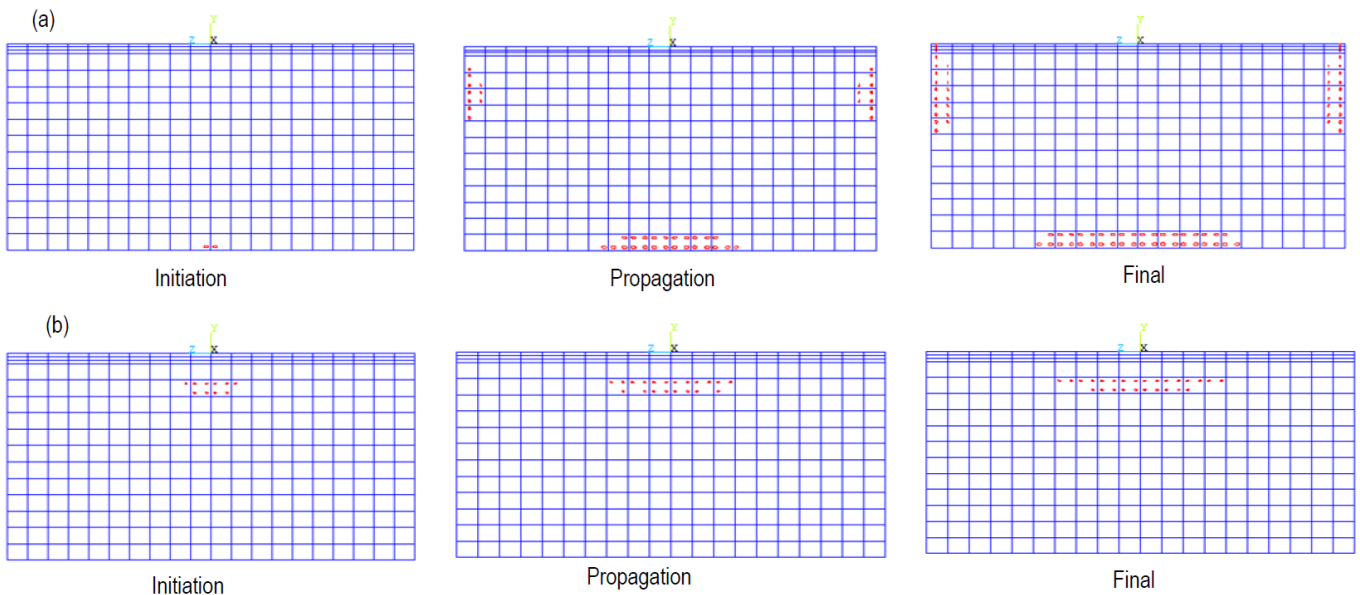


Fig. 13. Process of crack propagation in downstream face of Oued Fodda dam: (a) adhesive joints model; and (b) frictional joints model I

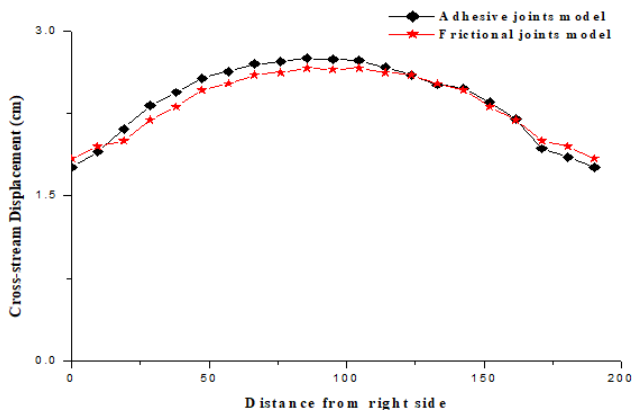
### 5. EFFECTS OF CROSS-STREAM SEISMIC MOVEMENT ON THE DAM DAMAGE RESPONSE

In order to present the effects of both the contact conditions and cross-stream seismic excitation on the cracking response of the CG dam, the Oued Fodda dam-foundation rock system presented in Section 3 is subjected to the 1980 El Asnam earthquake (M7) in a stream-cross direction. The distribution of maximum cross-stream displacements in upstream face along the dam crest is shown in Fig. 14 for the adhesive and frictional joints models. It is observed that the distribution of displacements is generally convergent in the two joints models as the maximum displacement at the middle crest attains a value of 2.81 cm. On the other hand, the envelopes of maximum cross-stream displacements of the dam for the adhesive and frictional joints formulations, depicted in Fig. 15, are also similar to each other with a small difference. This is owing to the fact that the dam related to the frictional joints model cannot slide, except for a very limited sliding at upper

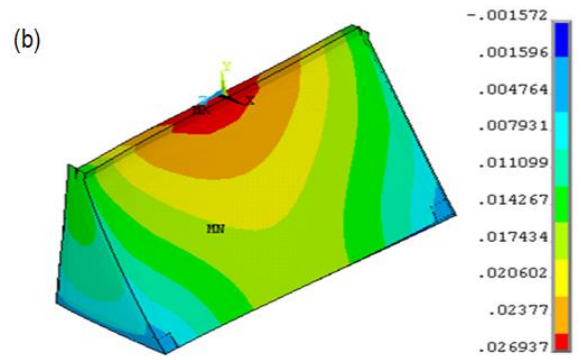
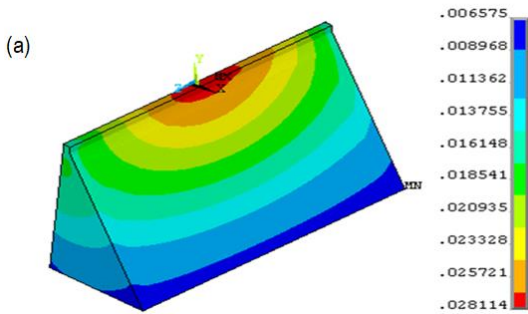
lateral parts, shown in Fig. 15(b), due to the effect of lateral rock blocks located along the dam-foundation right and left side interfaces that prevent the sliding of the dam along the cross-stream direction.

Fig. 16 represents the time history of stream-cross displacement at the upstream middle crest located along dam central axis for both of the two joints models. As indicated in Fig. 16, the displacement time histories are similar to each other. The time history of stream-cross displacement at both heel and toe of the dam is illustrated in Fig. 17. The profiles of final damage in up stream and downstream faces of the Oued Fodda dam under cross-stream earthquake excitation are illustrated in Figs. 18 and 19, respectively. It is observed that the time histories of stream-cross displacement at both heel and toe and the damage profiles for both the adhesive joints and frictional joints models are also similar to each other. In general, the earthquake performances of the dam under the adhesive and frictional joints models are generally similar, and thus the effect of the frictional joints model is

negligible in the case of cross-stream seismic movement. It is also important to note that when the excitation is applied in the inverse direction, the cracks are still the same but the damage profile is inverted.



**Fig. 14.** Distribution of maximum cross-stream displacements in upstream face along the dam crest



**Fig. 15.** Envelopes of maximum cross-stream displacements for the dam: (a) adhesive joints model; and (b) frictional joints model (Unit: m)

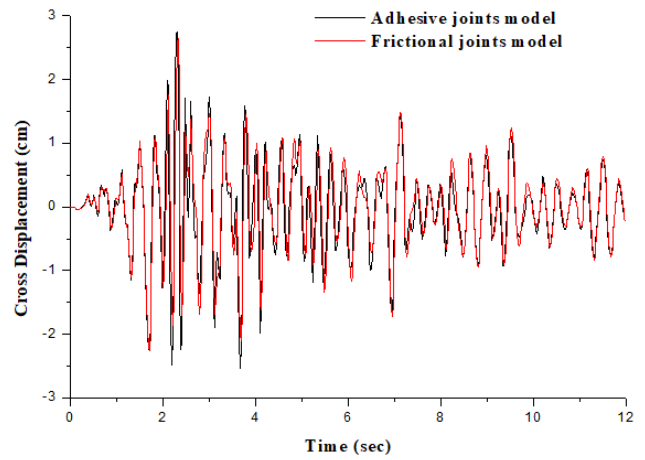


**Fig. 16.** Time history of cross-stream displacement at the dam crest for adhesive and frictional joints models

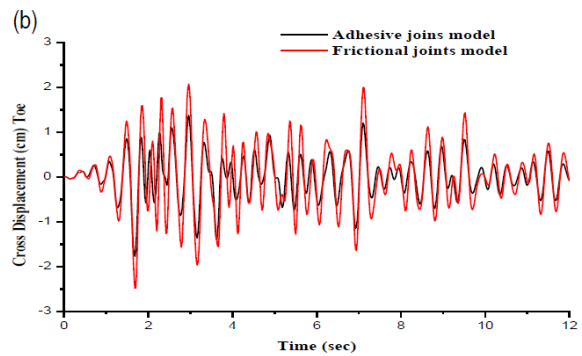
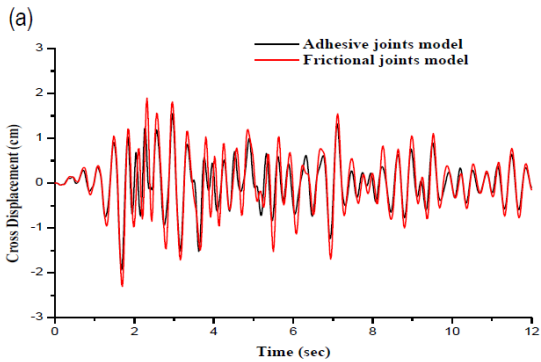


**Fig. 17.** Time history of cross-stream displacements at: (a) heel; and (b) toe of the dam

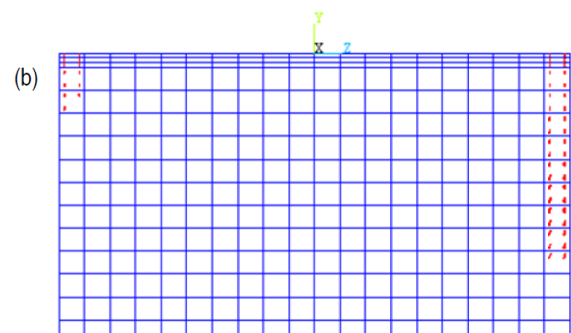
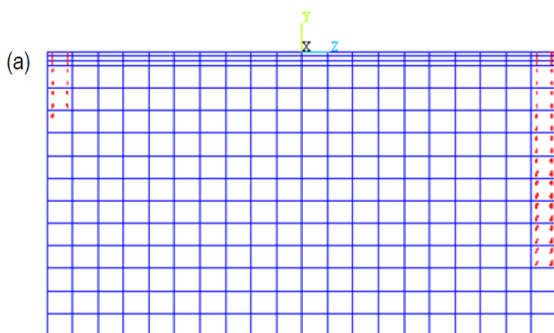


**Fig. 18.** Profiles of final damage in upstream face of Oued Fodda dam: (a) adhesive joints model; and (b) frictional joints model

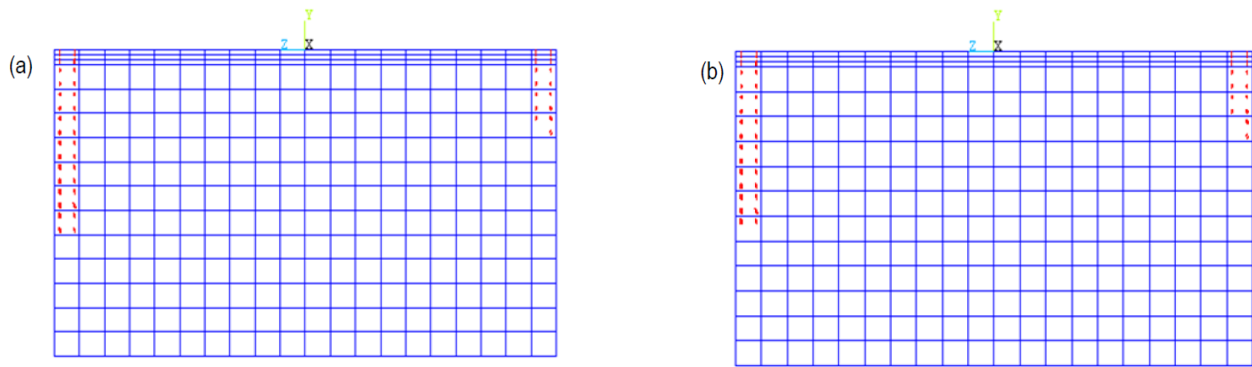


Fig.19. Profiles of final damage in downstream face of Oued Fodda dam: (a) adhesive joints model; and (b) frictional joints model

## 6. CONCLUSIONS

The present study presents the effects of contraction joints and cross-stream seismic excitation of the earthquake damage behaviour of the Oued Fodda dam using 3D finite element analyses. The material and contact nonlinearity are considered in this numerical investigation. We can draw the following conclusions from this study:

1. The nonlinear earthquake performance of the dam depends closely upon the properties of the joints model along the dam-foundation rock interface zone.
2. The frictional joints model can reduce the seismic response and damaged areas in the dam and lead to more stable solutions.
3. It is preferable to use higher tensile strength concrete in the damaged parts to decrease the predicted cracking and reinforce the stability and safety of the dam.
4. Frictional joints formulation may decrease the dam stiffness in interface zones and leads to larger nonlinear analysis for dam-foundation rock system.
5. Material and joints nonlinearity should be considered in dynamic performance analyses of the dam to achieve more reliable results.
6. A more realistic model of dam-foundation system may be obtained considering the frictional joints along dam-foundation rock interface.
7. Seismic interaction between the dam and foundation rock produced by cross-stream earthquake movement can result in significant damage to the dam.

## REFERENCES

1. Mridha S, Maity D. Experimental investigation on nonlinear dynamic response of concrete gravity dam-reservoir system. *Engineering Structures*. 2014;80:289-97. Available from: <https://doi.org/10.1016/j.engstruct.2014.09.017>
2. Valamanesh V, Estekanchi HE, Vafai A, Ghaemian M. Application of the endurance time method in seismic analysis of concrete gravity dams. *Scientia Iranica*. 2011;18(3):326-37. Available from: <https://doi.org/10.1016/j.scient.2011.05.039>
3. Hariri-Ardebili MA. Impact of foundation nonlinearity on the crack propagation of high concrete dams. *Soil Mechanics and Foundation Engineering*. 2014;51(2):72-82.
4. Pirooznia A, Moradloo AJ. Seismic fracture analysis of concrete arch dams incorporating the loading rate dependent size effect of concrete. *Structural Engineering and Mechanics, An Int'l Journal*. 2021;79(2):169-98. Available from: <https://doi.org/10.12989/sem.2021.79.2.169>
5. Lee J, Fenves GL. A plastic-damage concrete model for earthquake analysis of dams. *Earthquake engineering & structural dynamics*. 1998;27(9):937-56. Available from: [https://doi.org/10.1002/\(SICI\)1096-9845\(199809\)27:9<937::AID-EQE764>3.0.CO;2-5](https://doi.org/10.1002/(SICI)1096-9845(199809)27:9<937::AID-EQE764>3.0.CO;2-5)
6. Omid O, Valliappan S, Lotfi V. Seismic cracking of concrete gravity dams by plastic-damage model using different damping mechanisms. *Finite Elements in Analysis and Design*. 2013;63:80-97. Available from: <https://doi.org/10.1016/j.finel.2012.08.008>
7. Wang G, Wang Y, Lu W, Yu M, Wang C. Deterministic 3D seismic damage analysis of Guandi concrete gravity dam: A case study. *Engineering Structures*. 2017;148:263-76. Available from: <https://doi.org/10.1016/j.engstruct.2017.06.060>
8. Wang G, Lu W, Zhang S, Wang G, Lu W, Zhang S. Comparative analysis of nonlinear seismic response of concrete gravity dams using XFEM and CDP model. *Seismic Performance Analysis of Concrete Gravity Dams*. 2021;57:11-51. Available from: [https://doi.org/10.1007/978-981-15-6194-8\\_2](https://doi.org/10.1007/978-981-15-6194-8_2)
9. Ghrib F, Tinawi R. An application of damage mechanics for seismic analysis of concrete gravity dams. *Earthquake Eng Struct Dynam*. 1995;24(2):157-73. Available from: <https://doi.org/10.1002/eqe.4290240203>
10. Guanglun W, Pekau OA, Chuhan Z, Shaomin W. Seismic fracture analysis of concrete gravity dams based on nonlinear fracture mechanics. *Engineering Fracture Mechanics*. 2000;65(1):67-87. Available from: [https://doi.org/10.1016/S0013-7944\(99\)00104-6](https://doi.org/10.1016/S0013-7944(99)00104-6)
11. Wang G, Wang Y, Lu W, Zhou C, Chen M, Yan P. XFEM based seismic potential failure mode analysis of concrete gravity dam-water-foundation systems through incremental dynamic analysis. *Eng Struct*. 2015;98:81-94. Available from: <https://doi.org/10.1016/j.engstruct.2015.04.023>
12. Zhao E, Li B. Evaluation method for cohesive crack propagation in fragile locations of RCC dam using XFEM. *Water*, 2020;13(1):58. Available from: <https://doi.org/10.3390/w13010058>
13. Haghani M, Neya BN, Ahmadi MT, Amiri JV. Combining XFEM and time integration by  $\alpha$ -method for seismic analysis of dam-foundation-reservoir. *Theoretical and Applied Fracture Mechanics*. 2020;109:102-22. Available from: <https://doi.org/10.1016/j.tafmec.2020.102752>
14. Haghani M, Neya BN, Ahmadi MT, Amiri JV. A new numerical approach in the seismic failure analysis of concrete gravity dams using extended finite element method. *Engineering Failure Analysis*. 2022;132:105835. Available from: <https://doi.org/10.1016/j.engfailanal.2021.105835>
15. Wang Y, Waisman H. From diffuse damage to sharp cohesive cracks: a coupled XFEM framework for failure analysis of quasi-brittle materials. *Comput Methods Appl Mech Eng*. 2016;299:57-89. Available from: <https://doi.org/10.1016/j.cma.2015.10.019>
16. Ouzandja D, Tiliouine B. Effects of dam-foundation contact conditions on seismic performance of concrete gravity dams. *Arabian Journal for Science and Engineering*. 2015;40(11):3047-56. Available from: <https://doi.org/10.1007/s13369-015-1770-2>

17. Ouzandja D. (2016). Effets des conditions de contact à l'interface barrage-fondation sur la performance sismique des barrages-poids en béton. Thèse de doctorat, Ecole Nationale Polytechnique (E.N.P), Alger, Algérie.
18. Saichi T, Renaud S, Bouaanani N, Miquel B. Effects of rock foundation roughness on the sliding stability of concrete gravity dams based on topographic surveys. *Journal of Engineering Mechanics*. 2019;145(7):04019043. Available from: [https://doi.org/10.1061/\(ASCE\)EM.1943-7889.0001604](https://doi.org/10.1061/(ASCE)EM.1943-7889.0001604)
19. Gharibdoust A, Aldemir A, Binici B. Seismic behaviour of roller compacted concrete dams under different base treatments. *Structure and Infrastructure Engineering*. 2020;16(2):355-66. Available from: <https://doi.org/10.1080/15732479.2019.1661500>
20. Sen U, Okeil AM. Effect of biaxial stress state on seismic fragility of concrete gravity dams. *Earthquakes and Structures*. 2020;18(3):285-96. Available from: <https://doi.org/10.12989/eas.2020.18.3.285>
21. Ouzandja D, Messaad M. Seismic response analysis of concrete gravity dams considering base sliding. 1st International Conference on Geotechnical, Structural and Advanced Materials Engineering 2022.
22. Azmi M, Paultre p. Three-dimensional analysis of concrete dams including contraction joint non-linearity. *Eng Struct*. 2002;24(6):757-71. Available from: [https://doi.org/10.1016/S0141-0296\(02\)00005-6](https://doi.org/10.1016/S0141-0296(02)00005-6)
23. Dowdell DJ, Fan BH. Practical aspects of engineering seismic dam safety case study of a concrete gravity dam. *Proc - 13th World Conference on Earthquake Engineering* 2004.
24. Brand B, Dollar DA, Hasan H, Hernandez L, Nuss LK, Rowell R, Wallace, WA. Selecting analytic tools for concrete dams to address key events along potential failure mode paths. FEMA P-1016, Federal Emergency Management Agency. 2014.
25. New Zealand Society on Large Dams (NZSOLD). *New Zealand Dam Safety Guidelines*. 2015.
26. Wang H, Feng M, Yang H. Seismic nonlinear analyses of a concrete gravity dam with 3D full dam model. *Bull Earthq Eng*. 2012;10(6):1959-77. Available from: <https://doi.org/10.1007/s10518-012-9377-4>
27. Kartal ME. Three-dimensional earthquake analysis of roller compacted concrete dams. *Nat Hazards Earth Syst Sci*. 2012;12:2369-88. Available from: <https://doi.org/10.5194/nhess-12-2369-2012>
28. Wang JT, Lv DD, Jin F, Zhang, CH. Earthquake damage analysis of arch dams considering dam-water-foundation interaction. *Soil Dynamics and Earthquake Engineering*. 2013;49:64-74. Available from: <https://doi.org/10.1016/j.soildyn.2013.02.006>
29. Yilmazturk SM, Arici Y, Binici B. Seismic assessment of a monolithic RCC gravity dam including three dimensional dam-foundation-reservoir interaction. *Eng Struct*. 2015;100:137-48. Available from: <https://doi.org/10.1016/j.engstruct.2015.05.041>
30. Ouzandja D, Tiliouine B, Belharizi M, Kadri M. Three-dimensional nonlinear seismic response of oued fodda concrete gravity dam considering contact elements at dam-reservoir interaction interface. *Asian Journal of Civil Engineering (bhrc)*. 2017;18(6):977-92.
31. Omid O, Lotfi V. Seismic plastic-damage analysis of mass concrete blocks in arch dams including contraction and peripheral joints. *Soil Dynamics and Earthquake Engineering*. 2017;95:118-37.
32. Liang H, Tu J, Guo S, Liao J, Li D, Peng S. Seismic fragility analysis of a High Arch Dam-Foundation System based on seismic instability failure mode. *Soil Dynamics and Earthquake Engineering*. 2020;130:105981.
33. Ftima MB, Lafrance S, Léger P. Three-dimensional modelling of shear keys in concrete gravity dams using an advanced grillage method. *Water Science and Engineering*. 2020;13(3):223-32.
34. Khassaf SI, Chkheiw AH, Jasim MA. Effect of contraction joints on structural behavior of double curvature concrete dam subject to dynamic loading. *IOP Conference Series: Materials Science and Engineering*. 2020;888(1):012026. Available from: <https://doi.org/10.1088/1757-899X/888/1/012026>
35. Daneshyar A, Ghaemian M. Seismic analysis of arch dams using anisotropic damage-plastic model for concrete with coupled adhesive-frictional joints response. *Soil Dynamics and Earthquake Engineering*. 2019;125:105735. Available from: <https://doi.org/10.1016/j.soildyn.2019.105735>
36. Willam KJ, Warnke ED. Constitutive model for the triaxial behavior of concrete. *Proc - International Association for Bridge and Structural Engineering* 1975;19:1-30.
37. Westergaard HM. Water pressures on dams during earthquake. *Trans. ASCE*. 1933;98(2): 418-33. Available from: <https://doi.org/10.1061/TACEAT.0004496>
38. Drucker DC, Prager W. Soil mechanics and plastic analysis of limit design. *Q. Appl. Math*. 1952;10(2):157-65.
39. ANSYS. *Theory user's manual*. Swanson Analysis Systems Inc., Houston, PA, USA, 2018.

 Djamel Ouzandja:  <https://orcid.org/0000-0002-6152-8461>

 Amina Tahar Berrabah:  <https://orcid.org/0000-0003-2904-8342>


This work is licensed under the Creative Commons BY-NC-ND 4.0 license.



## SOLUTIONS OF THE NONLINEAR EVOLUTION PROBLEMS AND THEIR APPLICATIONS

Muhammad AMIR\*, Jamil Abbas HAIDER\*, Jamshaid UI RAHMAN\*, Asifa ASHRAF\*\*

\*Abdus Salam School of Mathematical Sciences, Government College University, Lahore 54600, Pakistan

\*\*Department of Mathematics, University of Management and Technology Lahore, Pakistan

[muhammadamir28295@gmail.com](mailto:muhammadamir28295@gmail.com), [jamilabbashaider@gmail.com](mailto:jamilabbashaider@gmail.com), [jamshaidrahman@gmail.com](mailto:jamshaidrahman@gmail.com), [asifaashraf9@gmail.com](mailto:asifaashraf9@gmail.com)

received 7 December 2022, revised 1 February 2023, accepted 26 February 2023

**Abstract:** In this article, a well-known technique, the variational iterative method with the Laplace transform, is used to solve nonlinear evolution problems of a simple pendulum and mass spring oscillator, which represents the duffing equation. In the variational iteration method (VIM), finding the Lagrange multiplier is an important step, and the variational theory is often used for this purpose. This paper shows how the Laplace transform can be used to find the multiplier in a simpler way. This method gives an easy approach for scientists and engineers who deal with a wide range of nonlinear problems. Duffing equation is solved by different analytic methods, but we tackle this for the first time to solve the duffing equation and the nonlinear oscillator by using the Laplace-based VIM. In the majority of cases, Laplace variational iteration method (LVIM) just needs one iteration to attain high accuracy of the answer for linearization and discretization, or intensive computational work is needed. The convergence criteria of this method are efficient as compared with the VIM. Comparing the analytical VIM by Laplace transform with MATLAB's built-in command Simulink that confirms the method's suitability for solving nonlinear evolution problems will be helpful. In future, we will be able to find the solution of highly nonlinear oscillators.

**Keywords:** Laplace variational iteration method, nonlinear problems, duffing equation, simple pendulum, mass and spring oscillator, Simulink

### 1. INTRODUCTION

The theory of nonlinear systems can be used to solve problems in economics, chemistry, astronomy, physiology of nerves, start of turbulence, control of heartbeats, electronic circuits, cryptography, secure communications and many other fields. In our modern world, the majority of systems are inherently nonlinear [1-2]. A collection of nonlinear equations known as a nonlinear system may be algebraic, differential, integral, fractional or a combination of these. A nonlinear system has been utilized to describe a wide range of phenomena throughout the last few decades in the physical, social and life sciences. In natural phenomena, nonlinear dynamical systems, which describe changes in variables over time, are sometimes chaotic, unpredictable or illogical. Nonlinear oscillations play a significant role in nonlinear systems that arise in a variety of engineering applications and our daily lives.

There are many methods to solve nonlinear problems, such as the Homotopy perturbation method (HPM) [3], which is used to solve attachment oscillations that occur in nanotechnology. The nonlinear oscillation system was studied using the Akbari Ganji method [4]. The energy balance method (EBM) [5] investigated the behavior of CNT nano resonators. The He-Elzaki method [6] is used to study the biological population model. The variational iteration method (VIM)—the Pade method [7]—is applied to solve a nonlinear oscillator with cubic and restoring forces. He's multiple-scale method [8] solved nonlinear vibrations. He's parameter-expansion method [9] solved the oscillation of the mass connected to the elastic wire. The damping duffing equation is solved using the multistage differential transform method [10]. Nonlinear one-dimensional K-dV equation arising in plasma physics is solved by using the auxiliary equation mapping method [11]. The

Zakharov–Kuznetsov (ZK) equation is an isotropic nonlinear evolution equation; the stability analysis of two-dimensional ZK equation is derived by applying the extended direct algebraic technique [12]. The solution for geophysical Korteweg–de Vries equation (GKdVE) is found with the help of the Hirota bilinear method (HBM) [13]. Marin et al. [14] solved mixed problems in thermoelasticity of type III for Cosserat media. The most famous model of nonlinear sciences namely  $(2 + 1)$ -dimensional nonlinear spin dynamics of Heisenberg ferromagnetic spin chains (HFSC) model for the evaluation of optical travelling waves by employing unified method (UM) [15]. The reciprocal impacts of Young moduli and mass density of the wave propagation behaviours of functionally graded (FG) nanobeams are investigated by Ebrahimi et al. [16].

In science and mathematics, a nonlinear system is the one where the change in output is not the same as the change in input. There is no well-established method for dealing with all types of nonlinear problems. The VIM was proposed in 1998 [17] and is widely used to solve a variety of nonlinear problems [18]. The major goal of this method is to build a correction function by using a general Lagrange multiplier that is properly chosen so that its correction solution is better than the initial trial function. A large number of results based on the VIM fail to explain it; in many situations, the integral of the correction function is convolution; as a result, a modification of the Laplace transform should be used. The Lagrange multiplier is a key part of the VIM. To do this, variational theory is used. The Lagrange multiplier is so much simpler to identify with the Laplace variational technique than with the variational theory [19].

Nonlinearity arising in the nature, science and technology does not hand easily. A number of difficulties are faced during

finding the solutions of nonlinear phenomena. The number of the above discussed exact solution methods has no capacity to deal all kind of nonlinear physical problems. Number of the computational methods used to solve the nonlinear dynamical problems [20-22] but analytical approaches are good as compared to the numerical approach because the physics of the problem understand easily in the case analytical and semi-analytical methods. Some nonlinear problems do not handle easily because the factor stability is much important. The identification of the Lagrange multiplier in the technique requires the knowledge of the variational theory, and the complex identification process might hinder applications of the method to practical problems. This paper suggests using the Laplace transform, which can be found in all math books, to make the process of identifying things easier. In this article, a Laplace variational iteration technique, combined with the VIM and the Laplace transform, presents a numerical solution to the duffing equation by using MATLAB's built-in command Simulink that confirms suitability for solving nonlinear evolution problems.

**2. METHOD SUMMARY**

Consider a general nonlinear oscillator equation is given as follows:

$$v''(t) + f(v) = 0 \tag{2.1}$$

Initial conditions are as follows:

$$v(0) = A, v'(0) = 0$$

Eq. (2.1) can be rewrite as follows:

$$v'' + \omega^2 v + h(v) = 0 \tag{2.2}$$

where  $\omega$  is the frequency which can be calculated as follows:

$$h(v) = f(v) - \omega^2 v$$

The correctional functional for Eq. (2.2) is defined as follows for the VIM:

$$v_{n+1}(t) = v_n(t) + \int_0^t \lambda(t, \eta) [v_n''(\eta) + \omega^2 v_n(\eta) + h^{\sim}(u_n)] d\eta, \quad n = 0, 1, 2, \dots \tag{2.3}$$

It is possible to derive the generic Lagrange multiplier  $\lambda$  from the immobile requirements of Eq. (3) with respect to  $v_n$  by using variational theory [17]. The letter h stands for the restricted variant, and the number n after it means the nth approximation. Here, the Lagrange multiplier written is this form [22]:

$$\lambda = \lambda(t - \eta)$$

corrective functional employed in Eq. (2.3) is essentially the convolution; therefore, the Laplace transform is applied. Then, Laplace transform is applied to both sides of the Eq. (2.3). In this form, the correctional functional will be converted as follows:

$$\mathcal{L}[v_{n+1}(t)] = \mathcal{L}[v_n(t)] + \mathcal{L}\left[\int_0^t \lambda(t - \eta) [v_n''(\eta) + \omega^2 v_n(\eta) + h^{\sim}(u_n)] d\eta\right] \tag{2.4}$$

$$\begin{aligned} &= \mathcal{L}[v_n(t)] + \mathcal{L}[\lambda(t) * (v_n''(\eta) + \omega^2 v_n(\eta) + h^{\sim}(u_n))] \\ &= \mathcal{L}[v_n(t)] + \mathcal{L}[\lambda(t)] \mathcal{L}[(v_n''(\eta) + \omega^2 v_n(\eta) + h^{\sim}(u_n))] \\ &= \mathcal{L}[v_n(t)] + \mathcal{L}[\lambda(t)] [(s^2 + \omega^2) \mathcal{L}[v_n(t)] - s v_n(0) - v_n'(0) + \mathcal{L}[h^{\sim}(u_n)]] \end{aligned} \tag{2.5}$$

The value of  $\lambda$  can be determined by taking Eq. (2.5) as a stationary one with respect to  $v_n(t)$ :

$$\frac{\delta}{\delta v_n} \mathcal{L}[v_{n+1}(t)] = \frac{\delta}{\delta v_n} \mathcal{L}[v_n(t)] + \frac{\delta}{\delta v_n} \mathcal{L}[\lambda(t)] [(s^2 + \omega^2) \mathcal{L}[v_n(t)] - s v_n(0) - v_n'(0) + \mathcal{L}[h^{\sim}(u_n)]]$$

$$\{1 + \mathcal{L}[\lambda(t)](s^2 + \omega^2)\} \frac{\delta}{\delta v_n} \mathcal{L}[v_n(t)] = 0$$

From above eq., we get the following equation:

$$\mathcal{L}[\lambda(t)] = \frac{1}{s^2 + \omega^2} \tag{2.6}$$

From the above calculation, we suppose that

$$\frac{\delta}{\delta v_n} \mathcal{L}[h^{\sim}(u_n)] = 0$$

Applying the inverse Laplace transform to the Eq. (2.6), we get the following equation:

$$\lambda(t) = -\frac{1}{\omega} \sin \omega t$$

By using Eq. (2.4), the required formula becomes in this form:

$$\begin{aligned} \mathcal{L}[v_{n+1}(t)] &= \\ \mathcal{L}[v_n(t)] - \frac{1}{\omega} \mathcal{L} \left[ \int_0^t \sin \omega(t - \eta) [v_n''(\eta) + \omega^2 v_n(\eta) + h^{\sim}(v_n)] d\eta \right] \end{aligned}$$

$$\begin{aligned} \mathcal{L}[v_{n+1}(t)] &= \mathcal{L}[v_n(t)] - \\ &\frac{1}{\omega} \mathcal{L}[\sin \omega t] [v_n''(\eta) + \omega^2 v_n(\eta) + h^{\sim}(v_n)] \end{aligned} \tag{2.7}$$

As a result, the Lagrange multiplier may be found considerably more quickly than with variational theory.

**3. APPLICATIONS**

Duffing's equation is described in Section 3 where it is provided an example of nonuniformity arising from the occurrence of secular terms. We will see how the asymptotic expansion of the solution of Duffing's equation can be rendered uniform by the laplace variational iteration method (LVIM) technique. In the following paper, we will see how it arises in the description of two different mechanical systems. It also governs certain electrical systems. It is an example of a class of nonlinear oscillators which we will study in some detail. The variable v can represent a variety of quantities such as an angle of oscillation, the deformation of an elastic system, a current or a voltage. The independent variable, t, is time.

This section thoroughly examines three distinct practical examples of nonlinear oscillators.

**3.1. Mathematical modeling of the simple pendulum**

Fig. (1.1) shows a mass M attached by a rod having length L at point A. The mass M oscillates in a vertical direction due to gravity. The length of the rod is connected to a fixed point, and its weight is negligible. The force of gravity acts on the mass and tension in the rod. The tangential component of the arc of the circle on which the mass moves is driven by the force —  $Mg \sin \theta$ . A particle travelling on a circle with fixed radius

experiences tangential acceleration, which equals  $L\left(\frac{d^2\theta}{dT^2}\right)$  and Newton's second law holds the governing Eq. [23]:

$$ML \frac{d^2\theta}{dT^2} = -Mg \sin\theta \tag{3.1.1}$$

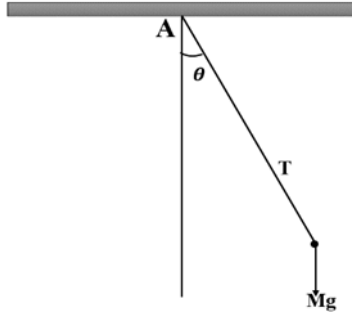


Fig.1. Motion of simple pendulum

Consider that the pendulum is lifted from static position when  $\theta = \theta_0$  at  $T=0$ . The angle of oscillation is  $v = \frac{\theta}{\theta_0}$ , and the parameter related to the frequency is  $\Omega = \sqrt{\frac{g}{L}}$ , the governing equation can be written as follows:

$$\frac{d^2v}{dT^2} = -\Omega^2 \frac{\sin(\theta_0 v)}{\theta_0} \tag{3.1.2}$$

with the initial conditions  $v = 1$  and  $\frac{dv}{dT} = 0$  when  $T=0$

If  $\theta_0$  is very small, a truncated Maclaurin can be used to approximate the sine term. When two terms are included in the expansion, we get the following:

$$\frac{d^2v}{dT^2} = -\Omega^2 \left(v - \frac{\theta_0^2 v^3}{6}\right) \tag{3.1.3}$$

Developing nondimensional time  $t = \Omega T$  and the parameter  $\varepsilon = \frac{\theta_0^2}{6}$  results to the Duffing's equation which is non-linear in nature [23].

$$v'' + v - \varepsilon v^3 = 0 \tag{3.1.4}$$

With initial condition:

$$v(0) = 1, v'(0) = 0$$

The general nonoscillator form of the Eq. (1) is given as follows:

$$v'' + \omega^2 v + h(v) = 0$$

where  $h(v) = -\omega^2 v - v'' - v + \varepsilon v^3$

The correctional functional is written as follows:

$$\begin{aligned} \mathcal{L}[v_{n+1}(t)] &= \mathcal{L}[v_n(t)] + \mathcal{L}\left[\int_0^t -\frac{1}{\omega} \sin\omega(t-\eta)[v_n''(\eta) + \omega^2 v_n(\eta) + h(v_n)] d\eta\right] \\ \mathcal{L}[v_{n+1}(t)] &= \mathcal{L}[v_n(t)] - \frac{1}{\omega} \mathcal{L}[\sin\omega t] \mathcal{L}[v_n'' + v_n - \varepsilon v_n^3] \end{aligned} \tag{3.1.5}$$

putting  $n = 0$  we have,

$$\mathcal{L}[v_1(t)] = \mathcal{L}[v_0(t)] - \frac{1}{\omega} \mathcal{L}[\sin\omega t] \mathcal{L}[v_0'' + v_0 - \varepsilon v_0^3] \tag{3.1.6}$$

Assume the initial solution is  $v_0(t) = A \cos\omega t$ ,

$$[v_1 \mathcal{L}(t)] = \mathcal{L}[A \cos\omega t] - \frac{1}{\omega} \mathcal{L}[\sin\omega t] \mathcal{L}[-A\omega^2 \cos\omega t + A \cos\omega t - \frac{\varepsilon A^3}{4} (\cos 3\omega t + 3 \cos\omega t)]$$

After some calculations, above expression is written as follows:

$$\begin{aligned} \mathcal{L}[v_1(t)] &= \mathcal{L}[A \cos\omega t] - \frac{1}{\omega} \left(-A\omega^2 + A - \frac{3\varepsilon A^3}{4}\right) \mathcal{L}[\sin\omega t] \mathcal{L}[\cos\omega t] + \frac{\varepsilon A^3}{4\omega} \mathcal{L}[\sin\omega t] \mathcal{L}[\cos 3\omega t] \end{aligned} \tag{3.1.7}$$

Taking the inverse Laplace transform to the Eq. (3.1.7), we get the first-order approximate results in this form:

$$v_1(t) = A \cos\omega t - \frac{1}{\omega} \left(-A\omega^2 + A - \frac{3\varepsilon A^3}{4}\right) \left(\frac{1}{2} t \sin\omega t\right) + \frac{1}{\omega} \left(\frac{\varepsilon A^3}{4}\right) \left(\frac{1}{8\omega} (\cos\omega t - \cos 3\omega t)\right) \tag{3.1.8}$$

For no secular term in Eq. (3.1.8), we have the following equation:

$$-\frac{1}{\omega} \left(-A\omega^2 + A - \frac{3\varepsilon A^3}{4}\right) = 0 \tag{3.1.9}$$

This results in the expression for the system's angular frequency.

$$\omega = \sqrt{1 - \frac{3\varepsilon A^2}{4}} \tag{3.1.10}$$

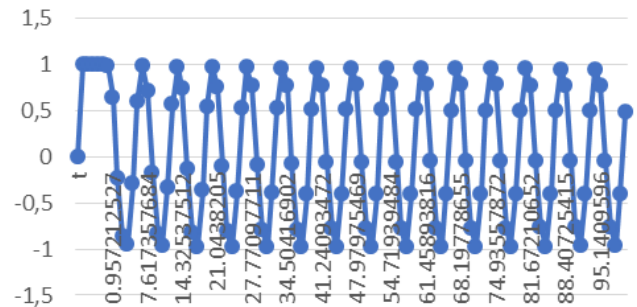


Fig. 2. Numerical results for simple pendulum obtained by Simulink

Mathematical modelling of the simple pendulum whose results are compared with MATLAB built-in command Simulink is shown in Figs 2, 3, 5, 7, and 8. Model-based design is an approach that market-leading firms use to revolutionize the creation of complex systems. This approach involves the systematic use of models throughout the entire process with the assistance of built-in tools from MATLAB. Model-based systems engineering (MBSE) refers to the process of applying models in order to support the entire lifespan of a system. The development process can be bridged with Simulink from requirements and system architecture all the way to the precise component design, implementation and testing of the entire system. The solution plots for all discussed problems are also shown in Figures 4 and 6. The graphical depiction of the general function is known as a sine wave. The sine wave can be recognised by its signature "W" shape, which indicates that it oscillates in a periodic and uniform manner both above and below 0. The sine function is a type of trigonometric function that maps the set of all nonnegative real numbers to the interval  $[-1, 1]$ . This means that the sine function accepts as an input any non-negative

real number and returns output as a value that falls somewhere in the range of  $[-1,1]$ . In the modelling of periodic occurrences and processes that adhere to recognizable cyclical patterns, the sine function and sine waves are two important building blocks.

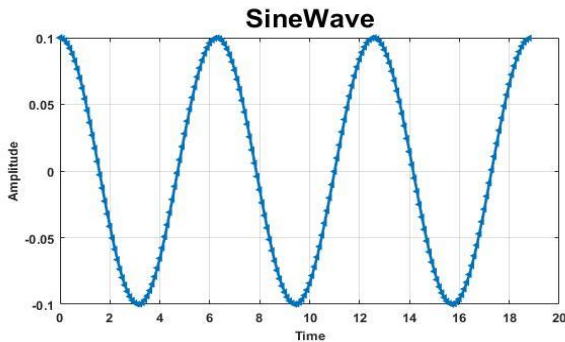


Fig.3. Sinewave plot for the solution of the Duffing equation of simple pendulum against  $\varepsilon = 0.18, A = 0.1$

### 3.2. Mathematical modelling of a mass and spring oscillator

Suppose a mass  $M$  is attached to the fixed ends  $A$  and  $B$ . Each spring's natural length is  $L$ , and its spring constant is  $\Lambda$ . The distance between  $A$  and  $B$  is  $2H$ , where  $H > L$ . The mass is released from  $AB$  by a perpendicular distance  $X_0$ . The mass swings along a path perpendicular to the point  $AB$ . The spring forces  $F$  fluctuate linearly with the extension while gravity is ignored [23].

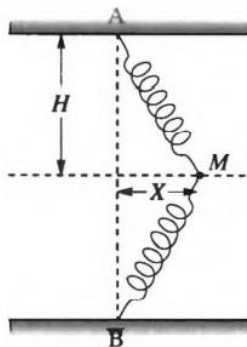


Fig. 4. Motion of mass and Spring oscillator

$$F = \Lambda \left( \frac{\sqrt{H^2 + X^2} - L}{L} \right) \quad (3.2.1)$$

Newton's seconds law holds.

$$M \frac{d^2 X}{dT^2} = -2F \cos \theta \quad \text{and} \quad \cos \theta = \frac{X}{\sqrt{H^2 + X^2}} \quad (3.2.2)$$

$$M \frac{d^2 X}{dT^2} = -\frac{2\Lambda}{L} X \left( 1 - \frac{L}{\sqrt{H^2 + X^2}} \right)$$

When the distance  $X$  is very small as compared with  $H$ , then inverse square root term can be changed by truncated Maclaurin expansion.

When two terms are established in the expression, we have the following equation:

$$\frac{d^2 X}{dT^2} = -\frac{2\Lambda}{L} X \left[ 1 - \frac{L}{H} \left( 1 - \frac{1}{L} \frac{X^2}{H^2} \right) \right] \quad (3.2.3)$$

Similarly, the nondimensional displacement  $v = \frac{X}{X_0}$  and the frequency parameter  $\Omega = \sqrt{2\Lambda(H-L)MLH}$  the govern the equation; then, we have the following equation:

$$\frac{d^2 v}{dT^2} = -\Omega^2 \left( v + \frac{L}{2(H-L)H^2} v^3 \right) \quad (3.2.4)$$

Then, for non-dimensional time  $t = \Omega T$  and the parameter  $\varepsilon = \frac{LX_0^2}{2(H-L)H_0^2}$ , we get the duffing Eq. [23]:

$$\frac{d^2 v}{dt^2} + v + \varepsilon v^3 = 0 \quad (3.2.5)$$

With initial conditions:

$$v(0) = 1, \quad v'(0) = 0$$

We use the VIM by Laplace transform to solve the Eq. (3.2.5). To obtain the correctional functional, the general nonoscillator form of the Eq. (3.2.5) is given as follows:

$$v'' + \omega^2 v + h(v) = 0$$

where  $h(v) = -\omega^2 v - v'' - v - \varepsilon v^3$

The correctional functional is written as follows:

$$\begin{aligned} \mathcal{L}[v_{n+1}(t)] &= \mathcal{L}[v_n(t)] + \mathcal{L}\left[\int_0^t -\frac{1}{\omega} \sin \omega(t-\eta) [v_n''(\eta) + \omega^2 v_n(\eta) + h^{\sim}(u_n)] d\eta\right] \\ \mathcal{L}[v_{n+1}(t)] &= \mathcal{L}[v_n(t)] \frac{1}{\omega} \mathcal{L}[\sin \omega t] \mathcal{L}[v_n'' + v_n + \varepsilon v_n^3] \end{aligned} \quad (3.2.6)$$

For an approximate solution, put  $n = 0$ ; then, we have the following equation:

Suppose the initial condition is  $v_0(t) = A \cos \omega t$ , the Eq. (3.2.7) is in this form:

$$\mathcal{L}[v_1(t)] = \mathcal{L}[v_0(t)] - \frac{1}{\omega} \mathcal{L}[\sin \omega t] \mathcal{L}[v_0'' + v_0 + \varepsilon v_0^3] \quad (3.2.7)$$

$$\mathcal{L}[v_1(t)] = \mathcal{L}[A \cos \omega t] - \frac{1}{\omega} \mathcal{L}[\sin \omega t] \mathcal{L}[-A\omega^2 \cos \omega t + A \cos \omega t + \varepsilon A^3 \cos^3 \omega t]$$

$$\mathcal{L}[v_1(t)] = \mathcal{L}[A \cos \omega t] - \frac{1}{\omega} \mathcal{L}[\sin \omega t] \mathcal{L}[-A\omega^2 \cos \omega t + A \cos \omega t + \frac{\varepsilon A^3}{4} (\cos 3\omega t + 3 \cos \omega t)]$$

After some calculations, we get the following expressions as follows:

$$\begin{aligned} \mathcal{L}[v_1(t)] &= \mathcal{L}[A \cos \omega t] - \frac{1}{\omega} \left( -A\omega^2 + A + \frac{3\varepsilon A^3}{4} \right) \mathcal{L}[\sin \omega t] \mathcal{L}[\cos \omega t] - \frac{\varepsilon A^3}{4\omega} \mathcal{L}[\sin \omega t] \mathcal{L}[\cos 3\omega t] \end{aligned} \quad (3.2.8)$$

Applying the inverse Laplace transform to the Eq. (3.2.8), we get the first-order approximate results in this form:

For no secular term in Eq. (3.2.9), we have the following equation:

$$v_1(t) = A \cos \omega t - \frac{1}{\omega} \left( -A\omega^2 + A + \frac{3\varepsilon A^3}{4} \right) \left( \frac{1}{2} t \sin \omega t \right) - \frac{1}{\omega} \left( \frac{\varepsilon A^3}{4} \right) \left( \frac{1}{8\omega} (\cos \omega t - \cos 3\omega t) \right) \quad (3.2.9)$$

$$-\frac{1}{\omega} \left( -A\omega^2 + \frac{3\varepsilon A^3}{4} \right) = 0 \quad (3.2.10)$$



This results in the expression for the system's angular frequency.

$$\omega = \sqrt{1 + \frac{3\varepsilon A^2}{4}} \tag{3.2.11}$$

The expression for angular frequency of the second problem in Eq. (3.2.11) is exactly the same Tables 1 and 2 as obtained by the EBM [27] in Eq. (4.4)

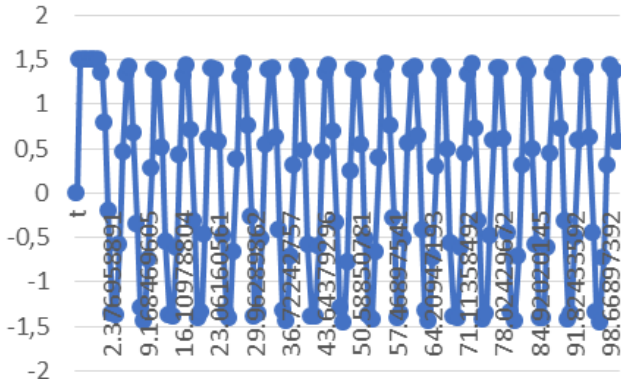


Fig.5. Numerical results for Mass and spring oscillator obtained by Simulink A1

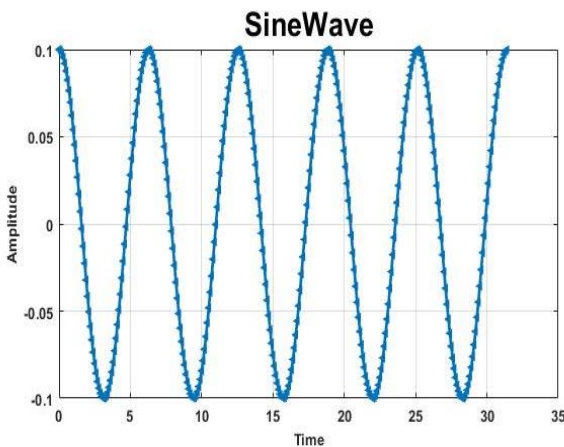


Fig.6. Sinewave plot for the solution of the Duffing equation of Mass and Spring Oscillator against  $\varepsilon = 0.18, A = 0.1$

Tab. 1. Comparison of obtained results of different kinds of analytical approaches for Eq. (3.2.5)

$\varepsilon A^2$	$\omega_{FEEM-c}$ [30]	$\omega_{SHBM}$ [32]	$\omega_{REBM}$ [27]	$\omega_{LVIM}$
0.5	1.1619	1.1707	1.1707	1.1707
	0.76%	0.001%	0.001%	0.001%
1	1.3038	1.3178	1.3178	1.3178
	1.06%	0.0043%	0.0043%	0.0043%
5	2.1213	2.1509	2.1507	2.1507
	1.35%	0.0262%	0.015%	0.015%
10	2.8284	2.8678	2.8672	2.8672
	1.33%	0.0419%	0.0217%	0.0217%
100	8.4261	8.5390	8.5360	8.5360
	1.25%	0.0643%	0.0287%	0.0287%
1000	26.476	26.8289	26.8187	26.8187
	1.24%	0.0681%	0.03011%	0.03011%
5000	59.169	59.9563	59.9337	59.9337
	1.24%	0.06783%	0.0301%	0.0301%

### 3.3. Mathematical modelling of the cubic quintic order duffing equation

Consider a fifth-order nonlinear duffing equation in this form [24-26]:

$$v'' + av + bv^3 + cv^5 = 0 \tag{3.3.1}$$

With initial condition,

$$v(0) = 1, \quad v'(0) = 0$$

To obtain the correctional functional, the general nonlinear oscillator form of the Eq. (3.3.1) is given as follows:

$$v'' + \omega^2 v + h(v) = 0$$

where  $h(v) = -\omega^2 v - v'' - av - bv^3 - cv^5$

The correctional functional of Eq. (3.3.1) can be rewrite as follows:

$$\begin{aligned} \mathcal{L}[v_{n+1}(t)] = \\ \mathcal{L}[v_n(t)] + \mathcal{L}\left[\int_0^t \sin\omega(t-\eta)[v_n''(\eta) + \omega^2 v_n(\eta) + h^-(v_n)]d\eta\right] \end{aligned} \tag{3.3.2}$$

Putting n=0 in Eq. (3.3.2), we get the following equation:

$$\mathcal{L}[v_1(t)] = \mathcal{L}[v_0(t)] - \frac{1}{\omega} \mathcal{L}[\sin\omega t] \mathcal{L}[v_0'' + av_0 + bv_0^3 + cv_0^5] \tag{3.3.3}$$

Let us consider the initial condition is  $v_0(t) = A\cos\omega t$ , then Eq. (3.3.3) in this form:

$$\mathcal{L}[v_1(t)] = \mathcal{L}[A\cos\omega t] - \frac{1}{\omega} \mathcal{L}[\sin\omega t] \mathcal{L}[-A\omega^2 \cos\omega t + Aa\cos\omega t + A^3 b\cos^3\omega t + A^5 c\cos^5\omega t]$$

After some modification, the above expression can be written as follows:

$$\begin{aligned} \mathcal{L}[v_1(t)] = \mathcal{L}[A\cos\omega t] - \frac{1}{\omega} \left( -A\omega^2 + Aa + \frac{3bA^3}{4} + \frac{5cA^5}{8} \right) \mathcal{L}[\sin\omega t] \mathcal{L}[\cos\omega t] - \frac{1}{\omega} \left( \frac{5cA^5}{16} + \frac{1bA^3}{4} \right) \mathcal{L}[\sin\omega t] \mathcal{L}[\cos 3\omega t] - \frac{1}{\omega} \left( \frac{A^5 c}{16} \right) \mathcal{L}[\sin\omega t] \mathcal{L}[\cos 5\omega t] \end{aligned} \tag{3.3.4}$$

Taking the inverse Laplace transform on Eq. (3.3.4), we obtain the first-order approximate results as follows:

For no secular term in Eq. (3.3.5), we get the following equation:

$$\begin{aligned} v_1(t) = A\cos\omega t - \frac{1}{\omega} \left( -A\omega^2 + Aa + \frac{3bA^3}{4} + \frac{5cA^5}{8} \right) \left( \frac{1}{2} t \sin\omega t \right) - \frac{1}{\omega} \left( \frac{5cA^5}{16} + \frac{1bA^3}{4} \right) \left( \frac{1}{8\omega} (\cos\omega t - \cos 3\omega t) - \frac{1}{\omega} \left( \frac{A^5 c}{16} \right) \left( \frac{1}{24\omega} (\cos\omega t - \cos 5\omega t) \right) \right) \end{aligned} \tag{3.3.5}$$

$$-\frac{1}{\omega} \left( -A\omega^2 + Aa + \frac{3bA^3}{4} + \frac{5cA^5}{8} \right) = 0$$

which leads to the expression for the system's angular frequency.

$$\omega^2 = 1 + \frac{3bA^2}{4} + \frac{5cA^4}{8} \tag{3.3.6}$$

$$\omega = \sqrt{1 + \frac{3bA^2}{4} + \frac{5cA^4}{8}} \tag{3.3.7}$$

The angular frequency of the problem third in Eq. (3.3.7) is also similar as calculated by the HPM [28] in Eq. (13) and gamma function method [29] in Eq. (3.7).

The Simulink comparison with the exact solution is as follows:

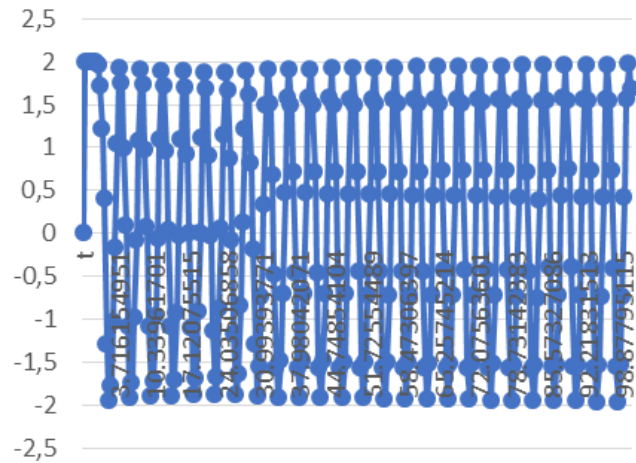


Fig. 7. Numerical results for Fifth order duffing equation obtained by Simulink A2

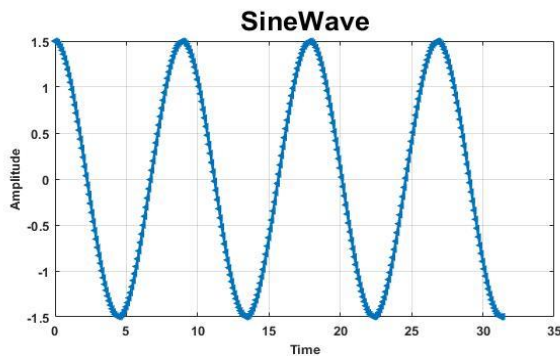


Fig.8. Sinewave plot for the solution of the fifth order Duffing equation against  $\epsilon = 0.3, A = 1.5$

Tab.2. Comparison of the approximate frequency of Eq. (3.3.6) with different A

A	GFM [29]	Ref [33]	Laplace-based VIM	Relative error
0.1	1.003774	1.003759	1.003774	0.0015
0.2	1.015382	1.015135	1.015382	0.0243
0.4	1.065833	1.062073	1.065833	0.3540
0.6	1.162325	1.144771	1.162325	1.5334
0.8	1.317574	1.268069	1.317574	3.9040
1	1.541104	1.436141	1.541104	7.3087

Nomenclature Table:  $\omega$  – angular frequency,  $\lambda$  – Lagrange multiplier,  $t$  – time,  $v$  – angle of oscillation or deformation of elastic system,  $\epsilon v^3$  – perturbation non-linear term,  $A \cos \omega t$  – initial trial function,  $\mathcal{L}$  – Laplace transform,  $\Omega T$ – non-dimensional time, VIM – variational iteration method, LVIM – Laplace variational iteration method, ZK – Zakharov–Kuznetsov, GKdVE– geophysical Korteweg–de Vries equation, HBM – Hirota bilinear method, FG – functionally graded

#### 4. CONCLUDING REMARKS


In this article, we use the Laplace transform to find the Lagrange multiplier quickly and easily. Laplace transform is a very powerful mathematical tool that is used in many areas of science and engineering. As engineering problems become significantly more difficult, Laplace transforms can help solve them using a simple method. Scientists who are trying to solve nonlinear problems can use the VIM by finding the Lagrange multiplier. This article will talk about how Laplace transforms are used in physics, and then, it will talk about how they are used in the simple pendulum, mass and spring oscillator. In the field of power systems engineering, a more complicated way to use load frequency control is also discussed in my recent research. The LVIM method is applied to solve the nonlinear problems, but there are a lot of nonlinear problems which are not solvable by this method because the limitations of our work are given as follows: if only the first derivative appears in the differential equation or only a constant term is added in the differential equation, noninformality occurs in the solution two times, and we obtained two different values of angular frequency and that is why we are unable to find the amplitude frequency relationship. Moreover, the Lagrange multiplier of higher order for this method is not established; so, the researcher tries to find the Lagrange multiplier of higher order and solves the highly nonlinear problems in future.

#### REFERENCES


1. Asghar S, Haider JA, Muhammad N. The modified KdV equation for a nonlinear evolution problem with perturbation technique. *International Journal of Modern Physics B*. 2022 Sep 30;36(24):2250160.
2. Amir M, Awais M, Ashraf A, Ali R, Ali Shah SA. Analytical Method for Solving Inviscid Burger Equation. *Punjab University Journal of Mathematics*. 2023 Dec 3;55(1).
3. Ali M, Anjum N, Ain QT, He JH. Homotopy perturbation method for the attachment oscillator arising in nanotechnology. *Fibers and Polymers*. 2021 Jun;22:1601-6.
4. Samadi H, Mohammadi NS, Shamoushaki M, Asadi Z, Ganji DD. An analytical investigation and comparison of oscillating systems with nonlinear behavior using AGM and HPM. *Alexandria Engineering Journal*. 2022 Nov 1;61(11):8987-96.
5. Koochi A, Goharimanesh M. Nonlinear oscillations of CNT nanoresonator based on nonlocal elasticity: The energy balance method. *Reports in Mechanical Engineering*. 2021 Feb 20;2(1):41-50.
6. Ul Rahman J, Lu D, Suleman M, He JH, Ramzan M. He–Elzaki method for spatial diffusion of biological population. *Fractals*. 2019 Aug 13;27(05):1950069.
7. Lu J, Ma L. The VIM-Pade technique for strongly nonlinear oscillators with cubic and harmonic restoring force. *Journal of Low Frequency Noise, Vibration and Active Control*. 2019 Dec;38(3-4):1272-8.
8. Ren ZF, Yao SW, He JH. He’s multiple scales method for nonlinear vibrations. *Journal of Low Frequency Noise, Vibration and Active Control*. 2019 Dec;38(3-4):1708-12.
9. Xu L. Application of He’s parameter-expansion method to an oscillation of a mass attached to a stretched elastic wire. *Physics Letters A*. 2007 Aug 20;368(3-4):259-62.
10. Aljahdaly NH, El-Tantawy SA. On the multistage differential transformation method for analyzing damping Duffing oscillator and its applications to plasma physics. *Mathematics*. 2021 Feb 22;9(4):432.
11. Seadawy AR, Cheemaa N. Some new families of spiky solitary waves of one-dimensional higher-order K-dV equation with power law nonlinearity in plasma physics. *Indian Journal of Physics*. 2020 Jan;94(1):117-26.


12. Seadawy AR. Stability analysis for Zakharov–Kuznetsov equation of weakly nonlinear ion-acoustic waves in a plasma. *Computers & Mathematics with Applications*. 2014 Jan 1;67(1):172-80.
13. Rizvi ST, Seadawy AR, Ashraf F, Younis M, Iqbal H, Baleanu D. Lump and interaction solutions of a geophysical Korteweg–de Vries equation. *Results in Physics*. 2020 Dec 1;19:103661.
14. Marin M, Seadawy A, Vlase S, Chirila A. On mixed problem in thermoelasticity of type III for Cosserat media. *Journal of Taibah University for Science*. 2022 Dec 31;16(1):1264-74.
15. Ali I, Seadawy AR, Rizvi ST, Younis M, Ali K. Conserved quantities along with Painleve analysis and Optical solitons for the nonlinear dynamics of Heisenberg ferromagnetic spin chains model. *International Journal of Modern Physics B*. 2020 Dec 10;34(30):2050283.
16. Ebrahimi F, Seyfi A, Dabbagh A. A novel porosity-dependent homogenization procedure for wave dispersion in nonlocal strain gradient inhomogeneous nanobeams. *The European Physical Journal Plus*. 2019 May;134:1-1.
17. He JH. Variational iteration method—a kind of non-linear analytical technique: some examples. *International journal of non-linear mechanics*. 1999 Jul 1;34(4):699-708.
18. Rahman JU, Mannan A, Ghoneim ME, Yassen MF, Haider JA. Insight into the study of some nonlinear evolution problems: Applications based on Variation Iteration Method with Laplace. *International Journal of Modern Physics B*. 2023 Jan 30;37(03):2350030.
19. He JH, Latifizadeh H. A general numerical algorithm for nonlinear differential equations by the variational iteration method. *International Journal of Numerical Methods for Heat & Fluid Flow*. 2020 Feb 20.
20. Haider JA, Muhammad N. Computation of thermal energy in a rectangular cavity with a heated top wall. *International Journal of Modern Physics B*. 2022 Nov 20;36(29):2250212.
21. Haider JA, Ahmad S. Dynamics of the Rabinowitsch fluid in a reduced form of elliptic duct using finite volume method. *International Journal of Modern Physics B*. 2022 Dec 10;36(30):2250217.
22. Anjum N, He JH. Laplace transform: making the variational iteration method easier. *Applied Mathematics Letters*. 2019 Jun 1;92:134-8.
23. Bush A. *Perturbation methods for engineers and scientists*. Routledge; 2018 May 4.
24. Beléndez A, Beléndez T, Martínez FJ, Pascual C, Alvarez ML, Arribas E. Exact solution for the unforced Duffing oscillator with cubic and quintic nonlinearities. *Nonlinear Dynamics*. 2016 Nov;86:1687-700.
25. Suleman M, Wu Q. Comparative solution of nonlinear quintic cubic oscillator using modified homotopy perturbation method. *Advances in Mathematical Physics*. 2015 Jan 1;2015.
26. Ganji DD, Gorji M, Soleimani S, Esmailpour M. Solution of nonlinear cubic-quintic Duffing oscillators using He's Energy Balance Method. *Journal of Zhejiang University-Science A*. 2009 Sep;10:1263-8.
27. Daeichin M, Ahmadpoor MA, Askari H, Yildirim A. Rational energy balance method to nonlinear oscillators with cubic term. *Asian-European Journal of Mathematics*. 2013 Jun 17;6(02):1350019.
28. He JH, Jiao ML, Gepreel KA, Khan Y. Homotopy perturbation method for strongly nonlinear oscillators. *Mathematics and Computers in Simulation*. 2023 Feb 1;204:243-58.
29. Wang KJ, Wang GD. Gamma function method for the nonlinear cubic-quintic Duffing oscillators. *Journal of Low Frequency Noise, Vibration and Active Control*. 2022 Mar;41(1):216-22.
30. Durmaz S, Kaya MO. High-order energy balance method to nonlinear oscillators. *Journal of Applied Mathematics*. 2012 Jan 1;2012.
31. Durmaz S, Demirbağ SA, Kaya MO. High order He's energy balance method based on collocation method. *International Journal of Nonlinear Sciences and Numerical Simulation*. 2010 Dec 1;11 (Supplement):1-6.
32. Wu BS, Sun WP, Lim CW. An analytical approximate technique for a class of strongly non-linear oscillators. *International Journal of Non-Linear Mechanics*. 2006 Jul 1;41(6-7):766-74.

33. Ali M, Anjum N, Ain QT, He JH. Homotopy perturbation method for the attachment oscillator arising in nanotechnology. *Fibers and Polymers*. 2021 Jun;22:1601-6.

Muhammad Amir:  <https://orcid.org/0009-0002-4871-4312>

Jamil Abbas Haider:  <https://orcid.org/0000-0002-7008-8576>

Jamshaid UI Rahman:  <https://orcid.org/0000-0001-8642-0660>

Asifa Ashraf:  <https://orcid.org/0009-0005-4786-7757>



This work is licensed under the Creative Commons BY-NC-ND 4.0 license.

APPENDIX

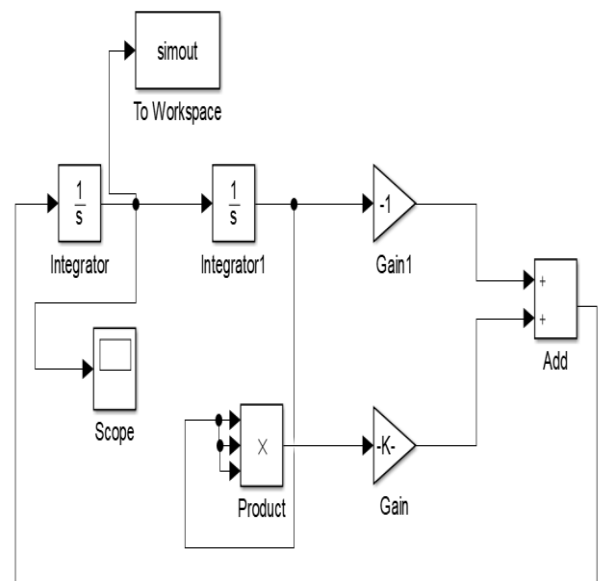


Fig. A1. Simulink model for duffing equation

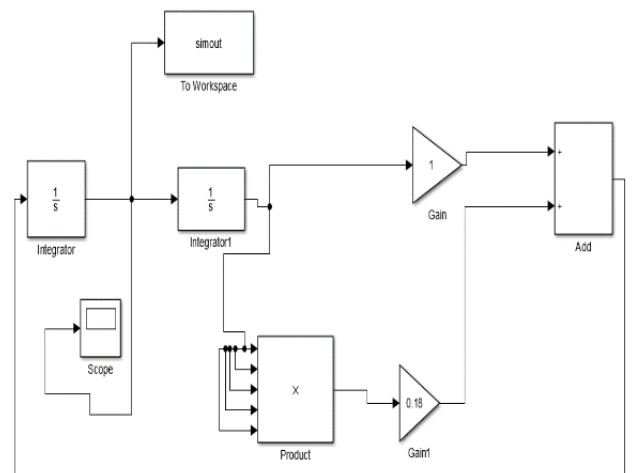


Fig.A2. Simulink model for duffing equation against  $\epsilon = 0.18$

## MINERALOGICAL ANALYSIS OF IRON ORE USING ULTRASONIC WAVE PROPAGATION PARAMETERS

Natalia MORKUN\*, Gerhard FISCHERAUER\*, Vitalii TRON\*\*, Alona GAPONENKO\*\*\*

\*Chair of Measurement and Control Systems, Bayreuth University, Universitätsstraße, 30, Bayreuth, Germany

\*\*Automation, Computer Science and Technologies Department, Kryvyi Rih National University,  
Vitalii Matusevich St., 11, Kryvyi Rih, Ukraine

\*\*\*Research Department, Kryvyi Rih National University, Vitalii Matusevich St., 11, Kryvyi Rih, Ukraine

[nmorkun@gmail.com](mailto:nmorkun@gmail.com), [mrt@uni-bayreuth.de](mailto:mrt@uni-bayreuth.de), [vtron@knu.edu.ua](mailto:vtron@knu.edu.ua), [a.haponenko@protonmail.com](mailto:a.haponenko@protonmail.com)

*received 28 September 2022, revised 26 February 2023, accepted 13 March 2023*

**Abstract:** Availability, relative simplicity and low cost, combined with ever-increasing capabilities, have led to a significant increase in the use of ultrasonic measurements of mining process variables in recent times. The scope of application varies from the study of the characteristics of raw materials and products of its processing to the operational assessment of the current parameters characterising the state of the process equipment. The purpose of this study is to develop methods for obtaining information about the characteristics of mineral raw materials as a result of ultrasonic logging of wells in a rock mass. The proposed approach makes it possible to improve the quality of information support for the management of technological processes of mining and processing of ore and thereby improve the quality of products supplied to the metallurgical stage and reduce overall production costs.

**Key words:** ultrasonic characteristics, scattering, estimation, mineral components

### 1. INTRODUCTION

Global demand for iron ores to meet the ever-growing needs of ferrous metallurgy requires the use of all available resources [1–3]. To estimate reserves of iron ore and design technological processes for its enrichment, in order to obtain a high-quality concentrate, knowledge about the mineralogical characteristics of the extracted raw materials is necessary [4, 5]. Although ultrasonic testing is non-destructive and relatively easy to implement, its potential has not yet been fully realised in rock characterisation, as the methodology and technical base strongly influence the obtained results [6–8].

At the same time, quantitative ultrasound (QUS) methods are widely used not only in technical applications but also in other branches of science and technology [9–11]. These methods make it possible to obtain estimates of attenuation, scattering and other acoustic properties of the medium under study from frequency-dependent probing signals. Specially equipped ultrasonic scanners produce ultrasonic echoes for online analysis [12]. The echo power spectra are obtained from the window segments of these signals. Echoes from a reference medium simulating certain formations are used to account for systemic data dependencies. Depth-dependent changes in the ratio of the power spectra of the studied formation to the reference medium make it possible to estimate the attenuation coefficient in the medium. Further processing gives estimates of the backscatter coefficient.

### 2. LITERATURE ANALYSIS

In geological and geotechnical engineering, various geomechanical parameters are widely used, such as modulus of elasticity, modulus of deformation, Poisson's ratio, uniaxial compressive

strength, shear strength, tensile strength and point load index to characterise the rock mass [13, 14]. However, there are no direct methods by which these properties can be assessed in the laboratory or in the field without a time-consuming procedure. An ultrasonic method based on indirect measurements is proposed to determine these characteristics of rocks [15]. It is known that there is a correlation between compression wave velocity and geomechanical properties of sedimentary rocks such as sandstones and carbonates. However, these dependencies do not consider the change in the mineralogical composition of the rock, its porosity and texture when deriving relationships. In this study, the authors evaluate compression wave velocity variability using fragmented analysis of major mineral constituents, porosity changes and saturation conditions to classify a rock mass. The resulting template can become the basis for lithology-based interpretation of more realistic geomechanical properties and thus emphasises the importance of a comprehensive study that includes geological, petrophysical and engineering data.

In paper [16], an assessment of rock properties was given using the method of pulsed ultrasonic measurements and correlation analysis of static and dynamic elastic constants. Formation elasticity characteristics, including Young's modulus, Poisson's ratio and shear modulus, are used as input parameters to predict well-bore instability and sanding. These parameters are usually estimated from the results of laboratory experiments on core samples and are called static elastic properties. This is a costly and time-consuming approach requiring special sample preparation. An alternative laboratory approach is to measure the dynamic modulus characteristics on a core sample using the acoustic method of acoustic travel time (ATT). The authors have conducted a large number of ATT tests on various types of rocks in combination with the measurement of other physical and mechanical properties of rocks, including density, porosity, water absorption, uniaxial com-



pressive strength and indirect tensile strength. Statistical analysis of the results made it possible to establish a correlation between the velocity of elastic waves and the physical and mechanical properties of the rock.

Several papers [17, 18] emphasise the critical importance of the physical and mechanical properties of rocks for their analysis and evaluation. Study [19] was aimed at studying some properties of quartz-mica schist (QMS). In an economical way, a correlation was established between the results of non-destructive and destructive test samples. With simple regression analysis, good correlations were obtained between ultrasonic wave velocities and QMS rock properties. The results were further improved with multiple regression analysis. They were also compared with data from other available empirical studies. General equations covering all types of rocks do not give a reliable assessment of the properties of rocks (the relative error range is from 23% to 1146%). It was proposed to study empirical correlations separately for different types of rocks. It is concluded that general empirical equations should not be used for design and planning purposes until they have been tested on at least one rock sample from the production site, as they may contain unacceptably large errors.

In paper [20], changes in the ultrasonic and mechanical properties of the rock are studied using velocity measurements of ultrasonic waves on limestone containing natural cracks and lamination, subjected to uniaxial compression tests. The results showed that these heterogeneities reduce the speed of ultrasonic waves and the mechanical strength of limestone. In combination with the analysis of X-ray images of the studied samples, it was found that the orientation of the layering and pre-existing penetrating cracks affects the direction of the subsequent crack propagation under uniaxial compressive load. According to the test results, the studied limestones were divided into four types: fissured-layered, filled cracks and lamination, basic filled cracks and almost intact.

In papers [21, 22], the focus was on the importance of selecting and using ultrasonic transducers for rock characterisation. It is theoretically and experimentally proved that the influence of various parameters of the transducer on the results of measurements of the speed of ultrasound is an indicator of changes in the characteristics of the test sample. It is concluded that the existing standards do not contain sufficient practical recommendations on several issues and require consideration of the proposed changes [23].

Modern methods of analysis and interpretation of information are widely used in processing the results of ultrasonic measurements [24–26]. In paper [27], it was suggested to use cluster and quantitative analysis of various characteristic features of ore-forming minerals for the classification of processed iron ore into blocks. As a result, ore material that requires higher degrees of enrichment was identified.

Thus, the existing technologies of ultrasonic measurements make it possible to evaluate various characteristics of rocks. However, due to the diversity and complexity of their structural and textural formations, it is rather difficult to identify unambiguous dependences of the ultrasound propagation process about their specific geological and mineralogical varieties.

### 3. RESEARCH METHODS

At the mining and beneficiation plants, the processed ore is classified according to the main chemical and mineralogical,

physical and mechanical characteristics into separate varieties. This division is used in the process of planning and organisation of ore mining in order to ensure a constant value of certain ore characteristics for the required time interval.

The most important stages required to solve this task include the identification, analysis and classification of distinctive features of various mineralogical-technological types of ore and minerals included in their composition.

Depending on the conditions of their formation and distribution, rocks have their inherent structural and textural features. They are characterised by a certain set of physical properties: porosity, permeability, density, elasticity, electrical resistivity, radioactivity, etc. [28].

Some physical and chemical properties of rocks can be studied in the conditions of their natural occurrence in the process of drilling exploratory and production wells by conducting appropriate geophysical surveys in them using the logging method.

Various types of logging are known [28–30], each of which has certain advantages and disadvantages. Fig. 1 shows a diagram of ultrasonic well logging, which is widely used in practice.

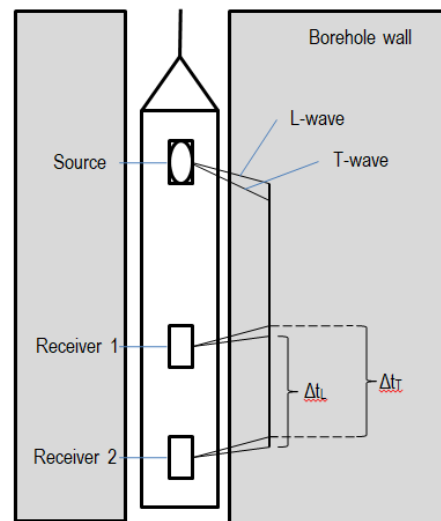


Fig. 1. Scheme of ultrasonic well logging

In the papers [31, 32], it is noted that as a result of ultrasonic well logging, speed and attenuation of ultrasonic waves in ore can be obtained. In turn, these parameters can be used to estimate the density and elastic qualities of the ore.

In rocks, the propagation speed of elastic waves varies widely and depends on physical properties, structure, texture, condition and other internal and external factors. The propagation velocities of elastic waves in an unbounded elastic medium can be determined by the formulas derived from the wave equations [33]. The velocity of the longitudinal wave in the studied volume is

$$C_L = \sqrt{\frac{E}{\rho} \frac{1-\sigma}{(1+\sigma)(1-2\sigma)}} \quad (1)$$

where the medium is assumed to be isotropic,  $\rho$  is its density,  $E$  is Young's modulus, and  $\sigma$  is Poisson's ratio.

The speed of transverse wave propagation is equal to

$$C_T = \sqrt{\frac{E}{\rho} \frac{1}{2(1+\sigma)}} = \sqrt{\frac{G}{\rho}}, \quad (2)$$

where  $G$  is the shear modulus.

The ratio of the speed of longitudinal waves to the speed of transverse waves depends only on the Poisson ratio of the rock:

$$\frac{C_L}{C_T} = \sqrt{2 \frac{1-\sigma}{1-2\sigma}} \quad (3)$$

In turn, all the elastic characteristics of rocks are connected by the following equations:

$$G = \frac{E}{2 \cdot (1 + \sigma)}, \quad (4)$$

$$K = \frac{E}{3 \cdot (1 - 2 \cdot \sigma)}, \quad (5)$$

where  $K$  is the volume modulus of elasticity (module of comprehensive compression), proportional to the ratio of stress under uniform comprehensive compression to the elastic relative change in the volume of the sample.

In contrast to the propagation speed of elastic waves, the damping coefficient is determined by significant frequency dependence. In a wide range of frequencies – from 1 Hz to 10 MHz, the attenuation coefficient of various rocks varies from  $1 \times 10^{-8}$  to  $2 \times 10^2 \text{ m}^{-1}$ . The attenuation decrement in the same frequency range varies from  $1 \times 10^{-2}$  to 1.0 on average  $\alpha$  [34, 35].

The attenuation coefficient increases with increasing frequency. However, a clearly defined and unambiguous functional dependence of attenuation on frequency for rocks has not been established. For example, in granites in the frequency range from 10 kHz to 1000 kHz, the best approximation is observed when describing the frequency dependence by the quadratic function  $\alpha = m f^2$ , where  $m$  is the proportionality factor. In gabbro-diabases, quartzites, granito-gneisses, sandstones, slates and other rocks, the frequency dependence in the interval from 500 kHz to 5,000 kHz follows the law  $\alpha = A_1 f + A_2 f^2$ . This dependence is observed for both longitudinal and transverse waves  $\alpha$  [34, 35].

The influence of the texture and intergrain boundaries on the attenuation coefficient is manifested in the fact that the value of this parameter, for example, in a single crystal is at least an order of magnitude lower than in a rock consisting of a given mineral. At low frequencies, ultrasound absorption prevails over scattering, so in this case, the radiation field is formed mainly by non-scattered acoustic vibrations. But even at high frequencies, there are regions where non-scattered radiation prevails over scattered radiation. This happens at short distances from the radiation source. Otherwise, the contribution of scattered radiation becomes significant. With an increase in frequency, the cross-section of the scattering of ultrasonic waves on mineral grains increases sharply. In this case, the radiation field is formed by both unscattered and scattered waves.

The ore bodies of the Kryvyi Rih iron ore basin (Ukraine) are divided into rich and poor. The texture of rich ores is shale-like and layered. The poor ones are represented by a series of layers of ferruginous quartzites with alternating ore and non-ore interlayers, usually 1–5 mm thick [36]. The ore layers are predominantly composed of martite, magnetite, hematite and hydrogoethite with minor amounts of quartz, chlorite and amphibole. Non-metallic interlayers consist of fine-grained quartz and contain inclusions of magnetite or martite. The iron content is 25%–45%. Rich ores (hematite and martite minerals) contain Fe >50% [36]. Average content is Fe = 46%–48%, S = 0.005%, Mn <0.45%, P = 0.02%–0.09%, SiO<sub>2</sub> = 14%.

Fig. 2 shows the main mineral formations of the Kryvyi Rih iron ore basin [36].



Fig. 2. Formations of magnetite (black) with other minerals (enlarged 40 times): (a) interspersed structure of magnetite grains; (b) replacement of magnetite with quartz; (c) relics of quartz and iron mica in the magnetite layer; (d) folded jaspilite; (e) development of cummingtonite in the ore layer; (f) replacement of magnetite with aegirine

Tab. 1 provides information on the main textural features of the most common geological and mineralogical varieties of iron ores mined and processed by magnetic enrichment at the Southern Mining and Processing Plant in Kryvyi Rih.

The analysis of the given textural and structural features of the geological and mineralogical varieties of iron ores led to the conclusion that it is possible to identify them by ultrasonic sounding, taking into account the size distribution of inclusions of individuals and aggregates of the minerals that make them up. For this purpose, it is proposed to evaluate the scattering of ultrasound on these formations.

Let us assume that a single disk source located in the plane  $z = z_0$  produces a directed beam of ultrasonic waves as it is shown in Fig. 3. Such a unit source of acoustic vibrations can be described by the radiation density

$$S_\lambda(\vec{r}, \vec{\Omega}) = \delta(z - z_0) \cdot \frac{\delta(\cos \nu - 1)}{2\pi} \cdot \frac{\text{St}(a - \rho)}{\pi a^2} \quad (6)$$

where  $\cos \nu \equiv \vec{\Omega} \circ \vec{u}_z$ ,  $\vec{u}_z$  is the unit vector directed along the  $z$ -axis,  $\rho = \sqrt{x^2 + y^2}$ ,  $a$  is the radius of the disk source,  $\delta(x)$  is the Dirac impulse, and  $\text{St}(x)$  is Heaviside's unit step function:

$$\text{St}(x) = \begin{cases} 1 & \text{for } x > 0 \\ 0 & \text{for } x < 0 \end{cases} \quad (7)$$

When a wave passes through a medium containing a large number of randomly located particles, the phases of waves scattered in any given direction and coming from randomly located centres are incoherent. As a result, the total intensity of the ultrasonic wave at a given point is equal to the sum of the intensities of the waves coming from all scattering centres. The scattering cross-sections in this case are additive, so the linear absorption and scattering coefficients,  $\Sigma_c(\lambda)$  and  $\Sigma_s(\lambda)$ , respectively, can be determined by the formulas:

$$\Sigma_c(\lambda) = n\sigma_c(\lambda), \quad \Sigma_s(\lambda) = n\sigma_s(\lambda) \quad (8)$$

Tab. 1. Characteristics of the mineral composition, as well as the size of individuals and aggregates of the Skelevatsky magnetite deposit (YUGOK)

Hornfels and jaspilites	Layer types	Magnetite			Quartz	
		Size (mm)		Content (%)	Grain size (mm)	Content (%)
		Grain	Unit			
Magnetite	Ore	0.15	0.35	90	0.04	8.5
	Mixed	0.11	0.18	37.5	0.04	59.5
	Nonmetallic	0.06	0.00	3	0.07	95
Chlorite-carbonate-magnetite	Ore	0.18	0.45	85	0.05	8
	Mixed	0.12	0.20	22	0.06	53.5
	Nonmetallic	0.05		2.5	0.075	73
Hematite-magnetite	Ore	0.15	0.6	87	0.03	5.5
	Mixed	0.12	0.33	38	0.05	55.6
	Nonmetallic	0.08	0.1	1.8	0.06	92
Magnetite-cumingtonite-chlorite-siderite	Ore	0.15	0.2	76	0.08	4
	Mixed	0.07	0.12	10.7	0.06	49.6
	Nonmetallic	0.04		5	0.1	52

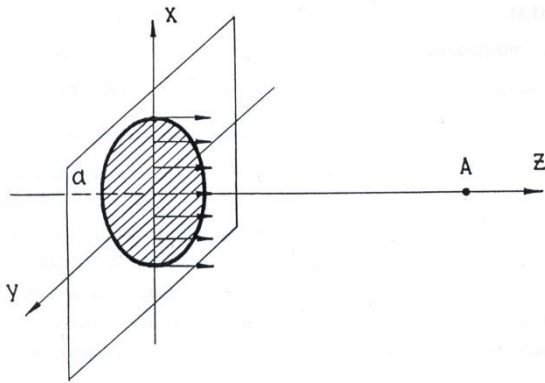


Fig. 3. Spatial orientation of the disk emitter of ultrasonic vibrations

Here,  $\lambda$  is the wavelength,  $n$  is the concentration of particles (number of particles per unit volume) and  $\sigma_c(\lambda)$  and  $\sigma_s(\lambda)$  are the respective total cross-sections for absorption and scattering of the acoustic wave by a single particle.

The field generated by the emitter of ultrasonic vibrations in the elementary volume of the phase space is described by the expression:

$$\vec{\Omega} \nabla I_\lambda(\vec{r}, \vec{\Omega}) = -\Sigma(\lambda) \cdot I_\lambda(\vec{r}, \vec{\Omega}) + \iint \Sigma_s(\vec{\Omega}' \rightarrow \vec{\Omega}) \cdot I_\lambda(\vec{r}, \vec{\Omega}') d\Omega' + S_\lambda(\vec{r}, \vec{\Omega}), \tag{9}$$

where  $S_\lambda(\vec{r}, \vec{\Omega})$ . The phase coordinates are the set of variables  $\vec{r}$  and  $\vec{\Omega}$ , and the elementary phase volume is determined by the product  $d\vec{r} \circ d\vec{\Omega}$ . The meaning of this equation is as follows: the change in the intensity of the ultrasonic beam  $I_\lambda(\vec{r}, \vec{\Omega})$  having a direction  $\vec{\Omega}$  at the point  $\vec{r}$  occurs, first, due to its weakening – absorption and scattering (the first term on the right-hand side); second, due to the scattering of the energy flow, which previously had a direction  $\vec{\Omega}'$ , in the direction  $\vec{\Omega}$  (the second term on the right-hand side); and finally, due to the energy arriving in this beam from sources (the last term on the right side).

When ultrasonic waves propagate in a rock mass, the radiation field is formed by both unscattered and scattered waves. Correct calculation of the radiation field of scattered waves is a

difficult task. To estimate the main characteristics of scattered radiation, we restrict ourselves to estimating the contribution of singly scattered ultrasonic waves.

From expression (9), kinetic equation can be obtained, the solution of which is the function  $I_\lambda(\vec{r}, \vec{\Omega})$ :

$$I_\lambda^s(\vec{r}, \vec{\Omega}) = \int \left( \iint \Sigma_s(\vec{\Omega}' \rightarrow \vec{\Omega}) \cdot \frac{e^{-\tau(\vec{r}, \vec{r}', \lambda)}}{|\vec{r} - \vec{r}'|} \cdot \delta(\vec{\Omega} - \frac{\vec{r} - \vec{r}'}{|\vec{r} - \vec{r}'|}) \cdot I_\lambda^s(\vec{r}', \vec{\Omega}') d\vec{\Omega}' \right) \circ d\vec{r}' \tag{10}$$

Then the integral intensity of singly scattered waves is determined by the expression:

$$I_\lambda^s(\vec{r}) = \iint_{4\pi} I_\lambda^s(\vec{r}, \vec{\Omega}) d\Omega \tag{11}$$

Substituting the right-hand side of expression (10) into (11) and integrating, we obtain the following:

$$I_\lambda^s(\vec{r}) = \iiint \Sigma_s(\vec{\Omega}' \rightarrow \frac{\vec{r} - \vec{r}'}{|\vec{r} - \vec{r}'|}) \cdot \frac{e^{-\tau(\vec{r}, \vec{r}', \lambda)}}{|\vec{r} - \vec{r}'|} \cdot I_\lambda^s(\vec{r}', \vec{\Omega}') d\vec{\Omega}' \circ d\vec{r}' \tag{12}$$

Let us estimate this value at point A on the axis of the ultrasonic beam (Fig. 3). We write expression (12) in a cylindrical coordinate system:

$$I_\lambda^s(z) = 2\pi \int_0^a \int_0^{\xi} I_\lambda^s \cdot e^{-\Sigma z} \Sigma_s(\mu) \frac{e^{-\Sigma \xi}}{\xi^2} \rho' d\rho' dz' \tag{13}$$

where  $\vec{\xi} = \vec{r} - \vec{r}'$ ,  $\xi = |\vec{\xi}| = \sqrt{(z - z')^2 + \rho'^2}$ , and  $\mu = \vec{u}_z \circ \vec{u}_\xi$  with  $\vec{u}_\xi = \vec{\xi} / \xi$  (unit vector in the direction of  $\vec{\xi}$ ).

To calculate (13), we will make several approximations. First, in the far field,  $z \gg a$  and therefore  $\xi \approx z - z'$ . Second, the scattering of particles is assumed to be isotropic, and then

$$\Sigma_s(\vec{\Omega} \rightarrow \vec{\Omega}') = \frac{n\sigma_s(\lambda)}{4\pi} \tag{14}$$

Taking these approximations into account, integrating in (13), we obtain the following:



$$I_{\lambda}^S(z) = \frac{n\sigma_S(\lambda)}{4} e^{-\sigma(\lambda)z} I_{\lambda}^{\circ} \left\{ z \ln\left(1 + \frac{a^2}{z^2}\right) + 2a \cdot \arctan \frac{z}{a} \right\}. \quad (15)$$

The solution of Eq. (15) can be obtained by a numerical method, for example, the Monte Carlo method [33].

To solve practical problems, we will evaluate the scattered radiation by measuring the attenuation of the probing pulse at a fixed angle to the central axis of propagation of the ultrasonic beam and compare the obtained values with the exemplary ones.

#### 4. RESEARCH RESULTS

The results of the analysis of the five main mineralogical and technological varieties of ores, which are mined and received for processing from one of the deposits of the Kryvyi Rih iron ore basin, are given in Tab. 2.

Tab. 2. The results of the analysis of different types of ores

Ore variety	Content (%)				Density (kg/m <sup>3</sup> )
	Quartz	Magnetite	Hematite	Siderite	
1	63.7	30.9	1.4	3.8	3,431
2	68.4	21.7	0.4	9.1	3,248
3	64.5	30.2	1.5	3.8	3,414
4	74.6	4.5	0.7	20.2	2,989
5	60.8	31.4	5.4	2.5	3,530

The following designations of ore varieties are used [37]: 1 – magnetite horns; 2 – silicate–carbonate–magnetite hornblende; 3 – red-striped magnetite and hematite–magnetite hornblende; 4 – silicate slates, ore-free hornblende and quartz; 5 – hematite–magnetite hornblendes.

Magnetite, hematite and siderite, which are part of the ore particles, differ in density, elastic qualities and textural–structural manifestations (Tab. 1), and the ore particles of different mineralogical and technological varieties differ in the content of these components (Tab. 2). For operational recognition of ore varieties, the results of following measurements were used: transverse  $C_T$  and longitudinal  $C_L$  propagation speed, total attenuation  $\alpha$  and scattering of ultrasonic waves in the studied environment. Tab. 3 shows the statistical parameters of the aforementioned parameters.

Tab. 3. Statistical characteristics of measured ultrasonic wave propagation parameters in the studied environment

Parameters	Min	Max	Mean	Variance
$\alpha$ (dB/m)	23	44	35	563
$\alpha_1$ (dB/m)	28	56	48	1,624
$C_L$ (m/s)	4 144	5 714	4 768	401 339
$C_T$ (m/s)	2 343	2 857	2 652	40 868

Fig. 4 shows the obtained interdependencies of rock characteristics, while Fig. 5 shows simultaneous dependences of transverse  $C_T$  and longitudinal velocity  $C_L$  of ultrasound on rock characteristics. Each point on Figs. 4 and 5 represents the average value

obtained as a result of the experiment series

It should be noted that in the case when the propagation speeds of elastic waves in the studied rocks change by 25%–40%, their attenuation and scattering coefficients change by several times.

Based on the fairly compact location of the obtained measurement results in the space of indirect features, it was concluded that their division into mineralogical-technological varieties should be represented by means of fuzzy clustering. In this case, the properties of the ore sample were characterised by a fuzzy membership function, which takes values in the range from 0 to 1.

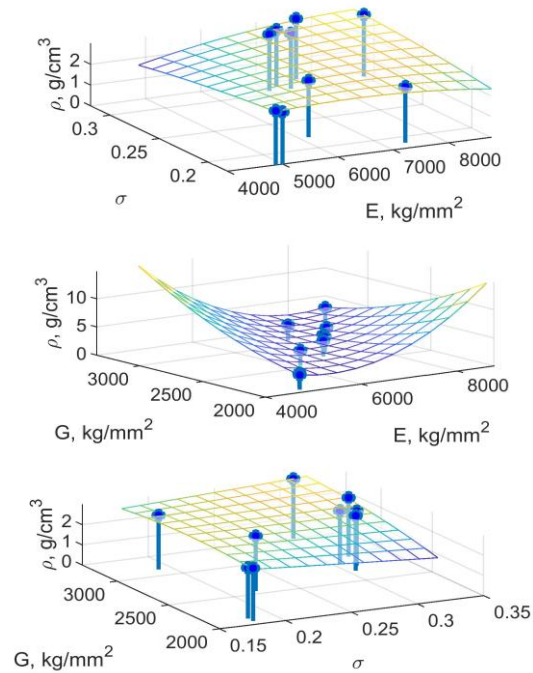
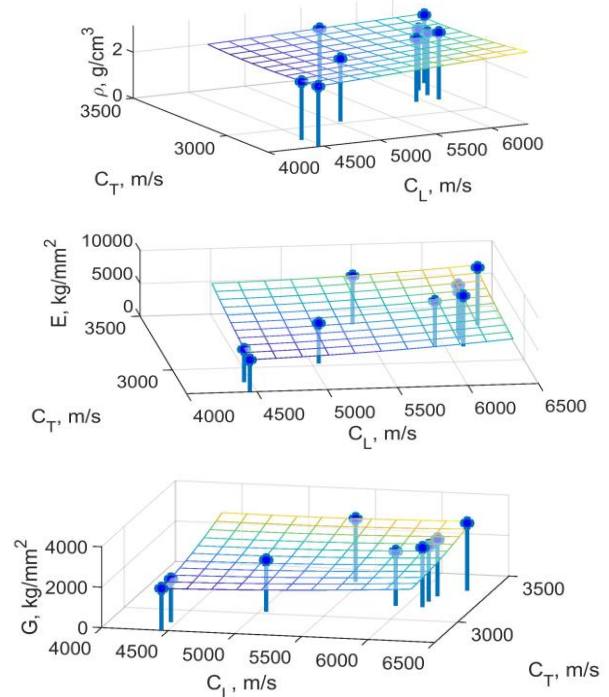


Fig. 4. Interdependencies of rock characteristics





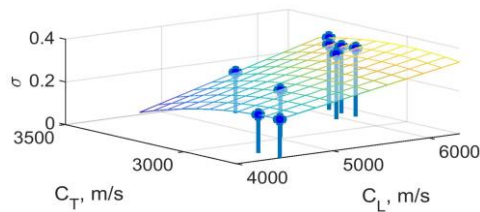


Fig. 5. Interdependencies of the speed of transverse ultrasonic waves Ct and the speed of longitudinal ultrasonic waves Cl and rock characteristics

Fuzzy clusters are described by a fuzzy partition matrix [38]:

$$F = [\mu_{ki}], \mu_{ki} \in [0, 1], k = \overline{1, M}, i = \overline{1, c}, \quad (16)$$

where the line with the number  $k$  contains the degrees of membership of the object  $(x_{k1}, x_{k2}, \dots, x_{kn})$  to the corresponding clusters  $A_1, A_2, \dots, A_c$ . The fuzzy C-means clustering algorithm that was used to divide the characteristics of ore samples into groups is based on the minimisation of the C-means functional [38]:

$$J(X; U, V) = \sum_{i=1}^c \sum_{k=1}^N (\mu_{ik})^m \|x_k - v_i\|_A^2 \rightarrow \min, \quad (17)$$

where  $\mu_{ik}$  is the degree of ownership of the element  $x_k$  to cluster  $v_i$  and  $V = [v_1, v_2, \dots, v_c], v_i \in R^n$  is a vector of cluster centres:

$$D_{ikA}^2 = \|x_k - v_i\|_A^2 = (x_k - v_i)^T A_i (x_k - v_i). \quad (18)$$

It was established that in the process of clustering, the results of measurements of the characteristics of the five studied mineralogical-technological varieties of ore, an average of 22 iterations must be performed, and the value of the objective function (17) is equal to 1.1562. Fuzzy functions belonging to the characteristics of ore samples that were assigned to a certain cluster, a given cluster and other clusters are presented in Fig. 6.

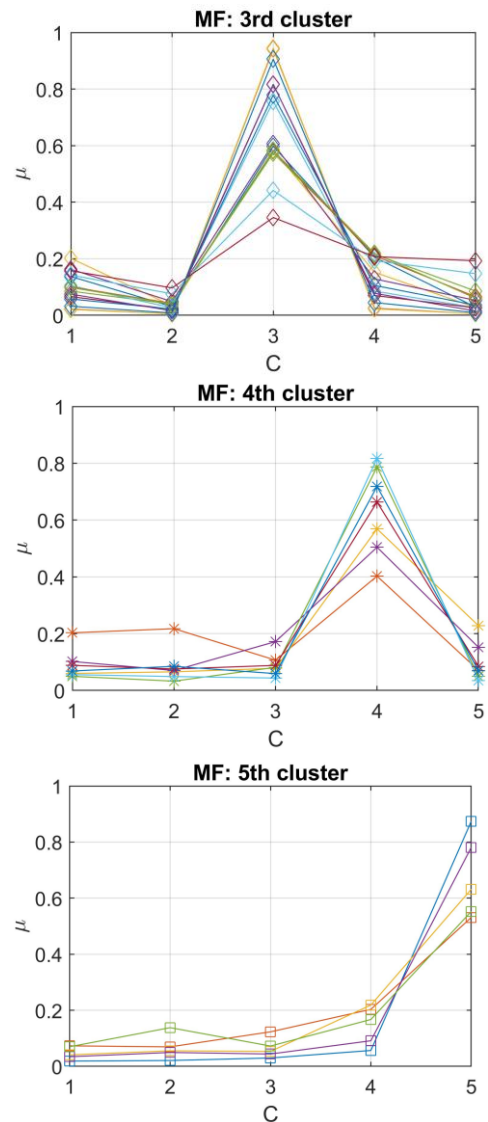
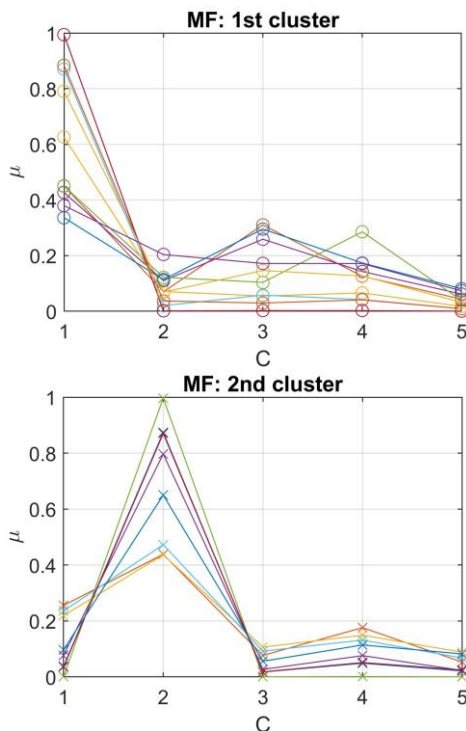


Fig. 6. Functions of points belonging to individual clusters



The analysis of the obtained results of fuzzy clustering showed that the obtained distribution of the results of ultrasonic measurements into clusters corresponds to the results of the system of classification of ores by mineralogical and technological varieties adopted at this enterprise and ensures the accuracy of their operational recognition in the mining process by at least 91.3%.

The frequency dependence of the ultrasound attenuation coefficient on the characteristics of the rock allows us to conclude about the prospects of using this parameter to improve the results of identification of its geological and mineralogical structures.

When performing technological tests of the proposed method, a mobile installation for well logging “Karrier-Kryvbas” was used, as well as a portable device for determining the content of iron in ore “PAKS-4KK” [40]. The acoustic measuring channel consists of sub-blocks for the formation, generation, reception, frequency and time selection of ultrasonic waves of the “Pulsar” granulometer of our development.

The preparation of ore samples (cores) and the study of their chemical composition were carried out using methods that are regulated and used at Ukrainian mining and mining processing plants in accordance with the State Standards of Ukraine. The chemical composition of the samples was studied with the help of

chemical and phase chemical analyses, studies under a microscope in transmitted and reflected light, as well as with the use of a diffractometer (X-ray diffraction, XRD) and an X-ray fluorescence (XRF) analyzer. The quantitative mineral composition of the studied ore samples was calculated based on the results of chemical and phase analyses. The actual density was measured by the pycnometric method.

## 5. CONCLUSIONS

Texture and combinations of minerals with different physical-mechanical and chemical-mineralogical properties are prerequisites for identifying the main mineralogical and technological varieties of iron ore by ultrasonic measurements. To take into account the textural features of the minerals that make up iron ore and their aggregations, it is proposed to evaluate the scattering of ultrasound on these formations.

The fuzzy clustering of measured transverse and longitudinal speeds of propagation, CT and CL, respectively, on the one hand and the estimated total and scattering-induced attenuation of ultrasonic waves in the studied environment,  $\alpha$  and  $\alpha_1$ , respectively, on the other hand correspond to the results of the accepted system of classification of ores into mineralogical and technological varieties: magnetite corneas; silicate-carbonate-magnetite hornblende; red-striped magnetite and hematite-magnetite hornblende; silicate slates, ore-free hornblende and quartz; and hematite-magnetite hornblendes. This ensures the accuracy of their operational recognition in the mining process with at least 91.3%.

A further direction of research is the use of the frequency dependence of the ultrasound attenuation coefficient on the characteristics of the rock to improve the results of identification of its geological and mineralogical structures.

## REFERENCES

- Zak A. Global Iron Ore Market to Reach 2.7 Billion Metric Tons by 2026. Global Industry Analysts (Internet). 2022. Available from: <https://www.prnewswire.com/news-releases/global-iron-ore-market-to-reach-2-7-billion-metric-tons-by-2026--301497721.html>.
- Falagán C, Grail BM, Johnson DB. New approaches for extracting and recovering metals from mine tailings, *Miner Eng*. 2017;106:71–8. 10.1016/j.mineng.2016.10.008.
- Golik V, Komashchenko V, Morkun V, Zaalishvili V. Enhancement of lost ore production efficiency by usage of canopies, *Metall Mining Ind*. 2015;7(4):325–9.
- Henckens T. Scarce mineral resources: Extraction, consumption and limits of sustainability. *Resour Conserv Recy*. 2021;169(105511): 1–12. 10.1016/j.resconrec.2021.105511.
- Morkun V, Semerikov S, Hryshchenko S, Slovak K. Environmental geo-information technologies as a tool of pre-service mining engineer's training for sustainable development of mining industry. *CEUR Workshop Proc* 1844. 2017;303–10.
- El Abassi D, Faiz B, Ibbi A, Aboudaoud I. A new ultrasound method for measuring the physical and mechanical properties of rocks. *J Environ Eng Geophys*. 2016;21(1):29–36. 10.2113/JEEG21.1.29.
- Bhave V, Chimankar OP, Dhoble SJ. Determination of compressive strength of rocks using ultrasound. *AIP Conf Proc*. 2104 (ICMBAT 2018). 2019;(020035):1–8. 10.1063/1.5100403.
- Morkun V, Morkun N, Pikilnyak A. Iron ore flotation process control and optimization using high-energy ultrasound. *Metall Mining Ind*. 2014;6(2):36–42.
- Ishimoto T, Suetoshi R, Cretin D, Hagihara K, Hashimoto J, Kobayashi A, Nakano T. Quantitative ultrasound (QUS) axial transmission method reflects anisotropy in micro-arrangement of apatite crystallites in human long bones: A study with 3-MHz-frequency ultrasound. *Bone*. 2019;127:82–90. 10.1016/j.bone.2019.05.034.
- Oelze ML. Statistics of scatterer property estimates. In: Mamou J, Oelze ML. *Quantitative Ultrasound in Soft Tissues*. Springer, Dordrecht etc. 2013:43–69.
- Morkun V, Morkun N, Tron V. Distributed control of ore beneficiation interrelated processes under parametric uncertainty. *Metall Mining Ind*. 2015;7(8):18–21.
- Zagzebski JA, Rosado-Mendez IM, Nasief HG, Hall TG. Quantitative ultrasound: Enhancing diagnosis using estimates of acoustic attenuation and backscatter. *AIP Conf Proc* 1747 (Medical Phys). 2016;(050001):1–10. 10.1063/1.4954108.
- Dunn MJ. Quantifying uncertainty in mining geomechanics design. *Proc First Int Conf Mining Geomech Risk (MGR 2019)*. 2019;391–402. 10.36487/ACG\_rep/1905\_23\_Dunn.
- Golik V, Komashchenko V, Morkun V, Gaponenko I. Improving the effectiveness of explosive breaking on the bade of new methods of borehole charges initiation in quarries. *Metall Mining Ind*. 2015;7(7):383–7.
- Garia S, Pal AK, Ravi K. Elastic wave velocities as indicators of lithology-based geomechanical behaviour of sedimentary rocks: an overview. *SN App Sci*. 2020;2(1521):1–21. 10.1007/s42452-020-03300-1.
- Soroush H, Qutob H. Evaluation of rock properties using ultrasonic pulse technique and correlating static to dynamic elastic constants. *Proc 2nd South Asian Geosci Conf Exhibition (GEO India 2011)*. 2011:1–12. Available from: [http://www.mkckorea.com/catalog/qseaman/UC-170/correlating\\_static.pdf](http://www.mkckorea.com/catalog/qseaman/UC-170/correlating_static.pdf).
- Arsyad M, Tiwow VA, Sulistiawaty, Sahdian IA. Analysis of physical properties and mechanics of rocks in the karst region of Pangkep Regency. *J Phys:Conf Ser*. 2020;1572(012008):1–8. 10.1088/1742-6596/1572/1/012008.
- Morkun V, Morkun N, Tron V. Distributed closed-loop control formation for technological line of iron ore raw materials beneficiation. *Metall Mining Ind*. 2015;7(7):16–9.
- Chawre B. Correlations between ultrasonic pulse wave velocities and rock properties of quartz-mica schist. *J Rock Mech Geotech Eng*. 2018;10(3):594–602. 10.1016/J.JRMGE.2018.01.006.
- Zuo JP, Wei X, Shi Y, Liu C, Li M, Wong RHC. Experimental study of the ultrasonic and mechanical properties of a naturally fractured limestone. *Int J Rock Mech Mining Sci*. 2020;125(104162). 10.1016/j.ijrmm.2019.104162.
- Bartoszek S, Stankiewicz K, Kost G, Ćwikła G, Dyczko A. Research on ultrasonic transducers to accurately determine distances in a coal mine conditions. *Energies*. 2021;14(2532). 10.3390/en14092532.
- Cerrillo C, Jiménez A, Rufo M, Paniagua J, Pachón FT. New contributions to granite characterization by ultrasonic testing. *Ultrasonics*. 2014;54(1):156–67. 10.1016/j.ultras.2013.06.006.
- Basu A, Aydin A. Evaluation of ultrasonic testing in rock material characterization. *Geotech Test J*. 2006;29(2):117–25. 10.1520/GTJ12652.
- McClements DJ. Ultrasonic Measurements in particle size analysis. In: Meyers, RA. *Encyclopedia of Analytical Chemistry*. Wiley Online. 2006. 10.1002/9780470027318.a1518.
- Samaitis V, Jasiūnienė E, Packo P, Smagulovala D. Ultrasonic methods. In: Sause MGR, Jasiūnienė E (eds.). *Structural Health Monitoring Damage Detection Systems for Aerospace*. Springer Nature, Cham, Switzerland. 2021;87–131. 10.1007/978-3-030-72192-3\_5.
- Morkun V, Morkun N. Estimation of the crushed ore particles density in the pulp flow based on the dynamic effects of high-energy ultrasound. *Arch Acoust*. 2018;43(1):61–7. 10.24425/118080.
- De Villiers JPR, Lu L. XRD analysis and evaluation of iron ores and sinters. *Iron Ore*. 2015;85–100. 10.1016/B978-1-78242-156-6.00003-4.


28. Gerali F. Well Logging, Engineering and Technology History Wiki. 2019. Available from: [https://ethw.org/Well\\_Logging](https://ethw.org/Well_Logging).
29. Haldar SK. Mineral Exploration: Principles and Applications Elsevier, Amsterdam etc. Second ed. 2018.
30. Liu CR. Laterolog tools and array laterolog tools. In: Liu CR, Theory of Electromagnetic Well Logging. Elsevier, Amsterdam etc. 2017;579-624.
31. Khan K, Vantala A, Mohiuddin M. Dependence of ultrasonic velocities and dynamic elastic rock properties on stress and saturation changes. Proc Int Symp Soc Core Analysts. 2005;(SCA2005-64): 1–6.
32. Kenigsberg AR, Rivière J, Marone C, Saffer DM. A method for determining absolute ultrasonic velocities and elastic properties of experimental shear zones. Int J Rock Mech Mining Sci. 2020;130(104306). 10.1016/j.ijrmmms.2020.104306.
33. Feynman R, Leighton R, Sands M. Sound. The wave equation. In: Lectures in Physics, vol 1, ch 47. Caltech. 2022. Available from: [https://www.feynmanlectures.caltech.edu/l\\_47.html](https://www.feynmanlectures.caltech.edu/l_47.html).
34. Acoustic properties of rocks [in Russian]. 2017. Available from: <http://ctcmetar.ru/volnovye-processy/9297-akusticheskie-svoystva-gornyh-porod.html>.
35. Acoustic velocity logging [in Russian]. 2019. Available from: <http://fccland.ru/dobycha-nefti/6826-akusticheskiy-karotazh-poskorosti.html>.
36. Lazarenko YK. Mineralogiya Krivorozhskogo basseyna [Mineralogy of the Kryvyi Rih basin; in Russian]. Naukova dumka, Kyiv. 1977.
37. Koryakov-Savoyskiy BA, Gulenko TI, Lopatin VI. Issledovaniye izmel'chayemosti rud s tsel'yu razrabotki sredstv avtomatizatsii [Study of the grindability of ores in order to develop automation tools; in Russian]. Avtomatizatsiya gornorudnogo i metallurgicheskogo proizvodstva: NIIAchermet, 7.13–20.38. 1971.
38. Shtovba SD. Vvedeniye v teoriyu nechetkikh mnozhestv i nechetkuyu logiku [Introduction to the theory of fuzzy sets and fuzzy logic; in Russian]. 2014. <http://matlab.exponenta.ru/fuzzylogic/book1>.
39. Morkun V, Morkun N, Tron V, Hryshchenko S, Serdiuk O, Dotsenko I. Basic regularities of assessing ore pulp parameters in gravity settling of solid phase particles based on ultrasonic measurements. Arch Acoust. 2019;44(1):161–7. 10.24425/aoa.2019.126362.
40. Azarian A, Azarian V, Morkun V. Operational Quality Control of Ferrous Metal Ores. Lambert Academic Publishing, London, UK. 2022.

Funded by the Alexander von Humboldt Foundation.

Natalia Morkun:  <https://orcid.org/0000-0002-1261-1170>

Gerhard Fischerauer:  <https://orcid.org/0000-0003-2000-4730>

Vitalii Tron:  <https://orcid.org/0000-0002-6149-5794>

Alona Haponenko:  <https://orcid.org/0000-0003-1128-5163>



This work is licensed under the Creative Commons BY-NC-ND 4.0 license.

## SOLUTION OF FRACTIONAL HEAT-LIKE AND FRACTIONAL WAVE-LIKE EQUATION BY USING MODERN STRATEGY

**Mohamed MOHAMED\***, **Amjad HAMZA\*\***, **Tarig ELZAKI\*\*\***, **Mohamed ALGOLAM\***, **Shiraz ELHUSSEIN\*\*\*\***

\*Department of Mathematics, Faculty of Sciences, Sudan University of Science and Technology, HGX7+M5F, Al Khartoum, Sudan

\*\*Department of Mathematics, Faculty of Sciences, University of Ha'il, Ha'il 2440, Saudi Arabia

\*\*\*Department of Mathematics, Faculty of Sciences and Arts-Alkamil, University of Jeddah,  
Hamzah Ibn Al Qasim St, Al Sharafeyah, Jeddah 23218, Saudi Arabia

\*\*\*\*Department of Mathematics, Faculty of Sciences, Taif University, Taif 21944, Saudi Arabia

[M.zain198327@hotmail.com](mailto:M.zain198327@hotmail.com), [ae.hamza@uoh.edu.sa](mailto:ae.hamza@uoh.edu.sa), [Tarig.alzaki@gmail.com](mailto:Tarig.alzaki@gmail.com), [m.sideeg2008@gmail.com](mailto:m.sideeg2008@gmail.com), [sehussein@tu.edu.sa](mailto:sehussein@tu.edu.sa)

*received 8 September 2022, revised 17 January 2023, accepted 5 February 2023*

**Abstract:** This paper introduces a novel form of the Adomian decomposition (ADM) method for solving fractional-order heat-like and wave-like equations with starting and boundary value problems. The derivations are provided in the sense of Caputo. In order to help understanding, the generalised formulation of the current approach is provided. Several numerical examples of fractional-order diffusion-wave equations (FDWEs) are solved using the suggested method in this context. In addition to examining the applicability of the suggested method to the solving of fractional-order heat-like and wave-like equations, a graphical depiction of the solutions to three instructive cases was constructed. Solution graphs were arrived at for integer and fractional-order problems. The derived and exact solutions to integer-order problems were found to be in excellent agreement. The subject of the present research endeavour is the convergence of fractional-order solutions. This strategy is considered to be the most successful way of addressing fractional-order initial-boundary value issues in science and engineering. This strategy is presented here.

**Key words:** fractional-order heat-like and wave-like equations, initial-boundary value problems, Adomian decomposition method

### 1. INTRODUCTION

Fractional calculus is the study of derivatives and integrals of fractional order. In addition to fluid dynamics, viscoelasticity, chemistry, physics and finance, these approaches may also be used in other fields. Fractional differential equations are used in several scientific and engineering fields.

The fractional method is currently regarded as the most powerful modelling tool in wave propagation, anomalous diffusion tools, turbulence and mechanics [1, 2, 3]. It is an extension of the conventional integer-order partial differential equations and fractional partial differential equations (FPDEs). In the past 10 years, scientists and engineers have paid a lot of attention to nonlinear equations due to the fact that nonlinearity is present in almost all physical situations. Nonlinear partial differential equations of fractional order are used in chemistry, biology, physics, vibration, acoustics, signal processing, electromagnetics, polymeric materials and fluid dynamics, as well as superconductivity, optics and quantum mechanics [4–7]. For the description of many elements of natural phenomena, such as the dynamics of complex materials, quasi-chaotic dynamical systems and random walks with memory, FPDEs are better suited than traditional PDEs [8,9,10].

Since FDEs typically lack accurate analytical solutions, the manner of solving these equations in approximate and numerical ways has been subject to much investigation [11–13]. Methods such as variational iteration, Adomian decomposition (ADM), homotopy perturbation, Lagrange multiplier technique and others are used to provide analytical approximations for linear and non-

linear FDEs. It is necessary to build an effective and user-friendly method for solving these equations. The ADM method may be used to solve this issue with ordinary, partial and nonlinear differential equations [14–17].

A broad class of linear or nonlinear differential equations has been approximated using the decomposition approach [18,19]. The method's use for fractional differential equations has recently been broadened [20–23]. Researchers are expected to work on the resolution of fractional-order diffusion-wave equations (FDWEs) using the ADM approach, which is a novel technology [24]. FDWEs are the most important type of anomalous diffusion equation derived from classical diffusion-wave equations [25]. Anh and Leonenko [26] provide the mean-square solution comprising the Green function and the spectral representation of FDWEs. Ali [27] uses a new ADM method to solve FDWEs having both starting and ending conditions.

In this paper, we will concentrate on solving FDWEs using a novel ADM methodological approach. Initial and boundary value issues are dealt with using ADM and its variants. The solutions to a few test problems and their graphical representation are arrived at using the Mathematica program to demonstrate the applicability of the current technique.

The remainder of the article is structured as follows: In Section 2, the details of the new iterative method, theorem proofs and its convergence are discussed. The model's description and how it is used to obtain the exact analytical solutions to the specified fractional heat-like and wave-like equations are also discussed. In Section 3, we demonstrate the proposed method's reliability,



convergence and efficiency using four exemplary instances. In Section 4, a debate over the examples provided in the article is presented, with the aid of some graphs and tables, and related discussion. Finally, Section 5 describes the conclusions we have drawn from the study.

**Definition 1:** provides the Reimann–Liouville (RL) integral operator of arbitrary order  $\tau (\tau \geq 0)$  for a function  $\chi(\beta)$  [28, 29]

$$J^\tau \chi(\beta) = \frac{1}{\Gamma(\tau)} \int_0^1 (\beta - t)^{\tau-1} \chi(t) dt. \tag{1}$$

The gamma function that permits Eq. (10) to converge on  $(0, \infty)$  point-wise is  $\Gamma(\tau) = \int_0^\infty \beta^{\tau-1} e^{-\beta} d\beta$ . The integral operator (RL) has the following properties.

$$\begin{cases} J^\tau J^\mu \chi(\beta) = J^{\mu+\tau} \chi(\beta), \\ J^\tau J^\mu \chi(\beta) = J^{\mu+\tau} \chi(\beta), \\ J^\tau \beta^\mu = \frac{\Gamma(\mu+1)}{\Gamma(\mu+\tau+1)}. \end{cases}$$

**Definition 2:** For the function  $\chi(\beta)$ , the Caputo operator of fractional order  $\tau$  is shown [28].

$$D^\tau \chi(\beta) = \frac{1}{\Gamma(\varepsilon-\tau)} \int_0^\varepsilon \frac{\chi^{(\varepsilon)}(t)}{(\beta-t)^{\tau+1-\varepsilon}} dt \quad \varepsilon - 1 < \tau < \varepsilon, \varepsilon = [\varepsilon] + 1. \tag{2}$$

The following conditions must be met by Eq. (2).

$$D^\tau \chi^k = \begin{cases} 0, & k \in N, k < |\tau|, \\ \frac{\Gamma(k+1)}{1+k-\tau} k^{k-\tau}. \end{cases}$$

**Definition 3:** The Mittag–Leffler function [30] is expressed as:

$$M_\tau(\beta) = \sum_{n=0}^\infty \frac{\beta^n}{\Gamma(n\tau+1)}, \tau > 0, \beta \in C. \tag{3}$$

## 2. BASED CONCEPT ON ADM

Adomian devised this approach for solving differentials and integrating differential problems in 1994. The following process can be used to illustrate the current method. Let

$$\phi(\chi(\gamma)) = \psi(\gamma) \tag{4}$$

If  $\psi(x)$  stands for the known function,  $\phi$  stands for the differential operator, which may be broken down as follows:

$$\phi(\chi) = L_\chi + R_\chi + N_\chi, \tag{5}$$

where  $R$  and  $N$  are linear and nonlinear terms, respectively, and  $L$  is the invertible operator of the largest derivative. Eq. (4) therefore has the following representation:

$$L_\chi + R_\chi + N_\chi = \psi \tag{6}$$

Taking  $L^{-1}$  of Eq. (5), we have

$$\chi = \eta + L^{-1}(\psi) - L^{-1}(R_\chi) - L^{-1} \tag{7}$$

The integration constant  $\eta$  is used here. The following are infinite series representations of the ADM

solution:

$$\chi = \sum_{\rho=0}^\infty \chi_\rho \tag{8}$$

The nonlinear term  $N_\chi$  is denoted by  $A_\rho$  Adomian polynomials and is defined as:

$$N_\chi = \sum_{\rho=0}^\infty A_\rho, \tag{9}$$

We can compute  $A_\rho$  with the aid of the formula below.

$$A_\rho = \frac{1}{\rho!} \frac{d^\rho}{d\lambda^\rho} N(\sum(\lambda^\rho \chi_K)), \quad \rho = 0, 1, 2, \dots$$

The following connection is used to represent the solution of Eq. (4):

$$\begin{cases} \chi_0 = \eta + L^{-1}(\psi), \rho = 0 \\ \chi_{\rho+1} = L^{-1}(R_\chi) - L^{-1}(A_\rho), \rho \geq 0 \end{cases} \tag{10}$$

## 3. MODIFIED ADM FOR INTINAL-BOUNDARY VALUE PROBLEMS

Consider the one-dimensional differential equation below to convey the key concept of treating initial and boundary conditions with the ADM approach for resolving initial-boundary value difficulties.

$$D_\beta^\tau \chi(\gamma, \beta) = D_{\gamma\gamma} \chi(\gamma, \beta) + R(\gamma, \beta), 0 < \gamma < 1, \beta > 0, 1 < T < 2. \tag{11}$$

The IC for Eq. (11) is of the following type:

$$\chi(\gamma, 0) = \delta_0(\gamma), \chi_\beta(\gamma, 0) = \delta_1(\gamma), 0 \leq \gamma \leq 1$$

Hence, the BC is defined as follows:

$$\chi(0, \beta) = \lambda_0(\beta), \chi(1, \beta) = \lambda_1(\beta), \quad \beta \geq 0$$

The operator form of ADM Eq. (11) is:

$$L_\chi = D_{\gamma\gamma} \chi(\gamma, \beta) + R(\gamma, \beta) \tag{12}$$

where  $L$  is defined as,

$$L = \frac{\partial^\tau}{\partial \beta^\tau}, 1 < T \leq 2.$$

Hence,  $L^{-1}$  is defined as,

$$L^{-1}(\cdot) = I^\tau(\cdot) d\beta. \tag{13}$$

Applying  $L^{-1}$  to Eq. (12), we obtain:

$$\chi(\gamma, \beta) = \eta + L^{-1} (D_{\gamma\gamma} \chi(\gamma, \beta) + R(\gamma, \beta)) \tag{14}$$

when using ADM, the initial approximation becomes more accurate.

$$\chi_0(\gamma, \beta) = \chi(\gamma, 0) + \beta (\partial_\beta \chi(\gamma, 0)) + L^{-1}(R(\gamma, \beta)).$$

The iteration formula becomes more powerful when used with the new ADM technique.

$$\chi_{\rho+1}(\gamma, \beta) = L^{-1}(D_{\gamma\gamma} \chi_\rho^*), \rho = 0, 1, 2, \dots \tag{15}$$

where the new  $\chi_\rho^*$  is then computed using the newly suggested method.

$$\begin{aligned} \chi_\rho^* &= \chi_\rho(\gamma, \beta) + (1 - \gamma) (\lambda_0(\beta) - \chi_\rho(0, \beta)) + \\ &\gamma (\lambda_1(\beta) - \chi_\rho(1, \beta)), \rho = 0, 1, 2, \dots \end{aligned} \tag{16}$$

It is clear that the new successive initial solutions  $\chi_\rho^*$  of Eq. (11) satisfy both the initial and boundary conditions when

$$\rho = 0, 1, 2, \dots$$

$$\text{At } \beta = 0, \quad \chi_\rho^*(\gamma, 0) = \chi_\rho(\gamma, 0),$$

$$\begin{aligned} \gamma = 0, & \quad \chi_\rho^*(0, \beta) = \lambda_0(\beta), \\ \gamma = 1, & \quad \chi_\rho^*(1, \beta) = \lambda_1(\beta). \end{aligned}$$

**Theorem 1.** (Uniqueness theorem) We consider the following general time FPDE.

$$L^T \chi(\gamma, \beta) + R\chi(\gamma, \beta) + N\chi(\gamma, \beta) = \psi(\gamma, \beta), \quad (17)$$

$m - 1 < T \leq m, \gamma > 0, \beta > 0$  where  $L$  is a fractional-order derivative,  $R$  is a linear differential operator, is a nonlinear operator and  $\psi$  is a source term, and where  $R(\chi)$  and  $N(\chi)$  satisfy the Lipschitz condition with the constants  $L_1$  and  $L_2$ . Then, Eq. (17) has a unique solution whenever  $0 < K < 1$  for  $K = \frac{(L_1+L_2)\beta^T}{\Gamma(T+1)}$ .

**Proof:** Let  $\theta$  be the Banach space of all continuous functions on  $I = [0, T]$  with the norm  $\|\chi(\beta)\| = \max |\chi(\beta)|$ . We define a mapping  $\omega : \theta \rightarrow \theta$ , where

$$\omega(\chi(\beta)) = \varphi(\beta) + T_\psi(\gamma, \beta) - J[R\psi(\gamma, \beta)] - J^T N\psi(\gamma, \beta) \quad (18)$$

Let  $\chi, \bar{\chi} \in \theta$

$$\begin{aligned} \|\omega_\chi - \omega_{\bar{\chi}}\| &= \max |\omega_\chi - \omega_{\bar{\chi}}|, \\ &= |\varphi(\beta) + J^T \psi(\gamma, \beta) - J^T [R\psi(\gamma, \beta)] - [J^T N\psi(\gamma, \beta)] \\ &\quad - \varphi(\beta) - J^T \psi(\gamma, \beta) + J^T [R\psi(\gamma, \beta)] \\ &\quad + [J^T N\psi(\gamma, \beta)]| \\ &= |J^T [R\psi(\gamma, \beta) - R\psi(\gamma, \beta)] + J^T [N\psi(\gamma, \beta) - N\psi(\gamma, \beta)]|, \end{aligned} \quad (19)$$

Now, we suppose that  $R(\chi)$  and  $N(\chi)$  satisfy the Lipschitz condition with the constants  $L_1$  and  $L_2$ .

Therefore,

$$\begin{aligned} \|\omega_\chi - \omega_{\bar{\chi}}\| &\leq \max [J^T |R\psi(\gamma, \beta) - R\psi(\gamma, \beta)| \\ &\quad + J^T |N\psi(\gamma, \beta) \\ &\quad - N\psi(\gamma, \beta)|], \end{aligned}$$

$$\begin{aligned} \|\omega_\chi - \omega_{\bar{\chi}}\| &\leq \max [L_1 J^T |\psi(\gamma, \beta) - \psi(\gamma, \beta)| \\ &\quad + L_2 J^T |\psi(\gamma, \beta) - \psi(\gamma, \beta)|], \end{aligned}$$

$$\begin{aligned} \|\omega_\chi - \omega_{\bar{\chi}}\| &\leq (L_1 + L_2) \|\psi(\gamma, \beta) - \psi(\gamma, \beta)\| \frac{\beta^T}{\Gamma(T+1)} \\ &\leq K \|\psi(\gamma, \beta) - \psi(\gamma, \beta)\|, \text{ where } K = \frac{(L_1+L_2)\beta^T}{\Gamma(T+1)} \end{aligned}$$

#### 4. APPLICATIONS

In this part, we will show how to solve various exemplary problems utilising the new ADM-based method.

**Example 1.** We examine a fractional heat-like equation in one dimension. [31]

$$D_{\beta}^{\tau} \chi = \frac{1}{2} \gamma^2 \frac{\partial^2 \chi}{\partial \gamma^2}, \quad 0 < \tau, \gamma \leq 1, \beta > 0. \quad (21)$$

Subject to the BC:

$$\chi(0, \beta) = 0, \quad \chi(1, \beta) = e^{\beta}, \quad \beta > 0. \quad (22)$$

and IC:

$$\chi(\gamma, 0) = \gamma^2. \quad (23)$$

By using ADM, Eq. (21) can be written in the form,

$$L\chi = \frac{1}{2} \gamma^2 \frac{\partial^2 \chi}{\partial \gamma^2}. \quad (24)$$

where  $L = D_{\beta}^{\tau}$ ,  $0 < \tau \leq 1$ .

Taking  $L^{-1}$ , of Eq. (24), we find that:

$$\chi(\gamma, \beta) = \chi(\gamma, 0) + L^{-1} \left[ \frac{1}{2} \gamma^2 \chi_{\gamma\gamma} \right].$$

Using the initial approximation, we find that:

$$\chi_0(\gamma, \beta) = \gamma^2. \quad (25)$$

By use of the new technique of initial approximation  $\chi_{\rho}^*$ , we have

$$\chi_{\rho+1} = \frac{1}{2} \gamma^2 L^{-1} [\chi_{\rho\gamma\gamma}^*], \quad \rho = 0, 1, 2, 3, \dots \quad (26)$$

By applying a new approximation  $\chi_{\rho}^*$ , we have:

$$\begin{aligned} \chi_{\rho}^*(\gamma, \beta) &= \chi_{\rho}(\gamma, \beta) + (1 - \gamma)[0 - \chi_{\rho}(0, \beta)] + \\ &\gamma [e^{\beta} - \chi_{\rho}(1, \beta)], \quad \rho = 0, 1, 2, \dots \end{aligned} \quad (27)$$

Let  $\rho = 0$ ; we then obtain:

$$\begin{aligned} \chi_0^*(\gamma, \beta) &= \chi_0(\gamma, \beta) + (1 - \gamma)[0 - \chi_0(0, \beta)] + \\ &\gamma [e^{\beta} - \chi_0(1, \beta)]. \end{aligned}$$

Using Eq. (26), we can obtain:

$$\chi_1(\gamma, \beta) = \frac{\gamma^2 \beta^{\tau}}{\Gamma(\tau+1)},$$

Let  $\rho = 1$ ; we then obtain:

$$\begin{aligned} \chi_1^*(\gamma, \beta) &= \chi_1(\gamma, \beta) + (1 - \gamma)[0 - \chi_1(0, \beta)] + \\ &\gamma [e^{\beta} - \chi_1(1, \beta)]. \end{aligned}$$

Using Eq. (26), we can obtain:

$$\chi_2(\gamma, \beta) = \frac{\gamma^2 \beta^{2\tau}}{\Gamma(2\tau+1)},$$

Let  $\rho = 2$ ; we then obtain:

$$\begin{aligned} \chi_2^*(\gamma, \beta) &= \chi_2(\gamma, \beta) + (1 - \gamma)[0 - \chi_2(0, \beta)] + \\ &\gamma [e^{\beta} - \chi_2(1, \beta)]. \end{aligned}$$

Using Eq. (26), we can obtain:

$$\chi_3(\gamma, \beta) = \frac{\gamma^2 \beta^{3\tau}}{\Gamma(3\tau+1)},$$

Thus, the new ADM solution for Eq. (21) can be written in a series form:

$$\begin{aligned} \chi(\gamma, \beta) &= \chi_0(\gamma, \beta) + \chi_1(\gamma, \beta) + \chi_2(\gamma, \beta) + \chi_3(\gamma, \beta) + \\ &\dots = \gamma^2 M_{\tau}(\beta). \end{aligned} \quad (28)$$

where  $M_{\tau}(\beta)$  is the Mittag-Leffler function.

If  $\tau = 1$ , we obtain:

$$\chi(\gamma, \beta) = \gamma^2 \left( 1 + \beta + \frac{\beta^2}{2!} + \frac{\beta^3}{3!} + \dots \right) = \gamma^2 e^{\beta}. \quad (29)$$

which is the exact solution of Eq. (21).

**Example 2.** We examine a fractional wave-like equation in one dimension [32].

$$D_{\beta}^{\tau} \chi = \frac{1}{2} \gamma^2 \frac{\partial^2 \chi}{\partial \gamma^2}, \quad 0 < \gamma < 1, 0 < \tau \leq 2, \beta > 0. \quad (30)$$

Subject to the BC:

$$\chi(0, \beta) = 0, \quad \chi(1, \beta) = 1 + \sinh \beta, \quad \beta > 0. \quad (31)$$

and IC:

$$\chi(\gamma, 0) = \gamma, \chi_\beta(\gamma, 0) = \gamma^2 \tag{32}$$

By using ADM, Eq. (30) can be written in the form,

$$L_{\beta\chi} = \frac{1}{2} \gamma^2 \frac{\partial^2 \chi}{\partial \gamma^2}. \tag{33}$$

where  $L = D_\beta^\tau$ ,  $1 < \tau \leq 2$ .

Taking  $L_\beta^{-1}$  of Eq. (33) enables us to find that:

$$\chi(\gamma, \beta) = \chi(\gamma, 0) + \beta \chi_\beta(\gamma, 0) + L^{-1} \left[ \frac{1}{2} \gamma^2 \chi_{\gamma\gamma} \right].$$

Using the initial approximation, we find that:

$$\chi_0(\gamma, \beta) = \gamma + \gamma^2 \beta. \tag{34}$$

By use of the new technique of initial approximation  $\chi_\rho^*$ , we have:

$$\chi_{\rho+1} = \frac{1}{2} \gamma^2 L^{-1} [\chi_{\rho\gamma\gamma}^*], \quad \rho = 0, 1, 2, 3, \dots \tag{35}$$

By applying a new approximation  $\chi_\rho^*$ , we have:

$$\chi_\rho^*(\gamma, \beta) = \chi_\rho(\gamma, \beta) + (1 - \gamma)[0 - \chi_\rho(0, \beta)] + \gamma[1 + \sinh\beta - \chi_\rho(1, \beta)], \quad \rho = 0, 1, 2, \dots \tag{36}$$

Let  $\rho = 0$ ; we then obtain:

$$\chi_0^*(\gamma, \beta) = \chi_0(\gamma, \beta) + (1 - \gamma)[0 - \chi_0(0, \beta)] + \gamma[1 + \sinh\beta - \chi_0(1, \beta)].$$

Using Eq. (35), we can obtain the following:

$$\chi_1(\gamma, \beta) = \frac{\gamma^2 \beta^{\tau+1}}{\Gamma(\tau+2)},$$

Let  $\rho = 1$ ; this enables us to obtain the following:

$$\chi_1^*(\gamma, \beta) = \chi_1(\gamma, \beta) + (1 - \gamma)[0 - \chi_1(0, \beta)] + \gamma[1 + \sinh\beta - \chi_1(1, \beta)].$$

Using Eq. (35), we can obtain:

$$\chi_2(\gamma, \beta) = \frac{\gamma^2 \beta^{2\tau+1}}{\Gamma(2\tau+2)},$$

Let  $\rho = 2$ ; we may then obtain:

$$\chi_2^*(\gamma, \beta) = \chi_2(\gamma, \beta) + (1 - \gamma)[0 - \chi_2(0, \beta)] + \gamma[1 + \sinh\beta - \chi_2(1, \beta)].$$

Using Eq. (35), we can obtain:

$$\chi_3(\gamma, \beta) = \frac{\gamma^2 \beta^{3\tau+1}}{\Gamma(3\tau+2)},$$

Thus, the new ADM solution for Eq. (30) can be written in a series form:

$$\chi(\gamma, \beta) = \chi_0(\gamma, \beta) + \chi_1(\gamma, \beta) + \chi_2(\gamma, \beta) + \chi_3(\gamma, \beta) + \dots = \gamma + \gamma^2 \beta + \gamma^2 \left[ \frac{\beta^{\tau+1}}{\Gamma(\tau+2)} + \frac{\beta^{\tau+3}}{\Gamma(\tau+4)} + \frac{\beta^{\tau+5}}{\Gamma(\tau+6)} + \dots \right], \tag{37}$$

If  $\tau = 2$ , we obtain:

$$\chi(\gamma, \beta) = \gamma + \gamma^2 \left( \beta + \frac{\beta^3}{3!} + \frac{\beta^5}{5!} + \frac{\beta^7}{7!} + \dots \right) = \gamma + \gamma^2 \sinh\beta. \tag{38}$$

which is the exact solution of Eq. (30).

**Example 3.** Consider the following two-dimensional linear [32].

$$D_{\beta\chi}^\tau \chi = \frac{\partial^2 \chi}{\partial \gamma^2} + \frac{\partial^2 \chi}{\partial \eta^2}, \quad 0 < \gamma, \eta < 2\pi, \quad 0 < \tau \leq 1, \beta > 0. \tag{39}$$

Subject to the BC:

$$\begin{aligned} \chi(0, \eta, \beta) &= \chi(2\pi, \eta, \beta) = 0 \\ \chi(\gamma, 0, \beta) &= \chi(\gamma, 2\pi, \beta) = 0 \end{aligned} \tag{40}$$

and IC:

$$\chi(\gamma, \eta, \beta) = \sin\gamma \sin\eta \tag{41}$$

By using ADM, Eq. (39) can be written in the form,

$$L_\chi = \frac{\partial^2 \chi}{\partial \gamma^2} + \frac{\partial^2 \chi}{\partial \eta^2}, \tag{42}$$

where  $L = D_\beta^\tau$ ,  $0 < \tau \leq 1$ .

Taking  $L^{-1}$  of Eq. (42), we find that:

$$\chi(\gamma, \eta, \beta) = \chi(\gamma, \eta, 0) + L^{-1} \left[ \frac{\partial^2 \chi}{\partial \gamma^2} + \frac{\partial^2 \chi}{\partial \eta^2} \right]. \tag{43}$$

Using the initial approximation, we find that:

$$\chi_0(\gamma, \eta, \beta) = \sin\gamma \sin\eta. \tag{44}$$

By use of the new technique of initial approximation  $\chi_\rho^*$ , we have:

$$\chi_{\rho+1} = L^{-1} [\chi_{\rho\gamma\gamma}^* + \chi_{\rho\eta\eta}^*], \quad \rho = 0, 1, 2, 3, \dots \tag{45}$$

By applying a new approximation  $\chi_\rho^*$ , we have:

$$\begin{aligned} \chi_\rho^*(\gamma, \eta, \beta) &= \chi_\rho(\gamma, \eta, \beta) + (1 - \gamma)[\chi(0, \eta, \beta) - \chi_\rho(0, \eta, \beta)] + \gamma[\chi(2\pi, \eta, \beta) - \chi_\rho(2\pi, \eta, \beta)] + \\ &+ (1 - \eta)[\chi(\gamma, 0, \beta) - \chi_\rho(\gamma, 0, \beta)] + \eta[\chi(\gamma, 2\pi, \beta) - \chi_\rho(\gamma, 2\pi, \beta)], \quad \rho = 0, 1, 2, \dots \end{aligned} \tag{46}$$

Let  $\rho = 0$ ; we then obtain:

$$\begin{aligned} \chi_0^*(\gamma, \eta, \beta) &= \chi_0(\gamma, \eta, \beta) + (1 - \gamma)[\chi(0, \eta, \beta) - \chi_0(0, \eta, \beta)] + \gamma[\chi(2\pi, \eta, \beta) - \chi_0(2\pi, \eta, \beta)] + \\ &+ (1 - \eta)[\chi(\gamma, 0, \beta) - \chi_0(\gamma, 0, \beta)] + \eta[\chi(\gamma, 2\pi, \beta) - \chi_0(\gamma, 2\pi, \beta)] = \sin\gamma \sin\eta. \end{aligned} \tag{47}$$

Using Eq. (45), we obtain:

$$\chi_1(\gamma, \eta, \beta) = L^{-1} [\chi_{0\gamma\gamma}^* + \chi_{0\eta\eta}^*] = -2\sin\gamma \sin\eta \frac{\beta^\tau}{\Gamma(\tau+1)}, \tag{48}$$

Let  $\rho = 1$ ; c

$$\begin{aligned} \chi_1^*(\gamma, \eta, \beta) &= \chi_1(\gamma, \eta, \beta) + (1 - \gamma)[\chi(0, \eta, \beta) - \chi_1(0, \eta, \beta)] + \gamma[\chi(2\pi, \eta, \beta) - \chi_1(2\pi, \eta, \beta)] + \\ &+ (1 - \eta)[\chi(\gamma, 0, \beta) - \chi_1(\gamma, 0, \beta)] + \eta[\chi(\gamma, 2\pi, \beta) - \chi_1(\gamma, 2\pi, \beta)] = -2\sin\gamma \sin\eta \frac{\beta^\tau}{\Gamma(\tau+1)}. \end{aligned} \tag{49}$$

Using Eq. (49), we obtain:

$$\chi_2(\gamma, \eta, \beta) = 4\sin\gamma \sin\eta \frac{\beta^{2\tau}}{\Gamma(2\tau+1)}, \tag{50}$$

Let  $\rho = 2$ ; we thus obtain:

$$\begin{aligned} \chi_2^*(\gamma, \eta, \beta) &= \chi_2(\gamma, \eta, \beta) + (1 - \gamma)[\chi(0, \eta, \beta) - \chi_2(0, \eta, \beta)] + \gamma[\chi(2\pi, \eta, \beta) - \chi_2(2\pi, \eta, \beta)] + \\ &+ (1 - \eta)[\chi(\gamma, 0, \beta) - \chi_2(\gamma, 0, \beta)] + \eta[\chi(\gamma, 2\pi, \beta) - \chi_2(\gamma, 2\pi, \beta)] = 4\sin\gamma \sin\eta \frac{\beta^{2\tau}}{\Gamma(2\tau+1)}. \end{aligned} \tag{51}$$

Us Eq. (45), we obtain:

$$\chi_3(\gamma, \eta, \beta) = -8\text{siny} \sin\eta \frac{\beta^{3\tau}}{\Gamma(3\tau+1)}, \quad (52)$$

Thus, the new ADM solution for Eq. (39) can be written in a series form:

$$\begin{aligned} \chi(\gamma, \eta, \beta) &= \chi_0(\gamma, \eta, \beta) + \chi_1(\gamma, \eta, \beta) + \chi_2(\gamma, \eta, \beta) + \\ \chi_3(\gamma, \eta, \beta) + \dots &= \text{siny} \sin\eta - 2\text{siny} \sin\eta \frac{\beta^\tau}{\Gamma(\tau+1)} + \\ 4\text{siny} \sin\eta \frac{\beta^{2\tau}}{\Gamma(2\tau+1)} - 8\text{siny} \sin\eta \frac{\beta^{3\tau}}{\Gamma(3\tau+1)} + \dots, \\ &= \text{siny} \sin\eta \left[ 1 - 2 \frac{\beta^\tau}{\Gamma(\tau+1)} + 4 \frac{\beta^{2\tau}}{\Gamma(2\tau+1)} - 8 \frac{\beta^{3\tau}}{\Gamma(3\tau+1)} + \dots \right] \end{aligned} \quad (53)$$

If  $\tau = 1$ , we obtain:

$$\chi(\gamma, \eta, \beta) = \text{siny} \sin\eta e^{-2\beta} \quad (54)$$

which is the exact solution of Eq. (39).

**Example 4.** We examine a fractional wave-like equation in two dimensions [33].

$$\begin{aligned} D_{\beta\beta}^\tau \chi &= \frac{1}{12} \left[ \gamma^2 \frac{\partial^2 \chi}{\partial \gamma^2} + \eta^2 \frac{\partial^2 \chi}{\partial \eta^2} \right], \\ 0 < \gamma, \eta < 1, \dots, 1 < \tau \leq 2, \beta > 0. \end{aligned} \quad (55)$$

Subject to the BC:

$$\begin{aligned} \chi(0, \eta, \beta) &= 0, \quad \chi(1, \eta, \beta) = 4\text{cosh}\beta \\ \chi(\gamma, 0, \beta) &= 0, \quad \chi(\gamma, 2\pi, \beta) = 4\text{sinh}\beta \end{aligned} \quad (56)$$

and IC:

$$\chi(\gamma, \eta, 0) = \gamma^2, \quad \chi_\beta(\gamma, \eta, 0) = \eta^2 \quad (57)$$

By using ADM, Eq. (58) can be written in the form,

$$L_{\beta\chi} = \frac{1}{12} \left[ \gamma^2 \frac{\partial^2 \chi}{\partial \gamma^2} + \eta^2 \frac{\partial^2 \chi}{\partial \eta^2} \right], \quad (58)$$

where  $L = D_{\beta\beta}^\tau, 1 < \tau \leq 2$ .

Taking  $L_{\beta}^{-1}$  of Eq. (58), we find that:

$$\chi(\gamma, \eta, \beta) = \gamma^4 + \eta^4 \beta + L_{\beta}^{-1} \left[ \frac{1}{12} \left( \gamma^2 \frac{\partial^2 \chi}{\partial \gamma^2} + \eta^2 \frac{\partial^2 \chi}{\partial \eta^2} \right) \right].$$

Using the initial approximation, we find that:

$$\chi_0(\gamma, \eta, \beta) = \gamma^4 + \eta^4 \beta. \quad (59)$$

By using the new technique of initial approximation  $\chi_\rho^*$ , we have:

$$\chi_{\rho+1} = \frac{1}{12} L_{\beta}^{-1} \left[ \gamma^2 (\chi_\rho^*)_{\gamma\gamma} + \eta^2 (\chi_\rho^*)_{\eta\eta} \right], \rho = 0, 1, 2, \dots \quad (60)$$

By applying a new approximation  $\chi_\rho^*$ , we have:

$$\begin{aligned} \chi_\rho^*(\gamma, \eta, \beta) &= \chi_\rho(\gamma, \eta, \beta) + (1-\gamma)[\chi(0, \eta, \beta) - \\ \chi_\rho(0, \eta, \beta)] &+ \gamma[\chi(1, \eta, \beta) - \chi_\rho(1, \eta, \beta)] + (1-\eta)[\chi(\gamma, 0, \beta) - \\ \chi_\rho(\gamma, 0, \beta)] &+ \eta[\chi(\gamma, 1, \beta) - \chi_\rho(\gamma, 1, \beta)], \quad \rho = 0, 1, 2, \dots \end{aligned} \quad (61)$$

Let  $\rho = 0$ ; we then obtain:

$$\begin{aligned} \chi_0^*(\gamma, \eta, \beta) &= \chi_0(\gamma, \eta, \beta) + (1-\gamma)[\chi(0, \eta, \beta) - \\ \chi_0(0, \eta, \beta)] &+ \gamma[\chi(1, \eta, \beta) - \chi_0(1, \eta, \beta)] + (1-\eta)[\chi(\gamma, 0, \beta) - \\ \chi_0(\gamma, 0, \beta)] &+ \eta[\chi(\gamma, 1, \beta) - \chi_0(\gamma, 1, \beta)] = \\ \gamma^4 + \eta^4 \beta. \end{aligned}$$

Using Eq. (60), we obtain:

$$\begin{aligned} \chi_1 &= \frac{1}{12} L_{\beta}^{-1} \left[ \gamma^2 (\chi_0^*)_{\gamma\gamma} + \eta^2 (\chi_0^*)_{\eta\eta} \right] \\ &= \gamma^4 \frac{\beta^\tau}{\Gamma(\tau+1)} + \eta^4 \frac{\beta^{\tau+1}}{\Gamma(\tau+2)} \\ \chi_2 &= \frac{1}{12} L_{\beta}^{-1} \left[ \gamma^2 (\chi_1^*)_{\gamma\gamma} + \eta^2 (\chi_1^*)_{\eta\eta} \right] \\ &= \gamma^4 \frac{\beta^{2\tau}}{\Gamma(2\tau+1)} + \eta^4 \frac{\beta^{2\tau+1}}{\Gamma(2\tau+2)} \\ \chi_3 &= \frac{1}{12} L_{\beta}^{-1} \left[ \gamma^2 (\chi_2^*)_{\gamma\gamma} + \eta^2 (\chi_2^*)_{\eta\eta} \right] \\ &= \gamma^4 \frac{\beta^{3\tau}}{\Gamma(3\tau+1)} + \eta^4 \frac{\beta^{3\tau+1}}{\Gamma(3\tau+2)} \end{aligned} \quad (62)$$

Thus, the new ADM solution for Eq. (55) can be written in a series form:

$$\begin{aligned} \chi(\gamma, \eta, \beta) &= \chi_0(\gamma, \eta, \beta) + \chi_1(\gamma, \eta, \beta) \\ &+ \chi_2(\gamma, \eta, \beta) + \chi_3(\gamma, \eta, \beta) + \dots \\ &= \gamma^4 \left[ 1 + \frac{\beta^\tau}{\Gamma(\tau+1)} + \frac{\beta^{2\tau}}{\Gamma(2\tau+1)} + \frac{\beta^{3\tau}}{\Gamma(3\tau+1)} + \dots \right] \\ &+ \eta^4 \left[ \beta + \frac{\beta^{\tau+1}}{\Gamma(\tau+2)} + \frac{\beta^{\tau+3}}{\Gamma(2\tau+2)} + \frac{\beta^{\tau+5}}{\Gamma(3\tau+2)} + \dots \right]. \end{aligned} \quad (63)$$

If  $\tau = 2$ , we obtain:

$$\begin{aligned} \chi(\gamma, \eta, \beta) &= \gamma^4 \left( 1 + \frac{\beta^2}{2!} + \frac{\beta^4}{4!} + \frac{\beta^6}{6!} + \dots \right) + \\ &\eta^4 \left( \beta + \frac{\beta^3}{3!} + \frac{\beta^5}{5!} + \frac{\beta^7}{7!} + \dots \right) \\ &= \gamma^4 \text{cosh}\beta + \eta^4 \text{sinh}\beta \end{aligned} \quad (64)$$

which is the exact solution of Eq. (55).

**Example 5.** Consider the following one-dimensional nonlinear heat – similar to Eq. (34):

$$\begin{aligned} D_{\beta\beta}^\tau \chi &= \gamma \chi \frac{\partial^2 \chi}{\partial \gamma^2} - 8\gamma^3 \frac{\beta^{2\tau+2}}{\Gamma(\tau+2)^2} + 2\gamma^2 \beta^\tau, \\ 0 < \gamma, \tau \leq 1, \dots, \beta > 0. \end{aligned} \quad (65)$$

Subject to the BC:

$$\chi(0, \beta) = 0, \quad \chi(1, \beta) = \frac{2\beta^{\tau+1}}{\Gamma(\tau+2)}, \quad \beta > 0 \quad (66)$$

and IC:

$$\chi(\gamma, 0) = 0 \quad (67)$$

By using ADM, Eq. (65) can be written in the form,

$$L_{\beta\chi} = \gamma \chi \frac{\partial^2 \chi}{\partial \gamma^2} - 8\gamma^3 \frac{\beta^{2\tau+2}}{\Gamma(\tau+2)^2} + 2\gamma^2 \beta^\tau, \quad (68)$$

where  $L = D_{\beta\beta}^\tau, 0 < \tau \leq 1$ .

Taking  $L^{-1}$  of Eq. (68), we find that:

$$\begin{aligned} \chi(\gamma, \beta) &= \chi(\gamma, 0) + L^{-1} [2\gamma^2 \beta^\tau] \\ &+ L^{-1} \left[ \gamma \chi \frac{\partial^2 \chi}{\partial \gamma^2} - 8\gamma^3 \frac{\beta^{2\tau+2}}{\Gamma(\tau+2)^2} \right]. \end{aligned} \quad (69)$$

Using the initial approximation, we find that:

$$\chi_0(\gamma, \beta) = 2\gamma^2 \frac{\beta^{2\tau}}{\Gamma(2\tau+1)}. \quad (70)$$

By using the new technique of initial approximation  $\chi_\rho^*$ , we have:

$$\chi_{\rho+1} = L^{-1} \left[ \gamma \chi_\rho^* \chi_{\rho\gamma\gamma} - 8\gamma^3 \frac{\beta^{2\tau+2}}{\Gamma(\tau+2)^2} \right], \rho = 0, 1, 2, 3, \dots \quad (71)$$



By applying a new approximation  $\chi_\rho^*$ , we have:

$$\chi_\rho^*(\gamma, \beta) = \chi_\rho(\gamma, \beta) + (1 - \gamma)[0 - \chi_\rho(0, \beta)] + \gamma \left[ \frac{2\beta^{\tau+1}}{\Gamma(\tau+2)} - \chi_\rho(1, \beta) \right], \quad \rho = 0, 1, 2, \dots \quad (72)$$

Let  $\rho = 0$ ; we then obtain:

$$\chi_0^*(\gamma, \beta) = \chi_0(\gamma, \beta) + (1 - \gamma)[0 - \chi_0(0, \beta)] + \gamma \left[ \frac{2\beta^{\tau+1}}{\Gamma(\tau+2)} - \chi_0(1, \beta) \right]$$

Using Eq. (71), we obtain:

$$\chi_1(\gamma, \beta) = 0, \quad (73)$$

Thus, the new ADM solution for Eq. (65) can be written in a series form:

$$\chi(\gamma, \beta) = \chi_0(\gamma, \beta) + \chi_1(\gamma, \beta) = 2\gamma^2 \frac{\beta^{2\tau}}{\Gamma(2\tau+1)} \quad (74)$$

Let  $\rho = 1$ ; we then obtain:

$$\chi(\gamma, \beta) = \gamma^2 \beta^2 \quad (75)$$

**Example 6.** Consider the following one-dimensional nonlinear wave – similar to Eq. (34):

$$D_\beta^\tau \chi = \gamma \chi \frac{\partial^2 \chi}{\partial \gamma^2} - 8\gamma^3 \frac{\beta^{2\tau}}{\Gamma(\tau+2)^2} + 2\gamma^2, \quad 1 < \gamma, \tau \leq 2, \beta > 0, \quad (76)$$

Subject to the BC:

$$\chi(0, \beta) = 0, \quad \chi(1, \beta) = \frac{2\beta^\tau}{\Gamma(\tau+1)}, \quad \beta > 0 \quad (77)$$

and IC:

$$\chi(\gamma, 0) = 0, \quad \chi_\beta(\gamma, 0) = 0 \quad (78)$$

By using ADM, Eq. (76) can be written in the form,

$$L_\chi = \gamma \chi \frac{\partial^2 \chi}{\partial \gamma^2} - 8\gamma^3 \frac{\beta^{2\tau}}{\Gamma(\tau+1)^2} + 2\gamma^2, \quad (79)$$

where  $L = D_\beta^\tau, 1 < \tau \leq 2$ .

Taking  $L^{-1}$  of Eq. (79), we find that:

$$\chi(\gamma, \beta) = \chi(\gamma, 0) + L^{-1}[2\gamma^2] + L^{-1} \left[ \gamma \chi \frac{\partial^2 \chi}{\partial \gamma^2} - 8\gamma^3 \frac{\beta^{2\tau}}{\Gamma(\tau+1)^2} \right]. \quad (80)$$

Using the initial approximation, we have:

$$\chi_0(\gamma, \beta) = 2\gamma^2 \frac{\beta^\tau}{\Gamma(\tau+1)}. \quad (81)$$

By using the new technique of initial approximation  $\chi_\rho^*$ , we have:

$$\chi_{\rho+1} = L^{-1} \left[ \gamma \chi_\rho^* \chi_{\rho\gamma}^* - 8\gamma^3 \frac{\beta^{2\tau}}{\Gamma(\tau+1)^2} \right], \quad \rho = 0, 1, 2, 3, \dots \quad (82)$$

By applying a new approximation  $\chi_\rho^*$ , we have:

$$\chi_\rho^*(\gamma, \beta) = \chi_\rho(\gamma, \beta) + (1 - \gamma)[0 - \chi_\rho(0, \beta)] + \gamma \left[ \frac{2\beta^\tau}{\Gamma(\tau+1)} - \chi_\rho(1, \beta) \right], \quad \rho = 0, 1, 2, \dots \quad (83)$$

Let  $\rho = 0$ ; we then obtain:

$$\chi_0^*(\gamma, \beta) = \chi_0(\gamma, \beta) + (1 - \gamma)[0 - \chi_0(0, \beta)] + \gamma \left[ \frac{2\beta^\tau}{\Gamma(\tau+1)} - \chi_0(1, \beta) \right]$$

Using Eq. (71), we obtain:

$$\chi_1(\gamma, \beta) = 0, \quad (84)$$

Thus, the new ADM solution for Eq. (76) can be written in a series form:

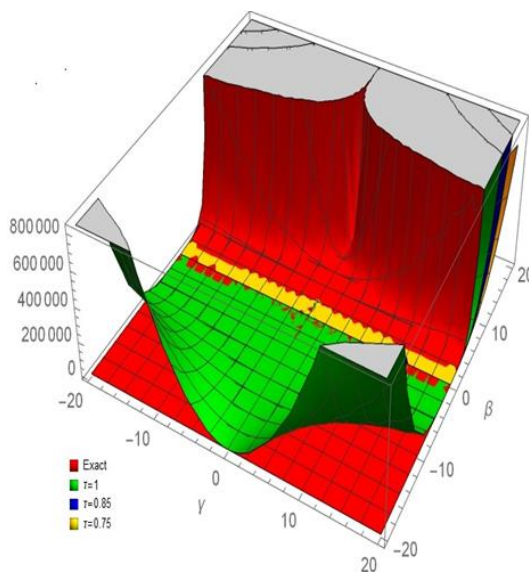
$$\chi(\gamma, \beta) = \chi_0(\gamma, \beta) + \chi_1(\gamma, \beta) = 2\gamma^2 \frac{\beta^\tau}{\Gamma(\tau+1)} \quad (85)$$

Let  $\rho = 1$ ; we then obtain:

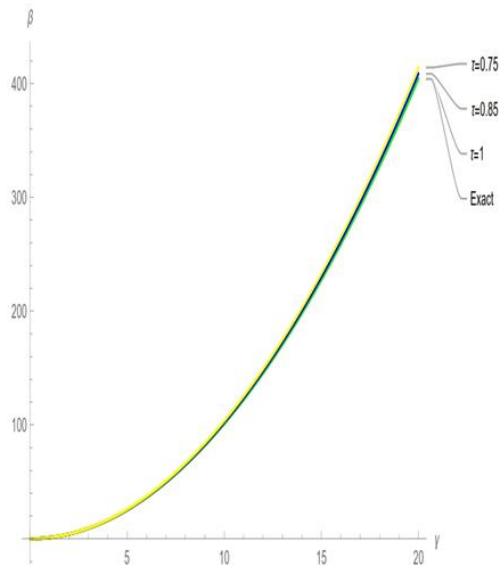
$$\chi(\gamma, \beta) = \gamma^2 \beta^2 \quad (86)$$

### 5. NUMERICAL RESULT

The derived solutions from Example 1 are displayed at various fractional orders of the derivatives in Figs. 1(a) and 1(b).



(a) 3D approximate solution – Example 1



(b) 2D approximate solution – Example 1

Fig. 1. Comparison between exact and approximate solutions

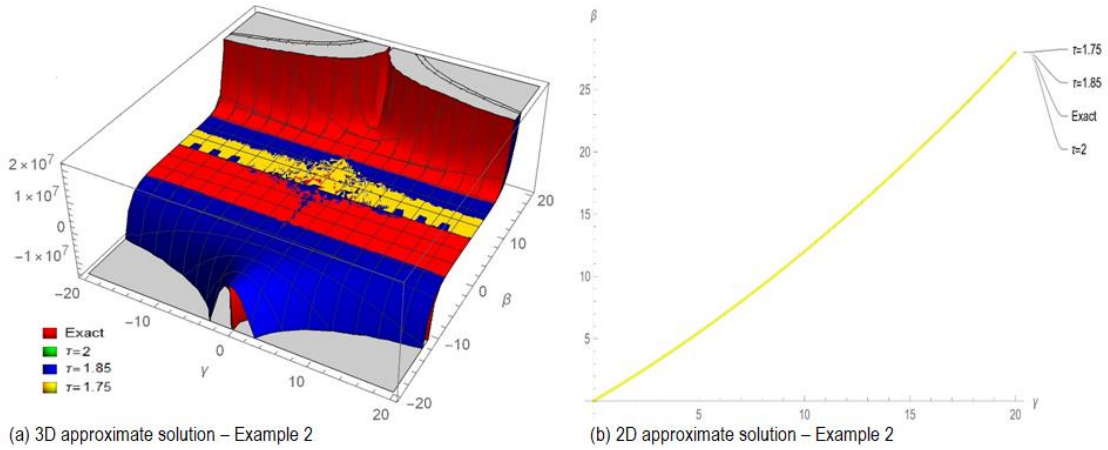


Fig. 2. Comparison between exact and approximate solutions

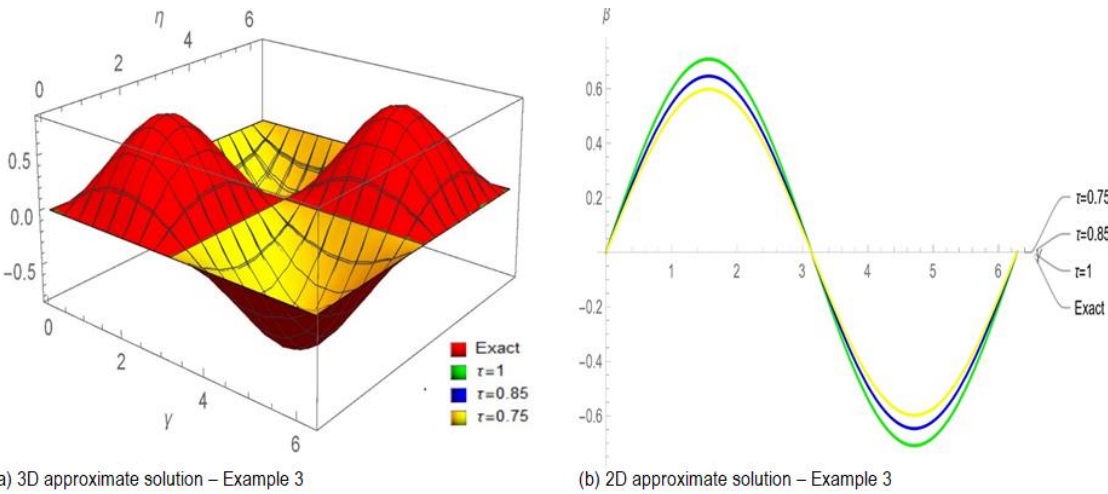


Fig. 3. Comparison between exact and approximate solutions

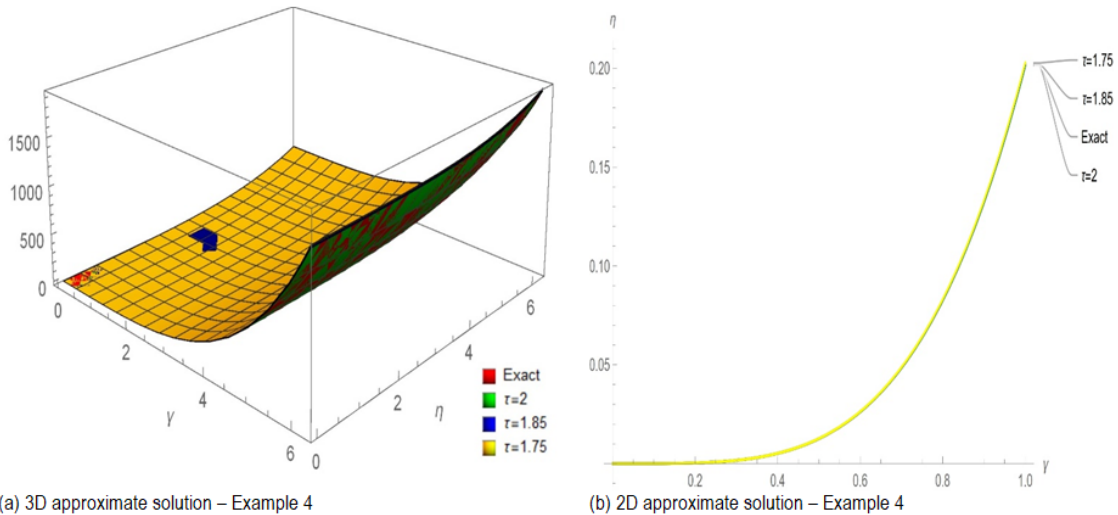


Fig. 4. Comparison between exact and approximate solutions

The graphs of the 2D and 3D ADM solutions in Figs. 1(a) and 1(b) corroborate the closed contact with the precise solution of Example 1 and show the 2D and 3D ADM solutions  $\tau$ . The closed contact between Example 1's precise and found solutions at the integer derivative order is being investigated. The graphs show how closely related the exact and derived outcomes are. The proposed approach yields an accurate solution for Example 1 as a

consequence. Figs. 2(a) and 2(b) show the obtained solutions from Example 2 at different fractional orders of the derivative solution for Example 1 as a consequence. Figs. 2(a) and 2(b) show the obtained solutions from Example 2 at different fractional orders of the derivatives. The closed contact with the exact solution of Example 2 is supported by the graphs of the 2D and 3D ADM solutions. As a consequence, using the provided technique,

it can be ascertained that Example 2's solution is correct. Figs. 3(a) and 3(b) show the analytical and exact solutions for  $\chi(\gamma, \beta)$  of Example 3 at  $\beta = 0.1, 0.2$  and  $0 < \gamma \leq 2\pi$  for various fractional-orders. The graphical behavior of the exact and analytical solutions to  $\chi(\gamma, \beta)$  Figs. 4(a) and 4(b) show the analytical and exact solutions for  $\chi(\gamma, \beta)$  of Example 4 at  $\beta = 0.2$  and  $0 < \gamma \leq 1$  for various fractional-orders. The graphical behaviour of the exact

and analytical solutions to  $\chi(\gamma, \beta)$ . Tabs. 1–4 contrast the exact answers that have been presented with the absolute inaccuracy at various fractional orders. The findings in the figures and tables clearly show that our approach to finding a solution quickly converges on a correct response. Last but not least, the images and figures show that the suggested processes are more exact and quickly converge to accurate results.

Tab. 1. Solution for the (first three approximations) with exact solution, with mesh points  $\beta = 0.01$ , for Eq. (21)

$\beta$	$\gamma$	$\tau = 0.75$	$\tau = 0.85$	$\tau = 1$	Exact	Error $\tau = 0.75$	Error $\tau = 0.85$	Error $\tau = 1$
0.01	0	0	0	0	0	0	0	0
	0.1	0	0.010213602	0.010100502	0.010100502	0.000251223	0.000113101	$8.34575 \times 10^{-15}$
	0.2	0.041406899	0.04085441	0.040402007	0.040402007	0.001004892	0.000452403	$3.3383 \times 10^{-14}$
	0.3	0.093165522	0.091922422	0.090904515	0.090904515	0.002261007	0.001017907	$7.51066 \times 10^{-14}$
	0.4	0.165627595	0.163417639	0.161608027	0.161608027	0.004019568	0.001809612	$1.33532 \times 10^{-13}$
	0.5	0.258793117	0.255340061	0.252512542	0.252512542	0.006280575	0.002827519	$2.08611 \times 10^{-13}$
	0.6	0.372662089	0.367689688	0.36361806	0.36361806	0.009044029	0.004071628	$3.00426 \times 10^{-13}$
	0.7	0.50723451	0.50046652	0.494924582	0.494924582	0.012309928	0.005541938	$4.0884 \times 10^{-13}$
	0.8	0.66251038	0.653670556	0.646432107	0.646432107	0.016078273	0.007238449	$5.34128 \times 10^{-13}$
	0.9	0.8384897	0.827301798	0.818140635	0.818140635	0.020349064	0.009161162	$6.7590377 \times 10^{-13}$
	1	1.035172469	1.021360244	1.010050167	1.010050167	0.025122301	0.011310077	$8.34443 \times 10^{-13}$

Tab. 2. Solution for the (first three approximations) with exact solution, with mesh points  $\beta = 0.02$ , for Eq. (30)

$\beta$	$\gamma$	$\tau = 1.75$	$\tau = 1.85$	$\tau = 2$	Exact	Error $\tau = 1.75$	Error $\tau = 1.85$	Error $\tau = 2$
0.02	0	0	0	0	0	0	0	0
	0.1	0.1002	0.1002	0.1002	0.1001	$1.18937 \times 10^{-7}$	$6.89018 \times 10^{-8}$	$2.66667 \times 10^{-8}$
	0.2	0.200801	0.2008	0.2008	0.2004	$4.75748 \times 10^{-7}$	$2.75607 \times 10^{-7}$	$1.06667 \times 10^{-7}$
	0.3	0.301801	0.301801	0.3018	0.3009	$1.07043 \times 10^{-6}$	$6.20116 \times 10^{-7}$	$2.4 \times 10^{-6}$
	0.4	0.403202	0.403201	0.403201	0.4016	$1.90299 \times 10^{-6}$	$1.10243 \times 10^{-6}$	$4.26667 \times 10^{-7}$
	0.5	0.505003	0.505002	0.505001	0.5025	$2.97343 \times 10^{-6}$	$1.72254 \times 10^{-6}$	$6.66667 \times 10^{-7}$
	0.6	0.607205	0.607203	0.607201	0.6036	$4.28173 \times 10^{-6}$	$2.48046 \times 10^{-6}$	$9.6 \times 10^{-7}$
	0.7	0.709806	0.709804	0.709802	0.7049	$5.82792 \times 10^{-6}$	$3.37619 \times 10^{-6}$	$1.30667 \times 10^{-6}$
	0.8	0.812808	0.812805	0.812803	0.8064	$7.61197 \times 10^{-6}$	$4.40971 \times 10^{-6}$	$1.70667 \times 10^{-6}$
	0.9	0.916211	0.916207	0.916203	0.9081	$9.6339 \times 10^{-6}$	$5.58104 \times 10^{-6}$	$2.16 \times 10^{-6}$
	1	1.02001	1.02001	1.02	1.01	$1.18937 \times 10^{-5}$	$6.89018 \times 10^{-6}$	$2.66667 \times 10^{-6}$

Tab. 3. Solution for the (first three approximations) with exact solution, with mesh points  $\beta = 0.02$ , for Eq. (30)

$\beta$	$\eta$	$\gamma$	$\tau = 0.75$	$\tau = 0.85$	$\tau = 1$	Exact	Error $\tau = 0.75$	Error $\tau = 0.85$	Error $\tau = 1$
0.1	$\frac{2\pi}{3}$	$\frac{2\pi}{3}$	0.517896942	0.559870154	0.614	0.614048065	0.096151123	0.05417791	4.80648E-05
		$\frac{4\pi}{3}$	-0.517896942	-0.559870154	-0.614	-0.614048065	0.096151123	0.05417791	4.80648E-05
0.2		$\frac{2\pi}{3}$	0.400780878	0.443831887	0.502	0.502740035	0.101959157	0.058908148	0.000740035
		$\frac{4\pi}{3}$	-0.400780878	-0.443831887	-0.502	-0.502740035	0.101959157	0.058908148	0.000740035

Tab. 4. Solution for the (first three approximations) with exact solution, with mesh points  $\beta = 0.2$ , for Eq. (55)

$\beta$	$\eta$	$\gamma$	$\tau = 1.75$	$\tau = 1.85$	$\tau = 2$	Exact	Error $\tau = 1.75$	Error $\tau = 1.85$	Error $\tau = 2$
0.2	0.1	0.25	0.000791879	0.000789268	0.000786479	0.000786479	$5.40013 \times 10^{-6}$	$2.78865 \times 10^{-6}$	$5.51412 \times 10^{-15}$
		0.5	0.01266991	0.012628127	0.01258351	0.01258351	0.0000864	0.0000446	$8.82159 \times 10^{-14}$
		0.75	0.064141377	0.063929852	0.06370398	0.06370398	0.000437397	0.000225873	$4.46601 \times 10^{-13}$
	0.05	0.25	0.000798353	0.00079569	0.000792844	0.000792844	$5.5089 \times 10^{-6}$	$2.84615 \times 10^{-6}$	$5.91053 \times 10^{-6}$
		0.5	0.012676384	0.01263455	0.012589876	0.012589876	0.0000865	0.0000447	$8.86131 \times 10^{-14}$
		0.75	0.064147851	0.063936275	0.063710345	0.063710345	0.000437506	0.00022593	$4.47004 \times 10^{-14}$

## 6. CONCLUSION

Fractional-order heat-like and wave-like equations with initial and boundary conditions are studied analytically in this paper. A novel approach based on ADM is provided for the solution of specified problems in a very easy and effective manner. For each case, fractional derivatives are defined in the Caputo sense. The approach is particularly well-suited to solving fractional PDEs with beginning and boundary conditions. Additionally, information demonstrating the output of this approach is presented in the form of graphs and tables to highlight the current technique's best applicability. The results also show that the techniques are a very effective, useful and accurate way to solve heat and wave equations with initial and boundary conditions.

## REFERENCES

1. Eltaib M Abd Elmohmoud, Mohamed Z Mohamed . Numerical treatment of some fractional nonlinear equations by Elzaki transform. *Journal of Taibah University for Science*.2022;16(1): 774-787.
2. Metzler, R Nonnenmacher TF. Space-and time-fractional diffusion and wave equations fractional Fokker–Planck equations and physical motivation. *Chem. Phys*.2002;284:67–90.
3. Metzler, R Klafter J. The random walk's guide to anomalous diffusion A fractional dynamics approach. *Phys Rep*.2000; 339: 1–77.
4. M Subramanian, M Manigandan , C Tunç, T N Gopal , J Alzabut . On system of nonlinear coupled differential equations and inclusions involving Caputo-type sequential derivatives of fractional order. *Journal of Taibah University for Science*.2022;16(1):1-23.
5. Imran Talib, Ali Raza, Abdon Atangana , Muhammad Bilal Riaz . Numerical study of multi- order fractional differential equations with constant and variable coefficients. *Journal of Taibah University for Science*.2022;16(1):608-620.
6. Jothimani, K Kaliraj, K Hammouch, Z Ravichandran C. New results on controllability in the framework of fractional integro differential equations with nondense domain. *Eur Phys J Plus* . 2019;134(9):441.
7. Khan H, Shah R, Kumam P, Arif M. Analytical Solutions of Fractional-Order Heat and Wave Equations by the Natural Transform Decomposition Method. *Entropy*. 2019; 21: 597.
8. Lei Y, Wang H, Chen X, Yang X, You Z, Dong S, Gao J. Shear property high-temperature rheological performance and low-temperature flexibility of asphalt mastics modified with bio-oil. *Constr Build Mater*.2018;174:30–37.
9. Zhang ZY. Symmetry determination and nonlinearization of a nonlinear time-fractional partial differential equation. *Proc R Soc*.2020;476:2019-0564.
10. Mohamed Z Mohamed, Amjad E Hamza , Abdelilah Kamal H Sedeeg .An Efficient Approximate Solutions of the fractional coupled Burger's equation by conformable double Sumudu transforms. *Ain shams journal*.2022;16: 101-879.
11. Shah R, Khan H, Arif M, et al. Application of Laplace–Adomian decomposition method for the analytical solution of third-order dispersive fractional partial differential equations. *Entropy* . 2019;21(4):335.
12. Shah HF, ur Rahman K, Shahzad M G. Numerical solution of fractional order smoking model via Laplace Adomian decomposition method. *Alex Eng J*. 2018;57(2):1061–1069.
13. Rubbab Q, Nazeer M, Ahmad F, et al. Numerical simulation of advection–diffusion equation with Caputo Fabrizio time fractional derivative in cylindrical domains applications of pseudo-spectral collocation method. *Alexandria Eng J*. 2021;60(1):1731–1738.
14. Agbata B C, Shior MM, Olorunni shola OA, Ezugorie IG, Obeng-Denteh. Analysis of Homotopy Perturbation Method (HPM) and its Application for Solving Infectious Disease Models. *IJMSS* 2021,9: 27-38.
15. Hamoud A, Dawood L, Ghadle K, Atshan S. Usage of the modified variational iteration technique for solving Fredholm integro-differential equations. *Int J Mech Prod Eng Res Dev*.2019; 9(2):895–902.
16. Osman M, Gong ZT, Mohammed A. Differential transform method for solving fuzzy fractional wave equation. *J Comput Anal Appl*.2021; 29(3):431–453.
17. Omer Acan1, Omer Firat , Yildiray Keskin, Galip Oturanc. Conformable variational iteration method. *NTMSCI*.2017;5(1):172-178.
18. G Adomian. A review of the decomposition method in applied mathematics. *J Math Anal Appl*.1988;135:501–544.
19. G. Adomian Solving Frontier Problems of Physics The Decomposition method. Kluwer Academic Publishers Boston. 1994.
20. S Momani, Z Odibat. Numerical comparison of methods for solving linear differential equations of fractional order. *Chaos Solitons Fractals*. 2007;31(5):1248–1255.
21. Z Odibat, S Momani. Approximate solutions for boundary value problems of time-fractional wave equation. *Appl Math Comput*.2006;181(1):767–774.
22. V Marinca. An approximate solution for one-dimensional weakly nonlinear oscillations. *J Nonlinear Sci Numer Simul*.2002;3(2): 107–110.
23. TH Hao. Search for variational principles in electrodynamics by Lagrange method. *Int J Nonlinear Sci Numer Simul*.2005;6(2): 209–210.
24. Mustafa S. Hajira, Khan H, Shah R, Masood S. A Novel Analytical Approach for the Solution of Fractional-Order Diffusion-Wave Equations. *Fractal Fract* .2021;5:206.
25. Mainardi F. Fractional Calculus and Waves in Linear Viscoelasticity An Introduction to Mathematical Models. World Scientific Singapore. 2010.
26. Anh VV, Leonenko NN. Harmonic analysis of random fractional diffusion–wave equations. *Appl Math Comput*.2003;141:77–85.
27. Ali EJ. A new technique of initial boundary value problems using Adomian decomposition method. *Int Math Forum* .2012;7:799–814.
28. Mohamed Z Mohamed , Tarig M Elzaki .Applications of new integral transform for linear and nonlinear fractional partial differential equations. *Journal of King Saud University – Science* . 2020;32:544–549.
29. Mustafa S, Hajira, Khan Hm Shah R, Masood S. A Novel Analytical Approach for the Solution of Fractional-Order Diffusion-Wave Equations. *Fractal Fract* . 2021;5:206.
30. Alia A, Shaha K, Lib Y, Khana RA. Numerical treatment of coupled system of fractional order partial differential equations. *J Math Comput Sci*. 2019;19:74–85.
31. Hassan Khan , Rasool Shah , Poom Kumam , and Muhammad Arif. Analytical Solutions of Fractional-Order Heat and Wave Equations by the Natural Transform Decomposition Method. *mdpi journal entropy*.2019;21:597.
32. S Sarwar, Salem Alkhalaf, S Iqbal, MA Zahid. A note on optimal homotopy asymptotic method for the solutions of fractional order heat- and wave-like partial differential equations. *Computers & Mathematics with Applications*. 2020;70(5):942-953.
33. Shah R, Khan H, Mustafa S, Kumam P, Arif M. Analytical Solutions of Fractional-Order Diffusion Equations by Natural Transform Decomposition Method. *Entropy*,2019, 557.
34. M A AL-Jawary. An Efficient Treatments For Linear And Nonlinear Heat-Like And Wave-Like Equations With Variable Coefficients. *IOSR Journal of Mathematics*.2015;11(4):01-13.

Mohamed Zain El Abden:  <https://orcid.org/0000-0002-8041-5841>

Amjad E. Hamza:  <https://orcid.org/0000-0002-8001-1548>

Tarig. M. Elzaki:  <https://orcid.org/0000-0002-6946-9267>

Mohamed S. Algolam:  <https://orcid.org/0000-0003-4005-9595>

Shiraz E. Elhoussein:  <https://orcid.org/0009-0007-8887-7673>



This work is licensed under the Creative Commons BY-NC-ND 4.0 license.



## STABILITY INVESTIGATION OF THE PCM NANOCOMPOSITES

Janusz T. CIEŚLIŃSKI\*<sup>ORCID</sup>, Paulina BOROŃ\*<sup>ORCID</sup>, Maciej FABRYKIEWICZ\*<sup>ORCID</sup>

\*Faculty of Mechanical Engineering and Ship Technology, Institute of Energy, Gdańsk University of Technology, ul. Narutowicza 11/12, 80-233 Gdańsk, Poland

[jcieslin@pg.edu.pl](mailto:jcieslin@pg.edu.pl), [s166585@student.pg.edu.pl](mailto:s166585@student.pg.edu.pl), [mac.fabrykiewicz@gmail.com](mailto:mac.fabrykiewicz@gmail.com)

received 21 September 2022, revised 13 March 2023, accepted 19 March 2023

**Abstract:** Ensuring the stability is a key issue to be solved for the technical application of nanocomposites. In this work, fatty acid P1801 served as base phase change material (PCM) P1801, and its main ingredients are palmitic acid (58%) and stearic acid (38%). Titania (TiO<sub>2</sub>) and alumina (Al<sub>2</sub>O<sub>3</sub>) with mass concentrations of 1% and 5% were selected as nanoparticles, while polyvinylpyrrolidone (PVP) or oleic acid (OA) with mass concentrations of 5% were tested as surfactants. On the basis of the measured temperature distributions in the sample, which is subject to melting and solidification processes, it was determined which of the tested nanocomposites are stable and which are not. In addition, a thermal test was proposed to assess the stability of the produced nanoPCM, which consists in measuring the temperature distribution versus time according to a precisely given procedure.

**Key words:** stability, nanoPCM, experiment, surfactant, alumina, titania, concentration

### 1. INTRODUCTION

The main obstacle to the widespread use of materials containing nanoparticles is their stability. This applies to both nanofluids and nanocomposites (nanoPCMs) [1–8]. While in the case of nanofluids there are reliable methods of determining their stability [9–11], in the case of nanocomposites these methods are still being developed. Wu et al. [12] studied the stability of paraffin-Cu-surfactant nanocomposites through heat capacity measurement by the use of differential scanning calorimetric (DSC). Although the heat transfer rate of nanoPCM was improved, the latent heats and the melting and freezing temperatures change very little after 100 thermal cycles. Choi et al. [13] tested the stability of stearic acid-carbon additives (multi-walled carbon nanotubes [MWCNT], CNT and graphene) nanocomposites by direct observation of examined nanoPCMs in the liquid state in a thermal chamber at a constant temperature. Jin et al. [14] proposed a thermal cycling test to evaluate the influence of the fabrication method of paraffin wax-expanded graphite nanocomposites on their thermal stability. A single test consisted of a melting and solidification process. Based on the time course of temperature, Jin et al. [14] found that both nanoPCMs produced in vacuum and those produced at atmospheric pressure were thermally stable. Zhichao et al. [15], basing their study on the Fourier transform infrared spectroscopy (FT-IR) spectrum, established that the optical micrographs of erythritol-TiO<sub>2</sub> nanocomposite with nanoparticles higher than 0.2%vol were more blurry than that for pure erythritol. Moreover, the solidification microstructure was changed. Nourani et al. [16] examined the stability of thermal properties (melting temperature and phase change enthalpy) of paraffin-Al<sub>2</sub>O<sub>3</sub> nanocomposites and stated that the DSC analysis after many melting/solidification cycles does not provide information on the stability of the nanocomposite. Measurement of the melting point does not provide information about the stability of the nanoPCM, as

it depends on chemical decay. In turn, the latent heat of fusion is an intensive property. Liu and Yang [17] used scanning electron microscopy (SEM) to study the microstructure and optical microscopy to examine the crystallography features of eutectic hydrate salt- $\alpha$ -Al<sub>2</sub>O<sub>3</sub> nanocomposite. Singh et al. [18], using field emission scanning electron microscopy (FESEM), determined that the distribution of CuO nanoparticles in the Myo-inositol based nanocomposite was more uniform than that observed in the case of Al<sub>2</sub>O<sub>3</sub> nanoparticles. Zhang et al. [19] studied the surface morphology and the chemical structure of stearic acid-expanded graphite nanocomposite by use of an SEM and an FT-IR spectrometer, respectively. Nourani et al. [20] evaluated the stability of the paraffin- $\gamma$ -Al<sub>2</sub>O<sub>3</sub>-surfactant nanocomposite by the use of spectrophotometry and measurement of Al<sup>3+</sup> concentration. Prabhu and ValanArasu [21] examined the stability of the paraffin wax-TiO<sub>2</sub>-Ag nanocomposites by visual analysis of the sedimentation photographs 12 h after nanoPCM production. Ibrahim et al. [22], based on the fact that the addition of nanoparticles to paraffin causes a change in the absorbance and transmittance of the mixture, proposed an optical method for determining the stability of the paraffin-TiO<sub>2</sub>/MgO nanocomposite. It was observed that the absorbance of the tested nanocomposites depends on the type and concentration of added nanoparticles. In turn, the transmittance for nanocomposites with a mass concentration of 1% changes significantly for short wavelengths and is stable for long wavelengths. To examine the distribution and dispersion of nanoparticles on the surface of the samples, Ibrahim et al. [22] used FESEM and energy dispersive spectroscopy (EDS). Zhang et al. [23] analysed the stability of nanophase change emulsions both by direct observation and particle size distribution and particle dispersion index (PDI) measurements. Venkateshwar et al. [24] analysed the potential techniques to quantify the concentration of nanoparticles after each melting–solidification cycle on nanoPCM. Limitations of the application of the thermal conductivity measurement, viscosity measurement, heat capacity measurement and microscopy for quanti-

fication of the nanoparticle concentration have been discussed. Instead, Venkateshwar et al. [24] have proposed a novel image analysis technique to measure the concentration and non-uniformity in the dispersion of nanoparticles in a vial of 4 cm height placed in the thermal bath. The method consists in making digital images of the sample, which are then converted to the red-green-blue (RGB) scale. Then, the RGB scale is converted to a hue-saturation-lightness (HSL) scale. A correlation between an individual component of the RGB and HSL scales and nanoparticles concentration has to be developed. The lightness (L) was observed to closely follow the change in the nanoparticle concentration. It was established that the rate of sedimentation depends on the density difference in the solid and liquid states of phase change material (PCM). Moreover, the effect of particle size dominates over nanoparticles density in the sedimentation process. Recently, the role of particle/molecules polarity has been highlighted in studies of the stability of nanocomposites [25–28]. Saydam and Duan [25] conducted a comprehensive study on the stability of the paraffin-based nanocomposites by use of visualisation and thermal conductivity measurement. Three different types of nanoparticles were tested, i.e. MWCNT, graphene nanoplatelets (GNP) and Al<sub>2</sub>O<sub>3</sub>. Significant coagulation and deposition of nanoparticles were found after a few thermal cycles regardless of the nanoparticle type, concentration or dispersion method (sonication, stirring). Different boundary conditions in heating were also examined for their effects. All tested nanocomposites showed an insignificant increase in thermal conductivity due to the agglomeration and sedimentation of nanoparticles. According to Saydam and Duan [25], the fundamental reason is related to the chemical nature of the PCM and nanoparticles: the paraffin wax has non-polar molecules while all the tested nanoparticles have polar molecules. Saroha et al. [28] tested the stability of paraffin-TiO<sub>2</sub> and sorbitol-TiO<sub>2</sub> nanoPCMs. According to the authors' concept, the paraffin-TiO<sub>2</sub> nanoPCM is thermally unstable, because n-alkane chains that create paraffin wax are nonpolar and TiO<sub>2</sub> nanoparticles are polar. Contrary to paraffin wax, sorbitol molecules are polar; therefore, sorbitol-TiO<sub>2</sub> nanoPCM is thermally stable.

According to the literature review, the methods for determining the stability of nanoPCM can be divided into several groups. The first method, the simplest, is the direct observation of the produced nanoPCMs over time. The second group includes the use of SEM to determine the microstructure of nanocomposites. The third group of methods is based on ascertainment of the optical properties of produced nanoPCM using spectrophotometry. The next group of methods is based on the measurements of thermophysical properties of the produced nanoPCM, with the use of DSC. Measurements of nanoparticle distribution and concentration are also used to determine the stability of nanoPCMs. Finally, the measurements of the rate of heating and cooling of nanoPCM during the melting and solidification process should be distinguished.

In the present study, the stability of a nanoPCM, composed of base PCM, nanoparticles and surfactant, was investigated. Fatty acid P1801 served as base PCM, and its main ingredients are palmitic acid (58%) and stearic acid (38%). As nanoparticles, TiO<sub>2</sub> and Al<sub>2</sub>O<sub>3</sub> with mass concentrations of 1% and 5% were used. Polyvinylpyrrolidone (PVP) or oleic acid (OA) with mass concentrations of 5% were selected as surfactants. The nanoPCMs were fabricated by the use of a two-step method in the liquid phase.

The paper presents the original results of stability studies of a series of fatty acid-based nanocomposites. Moreover, the effect of nanoparticles on the rate of heat transfer during the process of

heating and cooling nanoPCM was assessed. Finally, a simplified nanoPCM stability test was proposed, consisting in measuring the temperature in the sample with a single resistance thermometer placed along the axis of the sample in the middle of its height. The method used is an extension of the thermal cycling test proposed by Jin et al. [14]. However, while in the method of Jin et al. [14] the solidification process took place immediately after the melting process, in the present test, between the melting and solidification stages, there is a period of 12 h of keeping the nanoPCM at ambient temperature. It is believed that this is a more realistic representation of the operating mode of the thermal energy storage, which may affect the stability of the nanoPCM. In addition, the method of measuring the temperature of the nanoPCM sample was precisely defined, which was not specified in the study of Jin et al. [14].

## 2. MATERIALS AND METHODS

### 2.1. Materials

An organic commercial material fatty acid, P1801, supplied by Konimpex Chemicals (Konimpex Chemicals, Konin, Poland), was used as a base material. The detailed chemical composition of the tested material was determined on the basis of chromatographic tests using the GC-MS-QP2010 PLUS (Shimadzu Corp., Kyoto, Japan). The results of the analysis are presented in Fig. 1.

The range of phase transition temperatures, heat of phase transition and specific heat of the tested base material were estimated by the DSC method using DSC 404 F1 Pegasus instrument (Netzsch GmbH, Selb, Germany). The results of the analysis are presented in Fig. 2.

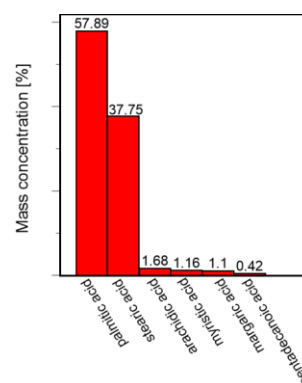


Fig. 1. Results of the chromatographic analysis of P1801

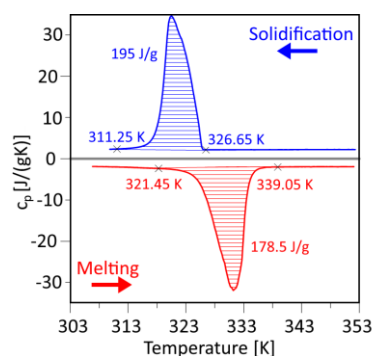


Fig. 2. Results of the DSC analysis of P1801. DSC, differential scanning calorimetric

The tested nanoparticles were titania (TiO<sub>2</sub>) and alumina (Al<sub>2</sub>O<sub>3</sub>), supplied by Sigma Aldrich Ltd. (Merck, KGaA, Darmstadt, Germany). Mass concentrations of particles in the composites were 1% and 5%. SEM images of the used nanoparticles are shown in Fig. 3.

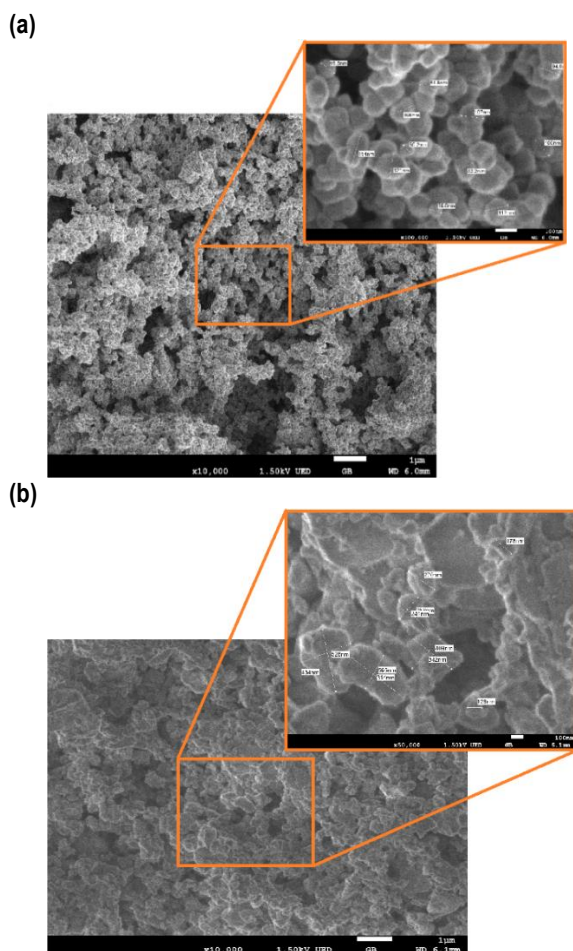


Fig. 3. SEM images of the nanoparticles; (a) TiO<sub>2</sub>, (b) Al<sub>2</sub>O<sub>3</sub>. SEM, scanning electron microscopy

Tab. 1. List of the tested PCMs

Sample	Melting	Solidification	Surfactant (wt [%])	Nanoparticles (wt [%])
nanoPCM1	nM1	nS1	OA (5%)	Al <sub>2</sub> O <sub>3</sub> (1%)
nanoPCM2	nM2	nS2		Al <sub>2</sub> O <sub>3</sub> (5%)
nanoPCM3	nM3	nS3		TiO <sub>2</sub> (1%)
nanoPCM4	nM4	nS4		TiO <sub>2</sub> (5%)
nanoPCM5	nM5	nS5	PVP (5%)	Al <sub>2</sub> O <sub>3</sub> (1%)
nanoPCM6	nM6	nS6		Al <sub>2</sub> O <sub>3</sub> (5%)
nanoPCM7	nM7	nS7		TiO <sub>2</sub> (1%)
nanoPCM8	nM8	nS8		TiO <sub>2</sub> (5%)
BPCM	BM	BS	-	-

BPCM, base phase change material; OA, oleic acid; PCMs, phase change materials; PVP, polyvinylpyrrolidone

The following surfactants were used to prepare nanocomposites: OA supplied by Warchem Ltd. (Warchem Ltd., Warsaw, Poland) and PVP supplied by Keten Ltd. (Keten Ltd., Wrocław, Poland).

A two-step method was used to prepare the tested nanoPCM. The process of producing nanoPCM started with melting the base phase change material (BPCM) in the container in a water bath at a temperature of 343 K. The melted BPCM was poured into measuring tanks in the amount of 80 g. The selected surfactant was added to the melted BPCM at a mass concentration of 5% and premixed. Then, nanoparticles in an amount corresponding to mass concentrations of 1% and 5% were added to the mixture prepared and mixed again. The containers with the prepared samples were placed in an ultrasonic cleaner for a period of 45 min. The list of nanoPCMs tested is presented in Tab. 1.

## 2.2. Apparatus and instrumentation

The setup consisted of a thermostat EBR<sup>c</sup> produced by Prüfgeräte-Werk Medingen (MLW, Medingen, Germany) and a computer-aided data acquisition system. The scheme of the experimental setup is shown in Fig. 4. A set of four containers with nanoPCM were simultaneously immersed in a water bath. The containers were made of glass, ensuring direct observation of the tested samples. Each container was equipped with a resistance thermometer placed halfway up the container axis.

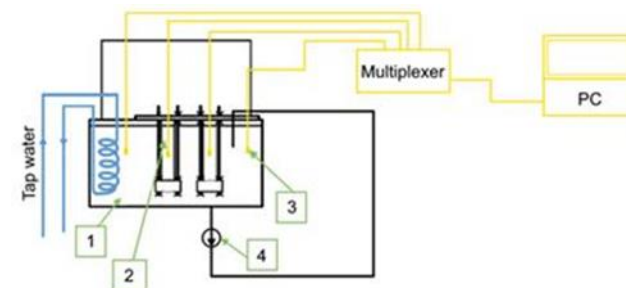


Fig. 4. Scheme of the experimental setup scheme: 1 – thermostat, 2 – set of containers with PCM, 3 – resistance thermometer, 4 – circular pump. PCM, phase change material

## 2.3. Methods

A single cycle included three measurement stages (Fig. 5). The first stage was started by placing the prepared molten sample at 343 K in a water bath of a thermostat at 293 K. During the solidification of the sample, the temperature was recorded using a resistance thermometer Pt100 (Termoaparatura Wrocław, Wrocław, Poland). The temperature values were recorded every 10 s. The measurement was performed until the temperature reading from the resistance thermometer did not deviate from 293 K by ± 0.5 K for 5 min. When the sample reached the expected temperature, it was removed from the water bath and left at the ambient parameters for about 20 min. After this time, the sample was placed again in the water bath at 343 K. The temperature measurement was carried out until the sample melted, i.e. it reached the temperature of 343 ± 0.5 K, and then the sample remained at the ambient temperature for 12 h. The second stage of the cycle started with the process of melting the sample in a water bath at a temperature of 343 K. The process was carried out until the sample reached the water bath temperature (± 0.5 K). Then the sample was placed in the water bath for about 20 min. After this time, the sample was placed back in the water bath at 293 K. After solidification, the sample was kept at ambient temperature for 12 h. The



third step was essentially a repetition of the second step, except for the 12-h phase involving keeping the sample at ambient temperature.

A simplified nanoPCM stability test was proposed, consisting in measuring the temperature in the sample according to the three-stage procedure involving three melting and three solidifica-

tion processes. If the time of reaching the melting temperature  $T_t''$  or solidification temperature  $T_k'$  of the nanoPCM after the third melting or solidification processes does not differ by more than 5% compared to the first melting or solidification processes, it can be assumed that the nanoPCM is stable.

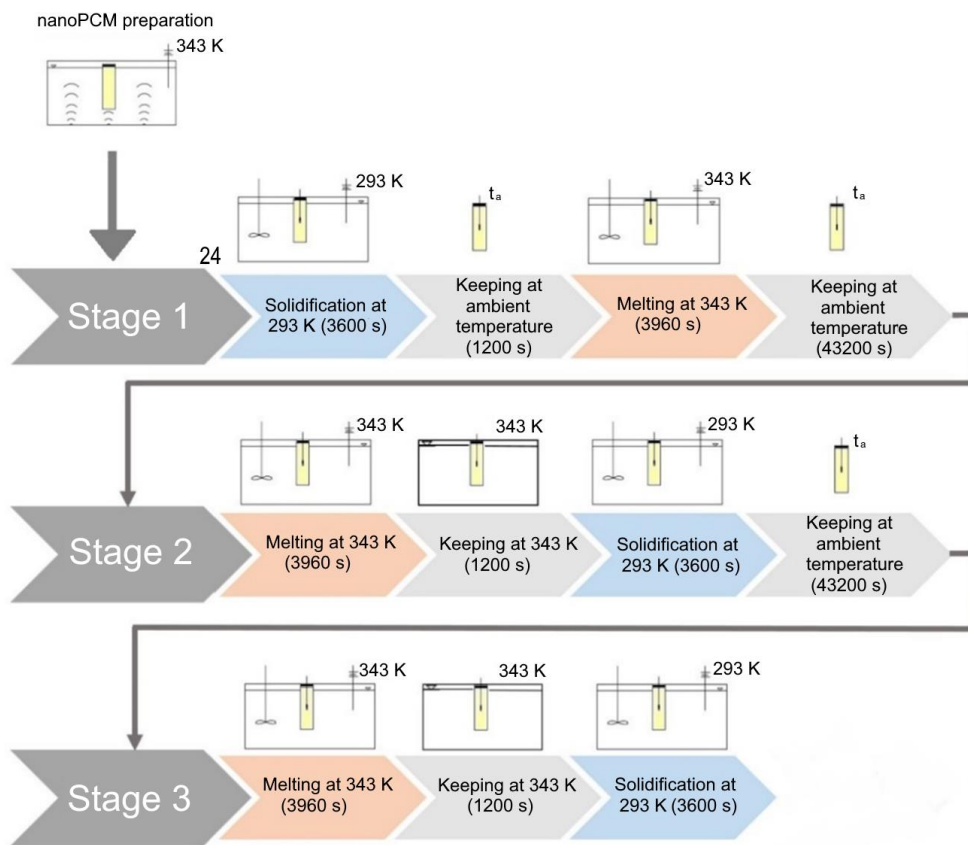


Fig. 5. Flow chart of the research cycle

### 3. RESULTS AND DISCUSSION

In order to check the measurement procedure and the reproducibility of the results, a full test cycle was performed for the BPCM according to the measurement procedure described in Section 2.3. Figures 6a and 6b show the temperature courses during the three melting processes (Run1, Run2 and Run3) and solidification processes (Run1, Run2 and Run3) of the tested BPCM, respectively. The black lines in Fig. 6 ( $BM_{AV}$  and  $BS_{AV}$ ) represent the average temperature calculated as an arithmetic mean of three runs for the melting and solidification processes, respectively. As shown in Fig. 6a, the temperature courses during the solidification processes, which took place every 15 h, practically overlap. The time after which the  $T_k'$  temperature was reached for the second solidification process (Run2) was about 4.7% longer in comparison with those for the first (Run1) and third (Run3) solidification processes. As can be seen in Fig. 6b, the time to reach the melting temperature  $T_t''$  was the same in all three melting processes (Run1, Run2 and Run3). The average times, calculated in each case as an arithmetic mean for the three processes, to reach

the temperatures  $T_t''$  and  $T_k'$  for BPCM were 2,190 s and 2,528 s, respectively.

In order to determine the stability of the tested nanoPCMs, the temperature courses were analysed for the three solidification and melting processes carried out according to the proposed procedure (Section 2.3). The obtained temperature courses are presented in Fig. 7. It is noticeable that nanoPCM1, nanoPCM2, nanoPCM5 and nanoPCM6 present the convergence of the temperature course of their cycles in the solidification process. For the melting process, this convergence is visible for nanoPCM1, nanoPCM5 and nanoPCM7.

As can be seen in Fig. 7a, the time to reach the melting temperature  $T_t''$  for nanoPCM1 was almost the same for the first and second melting processes (Run1 and Run2), while it was about 5% longer for the third solidification process (Run3) compared to the first process (Run1). In the case of the solidification process, the time of reaching  $T_k'$  for nanoPCM1 was almost the same in all three solidification processes (Run1, Run2 and Run3). So, it can be concluded that nanoPCM1 is relatively stable. It is worth noting that in the case of BPCM, the times to achieve  $T_k'$  and  $T_t''$  were



shorter by about 10% and 5% compared to nanoPCM1, which indicates heat transfer deterioration when using nanoPCM1.

Fig. 7b shows that the time of reaching the melting temperature  $T_t''$  for nanoPCM2 increases with the number of repetitions and is longer for Run2 and Run3 compared to Run1 by about 4% and 13%, respectively. The temperature courses for two solidification processes (Run1 and Run2) almost overlap. However, for the third process (Run3), the time to reach the temperature  $T_k'$  was about 4% longer compared to Run1. Hence, due to the systematic increase in melting and solidification times in subsequent runs, nanoPCM2 cannot be considered stable. As for nanoPCM1, it was observed that adding  $Al_2O_3$  with a mass concentration of 5% to BPCM deteriorated heat transfer. In the case of nanoPCM2, this applies to both the melting and solidification processes, for which the time to reach  $T_t''$  and  $T_k'$  was about 10% longer than for BPCM.

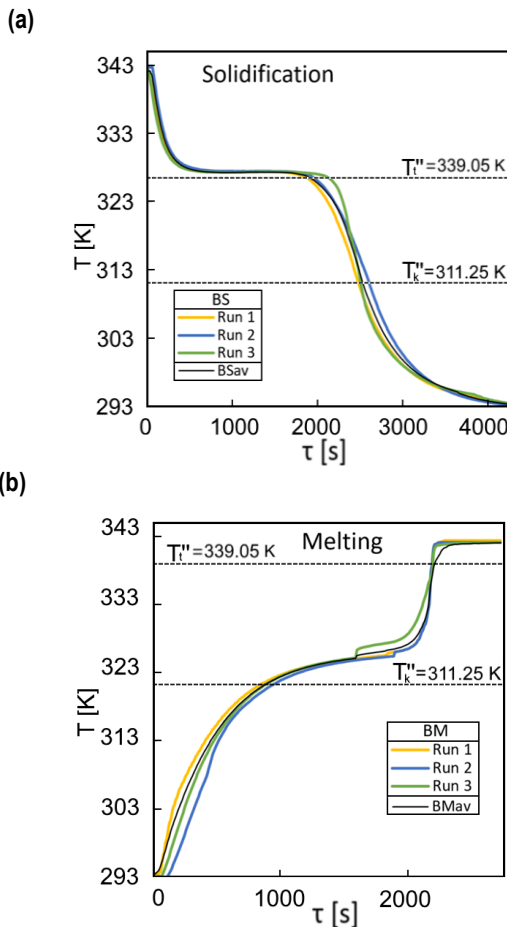


Fig. 6. Temperature courses for BPCM (a) solidification; (b) melting. BPCM, base phase change material

Fig. 7c shows the temperature courses for nanoPCM3. In the case of the melting process, the time to reach  $T_t''$  for subsequent runs slightly increases and is, respectively, about 2% and 3% longer for Run2 and Run3, compared to Run1. For the solidification process, the time to reach the temperature  $T_k'$  increases by about 5% for Run2 and about 15% for Run3 compared to Run1. Therefore, nanoPCM3 cannot be treated as stable. However, it is worth noting that the addition of  $TiO_2$  nanoparticles with a mass concentration of 1% improved heat transfer, especially for the melting

process for which the time to reach  $T_t''$  for BPCM was about 15% shorter than that observed for nanoPCM3.

Fig. 7d shows the temperature courses for nanoPCM4. It is seen that the time to reach the melting temperature  $T_t''$  increases substantially from run to run, and is about 12% and 40% longer for Run2 and Run3, respectively, compared to Run1. A similar trend is observed for the solidification process, where the time to reach  $T_k'$  is about 18% and 25% for Run2 and Run3, respectively, compared to Run1. Therefore, the nanoPCM4 should be treated as highly unstable. The intensification of heat transfer in the melting process is noteworthy, which admittedly decreases with each subsequent run, but the time to reach the melting temperature  $T_t''$  during Run3 is about 15% longer than for BPCM.

As seen in Fig. 7e, the time to reach the melting temperature  $T_t''$  for nanoPCM5 increases for each subsequent run, and finally for Run3 is about 40% longer than for BPCM. However, the addition of  $Al_2O_3$  nanoparticles with a mass concentration of 1% with PVP as a surfactant has no effect on the solidification process. The temperature courses for all three runs (Run1, Run2 and Run3) are almost identical. Therefore, the nanoPCM4 should be treated as highly unstable. Moreover, the addition of  $Al_2O_3$  nanoparticles with a mass concentration of 1% with PVP as a surfactant deteriorates heat transfer. The times to reach  $T_t''$  and  $T_k'$  for nanoPCM5 are longer than for BPCM.

Fig. 7f shows the temperature courses for nanoPCM6. For the melting process, the times to reach temperature  $T_t''$  for Run1 and Run2 are almost identical. However, the time to reach the melting temperature for Run3 is longer by about 15% compared to that observed for Run1. For the solidification process, the times to reach the temperature  $T_k'$  were almost the same for all the three runs. Nevertheless, nanoPCM6 cannot be considered stable. The addition of  $Al_2O_3$  nanoparticles with a mass concentration of 5% with PVP as a surfactant slightly deteriorates heat transfer. The time extension to reach the temperatures  $T_t''$  and  $T_k'$  for the third runs compared to BPCM was about 35% for the melting process and 8% for the solidification process.

Fig. 7g shows the temperature courses for nanoPCM7. For the melting process, after Run1 a kind of stabilisation is observed – the temperature courses for Run2 and Run3 overlap with each other. For the solidification process, the temperature courses for all three runs are almost identical. On this basis, nanoPCM7 can be considered stable. However, the addition of  $TiO_2$  nanoparticles with a mass concentration of 1% and PVP as a surfactant slightly deteriorates heat transfer during the melting process. The time to reach temperature  $T_t''$  for Run3 is about 13% longer compared to BPCM. The time to reach solidification temperature  $T_k'$  for nanoPCM7 is identical as for BPCM.

Fig. 7h shows the temperature courses for nanoPCM8. The time to reach the melting temperature  $T_t''$  increases for each subsequent run and finally for Run3 is about 19% longer than for Run1. For the solidification process, the times to reach temperature  $T_t''$  for Run1 and Run2 are nearly the same, while for Run3 the time extension was about 7% compared to Run1. On this basis, it was assessed that nanoPCM8 is not stable. The divergent impact of  $TiO_2$  nanoparticles with a mass concentration of 5% and PVP as a surfactant on heat transfer can be observed. For Run1, during the melting process, a heat transfer improvement is observed – the time to reach temperature  $T_t''$  is shorter by about 6% compared to that observed for BPCM. For Run2 and Run3, deterioration of heat transfer is noted – the time to reach temperature  $T_t''$  for Run3 is longer by about 12% compared to that observed for BPCM. For the solidification process, a slight improvement of heat transfer was

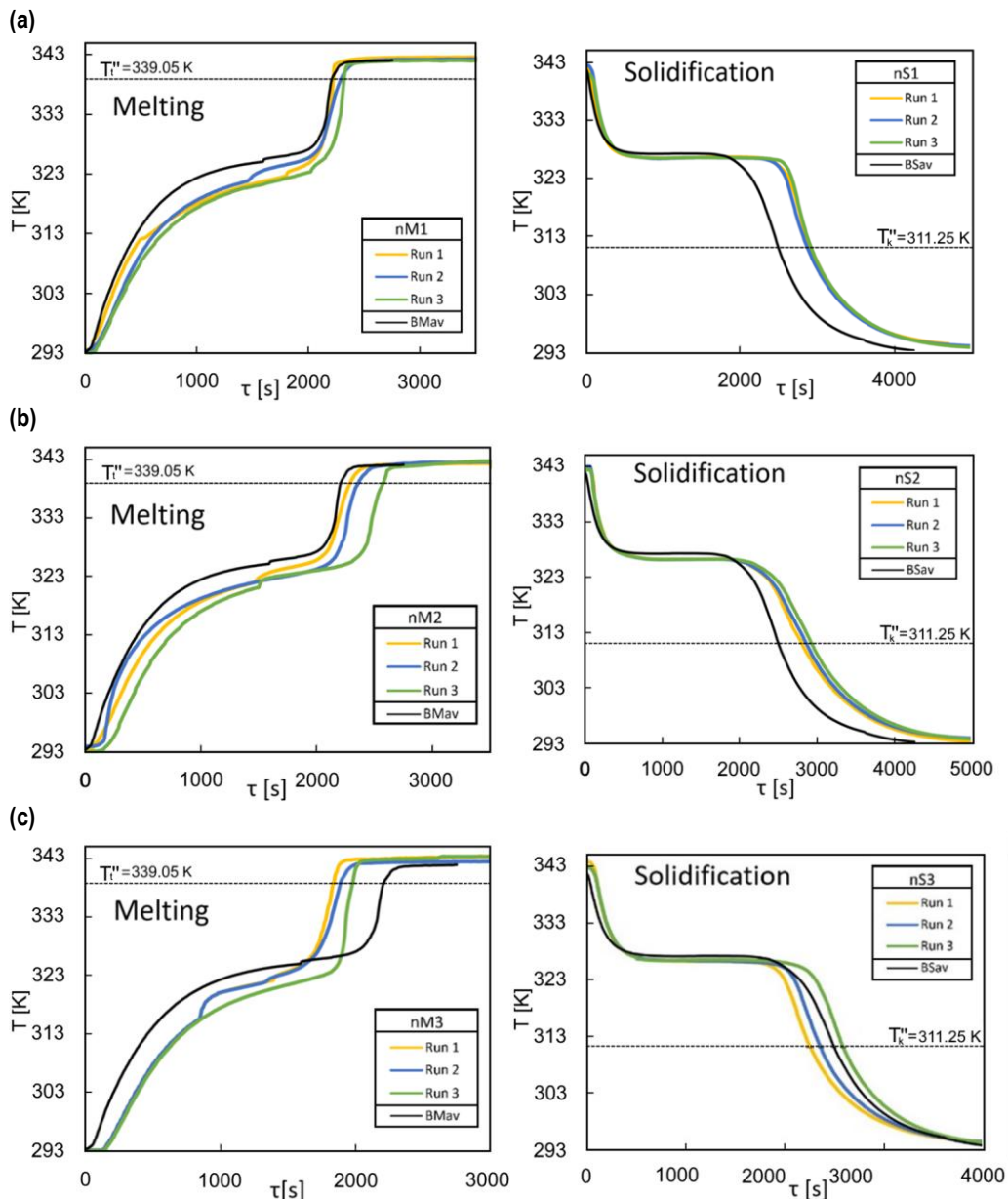
observed for Run1 and Run2, and a slight deterioration of heat transfer was observed for Run3 compared to BPCM.

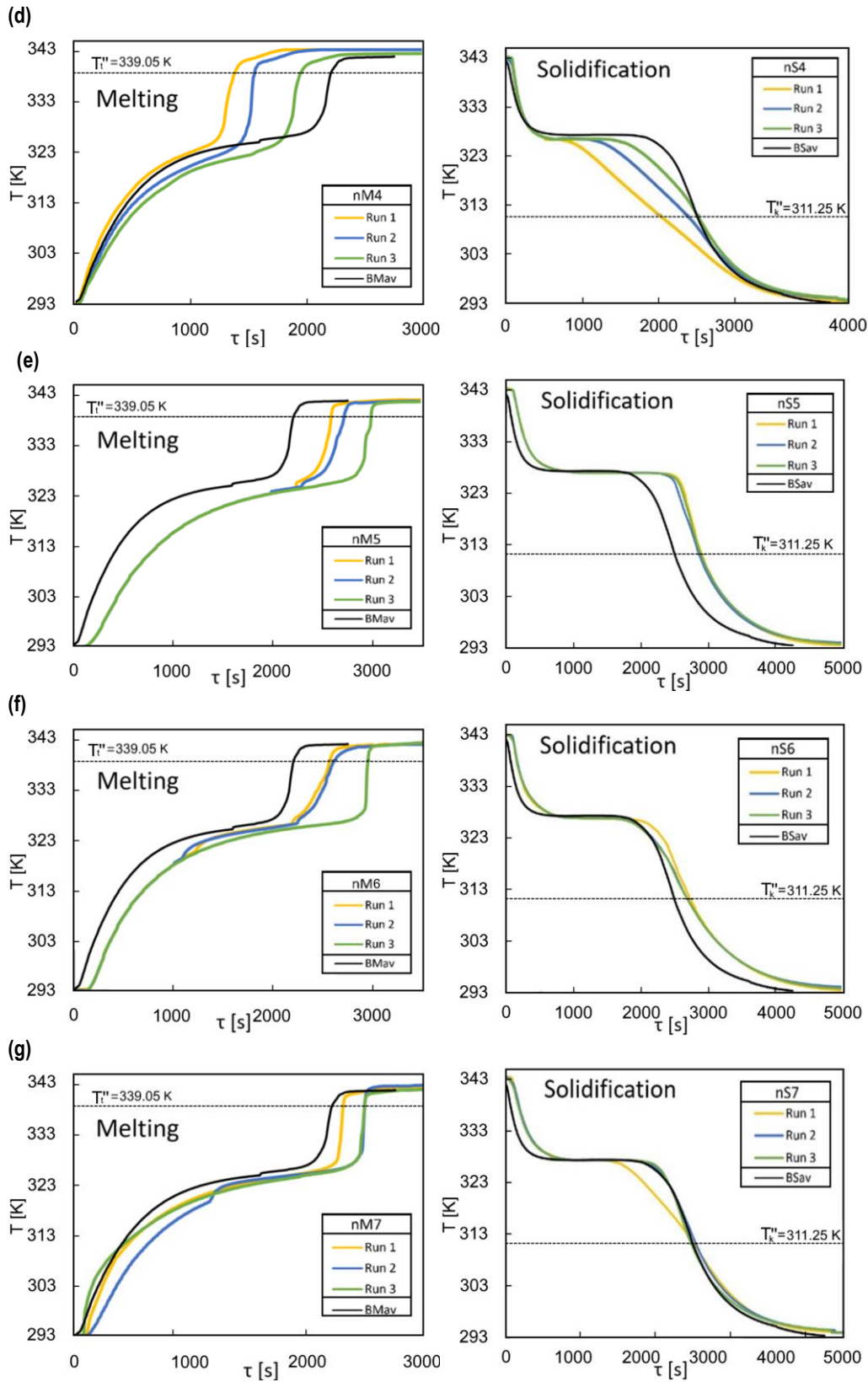
During the melting process, free convection dominates, which favours the possible sedimentation of nanoparticles. The melting process proceeds from the glass wall of the vessel with the nanoPCM sample towards the core in which the resistance thermometer is located. The front of the molten nanoPCM moves in an axisymmetric manner because the vessel with the nanoPCM sample is positioned vertically and is immersed in a large volume of liquid at a constant temperature (controlled by a thermostat). Initially, the layer of liquid nanoPCM is very thin and practically immobile.

As the layer thickness increases, the molten nanoPCM rises upwards along the vessel wall. The upward movement also results from the fact that the bottom of the cell is heated and the top of the sample is not heated. Fulfilling the mass continuity balance requires that the liquid nanoPCM that has reached the free surface begins to flow down, melting the solid nanoPCM around the resistance thermometer.

The solidification process starts from the vessel wall and the front of the solidified nanoPCM moves in an axisymmetric manner towards the core, which is in the liquid state. The heat transfer process is dominated by heat conduction, which means that the time of nanoPCM solidification is much longer compared to that involved in the melting process. Due to the axisymmetric nature of the heat transfer, there is no need to measure the angular temperature distribution, and accordingly it was decided to place the thermal resistance thermometer in the axis of the vessel.

The assessment of the stability of nanoPCM consists in maintaining the same temperature course after several cycles including the process of melting and solidification. It is assumed that the addition of nanoparticles improves heat conduction, and thus, above all, a shortening of the solidification time. The melting and solidification time of nanoPCM should be shorter than that of BPCM. The shift of the temperature distribution curves for nanoPCM towards the temperature distributions obtained for BPCM indicates the sedimentation of nanoparticles, and thus the lack of stability.





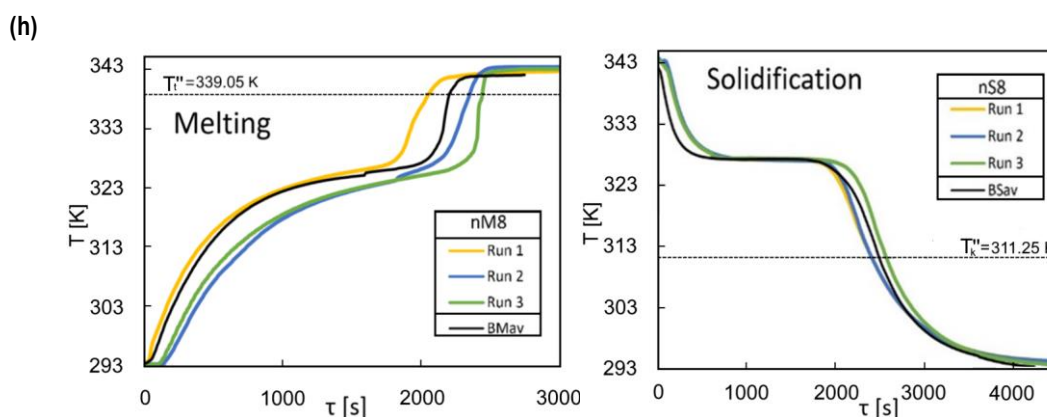


Fig. 7. Temperature courses for the melting and solidification processes of nanoPCM; (a) nanoPCM1; (b) nanoPCM2; (c) nanoPCM3; (d) nanoPCM4; (e) nanoPCM5; (f) nanoPCM6; (g) nanoPCM7; (h) nanoPCM8

#### 4. CONCLUSIONS

The stability of nanoPCMs is a major research challenge, as it will determine their potential application in practice. At present, there is no reliable method for assessing the stability of produced nanoPCMs. As stated by Saydam and Duan [25], multidisciplinary efforts to achieve a better understanding of the physical/chemical properties of nanoPCMs are required.

The paper presents the original results of stability studies of a series of fatty acid-based nanocomposites with the use of two types of nanoparticles and two stability-enhancing surfactants. Out of eight samples tested (as presented in Tab. 1), only two can be considered relatively stable, i.e. nanoPCM1 and nanoPCM7, and these are characterised by smaller nanoparticle concentrations. In the case of addition of Al<sub>2</sub>O<sub>3</sub>, it was observed that regardless of the concentration of nanoparticles (1%wt or 5%wt), nanoPCMs with OA surfactant were more stable. For nanoPCMs with TiO<sub>2</sub> nanoparticles, also irrespective of the nanoparticle concentration (1% wt or 5% wt), those in which PVP was used as a surfactant were more stable.

In addition to assessing the stability of nanoPCM, the effect of nanoparticles on the rate of heat transfer during the process of heating and cooling nanoPCM was assessed. It was observed that, regardless of surfactant type (OA or PVP), addition of Al<sub>2</sub>O<sub>3</sub> nanoparticles results in heat transfer deterioration, particularly during the melting process. Contrary to the effect observed with Al<sub>2</sub>O<sub>3</sub> nanoparticles, addition of TiO<sub>2</sub> nanoparticles, particularly when administered in the combination of OA surfactant, results in heat transfer enhancement, particularly during the melting process.

A thermal stability test of the produced nanocomposites, based on temperature measurement in the axis of the cylindrical sample placed in a constant temperature bath, was also proposed.

#### NOMENCLATURE

$c_p$	Specific heat	[J/(gK)]
$T_k'$	Initial solidification temperature	[K]
$T_k''$	Final solidification temperature	[K]
$T_t'$	Initial melting temperature	[K]
$T_t''$	Final melting temperature	[K]

#### ABBREVIATIONS

BM	BPCM melting
BPCM	Base phase change material
BS	BPCM solidification
DSC	Differential scanning calorimetry
EDS	Energy dispersive spectroscopy
FESEM	Field emission scanning electron microscopy
FT-IR	Fourier transform infrared spectroscopy
GNP	Graphene nanoplatelets
HSL	Hue-saturation-lightness
MWCNT	Multi-walled carbon nanotubes
OA	Oleic acid
PCM	Phase change material
PVP	Polyvinylpyrrolidone
RGB	Red-Green-Blue
SDBS	Sodium dodecyl benzene sulfonate
SEM	Scanning electron microscopy

#### REFERENCES

- Haghighi EB, Nikkam N, Saleemi M, Behi M, Mirmohammadi MA, Poth H, et al. Shelf stability of nanofluids and its effect on thermal conductivity and viscosity. *Measurement Science and Technology*. 2013;24:105301.
- Lofzadeh Dehkordi B., Ghadimi A., Metselaar H.S.C. Box–Behnken experimental design for investigation of stability and thermal conductivity of TiO<sub>2</sub> nanofluids. *Journal of Nanoparticle Research*. 2013;15:1369.
- Witharana S., Palabiyik I., Musina Z., Ding Y. Stability of glycol nanofluids — The theory and experiment. *Powder Technology*. 2013;239:72–77.
- Ilyas S.U., Pendyala R., Marneni N. Stability and Agglomeration of Alumina Nanoparticles in Ethanol-Water Mixtures. *Procedia Engineering*. 2016;148:290–297.
- Fuskele V., Sarviya R.M. Recent developments in Nanoparticles Synthesis. Preparation and Stability of Nanofluids. *Materials Today: Proceedings*. 2017;4:4049–4060.
- Yu F, Chen Y, Liang X, Xu J, Lee C, Liang Q, et al. Dispersion stability of thermal nanofluids. *Progress in Natural Science: Materials International*. 2017;27:531-542.
- Abdullah M, Malik SA, Iqbal MH, Sajid MM, Shad NA, Hussain SZ, et al. Sedimentation and stabilization of nano-fluids with dispersant. *Colloids and Surfaces*. 2018;554:86–92.
- Mahbulul IM, Elcioglu EB, Amalina MA, Saidur R. Stability, thermo-physical properties and performance assessment of alumina–water nanofluid with emphasis on ultrasonication and storage period. *Powder Technology*. 2019;345:668–675.



9. Lee L, Han K, Koo J. A novel method to evaluate dispersion stability of nanofluids. *International Journal of Heat and Mass Transfer*. 2014;70:421–429.
10. Lemes MA, Rabelo D, de Oliveira AE. A novel method to evaluate nanofluid stability using multivariate image analysis. *Analytical Methods*. 2017;9:5826.
11. Ilyas SU, Pendyala R, Marneni N. Stability of nanofluids. *Topics in Mining, Metallurgy and Materials Engineering*. Eds. Korada VS, Hamid NHB. *Engineering applications of nanotechnology. From energy to drug delivery*. Springer;2017. Available from: <https://www.springerprofessional.de/engineering-applications-of-nano-technology/11992454>
12. Wu S, Zhu D, Zhang X, Huang J. Preparation and Melting/Freezing Characteristics of Cu/Paraffin Nanofluid as Phase-Change Material (PCM). *Energy Fuels*. 2010; 24(3):1894–1898.
13. Choi DH, Lee J, Hong H, Kang Y T. Thermal conductivity and heat transfer performance enhancement of phase change materials (PCM) containing carbon additives for heat storage application. *International Journal of Refrigeration*. 2014;42:112-120.
14. Jin Y, Wan Q, Ding Y. PCMs Heat Transfer Performance Enhancement with Expanded Graphite and its Thermal Stability. *Procedia Eng*. 2015;102:1877-1884
15. Zhichao L, Qiang Z, Gaohui W. Preparation and enhanced heat capacity of nano-titania doped erythritol as phase change material. *International Journal of Heat and Mass Transfer*. 2015;80:653–659.
16. Nourani M, Hamdami N, Keramat J, Moheb A, Shahedi M. Thermal behavior of paraffin-nano-Al<sub>2</sub>O<sub>3</sub> stabilized by sodium stearyl lactylate as a stable phase change material with high thermal conductivity. *Renewable Energy*. 2016;88:474-482.
17. Liu Y, Yang Y. Use of nano- $\alpha$ -Al<sub>2</sub>O<sub>3</sub> to improve binary eutectic hydrated salt as phase change material. *Solar Energy Materials & Solar Cells*. 2017;160:18–25.
18. Singh DK, Suresh S, Singh H, Rose BAJ, Tassou S, Anantharaman N. Myo-inositol based nano-PCM for solar thermal energy storage. *Applied Thermal Engineering*. 2017;110:564–572.
19. Zhang JL, Wu N, Wu XW, Chen Y, Zhao Y, Liang JF, et al. High latent heat stearic acid impregnated in expanded graphite. *Thermo-chimica Acta*. 2018;663:118–124.
20. Nourani M, Hamdami N, Keramat J. Preparation and evaluation of a stable nanoalumina-paraffin composite: Melting rate investigation using image analysis. *Journal of Dispersion Science and Technology*. 2018;39(10):1385-1393.
21. Prabhu B, ValanArasu A. Stability analysis of TiO<sub>2</sub>-Ag nanocomposite particles dispersed paraffin wax as energy storage material for solar thermal systems. *Renewable Energy*. 2020;152:358-367.
22. Ibrahim SI, Ali AA., Hafidh SA, Chaichan MT, Kazem HA, Ali JM, Isahak WNR, Alamiery A. Stability and thermal conductivity of different nano-composite material prepared for thermal energy storage applications. *South African Journal of Chemical Engineering*. 2022;39:72-89.
23. Zhang G, Guo Y, Zhang B, Yan X, Lu W, Cui G, Du Y. Preparation and control mechanism of nano-phase change emulsion with high thermal conductivity and low supercooling for thermal energy storage. *Energy Reports*. 2022;8:8301-8311.
24. Venkateshwar K, Joshy N, Simha H, Mahmud S. Quantifying the nanoparticles concentration in nano-PCM. *Journal of Nanoparticle Research*. 2019;21:260.
25. Saydam V, Duan X. Dispersing Different Nanoparticles in Paraffin Wax as Enhanced Phase Change Materials – A Study on the Stability Issue. *Journal of Thermal Analysis and Calorimetry*. 2018;135(1):
26. Lee W, Yeop J, Heo J, Yoon YJ, Park SY, Jeong J, et al. High colloidal stability ZnO nanoparticles independent on solvent polarity and their application in polymer solar cells. *Scientific Reports*. 2020;10:18055.
27. Rajendran D, Ramalingame R, Adiraju A, Nouri H, Kanoun O. Role of Solvent Polarity on Dispersion Quality and Stability of Functionalized Carbon Nanotubes. *Journal of Composites Science*. 2022;6(1):26
28. Saroha J, Mehra S, Kumar M, Sharma SN. Thermo-physical properties of paraffin/TiO<sub>2</sub> and sorbitol/TiO<sub>2</sub> nanocomposites for enhanced phase change materials: a study on the stability issue. *Applied Physics A*. 2021;127:916.

Janusz T. Cieśliński  <https://orcid.org/0000-0002-8919-984X>

Paulina Boroń  <https://orcid.org/0009-0006-0263-3997>

Maciej Fabrykiewicz  <https://orcid.org/0000-0001-7648-8629>



This work is licensed under the Creative Commons BY-NC-ND 4.0 license.

## DEVELOPMENT OF A TEST RIG FOR THE MEASUREMENT OF SMALL WIND TURBINES IN A WIND TUNNEL

Heiko MEIRONKE\*, Thomas PANTEN\*, Martin HAYDUK\*, Frieder STRUBEL\*

\*Stralsund University of Applied Sciences, Faculty of Mechanical Engineering,  
Zur Schwedenschanze 15, 18435 Stralsund, Germany

[heiko.meironke@hochschule-stralsund.de](mailto:heiko.meironke@hochschule-stralsund.de), [thomas.panten@hochschule-stralsund.de](mailto:thomas.panten@hochschule-stralsund.de),  
[martin.hayduk@hochschule-stralsund.de](mailto:martin.hayduk@hochschule-stralsund.de), [frieder.strubel@hochschule-stralsund.de](mailto:frieder.strubel@hochschule-stralsund.de)

*received 5 October 2022, revised 7 February 2023, accepted 7 February 2023*

**Abstract:** This paper describes the development, design and function of a test rig for the measurement of small wind turbines in a wind tunnel and presents the first exemplary measurements of the performance characteristics of various horizontal and vertical rotors. A central part of this test rig is the developed control system with an electronic load, which enables an automated recording of the measured values for the evaluation of the power coefficients ( $c_p$ ) and tip-speed ratio ( $\lambda$ ) values. Another challenge emerges owing to the known differences in the power spectrum, because the power coefficients of drag rotors (<20%) are different from those of buoyancy rotors (<40%). The system was adapted to the different ranges by means of a stepless switching using various resistors. The entire control and regulation unit was compactly implemented using a programmable logic controller (PLC) and dynamically linked to the operating parameters of the wind tunnel. This enables an automated operation of the wind tunnel during the determination of the performance parameters of the investigated wind turbines.

**Key words:** wind tunnel testing, small wind turbine, performance measurement

### 1. INTRODUCTION

The currently anticipated challenges for energy technology in the coming years are enormous. Not only the realisation of the necessary energy transition but also increasing energy demands and geopolitical changes in the current energy supply make it necessary to rethink energy generation. In particular, energy generation by wind power plays an important role in this context. The study of small wind turbines, especially the vertical axis wind turbine (VAWT), is always a subject of research, especially in view of the current energy crisis [1–5].

With this in mind, a test rig was developed that allows investigation of the performances of different small wind turbines. This test rig allows various investigations to be carried out in the wind tunnel at Stralsund University. The size of the small wind turbines or the scaled models is limited by the boundary conditions of the wind tunnel. Wind energy converters with different operating principles and axis positions can be investigated.

This paper describes the development, design and function of the test rig and presents the first exemplary measurements of the performance characteristics of various horizontal and vertical rotors. A central part of this test rig is the developed control system with an electronic load, which enables an automated recording of the measured values for the evaluation of the power coefficients ( $c_p$ ) and tip-speed ratio ( $\lambda$ ) values. Another challenge emerges owing to the known differences in the power spectrum, because the power coefficients of drag-type rotors (<20%) are different from those of lift-type rotors (<40%). The system was adapted to the different ranges by means of a stepless switching using various resistors. The entire control and regulation unit was

compactly implemented using a programmable logic controller (PLC) and dynamically linked to the operating parameters of the wind tunnel. This enables an automated operation of the wind tunnel during the determination of the performance parameters of the investigated wind turbines.

### 2. THE WIND TUNNEL FACILITY AND THE CONTROL SYSTEM OF PERFORMANCE MEASUREMENTS

The tests to determine the performance characteristics of the small wind turbines were carried out in the subsonic wind tunnel at Stralsund University. The wind tunnel was developed and constructed completely through project work and final theses by students at the university. The control unit for the performance measurement is also the result of a final thesis and provides a strong simplification of the operation of the wind tunnel, as well as the automatic recording of the performance parameters of various rotors of wind turbines.

#### 2.1. The wind tunnel facility and test rigs for vertical and horizontal rotors

The wind tunnel is designed as a closed circuit wind tunnel (Göttingen-type) with an open test section (Fig. 1). The external dimensions are approximately 15 m x 2.4 m x 3.6 m (Fig. 1). The wind tunnel is equipped with two nozzle/collector configurations. It can be operated with a measuring cross-section of either 1,000 mm x 1,000 mm or 700 mm x 700 mm, with maximum possible

speeds of up to 30 m/s and 60 m/s. The length of the open test section is a maximum of 1.76 m in the case of the nozzle with the large outlet. The axial blower has a power of 45 kW. It produces a maximum flow rate of 90,000 m<sup>3</sup>/h at a pressure increase of 1,100 Pa (Tab. 1).

Tab. 1. General technical data of the wind tunnel

Dimension of wind tunnel (L/W/H)	15 m/2.8 m/3.6 m	
Air flow rate	90,000	m <sup>3</sup> /h
Total pressure increase	1,120	Pa
Power of axial blower	45	kW
Blower speed	1,500	1/min
Dimension of test section	Small	Big
Length	1.76 m	1.25 m
Cross-section	1.00 m <sup>2</sup>	0.50 m <sup>2</sup>
Maximum velocity	30 m/s	60 m/s

Following the axial blowers, the flow gets into the first diffuser. In the diffuser, the flow velocity is reduced. In order to form a flow with low losses as well as to meet the demand for the imposition of a wall boundary layer, a maximum opening angle of  $\varphi \leq 7^\circ$  has been considered in the formulation of the design of the diffusers. In the wind channel, a guidance of the flow in the duct bends is necessary. This takes place by means of guide vanes that have been placed in the duct bends. The installation of the guide vanes ensures that flow separation and related losses in the duct bends can be prevented.

Before the flow reaches the test area, it slows down once again in the settling chamber. Here the flow is guided through three fine-mesh grids. Still existing vortices are destroyed inside the fine grid, thus reducing the turbulence intensity. After that, the flow is accelerated in the nozzle and rendered still more uniform, so that at the outlet of the nozzle there forms a uniform velocity profile with a low turbulence intensity.

In order to cover a wide range of investigations, two nozzles with the contraction ratios of  $\epsilon = 4$  and  $\epsilon = 8$  were designed. The calculation of the profile of the nozzle contour is based on a method in which the ratio of the nozzle length of the nozzle outlet, the non-uniformity of the flow profile and the contraction ratio  $\epsilon$  of the nozzle are taken into account. The nozzle with a small outlet has a contraction ratio of  $\epsilon = 8$  and is designed with a specific nozzle length of 1.25 m. This results in a relatively large nozzle length. In order to ensure compliance with the guidelines for the design of the test section, which mandate that the maximum length of the channel should not be in excess of that stipulated, in the case of the large outlet, the nozzle cross section was determined at 1 m<sup>2</sup>, and a contraction ratio of  $\epsilon = 4$  and a ratio of the nozzle length to the nozzle outlet = 1 were reckoned appropriate. Furthermore, the nozzles are equipped with stiffening ribs and a stiffening frame, whereby an oscillation of the sheet metal parts is prevented.

To avoid oscillations of the air, which could result from the outflow of the open jet from the nozzle into the measuring room, small metal strips on the principle of Seiferth-wing [6] are attached to the inner edge of the outlet nozzle. After flowing through the open test section, the core flow is guided into the collector. Then, the air flow in the duct bend is redirected twice and then returned to the axial fans.

For the performance measurement of small wind turbines, a modular test rig has been developed for the measuring plenum,

which allows vertical and horizontal rotors to be measured [7, 8]. For the measurement of vertical rotors, the rotor-generator combination is placed vertically in a support rack and positioned about 0.5 m in front of the nozzle opening (Fig. 2, left).

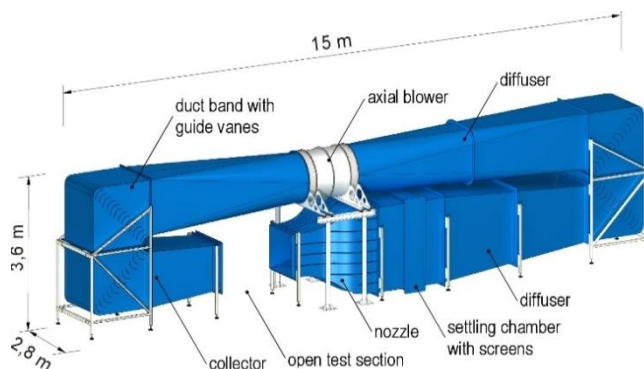


Fig. 1. The subsonic wind tunnel at Stralsund University

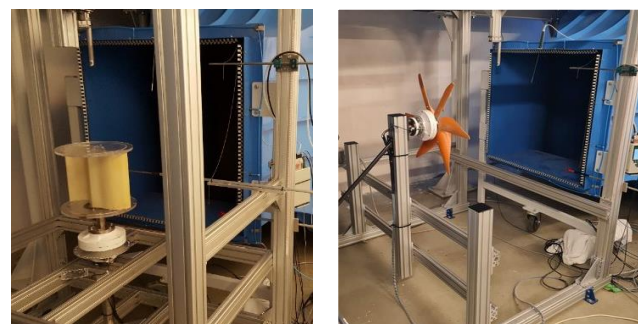


Fig. 2. Test rig for vertical rotors (left) and for horizontal rotors (right subsonic wind tunnel at Stralsund University)



Fig. 3. Vertical rotors: Standard-Savonius rotor (left), J-blade rotor (middle) and Benesh-V Rotor (right)



Fig. 4. Horizontal rotors: drag-type rotor (left) and lift-type rotor (right)

For the measurement of vertical rotors, three models (Standard-Savonius rotor, J-blade rotor and a variation of a Benesh rotor) are used as examples (Fig. 3), which mainly work according to the drag principle. All three vertical rotors have the same inflow



area (0.3 m x 0.25 m) of 0.075 m<sup>2</sup>. The blockage ratio defines the relationship between the cross-section of the nozzle outlet and the model and should not exceed 10%–20%. With a nozzle cross-section of 1 m<sup>2</sup>, the area blocked by the rotor is within the tolerable range at 7.5%.

For the measurement of horizontal rotors, the rotor–generator combination is supported by an additional vertical column approximately in the middle of the measurement plenum (Fig. 2, right) [8]. For the measurement of horizontal rotors, two models are used as examples. One rotor works according to the drag principle (Fig. 4) and the other uses the lift principle (Fig. 5). Both rotors can be equipped with two, three or six rotor blades. The cross-section of 0.4 m<sup>2</sup> (drag-type rotor) is about four times larger than that of the vertical rotors and therefore not quite optimal for the flow in the measurement plenum, which could lead to a slight deviation of the measurement results.

## 2.2. The control system of performance measurements

A major part of this work is the development and implementation of a control and measurement system to measure the output power of small wind energy converters [7]. This system should enable accurate measurement of the power curve of variable rotors.

The frequency inverter provides the power for the wind tunnel. It is activated and controlled externally via the central control. A PLC of the type LOGO 8 from Siemens is to be used as the central control.

The measured data are recorded on a memory card. The central control unit (Fig. 5) is the main component of the test rig. For example, the rotor parameters are entered and the speed profile for measurement is defined. Additionally, the remote control provides the user with a visualisation of the measurement data. Both of these systems were individually programmed with the software LOGO! (Soft Comfort V8.2 and TIA-Portal v.12.1, respectively) from Siemens. The mechanical power of the rotors is converted in a specially designed permanently excited synchronous generator. The range of rotational speeds to be expected is relatively large, as both different axis orientations and rotors with different operating principles (resistance and lift principles) are to be measured. With the relatively low speeds of the rotors operating according to the resistance principle, the tip-speed ratios are  $\lambda < 1$ . Contrastingly, the tip-speed ratios for the lift rotors are approx.  $\lambda = 4$ –6.

An electronic load serves as a load for the generator or the rotors, which has a power of 300 W in the first expansion stage and works in combination with a measuring and braking resistor. This assembly is a very important component of the test rig, as it allows the output power of the rotors to be controlled in very small steps. Additionally, the load and the resistor prevent the rotor from overspeeding during no-load operation by regulating the speed of the rotor.

The measurement of the electric current is carried out by means of the measuring resistor. This has a constant resistance value of 5  $\Omega$  in the operating range. Thus, the current can be easily determined by measuring the voltage drop at the resistor. This results in a voltage drop of 7.5 V over the measuring resistor with a current flow of 1.5 A. The measuring resistor with a power consumption of up to 500 W can easily absorb the converted power loss of 11.25 W. Since the controller has an analogue measuring range of 0–10 V with a resolution of 10 bits, the meas-

ured values are recorded with 10V/1,000 = 0.01 V steps. Divided by the constant resistance value of 5  $\Omega$ , this results in a current value of 2 mA and thus allows a very good measurement resolution. The measured output power in comparison to the mechanical power directly at the rotor is influenced by the losses on the complete path of energy transmission.

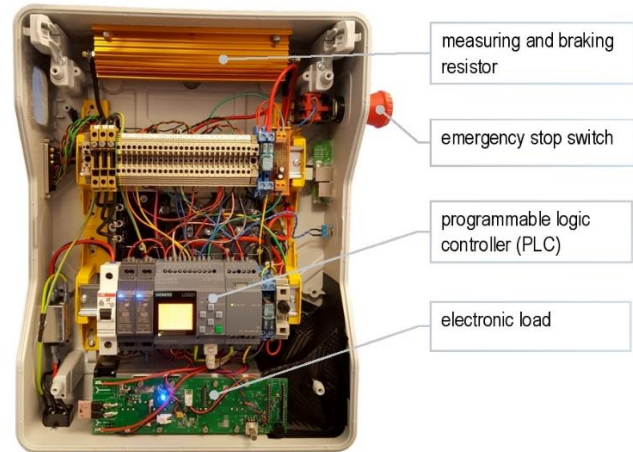


Fig. 5. Central control unit



Fig. 6. Remote control of wind tunnel and central control unit

The total power loss results from losses in the bridge rectifier, Ohmic losses in the supply lines, losses in the generator coils and the friction losses in the bearings. The fractions of the power losses can be easily estimated as a function of the rotational speed and are taken into account in the calculation of the final power coefficient.

## 3. MEASUREMENT OF PERFORMANCE CHARACTERISTICS OF VERTICAL ROTORS

In order to measure the rotors, the test rig was configured so that the wind tunnel can be automatically controlled from 6 m/s to 20 m/s in seven steps of speed. The load profile is run through in each step. The rotor speed is controlled from 50 rpm to 600 rpm in steps of 50 rpm. The aim is to determine the optimum tip-speed ratio of the rotor in order to subsequently record a performance curve in this range in high resolution. Approximately 100–150 measurements were carried out at each operating point in order to obtain a statistically reliable value. Software procedures are used to evaluate and calculate the performance parameters [7].

The optimum tip-speed ratio of the Standard-Savonius rotor could be determined from the measured values, e.g. at a rotational speed of 500 1/min (Fig. 7), which corresponds to a tip-speed ratio of  $\lambda = 0.65$ . This tip-speed ratio is independent of the speed



steps. The calculated power coefficient takes into account all losses, electrical as well as mechanical, in the bearings. It has been shown that the given Standard-Savonius achieves a power coefficient of  $c_p = 0.12$ . Furthermore, a vertical rotor with a shape similar to a Benesh rotor was measured. However, the geometry is not optimally designed, so that the rotor only has a power coefficient of  $c_p = 0.11$  with a tip-speed ratio of  $\lambda = 0.45$ . Among the three tested models, the one ascertained as being the most optimal was the vertical rotor with the J-blade design. It achieves a power coefficient of  $c_p = 0.15$  with a tip-speed ratio of  $\lambda = 0.6$ . It can be clearly seen that the last two rotors have very good start-up behaviour. This generally characterises the vertical rotors, which develop a strong torque at low speeds, a phenomenon that finds good corroboration in the literature [5, 9].

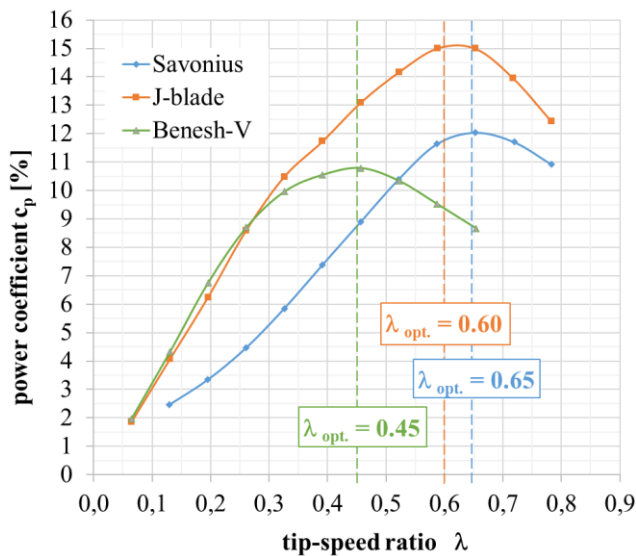


Fig. 7. Performance characteristics of vertical drag-type rotor (25°C)

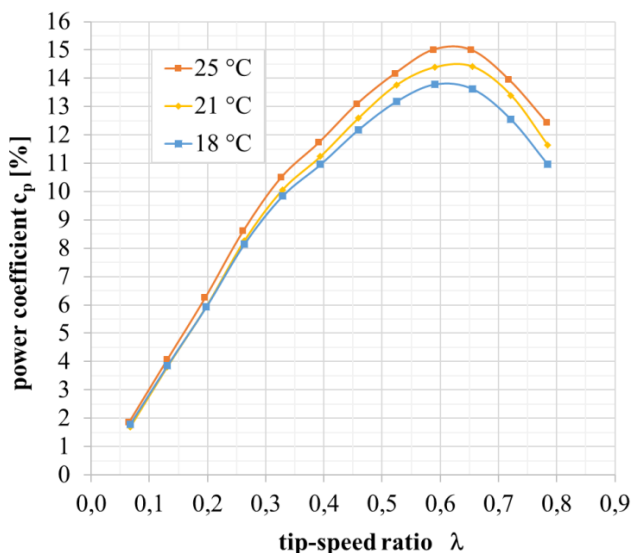


Fig. 8. Influence of temperature-dependent bearing friction on performance, e.g. J-blade rotor

A major problem with vertical rotors used in the low-power range of small wind turbines is the bearing friction of the rotors, which was also identified by Ricci et al. [10] in their research.

Power loss in the bearings can be of a magnitude that dominates in relation to the harvested wind power, especially in relation to the small inflow area of the rotors. An increase in the power coefficient is seen with increasing temperature, resulting in an increase of 2% for a temperature difference of just 7 K (Fig. 8). Friction in the bearings, which is strongly determined by the operating temperature of the rotors, is a factor that should not be neglected in relation to the relatively low wind power output. This effect is especially amplified if the small wind turbines are to be used reliably and effectively in different climatic zones or even in winter operation.

#### 4. MEASUREMENT OF PERFORMANCE CHARACTERISTICS OF HORIZONTAL ROTORS

For the measurements of the horizontal rotors, a self-built low-cost drag-type rotor was made from a commercially available plastic pipe (DN 110). An existing model was chosen as an example for a lift-type horizontal rotor. Since the two horizontal rotor types have different through-flow surfaces, a direct comparison is not possible. Nevertheless, the evaluation of the performance characteristics provides a very good insight into the behaviour of the rotors with the two different operating principles.

The measurements generally show a dependence of the number of rotor blades on the tip-speed ratio and the power coefficient. Especially for the drag-type rotors, an increase in the number of blades from two to three leads to a strong increase in the power coefficient by approx. 40% to  $c_p = 12.3$  (Fig. 9). The tip-speed ratio is reduced from  $\lambda = 2.41$  to  $\lambda = 2.20$ , as more surface is now available for harvesting the wind power.

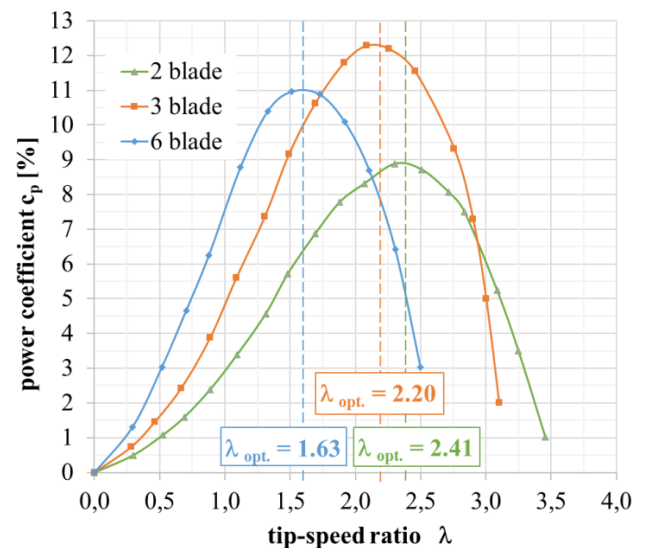


Fig. 9. Performance characteristics of horizontal drag-type rotor (average of speeds, 20°C)

The measurements of the drag-type model indicate that the investigated rotor with tip-speed ratio  $\lambda > 1$  is not a pure drag rotor. This rotor has the characteristics of both drag and lift rotors, due to the special shape of the rotor blades. With a lower number of rotor blades, the characteristics of a lift rotor became more evident. Nevertheless, the characteristics of a drag rotor predominated due to the rotor blade geometry and the relatively low power

coefficients. This low power coefficient is due to the non-optimal blade geometry, which in part negatively influences a good outflow of air at higher speeds. However, the horizontal drag-type rotor has very good start-up behaviour. Even in the lower speed range, relatively high torques are achieved, as can be seen from the strong gradient of the power coefficient.

The lift-type rotors also show an increase in the power coefficients with an increase in the number of blades from two to three. The increase of approx. 20% is significantly lower than that with the drag-type rotor (Fig. 10). With three blades, the optimum in the number of blades is also reached here, and a maximum power coefficient of  $c_p = 0.28$  with a tip-speed ratio of  $\lambda = 6.12$  is achieved.

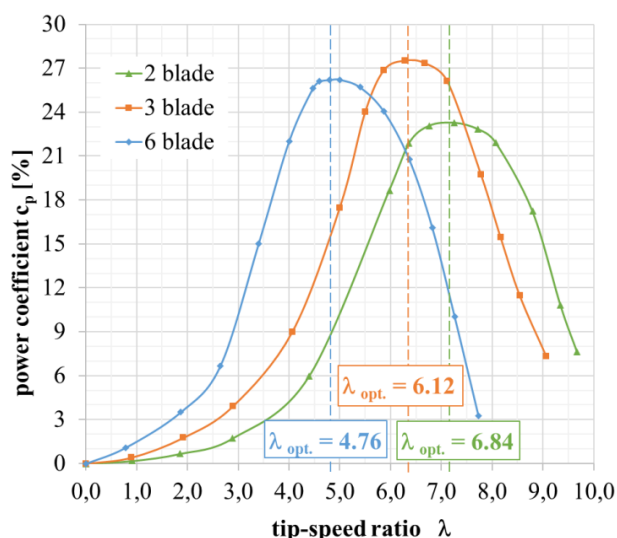


Fig. 10. Performance characteristics of horizontal lift-type rotor (average of speeds, 20°C)

Furthermore, the investigations show good agreement with the findings reported in the literature [9], in which a further increase in the number of blades (six blades) leads to a reduction in the power coefficient. This effect is due to negative flow phenomena between the blades.

## 5. CONCLUSIONS

This paper described the development, construction and function of the test rig used in the measurement plenum of the wind tunnel, and presented the first exemplary measurements of the performance characteristics of various horizontal and vertical rotors for small wind turbines.

With the developed automatic control system, the rotor test rig enables the measurement of the rotors with precisely specified parameters. The automated acquisition of the entire power spectrum is carried out systematically, very precisely and comprehensively. This developed control unit with the implemented data acquisition significantly simplifies the measurement processes for recording the performance parameters.

The measurement results of the rotors in the rotor test rig have shown that the energetic use of rotors in the drag-type rotor configuration, especially vertical rotors, offers technically usable potential, but that compared to lift rotors they have a relatively low power output. In particular, the friction in the bearings of the rotors

have a strong influence on the total performance of the small wind turbine in this low power range. Nevertheless, the use of these turbines in the form of small, decentralised systems could make sense. While the Savonius-type rotors are characterised by a low power coefficient, this limitation of theirs presents a strong contrast to several advantages that have been observed in them. The rotors have a low tip-speed ratio with a relatively high torque in the lower speed range. They are very robust and not sensitive to changes in wind direction, and pose only a very low risk to wildlife when used in sensitive landscape regions.

## REFERENCES

1. Savonius SJ. The wing rotor in theory and practice. Savonius Co., 1928
2. Akwa J, Vielmo H, Petry A. A review on the performance of Savonius wind turbines, Renewable and Sustainable Energy Reviews, 16, pp. 3054–3064, DOI: 10.1016/j.rser.2012.02.056, 2012
3. Roy S, Saha U. Wind tunnel experiments of a newly developed two-bladed Savonius-style wind turbine. Applied Energy, 137, pp. 117–125, DOI: 10.1016/j.apenergy.2014.10.022, 2015
4. Howell R, Qin N, Edwards J, Durrani N. Wind Tunnel and Numerical Study of a Small Vertical Axis Wind Turbine, Renewable Energy, 35, pp. 412-422, DOI: 10.1016/j.renene.2009.07.025, 2010
5. Sheldahl RE, Blackwell BF, Feltz LV. Wind tunnel performance data for two- and three-bucket Savonius rotors, Journal of Energy, Vol.2, No. 3, pp. 160-164, 1978
6. Seiferth R. Vorausberechnung und Beseitigung der Schwingungen von Freistrah-Windkanälen, Monograph. Fortschritte Deutsche Luftfahrtforschung, AVA Göttingen 1946
7. Hayduk M. Entwicklung und Fertigung eines Prüfstandes zur Vermessung der Leistungskurve von vertikalen Rotoren für Kleinwindenergieanlagen im Windkanal der Hochschule Stralsund, Bachelorarbeit, Hochschule Stralsund, 2020
8. Strubel F. Entwicklung, Aufbau und Erprobung eines universellen Versuchsstandes zur Messung aerodynamischer Größen von Rotoren horizontaler Windkraftanlagen im Windkanal, Bachelorarbeit, Hochschule Stralsund, 2022
9. Hau E. Windkraftanlagen, Springer-Verlag Berlin Heidelberg, 2016
10. Ricci R, Romagnoli R, Montepare S, Vitali D. Experimental study on a Savonius wind rotor for street lighting systems, Applied Energy, 161, pp. 143-152, DOI: 10.1016/j.apenergy.2015.10.012, 2016

The authors gratefully acknowledge the European Union – European Regional Development Fund (ERDF) for the financial support of the wind tunnel and measurement instruments (FHHST 10).



Heiko Meironke: <https://orcid.org/0000-0002-4808-1300>

Thomas Panten: <https://orcid.org/0009-0007-0301-4052>




Martin Hayduk: <https://orcid.org/0000-0002-8051-3214>

Frieder Strubel: <https://orcid.org/0009-0007-6996-4368>



This work is licensed under the Creative Commons BY-NC-ND 4.0 license.

## ADAPTATION AND APPLICATION OF A POLARISATION CURVE TEST PROTOCOL FOR A COMMERCIAL PEM ELECTROLYSER ON CELL AND STACK LEVEL

Nicol Daniela JARAMILLO RODRÍGUEZ\*,\*\* , Aline LUXA\*\* , Lars JÜRGENSEN\* 

\*Faculty of Nature and Technology, Energy Technology, Hochschule Bremen, Neustadtswall 30, Bremen, 28199, Germany

\*\*Application Center for Integration of Local Energy Systems ILES,

Fraunhofer Institute for Wind Energy Systems IWES, Am Seedeich 45, Bremerhaven, 27572, Germany

[nrodriguez001@stud.hs-bremen.de](mailto:nrodriguez001@stud.hs-bremen.de), [lars.juergensen@hs-bremen.de](mailto:lars.juergensen@hs-bremen.de), [aline.luxa@iwes.fraunhofer.de](mailto:aline.luxa@iwes.fraunhofer.de)

received 11 November 2022, revised 2 March 2023, accepted 4 March 2023

**Abstract:** The present study aims to develop a test protocol based on the literature for electrochemical characterisation of a polymer electrolyte membrane (PEM) electrolysis commercial stack using polarisation curves. For this, a 1-kW water electrolysis test stand with integrated temperature control and measurement systems was built around the stack. Afterwards, the stack performance was characterised under different operating pressure and temperature conditions by using polarisation curves. A measurement protocol was developed based on the literature. To ensure the reproducibility of the results, two rounds of experiments were performed. The experiments were carried out at temperatures between 20 and 60 °C and pressures up to 15 bar. The results show distinct regions in the polarisation curves related to the activation and ohmic overvoltage. The effect of temperature and pressure on the performance is shown and analysed. The performance of single cells in the stack is also measured. The stack polarisation curves are compared with those in the literature, which gives an understanding of the materials used in electrodes and types of membranes.

**Key words:** PEM water electrolysis, test protocol, electrochemical characterisation, polarisation curves

### 1. INTRODUCTION

In the future, green hydrogen is expected to be used as a chemical feedstock for industry and as long-term chemical storage for the energy grid. To support the establishment of the hydrogen market, the German government in the coalition agreement for 2021–2025 proposed an expansion of electrolysis capacity of up to 10 GW in Germany by 2030, based on the National Hydrogen Strategy [1]. Green hydrogen must be produced from renewable energy, which requires high reliability and dynamic capability of electrolyzers [2]. Therefore, the necessary development of the hydrogen economy entails many technical challenges that must be addressed early on for a successful implementation. For polymer electrolyte membrane water electrolysis (PEMWE), the stack is the most expensive component, accounting for about 60 % of the initial costs of an electrolysis plant [3,4]. For this reason, it is important to understand and improve the performance of the stack through electrochemical studies. In this field, one of the most common methods to study electrochemical cells is polarisation curves. These curves show the voltage behaviour of a cell under different current loads at constant temperature and pressure. In addition, a polarisation curve is a tool for comparing between the performance of electrolyzers.

In common data sheets of commercial PEMWE manufacturers, only a system efficiency at nominal load is given. This gives very little information about the stack performance in partial loads. Since polarisation curves cover the whole load range, they can serve as the base for optimising the electrolyser operation. Due to highly fluctuating renewable energy sources, PEMWE may often

have to operate under partial load. Furthermore, in commercial PEMWE plants, condition monitoring is essential to detect or prevent degradation. Polarisation curves can be a powerful tool to track cell degradation. Since high-power PEMWE stacks can have numerous cells, it is complicated to track every single one of them. Moreover, for the PEMWE stack description in modelling, often only the sum of identical single cells is considered for the total stack voltage [5]. However, this does not take account of the ohmic resistance of the end plates. Therefore, it is important to understand the difference and correlation between the polarisation curves of the stack and the individual cell. To the best of the authors' knowledge, there is no generic description of this. It is also necessary to examine the specific ways in which individual cells influence the overall performance of the PEMWE. In addition, the performance of the PEMWE is influenced not only by the power set point but also by temperature and pressure conditions. The effect of these factors has been widely described in the literature [6,7,8]. The findings of single cell examinations should be compared to the influence on a commercial stack on cell and stack level.

The Bremen University of Applied Sciences (HSB) is currently engaged in hydrogen technology research and the implementation of various electrolyser technologies. In this context, the main objective of this work was the electrochemical characterisation of a PEMWE stack using polarisation curves. For this purpose, a 1-kW electrolysis test bench was first set up for educational and research purposes at the Laboratory of Environmental Chemistry of the HSB. Since there is currently no technically standardised and recognised measurement protocol, especially for industrial plants, a suitable protocol was designed from various sources,

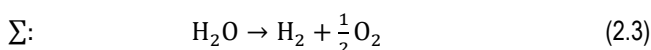
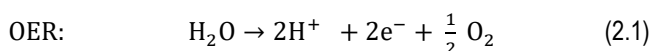
which tested a single cell at the laboratory level [9–11]. For complete characterisation over a wide operating range, experiments were carried out under multiple temperatures and pressures. To monitor the overall performance of the stack, measurements were performed at the stack level and compared with monitoring results of individual cells.

## 2. FUNDAMENTALS

In this chapter, the electrochemical basics are described, which are necessary for the general understanding of the study. Firstly, the redox reaction that occurs during the electrolysis is described, then the voltage necessary for the reaction to occur and the corresponding losses and, finally, the characterisation method, i.e., the polarisation curve.

### 2.1. Polymer electrolyte membrane (PEM) water reaction

In PEMWE, water is split into hydrogen and oxygen by an electrochemical potential. The redox reaction in (2.3) is described by the two half-cell reactions (2.1) and (2.2). The oxygen evolution reaction (OER) takes place at the anode with a required minimum anode potential of 1.23 V, while the hydrogen evolution reaction (HER) takes place at the cathode with a potential of 0 V. Both reactions must be catalysed, and a membrane is located between the electrodes for product separation and for efficient proton transport [12].



During the operation, water flows through the flow field of the bipolar plates, which ensures homogeneous distribution of water over the entire active surface and efficient removal of products from the cell. Within the cell, water flows through the porous transport layer (PTL) on the anode side to the catalyst-coated membrane (CCM), where it is converted into H<sup>+</sup> protons, electrons and oxygen (OER). Oxygen and excess water are transported through the PTL to the anode gas outlet. Electrons leave the anode through the external circuit, providing the driving force (cell voltage). Hydrogen ions move across the membrane to the cathode side, where they recombine with electrons to produce molecular hydrogen (HER). With the increase in current density, the transport of water from the anode to the cathode increases simultaneously due to electroosmotic movement. This entrained water is known as drag water. Hydrogen and drag water are released through the PTL into the flow channels and scrubbed through the cathode gas outlet. The membrane, electrodes and PTLs together form the membrane electrode assembly (MEA). The electrodes are located on both sides of the MEA, and together it is known as the CCM. The designation of CCMs in the literature usually follows this scheme: cathode-catalyst/membrane/anode-catalyst, e.g., Pt/Nafion®-117/IrO<sub>2</sub>, indicating the catalysts (Pt and IrO<sub>2</sub>) used on cathode and anode sides and the membrane (Nafion®-117) in between.

### 2.2. Overvoltage of PEM electrolysis

Previously, the voltage for OER and HER was described for the ideal case. Considering real-time operation, the voltage of an electrolysis cell

$$U_{\text{cell}} = U_{\text{ocv}} + \eta_{\text{act}} + \eta_{\text{ohm}} + \eta_{\text{mass}}, \quad (2.4)$$

can be calculated as the sum of the open-circuit voltage  $U_{\text{ocv}}$  and the losses: the activation overvoltage  $\eta_{\text{act}}$ , ohmic overvoltage  $\eta_{\text{ohm}}$  and mass transport overvoltage  $\eta_{\text{mass}}$ . The percentage of the individual losses depends, to a considerable part, on the design, the materials used and the operating parameters such as pressure and temperature. The open-circuit voltage  $U_{\text{ocv}}$  is the theoretical minimum potential difference between the two electrodes required to start the reaction.

At very low current densities, the total overvoltage is almost entirely determined by the activation overvoltage. The activation overvoltage describes the energy required to initiate the electrochemical reaction. Especially, the OER requires a high activation energy and occurs slower than the HER. The activation surge is directly influenced by temperature, catalyst material and catalyst loading.

The ohmic overvoltage is related to the proton resistance passing through the membrane and the electrical resistance of the components. The proton resistance of the membrane is significant as it is typically 10 times higher than the electrical resistance. With increasing current and proton flow, the ohmic overvoltage also increases linearly. Insufficient humidification of the membrane leads to a decrease in proton conduction, resulting in a higher voltage requirement. Intensified electrical resistance is caused, e.g., by poor contact between the current collectors and the bipolar plates or by passivation of the surfaces through the formation of oxide layers [15]. An increase in membrane thickness also has a negative effect on this overvoltage. However, a thinner membrane could increase the gas permeability [15].

The diffusion or concentration overvoltage refers to transport resistances resulting from insufficient inward transport of water into the stack or of gases and drag water out of the stack. At high current densities, gas bubbles may not be removed from the electrodes as quickly as they are generated. The voltage increases as the active surfaces are covered, the electrical resistance of the cell increases due to the non-conductivity of the bubbles, and the diffusion of water to the active surfaces is restricted.

Increasing the operating temperature of a PEMWE significantly improves the performance of the stack [14]. However, high temperatures increase gas permeability and decrease the mechanical stability of the membrane and may contribute to accelerated degradation [16]. This, along with the stability problems of ion exchange resins at temperatures above 60 °C, is the reason that the temperature in current commercial PEM plants does not usually exceed 60–70 °C [17].

### 2.3. Polarisation-Curve

The polarisation curve shows the relationship between cell voltage and current density, where lower cell potential at higher current density is desirable. It can be used to track cell degradation by comparing the curve at the beginning of life (BoL) and at the end of life (EoL). In addition, a polarisation curve is a



useful and standardised method for comparing the performance of different electrolyzers. During the measurement, constant operating conditions or thermodynamic equilibrium, including temperature and pressure, must be ensured. The polarisation curve can be measured in two ways, under galvanostatic or potentiostatic control. In the first variant, the current density is modified stepwise, while in the second variant, the voltage is changed.

In the following, the polarisation curve of an electrolysis cell is explained and illustrated with the help of Fig. 1. As it can be seen, the cell voltage increases with increasing current density, corresponding to increasing hydrogen production according to Faraday's law. The curve can be roughly divided into three overvoltage dominated ranges, the activation, ohmic, and mass transport range. The area with very low current densities is characterised by a strong voltage rise, which is due to the large influence of the activation overvoltage. Ohmic losses dominate most of the polarisation curve, which is characterised by a linear curve behaviour. With increasing current, a slope change by bending upwards is observed due to mass transport limitation. In this range, the efficiency is low, and the heat dissipation is very high.

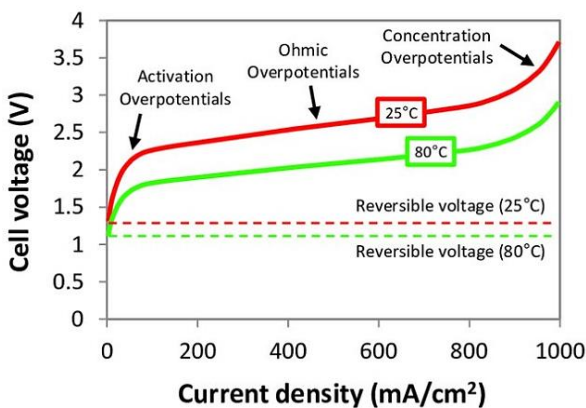


Fig. 1. Typical polarisation curves of an electrolysis cell at two different temperatures [18]

### 3. MATERIALS AND METHODS

For the characterisation process of the PEMWE, a test rig was built around a 1-kW commercial stack. The stack consists of 10 cells connected in series, with an active cell area of 30 cm<sup>2</sup> each. The characteristics of the stack according to the manufacturer are listed in Tab. 1. Details of the PEM cell materials are confidential by the commercial stack manufacturer and have not been provided to the stack owner.

The pressures referred to in this article are measured above atmospheric pressure and are expressed in units of bar. The stack operates under differential pressure, where the pressure on the cathode side can reach up to 20 bar, while the maximum allowable pressure on the anode side is limited to 0.5 bar. According to the manufacturer, a water inflow of 66 l/h at the anode side is needed to ensure a maximum temperature difference

$$\Delta T_s = T_{in,anode} - T_{out,anode}, \quad (3.1)$$

between the inlet and the outlet temperature of the

ode  $\Delta T_s$  of 10 K. While most of the water is used for cooling the stack, only a small amount is required for the reaction. Moreover, drag water is carried to the cathode side through the membrane, which is about 1 l per standard cubic meter of produced hydrogen.

Tab. 1. PEM stack technical specifications

Feature	Value	Unit	Feature	Value	Unit
Temperature $T_{in,anode}$	20–70	°C	Cells	10	-
Max. $\Delta T_s$	10	K	Active area	30	cm <sup>2</sup>
Max. voltage	25	V	O <sub>2</sub> operating pressure	<0.5	bar
Minimal current	15	A	H <sub>2</sub> operating pressure	Max 20	bar
Nominal current	52.5	A	H <sub>2</sub> O conductivity	0.1	μS/cm
Max. current	75	A	Cooling water flow rate	66	l/h
Nominal power	1	kW	H <sub>2</sub> O consumption	1	kg/h
Min. power	0.25	kW	$\eta_{nominal}$	78	%
Max. power	1.88	kW	H <sub>2</sub> -production	0.06 to 0.31	m <sup>3</sup> /h @STP

PEM, polymer electrolyte membrane

To operate the stack, the following subsystems have been installed: process water loop, stack power supply, thermal management, hydrogen production subsystem, nitrogen inertisation subsystem, measurement subsystem and a central data acquisition subsystem. In the following text, the systems mentioned are described with the help of the flow diagram in Figs. 2 and 3, which shows the setup in the laboratory. The process water circuit operates on the anode side. First, there is a peristaltic pump (P-1) to ensure a constant flow of water through the stack. Downstream, there are two counterflow glass heat exchangers (W- 1 and W-2). To operate the PEMWE, the conductivity of water must be less than 0.1 μS/cm. This is achieved with an ion exchange resin bed (F-2), which separates harmful metal ions and measured with a conductivity sensor (QI-1) placed in a parallel pipe. A filter (F-3) is used upstream of the stack and downstream of the ion exchanger to prevent contaminant particles coming into the stack, such as resin, that can be released from the ion exchanger. After the stack, the water with the produced oxygen flows to the oxygen tank (F-1), where gas and liquid are separated by gravity. To compensate for the water consumed by losses from the water splitting reaction, water can be added to the system through the oxygen tank. Water is added on the anode side because it is needed for OER, and the oxygen tank is not overpressurised. Two temperature sensors (TIRC-2 and TIR-3) are placed to measure the inlet  $T_{in,anode}$  and outlet water temperature of the stack  $T_{out,anode}$ . The sensors are used to record the temperature difference of the stack  $\Delta T_s$  (TDIC-1).

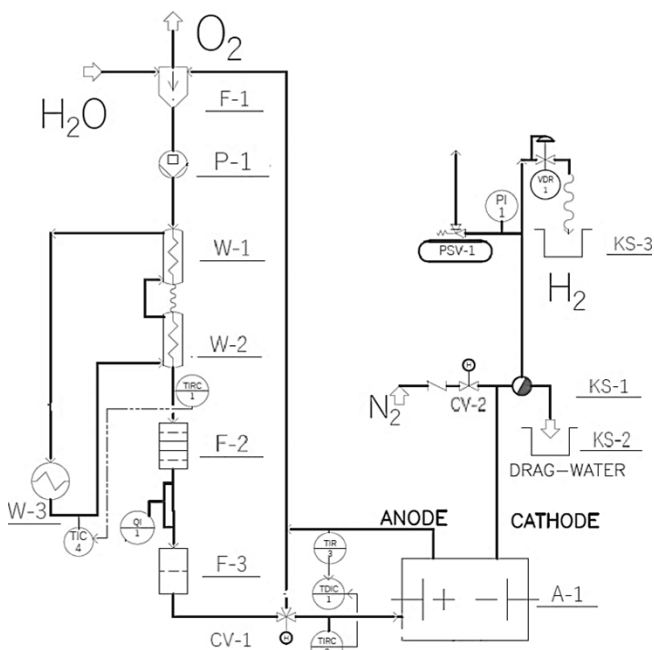


Fig. 2. Piping and instrument flow diagram of the test rig

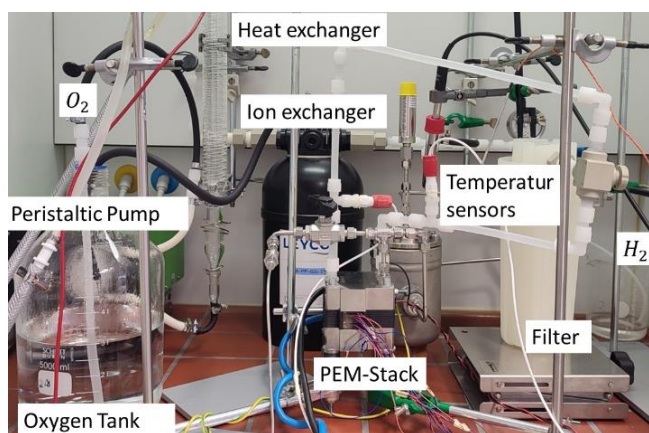


Fig. 3. Installed test bench for PEM electrolysis with 1 kW nominal power

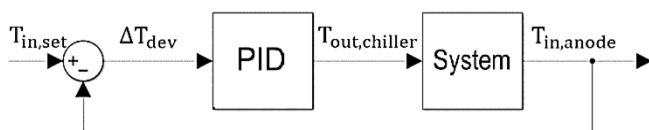


Fig. 4. Schematic of the stack anode inlet temperature control loop by means of the internal PID of the chiller.

For temperature regulation, a chiller (W-3) is connected to the heat exchangers and used to control the process water temperature feeding the stack  $T_{in,anode}$ . The temperature signal from the sensor before the stack is compared with the reference temperature  $T_{in,set}$ . According to the control error  $\Delta T_{dev}$ , the chiller regulates its water outlet temperature  $T_{out,chiller}$  by its internal proportional–integral–derivative (PID) controller. A schematic of the temperature control is shown in Fig. 4. This allows automatic regulation of the stack supply temperature. A proportional–integral (PI) controller would probably be sufficient, but the chiller with its PID was available in the laboratory for use.

The produced gases leave the stack (A-1) mixed with liquid

and gaseous water. In this system, liquid water is separated on the cathode side using a ball float steam trap (KS-1). A pre-pressure regulator (VDR-1) is installed to maintain the pressure in the system. Additionally, a safety valve (PSV-1) is placed upstream of the pressure regulator, which opens if the system pressure exceeds 18 bar, to ensure that the maximum pressure is not reached on the cathode side of the stack. The pressure is also monitored and displayed by a pressure gauge (PI-1). The inertisation subsystem is connected to the cathode side of the stack. Nitrogen is used as an inert gas for the inertisation of the hydrogen pipes and components.

To operate the stack, software of the power supply is used, in which it is possible to program what current or voltage the stack receives. To protect the stack from high voltages, the power supply is programmed to a cut-off voltage of 25 V according to the manufacturer’s specifications. Current and voltage measurements of the stack are also carried out by the power supply. Noise and impedance effects have been minimised with the addition of two twisted sense wires as recommended in the power supply manual. In addition to data collection by the power supply, a data acquisition program was developed in LabVIEW [19] to measure the temperature of the process water loop and voltage of the single cells. The individual cells were measured by attaching cables directly to the contacts of each cell and then the cables were connected to a National Instruments Module 9215. This way, the individual cells can be monitored, and short circuits between individual cells can be detected.

The measurement protocol for polarisation curves was also developed. The protocol can be used on all commercial electrolyzers, which can be installed on the test rig setup in this study. In general, it can be adapted to other test rigs, but there may be limitations that need to be considered such as temperature and flow rate.

The polarisation curves have been recorded under galvanostatic control. According to Ref [11], the cell voltage should not deviate by more than  $\pm 5$  mV during a 30-s period. For this reason, each step of the current density should last at least 30 s. To verify that the system is in thermodynamic equilibrium, two polarisation curves are recorded for each experiment. At atmospheric pressure, the ascending polarisation curve is first determined, i.e., the lowest allowable current is applied to the stack. The current is gradually increased until the maximum value of 75 A ( $2.5 \text{ A/cm}^2$ ) is reached. Then, the descending polarisation curve is recorded from the highest current to the lowest current. Under pressure, the process is reversed. If the curves strongly deviate from each other, this speaks of hysteresis and thus of a system that is not in equilibrium, and the experiment must be repeated [11]. Furthermore, each experiment was performed twice to ensure reproducibility of the measurement results.

The larger the current range over which the polarisation curve is taken, the more the information about a wide operating range of the stack is obtained. However, the lower part of the load range is limited by hydrogen permeation to the anode, which increases at low operating current densities [20], while at the upper part of the load range, a maximum current given by the manufacturer is the technical limiting aspect. The minimum current recommended by the manufacturer, that is applied to the PEMWE, is 15 A respectively  $0.5 \text{ A/cm}^2$ . To obtain more information about the activation losses of the stack, lower currents from  $0.006 \text{ A/cm}^2$  (0.2 A) were used with the low current density steps lasting

only 399 s, instead of the suggested 30 s due to safety aspects. The shorter steps avoid excessive hydrogen concentration on the anode side, which could lead to recombination of hydrogen with oxygen and thus could lead to a rupture of the membrane. The polarisation curve data acquisition is divided into three parts, which can be seen in Tab. 2. This table shows the current steps for each section and the duration of each step. It has been found in the literature that no mass transport losses are observed in

some commercial electrolysers even at 5 A/cm<sup>2</sup> [14]. However, depending on the design, mass transport losses can occur earlier. Therefore, several steps are initially performed in the range of 2–2.5 A/cm<sup>2</sup>. After no mass transport losses have been observed in the first experiments, the same step size as in the ohmic loss range is maintained. The current steps applied do not exceed the maximum current ramp of 5 A/s, as specified by the stack manufacturer.

**Tab. 2.** Operating procedure for recording of polarisation curves at atmospheric pressure. For 5 bar, 10 bar, and 15 bar, the data acquisition steps for the polarisation curves were performed in the reverse order

Step	Description	Details
Warm up	Start the system, set the temperature and wait until the operating conditions stabilise	(1) H <sub>2</sub> O conductivity 0.1 μS/cm (2) Pump volume flow 160 l/h (3) Stack inlet temperature 20 °C, 30 °C, 40 °C, 50 °C, 60 °C (4) Overpressure at the cathode 0, 5 bar, 10 bar, 15 bar
Data acquisition (polarisation curve)	Conduct current-controlled polarisation curves at constant temperature and pressure	(1) Ascending curve <ul style="list-style-type: none"> <li>• Activation overvoltage 1               <ul style="list-style-type: none"> <li>○ Step size: 0.025 A/cm<sup>2</sup></li> <li>○ Range: 0.006–0.15 A/cm<sup>2</sup></li> <li>○ Step duration: 5 s</li> </ul> </li> <li>• Activation overvoltage 2               <ul style="list-style-type: none"> <li>○ Step size: 0.05 A/cm<sup>2</sup></li> <li>○ Range: 0.2–0.5 A/cm<sup>2</sup></li> <li>○ Step duration: 30 s</li> </ul> </li> <li>• Ohmic overvoltage               <ul style="list-style-type: none"> <li>○ Step size: 0.1 A/cm<sup>2</sup></li> <li>○ Range: 0.6–2.5 A/cm<sup>2</sup></li> <li>○ Step duration: 30 s</li> </ul> </li> </ul> (2) Descending curve with the same steps
Shutdown	Prepare the system for the shutdown under security precautions	1) Turn off the power supply 2) Ensure water flow through the stack for a further 5 min 3) Open the nitrogen valve for purge

For each test, the temperature and pressure in the stack are kept constant during data acquisition. As the safety valve is set at 18 bar, pressures of 0 bar, 5 bar, 10 bar, and 15 bar are used on the cathode side, and the anode is not pressurised. The operation temperature is limited by the maximum operating temperature of the ion exchanger, which is 60 °C. For this reason, the experiments are carried out at five stack inlet temperatures: 20 °C, 30 °C, 40 °C, 50 °C, and 60 °C. For reliable results, the temperature difference in the stack ΔT<sub>s</sub> should be as small as possible, and the stack supply temperature T<sub>in,anode</sub> should be kept constant [11]. According to this, the flow rate of the pump is maintained at the maximum of 160 l/h for all experiments, allowing a temperature difference ΔT<sub>s</sub> of less than ±5 K. This is below the ±10 K limit specified by the manufacturer but higher than ±2 K, which is recommended by other reports [9–11]. In this work, ΔT<sub>dev</sub> is defined as follows:

$$\Delta T_{dev} = T_{in,set} - T_{in,anode} \leq \pm 2 \text{ K} \quad (3.2)$$

A deviation of ±2 K from the inlet temperature set ue T<sub>in,anode</sub> was tolerated.

#### 4. RESULTS AND DISCUSSION

The results are obtained from the polarisation curves of 7 of the 10 single cells and the entire stack, as well as the

temperatures and pressures in the system during the 32 experiments. The influence of the operating factors, temperature and pressure is shown by the polarisation curves. Since the cells are connected in series, the sum of the cell voltage should amount to the total stack voltage. Therefore, to compare the performance of the entire stack with the performance of the individual cells, the total voltage measured by the power supply is divided by the number of cells.

Fig. 5a shows the current density and voltage during an experiment at 60 °C and 5 bar. The decreasing current density steps are shown in red, and the resulting stack voltage is shown in green. Fig. 5b shows the behaviour of the inlet and the outlet temperature of the stack, as well as the temperature difference. The inlet temperature of the stack T<sub>in,anode</sub> remains almost constant and is independent of the current. It remained below the permitted value deviation of the set inlet temperature of ±2 K in this experiment as well as in all other experiments. The outlet temperature of the stack decreases until a current density of about 0.6 A/cm<sup>2</sup> (18 A) is reached. After that, the outlet temperature remains almost the same as the inlet temperature. The temperature difference in this experiment decreases from about 4 K to about 0 K from the highest current density of 2.5–0.6 A/cm<sup>2</sup>. Then, it remains almost constant at –0.25 K until the lowest current density is reached. The temperature difference ΔT<sub>s</sub> remains within the permissible range of ±5 K throughout all experiments.

The stack responds quickly to a current variation, with the

voltage value adjusting within 2 s of a change in current. Therefore, 30 s at each current density step was sufficient to guarantee the maximum variation of 5 mV. No significant hysteresis was observed in any of the experiments, indicating that the system was in thermodynamic equilibrium during all measurements, which can be seen in Fig. 9 of the Appendix. Furthermore, the feasibility of the experiment is proven with a second set of experiments. A minimal difference was found between the first and second series of tests, with the largest difference being 0.022 A/cm<sup>2</sup>, seen in the polarisation curve at 30 °C and 0 bar at maximum current density. The results can be seen in Fig. 10 of the Appendix.

In general, all the polarisation curves taken show two zones that are related to the activation and ohmic losses. From 0 to about 0.2 A/cm<sup>2</sup>, the polarisation curve has a behaviour analogous to the Butler-Volmer equation from Ref [14] used to describe the activation overvoltage, which is of the form  $\sinh^{-1}(x)$ . At approximately 0.2 A/cm<sup>2</sup>, the polarisation curve behaves linearly with increasing current density up to the maximum current density of 2.5 A/cm<sup>2</sup>. It can also be seen that most of the curve has a linear behaviour, i.e., the ohmic losses dominate most of the polarisation curve. As mentioned in Section 2.3, an exponential increase in voltage is expected at higher current densities due to the mass transport limitation. This behaviour was not observed up to current densities of 2.5 A/cm<sup>2</sup>, which also has been found in other studies [9,14,6]. Accurate identification of the precise limits of the loss regions requires further studies such as electrochemical impedance spectroscopy (EIS) [21].

#### 4.1 Effect of operating temperature and pressure

In this paragraph, the effect of the operating conditions on the stack performance are described. Fig. 6a shows the influence of temperature on the polarisation curve of the stack at a constant pressure of 0 bar. The polarisation curve is strongly dependent on the operating temperature. At a current density of 2.5 A/cm<sup>2</sup>, the voltage of the stack increases by 14 % when the temperature rises from 20 °C to 60 °C. The black square in Fig. 6a represents the nominal voltage efficiency  $\eta_V$  of the stack of 78% (1.48 V/1.90 V) at a nominal current density of 1.75 A/cm<sup>2</sup> according to the manufacturer. This point is closer to the polarisation curve of 60 °C.

In the first part of the polarisation curve from 0 to about 0.2 A/cm<sup>2</sup>, the curves differ slightly from each other, showing an influence of temperature on the voltage; however, it is small compared to the rest of the curve. At a constant current density of 0.2 A/cm<sup>2</sup>, the highest voltage difference is 31 mV between the temperatures of 20 °C and 30 °C. The smallest difference at the same current density is 19 mV and was found between the 50 °C and 60 °C curves. In the second part of the curve, from 0.2 A/cm<sup>2</sup> to 2.5 A/cm<sup>2</sup>, the voltage difference between the curves begins to increase linearly at different temperatures. At a current density of 2.5 A/cm<sup>2</sup>, the largest voltage difference is 108 mV, also between 20 °C and 30 °C.

The results indicate that the stack voltage decreases as the temperature increases, which brings the cell voltage closer to the thermoneutral voltage. This confirms that the electrolysers have better performance at higher temperatures. The reason for this could be the higher ionic conductivity of the membrane at higher temperatures, leading to lower ohmic losses. This is observed since the results showed a higher slope of the curve at 20 °C than the slope of the curve at 60 °C in the linear range of the polarisation curve. In addition, higher temperatures could also facilitate faster reaction kinetics, resulting in lower kinetic overvoltage. As shown in the small box in Fig. 6a, electrolysis starts faster at higher temperatures, indicating that the activation barrier is lower at higher temperatures. Another effect that may influence this behaviour is the dependence of the open-circuit voltage on temperature. At the lowest tested current density of 0.006 A/cm<sup>2</sup>, voltages of about 1.490 V at 20 °C and 1.433 V at 60 °C have been measured. The experiment that came closest to the thermoneutral voltage at standard conditions was the polarisation curve at 20 °C and atmospheric pressure. The slightly lower starting voltage at high temperatures can be explained by the partial pressure of the water vapour in the catalytic interface region of the electrolyte, and the same behaviour was observed in another test setup [6].

The polarisation curves of the 10-cell stack at different cathode pressures are shown in Fig. 6b. The voltage increases with increasing pressure at all current densities, which means that the performance of the stack decreases at higher pressure; however, this is not particularly dominant. The influence of pressure on the polarisation curve of the stack was mainly observed in the activation zone. With increasing current density, the pressure has barely any effect due to the lack of correlation between the pressure and ohmic resistance of the membrane, as described in the study in Ref [14]. For 2.5 A/cm<sup>2</sup>, the difference is about 13 mV between 0 bar and 15 bar.

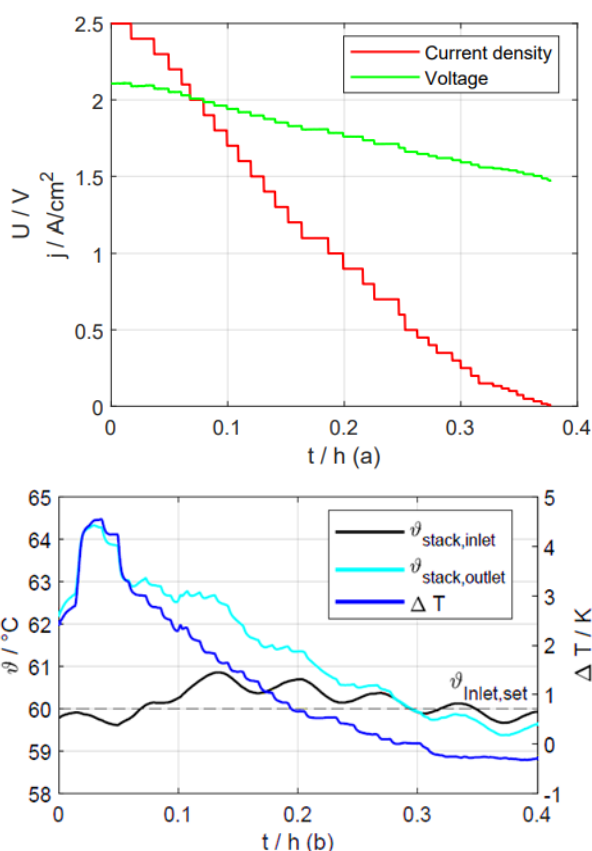


**Fig. 5.** (a) Current density steps and voltage for the polarisation curves, at 60 °C and 5 bar with decreasing current density (b) Course of the inlet and the outlet temperature as well as the temperature difference in the stack



### 4.2 Single cell measurements

Measurements were made in 7 out of 10 cells, as three of them could not be considered due to measurement errors. Fig. 7 shows the polarisation curves at 40 °C and 15 bar pressure. For the other tested temperatures and pressures, a similar behaviour as in Fig. 7 was observed.

The performance of the cells is generally similar at all current densities. At low current densities between 0 A/cm<sup>2</sup> and 0.5 A/cm<sup>2</sup>, in the overvoltage activation zone, the polarisation curves are almost overlapping and show a negligible difference. From this, it could be concluded that all cells have the same catalysts with the same loads and that the catalyst is applied homogeneously over the entire electrode. From about 0.5 A/cm<sup>2</sup>, where the linear region of the polarisation curve begins, the polarisation curve of the cells and of the stack start to diverge from each other as the current density increases. This may be due to the cells and the stack having different ohmic losses. Ohmic losses may differ between cells because of different electric contacts between the cells. Currently, electrolysis stacks are mostly produced manually, which can lead to inhomogeneities during the series connection or stacking of cells. The order of the cells at 2.5 A/cm<sup>2</sup> from best to lowest performance is 3, 6, 7, 8, 2, 10, and 4. Additionally, the stack always has higher voltage values than the cells.

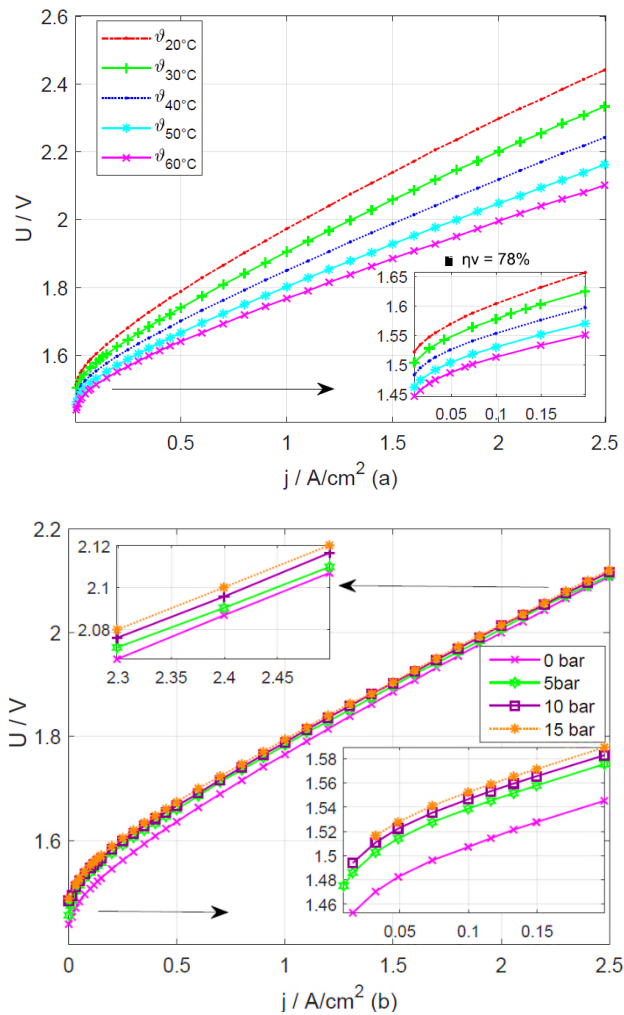


Fig. 6. (a) Effect of temperature on the performance of the stack at a constant pressure of 0 bar. (b) Effect of pressure on the performance of the stack at a constant temperature of 60 °C

The ohmic losses of the stack are higher than those of the cells since the stack measurement also considered the end plates, while the measurement of the cells was directly performed at the cell electrodes. Furthermore, as pressure increases, the voltage difference between the cells tends to widen, which is expected as high pressure can lead to reduction in the contact area. In particular, the cells far from the water inlet (e.g., cell 10) showed higher voltage at high currents than the first cells (e.g., cell 3). This may mean that irregular water distribution or more difficult gas removal may occur in the cells far from the water inlet. Since no clear mass transport losses are observed in general, this is unclear. Cell 4 shows the highest voltage values, which is inconsistent with the assumption of transport losses mentioned earlier. In this case, the explanation could be that in the middle part of the stack, the contact resistance between the membrane and the electrodes, as well as that between the bipolar plates and the CCMs, increases due to less compression of the cells.

However, it is important to note that the cells are generally very close to each other at all current densities, and the largest voltage difference is between the cells and the stack. In this study, the difference recorded between the cells is not considerable, as mentioned in the study in Ref [6]. It was found that improper contacts lead to uneven current distribution and a higher operating voltage to compensate for the non-active zones [6]. As high voltages were not seen in this work, it can be assumed that the CCMs of the stack have good contact with the bipolar plates and the cells to each other. However, in Ref [6], it was found that the effects of contact areas on stack performance at higher current densities were more pronounced, which could be an explanation for why the cell curves are further apart at current densities above 2 A/cm<sup>2</sup>.

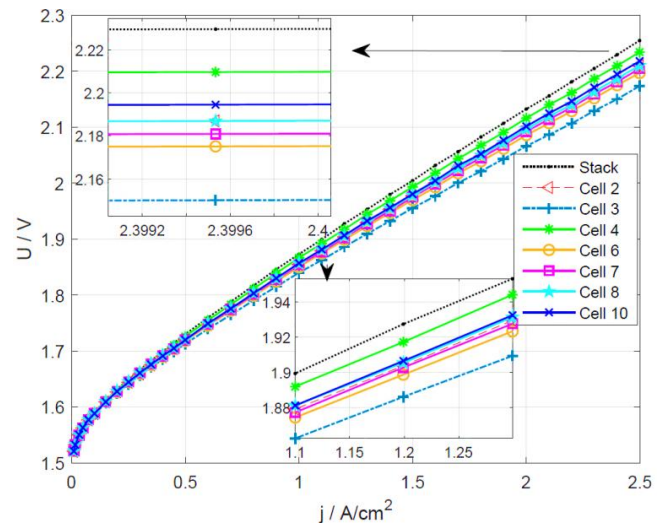
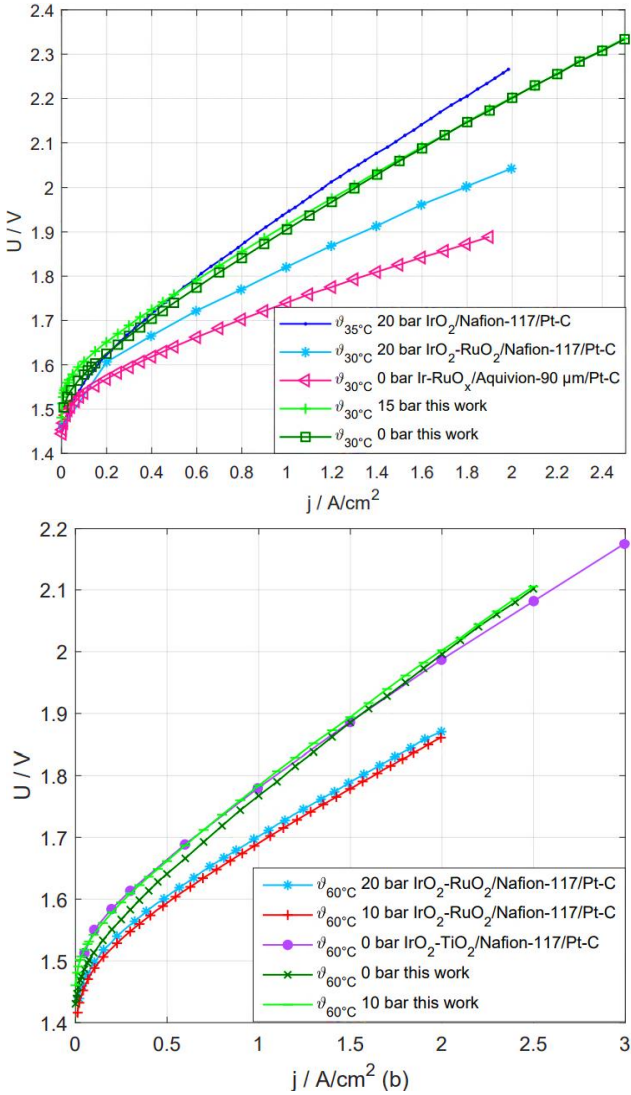


Fig. 7. Polarisation curve at 40 °C and 15 bar. Visualisation of the behaviour of the stack and 7 cells

### 4.3 Comparison with other PEM electrolysis systems

In this section, the experimental data obtained in this study are compared with those of four studies. It should be noted that the specific materials used in the PEMWE for this study were not disclosed by the commercial stack manufacturer and were not made available to the authors. Since the composition of the CCM of the stack used in this work is not known, it is of interest to the

authors for research purposes to draw general assumptions about the materials used in the commercial stack, through comparisons with the performance of other cells. Moreover, it should be noted that the polarisation lines of the present study shown in this section are from the stack, while all those in the literature are from a single cell since characterisation and fabrication of a single cell are generally easier.



**Fig. 8.** (a) Comparison of polarisation curves from this work and the literature in the temperature range of 30 °C and 35 °C and pressure range of 0 bar and 20 bar [2,23]. (b) Comparison of polarisation curves from this work and the literature at 60 °C and pressure range of 0 bar and 20 bar [17,22]

Fig. 8a illustrates the results presented in Ref [22] for temperatures near 30 °C and pressures of 0 bar and 20 bar, with the dark blue being a IrO<sub>2</sub>/Nafion®-117/Pt-C and the light blue an IrO<sub>2</sub>-RuO<sub>2</sub>/Nafion-117/Pt-C cell. The polarisation curve at 0 bar with a 90-µm-thick Aquivion® membrane with IrRuO<sub>x</sub> and Pt/C catalysts deposited on both sides of the membrane is shown in pink [23]. For comparison, the polarisation lines of this work closest to the operating conditions of the other works are also plotted in Fig. 8a. The polarisation curve at 35 °C and 20 bar with a IrO<sub>2</sub>/Nafion-117/Pt-C cell is the curve closest to the values of the investigated stack at 30 °C. It can also be noted that the other two

curves (pink and light blue) are far from the results obtained here. These show lower voltage values at the same current density, i.e., better performance. These two curves use a RuO<sub>x</sub> catalyst on the anode side. It has been found in the literature that the use of RuO<sub>x</sub> improves the rate of the OER. Although RuO<sub>x</sub> has a much lower overvoltage than other electrocatalysts in the OER, RuO<sub>x</sub> dissolves and becomes corroded at a higher rate during oxygen evolution [16]. This could be a reason why electrolyser manufacturers use IrO<sub>2</sub> instead of RuO<sub>x</sub> [14]. In addition, the Aquivion® membrane is thinner (90 µm) than that of Nafion® 117 (175 µm), which reduces ohmic losses.

Fig. 8b illustrates the results presented in Ref [22] at 60 °C and at pressures ranging from atmospheric to 20 bar. The polarisation curves from the study [22] are shown in blue for 20 bar and in red for 10 bar. The results from the present study at 10 bar are shown in light green, and the results at 0 bar are shown in dark green. A polarisation curve for a CCM with a Nafion®-117 membrane and a catalyst on the anode of IrO<sub>2</sub>/TiO<sub>2</sub> and Pt/C on the cathode from the study in Ref [17] at 60 °C and ambient pressure can also be found in purple. This polarisation curve is very close to the curve measured in this work at 60 °C and 10 bar. It could be assumed that the performance of the used commercial stack is close to that of a cell with IrO<sub>2</sub>/TiO<sub>2</sub> electrodes and a Nafion®-117 membrane. However, other factors of the stack design that affect the cell's performance must be considered such as the influence of ionomer content, catalyst loading, membrane wetting and other factors [17].

In the study in Ref [17], it was found that the cell voltage difference between 40 °C and 80 °C is about 160 mV at a current density of 1 A/cm² and increases to more than 250 mV at 3 A/cm². In the present study, a voltage difference of 212 mV was measured between 20 °C and 60 °C at a current density of 1 A/cm² and at 2.5 A/cm², the voltage difference increases to 397 mV. In [17] it was pointed out that this difference is due to a 50 % increase in membrane conductivity between 40 °C and 80 °C. In all the polarisation curves shown in this article, measured up to 3 A/cm², no mass transport overvoltage is visible.

## 5. CONCLUSIONS

A 1-kW water electrolysis test stand was set up at the Bremen University of Applied Sciences for hydrogen production. The electrochemical characterisation of the stack and the cells was realised using the polarisation curves. A galvanostatic control was used to characterise up to 2.5 A/cm², at 5 different temperatures of 20 °C, 30 °C, 40 °C, 50 °C, and 60 °C and at 4 different pressures of 0 bar, 5 bar, 10 bar, and 15 bar. The developed protocol for data collection was explained and can be used in future experiments. This work has shown that temperature is the most significant factor influencing the performance of the stack. Increasing the pressure also affects the stack performance, although by a lower percentage. High temperature and atmospheric pressure on the cathode side were found to be the most favourable operating conditions for best efficiency. However, the operation of the stack at higher pressures allows the production of pressurised hydrogen without severely affecting the performance on the stack level. Two zones of stack operation were also identified, one is dominated by activation voltage losses and the other is dominated by ohmic losses. No significant mass transport losses were found.

The stack has a higher voltage than the group of single cells due to its higher ohmic losses. It has also been found that not all cells have the same voltage value, especially in the area where ohmic losses dominate. However, the cells are generally very close together at all current densities. It could be assumed that the membranes of the stack have good contact with their catalyst layers, which also applies to the current collector with the bipolar plates and between them. In addition, it has been found not to be suitable to describe the total stack voltage by the sum of  $N$  identical individual cells. This is especially important for modelling and scaling of electrolyzers based on single cell tests. The comparison of the results of this work with those from the literature showed that the performance of the stack from this work is comparable to that of an IrO<sub>2</sub>-TiO<sub>2</sub> Nafion-117/Pt-C cell. However, this cannot be assured with the present results.

In future work, the parameters of an existing electrochemical model of the stack will be determined using the experimental data from this work. These electrochemical parameters will be integrated into a MATLAB-Simulink® model to simulate the stack and the complete system as part of the Hydrogen Lab Bremerhaven of the Fraunhofer Institute for Wind Energy Systems (IWES). In addition, the experimental data obtained in this work can be used to validate the modelling of the stack. Furthermore, it is desired to identify the percentage of voltage losses due to the end plates.

## 6 APPENDIX

The hysteresis was taken in all experiments, and in this section, the largest hysteresis is shown, which has been measured at 60 °C and 0 bar. In Fig. 10, the comparison between the first and the second round of experiments at 0 bar and at 4 different temperatures 30 °C, 40 °C, 50 °C, and 60 °C is given. The other experiments at 5 bar, 10 bar and 15 bar have a similar behaviour to the experiment presented in Fig. 10.

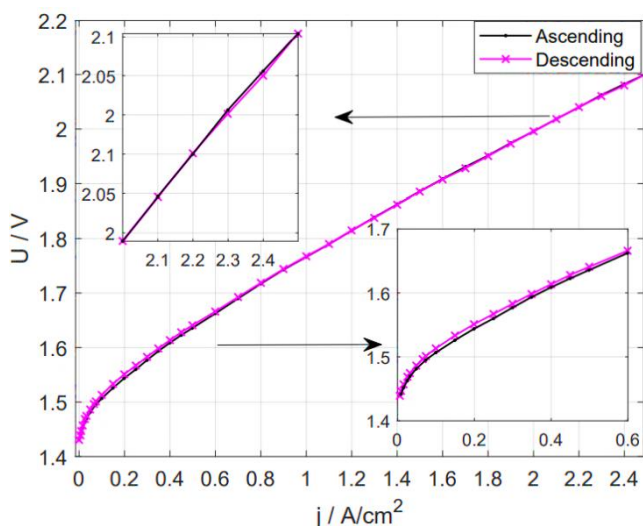


Fig. 9. Hysteresis at 60 °C and 0 bar

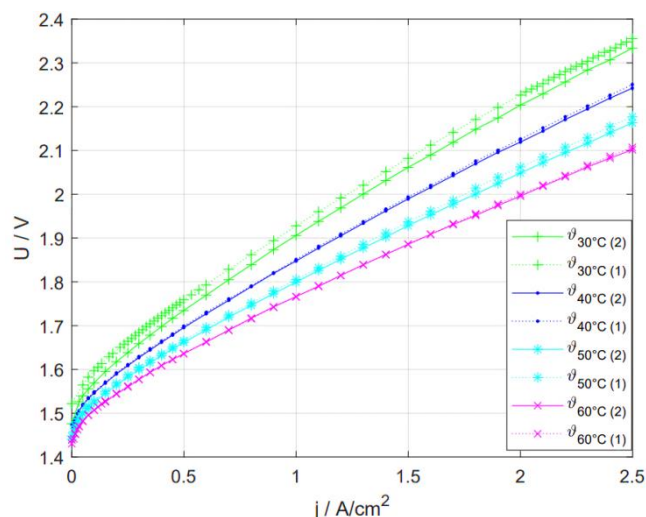


Fig. 10. Comparison between the first and second round of experiments at different temperatures and a constant pressure of 0 bar

## REFERENCES

1. Der Sozialdemokratischen Partei Deutschlands (SPD). BÜNDNIS 90/DIE GRÜNEN und den Freien Demokraten, Koalitionsvertrag 2021 – 2025: mehr fortschritt wagen Bündnis für Freiheit Gerechtigkeit und Nachhaltigkeit. 2021
2. European Commission. Hydrogen: The EU's hydrogen strategy explores the potential for renewable hydrogen to help decarbonise the EU in a cost-effective way [Internet]. 2022 [cited 2022 Nov 06]; Available from: [https://ec.europa.eu/info/index\\_en](https://ec.europa.eu/info/index_en)
3. Bertuccioli L, Chan A, Hart D, Lehner F, Madden B, Standen E. Study on development of water electrolysis in the EU: Fuel Cells and hydrogen Joint Undertaking. 2014
4. Lettenmeier P. Entwicklung und Integration neuartiger Komponenten für Polymerelektrolytmembran- (PEM) Elektrolyseure [PhD Dissertation]. Stuttgart: Fakultät Energie-, Verfahrens- und Biotechnik der Universität Stuttgart. 2018
5. Abomazid AM, El-Taweel NA, Farag HEZ. Novel Analytical Approach for Parameters Identification of PEM Electrolyzer. IEEE Transactions on Industrial Informatics. Sept. 2022; 18(9): 5870-5881. doi: 10.1109/TII.2021.3132941
6. Selamet ÖF, Acar MC, Mat MD, Kaplan Y. Effects of operating parameters on the performance of a high-pressure proton exchange membrane electrolyzer. Int. J. Energy Res. 2013; 37: 457-467. <https://doi.org/10.1002/er.2942>
7. Smolinka T, Ojong E, Garcke J. Hydrogen Production from Renewable Energies—Electrolyzer Technologies. Electrochemical Energy Storage for Renewable Sources and Grid Balancing. Elsevier; 2015. DOI 10.1016/B978-0-444-62616-5.00008-5.
8. Tjarks G. H, Stolten D, Wessling M. PEM-Elektrolyse-Systeme zur Anwendung in Power-to-Gas Anlagen. Forschungszentrum Julich GmbH, Zentralbibliothek (Schriften des Forschungszentrums Julich / Reihe Energie & Umwelt: Reihe Energie & Umwelt). 2017. – ISBN 9783958062177
9. Bender G, Carmo M, Smolinka T, Gago A, Danilovic N, Mueller M, Ganci F, Fallisch A, Lettenmeier P, Friedrich K A, Ayers K, Pivovar B, Mergel J, Stolten D. Initial approaches in benchmarking and round robin testing for proton exchange membrane water electrolyzers. International Journal of Hydrogen Energy. 2019; 44: 9174-9187. <https://doi.org/10.1016/j.ijhydene.2019.02.074>
10. European European Commission, Joint Research Centre, Tsotridis G, Pilega A. EU harmonized protocols for testing of low temperature water electrolysis. Publications Office of the European Union; 2021. Available from: [doi/10.2760/58880](https://doi.org/10.2760/58880)



11. Malkow T, Pilenga A, Tsoitridis G, De Marco G. EU harmonised polarisation curve test method for low-temperature water electrolysis. Publications Office of the European Union; 2018. Available from: doi:10.2760/179509
12. Godula-Jopek, A. Hydrogen production By electrolysis. Weinheim: Wiley-VCH-Verl., 2015
13. Mori M, Mržljak T, Drobnič B, Sekavčnik M. Integral Characteristics of Hydrogen Production in Alkaline Electrolysers. *Strojinski Vestnik*. Aug 2013; 59(10):585-594. doi: 10.5545/sv-jme.2012.858
14. Espinosa-López M, Darras C, Poggi P, Glises R, Baucour P, Raktondrainibe A, Besse S, Serre-Combe P. Modelling and experimental validation of a 46 kW PEM high pressure water electrolyzer. *Renewable Energy*. 2018; 119: 160–173. <https://doi.org/10.1016/j.renene.2017.11.081>
15. Bensmann, B. Systemanalyse der Druckwasser-Elektrolyse im Kontext [PhD Dissertation]. Magdeburg: Fakultät für Verfahrens- und Systemtechnik der Otto-von-Guericke-Universität Magdeburg. 2017
16. Feng Q, Yuan X, Liu G, Wei B, Zhang Z, Li H, Wang H. A review of proton exchange membrane water electrolysis on degradation mechanisms and mitigation strategies. *Journal of Power Sources*. 2017; 366: 33–55. <https://doi.org/10.1016/j.jpowsour.2017.09.006>
17. Bernt M. Analysis of Voltage Losses and Degradation Phenomena in PEM Water Electrolyzers [PhD Dissertation]. Munich: Fakultät für Chemie der Technischen Universität München. 2018
18. Amores E, Rodríguez J, Oviedo, Lucas-Consuegra A. Development of an operation strategy for hydrogen production using solar PV energy based on fluid dynamic aspects. *Open Engineering*. 2017; 7(1): 41–152. doi: 10.1515/eng-2017-0020
19. Bitter R, Mohiuddin T, Nawrocki M. LabVIEW: Advanced programming techniques. Crc Press; 2006
20. Stähler M, Stähler A, Scheepers F, Carmo M, Lehnert W, Stolten D. Impact of porous transport layer compression on hydrogen permeation. *PEM water electrolysis*. 2020; 45(7): 4008-4014.
21. Merwe J. Characterisation of a proton exchange membrane electrolyser using electrochemical impedance spectroscopy [PhD Dissertation]. Potchefstroom: School of Electrical, Electronic and Computer Engineering North-West University. 2012
22. Bessarabov D, Millet P. PEM Water Electrolysis [Internet]. 1th ed. Elsevier; 2018. Chapter 2, Key Performance Indicators; [cited 2022 Sep 30]. pp. 33–60. Available from: <https://www.elsevier.com/books/pem-water-electrolysis/pollet/978-0-08-102830-8>
23. Siracusano S, Trocino S, Briguglio N, Baglio V, Aricò AS. Electrochemical Impedance Spectroscopy as a Diagnostic Tool in Polymer Electrolyte Membrane Electrolysis. *Materials (Basel)*. 2018; 11(8):1368. doi: 10.3390/ma11081368

This work was partly supported by the Free and Hanseatic City of Hamburg.

Nicol D. Jaramillo Rodríguez:  <https://orcid.org/0000-0002-0745-8642>

Aline Luxa:  <https://orcid.org/0000-0002-3025-3274>

Lars Jürgensen:  <https://orcid.org/0000-0002-7742-8051>



This work is licensed under the Creative Commons BY-NC-ND 4.0 license.



## AERODYNAMIC INVESTIGATION ON THE ARTEFACT "BIRD OF SAQQARA"

Michel ZIEROW\*, Leon LESEMANN\*

\*City University of Applied Sciences, Faculty of Nature and Engineering,  
Institute of Aerospace Technology, Flughafenallee 10, 28199 Bremen, Germany

[michelzierow@gmail.com](mailto:michelzierow@gmail.com), [leonlesemann@gmail.com](mailto:leonlesemann@gmail.com)

received 9 October 2022, revised 4 April 2023, accepted 4 April 2023

**Abstract:** Lost, technical knowledge of ancient cultures is being rediscovered in modern times during archaeological excavations. A presumed example of the innovative power of ancient cultures is the artefact "Bird of Saqqara". In the context of this paper, the aerodynamic characteristics of the artefact are to be determined by a computational fluid simulation, in order to be able to make a statement about the actual flight suitability and to examine the theses of the pre-astronautics critically. Based on a 3D scan, a CAD model of the artefact is created and then a numerical flow simulation is performed. By varying the angle of attack, the dimensionless coefficients can be represented in corresponding polars. The results show that the artefact has a low maximum glide ratio and thus the glide properties are not sufficient for use as a handglider. The centre of gravity of the artefact is located at the trailing edge of the wing and behind the neutral point. The resulting longitudinal stability does not meet modern specifications. Asymmetric lift distribution in the spanwise direction results in uncontrolled roll. Consequently, the artefact cannot fly a straight path. Within the scope of this work, the connection between the "Bird of Saqqara" and an alleged knowledge of aerodynamics in ancient Egypt could not be confirmed.

**Key words:** Saqqara, bird, aerodynamics, archaeology, CFD, flight mechanics, Paleo-SETI, Egypt, Ancient Aliens

### 1. INTRODUCTION

Through findings and archaeological excavations in modern times, mankind continues to discover the advanced and highly technological knowledge that ancient cultures already possessed. To determine whether the findings are actually based on early inventive genius and knowledge of correlation, extensive research must be carried out. Thus, it happens that in the case of some ancient objects discovered by archaeological excavation, only assumptions can be made, which are taken up by pseudo-sciences and conspiracy theories. One of these pseudo-sciences is the so-called ancient-astronautics, which brings the alleged technical progress of some cultures into a connection with claims for the legitimacy of theories positing the existence of extraterrestrial life forms. The conspiracy theories refer to ancient religious writings or archaeological finds whose presumed purpose conflicts with the technical possibilities of the time of origin. One of these finds is the so-called "Bird of Saqqara", a wooden figure allegedly resembling a modern high-winged airplane. In pre-astronautics, this artefact is considered to indicate knowledge of aerodynamic and flight mechanics. In the context of this paper the aerodynamic characteristics of the artefact are to be determined by a computational fluid simulation, in order to be able to make a statement about the actual flight suitability and to examine the theses of the pre-astronautics critically.

### 2. INVESTIGATION OF THE ARTEFACT USING CFD SIMULATION

This section will describe the execution of the simulation with all associated work steps. For this purpose, the transfer of the

scan file into a suitable file format and the associated simplifications and abstractions are described first. Subsequently, the creation and optimisation of the mesh, as well as the setting of the solution parameters, will be discussed. The mathematical and flight-mechanical basics will not be explained further within this paper.

#### 2.1. Pre-processing

A 3D photoscan of the artefact, which was created by Mr. Maximilian Schecker and the staff of the Egyptian Museum in Cairo, serves as the basis for the flow simulation in Ansys Fluent 2020 R1. The point cloud, which is in .fbx format, is subjected to reengineering to convert the scan file into a solid and prepare it for a computational fluid dynamics (CFD) simulation. The process mainly consists of the following steps (conducted in this order):

- Modifying the scan file
- Converting the scan file format to a computer aided design (CAD) exchange format
- Scaling the CAD model to the original size
- Introduction of a body-fixed coordinate system
- Mapping the fuselage and wing through multiple section planes
- Transferring the sectional sketches to a new CAD model
- Creating a solid for the fuselage and wing
- Merging the individual parts into an assembly
- Prepare the assembly for a CFD simulation in Ansys SpaceClaim 2020 R1

In addition to the artefact, the original scan file still contains the pedestal of the model on which it is presented in the Egyptian Museum. This is removed in the first step using Autodesk Fu-

sion360 software to limit the amount of computing capacity required to process the model. The file is then converted into a surface model in .STEP-format and exported so that it can be further processed with more extensive CAD software.

The processing then takes place in Autodesk Inventor Professional 2022. Since scaling errors can occur during transfer to a CAD exchange format, the model first is scaled to its correct dimensions in Inventor. This is done by referring to drawings made by Messiha [1], although the exact dimensions are not decisive for the dimensionless coefficients. Due to the high level of detail of the 3D scan, it is not possible to convert the surface model directly into a solid in Inventor.

This goal can be achieved by cutting the fuselage and the wing of the bird into up to 44 partial segments and mapping the contour of the body in the cutting plane on each cut surface by means of a spline. To be able to transfer the resulting sectional surfaces to a separate CAD model and convert them there into a solid model, the sketches must be aligned with a common coordinate system. For this purpose, a longitudinal (Y), vertical (Z) and lateral (X) axis is added to the model (see Fig. 1).

Subsequently, 44 cutting planes are placed in the fuselage and 30 in the wing, on which the contour of the cross section is reproduced. The distance between the cutting planes is not specified with a constant value, but adjusted according to the curvature of the geometry. Finally, the cutting planes are connected to each other via an elevation so that a separate solid is created for the wing and fuselage, which get positioned in relation to each other in an assembly.



Fig. 1. STEP-file with additional coordinate system

Before the model could be subjected to a flow simulation, the simulation environment had to be defined in its geometry via Ansys SpaceClaim 2020. Accordingly, a higher resolution region in the near field of the artefact, a so-called body of influence (BOI), is also created. The simulation environment has dimensions of 1,240.95 mm × 1,032.74 mm × 1,178 mm, and the BOI is defined as 374.66 mm × 181 mm × 350 mm. In addition, the geometries get named via so-called named selections in order to be able to determine the flow inlet, the flow outlet and the artefact in the simulation software in the further course.

By exporting the file as .tgf, the computational grid can be generated in Ansys Fluent.

## 2.2. Generation of the mesh

An important step in CFD simulation is the discretisation of the differential equations by a mesh. First, a surface grid is generated for this purpose, which is then to be converted into a volume grid. For the surface grid, the cells are generated finer by applying the so-called sizings for certain regions. The goal is to effectively resolve the cell regions where high gradients of the flow variables

are expected. On the surface of the object, the sizing curvature is used, in which the cells are made finer at higher curvature of the surface. In addition, the cells on the surface of the BOI are generated finer than the global cell dimensions using the sizing of the corresponding name to better resolve the flow-field near the object. The far field of the flow is globally resolved coarser than the other regions, since high gradients of flow variables are not expected in that region. The parameters used to create the surface grid can be found in Tab. 1. By applying various optimisation mechanisms, it is possible to reduce the skewness of the grid to <0.6 in all regions. Thus, the surface grid has a sufficiently high quality. According to the workflow from Ansys Fluent, the volume regions are then computed. Poly-hexcore is used as cell type to reduce the memory usage. In addition, prism cells are used in the boundary layer of the artefact in order to resolve the high gradients normal to the surface well. Since the SST-kw model is to be used for computation afterwards, the standardised wall distance has to be  $y^+ \approx 1$  when generating the prism cells [2]. For this purpose, three iteration steps were performed, in which the height of the first layer of prism cells was varied. The number of layers was adjusted so that the total height remained constant. In the third iteration step, this goal was achieved. In addition, various optimisation mechanisms are again applied to optimise the mesh quality. Using the aspect ratio and the inverse orthogonal quality, the mesh quality is finally evaluated as high.

Tab. 1. Parameters of mesh-cells for different sizings

Sizing	Parameter	Values
Global	Min. size	0.1
	Max. size	25
	Growth rate	1.2
BOI (Body of influence)	Min. size	0.1
	Max. size	2.5
	Growth rate	1.2
Curvature	Min. size	0.1
	Max. size	2.5
	Growth rate	1.2
	Normal angle	9°

## 2.3. Setup of the solver

To set up the solver, the Ansys "Prepare to solve" function first applied several automated changes to the mesh to minimise the subsequent computational effort and fasten the convergence of the results.

As a first step, the boundary surfaces of the enclosure are assigned to the respective functions in the simulation. The leading face acts as a velocity inlet with an inflow velocity of 10 m/s. The airflow at different angles of attack is achieved by varying the directional components. The outflow surface behind the artefact is defined as a pressure outlet with a gauge pressure of 0 MPa. The remaining surfaces of the enclosure retain the type "Wall" and get set to be frictionless.

Report definitions for drag, lift and moment coefficients are generated to determine the coefficients. The reference values required for scaling are the projected wing area (as reference area) and inflow velocity (as reference velocity). As a discretisation method, a second-order method is used for the pressure

equations and the second-order-upwind method is used for the equations of momentum, turbulent kinetic energy and specific dissipation, so that the flow direction is also taken into account in the calculations. To accelerate the convergence of the solutions, explicit relaxation factors (sub-relaxation) are partially applied for the flow variables. As an additional implicit relaxation method, the calculation will be conducted as pseudo-transient.

To avoid the use of wall functions, the SST-k $\omega$ -model (Reynolds averaged Navier Stokes equations, RANS-method) is chosen for the calculation [2]. The results are assumed to be converged once the residuals have decreased by approximately three orders of magnitude.

### 3. EVALUATION OF THE SIMULATION RESULTS

In this section, the results of the CFD simulation are evaluated and characterised in order to make a determination about the glide characteristics and the flight performance of the artefact.

#### 3.1. Polars

Computational fluid simulation in a range of angles of attack from  $-5^\circ$  to  $14^\circ$  in  $1^\circ$  steps allows the aerodynamic coefficients of the artefact to be determined. The results are presented in polars.

The lift coefficient shows a linear course in the angle of attack range from  $-5^\circ$  to  $7^\circ$ , reaches a maximum of  $c_L = 0.4728$  at  $9^\circ$  and decreases with increasing angle of attack due to a progressive stall.

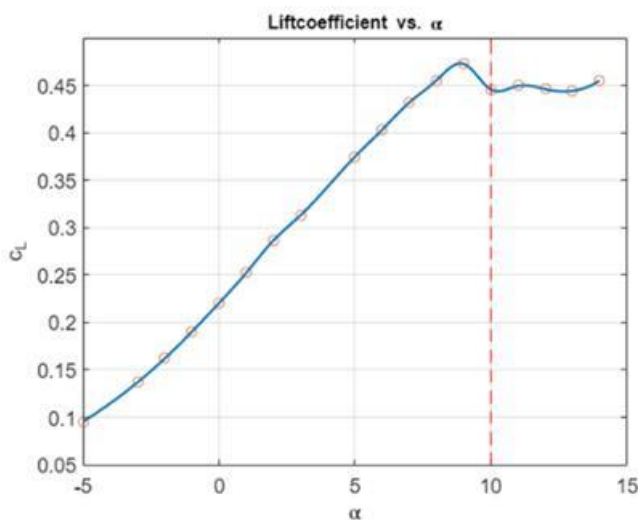


Fig. 2. Lift polar

The polar curve (see fig. 2 and fig. 3) shows that the flow breaks off even at a low angle of attack. Also, no particularly high maximum lift coefficient is achieved. In comparison, a NACA 0012 airfoil achieves a maximum lift coefficient of  $c_L \approx 0.9$  [2]. However, the artefact achieves positive lift coefficients even at negative angles of attack, which is due to the twisting of the airfoil in the spanwise direction.

Plotting the lift coefficient versus drag coefficient shows that the artefact has a high parasite drag coefficient of

$c_{D,0} = 0.1065$ . In comparison, general aviation aircrafts have zero parasite drag coefficients of approximately  $c_{D,0} = 0.02$  to  $0.05$  [3]. The high zero drag coefficient is due to the low curvature of the wings leading edge, which can also be seen in the pressure distribution in Fig. 7.

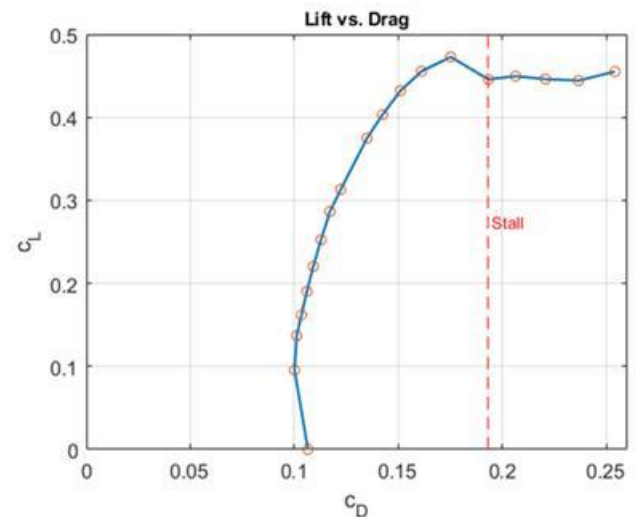


Fig. 3. Lift over drag polar

The combination of high drag coefficients and simultaneously low lift coefficients leads to a maximum lift/drag ratio of only  $E_{max} = 2.86$  at an angle of attack of  $7^\circ$  on the artefact. The artefact thus does not exhibit good glide characteristics. However, the glide characteristics of the flying object are decisive for engine-less, stationary straight flight, since a high drag cannot be compensated with an engine thrust.

#### 3.2. Flight mechanics calculation

To illustrate the simulation results, simple flight mechanics calculations are conducted. The artefact is assumed to be a mass point and the moment budget is neglected.

For this purpose, the minimum airspeed for engine-less, steady-state glide is first calculated for different flight path angles and angles of attack. In this case, at an angle of attack of  $10^\circ$ , the minimum airspeed for flight path angles from  $10-20^\circ$  is  $\approx 17$  m/s. This speed is significantly too high, for a stable, targeted launch by hand.

In addition, the maximum range (launch at best glide angle) and endurance (launch at minimum sink rate) are calculated for a drop from a height of 2 m. The maximum range is 5.48 m and the maximum endurance is 1.51 s. These values underline the poor glide characteristics derived from the polar axis and suggest that the object was not used as a hand glider.

#### 3.3. Position of the centre of gravity and the aerodynamic centre

The derivative  $\frac{\delta c_m}{\delta c_\alpha}$  is considered an essential stability measure. Thereby, the moment coefficient must decrease in case of a lift coefficient increase. Since the coefficient is usually nega-

five, it must increase in magnitude. Consequently, the pitching moment also increases, so that the pitch angle is reduced (stable behaviour) [4]. As shown in Fig. 4, the derivative is positive and therefore does not lead to flight stability.

In addition to the derivative  $\frac{\delta c_m}{\delta c_\alpha}$ , the position of the centre of gravity and aerodynamic centre (relative to each other) is used to assess flight stability. In this case, the centre of gravity is determined by the CAD model, whereas the aerodynamic centre can be calculated using the stability measure relative to a reference point. The neutral point should be located behind the centre of gravity, at  $\approx 15\%$  of the reference wing depth, for good flight stability in a wing-fuselage combination [5].

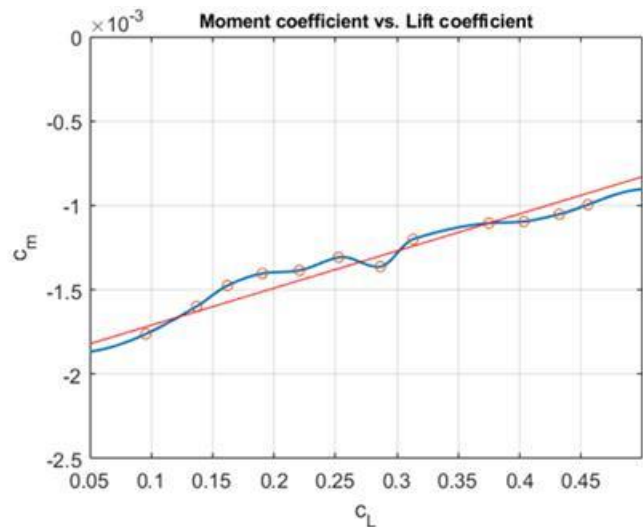


Fig. 4. Moment coefficient versus lift coefficient

The centre of gravity of the artefact is located shortly before the trailing edge of the wing (54 mm behind the nose tip) and thus clearly too far to the rear. The calculation of the aerodynamic centre shows that it is located in front of the centre of gravity and also too far in the rear. These characteristics do not indicate sufficient longitudinal stability, which means that the already poor glide characteristics of the artefact cannot be achieved in reality. The position of the centre of gravity and aerodynamic centre is shown in Fig. 5.

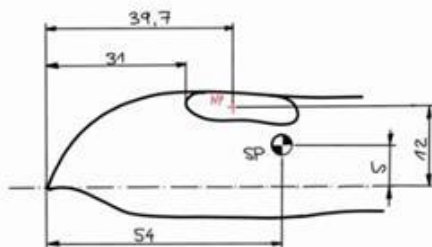


Fig. 5. Position of centre of gravity (SP) and the aerodynamic centre (NP); dimensions in millimetre

### 3.4. Distribution of pressure and velocity

After the characteristic aerodynamic values of the artefact

have been determined and classified in the previous subsection, the curves of pressures and velocities are now to be considered in order to describe the behaviour of the flow. The angles of attack  $6^\circ$  and  $11^\circ$  are considered, since a stall can be assumed between these angles.

The static pressure along the wing at the artefact is roughly similar to that at a typical airfoil (see Fig. 6).

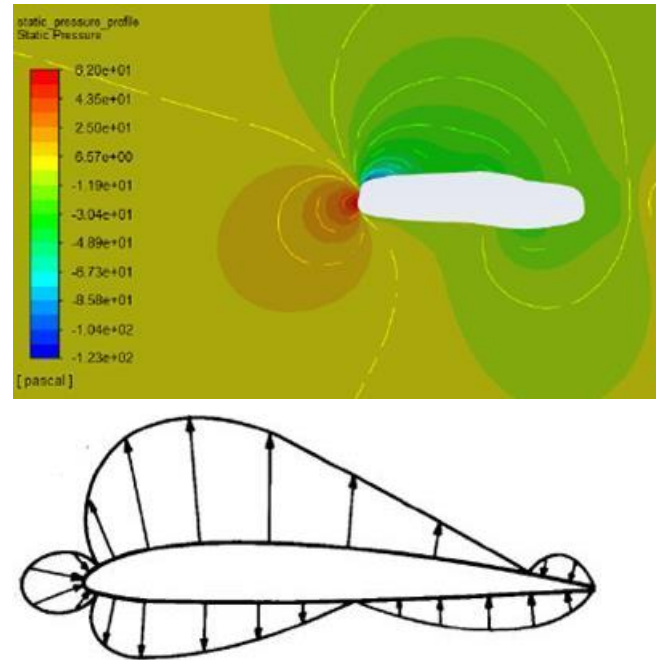


Fig. 6. Pressure distribution (top) and typical pressure distribution of an airfoil (bottom) [4]

Accordingly, a larger area of high static pressure is present at the leading edge of the artefact (shown in Fig. 6), which results from the low curvature of the wings leading edge. Static pressures of up to  $p_{stat} = 52\text{ Pa}$  occur here. Due to the different flow velocities, the static pressure on the upper side of the wing is lower than that on the lower side. Thus, as in the case of classic airfoils, it can be called a suction side. The values here are around  $-45\text{ Pa}$ , reaching up to  $-123\text{ Pa}$  in the front area of the profile.

The pressure distribution in the spanwise direction is shown in Fig. 7. As expected, the static pressure decreases in the direction of the wing tips. An asymmetry in the pressure distribution can be seen, with a larger pressure difference at the left wing (from the bird's perspective). This is particularly evident at the left wing tip, with a high overpressure.

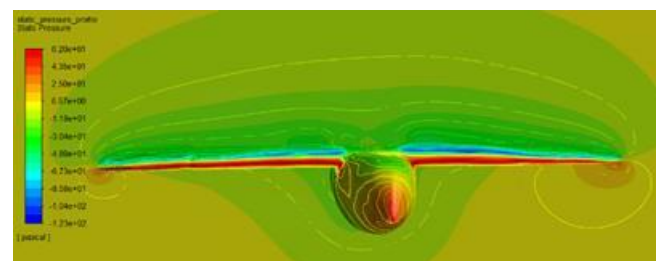


Fig. 7. Spanwise pressure distribution

It is expected that the asymmetric pressure or lift distribution



will cause the artefact to roll, with the right wing tilting downward. Since the total lift vector thus has an additional horizontal component, the bird would fly a right turn. Due to a lack of rudder, coordinated turn flight is not possible, resulting in a bank angle. After the initiation of the roll motion, the angle of bank would steadily increase, and at the same time the artefact, due to its pitching moment balance, would continue to pitch up. This non-stationary flight behaviour leads to a stall and thus to a crash of the bird.

Flow separation phenomena can be investigated by examining the velocity distribution along the wing depth. Similar to the pressure distribution, angles of attack of 6° and 11° were considered. By means of the display variant of vector fields in Ansys Fluent, the direction and height of the respective velocity vector can be visualised.

Fig. 8 shows the velocity field on the airfoil at 6° angle of attack. A thin, laminar boundary layer with low velocity (in blue) can be seen along the profile. Due to the abruptly ending trailing edge of the wing, backflows occur at this point. On modern airfoils, the reverse flows are reduced by tapering the trailing edge of the airfoil.

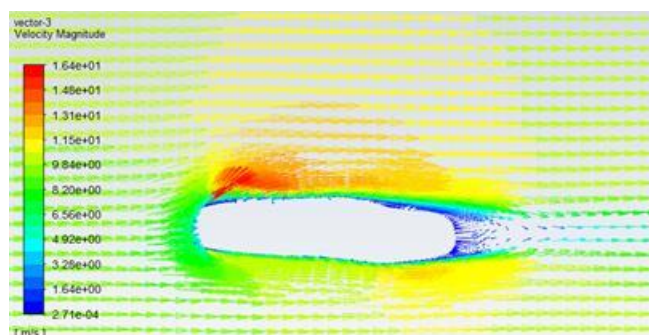


Fig. 8. Flow-field on the wing ( $\alpha = 6^\circ$ )

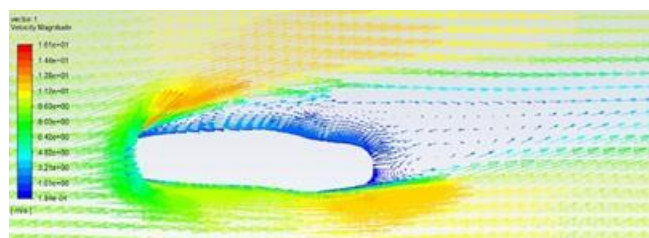


Fig. 9. Flow-field on the wing ( $\alpha = 11^\circ$ )

At an angle of attack of 11°, detachment of the boundary layer can be seen (s. fig. 9). The separation extends to the leading edge of the wing. Low flow velocities and the reverse flows reduce the effective lift, which can also be seen from the polars in Figs 2 and 3. A flight with an angle of attack of 11° is therefore not possible. With modern airfoils, flight at this angle of attack is usually possible, so that higher lift coefficients can also be achieved as a result of the higher angle of attack.

The flow separation phenomena are mainly favoured by the airfoil shape of the artefact, which does not have the characteristics of modern airfoils. It can be assumed that the airfoil shape was chosen to be approximately rectangular for manufacturing reasons. Removal of the leading and trailing edges due to the long-lasting weathering of the artefact is also conceivable.

#### 4. CONCLUSION

Due to the poor aerodynamic characteristics of the studied artefact, it cannot be confirmed within the scope of this study that the “Bird of Saqqara” is a product of ancient aerodynamic knowledge. The artefact has a very high parasite drag with only low lift at the same time. In addition, the pressure distribution, as well as the location of the centre of gravity and aerodynamic centre (with respect to each other) suggest poor flight stability characteristics. A straight trajectory is therefore not possible. The artefact would perform an uncontrolled rolling motion, which in combination with the pitching moment would result in a stall. Even without considering the moment balance, the artefact does not have good gliding characteristics, which also excludes its use as a hand glider. Additionally, simple hand throwing tests would have been possible to perform in ancient Egypt and, with an understanding of aerodynamics, would have quickly revealed opportunities for optimisation.

Subsequent research should primarily focus on possible application within a cultural or religious context. The vertical tail fin could also be an indication of its suitability as a weathervane.

#### REFERENCES

1. Messiha K. African Experimental Aeronautics: A 2,000-Year-old model glider. Blacks in Science - Ancient and Modern. Ivan Van Sertima. 1991;92-97.
2. Schwarze R. CFD-Modellierung - Grundlagen und Anwendungen bei. Berlin Heidelberg New York. Springer-Verlag. 2012.
3. Abbott IH. Theory of Wing Sections. New York. Dover Publ. 1959.
4. Raymer DP. Aircraft Design - A Conceptual Approach. Stanford. Stanford University. American Institute of Aeronautics und Astronautics. 1989.
5. Sachs X, Hafer G. Flugmechanik - Moderne Flugzeugentwurf und Steuerungskonzepte. Berlin Heidelberg New York. Springer-Verlag. 1993.
6. Hünecke K. Die Technik des modernen Verkehrsflugzeuges. Stuttgart. Motorbuch Verlag. 2017.

Michel Zierow:  <https://orcid.org/0000-0001-8724-972X>

Leon Lesemann:  <https://orcid.org/0000-0002-2119-3134>



This work is licensed under the Creative Commons BY-NC-ND 4.0 license.

## FORMATION OF INFORMATION BASE FOR CONTROLLING SETTLEMENT OF SOLID-PHASE ORE SLURRY PARTICLES IN A THICKENER

Vladimir MORKUN\*, Natalia MORKUN\*\*, Vitalii TRON\*  
 Oleksandra SERDIUK\*, Alona HAPONENKO\*\*\*, Iryna HAPONENKO\*\*\*

\*Faculty of Information Technologies, Department of Automation, Computer Science and Technology,  
 Kryvyi Rih National University, 11 Vitalii Matusevych St., Kryvyi Rih, 50027, Ukraine

\*\*Chair of Measurement and Control Systems, Bayreuth University, Universitätsstraße, 30, Bayreuth, Germany

\*\*\*Research Department, Kryvyi Rih National University, 11 Vitalii Matusevych St., Kryvyi Rih, 50027, Ukraine

[morkunv@knu.edu.ua](mailto:morkunv@knu.edu.ua), [nmorkun@knu.edu.ua](mailto:nmorkun@knu.edu.ua), [vtron@knu.edu.ua](mailto:vtron@knu.edu.ua)  
[serduik@knu.edu.ua](mailto:serduik@knu.edu.ua), [a.haponenko@protonmail.com](mailto:a.haponenko@protonmail.com), [haponenko@protonmail.com](mailto:haponenko@protonmail.com)

*received 18 May 2022, revised 25 February 2023, accepted 1 March 2023*

**Abstract:** Thickeners are process units that are often used at mining enterprises. There, they are involved in dehydration of mineral concentration products when water is removed from wet tailings containing metal concentrates. In mineral processing, large quantities of process water are used to separate different minerals from each other, so dehydration plays a major role in ore processing and preparation for concentration. This research aims to develop methods and tools of ultrasonic measurement of characteristics of settlement of solid-phase slurry particles and to assess their possible application to the automatic control system of the thickener to improve its efficiency.

**Key words:** thickener, ultrasonic, automatic control, modelling, parameter estimation

### 1. INTRODUCTION

The theory developed to date has provided the basis for designing, modelling and controlling industrial thickeners, where a product is a unit, an area, a concentration profile and the number of solids in the thickener [1–3].

However, mathematical models are useless if parameters of the corresponding equations cannot be determined experimentally. Knowledge of model parameters is necessary to form control and operation of mills, classifying units, flotation machines, magnetic separators (MS), equipment for separating solid and liquid phases, as well as the means of concentrate and tailings transportation. Synthesis of the thickener control is associated with certain problems due to their large time constants, non-linear characteristics, available disturbing influences and disturbances [4].

Quite a long period of slurry sampling for analysis in the existing control system for thickeners, as well as available disturbing influences due to changes in the flow rate, density and composition of the initial slurry do not enable maintaining slurry density in the discharge within technological regulations [5]. To overcome this drawback, the magnetic thickener control system is upgraded along the following lines:

- installation of a sensor on the slurry discharge to enable continuous measurement of density of the thickened slurry;
- development of an additional loop to control the density of the thickened slurry by changing its flow rate;
- development of a module for activating a magnetite level control loop or a slurry density stabilisation loop depending on the current technological situation.

The results of studying slurry dehydration with the solid phase composed mainly of superfine particles are presented in [6]. This approach does not consider formation of controlling actions directly during the process to increase the efficiency of thickening. In [7], to improve the design and efficiency of thickening, methods for calculating the fluid dynamics are used. The authors apply a balance model of the number of particles. The approach requires additional investigations to form an information support system for controlling operational data on the distribution of particles in the thickener and their physical–mechanical and chemical–mineralogical characteristics.

A method of measuring the ultrasound phase velocity and attenuation in slurries to evaluate their characteristics was considered in [8]. The results show that the phase velocity of ultrasonic waves increases with the number of fine particles in the slurry. Dispersion is due to the solid phase present and correlates with its mass fraction. The results of attenuation experiments show that it is possible to back-calculate the slurry properties by fitting the model to experimental data if size distribution of the solid-phase particles is known. It is concluded that it is difficult to determine the accuracy of these calculations and therefore more research in this area is needed.

When concentrating on flocculant solutions, the sand concentration varies significantly with and without displacement. In order to use the presented dependencies when controlling thickening and desliming, it is necessary to take into account the differences in characteristics of certain mineral and technological types of ore materials as well as contamination of ore particle surfaces [9]. Removal of high-dispersed impurities from process water by

means of flocculation of iron ore particles was studied in [10]. The main aspects of chemical influence on thickening and desliming are indicated.

When controlling thickeners, fluctuations in the process flow should be considered [11]. This is achieved by changing both the amount of flocculant and the pumping rate of the bottom product. However, variations in the ore type cause relevant changes in the required flocculant dosage. It is noted that with the PID control loop, the amount of flocculant can be adjusted via a feedback from either the layer level or the turbidity of the overflow. Care is taken to ensure that the location of the flocculant injection point provides good flocculant dispersion. In some cases, it may be necessary to add some flocculant at several points, thus improving its contact with the medium. The density of the bottom product of the thickener is a function of the ability of solids to settle as well as the residence time in the thickener. Systems designed to adjust density according to the results of measuring this parameter tend to cause cyclic instability. It is concluded that the strategy of controlling the stock by regulating the pumped bottom product to maintain a constant mass provides consistently high density of the bottom flow.

A control strategy based on measuring density and the flow rate of the feed product, density and the flow rate of the thickened product to maintain the amount of solid materials at the input, output and directly in the thickener by adjusting the pump performance was suggested in [12]. The following controlled variables are either corrected or limited: density of the thickened product, the drive torque and the level of solids stock in the thickener. This implements the following control logic. If the outflow is smaller than the inflow, the pump capacity will not increase until density is such that the upper torque limit or the maximum solids stock in the thickener is reached. If the outflow is greater than the inflow and the outflow density is lower than the required one, the pump capacity will be reduced provided the torque limit is in the safe operating range and the amount of solids is below the upper limit.

Conventional control of the thickener is based on single-loop auto-control systems with PI-controllers (control of the bottom product pumping, the density-dependent flow rate of the thickened product) [13]. However, practice shows that this control architecture is not optimal for controlling a process of slow and complex dynamics. Depending on the process flowchart used at a plant, different objectives can be set to optimise the thickener capacity: the target density of the bottom product is used to ensure optimal solids content in the tailings pond, the efficient drainage rate for the mill, and so on. The target slurry level is used to obtain optimal thickener loading without overloading the drive. The pressure at the thickener bottom is used as an indicator of the solids stock. This helps the system determine whether the high layer level is the result of a decrease in the settling rate or an increase in solids concentration. In some cases, the target torque is used as an indicator of acceptable rheology of the bottom flow.

While ensuring optimal control of solids percentage in the flow, keeping all relevant variables within acceptable limits is what many authors are striving for when forming a control strategy for thickeners [14–16].

However, in any control strategy, it is good to have as much information as possible about the values of the important variables. In the case of the thickener, several values can be measured, for example, torque of the rake drive, the layer level, pressure at the thickener bottom, in/outflow rates and percentage of solids in the flows. Additional measurements also allow for more effective control strategies [17].

This research is aimed at the formation of an information base for controlling the settlement of solid-phase ore slurry particles in a thickener by determination of such characteristics as dynamics of slurry density and particle size distribution of its solid phase at the initial stage of ground ore settlement in the thickener. This approach will allow to consider the nature of the size distribution of solid-phase particles of the ore material in the thickener, and determine the characteristics of the output product in the thickener in accordance with the parameters of ore particles settlement, which as a result will reduce the loss of the useful component in the iron ore concentrate.

## 2. PROPOSED METHODOLOGY

Process lines of concentration usually consist of several successive stages, each of which includes the following main operations: grinding, classification/sizing and magnetic separation. The operations are aimed at ore aggregate release and separation of particles of various minerals from each other by reducing the size of mineral grains to 0.1 mm or less.

Fig. 1 depicts a concentration flowchart at the ore concentration plant of the Northern Mining and Concentration Plant in Kryvyi Rih MS, hydrocyclone (H/c), thickener (T-r). Despite some differences in the operations and concentration units, the flowchart can be considered typical for most mining and concentration plants of Ukraine.

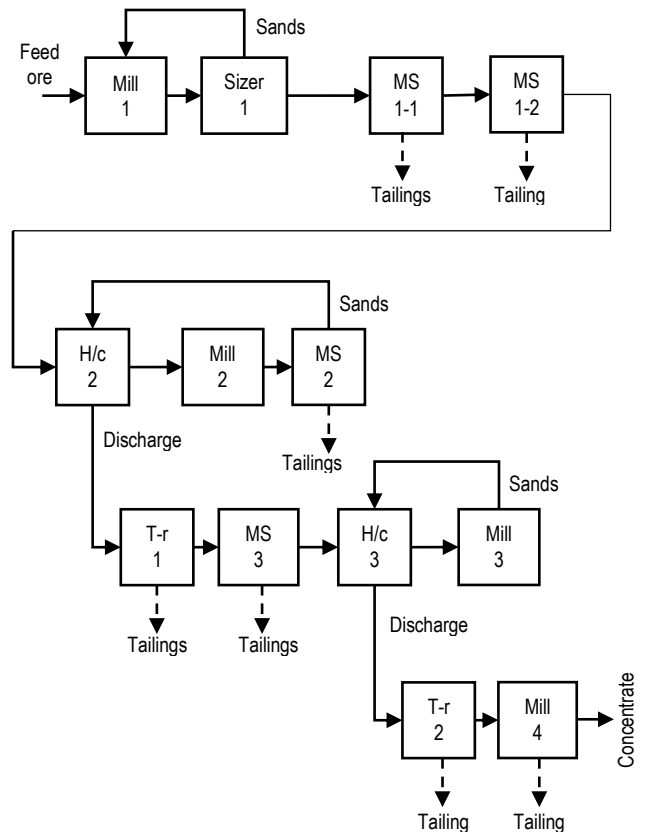


Fig. 1. Concentration flowchart at the ore concentration plant of the Northern GZK

To assess the quantity of mineral products, besides distribution of mineral particles  $\gamma$  ( $\xi$ ) by fractions with different physical properties  $\xi$ , the indicator of distribution of useful components  $\beta$  ( $\xi$ )

is generally used as well.  $\gamma(\xi)$  and  $\beta(\xi)$  allow to perform a quantitative evaluation of ore materials. Separation characteristics  $f \epsilon (\xi)$  are used to quantify the efficiency of process devices.

Surfaces of indicators of released ore sizes and the content of the useful component in them, which are distributed along the concentration line (control points 1...15 in Fig.1), are presented in Fig. 2 (a) and (b).

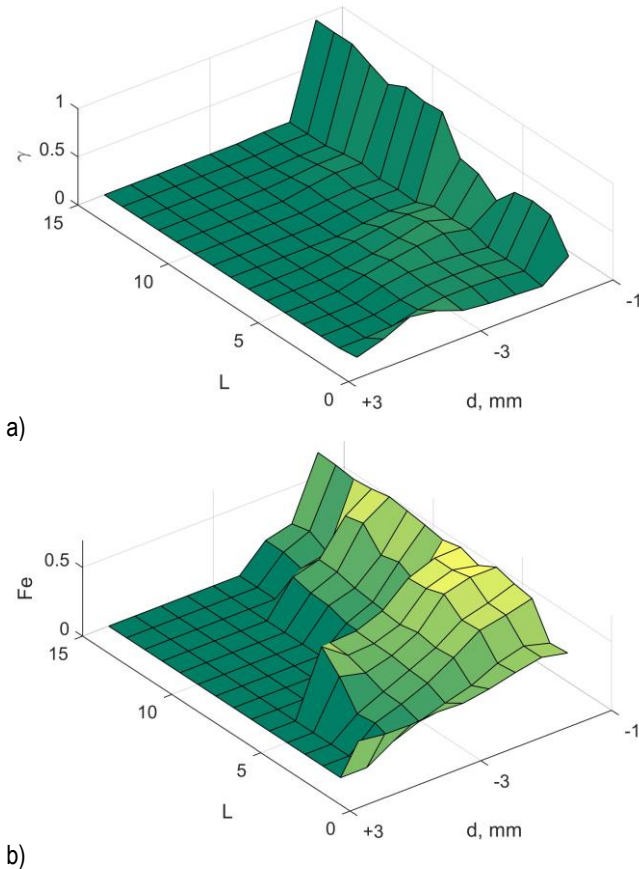


Fig. 2. Indicators distributed along the concentration line: (a) the yield of sizes of the solid-phase slurry; (b) the total Fe content in the intermediate product

The thickener is an integral part of the ore concentration line and the results of its operation directly affect qualitative and quantitative indices of products obtained.

In [1,17] it is shown that the automatic control system (ACS) of the thickener should enhance its efficiency, namely: stabilise thickening indicators, form concentration of the thickened product taking into account process requirements, reduce the flow rate of flocculant considering torque limitations and properties of the transported slurry. The control system performs continuous correction of process parameters on the basis of their promptly measured characteristics. The optimal operating conditions of the thickener are determined by steady-mode characteristics, and the ACS is used to stabilise its operation at the selected values of process variables.

In the thickening process, we can distinguish the following variables by output: concentration of the thickened product and the settlement level; adjustable variables: the volume flow rate of the thickened product and the flocculant flow rate; parameters: the function of solids density and effective solids pressure; and disturbances: granulometric composition, density of the feed product

and its flow rate. In practice, the following measurements are available: density of feed and thickened products, the settlement level, bottom pressure, torque, overflow turbidity, and pumping current of the thickened product.

Fig. 3 presents main processes associated with the thickener operation; i.e. flocculation, which results from adding flocculants to the slurry, and settlement of its solid phase [1].

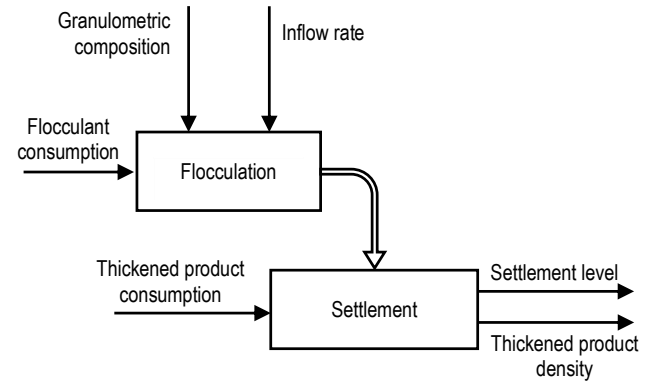


Fig. 3. Diagram and main variables of the thickening process

Various mathematical models of the thickening process of ore raw materials were suggested in [18–20]. For example, the internationally accepted phenomenological model describes slurry compaction in the thickener based on the degenerate parabolic differential equation of the second order [21–22]:

$$\frac{\partial \varphi}{\partial t} + \frac{\partial}{\partial z} (q\varphi + f_{bk}(\varphi)) = \frac{\partial}{\partial z} \left( \frac{f_{bk}(\varphi)\sigma'_c(\varphi)}{\Delta\rho\varphi g} \frac{\partial \varphi}{\partial z} \right) \quad (1)$$

where  $(z, t)$  are the vertical upward spatial coordinate and time,  $\varphi$  is the volume fraction of solids,  $q(t)$  is the volume flow rate (volume of the thickened product per unit area of thickeners),  $f_{bk}(\varphi) - \varphi v_s(\varphi)$  is Kinch solid flow density, where  $v_s(\varphi)$  is the initial rate of the concentrated product settling,  $\varphi, \sigma_c(\varphi)$  is effective pressure of solids representing compressibility of sediments,  $\Delta\rho = \rho_s - \rho_f$  is a difference in solid-liquid density and  $g$  is acceleration of gravity.

The above and other proposed models prove that availability of information on the actual behaviour of solid-phase particles of the slurry during its settlement allows for significant simplification of slurry control formation.

We propose a method of forming control over thickening based on assessing changes in slurry density and particle size distribution of its solid phase in the initial settlement stage in the thickener, which makes it possible to predict the characteristics of the thickened product and thereby counteract high inertia of the system. For this purpose, the characteristics of ultrasonic waves passing through the controlled volume of the slurry settling in the thickener are measured [8, 23–25].

Let us denote the intensity of the ultrasonic signal passing a fixed distance in the slurry as [26]

$$\xi = I_0 \exp \left\{ -\frac{1}{V} \sum_{i=1}^k \sigma(r_i) Z \right\} \quad (2)$$

where  $\sigma(r_i)$  is a cross section of ultrasound attenuation on particles of the radius  $r_i$ .



Dispersion of this value is determined by the expression

$$D_{\xi} = M(\xi - \langle \xi \rangle)^2 = M(\xi^2 - 2\xi \langle \xi \rangle + \langle \xi \rangle^2) = M\xi^2 - \langle \xi \rangle^2 \quad (3)$$

Considering that

$$\xi^2 = I_0 \exp \left\{ -\frac{2}{V} \sum_{i=1}^k \sigma(r_i) Z \right\} \quad (4)$$

we obtain

$$M\xi^2 = \sum_{k=0}^{\infty} M \left( \frac{\xi^2}{k} \right) F(k) \quad (5)$$

Mathematical expectation of the value for the fixed number of particles  $k$  of the ground material in the controlled volume makes:

$$M \left( \frac{\xi^2}{k} \right) = \left[ \int_0^{\infty} e^{\frac{2}{V} \sigma(r) Z} F(r) dr \right]^k = \eta_1^k \quad (6)$$

$$M(\xi^2) = \sum_{k=0}^{\infty} \frac{\eta_1^k \bar{N}^k e^{-\bar{N}}}{k!} = e^{-\bar{N}(1-\eta_1)} \quad (7)$$

$$M(\xi^2) = I_0^2 \exp \left\{ -nV \left( 1 - \int_0^{\infty} e^{-\frac{2}{V} \sigma(r) Z} F(r) dr \right) \right\} \quad (8)$$

The average value of the signal passing through the controlled volume of the slurry  $V$  is

$$\langle \xi \rangle = I_0 \exp \left\{ -nV \left( 1 - \int_0^{\infty} e^{-\frac{1}{V} \sigma(r) Z} F(r) dr \right) \right\} \quad (9)$$

We substitute the determined values into expression (3)

$$D_{\xi} = I_0^2 \exp \left\{ -nV \left( 1 - \int_0^{\infty} e^{-\frac{2}{V} \sigma(r) Z} F(r) dr \right) \right\} - I_0^2 \exp \left\{ 2nV \left[ 1 - \int_0^{\infty} e^{-\frac{1}{V} \sigma(r) Z} F(r) dr \right] \right\} \quad (10)$$

Let us represent summands of the obtained expression in the form of

$$\int_0^{\infty} F(r) e^{-\frac{2}{V} \sigma(r) Z} dZ \approx \int_0^{\infty} F(r) \left[ 1 - \frac{2}{V} \sigma(r) Z + \frac{4\sigma^2(r) Z^2}{2V^2} \right] dZ \quad (11)$$

$$\int_0^{\infty} F(r) dr \cdot e^{-\frac{1}{V} \sigma(r) Z} = 1 - \frac{Z}{V} \int_0^{\infty} \sigma(r) F(r) dr + \frac{Z^2}{2V^2} \int_0^{\infty} F(r) \sigma^2(r) dr \quad (12)$$

Dispersion of the signal passing through a layer of the slurry of thickness  $Z$  is determined from the expression

$$D_{\xi} = I_0^2 \exp \left\{ -nV \left( 1 - 1 + \frac{2Z}{V} \int_0^{\infty} \sigma(r) F(r) dr - \frac{2Z^2}{V^2} \int_0^{\infty} \sigma^2(r) F(r) dr \right) \right\} - I_0^2 \exp \left\{ -2nV \left( 1 - 1 + \frac{Z}{V} \int_0^{\infty} \sigma(r) F(r) dr - \frac{Z^2}{2V^2} \int_0^{\infty} \sigma^2(r) F(r) dr \right) \right\} = I_0^2 \exp \left\{ 2nZ \int_0^{\infty} \sigma(r) F(r) dr \right\} \times \left[ \exp \frac{2nZ^2}{V} \int_0^{\infty} \sigma^2(r) F(r) dr - \exp \frac{nZ^2}{V} \int_0^{\infty} \sigma^2(r) F(r) dr \right] \quad (13)$$

Let us introduce the designation

$$\psi = \exp \left\{ \frac{nZ^2}{V} \int_0^{\infty} \sigma^2(r) F(r) dr \right\} \quad (14)$$

Then

$$D_{\xi} = I_0^2 \exp \left\{ 2nZ \int_0^{\infty} \sigma(r) F(r) dr \right\} [\psi^2 - \psi] \quad (15)$$

In (9), we decompose the integrand into a series. Leaving three terms of this series, we obtain

$$\langle \xi \rangle = I_0 \exp \left\{ -nV \left( 1 - 1 + \frac{Z}{V} \int_0^{\infty} \sigma(r) F(r) dr - \frac{1}{2} \frac{Z^2}{V^2} \int_0^{\infty} \sigma^2(r) F(r) dr \right) \right\} = I_0 \exp \left\{ -nZ \int_0^{\infty} \sigma(r) F(r) dr \right\} \sqrt{\psi} \quad (16)$$

Let us determine the relative value

$$\frac{\sqrt{D_{\xi}}}{\langle \xi \rangle} = \frac{I_0 \exp \left\{ -nZ \int_0^{\infty} \sigma(r) F(r) dr \right\} \sqrt{\psi^2 - \psi}}{I_0 \exp \left\{ -nZ \int_0^{\infty} \sigma(r) F(r) dr \right\} \sqrt{\psi}} = \sqrt{\psi - 1} \quad (17)$$

We present (14) as

$$\psi = \exp \left\{ \frac{WZ^2}{V} \cdot \frac{\int_0^{\infty} \sigma^2(r) F(r) dr}{\int_0^{\infty} \frac{4}{3\pi r^3} F(r) dr} \right\} \quad (18)$$

We determine the logarithm of this value as

$$\log \psi = \frac{WZ^2}{V} \cdot \frac{\int_0^{\infty} \sigma^2(r) F(r) dr}{\int_0^{\infty} \frac{4}{3\pi r^3} F(r) dr} \quad (19)$$

We introduce the designation

$$\frac{\sqrt{D_{\xi}}}{\langle \xi \rangle} = \sqrt{\psi - 1} = a \quad (20)$$

Then  $\psi = 1 + a^2$

Considering that  $\sqrt{\psi} \approx 1$ , we obtain

$$\langle \xi \rangle = I_0 \exp \left\{ \frac{-ZW \int_0^{\infty} \sigma(r) F(r) dr}{\int_0^{\infty} \frac{4}{3\pi r^3} F(r) dr} \right\} \quad (21)$$

and thus

$$\ln \frac{I_0}{\langle \xi \rangle} = ZW \frac{\int_0^{\infty} \sigma(r) F(r) dr}{\int_0^{\infty} \frac{4}{3\pi r^3} F(r) dr} \quad (22)$$

We determine the characteristic function

$$S' = \frac{\ln \psi}{\ln I_0 / \langle \xi \rangle} = \frac{Z \int_0^{\infty} \sigma^2(r) F(r) dr}{V \int_0^{\infty} \sigma(r) F(r) dr} \quad (23)$$

The last expression reveals that the value  $S'$  is a function of the solid particle size in the slurry. Thus, by measuring the parameters  $I_0$ ,  $\langle \xi \rangle$ ,  $D_{\xi}$  and calculating the parameter  $S'$ , we can assess particle size distribution of the slurry settled in the thickener.

### 3. RESULTS

The amplitude–frequency characteristic of the signal reflected from the ultrasonic oscillation reflector in the slurry depends on the distribution of solid-phase particles of the ore slurry during their free settlement, whose parameters are determined by both the particle size and slurry density [27, 28].

The proposed ACS of thickener 1 (Fig. 4) contains waveguide 2 with piezoelectric transducer 3 mounted. Driving oscillator 4 on command from computing-control unit 5 generates a trigger pulse of normalised amplitude and duration, which through the OR logic circuit 6 goes to the input of controlled electromagnetic sinusoidal oscillator 7 switched on for the duration of the pulse. A train of ultrasonic oscillations is formed by piezoelectric transducer 3 and through waveguide 2 is radiated in the direction of ultrasonic wave reflector 8 in the tank of thickener 1. The reflected ultrasonic oscillations via waveguide 2, piezoelectric transducer 3 and selection unit 9 arrive at the receiving amplifier 10. Thus, at the output of receiving amplifier 10, the signal coming from ultrasonic wave reflector 8, the amplitude–frequency characteristic of which is

determined in analyzer 11, is formed. In computing-control unit 5 the value  $S$  characterising granulometric composition of the medium under study is calculated.

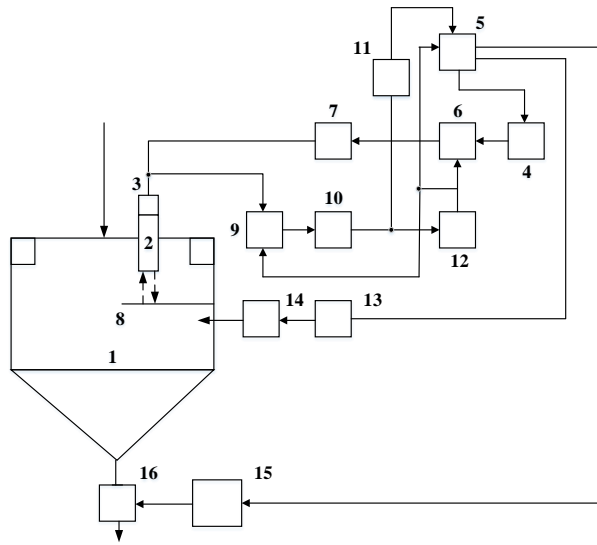


Fig. 4. Ultrasound-based ACS of the thickener. ACS, automatic control system

Pulse former 12 receiving a signal from receiving amplifier 10 through OR logic circuit 6 again starts controlled electromagnetic sinusoidal oscillation generator 7. The frequency of the formed pulses  $f$  is a function of the distance to ultrasonic wave reflector 12 of and the velocity of ultrasonic wave propagation in the studied medium:

$$f = v / 2d \tag{24}$$

where  $v$  is the velocity of ultrasonic wave propagation and  $d$  is the distance from waveguide 2 to ultrasonic wave reflector 12 in thickener tank 1.

In liquid media, ultrasound propagates as volume rarefaction-compression waves and the process is adiabatic, that is, the temperature in the sound wave has no time to equalise [29]. The adiabatic sound velocity is determined by the pressure transmission velocity:

$$C = \sqrt{\left(\frac{dP}{d\rho}\right)_s} \tag{25}$$

where  $P$  is pressure in the material,  $\rho$  is density of the material and  $s$  indicates that the derivative is taken at constant entropy.

The ultrasound velocity can be expressed in the following form:

$$C = \sqrt{\frac{K_{\alpha\partial}}{\rho}} = \sqrt{\frac{1}{\beta_{\alpha\partial}}} = \sqrt{\frac{\gamma}{\beta_{us}\cdot\rho}} \tag{26}$$

where  $K_{\alpha\partial}$  is an adiabatic comprehensive compression module;  $\beta_{\alpha\partial} = \frac{1}{K_{\alpha\partial}} = \frac{1}{\rho} \left(\frac{\partial\rho}{\partial P}\right)_s$  is adiabatic compression;  $\beta_{us} = \gamma \cdot \beta_{\alpha\partial}$  is isothermal compressibility; and  $\gamma = \frac{C_p}{C_v}$  is a ratio of heat capacities at constant pressure and volume.

Thus, given the invariability of distance  $d$  from waveguide 2 to ultrasonic wave reflector 12 in thickener tank 1, the frequency  $f$  is determined by the ultrasound propagation velocity, which, in turn, depends on the density of the controlled medium  $\rho$ .

To increase noise immunity of the measurement results, the frequency of pulses generated by driving oscillator 8 is selected by an order of magnitude less than the repetition rate of circulating pulses. Therefore, without a reflected signal, for example, in case of a foreign object in the control plane, after some time driving oscillator 8 again starts controlled electromagnetic sinusoidal oscillations generator 11 and the system resumes its operation.

Taking into account the applied approach and the formed information base, the control algorithm for the thickener can be formulated as an optimisation problem [15, 30–32]:

$$\min = \int_{t_k}^{t_k+\Delta k} (W_x(\tilde{x}(t) - x_{SS})^2 + W_u(u(t) - u_{SS})^2) dt \tag{27}$$

where the state equation looks like

$$\tilde{x}(t) = f(\tilde{x}(t)) + g(x(t))u(t) \tag{28}$$

where  $\tilde{x}$  is the forecast value of  $x$ ;  $k$  is the time horizon;  $W_x, W_u$  - bara is weight.

The  $u$ -function minimising the optimisation problem should be in the set of piecewise continuous functions (with the sampling time which is the time difference between two steps  $t_k$  and  $t_{k+1}$ ) [33]. The steady-state input  $u_{SS}$  corresponds to the steady-state  $x_{SS}$ . In the context of the thickener model, it is clear from the above equation that the state vector  $x$  coincides with the vector  $\phi$  in the model [34, 35].

Computing-control unit 9 based on the calculated value  $f$  through actuator 13 and operating member 14 regulates the flow rate of thickened products in thickener 1 to stabilise their density.

The calculated values of  $S'$  are used to control the rate of solid-phase particles settlement by controlling the amount of flocculant by means of actuator 15 and regulator 16. Fig. 5 shows the calculated dependence of the parameter  $S'$  on the content of the 74  $\mu\text{m}$  class in the solid phase of the slurry settling in the thickener.

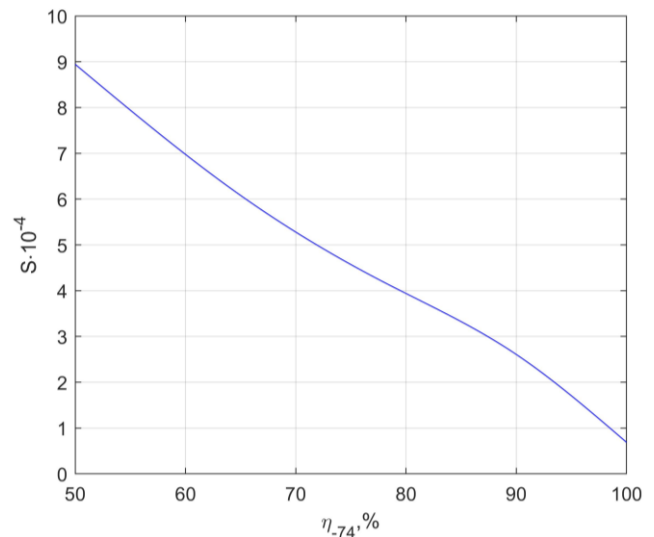


Fig. 5. Granulometric composition of the medium on the content of the 74  $\mu\text{m}$  class in the solid phase

The specified parameters allow maintaining the efficiency of the thickening process in accordance with the characteristics of the ore slurry without losing the useful component. Due to obtaining operational information about the characteristics of the settlement of the solid phase particles of the ore slurry already at its

initial stage, it is possible to reduce the duration of transient processes in the ACS.

According to the results of industrial tests of the ACS for the thickener control on the basis of ultrasonic control devices, it is found that the use of this system within the iron ore concentration ACS at mining enterprises of Kryvyi Rih iron ore basis will reduce the loss of  $Fe_{mag}$  by 0.6%–0.7%.

#### 4. CONCLUSIONS

Determination of such characteristics as dynamics of slurry density and particle size distribution of its solid phase at the initial stage of ground ore settlement in the thickener allows us to take into account fluctuations in the parameters of the process flow. This is achieved by controlling both the amount of flocculants and the pumping rate of the bottom product.

The ACS based on the obtained information and modern software and hardware tools makes it possible to overcome slow dynamics of the response to control actions and cross-impacts of controlled variables. To achieve optimal efficiency of the thickening processes, their ACS should be formed as modules of the hierarchical control structure of the entire technological process of ore concentration.

The proposed approach allows us to consider the nature of size distribution of solid-phase particles of the ore material in the thickener, and determine the characteristics of the output product in the thickener in accordance with the parameters of ore particles settlement, thus reducing the loss of the useful component by 0.6%–0.7%.

#### REFERENCES

- Segovia J.P., Concha F., Sbarbaro D. On the control of sludge level and underflow concentration in industrial thickeners. Preprints of the 18th IFAC World Congress Milano (Italy) August 28 - September 2. 2011: 8571-8576
- Jiao H., Chen W., Wu A., Yu Y., Ruan Z., Honaker R., Chen X., Yu J. Flocculated unclassified tailings settling efficiency improvement by particle collision optimization in the feedwell. *Int. J. Miner. Metall. Mater.* 2021; 29: 2126–2135. <https://doi.org/10.1007/s12613-021-2402-3>.
- Jiao H., Wu Y., Wang H., Chen X., Li Z., Wang Y., Zhang B., Liu J. Micro-scale mechanism of sealed water seepage and thickening from tailings bed in rake shearing thickener. *Minerals Engineering*. 2021; 173:107043. <https://doi.org/10.1016/j.mineng.2021.107043>.
- Betancourt F., Urger R., Diehl S., Faras S. A model of clarifier-thickener control with time-dependent feed properties. Presented at Physical Separation '13, Falmouth, UK, June 20 and 21, 2013: 1-21
- Krivososov V.A., Kozyr O.F. Control system for a magnetic thickening in the technological process of iron ore enrichment. *Scientific and practical electronic journal Alley of Science*. 2018; 4(20): 125-129.
- Tripathy S.K., Murthy Y.R., Farokhpay S., Filippov L.O. Design and analysis of dewatering circuits for a chromite processing plant tailing slurry. *Mineral Processing and Extractive Metallurgy Review*. 2021;42(2):102-114. <https://doi.org/10.1080/08827508.2019.1700983>.
- Fawell P.D., Nguyen T.V., Solnordal C.B., Stephens D.W. Enhancing gravity thickener feedwell design and operation for optimal flocculation through the application of computational fluid dynamics. *Mineral Processing and Extractive Metallurgy Review*. 2021;42(7):496-510. <https://doi.org/10.1080/08827508.2019.1678156>.
- Aitomaki Y. Towards a measurement of paper pulp quality: ultrasonic spectroscopy of fibre suspensions [licentiate thesis] Lulea(Sweden): Lulea University of Technology; 2006
- Chen X., Jin X., Jiao H., Yang Y., Liu J. Pore connectivity and dewatering mechanism of tailings bed in raking deep-cone thickener process. *Minerals*. 2020;10:375. <https://doi.org/10.3390/min10040375>
- Liang G., Zhao Q., Liu B., Du Z., Xia X. Treatment and reuse of process water with high suspended solids in low-grade iron ore dressing. *Journal of Cleaner Production*. 2021;278:123493. <https://doi.org/10.1016/j.jclepro.2020.123493>
- Advanced thickener control [Internet] [place unknown]: Metso Outotec; 2017 Jun 13; cited 2022 May 18. Available from: <https://www.mogroup.com/insights/blog/mining-and-metals/advanced-thickener-control/> Jun 14, 2017
- Michaud L.D. Thickener Process Control Strategy [Internet] [place unknown]: 911 Metallurgist; 2017 Oct 1. cited 2022 May 18. Available from: <https://www.911metallurgist.com/blog/thickener-process-control-strategy>
- Control strategies for thickeners [Internet] [place unknown]: Rhosonics; 2021 Mar 11; cited 2022 May 18. Available from: <https://rhosonics.com/news/control-strategies-for-thickeners>
- Xu N., Wang X., Zhou J., Wang Q., Fang W., Peng X. An intelligent control strategy for thickening process. *International Journal of Mineral Processing*. 2015;142:56-62. <https://doi.org/10.1016/j.minpro.2015.01.007>
- Zhang J., Yin X., Liu J. Economic MPC of deep cone thickeners in coal benedication. *The Canadian Journal of Chemical Engineering*. 2016;94(3):498-505. <https://doi.org/10.1002/cjce.22419>
- Tan C.K., Setiawan R., Bao J., Bickert G. Studies on parameter estimation and model predictive control of paste thickeners. *Journal of Process control*. 2015;28:1-8. <https://doi.org/10.1016/j.jprocont.2015.02.002>
- Basics in Minerals Processing Handbook [Internet] [place unknown]: Metso Outotec; cited 2022 May 18. Available from: <https://www.mogroup.com/insights/e-books/basics-in-minerals-processing-handbook/>
- Teerikoski S. Optimal control of clarifier-thickeners [Independent thesis Advanced level (professional degree)]. Uppsala(Sweden): Uppsala University; 2017
- Chai T., Li H., Wang H., An intelligent switching control for the intervals of concentration and flow-rate of underflow slurry in a mixed separation thickener. *IFAC Proceedings Volumes*. 2014;47:338-345. <https://doi.org/10.3182/20140824-6-ZA-1003.02114>
- Golik V., Komashchenko V., Morkun V., Zaalishvili V.. Enhancement of lost ore production efficiency by usage of canopies. *Metallurgical and Mining Industry*. 2015;7(4):325-329
- Burger R., Diehl S., Faras S., Nopens I., Torfs E. A consistent modelling methodology for secondary settling tanks: a reliable numerical method. *Water Science & Technology*. 2013;68(1):192-208. <https://doi.org/10.2166/wst.2013.239>
- Barth A., Burger R., Kroker I., Rohde C. Computational uncertainty quantification for a clarifier-thickener model with several random perturbations: A hybrid stochastic Galerkin approach. *Computers & Chemical Engineering*. 2016;89:11-26. <http://dx.doi.org/10.1016/j.compchemeng.2016.02.016>.
- Morkun V., Morkun N., Pikilnyak A. Iron ore flotation process control and optimization using high-energy ultrasound. *Metallurgical and Mining Industry*. 2014;6(2):36–42
- Morkun V., Morkun N., Pikilnyak A.. The gas bubble size distribution control formation in the flotation process. *Metallurgical and Mining Industry*. 2014;6(4):42–45
- Morkun V., Morkun N., Pikilnyak A. Simulation of high-energy ultrasound propagation in heterogeneous medium using k-space method. *Metallurgical and Mining Industry*. 2014;6(3):23–27
- Morkun V., Morkun N. Estimation of the crushed ore particles density in the pulp flow based on the dynamic effects of high-energy ultrasound. *Archives of Acoustics*. 2018;43(1):61–67. <http://dx.doi.org/10.24425/118080>

27. Kilic O. Application of ultrasonic velocity measurement and thermal analysis for the determination of the limestone quality. *Physicochemical Problems of Mineral Processing*. 2014;50(2):525-534. <http://dx.doi.org/10.5277/ppmp140209>
28. Morkun V., Morkun N., Tron V., Hryshchenko S., Serdiuk O., Dotsenko I. Basic regularities of assessing ore pulp parameters in gravity settling of solid phase particles based on ultrasonic measurements. *Archives of Acoustics*. 2019;44(1):161-167. <http://dx.doi.org/10.24425/aaa.2019.126362>
29. Kapranov B.I., Kalinichenko A.N. Determination of the speed of sound propagation in metallic and non-metallic materials [lecture notes], Tomsk(RU), National Research Tomsk Polytechnical University; 2018
30. Morkun V., Tron V. Automation of iron ore raw materials beneficiation with the operational recognition of its varieties in process streams. *Metallurgical and Mining Industry*. 2014;6(6):4-7
31. Morkun V., Morkun N., Tron V. Model synthesis of nonlinear nonstationary dynamical systems in concentrating production using Volterra kernel transformation. *Metallurgical and Mining Industry*. 2015;7(10):6–9
32. Morkun V., Morkun N., Tron V. Identification of control systems for ore-processing industry aggregates based on nonparametric kernel estimators. *Metallurgical and Mining Industry*. 2015;7(1):14–17
33. Burger R., Diehl S., Faras S., Nopens I. On reliable and unreliable numerical methods for the simulation of secondary settling tanks in wastewater treatment. *Computers and Chemical Engineering*. 2012;41:93-105. <https://doi.org/10.1016/j.compchemeng.2012.02.016>
34. Betancourt F., Burger R., Diehl S., Faras S., Modeling and controlling clarifier-thickeners fed by suspensions with time-dependent properties. *Minerals Engineering*. 2014;62:91-101. <https://doi.org/10.1016/j.mineng.2013.12.011>
35. Bergh L., Ojeda P., Torres L. Expert Control Tuning of an Industrial Thickener. *IFAc-PapersOnLine*. 2015;48(17):86-91. <https://doi.org/10.1016/j.ifacol.2015.10.083>

Funded by the Alexander von Humboldt Foundation.

Vladimir Morkun:  <https://orcid.org/0000-0003-1506-9759>

Natalia Morkun:  <https://orcid.org/0000-0002-1261-1170>

Vitalii Tron:  <https://orcid.org/0000-0002-6149-5794>

Oleksandra Serdiuk:  <https://orcid.org/0000-0003-1244-7689>

Alona Haponenko:  <https://orcid.org/0000-0003-1128-5163>

Iryna Haponenko:  <https://orcid.org/0000-0002-0339-4581>



This work is licensed under the Creative Commons BY-NC-ND 4.0 license.



## APPROXIMATE SOLUTION OF PAINLEVÉ EQUATION I BY NATURAL DECOMPOSITION METHOD AND LAPLACE DECOMPOSITION METHOD

Muhammad AMIR<sup>\*✉</sup>, Jamil Abbas HAIDER<sup>\*✉</sup>, Shahbaz AHMAD<sup>\*✉</sup>, Sana GUL<sup>\*✉</sup>, Asifa ASHRAF<sup>\*\*✉</sup>

<sup>\*</sup>Abdus Salam School of Mathematical Sciences, Government College University, Lahore 54600, Pakistan

<sup>\*\*</sup>Department of Mathematics, University of Management and Technology Lahore, Pakistan

[muhammadamir28295@gmail.com](mailto:muhammadamir28295@gmail.com), [jamilabbashaider@gmail.com](mailto:jamilabbashaider@gmail.com), [shahbazahmad@sms.edu.pk](mailto:shahbazahmad@sms.edu.pk)  
[sana\\_qul\\_22@sms.edu.pk](mailto:sana_qul_22@sms.edu.pk), [asifaashraf9@gmail.com](mailto:asifaashraf9@gmail.com),

*received 8 December 2022, revised 19 March 2023, accepted 19 March 2023*

**Abstract:** The Painlevé equations and their solutions occur in some areas of theoretical physics, pure and applied mathematics. This paper applies natural decomposition method (NDM) and Laplace decomposition method (LDM) to solve the second-order Painlevé equation. These methods are based on the Adomain polynomial to find the non-linear term in the differential equation. The approximate solution of Painlevé equations is determined in the series form, and recursive relation is used to calculate the remaining components. The results are compared with the existing numerical solutions in the literature to demonstrate the efficiency and validity of the proposed methods. Using these methods, we can properly handle a class of non-linear partial differential equations (NLPDEs) simply.

**Novelty:** One of the key novelties of the Painlevé equations is their remarkable property of having only movable singularities, which means that their solutions do not have any singularities that are fixed in position. This property makes the Painlevé equations particularly useful in the study of non-linear systems, as it allows for the construction of exact solutions in certain cases. Another important feature of the Painlevé equations is their appearance in diverse fields such as statistical mechanics, random matrix theory and soliton theory. This has led to a wide range of applications, including the study of random processes, the dynamics of fluids and the behaviour of non-linear waves.

**Keywords:** natural decomposition method, Laplace decomposition method, series solution, Adomain polynomial, Painlevé equation

### 1. INTRODUCTION

The special functions are vital in studying linear differential equations (LDEs) and are significant in mathematical physics. These functions include the Bessel, Whittaker, parabolic cylindrical, Airy and hypergeometric functions. A few of them have the same names as those functions because they are solutions to LDEs with rational coefficients. The Bessel functions are solutions of the Bessel equation, the second-order LODEs with single irregular singularity, and are utilised to explain the motion of planets and artificial satellites by employing the Kepler equation. The Painlevé equations were first discovered by Paul Painlevé and Gambier more than 100 years ago [1]. Painlevé investigated many second-order equations and categorised the singularities form. Painlevé [2] and some of his collaborators derived the Painlevé equations while investigating the non-linear partial differential equations (NLPDEs).

Consider the second-order non-linear equation of the form:

$$\left(\frac{d^2y}{dt^2}\right) = R\left(t, v, \frac{dv}{dt}\right),$$

where  $R\left(t, v, \frac{dv}{dt}\right)$  is rational in  $v$  and  $v'$  and function is analytic in  $t$ .

The only movable singularity in these differential equations is a pole known as the Painlevé property. This significant property is expressed for all linear equations, but non-linear equations rarely have it. Painlevé and Gambier focused on the arrangement of the

singularity structure with the polynomial coefficient of the second-order differential equation. They established that subject to a certain transformation; any such equations can be transformed into one of the 50 canonical forms, which is a significant achievement. The question arose: Which of the following equations are irreducible and need to specify new transcendental functions? Painlevé described that 44 of these 50 equations are reducible, except only these six equations that require a new function for their solution, which are named Painlevé equations. Moreover, some experts believe that Painlevé functions will arise as a unique member of the special function in the 21st century. Many mathematicians have used Painlevé equations to explain the growing nature of the systems since their discovery. Painlevé equations play a vital role in many physical problems such as the asymptotic behaviour of the non-linear equation [3], superconductivity [4], negative curvature surfaces [5], Bose–Einstein condensation, Stokes phenomena [6], hyperasymptotics solution [7] and non-linear optics [8]. Furthermore, some NLPDEs, including the Boussinesq and Korteweg–de Vries (Kdv) equations, may be expressed in terms of the Painlevé transcendent [9, 10].

These six equations have a wide range of remarkable characteristics and applications. The Painlevé equations were initially discovered from primarily mathematical considerations, but more recently, they have been used in several significant physical applications, such as statistical mechanics, plasma physics, non-linear waves, quantum gravity, quantum field theory, general relativity, non-linear optics and fibre optics [11]. The Painlevé equations have also attracted significant interest because they are

reductions of the soliton equations that can be solved by inverse scattering [12] transform, such as the Kdv, the modified Kortewegde Vries equation (MKdv), the cylindrical Kortewegde Vries equation, the equations of the Boussinesq and Kadomtsev–Petviashvili type, the non-linear Schrodinger equation and the sine-Gordon equation. Connections are briefly described in [13–15]. Moreover, the Painlevé equations can be represented as equations of isomonodromic deformations of auxiliary linear systems of differential equations [16].

In recent years, a wide range of numerical methods has been developed to solve the second-order Painlevé differential equation, such as homotopy perturbation method (HPM) [17], sinc-collocation method [18], optimisation method [19], variational iteration algorithm-I [20] and quasilinearisation method (QM) [21].

In this paper, the solution of the second-order Painlevé equation is obtained by two techniques Laplace decomposition method (LDM) and the natural decomposition method (NDM). Laplace transformation is the famous integral transform available to every researcher and can be used to solve linear ordinary, partial and integral equations in the time domain. Khan and his co-researcher [22] derived a new integral transform called N-transform; in 2012, it was renamed the natural transform [23]. The natural transform resembles Laplace [24] and Sumudu transforms [25]. Natural decomposition is used to solve a large number of the NLPDEs such as the sine-Gordon equation [26], time-fractional coupled KdV equation [27], gas dynamics equation [28] and inviscid burger equation [29].

There are several avenues of future work on the Painlevé I equation that could lead to new insights into its behaviour and applications in physics and mathematics.

One area of research is the study of its solutions and their properties. While the Painlevé I equation is known to have special types of solutions, such as the Painlevé transcendents, there is still much to be understood about their behaviour and how they can be used to describe physical systems. In particular, the study of the Painlevé I equation in the context of complex analysis and differential geometry could lead to new insights into its solutions and their properties.

Another area of research is the connection between the Painlevé I equation and other mathematical and physical systems. For example, recent work has shown that the Painlevé I equation arises in the study of the stability of certain non-linear waves in fluids. Investigating these connections could lead to new applications of the Painlevé I equation in other areas of physics and engineering. Finally, there is ongoing work on the numerical and computational aspects of the Painlevé I equation. While exact solutions can be constructed using certain methods, it is often necessary to use numerical techniques to study the behaviour of the equation in more complex settings. Developing efficient and accurate numerical methods for the Painlevé I equation could help to expand its use in a wide range of applications in physics and engineering. Overall, future work on the Painlevé I equation is likely to involve a combination of theoretical and computational approaches, with the goal of understanding its behaviour and applications in a wide range of contexts.

The paper is structured as follows. In Section 2, methodologies and its implementations of proposed techniques are briefly discussed. In Section 3, we apply NDM and LDM to the Painlevé equation to show the efficiency and accuracy of our methods. In Section 4, the important results related to the Painlevé equations are explained briefly. Section 5 ends this paper with the conclusions.

## 2. METHODOLOGY

In this section, we will discuss the methodologies of two proposed methods and also discuss how these methods handle the NLPDEs.

### 2.1. LDM

The general form of the NLPDE is given as follows with conditions:

$$Lv(x, t) + Rv(x, t) + Nv(x, t) = f(x, t) \tag{2.1.1}$$

(with initial conditions:

$$v(x, 0) = g(x) , \quad v_t(x, 0) = h(x),$$

(where L denotes the linear differential operator of the second order:

$$L = \frac{\partial^2}{\partial t^2}, \tag{2.1.2}$$

where R represents the remaining less order linear operator, Nv is the non-linear operator and f(x, t) is the non-homogeneous term.

Applying Laplace transformation of Eq. (2.1.1) with initial conditions:

$$\mathcal{L}[Lv(x, t)] + \mathcal{L}[Rv(x, t)] + \mathcal{L}[Nv(x, t)] = \mathcal{L}[f(x, t)] \tag{2.1.3}$$

Using the differentiation property of the Laplace transform, we have

$$\mathcal{L}[Lv(x, t)] = \frac{1}{s}g(x) + \frac{1}{s^2}h(x) - \frac{1}{s^2}\mathcal{L}[Rv(x, t) + Nv(x, t)]. \tag{2.1.4}$$

In the next step, the solution of Laplace transform in the form of infinite series is given as follows:

$$v(x, t) = \sum_{n=0}^{\infty} v_n(x, t). \tag{2.1.5}$$

So that the non-linear operator is decomposed as

$$Nv(x, t) = \sum_{n=0}^{\infty} A_n, \tag{2.1.6}$$

where  $A_n$  denotes the Adomain polynomials of the terms  $v_0, v_1, v_2, \dots, v_n$  and can be calculated using this formula:

Substituting Eqs (2.1.5) and (2.1.6) into Eq. (2.1.4), we will get

$$A_n = \frac{1}{n!} \frac{d^n}{dx^n} \left[ N \left( \sum_{i=0}^{\infty} \lambda^i v_i(x, t) \right) \right], \quad n = 0, 1, 2, \dots \tag{2.1.7}$$

$$\mathcal{L} \left[ \sum_{n=0}^{\infty} v_n(x, t) \right] = \frac{g(x)}{s} + \frac{h(x)}{s^2} + \frac{1}{s^2} \mathcal{L}[f(x, t)] - \frac{1}{s^2} \mathcal{L}[Rv(x, t)] \tag{2.1.8}$$

Using the linearity property to the Laplace transform,

$$\sum_{n=0}^{\infty} \mathcal{L}[v_n(x, t)] = \frac{g(x)}{s} + \frac{h(x)}{s^2} + \frac{1}{s^2} \mathcal{L}[f(x, t)]$$

$$-\frac{1}{s^2} \mathcal{L}[Rv(x, t)] - \frac{1}{s^2} [\sum_{n=0}^{\infty} \mathcal{L}[A_n]] \tag{2.1.9}$$

Now, comparing Eq. (2.1.9) on both sides, we have

$$\mathcal{L}[v_0(x, t)] = \frac{g(x)}{s} + \frac{h(x)}{s^2} + \frac{1}{s^2} \mathcal{L}[f(x, t)] = H(x, s), \tag{2.1.10}$$

$$\mathcal{L}[v_1(x, t)] = -\frac{1}{s^2} \mathcal{L}[Rv_0(x, t)] + A_0, \tag{2.1.11}$$

$$\mathcal{L}[v_2(x, t)] = -\frac{1}{s^2} \mathcal{L}[Rv_1(x, t)] + A_1. \tag{2.1.12}$$

In general, we have

$$\mathcal{L}[v_{n+1}(x, t)] = -\frac{1}{s^2} \mathcal{L}[Rv_n(x, t)] + A_n \tag{2.1.13}$$

Applying the inverse Laplace transform to Eqs (2.1.10) – (2.1.13), the required recurrence relation is given as follows:

$$v_0(x, t) = H(x, t),$$

$$v_{n+1}(x, t) = -\mathcal{L}^{-1} \left[ \frac{1}{s^2} \mathcal{L}[Rv_n(x, t)] + A_n \right], \quad n \geq 0.$$

$H(x, t)$  Specifies specifies the initial conditions for the term occurring from the source term.

By taking the Laplace transform of Eq. (2.1.13) and applying the Laplace inverse transform, we obtain the remaining terms of  $v_0, v_1, v_2 \dots \dots v_n$  recursively.

## 2.2. Analysis of the NDM

The general form of the NDM is given below as follows:

$$Lv(x, t) + Mv(x, t) + Nv(x, t) = h(x, t), \tag{2.2.1}$$

with initial conditions:

$$v(x, 0) = f(x), \quad v_t(x, 0) = g(x). \tag{2.2.2}$$

Suppose  $L$  is the differential operator of the second order:

$$L = \frac{\partial^2}{\partial t^2}.$$

$M$  is the less order remainder operator,  $Nv$  denotes the non-linear operator and  $h(x, t)$  represents the source term.

Now, taking the N-transform of Eq. (2.2.1) on both sides,

$$N^+[Lv(x, t)] + N^+[Mv(x, t)] + N^+[Nv(x, t)] = N^+[f(x, t)]. \tag{2.2.3}$$

Using the N-transform properties, we have

$$\frac{s^2}{v^2} R(s, v) - \frac{s}{v^2} v(x, 0) - \frac{1}{v} v'(x, 0) + N^+[Mv(x, t)] + N^+[Nv(x, t)] = N^+[f(x, t)]. \tag{2.2.4}$$

Substitute Eq.(2.2.2) into Eq.(2.2.4), we obtain

$$R(s, v) = \frac{f(x)}{u} + \frac{vg(x)}{s^2} + \frac{v^2}{s^2} N^+[h(x, t)] - \frac{v^2}{s^2} N^+[Mv(x, t) + Nv(x, t)]. \tag{2.2.5}$$

Now, applying the inverse of the natural transform of Eq.(2.2.5), we get

$$v(x, t) = E(x, t) - N^{-1} \left[ \frac{v^2}{s^2} N^+[Mv(x, t) + Nv(x, t)] \right] \tag{2.2.6}$$

where  $E(x, t)$  illustrates the term developed from initial conditions and source term.

The next step is that we present the solution of non-linear terms in the form of infinite series:

$$v(x, t) = \sum_{n=0}^{\infty} v_n(x, t). \tag{2.2.7}$$

So that the non-linear operator is decomposed as

$$Nv(x, t) = \sum_{n=0}^{\infty} A_n, \tag{2.2.8}$$

where  $A_n$  denotes the Adomain polynomials of  $v_0, v_1, v_2 \dots \dots v_n$  and can be determined by this formula:

$$A_n = \frac{1}{n!} \frac{d^n}{dx^n} [N(\sum_{i=0}^{\infty} \lambda^i v_i(x, t))], \quad = 0, 1, 2, \dots \tag{2.2.9}$$

Substituting Eqs (2.2.7) and (2.2.8) into Eq. (2.2.6), we will get

$$\sum_{n=0}^{\infty} v_n(x, t) = E(x, t) - N^{-1} \left[ \frac{v^2}{s^2} N^+[M \sum_{n=0}^{\infty} v_n(x, t) + N \sum_{n=0}^{\infty} A_n(x, t)] \right]. \tag{2.2.10}$$

Now, comparing Eq. (2.2.10) on both sides, we get

$$v_0(x, t) = E(x, t),$$

$$v_1(x, t) = -N^{-1} \left[ \frac{v^2}{s^2} N^+[Mv_0(x, t) + A_0] \right],$$

$$v_2(x, t) = -N^{-1} \left[ \frac{v^2}{s^2} N^+[Mv_1(x, t) + A_1] \right].$$

In general, we have

$$v_{n+1}(x, t) = -N^{-1} \left[ \frac{v^2}{s^2} N^+[Mv_n(x, t) + A_n] \right], \quad n \geq 0. \tag{2.2.11}$$

By using the general recurrence relation given in Eq. (2.2.11), we determine easily the remaining terms of  $v(x, t)$  as  $v_0, v_1, v_2 \dots \dots v_n$  where  $v_0$  is given the initial condition.

## 3. APPLICATIONS

In this section, we show the efficiency and high accuracy of the NDM and LDM for the solution of Painlevé equation I.

### 3.1. NDM for Painlevé equation

The second-order Painlevé equation [20,32] can be formulated as

$$v''(t) = 6v^2 + t, \tag{3.1.1}$$

subject to the initial conditions:

$$v(0) = 0, \quad v'(0) = 1. \tag{3.1.2}$$

By applying N-transform on both sides of Eq. (3.1.1),

$$N^+[v''(t)] = N^+[6v^2 + t]. \tag{3.1.3}$$

Using the properties of N-transform, we obtain

$$\frac{s^2}{v^2} R(s, v) - \frac{k}{v^2} v(0) - \frac{1}{v} v'(0) = N^+[6v^2] + \frac{v}{s^2}, \quad (3.1.4)$$

Substituting Eq. (3.1.2) into Eq. (3.1.2), we have

$$R(s, v) = \frac{v}{s^2} + \frac{v^3}{s^4} + \frac{v^2}{s^2} N^+[6v^2]. \quad (3.1.5)$$

Now, applying the inverse of N-transform, we have

$$N^{-1}[R(s, v)] = N^{-1}\left[\frac{v}{s^2} + \frac{v^3}{s^4} + \frac{v^2}{s^2} N^+[6v^2]\right] \quad (3.1.6)$$

Eq. (3.1.6) becomes

$$v(x, t) = t + \frac{t^3}{3!} + N^{-1}\left[\frac{v^2}{s^2} N^+[6v^2]\right]. \quad (3.1.7)$$

Eq. (3.1.7) can be written as

$$v(x, t) = t + \frac{t^3}{3!} + N^{-1}\left[\frac{v^2}{s^2} N^+[\sum_{n=0}^{\infty} A_n]\right]. \quad (3.1.8)$$

From Eq. (3.1.8), we can conclude that

$$\begin{aligned} v_0(x, t) &= t + \frac{t^3}{3!}, \\ v_1(x, t) &= N^{-1}\left[\frac{v^2}{s^2} N^+[A_0]\right], \\ v_2(x, t) &= N^{-1}\left[\frac{v^2}{s^2} N^+[A_1]\right], \\ v_{n+1}(x, t) &= N^{-1}\left[\frac{v^2}{s^2} N^+[A_n]\right], \quad n \geq 1. \end{aligned} \quad (3.1.9)$$

Therefore, from Eq. (3.1.9), the remaining terms of function  $v(x, t)$  can easily be computed as follows:

$$\begin{aligned} v_1(x, t) &= \frac{1}{2}t^4 + \frac{1}{15}t^6 + \frac{1}{336}t^8, \\ v_2(x, t) &= \frac{1}{7}t^7 + \frac{1}{40}t^9 + \frac{71}{46200}t^{11} + \frac{1}{26208}t^{13}, \\ v_3(x, t) &= \frac{1}{28}t^{10} + \frac{23}{3080}t^{12} + \frac{5219}{8408400}t^{14} + \frac{3551}{144144000}t^{16} + \frac{95}{224550144}t^{18}, \\ v_4(x, t) &= \frac{3}{364}t^{13} + \frac{131}{64680}t^{15} + \frac{19867}{95295200}t^{17} + \frac{163469}{14378364000}t^{19} + \frac{163451}{491203440000}t^{21} + \frac{131}{7101398304}t^{23}. \end{aligned}$$

In this way, we obtained the approximate result of the function  $v(x, t)$ , which is given as

$$v(x, t) = \sum_{n=0}^{\infty} v_n(x, t), \quad (3.1.10)$$

$$\begin{aligned} v(x, t) &= t + \frac{t^3}{3!} + \frac{1}{2}t^4 + \frac{1}{15}t^6 + \frac{1}{336}t^8 + \frac{1}{7}t^7 + \frac{1}{40}t^9 + \frac{71}{46200}t^{11} + \frac{1}{26208}t^{13} + \frac{1}{28}t^{10} + \frac{23}{3080}t^{12} + \frac{5219}{8408400}t^{14} + \frac{3551}{144144000}t^{16} + \frac{95}{224550144}t^{18} + \frac{3}{364}t^{13} + \frac{131}{64680}t^{15} + \frac{144144000}{19867}t^{17} + \frac{224550144}{163469}t^{19} + \frac{364}{491203440000}t^{21} + \frac{19867}{163451}t^{23} + \dots \end{aligned}$$

### 3.2. LDM for Painlevé equation

Consider the general form of the Painlevé equation:

$$v''(t) = 6v^2 + t, \quad (3.2.1)$$

subject to the initial conditions:

$$v(0) = 0, \quad v'(0) = 1. \quad (3.2.2)$$

Now, applying Laplace transform on both sides of Eq. (3.2.1)

with initial conditions:

$$\begin{aligned} \mathcal{L}[v''] &= \mathcal{L}[6v^2] + \mathcal{L}[t], \\ s^2 v(x, s) + v(0)s - v'(0) &= \mathcal{L}[6v^2] + \mathcal{L}[t]. \end{aligned} \quad (3.2.3)$$

Substituting Eq. (3.2.2) into Eq. (3.2.3), we have

$$v(x, s) = \frac{1}{s^2} + \frac{1}{s^4} + \mathcal{L}[6v^2]. \quad (3.2.4)$$

Now, taking the inverse of the Laplace transform, we obtain

$$\mathcal{L}^{-1}[v(x, s)] = \mathcal{L}^{-1}\left[\frac{1}{s^2} + \frac{1}{s^4} + \frac{1}{s^2} \mathcal{L}[6v^2]\right]. \quad (3.2.5)$$

Eq. (3.2.5) becomes

$$v(x, t) = t + \frac{t^3}{3!} + \mathcal{L}^{-1}\left[\frac{1}{s^2} \mathcal{L}[6v^2]\right]. \quad (3.2.6)$$

Eq. (3.2.6) can be written as

$$v(x, t) = t + \frac{t^3}{3!} + \mathcal{L}^{-1}\left[\frac{1}{s^2} \mathcal{L}[\sum_{n=0}^{\infty} A_n]\right]. \quad (3.2.7)$$

From Eq. (3.2.7), we can conclude that

$$\begin{aligned} v_0(x, t) &= t + \frac{t^3}{3!}, \\ v_1(x, t) &= \mathcal{L}^{-1}\left[\frac{1}{s^2} \mathcal{L}[A_0]\right], \\ v_2(x, t) &= \mathcal{L}^{-1}\left[\frac{1}{s^2} \mathcal{L}[A_1]\right], \\ v_3(x, t) &= \mathcal{L}^{-1}\left[\frac{1}{s^2} \mathcal{L}[A_2]\right]. \end{aligned}$$

Eventually,

$$v_{n+1}(x, t) = \mathcal{L}^{-1}\left[\frac{1}{s^2} \mathcal{L}[A_n]\right], \quad n \geq 0. \quad (3.2.8)$$

Therefore, from Eq. (3.2.8), the other remaining terms of the function  $u(x, t)$  can easily be computed as follows:

$$\begin{aligned} v_1(x, t) &= \frac{840t^4 + 112t^6 + 5t^8}{1680}, \\ v_2(x, t) &= \frac{1029600t^7 + 180180t^9 + 11076t^{11} + 275t^{13}}{7207200}, \\ v_3(x, t) &= \frac{11027016000t^{10} + 2305648800t^{12} + 191641680t^{14} + 7606242t^{16} + 130625t^{18}}{308756448000}, \\ v_4(x, t) &= \frac{19460562660000t^{13} + 4782299886000t^{15} + 492262539300t^{17}}{19460562660000t^{13} + 19460562660000t^{13} + 19460562660000t^{13}} + \frac{26844879180t^{19}}{785708957t^{21}} + \frac{19460562660000t^{13}}{19460562660000t^{13}} + \frac{10307500t^{23}}{10307500t^{23}} + \dots \\ v(x, t) &= t + \frac{t^3}{3!} + \frac{840t^4 + 112t^6 + 5t^8}{1680} + \frac{1029600t^7 + 180180t^9 + 11076t^{11} + 275t^{13}}{7207200} + \frac{11027016000t^{10}}{308756448000} + \frac{2305648800t^{12}}{308756448000} + \frac{191641680t^{14}}{308756448000} + \frac{7606242t^{16}}{308756448000} + \frac{130625t^{18}}{130625t^{18}} + \frac{19460562660000t^{13}}{19460562660000t^{13}} + \frac{4782299886000t^{15}}{4782299886000t^{15}} + \frac{492262539300t^{17}}{492262539300t^{17}} + \frac{26844879180t^{19}}{26844879180t^{19}} + \frac{785708957t^{21}}{785708957t^{21}} + \frac{10307500t^{23}}{10307500t^{23}} + \dots \\ v(x, t) &= \sum_{n=0}^{\infty} v_n(x, t), \end{aligned} \quad (3.2.9)$$



**Tab. 1.** Comparison of the approximate solution of Painlevé equation I

t	MADM [30]	VIM [31]	LDM	NDM
0.1	0.1002601271	0.1002167477	0.1002167476	0.1002167476
0.2	0.2021288956	0.2021394527	0.2021394527	0.2021394527
0.3	0.3086306987	0.3086307490	0.3086307491	0.3086307491
0.4	0.4239860367	0.4239862788	0.4239862886	0.4239862891
0.5	0.5543370146	0.5543399110	0.5543400885	0.5543401061
0.7	0.8992199875	0.8992296944	0.899242462	0.8992475639
0.9	1.4814889672	1.481778951	1.482022918	1.48237693
1.0	1.9416721356	1.959421042	1.960056483	1.962154582

LDM, laplace decomposition method;  
NDM, natural decomposition method.

The numerical results in Tab.1 show that the second-order Painlevé equation is convergence with four iterations by applying NDM. The given comparison in Tab.1 demonstrates that NDM converges more rapidly than LDM and others (VIM, MADM and VIA-1).

#### 4. IMPORTANT RESULTS OF THE PAINLEVE EQUATION I

The Painlevé equation has a number of important results and applications in mathematics and physics. Some of the key results include the following:

The Painlevé I equation is a completely integrable system, meaning that its solutions can be constructed using certain algebraic and analytic methods. This property has led to a deeper understanding of the behaviour of non-linear systems and their applications in physics and mathematics. The solutions of the Painlevé I equation are known as the Painlevé transcendent, which are a special class of functions with remarkable properties. They have been extensively studied in the context of special functions and have applications in a variety of areas, including random matrix theory, non-linear optics and statistical physics. The Painlevé I equation arises in the study of a wide range of physical systems, including the propagation of non-linear waves in fluids, the dynamics of magnetic vortices in superconductors and the behaviour of certain quantum mechanical systems. Its integrability properties make it a powerful tool for understanding the behaviour of these systems. The Painlevé I equation has connections to a number of other important mathematical and physical systems, including the Korteweg–de Vries equation, the using model in statistical physics and the theory of algebraic curves. Understanding these connections has led to new insights into the behaviour of the Painlevé I equation and its applications in various fields.

Overall, the Painlevé I equation represents a significant contribution to the study of integrable systems and their applications in physics and mathematics. Its important results and connections to other systems continue to make it a subject of active research and interest in the scientific community.

#### 5. CONCLUSION

This article applies the NDM and LDM to find the approximate solutions of the second-order Painlevé equation. The properties of the NDM are used to obtain a series solution that converges rapidly to the approximate solution. Also, LDM was applied successfully to solve the Painlevé equation. Furthermore, LDM does not require discretisation of the variable and avoids round-off errors. The numerical result shows that NDM is more attractive and powerful than LDM. In the future, we employ NDM and LDM to solve NLPDEs in science and engineering.

The Painlevé equations are a set of NLODEs that are notable for their integrability properties and their appearance in various areas of physics and mathematics. They were first introduced by the French mathematician Paul Painlevé in the early 20th century.

The novelty of this equation is described as follows:

- One of the key novelties of the Painlevé I equation is its integrability properties. Like the other Painlevé equations, it is integrable, meaning that its solutions can be constructed using certain algebraic and analytic methods. This property has led to a deeper understanding of the behaviour of non-linear systems and their applications in physics and mathematics.
- Another important feature of the Painlevé I equation is its appearance in the study of random matrix theory, where it plays a crucial role in the description of the distribution of eigenvalues of certain random matrices. In particular, it is used to describe the scaling limit of the Tracy–Widom distribution, which arises in the study of the largest eigenvalue of random matrices.


Overall, the Painlevé I equation represents a significant contribution to the study of non-linear systems and their applications in mathematics and physics. Its simplicity and wide-ranging connections continue to make it a subject of active research and interest in the scientific community.

Overall, future work on the Painlevé I equation is likely to involve a combination of theoretical and computational approaches, with the goal of understanding its behaviour and applications in a wide range of contexts.


#### REFERENCES


1. Painlevé P. Sur les équations différentielles du second ordre et d'ordre supérieur dont l'intégrale générale est uniforme. Acta mathematica. 1902 Dec;25:1-85.
2. Borisov AV, Kudryashov NA. Paul Painlevé and his contribution to science. Regular and Chaotic Dynamics. 2014 Feb;19:1-9.
3. Segur H, Ablowitz MJ. Asymptotic solutions of nonlinear evolution equations and a Painlevé transcendent. Physica D: Nonlinear Phenomena. 1981 Jul 1;3(1-2):165-84.
4. Kanna T, Sakkaravarthi K, Kumar CS, Lakshmanan M, Wadati M. Painlevé singularity structure analysis of three component Gross–Pitaevskii type equations. Journal of mathematical physics. 2009 Nov 25;50(11):113520.
5. Cao X, Xu C. ABäcklund transformation for the Burgers hierarchy. In Abstract and Applied Analysis 2010 Jan 1 (Vol. 2010). Hindawi.
6. Lee SY, Teodorescu R, Wiegmann P. Viscous shocks in Hele–Shaw flow and Stokes phenomena of the Painlevé I transcendent. Physica D: Nonlinear Phenomena. 2011 Jun 15;240(13):1080-91.
7. Dai D, Zhang L. On tronquée solutions of the first Painlevé hierarchy. Journal of Mathematical Analysis and Applications. 2010 Aug 15;368(2):393-9.


8. JFlorjańczyk M, Gagnon L. Exact solutions for a higher-order nonlinear Schrödinger equation. *Physical Review A*. 1990 Apr 1;41(8):4478.
9. Ablowitz MJ, Segur H. *Solitons and the inverse scattering transform*. Society for Industrial and Applied Mathematics; 1981 Jan 1.
10. Tajiri M, Kawamoto S. Reduction of KdV and cylindrical KdV equations to Painlevé equation. *Journal of the Physical Society of Japan*. 1982 May 15;51(5):1678-81.
11. Dehghan M, Shakeri F. The numerical solution of the second Painlevé equation. *Numerical Methods for Partial Differential Equations: An International Journal*. 2009 Sep;25(5):1238-59.
12. Clarkson PA. Special polynomials associated with rational solutions of the fifth Painlevé equation. *Journal of computational and applied mathematics*. 2005 Jun 1;178(1-2):111-29.
13. El-Gamel M, Behiry SH, Hashish H. Numerical method for the solution of special nonlinear fourth-order boundary value problems. *Applied Mathematics and Computation*. 2003 Dec 25;145(2-3):717-34.
14. Ellahi R, Abbasbandy S, Hayat T, Zeeshan A. On comparison of series and numerical solutions for second Painlevé equation. *Numerical Methods for Partial Differential Equations*. 2010 Sep;26(5):1070-8.
15. Gromak VI, Laine I, Shimomura S. Painlevé differential equations in the complex plane. In *Painlevé Differential Equations in the Complex Plane 2008 Aug 22*. de Gruyter.
16. Bobenko AI, Eitner U, editors. *Painlevé equations in the differential geometry of surfaces*. Berlin, Heidelberg: Springer Berlin Heidelberg; 2000 Dec 12.
17. Dehghan M, Shakeri F. The numerical solution of the second Painlevé equation. *Numerical Methods for Partial Differential Equations: An International Journal*. 2009 Sep;25(5):1238-59.
18. Saadatmandi A. Numerical study of second Painlevé equation. *Comm. Numer. Anal*. 2012;2012.
19. Sierra-Porta D, Núñez LA. On the polynomial solution of the first Painlevé equation. *Int. J. of Applied Mathematical Research*. 2017;6(1):34-8.
20. Ahmad H, Khan TA, Yao S. Numerical solution of second order Painlevé differential equation. *Journal of Mathematics and Computer Science*. 2020;21(2):150-7.
21. Izadi M. An approximation technique for first Painlevé equation.
22. Khan ZH, Khan WA. N-transform properties and applications. *NUST journal of engineering sciences*. 2008 Dec 31;1(1):127-33.
23. Belgacem FB, Silambarasan R. Theory of natural transform. *Math. Engg. Sci. Aeros*. 2012 Feb 25;3:99-124.
24. Spiegel MR. *Laplace transforms*. New York: McGraw-Hill; 1965.
25. Belgacem FB, Karaballi AA. Sumudu transform fundamental properties investigations and applications. *International Journal of Stochastic Analysis*. 2006;2006.
26. Maitama S, Hamza YF. An analytical method for solving nonlinear sine-Gordon equation. *Sohag Journal of Mathematics*. 2020;7(1):5-10.
27. Elbadri M, Ahmed SA, Abdalla YT, Hmidi W. A new solution of time-fractional coupled KdV equation by using natural decomposition method. In *Abstract and Applied Analysis 2020 Sep 1* (Vol. 2020, pp. 1-9). Hindawi Limited.
28. Maitama S, Kurawa SM. An efficient technique for solving gas dynamics equation using the natural decomposition method. In *International Mathematical Forum 2014* (Vol. 9, No. 24, pp. 1177-1190). Hikari, Ltd..
29. Amir M, Awais M, Ashraf A, Ali R, Ali Shah SA. Analytical Method for Solving Inviscid Burger Equation. *Punjab University Journal of Mathematics*. 2023 Dec 3;55(1).
30. Behzadi SS. Convergence of iterative methods for solving Painlevé equation. *Applied Mathematical Sciences*. 2010;4(30):1489-507.
31. Hesameddini E, Peyrovi A. The use of variational iteration method and homotopy perturbation method for Painlevé equation I. *Applied Mathematical Sciences*. 2009;3(37-40):1861-71.
32. Behzadi SS. Convergence of iterative methods for solving Painlevé equation. *Applied Mathematical Sciences*. 2010;4(30):1489-507.

Muhammad Amir:  <https://orcid.org/0009-0002-4871-4312>

Jamil Abbas Haider:  <https://orcid.org/0000-0002-7008-8576>

Shahbaz Ahmad:  <https://orcid.org/0000-0002-9901-0924>

Sana Gul:  <https://orcid.org/0000-0002-5075-2599>

Asifa Ashraf:  <https://orcid.org/0009-0005-4786-7757>



This work is licensed under the Creative Commons BY-NC-ND 4.0 license.

## A SUPERVISORY CONTROL SYSTEM FOR AUTOMATION OF HORIZONTAL FORM-FILL-SEAL PACKAGING PLANT BASED ON MODIFIED ATMOSPHERE TECHNOLOGY

**Mohammad Reza SEIFI\***, **Reza ALIMARDANI\*\***, **Seyed Saeid MOHTASEBI\*\***  
**Hossein MOBLI\*\***, **Maumoud Soltani FIROUZ\*\***

\*Department of Biosystem Mechanics, Arak University, Ali-Ebne-Abitaleb, Daneshjoo Blvd, 3MHG+VX3, Arak, Iran

\*\*Department of Agricultural Machinery Engineering, Faculty of Agricultural Engineering and Technology,  
University of Tehran, R232+G78 Mesbah, Karaj, Iran

[m-r-seifi@araku.ac.ir](mailto:m-r-seifi@araku.ac.ir), [rmardani@ut.ac.ir](mailto:rmardani@ut.ac.ir), [mahsoltani@ut.ac.ir](mailto:mahsoltani@ut.ac.ir), [mohtaseb@ut.ac.ir](mailto:mohtaseb@ut.ac.ir), [hmobli@ut.ac.ir](mailto:hmobli@ut.ac.ir)

*received 6 January 2023, revised 6 March 2023, accepted 26 March 2023*

**Abstract:** The packaging industry is one of the most important parts of agricultural products processing. A popular method of increasing the shelf life of agricultural products is modified atmosphere packaging (MAP). The main objective of this paper was to increase the adaptability and flexibility of the machines for packaging of different vegetables including lettuces, broccolis, cabbages, cauliflowers, etc. To achieve this goal, a supervisory control and data acquisition (SCADA)-based system was designed and developed for controlling and monitoring of MAP process of fresh vegetables. The system was divided into three physical layers: field devices, remote terminal unit (RTU) and master terminal unit (MTU). For packaging width adjuster system, the  $R^2$ , maximum error (ME), mean absolute error (MAE) and root mean square error (RMSE) were obtained as 0.999, 8 mm, 2.96 mm and 3.44 mm, respectively. For packaging height adjuster system, the  $R^2$ , ME, MAE and RMSE were obtained as 0.994, 10 mm, 3.53 mm and 4.57 mm, respectively. The SCADA system can be able to accurately adjust the speed of the conveyor and the temperature of the sealing jaws, based on the desired values. For gas injection unit, the value of 1.66 L/min, 0.557 L/min and 0.667 L/min were recorded for ME, MAE and RMSE, respectively. Four types of trends including temperature, speed, flow and digital parameter trends were designed. In addition to displaying screen alarms, the occurred alarms are stored, automatically as a text file for troubleshooting. Finally, the results showed that the designed system can be reliably used for MAP of various varieties of fresh vegetables.

**Key words:** packaging, food industry, SCADA systems

### 1. INTRODUCTION

Packaging engineering is a profitable, important and substantial part of agricultural and food products processing. Packaging of fresh vegetables and fruits is more significant. After harvesting and due to breathing and also dealing with environmental air, a series of chemical reactions occur in the produce, and thus, the moisture is lost. Therefore, wrinkles, discolouration, dehydration, changes in texture and freshness loss or corruption occur in the products. A popular method of increasing the shelf life of agricultural produces is to use modified atmosphere packaging (MAP). In this technique, the headspace of the package is replaced with a specific pure gas or a mixture of several gases such as oxygen ( $O_2$ ), nitrogen ( $N_2$ ) and carbon dioxide ( $CO_2$ ) with a certain proportion. The mixture of gases and the ratio of each gas in the mixture are important and are chosen as a function of the product that is packaged by the modified atmosphere technique. In order to eliminate hygienic problems related to human health and minimise human intervention, the packaging process requires adequate control and a high level of automation of fresh vegetable packaging plants, to improve the quality of products and efficiency of the system. In order to automate the plant, there is a need to develop a system that monitors the plant and helps reduce the errors caused by humans.

Nowadays, more and more complex, safe and trustworthy automation and control systems are required to support the technological change towards the factories of the future concept. This means that automation and control systems must automate, control and optimise the production processes ensuring plant availability while providing high-quality production with zero defects [1]. In particular, the automation system should facilitate a great deal of online modification including I/O interfacing, instrumentation hardware, diagnostics, prognostics, and data collection and operator interfaces [2]. The processing and packaging control system of agricultural products (especially fresh fruits and vegetables) embeds a generic set of essential requirements with regard to timing, error diagnostics, coordination and synchronisation. Moreover, the imperative error recovery and fault corrections are needed during run time. Furthermore, the control systems should satisfy other fault-tolerant features such as interlock checking and intuitive status display with error messaging [3].

Several controlling methods of agricultural crops processing especially in the field of packaging have been utilised. One of the most proper automation technology seems to be supervisory control and data acquisition (SCADA). This technology has been widely applied in the recent decade in the food industry [4].

The SCADA system has been extensively used in the food industry. Kumar and Rani [5] proposed an automation system using SCADA for the preparation, bottling and packaging of soft drinks.

Kulkarni and Elango [6] developed an automatic filling system by SCADA. They reported that the controlling and monitoring process by SCADA reduced errors in the system. Singh et al. [7] presented a method aimed towards providing a smart automation system in sugar mill. The graphical programming software LabVIEW has been utilised to develop SCADA software. By using a smart SCADA system, the performance and reliability of the sugar mill have been improved [7]. Lima et al. [8] developed a remote monitoring system based on the SCADA model in the field of food industry. They used the SCADA system for monitoring of production rate, packed quantity and Overall Equipment Effectiveness (OEE). The system also included alarms management, process trending and data logging [8]. The paper of Jain et al. [9] proposed a SCADA simulation model for packaging system in dry ice plant to improve packaging and extensively reduce operating labour costs. Sinha et al. [10] focused on a real-time flow measurement system using the Hall probe sensor and personal computer (PC)-based SCADA. In the paper, a float carrying a thin circular permanent magnet was used and a Hall probe sensor was placed outside the rotameter tube to sense the variation of magnetic field of a magnet with variation of float position. The DC signal output of the measuring system has been sent to a PC-based flow indicator. The flow indicator has been designed using Lab Tech Note Book Pro software and PC-based SCADA system. The performance of the system has been tested experimentally. A very good repeatability and a linearity of results have been reported [10]. Also, an oxygen control system was designed and developed by Catania et al. [11] for malaxation machine to improve virgin olive oil quality. The developed system is composed of an oxygen concentration sensor directly connected to the malaxation chamber and a data acquisition system to analyse and store the measured values in a process database [11]. The automation of systems in other aspects of manufacturing systems related to agriculture has been investigated by researchers. The paper of Szymenderski and Typańska [12] presented a model of controlling the flow of energy in agricultural biogas plant. The biogas plant control algorithm has been modelled using SCADA software, and an analysis of cost performance and life of the investment have been performed [12]. Aziz et al. [13] proposed a SCADA system to monitor and predict changes of humidity and temperature level in the greenhouse atmosphere. The system included active measurements, which were capable of detecting degradation level for humidity and temperature, were equipped with an alert mechanism to notify workers about the atmosphere quality in the greenhouse [13]. The paper of Bhutada et al. [14] discussed the automation of a free-standing greenhouse using SCADA system. The system was designed to achieve the optimal level of environment and growth factors inside the greenhouse and also present an efficient and user-friendly way of greenhouse automation [14].

In the field of fruit and vegetables, SCADA-based systems were scarcely implemented. Fresh vegetable packaging machinery usually does not have an advanced control system, while many packaging parameters are manually adjusted which necessitates the presence of the operator. However, the modern multi-target concept of fruit and vegetables packaging machinery is more attractive with recent technologies to develop the packaging systems having the ability to pack different agricultural products with different sizes, modified atmosphere conditions and packaging materials. Nevertheless, some researchers have focused on applying SCADA in preserving fruit and vegetables during stor-

age. Ramesh Babu et al. [15] studied on applying SCADA systems in the automation of controlled atmosphere stores and suggested suitable systems for automatic control and remote monitoring of all the parameters for a better shelf life of fruit and vegetables. Yu et al. [16] developed a remote SCADA system for keeping fruits and vegetables fresh. The system was divided into three physical layers: the field control unit at the bottom, a host computer control system in the middle and the remote monitoring layers at the top [16].

In order to preserve the quality of fresh vegetables using the MAP technique, different parameters such as flow rate and ratio of injecting gases, sealing temperature and packaging speed should be accurately controlled and then many true decisions should be made. Also, manufacturing processes in the agricultural industry are usually hard to be automated due to their non-uniformity, high variability of raw materials and also due to the scarcity of sensors for real-time monitoring of the key variables. To the best of our knowledge, there is no effort given to the automation of the whole process of fresh vegetable packaging systems, and many affecting parameters are manually changed by operators such as packaging width and height. Also, the present systems do not have an appropriate compatibility to use for packaging of different types of fresh vegetables.

Although Programmable Logic Controller (PLC)-based architecture is commonly used in packaging machinery, they are not developed for making data records, connecting to a central control system, alarms, etc., whereas the implementation of advanced automation and control strategy in the vegetable packaging domain plays a vital role. In comparison with the traditional methods, advanced control systems have several advantages. The traditional methods use discrete electronics, PLCs, Industrial computers and even high-computing systems such as the Digital Signal Processor (DSP) platform. These automation platforms have issues such as reliability, flexibility and scalability [17]. In a competitive and constantly changing environment, it is critical to identify and select the most current and appropriate technology that will satisfy the new need at the least cost. In the packaging of vegetables, the key aspects that should be considered are the product characteristics, packaging requirements and production facilities [18].

Motivated by the shortcomings in the current state-of-the-art, and to increase the adaptability and flexibility of the machines for packaging of different vegetables including lettuces, broccolis, cabbages, cauliflowers, Brussels sprouts, etc., this paper establishes research on automation of these systems based on supervisory control technology.

The most innovative aspect is the transition from an old rigid concept to a conception with distributed unit operation-based systems in a packaging factory controlled by a central unit. This allowed great freedom of action in packaging different types of vegetables with different shapes, dimensions and sizes. Therefore, flexibility is an important factor that makes it possible to change the packaged good characteristic, weight, size, wrapping materials, etc. [19]. The majority of vegetable packaging machine factories build their product in small batches or in individual operating modes which makes it necessary to supervise a human operator on each unit machine.

Based on the aims of this paper, a SCADA-based system was designed and developed for controlling and monitoring of packaging process of fresh vegetables using modified atmosphere technology. The designed SCADA system was implemented on the



fabricated Horizontal Form-Fill-Seal (HFFS) plant. It allows to visualise the entire system and inspect of individual influencing factors so that it is possible to continuously and precisely control the process. The possibility of recording data is another advantage which allows us for subsequent analysis in order to evaluate the correctness of the system. Computer, controllers, instruments, actuators and interfaces provide supervisory control of the automated process and allow analysis of the system through data acquisition.

2. MATERIALS AND METHODS

2.1. Experimental HFFS plant

A HFFS plant was designed and fabricated for packaging of fresh vegetables such as lettuce and cabbage. Fig. 1 shows the fabricated packaging plant.

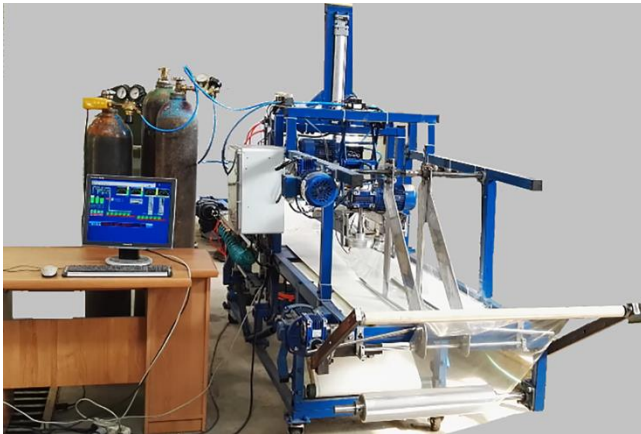


Fig. 1. The fabricated HFFS plant for MA packaging of fresh vegetables. HFFS, horizontal form-fill-seal

The packaging process of the HFFS plant includes the following tasks. First, fresh wholesome and cleaned vegetables are put on the conveyor, consecutively and in a line. At the entrance of the machine, a polymeric film is pulled and stretched on the conveyor and beneath the fresh products. The polymeric film passes through a forming collar, named the folding box, and then is transformed into a tube and after that, the two edges of the polymer are sealed together by the heated wheel sealers under a definite pressure and temperature. Gas flushing is used for atmosphere modification by a lance that is entered into the tube when the HFFS plant is operated [20]. The gas mixture used for modification of the packaging headspace usually includes O<sub>2</sub>, CO<sub>2</sub> and N<sub>2</sub>. The box motion cross-sealing unit is designed to extend the dwelling time by which the cross-sealing jaws that are in contact with the polymeric film. So it can be able to transfer more heat and long-time press into the film as opposed to increasing temperature which can potentially melt the film. To make a box motion unit, separate pneumatic actuators were used for the horizontal and vertical motions allowing a variable amount of jaw separation and dwell distance to be achieved. A knife, integral with the sealing jaws, cuts through adjacent packs to produce the separation. Fig. 2 illustrates the components of the fabricated HFFS plant.

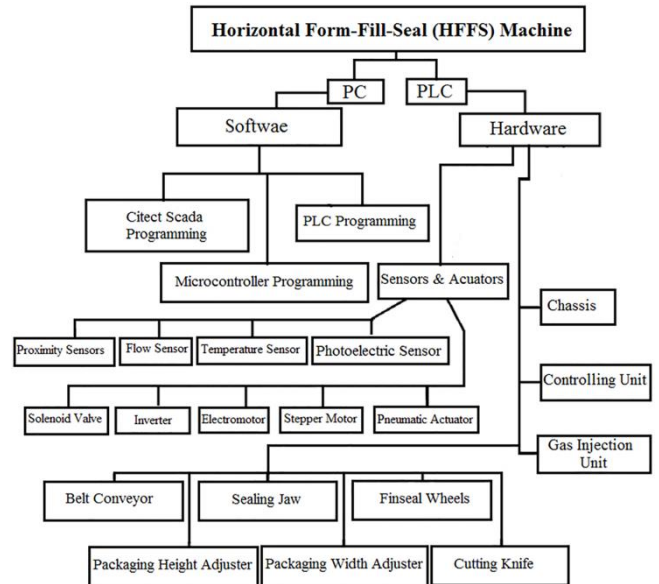


Fig. 2. The components of the fabricated HFFS plant. HFFS, horizontal form-fill-seal

2.2. SCADA system structure

The developed SCADA system is illustrated in Figs. 3 and 4. The system as a whole is divided into three physical layers: field devices at the bottom including instruments, sensors and actuators being responsible for the acquisition of input signals and delivery of control ones to the processes [21]; remote terminal unit (RTU) including a PLC; the supervision control layer is implemented by the Master Terminal Unit (MTU), typically a computer (e.g. a personal computer), that periodically collects data from the process control layer. The MTU ensures essential functionalities such as alarms management, data logging, processes trending and reports generation [8].

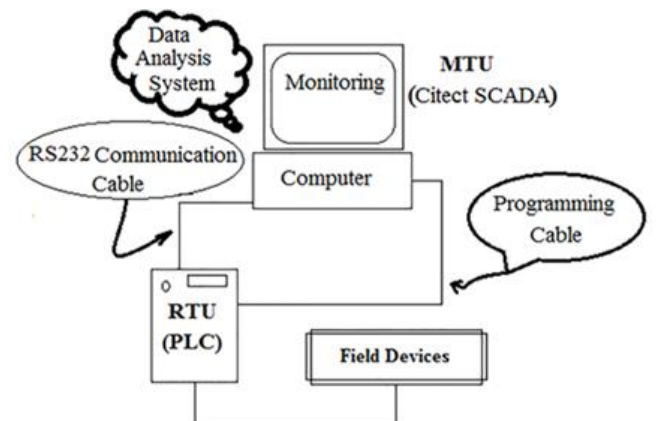


Fig. 3. The developed SCADA system architecture for the HFFS Machine. HFFS, horizontal form-fill-seal; SCADA, supervisory control and data acquisition

The applied sensors for measuring the physical parameters in the controlling system of the HFFS plant are composed of temperature sensor for sealing jaws, infrared distance measuring sensor for packaging width and height adjuster units, magnetic position detector for pneumatic cylinders, inductive proximity sensor for speed measurement of the conveyors and fin-wheel

sealing jaw and photoelectric sensor for vegetable passing detection and digital gas flow sensor for gas injection treatment.

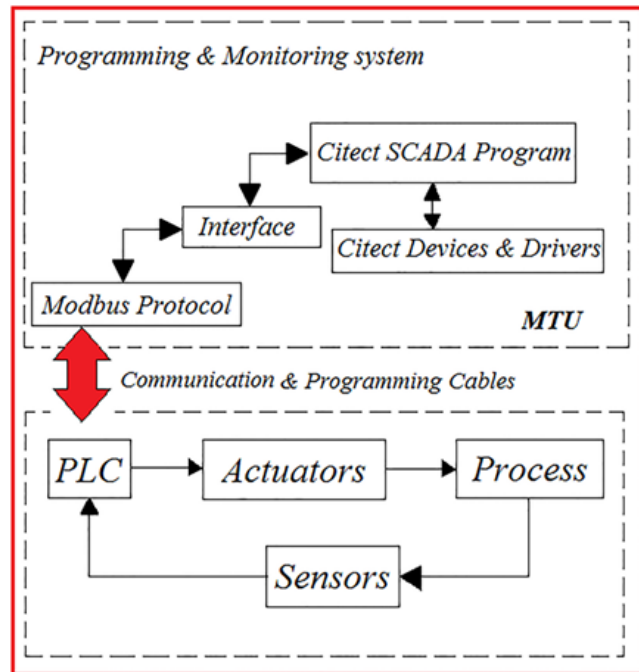


Fig. 4. Diagram of monitoring and controlling system

Two precision centigrade temperature sensors (LM35) were used for measuring the temperature of the cross-sealing and fin-wheel sealing jaws. The output voltage of the sensor is proportional to the sensed temperature with sensitivity of 10 mV/°C. To install the sensors, a hole with diameter and depth of 6 mm was drilled on the cross-sealing and fin-wheel sealing jaws, and then the sensors were fixed into the holes.

To measure the packaging width and height, two infrared distance measuring sensors (Model: GP2Y0A21YK0F, SHARP) were installed on the chassis of the HFFS plant. The output voltage of the sensor is corresponding to the detection distance, but there is a nonlinear relationship between the output voltage and the detected distance, so a pre-experiment was performed for extraction of the best calibration equations.

A magnetic sensor was applied for position detection of the pneumatic actuators that should be installed on the cylinders. For each actuator, two sensors were used to recognise if the actuator is in the open mode or closed one.

For conveyor and wheel seal speed measurement, the inductive proximity sensors (FOTEK, PM-18-08) were used as a rotational speed counter (rpm). By multiplying the diameter of the roller and the rotational speed, the linear speed of the roller or wheel would be calculated.

The photoelectric sensor (OMRON, E3JK) was used for vegetable passing detection through the vertical sealing jaws. When the sensor detected the vegetable, a positive pulse is sent to the PLC and the end seal of the package is performed by sealing jaws.

Three gas flow sensors (Honeywell Zephyr, HA-FUHT00300L4AXT) were used for measuring the flow rates of N<sub>2</sub>, O<sub>2</sub> and CO<sub>2</sub> gases through atmosphere modification. The sensors provide Inter-Integrated Circuit (I<sup>2</sup>C) protocol for reading gas flow over specified full-scale flow and compensated temperature rang-

es. So, a digital interface was designed for the sensors. The interface receives the output of the gas flow sensor and then converts it to analogue voltage. Also, the PLC receives the analogue voltage and converts it to digital form again. Fig. 5 shows the designed interface for the gas flow sensors. The gas flow rate is calculated as follows:

$$F = 300 \times \frac{DOC - 0.1}{0.8} \quad (1)$$

where  $F$  is the gas flow (L/min) and  $DOC$  is the digital output code of the sensor.

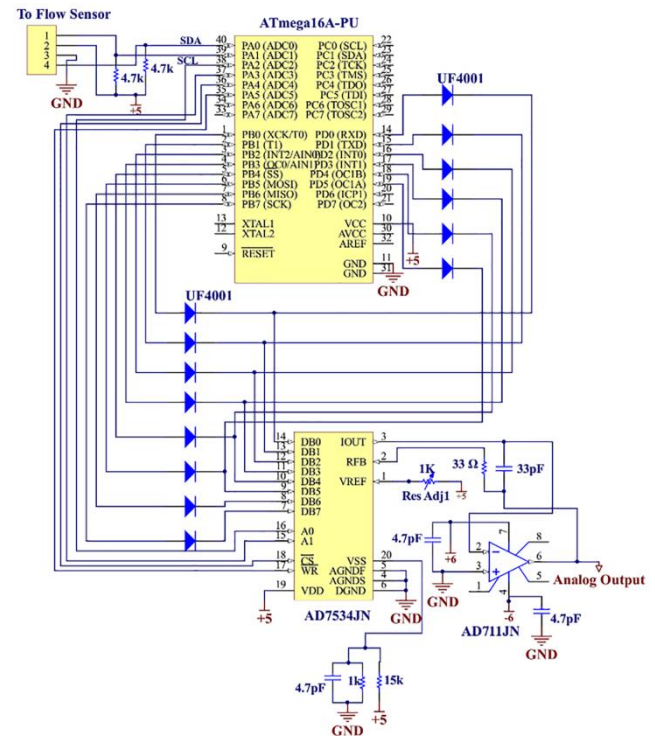


Fig. 5. The electronic circuit diagram of the designed digital interface for communication between the gas flow sensor and PLC. PLC, programmable logic controller

The duty of the actuators is to receive commands from RTU and carry out relevant operations. RTU by analysing the received data from the sensors sends specified commands to the actuators and decides for the next step after the reception of appropriate feedback. The actuators of the HFFS plant are LS IG5A frequency inverter, pneumatic solenoid valves, flow control valves for injecting gases, relays for turning on or off the electromotors and heating elements of sealing jaws. Two IG5A inverters were used for controlling the speed of the conveyors and wheel seal jaw.

The control unit of IG5A has analogue and digital inputs, so that it can take commands from PLC to turn on and off the electromotor and adjust the speed of the motors, also provides forward and reverse turns to change the rotating direction of the motors. Three 5/2-way single solenoid valve spring return were used for controlling the pneumatic cylinders of the upper and bottom vertical sealing jaws and cutting knife. Also, to control the pneumatic cylinder of the carrier of the vertical jaws, a 5/3-way double solenoid valve closed mid-position was used. Three automatic flow control valves were fabricated using a manual flow control valve, stepper motor and driving system for adjusting the

ratio of injecting gas mixture. An electronic driver module was designed as a control unit of flow valves to receive command signals from the PLC. The N<sub>2</sub>, O<sub>2</sub> and CO<sub>2</sub> gases are usually used for headspace modification in packaging engineering. Fig. 6 shows the fabricated automatic flow control valves and the driving module.

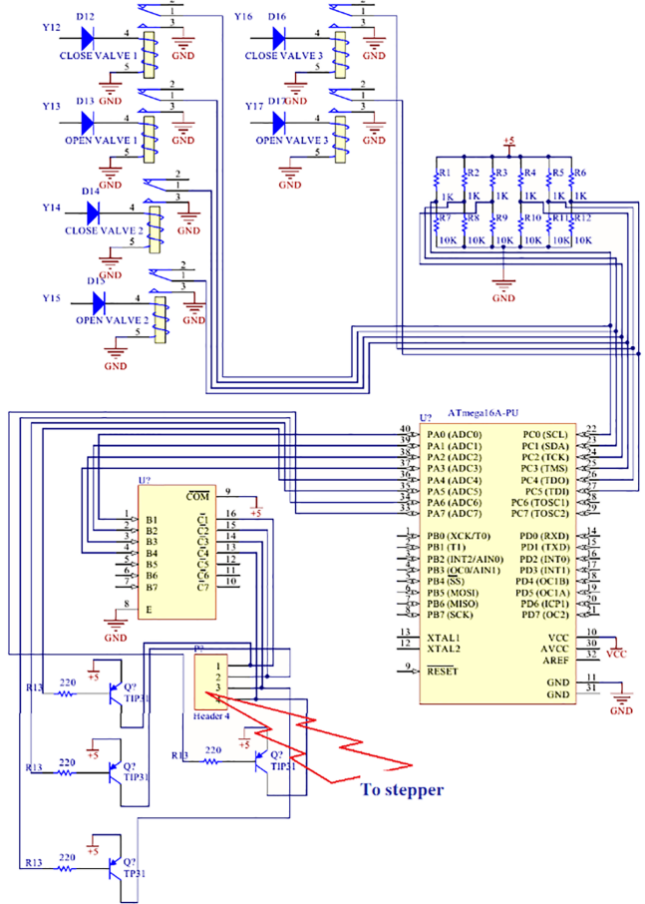
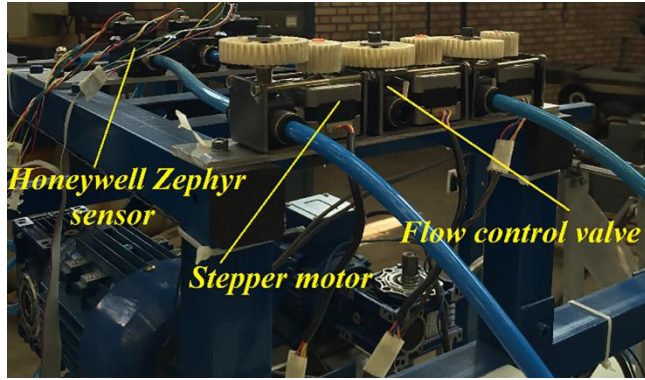


Fig. 6. The injection system for N<sub>2</sub>, O<sub>2</sub> and CO<sub>2</sub> gases

According to Tab. 1, the total number of input and output digital parameters and input and output analogue parameters are 8, 20, 7 and 2, respectively. So, a PLC with 20 digital inputs and 12 digital outputs (Model: FBs-32MBR2-AC, FATEK) was used as RTU. Also, a digital output module (FBs-8Y), an analogue input module (FBs-6AD), an analogue output module (FBs-2DA) and a serial communication board (FBs-CB2) were used for extension of the selected PLC.

Tab. 1. Identification of input and output parameters of PLC

Device	Type	Supply voltage (V)	Output voltage (V)	No .
Temperature sensor	Analogue input	5	0–1.55	2
Distance measuring sensor	Analogue input	5	0–3.5	2
Flow rate sensor	Analogue input	5	0–5	3
Photoelectric sensor	Digital input	24	24	1
Inductive proximity sensor	Digital input	24	24	3
Magnetic sensor	Digital input	24	24	4
Inverter speed adjuster	Analogue output	0–10	–	2
Solenoid valve	Digital output	24	–	5
Flow control valve	Digital output	24	–	6
Gas injection valve	Digital output	24	–	1
Relay for electromotor	Digital output	24	–	3
Relay for heat element	Digital output	24	–	2
Starter relay for inverter	Digital output	24	–	3

PLC, programmable logic controller

The developed RTU supports the industrial ModBus RTU protocol. So, the used devices for communicating the RTU and MTU are ModBus/RTU protocol, RS232 interface, communication cable and communication board (FBs-CB2, which was installed on the RTU). The ModBus protocol is widely used in the agricultural industry and was developed in 1979 by Modicon Inc. ModBus communicates using a master–slave technique as a messaging structure, and so does not define a physical layer. Normally, the RS232, RS422 or RS485 protocols are used as the physical layer. ModBus allows flexible access to the measured values and configuring parameters of the intelligent devices. Depending on the complexity of the processing flow, different devices can be connected to the network [22, 23].

The supervision control layer is implemented by MTU, typically a computer (e.g. a personal computer) and SCADA-based software. The master computer performs two-way data exchange with the slave computer (PLC) using ModBus protocol. The supervisory computer system periodically collects the data from the process control layer. The system software used in this research is CitectSCADA-7.1 (Schneider Electric). The software consists of two distinctive parts: configuration environment and runtime. The configuration environment includes tools for making runtime, designing and managing of the supervisory system. The runtime environment is a graphical interface that communicates with the I/O devices so the administrator can perform the supervisory control and manages the overall system. To develop the SCADA system, in the first phase, a new project was created in Citect Explore. The next steps are defining labels for control variables, communication settings, server settings, system settings, alarms, monitor screen design and programming in Cicode Editor.



The variable database is the most essential part of the SCADA system that has different formats such as digital, integer and real. Tab. 2 shows the defined variables in the developed SCADA system.

**Tab. 2.** Defined variables in CITECT SCADA and memory of the PLC

Tag name	Type	Unit	Tag name	Type	Unit
Conveyor 1 Speed Sensor	DIGITAL	None	Reverse Run M2 M3 M4	DIGITAL	None
Wheel Seal Speed Sensor	DIGITAL	None	Gas Injection Valve	DIGITAL	None
Product Passing Detector	DIGITAL	None	Actual Value Wheel Seal Temperature	REAL	°C
Conveyor 2 Speed Sensor	DIGITAL	None	Actual Value Sealing Jaw Temperature	REAL	°C
Position Detector Cutting Knife	DIGITAL	None	Operator Input Wheel Seal Temperature	INT	°C
Position Detector Vertical Actuator	DIGITAL	None	Operator Input Sealing Jaw Temperature	INT	°C
Closing Detector Horizontal Actuator	DIGITAL	None	Actual Value Packaging Width	INT	0.1 V
Opening Detector Horizontal Actuator	DIGITAL	None	Operator Input Packaging Width	INT	mm
Product Passing Detector	DIGITAL	None	Actual Value Packaging Height	INT	0.1 V
Up Vertical Actuator	DIGITAL	None	Operator Input Packaging Height	INT	mm
Cutting Knife Actuator	DIGITAL	None	Reference Conveyor Speed	INT	m/s
Down Vertical Actuator	DIGITAL	None	Actual Value Conveyor Speed M1	REAL	m/s
Opening Horizontal Actuator	DIGITAL	None	Actual Value Conveyor Speed M5	REAL	m/s
Closing Horizontal Actuator	DIGITAL	None	Actual Value Wheel Seal Speed M3	REAL	m/s
Packaging Width M2	DIGITAL	None	Dueling Time	INT	10 ms

Wheel Seal M3	DIGITAL	None	Gas Flow Sensor 1	REAL	SLPM
Packaging Height M4	DIGITAL	None	Gas Flow Sensor 2	REAL	SLPM
Heat Element Sealing Jaw	DIGITAL	None	Gas Flow Sensor 3	REAL	SLPM
Heat Element Wheel Seal	DIGITAL	None	Carrier Opening Speed	REAL	m/s
Forward Run Conveyor M1 & M2	DIGITAL	None	Carrier Closing Speed	REAL	m/s
Forward Run M2 M3 M4	DIGITAL	None	Gas Flow Sensor 1	REAL	SLPM
Close Flow Valve 1	DIGITAL	None	Gas Flow Sensor 2	REAL	SLPM
Open Flow Valve 1	DIGITAL	None	Gas Flow Sensor 3	REAL	SLPM
Close Flow Valve 2	DIGITAL	None	Heat Element Control	DIGITAL	None
Open Flow Valve 2	DIGITAL	None	O <sub>2</sub> Flow Control	DIGITAL	None
Close Flow Valve 3	DIGITAL	None	CO <sub>2</sub> Flow Control	DIGITAL	None
Open Flow Valve 3	DIGITAL	None	N <sub>2</sub> Flow Control	DIGITAL	None

PLC, programmable logic controller, SCADA, supervisory control and data acquisition

The communication settings connecting the master computer and the slave PLC are shown in Tab. 3. Citect acquires the data sent by the slave computer and displays some needed data on the monitor display. Moreover, operator may manually transmit commands to the PLC through the RS232 port.

**Tab. 3.** Communication settings of MTU and RTU

Parameter	MTU	RTU
Protocol	ModBus/RTU	ModBus RTU (Slave)
Baud rate	115,200	115,200
Stop bit	1	1bit
Data bit	8bits	8bits
Parity	EVEN-P	Even parity

MTU, master terminal unit; RTU, remote terminal unit

The functionality of alarms is to declare abnormality occurrence in the system, warning to operator if the current situation causes damage to the machine, defective product or imperfect process. For instance, if the temperature of the sealing jaws would be lower than the adjusted value, the packaging process would not be completely implemented and faulty sealing edges would be produced. The defined alarms are categorised into three groups: digital, analogue and advanced. The defined alarms are presented in Tabs. 4–6.



Tab. 4. Communication settings of MTU and RTU

Alarm tag	Alarm description
Conveyor_Motor	Conveyor Motor STOPPED
Gas_Injection	Gas Valve Injection CLOSED
Jaw_Element	Jaw Element Seal Turned OFF
Wheel_Element	Wheel Seal Element Turned OFF
Wheel_Motor	Wheel Seal Motor STOPPED

MTU, master terminal unit; RTU, remote terminal unit.

Tab. 5. The analogue alarms defined in Citect

Alarm tag	High-high	High	Low	Low-low	Deviation
Seal temperature	140	135	100	95	5
Wheel temperature	180	160	125	120	5
Conveyor speed	0.2	0.18	0.08	0.06	0.01

Tab. 6. The advanced alarms for HFFS

Alarm tag	Alarm description	Cicode expression
OverFlow1	O <sub>2</sub> Flow>=300	GAS_FLOW_OXYGEN>=300
OverFlow2	N <sub>2</sub> Flow>=300	GAS_FLOW_NITROGEN>=300
OverFlow3	CO <sub>2</sub> Flow>=300	GAS_FLOW_CO2>=300

HFFS, horizontal form-fill-seal



Fig. 7. The graphic page designed for the HFFS system.  
HFFS, horizontal form-fill-seal

The graphic page establishes a visual communication between the user and the SCADA system. On the graphic page, objects and buttons trigger a process or do an action. The parameters that should be assignable for the user are temperature of sealing jaws, speed of conveyor and fin-wheel sealing jaws, width and height of packaging, duelling time, injecting gas flow rate, gas injection valve and conveyor status (ON or OFF) and type of the product (lettuce, cabbage, etc.). All these parameters are configurable and operator can be able to change their values. The triggered alarms are displayed at the bottom of the screen. Citect

audio features also were used to notify the user the occurrence of alarms. Fig. 7 illustrates the graphic page designed for the packaging system.

### 2.3. MAP conditions of fresh vegetables

The composition of the required gas in the MAP approach depends on the type of the product, its moisture content, microbiological specifications, breathing rate, the preservation of its colour and the storage temperature. Tab. 7 shows the optimum value of components in the modified atmosphere. The required value of each component was saved in the SCADA system and determined regarding the target product.

Tab.7. Required gas portion for different horticultural products [24]

Horticultural products	Temperature (°C)	Oxygen (%)	Carbon dioxide (%)	Nitrogen (%)
Artichokes	0–5	2–3	2–3	94–96
Asparagus	0–5	15–20	5–10	70–80
Beans	5–10	2–3	4–7	90–94
Beets	0–5	2–5	2–5	90–96
Broccoli	0–3	1–2	5–10	88–94
Brussels sprouts	0–5	1–2	5–7	91–94
Cabbage	0–5	2–3	3–7	90–95
Cantaloupes	3–7	3–5	10–15	80–87
Carrots	0–5	3–5	2–5	90–95
Cauliflower	0–2	2–3	2–5	92–96
Celery	0–5	1–1	0–5	94–99
Com, sweet	0–5	2–4	5–10	86–93
Cucumbers	8–12	3–5	0–2	93–97
Honeydews	10–12	3–5	0–2	93–97
Leeks	0–5	1–2	3–5	93–96
Lettuce	0–5	1–3	0–3	94–99
Mushroom	0–3	Air	10–15	Air
Okra	8–12	3–5	0–2	93–97
Onions, dry	0–5	1–2	0–5	93–99
Onions, green	0–5	1–2	10–20	78–89
Peppers, bell	8–12	3–5	0–2	93–97
Peppers, chilli	8–12	3–5	0–3	92–97
Potatoes	4–10	2–3	2–5	92–96
Radish	0–5	1–5	2–3	92–97
Spinach	0–5	18–21	10–20	72–59
Tomato	15–20	3–5	0–3	92–97

## 3. RESULTS AND DISCUSSION

### 3.1. Calibration of distance sensor

For the infrared distance measuring sensors, there is a linear relationship between output voltage and inverse value of the sensed distance. However, the following hyperbolic model was developed to extract an accurate calibration equation for the distance sensors:

$$D = \frac{aV+b}{cV+d} \tag{2}$$

where D is the sensed distance (cm), V is the output voltage of the sensor (0.1×V) and a,b,c,d are the calibration equation constants.

The Levenberg–Marquardt method of curve fitting and cftool of MATLAB R2013a was used to extract the calibration constants; the initial value of constants (a, b, c and d) was assumed equal to 1. The Levenberg–Marquardt method has been widely used in many fields due to its high converging efficiency to obtain the global optimal solution. This method takes advantage of the steepest descent method, the Newton method and the Gauss–Newton method. The steepest descent method obtains the local optimal solution with the first-order convergence and has no limitation on the initial values of parameters [25]. The obtained results are presented in Tab. 8.

Tab. 8. The obtained regression coefficients for infrared distance measuring sensor

Parameter	a	b	C	d	R <sup>2</sup>	RMSE
Packaging width	0.0662	-5.749	9.5×10 <sup>-5</sup>	0.0016	0.9998	2.102
Packaging height	-0.0117	1.918	5.06×10 <sup>-5</sup>	0.00035	0.9973	3.771

RMSE, root mean square error

The maximum error (ME) of packaging width and height measurements were obtained as 3.5mm and 5.2mm, respectively. Evaluation of the SCADA system is presented as follows.

### 3.2. Packaging width and height system

The packaging width and height adjuster units were designed so that to be adjustable in the range of 130–400 mm and 150–300 mm, respectively. To evaluate this section of the system, the reference values of width and height of packaging were changed in the monitoring system with interval of 10mm, and the corresponding actual value of these variables was measured using a vernier calliper with an accuracy of 0.1 mm. Fig. 8 shows the reference and actual values of the packaging width.

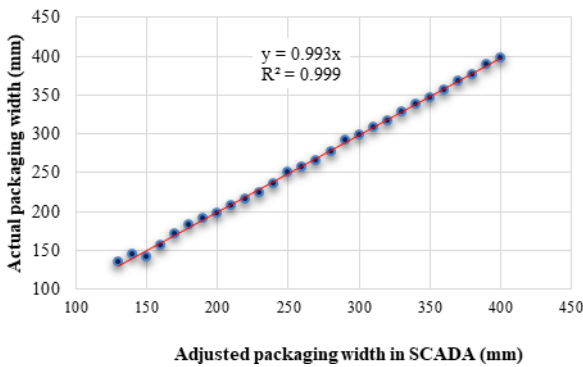


Fig. 8. Fitness of the adjusted and the measured values of packaging width

The R<sup>2</sup>, ME, mean absolute error (MAE) and root mean square error (RMSE) were obtained as 0.999, 8 mm, 2.96 mm and 3.44 mm, respectively. Fig. 9 shows the adjusted value of

packaging height versus measured ones.

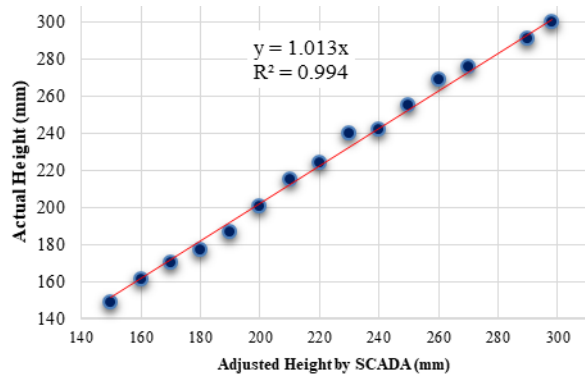


Fig. 9. Adjusted packaging height versus measured values

For packaging height adjuster unit, the R<sup>2</sup>, ME, MAE and RMSE were obtained as 0.994, 10 mm, 3.53 mm and 4.57 mm, respectively.

### 3.3. Conveyor and fin-wheel speed

The speed of the conveyor was changed in the SCADA system in the range of 0.06–0.2 m/s with interval of 0.01 m/s and the response of the system was recorded in the database. In Fig. 10 in the square point, the conveyor speed has been increased by the operator with step of 0.01m/s and as can be seen, the actual values of the conveyor speed were equal to the desired ones. So the system can accurately adjust the speed of the conveyor based on the desired speed.

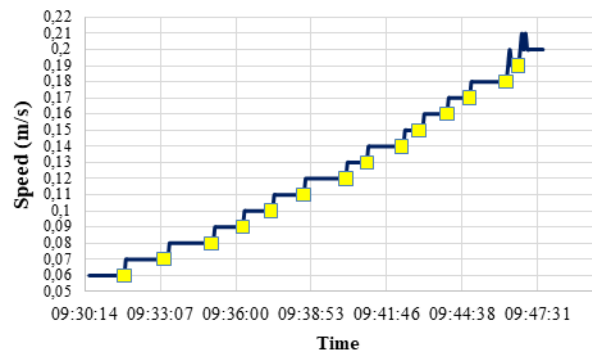


Fig. 10. Response of the SCADA system to changes in the speed of the conveyor in the range of 0.06–0.2 m/s. SCADA, supervisory control and data acquisition

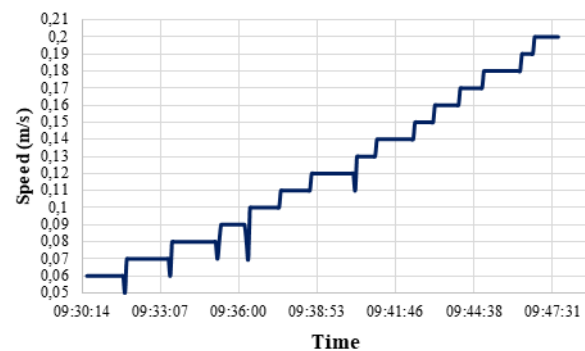


Fig. 11. The recorded values of the wheel sealing jaw speed as a function of the conveyor speed

The speed of the fin-wheel sealing jaw should be a function of the conveyor and so when a change happens at the speed of the conveyor belt, the system should adjust the speed of the wheel sealing jaw. Fig.11 presents changes in the fin-wheel speed that pursues the conveyor speed.

As shown in Figs. 10 and 11, the wheel seal treatment is exactly in compliance with the conveyor speed.

### 3.4. Temperature of sealing jaws

To evaluate the SCADA system in temperature controlling of the sealing jaws, the values of 125°C and 135°C for vertical jaws and 170°C and 180°C for wheel jaws were used as the reference temperatures, and the response of the system was recorded. In designing of the heat elements, the desired time for heating the sealing jaws from room temperature (25°C) to reference value was assumed as 20 min. As shown in Fig. 12, the actual temperatures were linearly increased until reached the reference value. Upon reaching the jaw temperature to the value that has been set by the user, the system turns off the heating elements. The heating time (reaching to the desired temperature) was recorded at about 18 min, which was close to the chosen time (20 min). In Fig. 12, a fluctuation of 5°C and 3°C is visible for vertical and fin-wheel jaws, respectively.

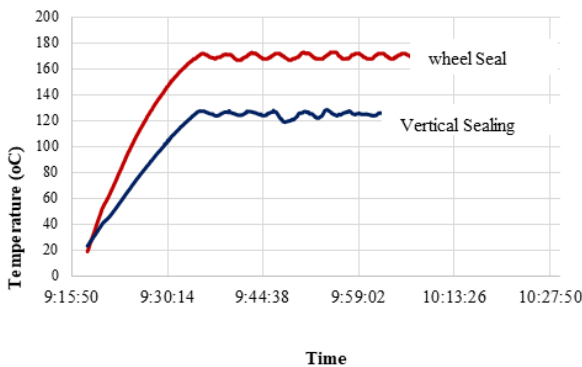


Fig. 12. Temperature changes in vertical and fin-wheel jaws at reference temperatures of 125°C and 170°C, respectively

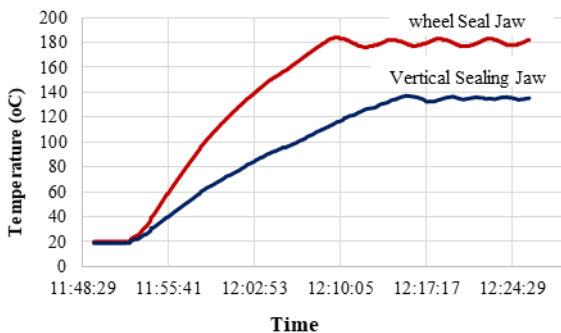


Fig. 13. Recorded temperature of sealing jaws at reference temperatures of 135°C and 180°C

Fig. 13 shows the recorded temperature of the sealing jaws at the reference temperatures of 135°C and 180°C. The needed time for reaching the reference temperature was recorded as 22 min and 20 min for the vertical and fin-wheel sealing jaws, respectively, which are close to the desired time (20 min). The temperature fluctuation of 3°C is observed in Fig. 13 for vertical and wheel seal jaws.

### 3.5. Gas injection unit

To evaluate the gas injection unit, the reference flow rate was changed in the SCADA system in the range of 1–10 L/min and 10–100 L/min with interval of 1 L/min and 10 L/min, respectively. Fig. 14 shows the first step of the experiment.

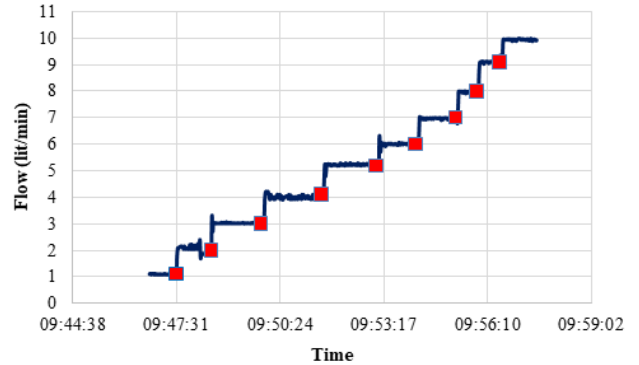


Fig. 14. Changes in injected gas flow rate in the range 1–10 L/min. Square points indicate that flow increment has been done by the user in the SCADA system. SCADA, supervisory control and data acquisition

At this stage, ME, MAE and RMSE were obtained as 0.3 L/min, 0.08 L/min and 0.12 L/min, respectively. At flow rate of 0.3 L/min and 6 L/min, feedback of the system and modification of flow by SCADA are clearly visible.

Fig. 15 presents the response of SCADA to changes in injected gas flow rate in the range of 10–100 L/min. Square points determine times that the user increased the reference value of flow rate. For ME, MAE and RMSE, the value of 1.66 L/min, 0.557 L/min and 0.667 L/min were recorded. ME has occurred at flow of 100 L/min.

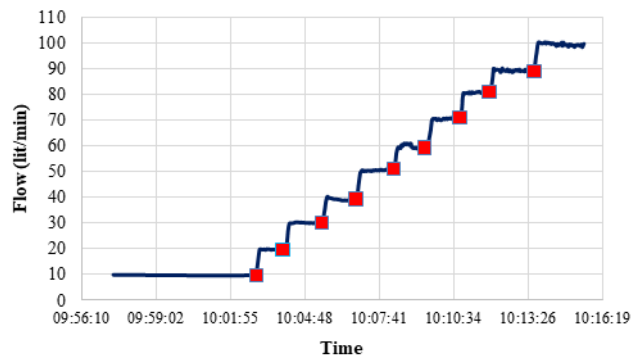


Fig. 15. Measured gas flow at different reference values adjusted by the user

Trend in the SCADA system provides graphs that help manager to supervise and analyse the system. For HFFS, four types of trends including temperature, speed, flow rate and digital parameters trend were designed. Operator can select each type trend and inspect probable problems. For instance, Fig. 16 shows the temperature trends that were recorded during the evaluation of the system.

Since alarms usually notify the user the events that are critical or harmful to a machine or process, so should be always visible for the user. In the developed SCADA system, alarms are shown



at the bottom of the runtime environment (Fig. 16). In addition to displaying screen alarms, the occurred alarms are stored as a text file for a 24-h period.

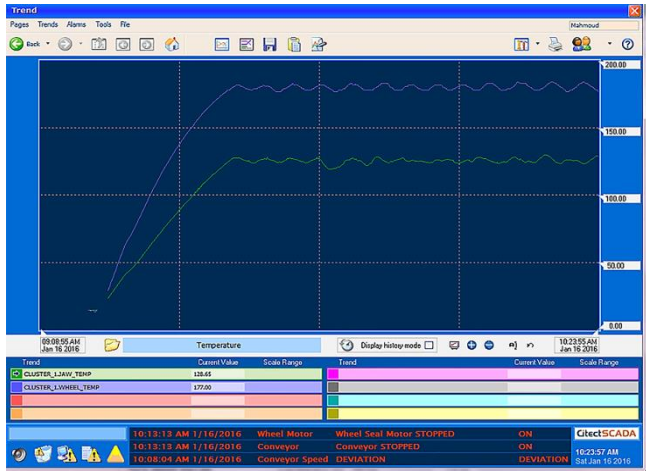


Fig. 16. Temperature trend of fin-wheel and vertical sealing jaws

### 3.6. The effect of MAP process on the shelf life

The evaluation of the fabricated apparatus was carried out using lettuce and cabbage. The packaged and fresh unpackaged products were kept in the same condition in a refrigerator. The pictures of crops were captured daily to evaluate the degree of corruption and decay. Fig. 17a–c shows lettuces on the 5th, 15th and 20th storage days. While no change was observed in the MAP process, the corruption of unpackaged lettuces was evident from the first sampling step, which increased when increasing the storage time. The corruption locations were flagged with yellow ovals in unpackaged lettuces stored for 5 days to make their visibility easier. Brown spots were seen in ones without packaging after 20 days. The obtained results for cabbage are similar to lettuce and the packaged products maintain their quality during the storage time. To keep the article concise, only the pictures of cabbages stored for 20 days were given in Fig. 17d. The colour and quality of packaged products were maintained during this period.







Fig. 17. Comparison of packaged (right side) and unpackaged products (left side) stored for (a)5, (b)15, (c)20 days for lettuce and (d)20 days for cabbage

#### 4. CONCLUSION

In this research, the SCADA real system was designed and developed for supervisory control and automation of modified atmosphere technology-based fresh vegetable packaging processing. The developed system provides monitoring and process control, Human–Machine Interface (HMI), data acquisition and system troubleshooting. The monitoring system accurately reflects the performance of equipment. The system also generates appropriate alarms to indicate unusual issues with the equipment. Each alarm is accurately described, which allows for quick finding and eliminating defects. The use of SCADA allows for making remote adjustments such as packaging speed, polymer type and heat sealing temperature to optimise the system operation. The system provides the ability to carry out automatic packaging operations for a wide range of fresh vegetables. The data were acquired during the operation of the plant and displayed the current value of significant parameters in the form of appropriate tables and graphics. By using SCADA, we established supervisory management at different levels from sensors and actuators to computer systems and analysis of the acquired data. The most important advantages of SCADA in this project are the increment of productivity and the downtime reduction due to the increase in the visibility in each subsystem within the plant. It also provides the capability

of monitoring the work in progress in real time and a better understanding of the production process, which decreases labour with improving quality. However, the life cycle assessment (LCA), which is the investigation and valuation of the environmental impact of a given product, is needed to be studied.

#### Nomenclature:

<b>MAP</b>	Modified Atmosphere Packaging
<b>SCADA</b>	Supervisory Control and Data Acquisition
<b>HFFS</b>	Horizontal Form-Fill-Seal
<b>PLC</b>	Programmable Logic Controller
<b>DSP</b>	Digital Signal Processor
<b>RTU</b>	Remote Terminal Unit
<b>MTU</b>	Master Terminal Unit
<b>Lm35</b>	Temperature Sensors
<b>F</b>	Gas Flow (L/min)
<b>DOC</b>	Digital Output Code of the Sensor
<b>D</b>	Sensed Distance (cm)
<b>R<sup>2</sup></b>	Coefficient of Determination
<b>V</b>	Output Voltage of the Sensor
<b>ME</b>	Maximum Error
<b>MAE</b>	Mean Absolute Error
<b>RMSE</b>	Root Mean Square Error

**HMI** Human–Machine Interface  
**LCA** Life Cycle Assessment  
**PC** personal computer

## REFERENCES

- Alvarez ML, Sarachaga I, Burgos A, Estévez E, Marcos M. A Methodological Approach to Model-Driven Design and Development of Automation Systems. *IEEE Transactions on Automation Science and Engineering* 2018;15(1):67-79.
- Mahalik NP, Nambiar AN. Trends in food packaging and manufacturing systems and technology. *Trends in food science & technology*. 2010;21(3):117-128.
- Mahalik NP. Advances in packaging methods, processes and systems. *Challenges* 2014;5(2):374-89.
- Caldwell DG. Robotics and automation in the food industry," 1518 Walnut Street, Suite 1100, Philadelphia, PA 19102-3406, USA, Woodhead Publishing, 2013.
- Kumar A, Rani, P. Automation of Beverage Vending Machine using PLC and SCADA. *An International Journal of Engineering & Technology* 2016; 3(5): 78-84.
- Kulkarni SL, Elango M. Development of PLC based controller for bottle filling machine. *International Journal of Innovations in Engineering Research and Technology* 2016;3(4) 1-10.
- Singh B, Mathew L, Patel S. Design and Implementation of Smart SCADA in Sugar Mill using LabVIEW. *European Journal of Advances in Engineering and Technology*. 2015;2(10): 61-5.
- Lima J, Moreira JF, Sousa RM. Remote supervision of production processes in the food industry. In *Industrial Engineering and Engineering Management (IEEM)*, 2015 IEEE International Conference on 2015 Dec 6 (pp. 1123-1127). IEEE.
- Jain P, Nithiyanthan K, Raghuraman R, Kasilingam G. Logixpro Based Scada Simulations Model for Packaging System in Dry ICE Plant. *International Journal of Electrical and Computer Engineering* 2015;5(3):443-53.
- Sinha S, Banerjee D, Mandal N, Sarkar R, Bera SC. Design and implementation of real-time flow measurement system using Hall probe sensor and PC-based SCADA. *IEEE Sensors Journal* 2015;15(10):5592-6000.
- Catania P, Vallone M, Pipitone F, Inglese P, Aiello G, La Scalia G. An oxygen monitoring and control system inside a malaxation machine to improve extra virgin olive oil quality. *Biosystems Engineering* 2013;114(1):1-8.
- Szymenderski J, Typańska D. Control model of energy flow in agricultural biogas plant using SCADA software. In *Computational Problems of Electrical Engineering (CPEE)*, 2016 17th International Conference 2016 Sep 14 (pp. 1-4). IEEE.
- Aziz IA, Ismail MJ, Haron NS, Mehat M. Remote monitoring using sensor in greenhouse agriculture. In *Information Technology, 2008. ITSIM 2008. International Symposium on 2008 Aug 26 (Vol. 4, pp. 1-8)*. IEEE.
- Bhutada S, Shetty S, Malye R, Sharma V, Menon S, Ramamoorthy R. Implementation of a fully automated greenhouse using SCADA tool like LabVIEW. In *Advanced Intelligent Mechatronics. Proceedings, 2005 IEEE/ASME International Conference on 2005 Jul 24 (pp. 741-46)*. IEEE.
- Ramesh Babu D, Gayatri N, Issac Prasad P, Rao SJM, Rao KVN. Automatic systems for controlling fruit movement, grading and storing under low temperature controlled atmosphere storage. *International Journal of Mechanical and Production* 2020;10:4541-56.
- Yu X, Wu P, Han W, Zhang Z. A remote SCADA system for keeping fruits and vegetables fresh with ozone. *Journal of Food, Agriculture and Environment* 2013;11(2):187-192.
- Mahalik NP. Advances in packaging methods, processes and systems. *Challenges* 2014,5(2):374-89.
- Wandelen CV. Modified Atmosphere Packaging Machinery Selection and Specification. *Modified Atmosphere Packaging for Fresh-Cut Fruits and Vegetables* 2011:219-28.
- Freddi A, Salmon M, Freddi A, Salmon M. Design of a Packaging Machine: General Description and Conceptualization. *Design Principles and Methodologies: From Conceptualization to First Prototyping with Examples and Case Studies* 2019:205-37.
- Parry RT. Principles and applications of modified atmosphere packaging of foods. Springer Science & Business Media; 2012.
- Moreira F, Sousa R. Automatic Production Systems (in Portuguese), pedagogical publication, University of Minho, 2013.
- Sebestyen G, Nicoara D, Rusu M, Buzdugan L, Cerghizan M, Saplacan G. Supervisory control and quality assurance in food industry. In *Automation, Quality and Testing, Robotic. AQTR 2008. IEEE International Conference (Vol. 1, pp. 195-199)*. IEEE.
- Mahalik NP, Yen M. Extending fieldbus standards to food processing and packaging industry: A review. *Computer Standards & Interfaces* 2009;31(3):586-98.
- Kargwal R, Garg MK, Singh VK, Garg R, Kumar N. Principles of modified atmosphere packaging for shelf life extension of fruits and vegetables: An overview of storage conditions. *IJCS* 2020;8(3): 2245-52.
- Transtrum MK, Sethna JP. Improvements to the Levenberg-Marquardt algorithm for nonlinear least-squares minimization. arXiv preprint arXiv 2012; 1201.5885.

Acknowledgment: This work was financially supported by the Iran National Science Foundation (INSF) (Research Project Reference Number: 9230796).

Mohammad Reza Seifi:  <https://orcid.org/0000-0002-8296-3489>

Reza Alimardani:  <https://orcid.org/0000-0002-9756-3373>

Seyed Saeid Mohtaseb:  <https://orcid.org/0000-0002-4031-1095>

Hossein Mobli:  <https://orcid.org/0000-0003-3822-8804>

Maumoud Soltani Firouz:  <https://orcid.org/0000-0001-9155-1016>



This work is licensed under the Creative Commons BY-NC-ND 4.0 license.

## NEURAL CONTROL OF A ROBOTIC MANIPULATOR IN CONTACT WITH A FLEXIBLE AND UNCERTAIN ENVIRONMENT

Piotr GIERLAK\* 

\*Faculty of Mechanical Engineering and Aeronautics, Department of Applied Mechanics and Robotics  
Rzeszow University of Technology, al. Powstańców Warszawy 12, 35-959 Rzeszów, Poland

[pgierlak@prz.edu.pl](mailto:pgierlak@prz.edu.pl)

*received 13 December 2022, revised 15 February 2023, accepted 27 March 2023*

**Abstract:** This article presents the synthesis of a neural motion control system of a robot caused by disturbances of constraints limiting the movement, which are the result of flexibility and disturbances of the contact surface. A synthesis of the control law is presented, in which the knowledge of the robot's dynamics and the parameters of a susceptible environment is not required. Moreover, the stability of the system is guaranteed in the case of an inaccurately known surface of the environment. This was achieved by introducing an additional module to the control law in directions normal to the surface of the environment. This additional term can be interpreted as the virtual viscotic resistance and spring force acting on the robot. This approach ensured the self-regulation of the robot's interaction force with the compliant environment, limiting the impact of the geometrical inaccuracy of the environment.

**Key words:** robotics, robot control, nonlinear control systems

### 1. INTRODUCTION

The development of industrial robotics is related to robots performing more and more complex tasks that often require simultaneous execution of a desired trajectory and the interaction force of the end effector with the environment [1-4]. This refers to, among other, tasks regarding the robotisation of mechanical processing. The performance of the above-mentioned tasks is possible with simultaneous movement in one direction and exerting forces on directions perpendicular to them [5-7]. Currently, two basic control strategies are widespread in relation to robotisation of machining [8]. In the first strategy, the desired interaction force is maintained at a constant speed of movement, while the motion path of the robot end effector automatically adjusts to the shape of the contact surface. In the second control strategy [8], the robot end effector moves along the desired trajectory, regardless of the shape of the surface. A variable value is the speed, which is reduced with increasing resistance to motion resulting from the surface allowance. However, the force is not a controlled value.

The main disadvantage of the discussed solutions is that the control algorithm takes into account only one criterion, which is either minimising the error of the interaction force or minimising the deviation from the desired motion path. However, in some applications, it is necessary to consider both criteria simultaneously. This applies, for example, to the machining of castings, which have a large change in shape due to the phenomenon of foundry shrinkage [9]. Another example of difficulties is the processing of thin-walled elements, which show high compliance and deformability during machining [10]. Then, taking into account only the pressure force or only the desired path of movement of the robot end effector leads to large errors in the shape of the machined surface. An important and current issue is the development of a robot control strategy that will ensure the appropriate quality of machining, despite the presence of unmodelled effects, such as

inaccurately known geometry of the workpieces and their flexibility [11,12].

This paper deals with the synthesis of the control system in cases of disturbances in the robot's contact with the environment, which result from the flexibility of the surface and the inaccuracy of its description. This article is an extension and development of the topics presented in [6,7,10]. In the paper [10], an adaptive control system was used, which was stable in the case of contact of the robot with a flexible surface, and the algorithm did not require the knowledge of the surface elasticity coefficient. The article [6] solves a similar problem with the use of neural networks, which was aimed at eliminating the need to know the dynamics model of the robot–environment system. In [7], in addition to the flexibility of the contact surface, the possibility of its inaccuracy was taken into account, and the control problem was solved with the use of an adaptive system. Finally, this article deals with control taking into account the flexibility and inaccuracy of the contact surface, and the control system uses an artificial neural network in order to eliminate the need to know the mathematical model of the robot–environment system.

In order to solve the problem, a cooperative control strategy was used, combining two elementary strategies. One of them aims to achieve the desired force and the other aims to implement the desired path of motion of the end effector. In the absence of surface inaccuracy, only the first strategy is active. Otherwise, the second strategy is activated with the first strategy running simultaneously. This leads to the “competition” of the two strategies, which allows the control algorithm to include two criteria, rather than simply switching between strategies.

### 2. LITERATURE REVIEW

The issue of position–force control of robots has its genesis in the practical applications of robots for the implementation of pro-



cesses in which the interaction between the robot and the environment is important. The most common applications where this interaction is crucial are robotic machining processes, such as milling [13,14], deburring [9,15], grinding [16,17] and polishing [2,18]. Implementation of the aforementioned processes requires the movement of the tool along a given path, which results from the shape of the machined surface, while exerting pressure on this surface, ensuring contact between the tool and the workpiece. Control algorithms that simultaneously perform position and force control belong to the hybrid group [19,20].

An important element of designing a robot control algorithm for such a task is to formulate an appropriate model of the robot–environment system. In general, various classes of models of both robots and the environment with which the robot interacts are known in the literature. Depending on the purpose of modelling and the significance of the phenomena, the following robot models are distinguished: robots as connections of rigid bodies without the flexibility of joints [21], robots as connections of rigid bodies with the flexibility of joints [22,23] and robots with the flexibility of both joints and links [24,25,26]. Similarly, there are many ways to model the environment with which the robot physically interacts. The simplest models describe the interaction surface as rigid and smooth [27]. In justified cases, flexibility and roughness of surface are taken into account [6,7]. In more complex analyses, surface models are used, described by differential equations that take into account the mass, damping and stiffness of the object with which the robot is in contact [28]. In the control synthesis issues, the models contain the most important features of robot–environment systems and, at the same time, are simple enough to be used to demonstrate the stability of a closed system [27].

The formulation of an uncomplicated model of the robot–environment system allows for the decomposition of the problem into a control task on directions tangential to the interaction surface and on normal directions. In tangential directions, the positional control is responsible for moving the robot tool along the

path. In normal directions, the interaction force of the robot with the surface is controlled. In the position control part, linearisation is typically used in the inner loop, and the outer loop uses a PID (proportional–integral–derivative), PD (proportional–derivative) or PI (proportional–integral) controller. Feedback linearisation can be implemented, e.g., in the form of calculated torque [27], adaptive control [28], neural control [29], fuzzy control [30], neuro-fuzzy control [31], reinforcement learning [32] and many others. In the part of the system responsible for controlling the force, a simple proportional or proportional integral controller is usually used, sometimes in the form of a fuzzy controller.

There is a significant number of works devoted to the use of neural networks in the control of robots interacting with the environment. Neural networks are used, for example, to compensate for the non-linearity of the robot [33] or in the structure of the state observer [34]. Numerous works concern the use of fuzzy or neuro-fuzzy systems in the positional control of robots [31,35]. In order to increase the efficiency of controller tuning, advanced methods are used, using, for example, genetic algorithms [36] or particle swarm optimisation [37]. When it comes to hybrid position–force control of robots using neuro-fuzzy systems, the basics of the theory are included in the article [38], while more advanced issues taking into account the uncertainty of the environment or robot kinematics are described in papers [12,39,40]. Among the cited works, only [39] presents the results of the experimental verification of the solution. Usually, only theoretical and simulation results are described, especially for more advanced solutions.

### 3. APPROACH TO THE PROBLEM

The article proposes an approach to the problem of robot control in interaction with the environment, which consists in combining two elementary control strategies (Fig. 1).

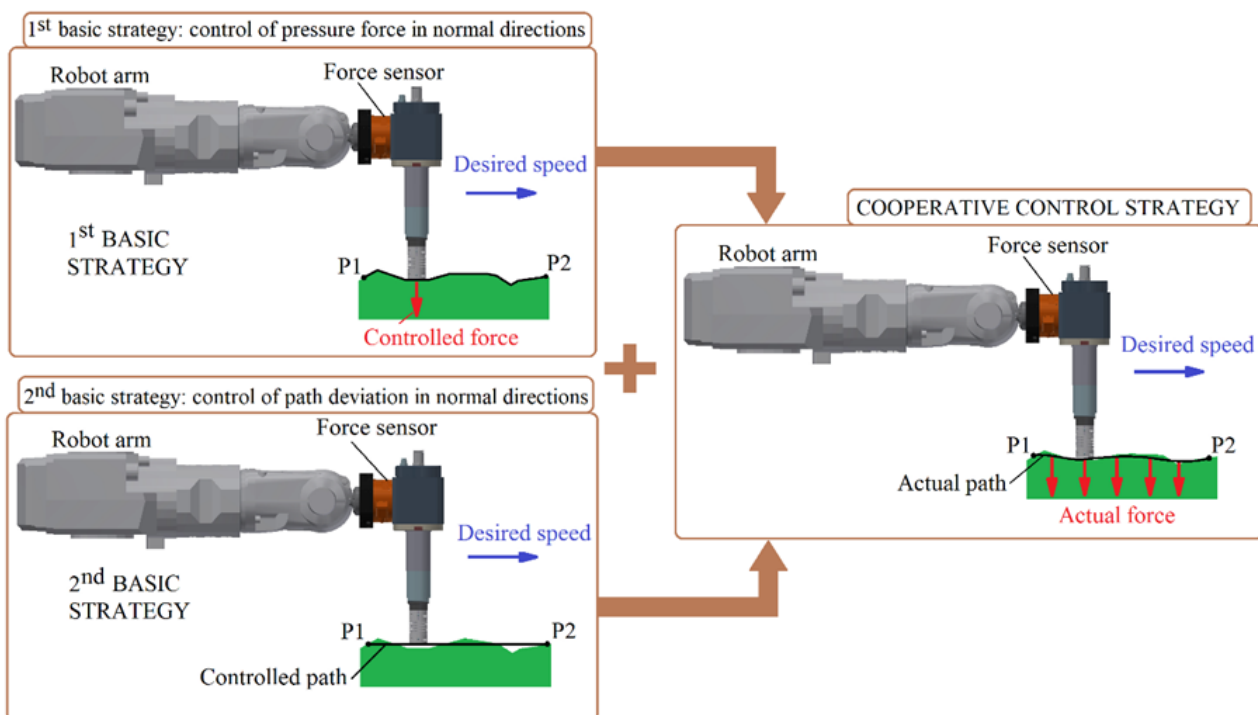


Fig. 1. Cooperative strategy for robot control



The task of the first one is to maintain a given interaction force at a given speed of movement. As a result, the path of the robot's end effector adjusts itself to the shape of the contact surface. The task of the second strategy is to execute the given motion path of the robot's end effector, regardless of the actual shape of the machined surface. The cooperative combination of these strategies leads to their interaction in such a way that the goals of each strategy are realised in a "soft" manner. The resulting operation of the control system may be closer to the first or second strategy depending on the adopted cooperation coefficient, which is responsible for adjusting the priority of force or position execution.

If the adopted surface model coincides with the actual shape of the machined surface, the first elementary strategy (Fig. 2a) is implemented, consisting in maintaining the given force in the direction normal to the surface. It is obvious that in the event of an inaccuracy of the machined surface in relation to the adopted surface model, and this is most often the case in fact, the operation of the elementary force control strategy will be weakened in favour of the strategy of minimising the deviation of the robot's end effector from the given path. Thus, neither strategy will be fully implemented. The activation of the second strategy causes the system to operate in such a way that in the place where the real surface was disturbed, virtual elastic and damping forces acted on the robot's end effector, replacing the interaction surface (Fig. 2b). Thanks to this, the end effector is attracted to the given path of movement.

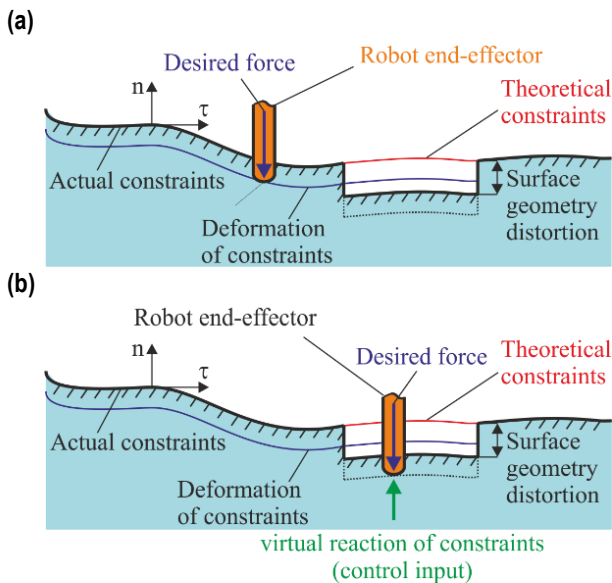


Fig. 2. The activity of the control strategy in the case of distortions in the surface: (a) movement on the surface without distortion and (b) movement on the distorted surface

The combination of strategies prevents extreme cases of system operation and at the same time ensures a smooth transition between strategies. It takes place automatically depending on the condition of the machined surface, which is an unquestionable advantage of the proposed method.

#### 4. DYNAMICS OF THE ROBOT – FLEXIBLE ENVIRONMENT SYSTEM

In industrial practice, robotic tasks are usually not defined in the robot's configuration space but in a task space, which is usual-

ly Cartesian space. Therefore, in the further discussion, the description of the robot's dynamics in the task space was used, which has the following form [10]:

$$A(q)E\ddot{\theta} + H(q, \dot{q})E\dot{\theta} + B(q, \dot{q}) + \Psi(q, t) = U + \lambda \quad (1)$$

where  $q \in R^n$  is the vector of generalised coordinates (joint coordinates),  $\theta \in R^m$  is the vector of task variables,  $A(q) \in R^{m \times m}$  is inertia matrix,  $H(q, \dot{q}) \in R^{m \times m}$  is the matrix of coefficients of centrifugal and Coriolis forces,  $B(q, \dot{q}) \in R^m$  is the vector of friction and gravitational forces,  $\Psi(q, t) \in R^m$  is the vector of limited interference,  $U \in R^m$  is the vector of control inputs,  $\lambda \in R^m$  is the vector of interaction forces,  $E \in R^{m \times m}$  is the matrix of system vulnerability and  $m$  is the dimension of the task space (it was assumed that  $m = n$ ).

The vector of interaction forces can be represented by two components:

$$\lambda = \begin{bmatrix} F_{e\tau} \\ F_{en} \end{bmatrix} \quad (2)$$

where  $F_{en} \in R^r$  is the vector of normal forces and  $F_{e\tau} \in R^{m-r}$  is the vector of tangent forces. Similarly, the vector of task variables can be expressed with two components:

$$\theta = \begin{bmatrix} c_\tau \\ F_{en} \end{bmatrix} \in R^m \quad (3)$$

where  $c_\tau \in R^{m-r}$  is the vector of tangential displacement. Decomposition in Eqs (2) and (3) results from the decomposition of the  $m$ -dimensional task space  $\{C\}$  into  $r$ -dimensional normal subspace  $\{N\}$  and  $(m - r)$  - dimensional tangential subspace  $\{T\}$ . The vulnerability of the interaction surfaces, which limits the movement of the robot's end effector, is included in the dynamics description and the system vulnerability matrix has the following form:

$$E = \begin{bmatrix} I_{(m-r) \times (m-r)} & 0 \\ 0 & P_e \end{bmatrix} \in R^{m \times m} \quad (4)$$

where  $P_e = R^{r \times r}$  is the environmental vulnerability matrix. Eq. (1) describes the dynamics of the system in task coordinates using kinematic motion parameters in tangent directions and forces in normal directions. Such a description facilitates the definition and implementation of the task, i.e., the execution of movement on the surface with the pressure force. Introducing the interaction forces into the vector of task variables enables effective control of these forces with the use of techniques known in the field of position control. The paper [10] provides information on the transformation of the dynamic description from the robot's configuration space to the task space.

#### 5. NEURAL POSITION/FORCE TRACKING CONTROL

This section proposes a cooperative control strategy, which combines two different control strategies on the basis of cooperation (Fig. 3). The purpose of this approach is to supplement one strategy by the other in situations in which a given elementary strategy applied individually leads to unfavourable behaviour of the robot. The neural control algorithm presented in this section does not require the knowledge of the system dynamics model. Implementation of a cooperative control strategy requires the assumption of nominal contact surface geometry (theoretical constraints), desired trajectory of motion and force and knowledge of the current position of the robot's end effector.

**Assumption 1:** For dynamical system (1), the following trajectories are given:

- limited trajectory of motion of the robot's end effector in the tangential plane  $c_{\tau d}(t) \in R^{m-r}$ ,  $\dot{c}_{\tau d}(t)$ ,  $\ddot{c}_{\tau d}(t)$ ,
- limited force trajectory in normal directions  $F_{end}(t) \in R^r$ ,  $\dot{F}_{end}(t)$ ,  $\ddot{F}_{end}(t)$ ,
- limited nominal trajectory of motion of the robot's end effector in normal directions  $c_{n\ nom}(t) \in R^r$ ,  $\dot{c}_{n\ nom}(t)$ ,  $\ddot{c}_{n\ nom}(t)$ , which results from the assumed surface shape.

Assumption 1 concerning simultaneous knowledge of the description of the nominal motion path and the force trajectory in the same direction (normal) is a significant difference in comparison to the assumptions formulated in typical issues related to position/force control. It also allows the definition of a modified control objective, by an appropriate definition of the filtered tracking error, which in the case of taking into account the inaccuracy of constraints must be different than in the case of knowing the environment surface or omitting its inaccuracy.

To define the control objective, control errors were introduced, where

$$\tilde{c}_{\tau} = c_{\tau d} - c_{\tau} \tag{5}$$

is the error of motion in the tangential plane, and

$$\tilde{F}_{en} = F_{end} - F_{en} \tag{6}$$

is the error of force in the normal direction. An auxiliary variable  $\delta \in R^r$  is defined such that

$$\delta = c_n - c_{n\ nom} - \delta_0 \tag{7}$$

which is related to the difference between the nominal position of the robot end effector  $c_{n\ nom}$  resulting from the theoretically existing constraints and the real position  $c_n$  in the normal direction (Fig. 3).

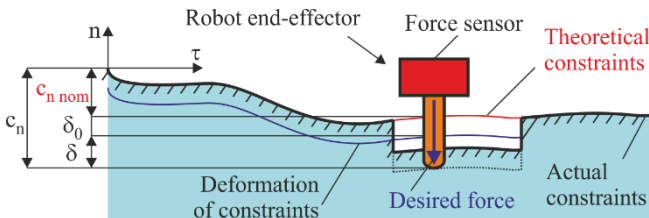


Fig. 3. Variables related to the position of the robot's end effector in the normal direction

That is,  $\delta$  is the deviation of the end effector from the assumed constraints in the normal direction. In detail, it should be added that the expression  $\delta_0 = K_e^{-1}F_{end}$  is the predicted surface deformation derived from the pressure force,  $F_{en}$ . With high surface rigidity, this deformation is negligible.

To achieve the control objective, a filtered tracking error was introduced:

$$s = \begin{bmatrix} s_{\tau} \\ s_n \end{bmatrix} \tag{8}$$

in which

$$s_{\tau} = \dot{\tilde{c}}_{\tau} + \Lambda_{\tau}\tilde{c}_{\tau} \tag{9}$$

$$s_n = \dot{\tilde{F}}_{en} - w_{\delta}\dot{\delta} + \Lambda_n(\tilde{F}_{en} - w_{\delta}\delta) \tag{10}$$

where  $\Lambda_{\tau} \in R^{(m-r) \times (m-r)}$  and  $\Lambda_n \in R^{r \times r}$  are diagonal gain matrices and  $w_{\delta} \in R^{r \times r}$  is the cooperation gain matrix. Expression (10) introduces a new approach to the problem of control in

the normal direction to the surface of constraints. Compared with the approach presented in papers [6,10], in which the generalised error  $s_n$  for normal directions depends on the force error and its derivative, here it also depends on deviation  $\delta$  from the desired nominal motion path in the normal direction and from the derivative  $\dot{\delta}$ .

Eqs (8)–(10) make it possible to write the description of the dynamics as a function of the filtered tracking error:

$$A(q)E\dot{s} = -H(q, \dot{q})Es + f + \Psi(q, t) - U - \lambda \tag{11}$$

with the non-linear part  $f \in R^m$  dependent on both the robot mathematical model and the environment designated as follows:

$$f = A(q)E\dot{v} + H(q, \dot{q})Ev + B(q, \dot{q}) \tag{12}$$

where there is an auxiliary variable that has the following form:

$$v = \begin{bmatrix} \dot{c}_{\tau d} \\ \dot{F}_{end} - w_{\delta}\dot{\delta} \end{bmatrix} - \begin{bmatrix} \Lambda_{\tau} & 0 \\ 0 & \Lambda_n \end{bmatrix} \begin{bmatrix} \tilde{c}_{\tau} \\ \tilde{F}_{en} - w_{\delta}\delta \end{bmatrix} \tag{13}$$

Next, the control law including the PD controller (term  $K_D s$ ), the non-linearity compensating control  $\hat{f} \in R^m$ , the term compensating the interaction force  $\lambda$  and the robust term  $r \in R^m$  was assumed:

$$U = K_D s + \hat{f} - \lambda - r \tag{14}$$

where  $K_D \in R^{m \times m}$  is a gain matrix such that  $K_D = K_D^T > 0$ , and function  $\hat{f}$  approximates  $f$ . Regarding the first control part, it is possible to decompose the  $K_D$  matrix according to the equation:

$$K_D = \begin{bmatrix} K_{D\tau} & 0 \\ 0 & K_{Dn} \end{bmatrix} \tag{15}$$

where  $K_{D\tau} \in R^{(m-r) \times (m-r)}$  and  $K_{Dn} \in R^{r \times r}$  are diagonal gain matrices.

The part  $\hat{f}$  was introduced into the control law of Eq. (14) to compensate for the non-linear function  $f$ , which depends on, inter alia, the inaccuracy of the surface  $\delta$ , not just from the force error  $\tilde{F}_{en}$ . The function  $f$  can be decomposed into two parts, one of which corresponds to the tangential directions and the other the normal direction:

$$f = \begin{bmatrix} f_{\tau} \\ f_n \end{bmatrix} \tag{16}$$

The constituent functions  $f_{\tau}$  and  $f_n$  described by Eq. (17) can be approximated with the help of various techniques. The nonlinear components  $f_{\tau}$  and  $f_n$  can be written as outputs from ideal RVFL (Random Vector Functional Link) neural networks with limited approximation errors as follows [41,42]:

$$f = \begin{bmatrix} f_{\tau} \\ f_n \end{bmatrix} = \begin{bmatrix} W_{\tau}^T \Phi_{\tau}(x_{\tau}) + \varepsilon_{\tau}(x_{\tau}) \\ W_{n1}^T \Phi_{n1}(x_{n1}) + \varepsilon_{n1}(x_{n1}) \\ \vdots \\ W_{ni}^T \Phi_{ni}(x_{ni}) + \varepsilon_{ni}(x_{ni}) \\ \vdots \\ W_{nr}^T \Phi_{nr}(x_{nr}) + \varepsilon_{nr}(x_{nr}) \end{bmatrix} \tag{17}$$

where  $x_{\tau}$  and  $x_{ni}$  are network input signals vectors,  $W_{\tau}$  and  $W_{ni}$  are ideal output weights matrices,  $\Phi_{\tau}(\cdot)$  and  $\Phi_{ni}(\cdot)$  are neurons activation functions vectors and  $\varepsilon_{\tau}$  and  $\varepsilon_{ni}$  are vectors of errors of function mapping by networks that  $\|\varepsilon_{\tau}\| \leq \varepsilon_{b\tau}$  and  $|\varepsilon_{ni}| \leq \varepsilon_{bni}$  where  $\varepsilon_{b\tau} > 0$ ,  $\varepsilon_{bni} > 0$ . If neuron activation functions are selected in the form of a basic functions' group, then the network with ideal limited weights has the feature of approximation of any

function defined on a compact set with a finite number of discontinuity points. Since network ideal weights are unknown, function estimate Eq. (19) should be used, in the following form:

$$\hat{f} = \begin{bmatrix} \hat{f}_\tau \\ \hat{f}_n \end{bmatrix} = \begin{bmatrix} \hat{W}_\tau^T \Phi_\tau(x_\tau) \\ \hat{W}_{n1}^T \Phi_{n1}(x_{n1}) \\ \vdots \\ \hat{W}_{ni}^T \Phi_{ni}(x_{ni}) \\ \vdots \\ \hat{W}_{nr}^T \Phi_{nr}(x_{nr}) \end{bmatrix} \quad (18)$$

where  $\hat{W}_\tau$  and  $\hat{W}_{ni}$  are network ideal weights estimates. Each nonlinear function  $f_n$  was decomposed into functions  $f_{ni}$ , each of which corresponds to the normal  $i$ -th direction and is approximated by a separate neural network. The decomposition was performed in order to facilitate the proving of closed-loop system stability.

Assuming the control law of Eq. (14) and taking into account relationships of Eqs (16)–(18), a description of a closed system was obtained in the form:

$$AE\dot{s} = -HEs - K_D s + r + \begin{bmatrix} \tilde{W}_\tau^T \Phi_\tau(x_\tau) \\ \tilde{W}_{n1}^T \Phi_{n1}(x_{n1}) \\ \vdots \\ \tilde{W}_{ni}^T \Phi_{ni}(x_{ni}) \\ \vdots \\ \tilde{W}_{nr}^T \Phi_{nr}(x_{nr}) \end{bmatrix} + \begin{bmatrix} \varepsilon_\tau(x_\tau) \\ \varepsilon_{n1}(x_{n1}) \\ \vdots \\ \varepsilon_{ni}(x_{ni}) \\ \vdots \\ \varepsilon_{nr}(x_{nr}) \end{bmatrix} + \Psi(q, t) \quad (19)$$

where

$$\tilde{W}_\tau = W_\tau - \hat{W}_\tau \quad (20)$$

$$\tilde{W}_{ni} = W_{ni} - \hat{W}_{ni} \quad (21)$$

are errors of weights estimates.

Appropriate assumptions were made to prove the stability of the control system.

**Assumption 2:** There is limited interference on the dynamic system (1):

$$\Psi(q, t) = \begin{bmatrix} \Psi_\tau(q, t) \\ \Psi_n(q, t) \end{bmatrix} \quad (22)$$

where  $\Psi_\tau(q, t) \in R^{m-r}$ ,  $\Psi_n(q, t) \in R^r$  and  $b_\tau$ ,  $b_{ni}$  are known constants such that  $\|\Psi_\tau(q, t)\| \leq b_\tau$  and  $\|\Psi_n(q, t)\| \leq b_{ni}$ .

**Assumption 3:** The vector of filtered tracking error in the form of Eq. (8) can be decomposed according to the following equation:

$$s = \begin{bmatrix} s_\tau \\ s_n \end{bmatrix} \quad (23)$$

where  $s_\tau \in R^{m-r}$  and  $s_n = [s_{n1} \dots s_{ni} \dots s_{nr}]^T \in R^r$ .

**Assumption 4:** A robust term can be decomposed in the following way:

$$r = \begin{bmatrix} r_\tau \\ r_n \end{bmatrix} \quad (24)$$

where

$$r_\tau = -\frac{K_\tau}{\|s_\tau\|} s_\tau \quad (25)$$

$$r_{ni} = -K_{ni} \frac{s_{ni}}{|s_{ni}|} \quad (26)$$

and  $K_\tau > b_\tau \geq \|\Psi_\tau(q, t)\|$  and  $K_{ni} > b_{ni} \geq \|\Psi_{ni}(q, t)\|$ .

**Assumption 5:** The weights matrices are limited so that

$$\|W_\tau\|_F \leq W_{\tau \max} \quad (27)$$

$$\|W_{ni}\|_F \leq W_{ni \max} \quad (28)$$

**Assumption 6:** The weights adaptation law takes the form of the equations [43]:

$$\dot{\hat{W}}_\tau = \Gamma_\tau \Phi_\tau(x_\tau) s_\tau^T - k_\tau \|s_\tau\| \Gamma_\tau \hat{W}_\tau \quad (29)$$

$$\dot{\hat{W}}_{ni} = \Gamma_{ni} \Phi_{ni}(x_{ni}) s_{ni} - k_{ni} |s_{ni}| \Gamma_{ni} \hat{W}_{ni} \quad (30)$$

where  $\Gamma_\tau = \Gamma_\tau^T > 0$ ,  $\Gamma_{ni} = \Gamma_{ni}^T > 0$ ,  $k_\tau > 0$  and  $k_{ni} > 0$  are design parameters.

**Theorem 1:** If the system described by Eq. (1) is controlled by Eq. (14) and Assumptions 1–6 are fulfilled, the filtered tracking errors  $s_\tau$  and  $s_{ni}$  and estimation errors  $\tilde{W}_\tau$  and  $\tilde{W}_{ni}$  are uniformly ultimately bounded with practical limits given by the right-hand side of the Eqs (41)–(44), respectively.

**Proof of Theorem 1.** The description of the system given by Eq. (1) was transformed into a description in terms of the filtered tracking error of Eq. (11), and after the introduction of the control law of Eq. (14), a closed-loop system description [Eq. (20)] was obtained, including disturbances and a robust term. To demonstrate the stability of the closed system, the Lyapunov stability theory was used. The following function was assumed:

$$V = \frac{1}{2} s^T E^T A(q) E s + \frac{1}{2} \text{tr}[\tilde{W}_\tau^T \Gamma_\tau^{-1} \tilde{W}_\tau] + \frac{1}{2} \sum_{i=1}^r P_{eii} \text{tr}[\tilde{W}_{ni}^T \Gamma_{ni}^{-1} \tilde{W}_{ni}] \quad (31)$$

where  $P_{eii}$  is an element of the matrix of environmental vulnerability. By calculating the derivative of function Eq. (31) with respect to time and taking into account Eq. (19), the following was obtained:

$$\dot{V} = s^T E^T (-K_D s + r + \Psi(q, t)) + s^T E^T \begin{bmatrix} \tilde{W}_\tau^T \Phi_\tau(x_\tau) \\ \tilde{W}_{n1}^T \Phi_{n1}(x_{n1}) \\ \vdots \\ \tilde{W}_{ni}^T \Phi_{ni}(x_{ni}) \\ \vdots \\ \tilde{W}_{nr}^T \Phi_{nr}(x_{nr}) \end{bmatrix} + \begin{bmatrix} \varepsilon_\tau(x_\tau) \\ \varepsilon_{n1}(x_{n1}) \\ \vdots \\ \varepsilon_{ni}(x_{ni}) \\ \vdots \\ \varepsilon_{nr}(x_{nr}) \end{bmatrix} + \text{tr}[\tilde{W}_\tau^T \Gamma_\tau^{-1} \dot{\tilde{W}}_\tau] + \sum_{i=1}^r P_{eii} \text{tr}[\tilde{W}_{ni}^T \Gamma_{ni}^{-1} \dot{\tilde{W}}_{ni}] \quad (32)$$

where the following property [10] was used:

$$s^T E^T [A(q) - 2H(q, \dot{q})] E s = 0 \quad (33)$$

Given that  $E^T = E$  and taking into account Eq. (8), the fourth element of Eq. (32) was transformed into the following form:

$$s_\tau^T \tilde{W}_\tau^T \Phi_\tau(x_\tau) + \sum_{i=1}^r s_{ni} P_{eii} \tilde{W}_{ni}^T \Phi_{ni}(x_{ni}) \quad (34)$$

The disturbance vector and robust control vector were also decomposed as follows:

$$\Psi(q, t) = [\Psi_\tau^T(q, t) \quad \Psi_{n1}(q, t) \quad \dots \quad \Psi_{ni}(q, t) \quad \dots \quad \Psi_{nr}(q, t)]^T \quad (35)$$

$$r = [r_\tau^T \quad r_{n1} \quad \dots \quad r_{ni} \quad \dots \quad r_{nr}]^T \quad (36)$$

Taking into account Eqs (4), (15), (23) and (34)–(36) and the weights adaptation laws of Eqs (29) and (30), the following equation was obtained:

$$\dot{V} = -s_\tau^T K_{D\tau} s_\tau - s_n^T P_e K_{Dn} s_n + k_\tau \|s_\tau\| \text{tr}[\tilde{W}_\tau^T \hat{W}_\tau] + \sum_{i=1}^r P_{eii} k_{ni} |s_{ni}| \text{tr}[\tilde{W}_{ni}^T \hat{W}_{ni}] + s_\tau^T [\varepsilon_\tau(x_\tau) + \Psi_\tau(q, t)] + s_\tau^T r_\tau + \sum_{i=1}^r s_{ni} P_{eii} (\varepsilon_{ni}(x_{ni}) + \Psi_{ni}(q, t)) + \sum_{i=1}^r s_{ni} P_{eii} r_{ni} \quad (37)$$

The ideal weights of neural networks are by definition limited,

which means that they meet the conditions (28) and (29), which were used for the transformations:

$$tr[\tilde{W}_\tau^T \tilde{W}_\tau] = tr[\tilde{W}_\tau^T (W_\tau - \tilde{W}_\tau)] \leq \|\tilde{W}_\tau\|_F W_{\tau max} - \|\tilde{W}_\tau\|_F^2 \quad (38)$$

$$tr[\tilde{W}_{ni}^T \tilde{W}_{ni}] = tr[\tilde{W}_{ni}^T (W_{ni} - \tilde{W}_{ni})] \leq \|\tilde{W}_{ni}\|_F W_{ni max} - \|\tilde{W}_{ni}\|_F^2 \quad (39)$$

Taking into account network weight limitations, robust term elements of Eqs (25) and (26), Eq. (37) was transformed into the form:

$$\dot{V} \leq -\|s_\tau\| [K_{D\tau min} \|s_\tau\| + k_\tau \|\tilde{W}_\tau\|_F (\|\tilde{W}_\tau\|_F - W_{\tau max}) - \varepsilon_{b\tau}] - \sum_{i=1}^r P_{eii} |s_{ni}| [K_{Dni} |s_{ni}| + k_{ni} \|\tilde{W}_{ni}\|_F (\|\tilde{W}_{ni}\|_F - W_{ni max}) + \varepsilon_{bni}] \quad (40)$$

The function  $\dot{V}$  is negative if the expressions in square brackets are positive. They are positive if the errors meet the following inequalities:

$$\|s_\tau\| > \frac{k_\tau W_{\tau max}^2 + 4\varepsilon_{b\tau}}{4K_{D\tau min}} \equiv b_{s\tau} \quad (41)$$

$$|s_{ni}| > \frac{k_{ni} W_{ni max}^2 + 4\varepsilon_{bni}}{4K_{Dni}} \equiv b_{sni} \quad (42)$$

or

$$\|\tilde{W}_\tau\|_F > \frac{W_{\tau max}}{2} + \sqrt{\frac{W_{\tau max}^2}{4} + \frac{\varepsilon_{b\tau}}{k_\tau}} \equiv b_{W\tau} \quad (43)$$

$$\|\tilde{W}_{ni}\|_F > \frac{W_{ni max}}{2} + \sqrt{\frac{W_{ni max}^2}{4} + \frac{\varepsilon_{bni}}{k_{ni}}} \equiv b_{Wni} \quad (44)$$

It follows that  $\dot{V}$  is negative outside the compact sets defined by Eqs (41)–(44). According to the extension of the standard Lyapunov theory, it can be concluded that  $\|s_\tau\|$ ,  $|s_{ni}|$ ,  $\|\tilde{W}_\tau\|_F$  and  $\|\tilde{W}_{ni}\|_F$  are uniformly ultimately bounded, and the control system is stable. Therefore, the filtered tracking error  $s$  and its derivative are limited, similar to the matrices of weight estimates  $\tilde{W}_\tau$  and  $\tilde{W}_{ni}$ . □

## 6. SIMULATION RESULTS

The manipulator model was used in the simulation tests; the diagram of which is shown in Fig. 4. Its arm has three links, used to achieve the position, and the other links responsible for orientation are not used in these studies. Details on kinematics, dynamics, parameters and path planning used in the simulation are given in Appendix A in a paper [7].

End effector of the robot (point D) should move on a surface lying in the plane parallel to the plane  $x_0 y_0$  and simultaneously exert pressure force perpendicular to the surface. The Fig. 5 shows the desired motion path of point D (Figs. 5a,b) and the desired velocity (Fig. 5c). To test the properties of the control system, the simulation was carried out assuming an inaccuracy in the surface, consisting in a depression in the surface of 0.001 m, which is shown in Fig. 6a. Changing the surface can also be represented as a change of surface profile in terms of time during the motion of the end effector (Fig. 6b).

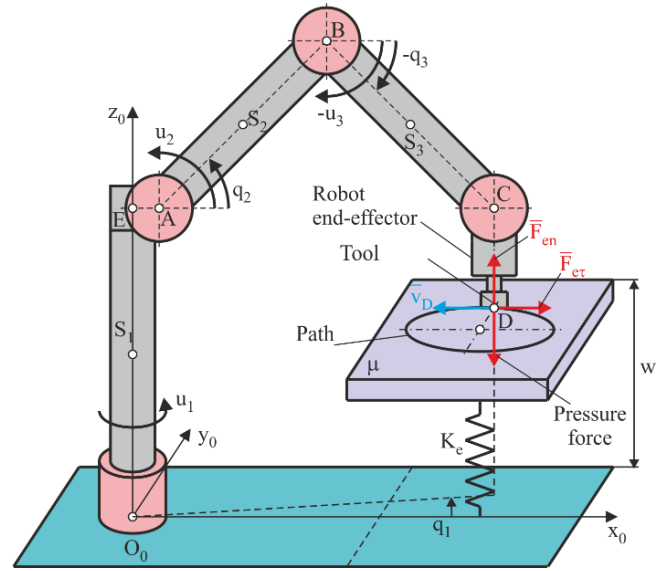


Fig. 4. Model of a robotic manipulator in contact with a flexible environment:  $O_0E = d_1$ ,  $EA = l_1$ ,  $AB = l_2$ ,  $BC = l_3$  and  $CD = d_5$  are geometrical parameters characterising the robot arm;  $q_1$ ,  $q_2$  and  $q_3$  are angles of link rotation assumed as generalised coordinates;  $u_1$ ,  $u_2$  and  $u_3$  are input moments;  $K_e$  is stiffness coefficient and  $\mu$  is coefficient of dry friction

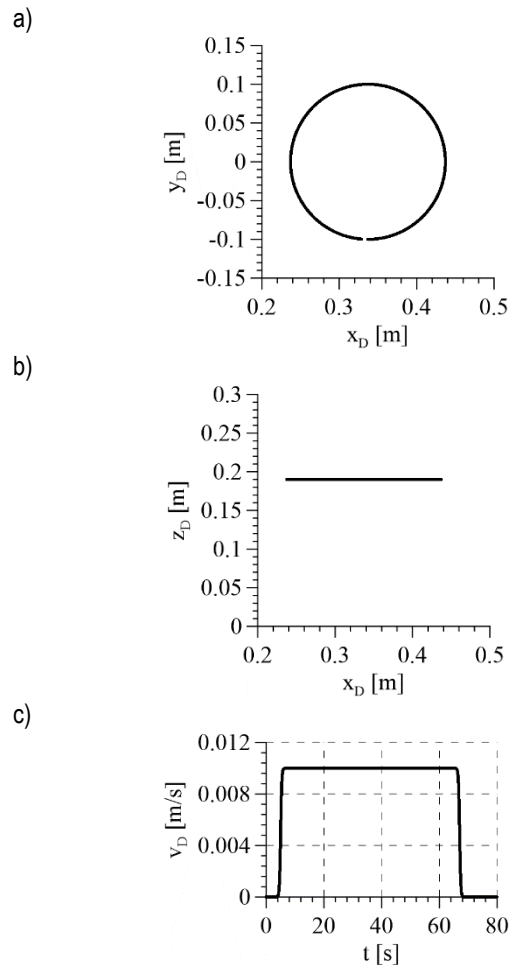


Fig. 5. The desired motion: (a) motion path of point D in the xy plane; (b) motion path of point D in the xz plane and (c) the desired velocity of motion of point D



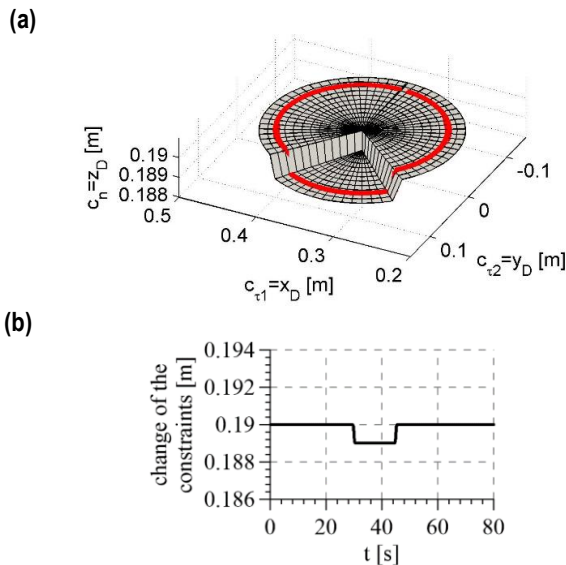


Fig. 6. Disruption of the surface of constraints: (a) defect in the surface and (b) change of the surface of constraints in time along the desired motion path

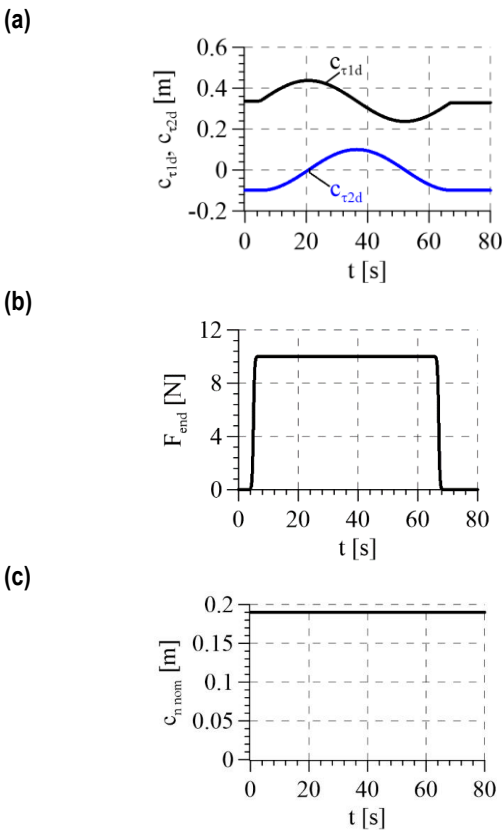


Fig. 7. The desired trajectory: (a) coordinates of point D; (b) pressure force and (c) nominal coordinate of point D in normal direction

The desired positional trajectory is shown in Fig. 7a, the desired force trajectory is shown in Fig. 7b and the nominal coordinate of point D in the normal direction is shown in Fig. 7c. The developed control algorithm requires the nominal trajectory of motion in the normal direction  $c_{n,nom}$  to be given. A trajectory deviation from nominal trajectory in the normal direction will activate the second control strategy. Moreover, due to the flexibility of contact surface, it will be deformed proportional to the pressure force.

To implement the robot's task, a control given by Eq. (14) was used in which the gain matrices have the form  $K_D = diag\{K_{D\tau 1}, K_{D\tau 2}, K_{Dn}\}$  and  $\Lambda = diag\{\Lambda_{\tau 1}, \Lambda_{\tau 2}, \Lambda_n\}$ , and in the analysed case,  $w_\delta$  is a one-dimensional coefficient, which determines the behaviour of the system in the presence of surface disturbances. The environmental vulnerability matrix is one dimensional; the vulnerability coefficient is  $P_e = 0.0001$  m/N. In order to compensate for nonlinearities in each of the directions, neural networks with 15 bipolar sigmoid neurons were used. Table 1 shows the parameters of the control system.

Tab. 1. Parameters of control system used in numerical tests

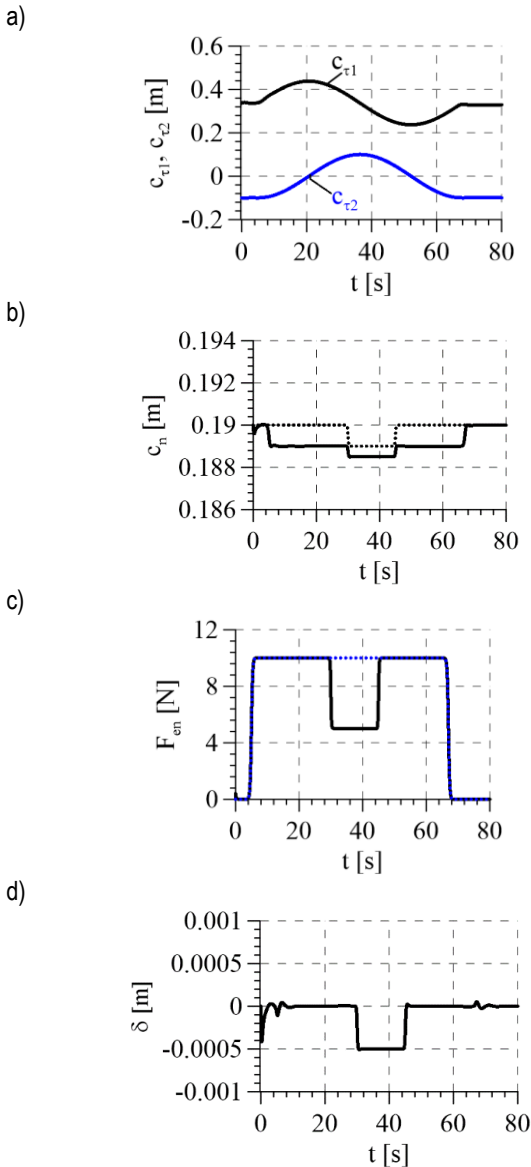
Parameter	Unit	Value
$K_{D\tau 1}$	kg/s	1
$K_{D\tau 2}$	kg/s	1
$K_{Dn}$	s	0.002
$\Lambda_{\tau 1}$	s <sup>-1</sup>	3
$\Lambda_{\tau 2}$	s <sup>-1</sup>	3
$\Lambda_n$	s <sup>-1</sup>	3.5
$k_{\tau 1}$	-	0.1
$k_{\tau 2}$	-	0.1
$k_n$	-	0.1
$K_\tau$	N	0.0001
$K_n$	N	0.00001
$\Gamma_{\tau 1}$	-	$5 \cdot I_{15 \times 15}$
$\Gamma_{\tau 2}$	-	$5 \cdot I_{15 \times 15}$
$\Gamma_n$	-	$0.003 \cdot I_{15 \times 15}$
$w_\delta$	N/m	10,000

Fig. 8a shows the realised trajectory in the tangent directions. The pressure force in the normal direction together with the desired force (indicated by the dashed line) is shown in Fig. 8c. In the area of surface disturbance, the actual pressure force was reduced, which fulfills the goal of the control strategy. The surface profile (dashed line) and surface deformation under pressure force are shown in Fig. 8b. Fig. 8d shows the deviation of the robot end effector from the desired path in the normal direction.

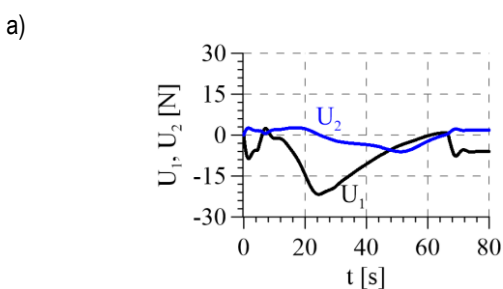
The overall control signals in the task space are shown in Fig. 9. It is clearly seen in Fig. 9b that, in the surface disturbance region, the control changes to reduce the end effector pressure on the surface (from 30 s to 45 s). The components of the control signals resulting from Eq. (14) are shown in Fig. 10: PD control (Fig. 10a,b), compensatory control (Fig. 10c,d), interaction force compensation (Fig. 10e,f) and robust control (Fig. 10g,h). The most sensitive to surface inaccuracies are the PD controls (Fig. 10b) and the control compensating for the effect of normal force (Fig. 10f).

Control errors in tangential directions are shown in Fig. 11a. These are typical waveforms showing oscillations resulting from the acceleration and deceleration phases in the initial and final phases of the movement. The pressure force error (Fig. 11b) also shows oscillations in these movement phases, but more importantly, it increases when the surface disturbance occurs. It is related to the deviation of the robot end effector from the desired motion path (Fig. 8d). The component goals of minimising the force error and minimising the robot's deviation from the path are not fully achieved because they are competitive and cannot be achieved simultaneously in a surface disturbance situation. However, this is consistent with the definition of the filtered tracking

error given by Eq. (10), which indicates that the simultaneous occurrence of a force error and a position error in the normal direction does not contradict the possibility of minimising the filtered tracking error. Such formulation of the control objective is conducive to achieving a “balance” between minimising the force error and minimising the deviation from the nominal surface.



**Fig. 8.** Realised trajectory: (a) coordinates of point D in the tangential directions; (b) coordinates of point D in the normal direction related to surface deformation; (c) pressure force and (d) deviation of robot’s end effector from assumed constraints in the normal direction



b)

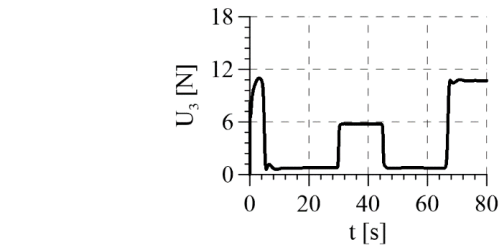
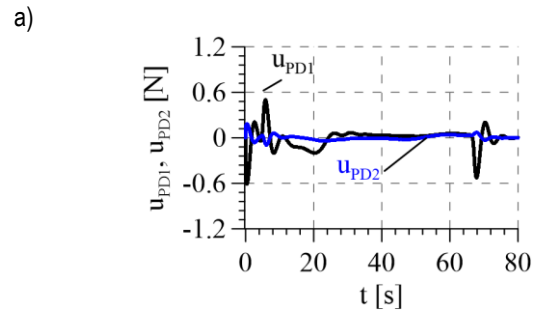
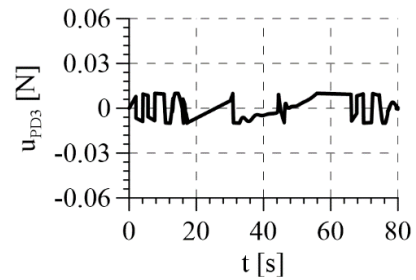


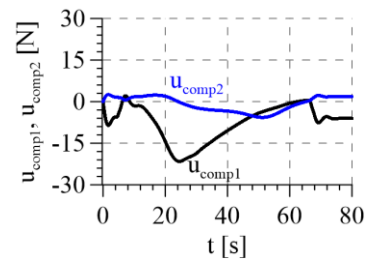
**Fig. 9.** The overall control signals: (a) in tangential directions and (b) in the normal direction



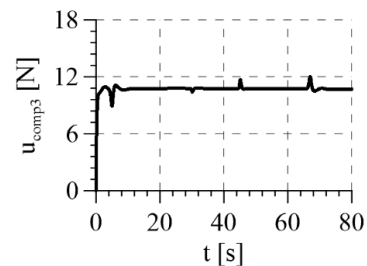
b)



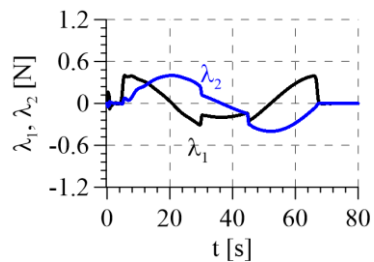
c)



d)



e)



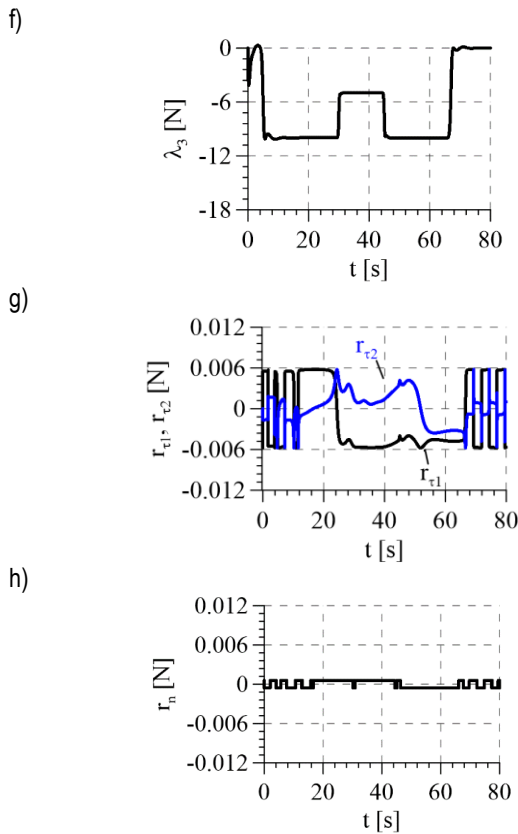


**Fig. 10.** Control signals: (a) PD control in tangential directions, where  $u_{PD1} = K_{D\tau1} s_{\tau1}$  and  $u_{PD2} = K_{D\tau2} s_{\tau2}$ ; (b) PD control in the normal direction, where  $u_{PD3} = K_{Dn} s_n$ ; (c) compensatory control in tangential directions, where  $u_{komp1} = \hat{f}_{\tau1}$  and  $u_{komp2} = \hat{f}_{\tau2}$ ; (d) compensatory control in the normal direction, where  $u_{komp3} = \hat{f}_n$ ; (e) control compensating for the influence of friction forces; (f) control compensating for normal force; (g) robust control in tangential directions and (h) robust control in the normal direction

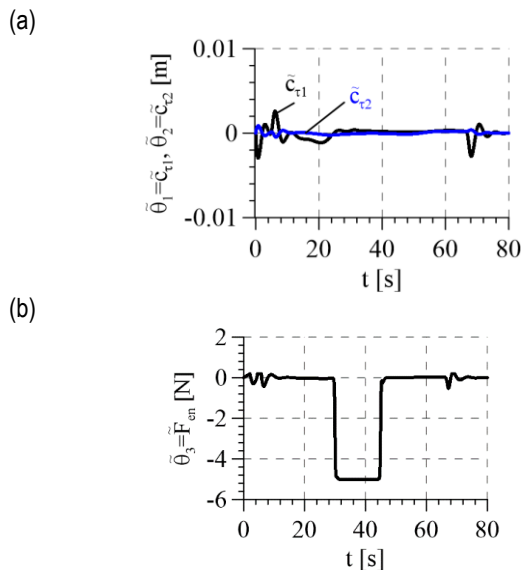


**Fig. 11.** Tracking errors: (a) motion errors in tangential directions and (b) normal force error

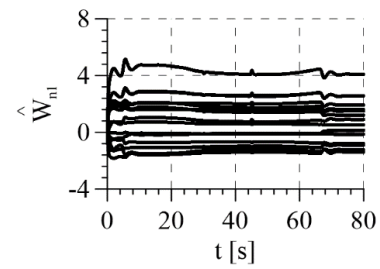


**Fig. 12.** Estimates of the weights of neural network compensating nonlinearities in the normal direction

The estimates of the weights of the neural network generating the compensatory control for the normal direction are shown in Fig. 12. They are limited, according to the stability proof, and their greatest variability occurs in the initial phase of motion, which is also the stage of the most intensive training of the neural network.

## 7. CONCLUSIONS

The article presents the synthesis of the control system for the robot-flexible environment system. The influence of the contact surface disturbance on the robot's behaviour was taken into account. The results of the simulation tests show that the requirements for the control system were met, i.e., firstly, the control system was stable, and secondly, the cooperative control strategy was correctly implemented. By appropriately combining the two elemental control strategies, a compromise is ensured between the execution of the desired pressure force and the maintenance of the desired movement path.

The main contribution of the article is as follows: the use of additional control components, which can be interpreted as reactions of virtual constraints, ensures a self-regulation of the robot's interaction force with a flexible environment, minimising the influence of the geometric inaccuracy of the environment. The presented method was developed for the use in robotic machining of elements with imprecise shape, e.g., thin-walled castings or parts made of plastics, which have low precision and are very flexible. The difficulty in its application in practice is the need to modify standard industrial robot controllers [44].

## REFERENCES

1. Iglesias I, Sebastián MA, Ares JE. Overview of the State of Robotic Machining: Current Situation and Future Potential. *Procedia Eng.* 2015;132:911–7.
2. Tian F, Lv C, Li Z, Liu G. Modeling and control of robotic automatic polishing for curved surfaces. *CIRP J Manuf Sci Technol.* 2016;14:55–64.
3. Denkena B, Bergmann B, Lepper T. Design and optimization of a machining robot. *Procedia Manuf.* 2017;14:89–96.
4. Gracia L, Solanes JE, Muñoz-Benavent P, Valls Miro J, Perez-Vidal C, Tornero J. Adaptive Sliding Mode Control for Robotic Surface Treatment Using Force Feedback. *Mechatronics.* 2018;52:102–18.
5. Vukobratović M, Ekalo Y, Rodič A. How to Apply Hybrid Position/Force Control to Robots Interacting with Dynamic Environment. W: Bianchi G, Guinot JC, Rzymkowski C, Eds. *Romansy 14* [Internet]. Vienna: Springer Vienna; 2002 [cited 13 december 2022]. 249–58. Available from: [http://link.springer.com/10.1007/978-3-7091-2552-6\\_27](http://link.springer.com/10.1007/978-3-7091-2552-6_27)
6. Gierlak P. Position/Force Control of Manipulator in Contact with Flexible Environment. *Acta Mech Autom.* 2019;13(1):16–22.

7. Gierlak P. Adaptive Position/Force Control of a Robotic Manipulator in Contact with a Flexible and Uncertain Environment. *Robotics*. 2021;10(1):32.
8. Application Manual. Force Control for Machining. Zürich: ABB Robotics; 2011.
9. Burghardt A, Szybicki D, Kurc K, Muszyńska M, Mucha J. Experimental Study of Inconel 718 Surface Treatment by Edge Robotic Deburring with Force Control. *Strength Mater*. 2017;49(4):594–604.
10. Gierlak P, Szuster M. Adaptive position/force control for robot manipulator in contact with a flexible environment. *Robot Auton Syst*. 2017;95:80–101.
11. Duan J, Gan Y, Chen M, Dai X. Adaptive variable impedance control for dynamic contact force tracking in uncertain environment. *Robot Auton Syst*. 2018;102:54–65.
12. Ravandi KA, Khanmirza E, Daneshjou K. Hybrid force/position control of robotic arms manipulating in uncertain environments based on adaptive fuzzy sliding mode control. *Appl Soft Comput*. 2018;70:864–74.
13. Guo K, Zhang Y, Sun J. Towards stable milling: Principle and application of active contact robotic milling. *Int J Mach Tools Manuf*. 2022;182:103952.
14. Wang W, Guo Q, Yang Z, Jiang Y, Xu J. A state-of-the-art review on robotic milling of complex parts with high efficiency and precision. *Robot Comput-Integr Manuf*. 2023;79:102436.
15. Chen SC, Tung PC. Trajectory planning for automated robotic deburring on an unknown contour. *Int J Mach Tools Manuf*. 2000;40(7):957–78.
16. Robotic Grinding Process of Turboprop Engine Compressor Blades with Active Selection of Contact Force. *Teh Vjesn - Tech Gaz* [Internet]. 2022 Feb 15 [cited 2022 Dec 7];29(1). Available from: <https://hrcak.srce.hr/269299>.
17. Wang Z, Zou L, Luo G, Lv C, Huang Y. A novel selected force controlling method for improving robotic grinding accuracy of complex curved blade. *ISA Trans*. 2022;129:642–58.
18. Ke X, Yu Y, Li K, Wang T, Zhong B, Wang Z, et al. Review on robot-assisted polishing: Status and future trends. *Robot Comput-Integr Manuf*. 2023;80:102482.
19. Gierlak P. Hybrid Position/Force Control of the SCORBOT-ER 4pc Manipulator with Neural Compensation of Nonlinearities. In: Rutkowski L, Korytkowski M, Scherer R, Tadeusiewicz R, Zadeh LA, Zurada JM, editors. *Artificial Intelligence and Soft Computing* [Internet]. Berlin, Heidelberg: Springer Berlin Heidelberg; 2012 [cited 2020 Nov 21]. p. 433–41. (Hutchison D, Kanade T, Kittler J, Kleinberg JM, Mattern F, Mitchell JC, et al., editors. *Lecture Notes in Computer Science*; vol. 7268). Available from: [http://link.springer.com/10.1007/978-3-642-29350-4\\_52](http://link.springer.com/10.1007/978-3-642-29350-4_52).
20. Gierlak P. Hybrid Position/Force Control in Robotised Machining. *Solid State Phenom*. 2013;210:192–9.
21. Dwivedy SK, Eberhard P. Dynamic analysis of flexible manipulators, a literature review. *Mech Mach Theory*. 2006;41(7):749–77.
22. Do TT, Vu VH, Liu Z. Linearization of dynamic equations for vibration and modal analysis of flexible joint manipulators. *Mech Mach Theory*. 2022;167:104516.
23. Cheng X, Zhang Y, Liu H, Wollherr D, Buss M. Adaptive neural backstepping control for flexible-joint robot manipulator with bounded torque inputs. *Neurocomputing*. 2021;458:70–86.
24. Endo T, Kawasaki H. Bending moment-based force control of flexible arm under gravity. *Mech Mach Theory*. 2014;79:217–29.
25. Thomsen DK, Sørensen R, Balling O, Zhang X. Vibration control of industrial robot arms by multi-mode time-varying input shaping. *Mech Mach Theory*. 2021;155:104072.
26. Cheong J, Youm Y. System mode approach for analysis of horizontal vibration of 3-D two-link flexible manipulators. *J Sound Vib*. 2003;268(1):49–70.
27. Lewis FL, Jagannathan S, Yesildirek A. *Neural network control of robot manipulators and nonlinear systems*. London: Taylor & Francis; 1999. 442 p. (The Taylor & Francis systems and control book series).
28. Wei B. Adaptive Control Design and Stability Analysis of Robotic Manipulators. *Actuators*. 2018;7(4):89.
29. Gupta P, Sinha NK. Intelligent control of robotic manipulators: experimental study using neural networks. *Mechatronics*. 2000;10(1–2):289–305.
30. Yin X, Pan L, Cai S. Robust adaptive fuzzy sliding mode trajectory tracking control for serial robotic manipulators. *Robot Comput-Integr Manuf*. 2021;72:101884.
31. Pham DT, Fahmy AA. NEURO-FUZZY MODELLING AND CONTROL OF ROBOT MANIPULATORS FOR TRAJECTORY TRACKING. *IFAC Proc Vol*. 2005;38(1):170–5.
32. Szuster M, Gierlak P. Approximate Dynamic Programming in Tracking Control of a Robotic Manipulator. *Int J Adv Robot Syst*. 2016;13(1):16.
33. Kumar N, Rani M. Neural network-based hybrid force/position control of constrained reconfigurable manipulators. *Neurocomputing*. 2021;420:1–14.
34. Yang Z, Peng J, Liu Y. Adaptive neural network force tracking impedance control for uncertain robotic manipulator based on nonlinear velocity observer. *Neurocomputing*. 2019;331:263–80.
35. de Campos Souza PV. Fuzzy neural networks and neuro-fuzzy networks: A review the main techniques and applications used in the literature. *Appl Soft Comput*. 2020;92:106275.
36. Refoufi S, Benmahammed K. Control of a manipulator robot by neuro-fuzzy subsets form approach control optimized by the genetic algorithms. *ISA Trans*. 2018;77:133–45.
37. Vijay M, Jena D. PSO based neuro fuzzy sliding mode control for a robot manipulator. *J Electr Syst Inf Technol*. 2017;4(1):243–56.
38. Fanaei A, Farrokhi M. ADAPTIVE NEURO-FUZZY CONTROLLER FOR HYBRID POSITION/FORCE CONTROL OF ROBOTIC MANIPULATORS. *IFAC Proc Vol*. 2005;38(1):127–32.
39. Wang Z, Zou L, Su X, Luo G, Li R, Huang Y. Hybrid force/position control in workspace of robotic manipulator in uncertain environments based on adaptive fuzzy control. *Robot Auton Syst*. 2021 Nov;145:103870.
40. Garcia-Rodriguez R, Parra-Vega V. Normal and tangent force neuro-fuzzy control of a soft-tip robot with unknown kinematics. *Eng Appl Artif Intell*. 2017 Oct;65:43–50.
41. Pao YH, Park GH, Sobajic DJ. Learning and generalization characteristics of the random vector functional-link net. *Neurocomputing*. 1994;6(2):163–80.
42. Kumar N, Panwar V, Sukavanam N, Sharma SP, Borm JH. Neural network based hybrid force/position control for robot manipulators. *Int J Precis Eng Manuf*. 2011;12(3):419–26.
43. Lewis FL, Liu K, Yesildirek A. Neural net robot controller with guaranteed tracking performance. *IEEE Trans Neural Netw*. 1995;6(3):703–15.
44. Obal P, Gierlak P. EGM Toolbox—Interface for Controlling ABB Robots in Simulink. *Sensors*. 2021;21(22):7463.

Piotr Gierlak:  <https://orcid.org/0000-0003-4545-8253>



This work is licensed under the Creative Commons BY-NC-ND 4.0 license.



## METHOD OF MACHINING CENTRE SLIDING SYSTEM FAULT DETECTION USING TORQUE SIGNALS AND AUTOENCODER

Damian AUGUSTYN\*, Marek FIDALI\*

\*Department of Fundamentals of Machinery Design, Faculty of Mechanical Engineering, Silesian University of Technology, ul. Akademicka 2A, 44-100 Gliwice, Poland

damian.augustyn@polsl.pl, marek.fidali@polsl.pl

received 31 December 2022, revised 23 March 2023, accepted 8 April 2023

**Abstract:** The sliding system of machining centres often causes maintenance and process problems. Improper operation of the sliding system can result from wear of mechanical parts and drives faults. To detect the faulty operation of the sliding system, measurements of the torque of its servomotors can be used. Servomotor controllers can measure motor current, which can be used to calculate motor torque. For research purposes, the authors used a set of torque signals from the machining centre servomotors that were acquired over a long period. The signals were collected during a diagnostic test programmed in the machining centre controller and performed once per day. In this article, a method for detecting anomalies in torque signals was presented for the condition assessment of the machining centre sliding systems. During the research, an autoencoder was used to detect the anomaly, and the condition was assessed based on the value of the reconstruction error. The results indicate that the anomaly detection method using an autoencoder is an effective solution for detecting damage to the sliding system and can be easily used in a condition monitoring system.

**Key words:** condition monitoring, torque signal, machining centre, anomaly detection, autoencoder

### 1. INTRODUCTION

Contemporary machining centres used in production are usually fully automated and complex mechatronic systems. Among many state-of-the-art systems that can be found in machining centres, sliding system plays a very important role. It is the mechanical system that enables the movement of the machine's table or spindle along the axes (X, Y, Z) to position the cutting tool precisely relative to the workpiece. The sliding system in contemporary machining centres plays a critical role in ensuring the precision and accuracy of the machining process. Fig. 1 presents an exemplary sliding system of a multi-axis machining centre.

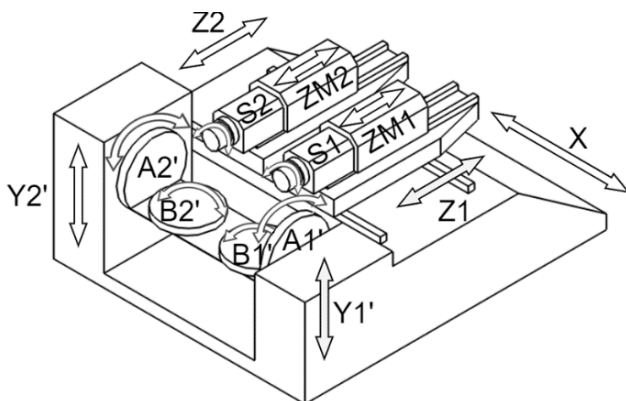


Fig. 1. Diagram of the axis sliding systems of a double-spindle machining centre

The sliding system is typically composed of several components, as shown in Fig. 2.

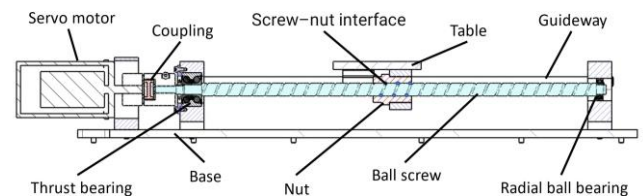


Fig. 2. Schematic diagram of the exemplary ball-screw drive system used in sliding system of machining centres

According to the different publications [1, 2] and reports of maintenance services, common faults of sliding systems are as follows:

- servomotor problems (bearings, electrical system);
- increased resistance to movement;
- decay of preload;
- increased clearance;
- ball screw damage;
- bearing damage.

Failures and damage to sliding systems can lead to serious problems and limitations in the operation of the machining centre, which can lead to loss of production, high repair costs and even the need to stop the production line. In recent years, much attention has been devoted to the development of various diagnostic methods for the sliding systems of the machining centre. Their goal is to enable the quick detection of failures and damages, which allows for quick intervention and minimising downtime.

**1.1. Condition monitoring and diagnostics of sliding systems**

Condition monitoring of the sliding system in machining centres is an essential aspect of ensuring their operational efficiency and avoiding costly downtime due to unscheduled maintenance. There are various techniques available for condition monitoring, ranging from simple diagnostic signals from sensors and devices installed by the manufacturer to more sophisticated methods based on machine learning and deep learning.

Sliding system of machining centres could be monitored and diagnosed in different ways. Very often sliding systems are assessed indirectly by evaluating the quality of machining parts [3]. Direct assessment of the components of the sliding system can be performed using both off-line and on-line techniques, based on methods such as vibration analysis [4–7], laser interferometry [8, 9], noise analysis [10, 11], visual inspection [12, 13], temperature monitoring [14, 15], acoustic emission monitoring [16, 17], motor current signature analysis [18, 19] and thermal imaging [20–22].

One of the most commonly used techniques for condition monitoring of sliding systems is vibration analysis. This technique involves analysing the vibration signals generated by the sliding system and extracting various parameters based on time, spectral and time–frequency analysis [23, 24]. These parameters can be used to indicate the operating condition and mechanical performance of the sliding system.

Another technique for condition monitoring is torque signal analysis [25]. This technique involves analysing the torque signal generated by the servomotors of the sliding system and their controllers. The servomotor controllers measure and monitor various operational parameters such as temperature or electric current, which can be used to calculate a torque signal that is useful for assessing the condition of sliding systems. Servo torque signal analysis methods are based on long-term trends and short-term fluctuations, using signal models and the least squares method.

Methods based on machine learning and deep learning are also being used for condition monitoring of sliding systems. These methods can extract data from many available sensors and then fuse them to predict the remaining useful life (RUL) [26]. Convolutional neural networks consisting of two modules – feature extractor and classifier – are commonly used for this purpose [27–29].

More recently, deep adversarial networks and autoencoders [30, 31] have been used for fault detection and identification of sliding system. Deep adversarial networks have been used for RUL prediction with partial sensor malfunctions. Autoencoders have been used for fault detection and identification of sliding systems.

Overall, condition monitoring of sliding systems in machining centres is an active research area, with ongoing efforts to develop more accurate and reliable techniques for fault detection and identification. These efforts are aided by the availability of data acquisition systems, advances in machine learning and deep learning and the development of decentralised federated transfer learning methodologies.

**2. SIGNALS OF SLIDING DRIVE TORQUE AND ITS ANALYSIS**

During the research, we analysed the torque signals that were collected by our industrial partner from December 2019 to Sep-

tember 2022. Torque was measured during diagnostic tests on the sliding system drives of the X, Y, Z and A axes of machining centres. For the purposes of our research, we considered a set of 100,000 torque signals from 47 machining centres. The maintenance service reported that no faults were detected in the sliding systems during the signal collection period. The machining centre diagnostic test was performed periodically, at least once a day. This test involved performing a sequence of axis drive movements, during which the sliding travelled throughout the entire operating range and then returned to the initial position. Plots of exemplary torque signals for the X, Y, Z and A axes gathered during one of the diagnostic tests are presented in Figs. 3–6, respectively. We assumed that the torque signals acquired during the diagnostic test could be a source of information about the general condition of the entire sliding system, including the drive and sliding mechanisms. Therefore, we proposed a method for sliding fault detection based on these signals.

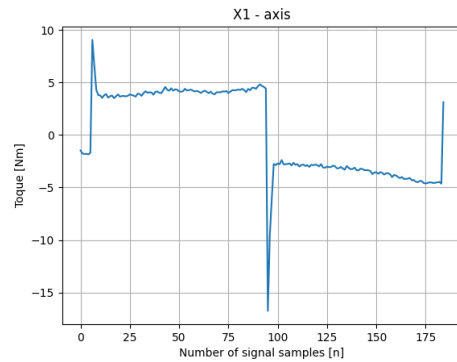


Fig. 3. Torque signal of the sliding servo drives for the X-axis

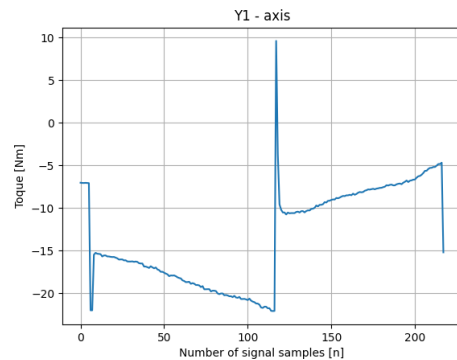


Fig. 4. Torque signal of the sliding servo drives for the Y-axis

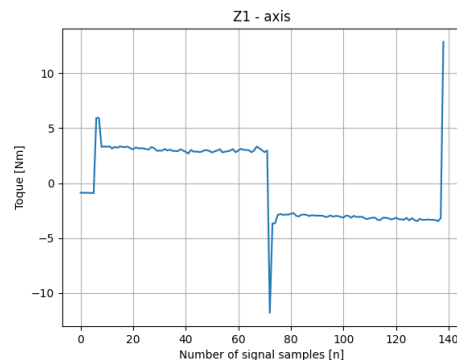


Fig. 5. Torque signal of the sliding servo drives for the Z-axis

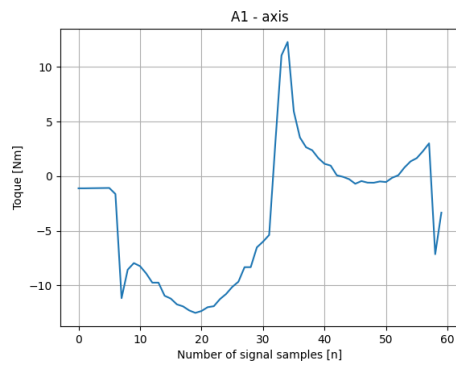


Fig. 6. Torque signal of the sliding servo drives for the A-axis

### 3. METHOD OF SLIDING FAULT DETECTION

The general idea of the method is based on detecting anomalies and deviations between the acquired torque signal and the model of the torque signal of a correctly operating sliding system. This is due to the fact that all collected signals represent good sliding system conditions. A flow of operations necessary to implement and verify the method is presented in Fig. 7. First, torque signals from the servo drives of individual axes are acquired and stored in a database after each periodic sliding system diagnostic test. In the next step, the recorded data are processed and analysed. Based on the properly recorded time series, anomalies are detected, and the value of the status indicator is calculated. The status indicator can be used to build long-term time series for trend analysis purposes. In the case of sliding system degradation, an increase in the value of the status indicator should be expected. By using the upper limit control method, it will be possible to detect the change in sliding condition and warn the maintenance services that additional inspection is necessary. The aim of this method is to improve efficiency, product quality and worker safety.

#### 3.1. Anomaly detection and status indicator calculation

A crucial operation in the proposed method is the detection of anomalies in the torque signal and the calculation of the value of the sliding system condition indicator. There are several ways to detect anomalies in torque signals, such as model-based and residue analysis or feature extraction and neural models [32]. The second approach was tested during preliminary research and the results were very promising [33]. As part of the research continuation, it was decided to verify the potential of another type of feed-forward artificial neural network called an autoencoder. This diagnostic method, based on the torque signal and using an autoencoder, is particularly useful in cases where there is a lack of data regarding the fault or where such data are rare or costly to obtain. This method can help to detect subtle and complex problems in sliding system of machining centre in real-time during diagnostic tests, allowing maintenance personnel to quickly respond and prevent further issues. Additionally, this method enables the evaluation and tracking changes of sliding system condition. In contrast to traditional diagnostic methods, the proposed method utilises the ability to learn complex data patterns and has the potential to detect subtle or difficult-to-identify faults using traditional methods. This method can be used in automated diagnostic systems and does not require extensive knowledge of technical

diagnostics, making it more accessible and easier to implement in industry.

The threshold reconstruction autoencoder is the basic deep learning approach for anomaly detection. Autoencoders are used for an unsupervised learning process [34–36], while the developed method uses a supervised learning process [37], similar to a self-supervised process [38, 39]. The choice of the learning method was dictated by the unreliability of the assumption adopted in practice, which was revealed during the ablation studies [40]. The results of ablative studies showed the disadvantages of the method based on unsupervised learning compared to the applied method of supervised learning, which achieved higher performance. In unsupervised learning, where the training data may contain anomalous examples, the autoencoder could also reconstruct anomalies, which would reduce the ability to detect anomalies based on reconstruction errors. The autoencoder, for a set of input values, creates a hidden representation from which to recreate the batch data. The assumption of the developed diagnostic method is higher values of the reconstruction error for anomalous waveforms of the torque signal compared with normal waveforms.

It was assumed that the autoencoder is trained on the time series of the torque signals represented by sliding in good condition. The result of the autoencoder operation is the value of the reconstruction error, which can be treated as a status indicator. The application of autoencoder requires the preparation of input data. In the next step, torque signals were selected and pre-processed for further computation.

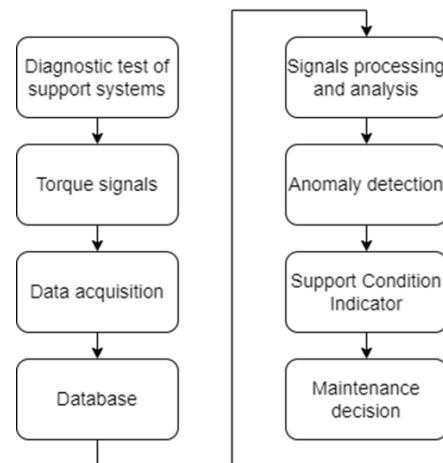


Fig. 7. Method of diagnosing a sliding system

#### 3.2. Data preparation

The set of torque signals acquired during diagnostic tests of a sliding system of machining centres required verification and pre-processing. During the verification process, it was observed that some of the signals differed in the number of time points and time positions in relation to the beginning of the diagnostic test. Additionally, some signals were found to be cut off, most likely due to a lack of signal synchronisation. The cut-off signals were rejected. For the time-shifted signals, we developed a procedure to match them in time. In the next step, we divided the signals into two subsets: a subset of signals describing good conditions and a subset of signals with anomalies. To achieve this, a statistical analysis of the torque signal values was performed. The values of the torque variance were ordered in ascending order and 25% of

the lowest and highest values were treated as outliers with probable anomalies (Fig. 8). Further analysis of the signals connected with the outliers allowed us to identify a small number of signals where anomalies were clearly visible (Fig. 9). The remaining 50% of feature values were assumed to be connected with torque signals describing good sliding system conditions and could be used for autoencoder training. The outliers were used for autoencoder testing. The process of selecting torque signals based on their feature values is presented in Fig. 8.

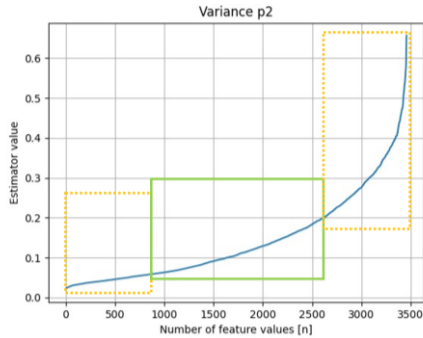


Fig. 8. Distribution of signal variance and way of values dividing into training (continuous line box) and testing (dotted line box) set

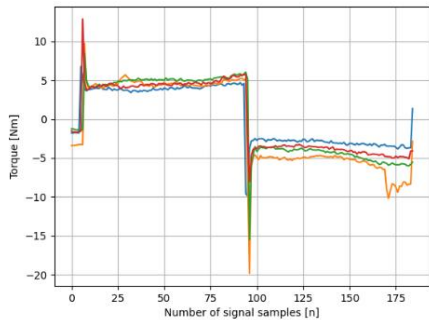


Fig. 9. Selected anomalous signals

The corrected torque signals, along with a small number of selected anomalous signals, were marked for the prepared training and test data sets. Both torque signal values in both data sets were then normalised. Fig. 10 shows the normalised torque signals for both good operation and anomalous sliding system operation. However, the reason for the detected anomalies was not identified by the maintenance personnel.

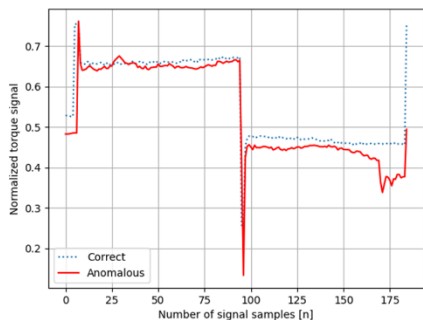


Fig. 10. Comparison of normalised torque signals for correct and anomalous sliding system operation

### 3.3. Anomaly detection using autoencoder

Pre-processed signals were utilised to train and test an autoencoder using a Python environment with TensorFlow and Keras libraries. A deep autoencoder with a symmetrical architecture was employed to detect anomalies. The autoencoder is composed of two components: an encoder and a decoder. The encoder part comprises three layers that utilise the Rectified Linear Unit (ReLU) activation function for ease of neural network optimisation. The decoder part also has three layers, with the ReLU activation function applied to the first two layers and the Sigmoid activation function applied to the final layer. The Adam optimisation method and Mean Absolute Error (MAE) [41] loss function were used for the autoencoder learning process, which was run only on the correct torque signals. A limited number of recorded anomalous torque signals were used to test the developed autoencoder model. The autoencoder model was trained over 30 epochs, and Fig. 11 shows the learning curve consisting of the training and validation loss.

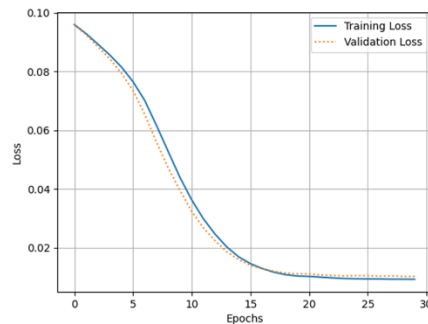


Fig. 11. Learning curve of the autoencoder model

## 4. ANOMALY DETECTION RESULTS AND DISCUSSION

The developed autoencoder was tested on data that was not used during the training process. The model was able to determine the good condition of the machining centre sliding systems with an average accuracy of 99% for the selected threshold values. Fig. 12 shows the performance of the autoencoder model on an example of a correct torque signal (represented by the blue dotted line). The reconstructed torque signal is shown in red, while the reconstruction error is shown in light red. As one can see, error is very small and almost not visible on the plot.

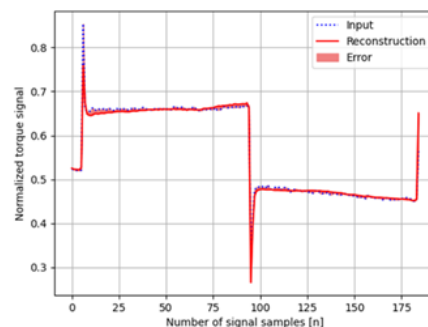


Fig. 12. Reconstruction error graph for a normal torque signal



In Fig. 13, the effect of the developed autoencoder model for an exemplary anomalous torque signal is shown. In this case, error is clearly visible and is close to 0.022.

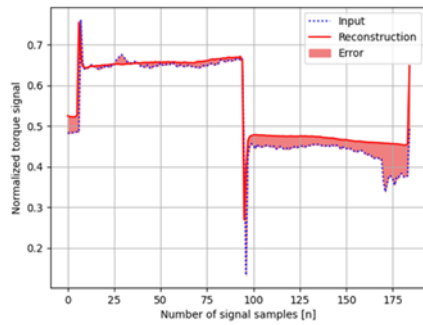


Fig. 13. Reconstruction error graph for an anomalous torque signal

The developed autoencoder allows for the visual representation of the reconstruction error in diagrams. For the purpose of the developed diagnostic system, anomaly detection is based on the reconstruction error, for which the average reconstruction error for the training set and the test set was calculated, as shown in Fig. 14.

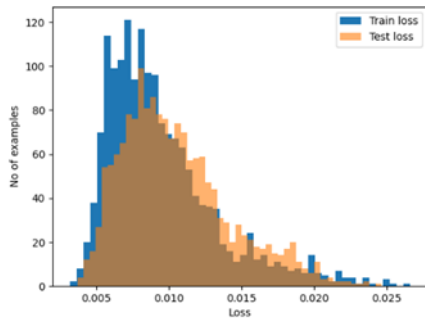


Fig. 14. Reconstruction error graph for torque signals from training set (blue) and test set (orange)

Based on the reconstruction error, graphs are generated to show the changes for the recorded time series. To make the system resistant to single isolated values of increased reconstruction error that may not be related to changes in the conditions of the sliding system drives, a moving average was used. This enables observation of the reconstruction error trend and prediction of the condition of the machining centre drives. Fig. 15 shows the reconstruction error for the time series from the training set.

Fig. 16 shows the reconstruction error for the test set. Time series in the test set were ordered according to ascending order of variance values (Fig. 9) of outliers.

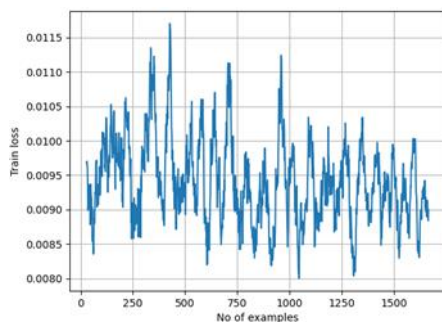


Fig. 15. Reconstruction error changes for the training set

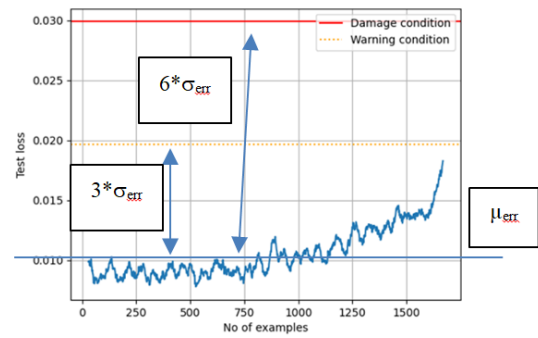


Fig. 16. Reconstruction error changes for the test set

Two threshold values were determined based on the analysis of the time series of reconstruction errors. The first threshold was determined by three standard deviations above the mean reconstruction error. The diagnostic system warning state has been assigned to it. The warning status is information for the maintenance department about the need to observe a given axis of the machining centre and control changes in its condition. The second was determined by six standard deviations above the mean reconstruction error. The fault condition of the machining centre servo drive was assigned to the second threshold. Exceeding the value of the second threshold determines the need for repair or accelerated maintenance of the machining centre sliding drive.

## 5. CONCLUSIONS

The use of servo drive torque signal measurement is an interesting alternative to assess the condition of the machining centre sliding system. This article presents an anomaly detection method which uses the autoencoder and allows the assessment of the conditions of the sliding system based on the reconstruction error value, which could be treated as a sliding system condition indicator. The autoencoder was trained based on the torque time series of the machining centre sliding systems. The training process was supervised, resembling a self-supervised process. Based on the selected error thresholds of the autoencoder reconstruction, it enables the assessment of the condition of the sliding system. The developed anomaly detection method enables the detection of registered anomalies in time series and the determination of the sliding system condition of the machining centre. Compared to the artificial neural network developed during earlier research, the method based on the autoencoder is characterised by greater efficiency and effectiveness in assessing the condition of sliding systems. The plans for future research include extending the ablative tests for the developed method in order to fully use its potential and capabilities.


## REFERENCES

- Kim Y, Bae H, Kim S, Vachtsevanos G. Fault Diagnosis of AC Servo Motor with Current Signals Based on Wavelet Decomposition and Template Matching Methods. IFAC Proceedings Volumes. 2008;41(2):7239–44. <https://doi.org/10.3182/20080706-5-kr-1001.01225>
- Lee WG, Lee JW, Hong MS, Nam S-H, Jeon Y, Lee MG. Failure Diagnosis System for a Ball-Screw by Using Vibration Signals. Shock and Vibration. 2015;2015:1–9. <https://doi.org/10.1155/2015/435870>

3. Archenti A, Laspas T. Accuracy and Performance Analysis of Machine Tools. *Precision Manufacturing*. 2019;215–44. [https://doi.org/10.1007/978-981-10-4938-5\\_7](https://doi.org/10.1007/978-981-10-4938-5_7)
4. Jamil N, Hassan MF, Lim SK, Yusoff AR. Predictive maintenance for rotating machinery by using vibration analysis. *Journal of Mechanical Engineering and Sciences*. 2021 Sep 19;15(3):8289–99. <https://doi.org/10.15282/jmes.15.3.2021.07.0651>
5. Polat K. The Fault Diagnosis based on Deep Long Short-Term Memory Model from the Vibration Signals in the Computer Numerical Control Machines. *Journal of the Institute of Electronics and Computer*. 2020;2(1):72–92. <https://doi.org/10.33969/jiec.2020.21006>
6. Desavale RG, Katiyar JK, Jagadeesha T. Vibrations Characteristics Analysis of Rotor-Bearings System Due to Surface Defects Based in CNC Machines. *Recent Advances in Manufacturing, Automation, Design and Energy Technologies*. 2021 Oct 12;705–10. [https://doi.org/10.1007/978-981-16-4222-7\\_78](https://doi.org/10.1007/978-981-16-4222-7_78)
7. Alghassi A, Yu Z, Farbiz F. Machine Performance Monitoring and Fault Classification using Vibration Frequency Analysis. 2020 Prognostics and Health Management Conference (PHM-Besançon). 2020 May; <https://doi.org/10.1109/PHM-Besancon49106.2020.00009>
8. Józwick J, Kuric I, Sága M, Lonkwić P. Diagnostics of CNC Machine Tools in Manufacturing Process with Laser Interferometer Technology. *Manufacturing Technology*. 2014 Mar 1;14(1):23–30. <https://doi.org/10.21062/ujep/x.2014/a/1213-2489/mt/14/1/23>
9. Winarno A, Prayoga BT, Hendaryanto IA. Linear Motion Error Evaluation of Open-Loop CNC Milling Using a Laser Interferometer. *Acta Mechanica et Automatica*. 2022 Mar 24;16(2):124–9. <https://doi.org/10.2478/ama-2022-0016>
10. Józwick J, Wac-Włodarczyk A, Michałowska J, Kłoczko EngM. Monitoring of the Noise Emitted by Machine Tools in Industrial Conditions. *Journal of Ecological Engineering*. 2018 Jan 1;19(1):83–93. <https://doi.org/10.12911/22998993/79447>
11. Madhusudana CK, Kumar H, Narendranath S. Fault Diagnosis of Face Milling Tool using Decision Tree and Sound Signal. *Materials Today: Proceedings*. 2018;5(5):12035–44. <https://doi.org/10.1016/j.matpr.2018.02.178>
12. Sun WH, Yeh SS. Using the Machine Vision Method to Develop an On-machine Insert Condition Monitoring System for Computer Numerical Control Turning Machine Tools. *Materials*. 2018 Oct 14;11(10):1977. <https://doi.org/10.3390/ma11101977>
13. Xing K, Liu X, Liu Z, Mayer JRR, Achiche S. Low-Cost Precision Monitoring System of Machine Tools for SMEs. *Procedia CIRP*. 2021;96:347–52. <https://doi.org/10.1016/j.procir.2021.01.098>
14. Zhou ZD, Gui L, Tan YG, Liu MY, Liu Y, Li RY. Actualities and Development of Heavy-Duty CNC Machine Tool Thermal Error Monitoring Technology. *Chinese Journal of Mechanical Engineering*. 2017 Jul 25;30(5):1262–81. <https://doi.org/10.1007/s10033-017-0166-5>
15. Sudianto A, Jamaludin Z, Abdul Rahman AA, Novianto S, Muharrom F. Automatic Temperature Measurement and Monitoring System for Milling Process of AA6041 Aluminum Alloy using MLX90614 Infrared Thermometer Sensor with Arduino. *Journal of Advanced Research in Fluid Mechanics and Thermal Sciences*. 2021 Apr 30;82(2):1–14. <https://doi.org/10.37934/arfmts.82.2.114>
16. Duro JA, Padgett JA, Bowen CR, Kim HA, Nassehi A. Multi-sensor data fusion framework for CNC machining monitoring. *Mechanical Systems and Signal Processing*. 2016 Jan;66-67:505–20. <https://doi.org/10.1016/j.ymssp.2015.04.019>
17. Goli A, Tirkolaee EB, Weber GW. An Integration of Neural Network and Shuffled Frog-Leaping Algorithm for CNC Machining Monitoring. *Foundations of Computing and Decision Sciences*. 2021 Mar 1;46(1):27–42. <https://doi.org/10.2478/fcds-2021-0003>
18. Zou Z, Lin Y, Lin D, Gu F, Ball AD. Online Tool Condition Monitoring of CNC Turnings Based on Motor Current Signature Analysis. 2021 26th International Conference on Automation and Computing (ICAC). 2021 Sep 2; <https://doi.org/10.23919/ICAC50006.2021.9594219>
19. Aouabdi S, Taibi M, Bouras S, Boutasseta N. Using multi-scale entropy and principal component analysis to monitor gears degradation via the motor current signature analysis. *Mechanical Systems and Signal Processing*. 2017 Jun;90:298–316. <https://doi.org/10.1016/j.ymssp.2016.12.027>
20. Choudhary A, Mian T, Fatima S. Convolutional neural network based bearing fault diagnosis of rotating machine using thermal images. *Measurement*. 2021 May;176:109196. <https://doi.org/10.1016/J.MEASUREMENT.2021.109196>
21. Rotating machinery fault diagnosis based on convolutional neural network and infrared thermal imaging. *Chinese Journal of Aeronautics*. 2020 Feb 1;33(2):427–38. <https://doi.org/10.1016/j.cja.2019.08.014>
22. Janssens O, Loccufer M, Van Hoecke S. Thermal Imaging and Vibration-Based Multisensor Fault Detection for Rotating Machinery. *IEEE Transactions on Industrial Informatics*. 2019 Jan;15(1):434–44. <https://doi.org/10.1109/TII.2018.2873175>
23. Nayana BR, Geethanjali P. Analysis of Statistical Time-Domain Features Effectiveness in Identification of Bearing Faults From Vibration Signal. *IEEE Sensors Journal*. 2017 Sep 1;17(17):5618–25. <https://doi.org/10.1109/JSEN.2017.2727638>
24. Moussa MA, Boucherma M, Khezzar A. A Detection Method for Induction Motor Bar Fault Using Sidelobes Leakage Phenomenon of the Sliding Discrete Fourier Transform. *IEEE Transactions on Power Electronics*. 2017 Jul;32(7):5560–72. <https://doi.org/10.1109/TPEL.2016.2605821>
25. Zhang X, Zhang Q, Tan L, Xu G. Running state detection and performance evaluation method for feed mechanism of numerical control machine. 2017 IEEE International Conference on Prognostics and Health Management (ICPHM). 2017 Jun; <https://doi.org/10.1109/ICPHM.2017.7998332>
26. Li X, Xu Y, Li N, Yang B, Lei Y. Remaining Useful Life Prediction With Partial Sensor Malfunctions Using Deep Adversarial Networks. *IEEE/CAA Journal of Automatica Sinica*. 2023 Jan 1;10(1):121–34. <https://doi.org/10.1109/JAS.2022.105935>
27. Zhang W, Wang Z, Li X. Blockchain-based decentralized federated transfer learning methodology for collaborative machinery fault diagnosis. *Reliability Engineering & System Safety*. 2023 Jan; 229: 108885. <https://doi.org/10.1016/j.res.2022.108885>
28. Neupane D, Kim Y, Seok J, Hong J. CNN-Based Fault Detection for Smart Manufacturing. *Applied Sciences*. 2021 Dec 10;11(24):11732. <https://doi.org/10.3390/APP112411732>
29. Sun Y, Li S. Bearing fault diagnosis based on optimal convolution neural network. *Measurement*. 2022 Feb;190:110702. <https://doi.org/10.1016/J.MEASUREMENT.2022.110702>
30. Canbaz H, Polat K. Fault Detection of CNC Machines from Vibration Signals Using Machine Learning Methods. *Artificial Intelligence and Applied Mathematics in Engineering Problems*. 2020;365–74. [https://doi.org/10.1007/978-3-030-36178-5\\_27](https://doi.org/10.1007/978-3-030-36178-5_27)
31. Alghassi A. Generalized Anomaly Detection Algorithm Based on Time Series Statistical Features. *Intelligent Systems Reference Library*. 2021;177–200. [https://doi.org/10.1007/978-3-030-67270-6\\_7](https://doi.org/10.1007/978-3-030-67270-6_7)
32. Korbicz J, Kowalczyk Z, Kościelny JM, Cholewa W, editors. *Fault Diagnosis*. Berlin, Heidelberg: Springer Berlin Heidelberg; 2004. <https://doi.org/10.1007/978-3-642-18615-8>
33. Augustyn D, Fidali M. Application of torque signal analysis of servomotors to assess of support system condition of industrial machining centre. *Applied Condition Monitoring*. 2023
34. Provotar OI, Linder YM, Veres MM. Unsupervised Anomaly Detection in Time Series Using LSTM-Based Autoencoders. 2019 IEEE International Conference on Advanced Trends in Information Theory (ATIT). 2019 Dec; <https://doi.org/10.1109/ATIT49449.2019.9030505>
35. Bampoula X, Siaterlis G, Nikolakis N, Alexopoulos K. A Deep Learning Model for Predictive Maintenance in Cyber-Physical Production Systems Using LSTM Autoencoders. *Sensors [Internet]*. 2021 Jan 1;21(3):972. <https://doi.org/10.1109/ATIT49449.2019.9030505>

36. Ahmad S, Styp-Rekowski K, Nedelkoski S, Kao O. Autoencoder-based Condition Monitoring and Anomaly Detection Method for Rotating Machines. 2020 IEEE International Conference on Big Data (Big Data). 2020 Dec 10; <https://doi.org/10.1109/BigData50022.2020.9378015>
37. Lei Le, Andrew Patterson, Martha White. Supervised autoencoders: Improving generalization performance with unsupervised regularizers. In *Advances in Neural Information Processing Systems 31: Annual Conference on Neural Information Processing Systems 2018, NeurIPS 2018, 3-8 Dec 2018, Montréal, Canada 2018*: 107-117.
38. Tran DH, Nguyen VL, Nguyen H, Jang YM. Self-Supervised Learning for Time-Series Anomaly Detection in Industrial Internet of Things. *Electronics*. 2022 Jul 8;11(14):2146. <https://doi.org/10.3390/electronics11142146>
39. Serradilla O, Zugasti E, Ramirez de Okariz J, Rodriguez J, Zurutuza U. Adaptable and Explainable Predictive Maintenance: Semi-Supervised Deep Learning for Anomaly Detection and Diagnosis in Press Machine Data. *Applied Sciences*. 2021 Aug 11;11(16):7376. <https://doi.org/10.3390/app11167376>
40. Amjad RA, Liu K, Geiger BC. Understanding Neural Networks and Individual Neuron Importance via Information-Ordered Cumulative Ablation. *IEEE Transactions on Neural Networks and Learning Systems*. 2022 Dec;33(12):7842–52. <https://doi.org/10.1109/TNNLS.2021.3088685>
41. Jais IKM, Ismail AR, Nisa SQ. Adam Optimization Algorithm for Wide and Deep Neural Network. *Knowledge Engineering and Data Science*. 2019 Jun 23;2(1):41. <https://doi.org/10.17977/um018v2i12019p41-46>

Damian Augustyn:  <https://orcid.org/0000-0002-4896-4090>

Marek Fidali:  <https://orcid.org/0000-0002-3667-5582>



This work is licensed under the Creative Commons BY-NC-ND 4.0 license.

## EFFECT OF DAM–ROCK FOUNDATION INTERACTION MODELING ON THE MODAL RATIO-RELATED QUANTITY OF BENI BEHDEL AND `EL MEFROUCH MULTI-ARCH DAMS

Amina Tahar BERRABAH\*, Amina ATTIA\*\*, Daoudi Mohammed HABIB\*\*\*, Djamel OUZANDJA\*\*\*\*

\*Faculty of Science and Technology, Department of Civil Engineering and Public Works,  
University of Ain Temouchent, Route de Sidi Bel Abbes - BP 284, 'Ain Temouchent, Algeria

\*\*Faculty of Science and Technology, Department of Civil Engineering and Public Works,  
Engineering and Sustainable Development Laboratory, University Of Ain Temouchent,  
Route de Sidi Bel Abbes - BP 284, 'Ain Temouchent, Algeria

\*\*\* Faculty of Science and Technology, Department of Civil Engineering And Public Works,  
Smart Structure Laboratory, University of Ain Temouchent, Route de Sidi Bel Abbes - BP 284, 'Ain Temouchent, Algeria

\*\*\*\*Faculty of Technology, Department of Civil Engineering,  
Laboratory of Materials and Mechanics of Structures (LMMS), University of Msila, PB 166 M'sila 28000, Algeria

[amina.taharberrabah@univ-temouchent.edu.dz](mailto:amina.taharberrabah@univ-temouchent.edu.dz), [amina.attia@univ-temouchent.edu.dz](mailto:amina.attia@univ-temouchent.edu.dz)  
[habib.daoudi@univ-temouchent.edu.dz](mailto:habib.daoudi@univ-temouchent.edu.dz), [djamel.ouzandja@univ-msila.dz](mailto:djamel.ouzandja@univ-msila.dz)

*received 1 February 2023, revised 9 April 2023, accepted 3 May 2023*

**Abstract:** Using the Beni Behdel dam and the El Mefrouch dam as example studies, this paper intends to clearly demonstrate how modeling of the interactions between rock foundations and dams impacts the modal behavior of these two multi-arch dams. The uniqueness of this study is that the modal behavior of each dam is represented in terms of related parameters (period, participation factor, ratio, and effective mass), and more precisely in terms of ratio (defined as the ratio between the participation factor of the mode  $i$  and the maximum participation factor), as opposed to other works that have expressed this behavior in terms of frequency. In this article, stiff rock foundation, massless rock foundation, and massed rock foundation are the three methods used to simulate dynamic interactions. The investigated dams are three-dimensionally simulated using the ANSYS finite elements code. The modeling of the rock foundation–dam interaction has an effect on the fundamental mode value, its location, and the related parameters, according to the results. Furthermore, it is found that the upstream–downstream direction is not always the most important direction for dams and that interaction modeling influences the resonance bandwidth, which affects the forecast of the resonance phenomenon.

**Key words:** related quantities, modal behavior, dam–rock foundation interaction, ANSYS code

### 1. INTRODUCTION

In the design and safety analysis of the dam structures, the dynamic dam–foundation interaction is crucial. Numerous computational techniques, such as rigid, massless, and massed foundation models, have been employed to investigate the dynamic dam–foundation interaction [5,10,16,18,20,21]. Using large foundation models is not necessary. A massless foundation model, in which only the impacts of foundation flexibility are taken into account, was put forth by Clough et al. in the 1970s [7]. This model is employed by the well-known EACD-3D [11] and ADAP-88 [12] programs, and it is viewed as a standard procedure by the U.S. Army Corps of Engineers [19]. However, using the massless foundation model has some defaults. According to Pan et al. [22], the massless foundation model could successfully replicate the seismic response of the gravity dam by adding a number of viscous dampers at the dam–foundation interface.

Models of the dam, dam–reservoir, and dam–foundation–reservoir were used by Ghaedi et al. [23] to compare the acceleration, displacement, stress, and dynamic damage of the 81.8 m high Kinta roller compacted concrete gravity dam. The results

revealed that foundation flexibility had a significant impact on the seismic response of the RCC dam–reservoir–foundation system.

According to Bayraktar et al.'s [24] investigation into the impact of base-rock characteristics on the dynamic response of dam–foundation interaction systems subjected to three different earthquake input mechanisms, the rigid-base input model was found to be insufficient to accurately describe the dynamic interaction of dam–foundation systems, whereas the massless foundation input model could be used for practical analysis. The simulation results with a 90 m high concrete gravity dam supported this finding.

For instance, it is impossible to take into account how radiation damping affects energy dispersion for a far-field foundation. A. K. Chopra found in 2012 that if the foundation–rock mass and damping are ignored, stresses may be overestimated by a ratio of 2:3 [6].

When subjected to seismic disturbances, concrete dams are structures that could be excited to resonance [8,9,17]. It is common knowledge that resonance can occur if the excitation frequency is within the structural natural frequency's bandwidth. Through modal analysis, the structural natural frequency is determined.



The primary step of any structure's dynamic study is modal analysis [4,13,14]. Modal analysis reveals the structure under the study's dynamic properties. Frequencies and their related quantities are a structure's main dynamic properties. One of the crucial capabilities when utilizing the "ANSYS" finite element code is the modal analysis type [1].

## 2. MATERIALS AND METHODS

The uniqueness of this study lies in the expression of the modal behavior of each dam in terms of related quantities. Related quantities given by ANSYS are the modal period, the modal participation factor, effective mass, and the ratio [1–3].

The participation factor for a given excitation is given as [1,3]:

$$P_{fi} = \{\varphi\}_i^T [M] \{D\} \quad (1)$$

where:

$P_{fi}$ : Participation factor for the  $i$ th mode.

$\{D\}$ : vector describing the excitation direction

$\{\varphi\}_i$ : Normalized eigenvector

$\{\varphi\}_i^T$ : Normalized eigenvector transpose.

$[M]$ : Structural mass (global structural mass)

The effective mass in a given direction is defined as:

$$M_{ei} = \frac{P_{fi}^2}{\{\varphi\}_i^T [M] \{\varphi\}_i} \quad (2)$$

$M_{ei}$ : The effective mass for the  $i$ th mode with:

$$\{\varphi\}_i^T [M] \{\varphi\}_i = 1 \quad (3)$$

It is important to note that in ANSYS code the frequencies are normalized by default with respect to the mass, but it is also possible to normalize it with respect to the unity.

The modal ratio is defined as:

$$\text{Ratio} = \frac{P_{fi}}{P_{fi \max}} \quad (4)$$

$P_{fi \max}$ : The maximal participation factor.

All related quantities presented above depend on the excitation direction (Eqs. 1, 2, 3 and 4).

Numerous studies have found that the phenomena of soil–structure interaction had an impact on the modal behavior of the structure. The rigid foundation model, the massless foundation model, and the massed foundation model are three approaches to modeling the soil–structure interaction phenomenon that have been described in the literature.

This article examines the effects of the rock–dam interaction phenomenon on the modal-related quantities of the two multi-arch dam study cases, with an emphasis on the ratio-related quantities. The two dams are the El Mefrouch arch dam and the multi-arch dam of Beni Behdel.

The originality of this work lies in the fact that, unlike earlier works that have expressed this behavior in terms of frequency, it expresses the modal behavior of each dam in terms of related quantities (period, participation factor, ratio, and effective mass), and more specifically, in terms of ratio (defined as the ratio between the participation factor of the mode I and the maximum participation factor).

Three finite element dam–foundation soil models are presented in Section 2. Sections 3 and 4 give the results of the modal analysis [14]. In the final section, the conclusions are drawn.

## 2.1. Dam–foundation rock finite element models

The two dams that are the subject of the current study and their finite element models are presented in this section.

The first case study is the Beni Bahdel multi arch dam in Algeria, which is 25 km to the southwest of Tlemcen. It was constructed in 1934 on the Oued Tafna for a retention volume of 63 million m<sup>3</sup>, and it was impounded in 1944 (see Fig. 1). The detailed geometry is given in Tab. 1.



Fig. 1. Beni Bahdel multi-arch dam [27]

Tab. 1. Geometry of the Beni Bahdel dam [25]

Element	Dimensions	The measures
Foothills	Height above ground level of the foundation	57 m
	Spacing	20 m d'axe en axe
	The shape	Sensiblement triangulaire
	The slope of the upstream face	1 : 0.95
	Slope of the downstream face	0.30
	Thickness at the top	3 m
	Thickness at the lower end	4.80 m
	Arches	The length of the ridge
Number of arches		11
The shape		Circular cylinder
Inside diameter		17.20 m
Inclination		1 : 0.95
Thickness at top		0.70 m
Thickness at the lower end		1.30 m

The second case study is El Mefrouch multi arch dam, which is made up of 17 concrete arches and is located in the same area as the first dam in Tlemcen, Algeria (Fig. 2). The dam on the wadi El Nachef started to be built at the end of 1952. It was placed into service in 1963 and has a 15 million m<sup>3</sup> capacity. A detailed geometry is given in Tab. 2.



Fig. 2. El Mefrouch multi-arch dam [26]

**Tab. 2.** Geometry of El Mefrouch multi-arch dam [27]

Element	The measures
Maximum height above lowest point of foundation	35 m
Capping height (N.G.A)	1,125.00 m
Exceptional high water mark (N.G.A)	1,124.50 m
Normal impoundment elevation	1,122.00 m
Surface area of the reservoir at normal water level	189.35 ha
Safety embankment above the normal reservoir	2.80 m
Width at crest (service bridge)	2.30 m
Thickness of the buttresses at the base	2.50 m
Thickness of the vaults	0,80 m
Slopes of the upstream face	0,80
Downstream face slopes	0.5665
Volume of the reservoir	14,993 hm <sup>3</sup>
Regulated annual volume	14 hm <sup>3</sup> /year
Maximum depth	19 m

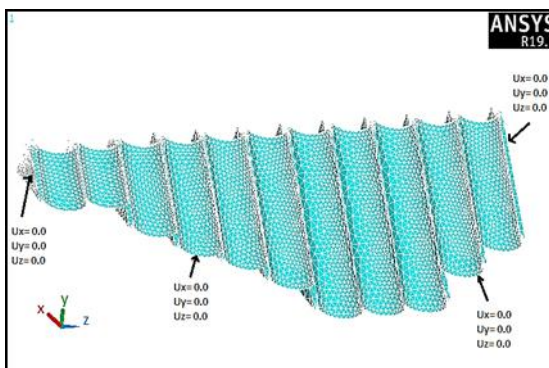
**3. ANALYSES AND RESULTS**

The following analyses are carried out using the finite element commercial program ANSYS to examine the effects of rock foundation–dam interaction on the modal response of the studied multi-arch dams.

Linear modal analysis without rock foundation of both multi-arch dams, which means that the bases of both multi-arch dams are clamped.

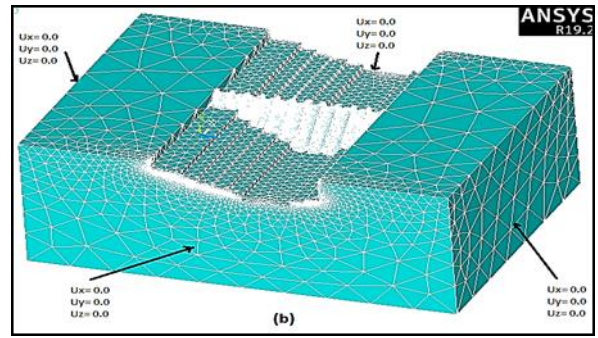
Linear modal evaluation of the dam and rock foundation system. Here, two studies are conducted with regard to the mass of the rock foundation; the first analysis takes into account the mass of the rock foundation, and the second study ignores it.

Fig. 3 sketches the finite element simulation of the multi-arch Beni Bahdel dam without rock foundation. A total of 41,598 quadratic solid elements (SOLID185) and 13,926 nodes are used in the model. The model base is blocked in the three directions x, y, and z to simulate the absence of Beni Bahdel multi-arch dam–rock foundation interaction phenomenon.



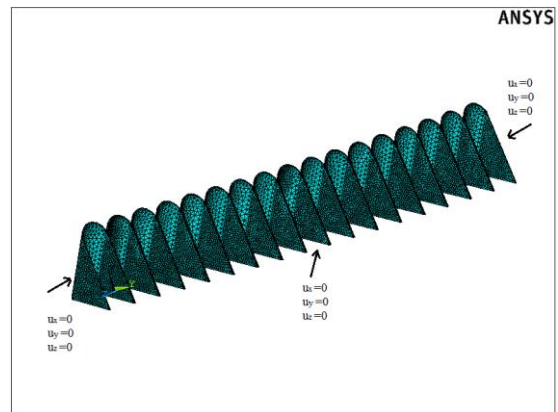
**Fig. 3.** ANSYS Finite element model of Beni Bahdel multi-arch dam with rigid rock foundation

Sketches for Fig. 4 Finite element model for the Beni Bahdel multi-arch dam–rock foundation. The model has 27,424 nodes and 97,519 quadratic solid elements (SOLID185). As boundary conditions, the three directions of x, y, and z are blocked on the model base.



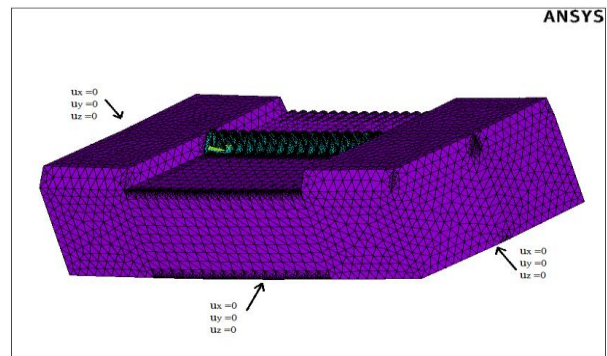
**Fig. 4.** Finite element model of Beni Bahdel multi-arch dam–rock foundation system

Fig. 5 depicts the El Mefrouch arch dam with rigid rock foundation as a finite element model in ANSYS. The model contains 19,619 nodes and 55,819 quadratic solid components (SOLID185). The model base is constrained in the x, y, and z axes to simulate the rigid rock foundation.



**Fig. 5.** ANSYS Finite element model of El Mefrouch multi-arch dam with rigid rock foundation

Sketches from Fig. 6 El Mefrouch finite element model system for multi-arch dams with rock foundations. The model has 43,108 nodes and 178,047 quadratic solid elements (SOLID185). It is crucial to remember that the model's base is fixed in the x, y, and z directions.



**Fig. 6.** ANSYS Finite element model of El Mefrouch multi-arch dam–rock foundation system

For both examples under study, it is assumed that the foundation rock's length and width, measured along the global x, y, and z

axes, respectively, exceed 2.5 H, where H is the level of the reservoir. These sizes are big enough that the modal responses of the investigated dams are unaffected by the boundary conditions that are used. To ensure a proper representation of the foundation rock, it is customary to take the factor of 2.5; for example, see Ref. [15].

The materials characteristics for the Beni Behdel and El Mefrouch arch dams, as well as their rock base foundation, are provided in Tabs. 3 and 4.

Tab. 3. Material properties of Beni Behdel multi-arch dam and its rock foundation

Material	Young's modulus (N/m <sup>2</sup> )	Poisson coefficient	Density (kg/m <sup>3</sup> )
Beni Behdel concrete dam	3 E+10	0.2	2,500
Foundation rock	3.25 E+10	0.3	2,600

Tab. 4. Material properties of El Mefrouch multi-arch dam and its rock foundation

Material	Young's modulus (N/m <sup>2</sup> )	Poisson coefficient	Density (kg/m <sup>3</sup> )
El Mefrouch concrete dam	2.85 E+10	0.2	2,500
Foundation rock	6.22 E+9	0.25	2,100

### 3.1. Modal behavior of multi-arch dams without rock foundation modeling

Without accounting for the rock foundation–dam interaction phenomenon, this section discusses the modal responses of the two analyzed dam examples.

Block Lanczos is used to extract the modal responses (ANSYS v19). The first natural mode number frequencies, the associated frequency, period, participation factor Pfi, its ratio to the maximum participation factor, and effective mass are the related quantities discussed in this article. It is important to note that ANSYS finite element code gives modal results in the three directions of x, y, and z.

The “x” axis represents the upstream–downstream direction in both of the multi-arch dam study cases, while the “y” and “z” axes represent the transverse and vertical directions, respectively.

For Beni Behdel multi-arch dam without interaction phenomenon modeling (multi-arch dam clamped at its base), the related quantities of the first eigenmodes are listed in Tabs. 5–7 in the x, y, and z directions, respectively.

The dam frequencies (and consequently the dam periods) are evident in Tabs. 5–7 to be independent of the motion directions; the same frequencies are in the x, y, and z directions; the only parameters that change are the participation factors, which affect the ratio and effective mass.

The most dominating mode, or the fundamental mode, is the one that involves the most mass. This mode is described in ANSYS code as the mode with a modal ratio quantity of “one” (1) for the direction taken into consideration [3].

The fundamental mode of the Beni Behdel multi-arch dam is mode number 12 in the x direction (see Tab. 5), mode number 1

in the y direction (see Tab. 4), but mode number 35 in the z direction (see Tab. 7).

Tab. 5. First frequencies in x direction for Beni Behdel multi-arch dam with rigid rock foundation

Mode	Frequency	Period	Participation Factor	Ratio	Effective Mass
1	5.02949	0.19883	−5.2983	0.000849	28.0719
2	5.51075	0.18146	−254.05	0.040704	64,540.1
.	.	.	.	.	.
12	12.2534	0.81610E−01	6,241.3	1.000000	0.389537 E + 08
13	12.6866	0.78824E−01	−15.382	0.002465	236.621

Tab. 6. First frequencies in y direction for Beni Behdel multi-arch dam with rigid rock foundation

Mode	Frequency	Period	Participation Factor	Ratio	Effective Mass
1	5.02949	0.19883	7,771.8	1.000000	0.604002 E + 08
2	5.51075	0.18146	76.410	0.009832	5,838.50

Tab. 7. First 10 frequencies in z direction for Beni Behdel multi-arch dam with rigid rock foundation

Mode	Frequency	Period	Participation Factor	Ratio	Effective Mass
1	5.02949	0.19883	−6.9136	0.000981	47.7980
2	5.51075	0.18146	−34.644	0.004918	1200.18
.	.	.	.	.	.
35	21.6018	0.46292E−01	7,044.2	1.000000	0.496214 E + 08

The ratio value of the Beni Behdel arch dam with rigid rock foundation is presented in Fig. 7 as a function of the analysis directions. This image makes it evident that ratio values are more significant in the x and y directions than in the vertical direction, or z. This indicates that the range of frequencies that capture significant mass values is larger in the x and y directions than in the vertical direction, or z.

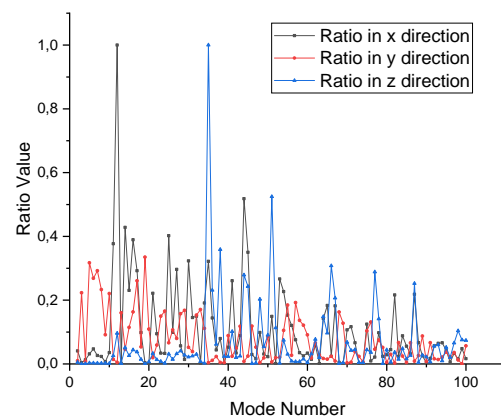


Fig. 7. Effect of analysis direction on the ratio value for Beni Behdel arch dam with rigid rock foundation



To avoid resonance phenomena, it is crucial to consider the fundamental mode seriously as a dynamic property. According to modal analyses, the dam is more susceptible in both the transverse and upstream–downstream directions, so for dams, the upstream–downstream direction is not already the most unfavorable direction. Instead, it is necessary to study the dynamic behavior of the Beni Behdel multi-arch dam due to excitation in both the transverse and upstream–downstream directions (x and y).

Without taking interaction phenomenon into account, the same analysis is done for the El Mefrouch multi-arch dam. The first frequencies and their associated values in the x, y, and z directions are summarized in Tabs. 6–8, respectively.

It is clear from Tabs. 8–10 that the dam-related quantities depend on the motion directions.

The fundamental mode of El Mefrouch multi arch dam in x direction is the mode number 17 (see Tab. 8), in y direction is the mode number 16 (see Tab. 9); however, in z direction is the mode number 79 (see Tab. 10).

**Tab. 8.** First 10 frequencies in x direction for El Mefrouch multi-arch dam with rigid rock foundation

Mode	Frequency	Period	Participation factor	Ratio	Effective mass
1	7.31985	0.13661	-5.3568	0.001338	28.6951
2	7.38362	0.13543	-2.2185	0.000554	4.92174
.	.	.	.	.	.
17	9.51602	0.10509	4,004.5	1.000000	0.160358 E + 08

**Tab. 9.** First 10 frequencies in y direction for El Mefrouch multi-arch dam with rigid rock foundation

Mode	Frequency	Period	Participation factor	Ratio	Effective mass
1	7.31985	0.13661	-0.90156	0.000153	0.812807
2	7.38362	0.13543	50.952	0.008656	2,596.14
.	.	.	.	.	.
16	8.76738	0.11406	5,886.5	1.000000	0.346507 E + 08

**Tab. 10.** First frequencies in z direction for El Mefrouch multi-arch dam with rigid rock foundation

Mode	Frequency	Period	Participation factor	Ratio	Effective mass
1	7.31985	0.13661	-2.4075	0.000548	5.79619
2	7.38362	0.13543	-1.5863	0.000361	2.51631
.	.	.	.	.	.
79	25.2994	0.39527E-01	4,392.2	1.000000	0.192910 E + 08

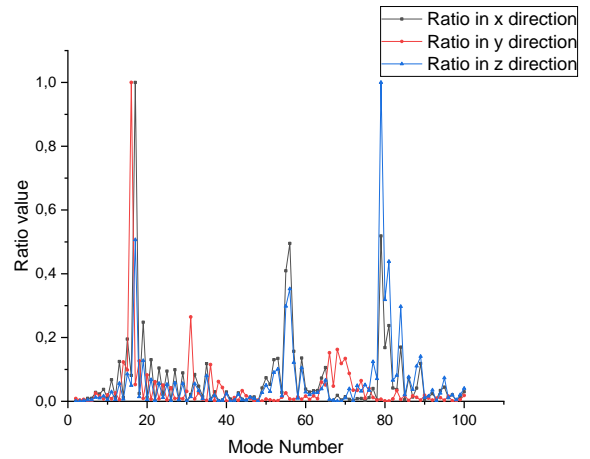


**Fig. 8.** Effect of analysis direction on the ratio value of El Mefrouch arch dam with rigid rock foundation

According to Fig. 8, the number of modes with a significant ratio value is more significant in the x and y directions than the z directions. This is because the El Mefrouch dam ratio value is more prominent in the x and y directions than the z directions.

The upstream–downstream direction is not already the most unfavorable direction for dams, according to El Mefrouch modal analyses, which also show that this dam is more sensitive in the transverse and upstream–downstream directions. Instead, it is essential to examine the El Mefrouch multi-arch dam’s dynamic behavior as a result of excitation in both the transverse and upstream–downstream directions (x and y).

### 3.2. Modal behavior of multi-arch dams with rock foundation modeling (taking into account interaction phenomenon)

The interaction phenomenon is taken into account for both multi-arch dam cases in the section that follows. The massless rock foundation model and the mass-rock foundation model are the two models that are used for dynamic interaction modeling.

The effects of the Beni Behdel multi-arch-rock foundation interaction modeling on the ratio value in the x, y, and z directions are shown in Figs. 9–11, respectively. These graphs demonstrate how the fundamental frequencies shift as a result of the rock foundation modeling; this shift is particularly pronounced in the vertical direction (z-axis).

The ratio values are also modified by the dam–rock foundation interaction models. This means that accounting for the presence of the rock foundation modifies the participation factor of each mode, which in turn modifies the dynamic properties of the dam.

Figs. 12–14 show the impact of El Mefrouch multi-arch and rock foundation interaction modeling on the ratio value in the x, y, and z directions, respectively. These figures also demonstrate how the rock foundation modeling affects the shifting of fundamental frequencies.

As for the Beni Behdel arch dam, the El Mefrouch arch dam’s fundamental mode shifting is more pronounced in the vertical direction z than in the other two directions. This is because the entire system (dam with rock foundation) is more sensitive to changes in mass and stiffness in the z direction (gravity direction) than in the other two directions (knowing that adding foundation to the dam leads only to a decrease in the system stiffness for the case of dam with massless rock foundation and to a decrease in



stiffness and increase in the mass for the case of dam with mass rock foundation).

which also has an impact on the prediction of resonance bandwidth and the resonance phenomenon in general.

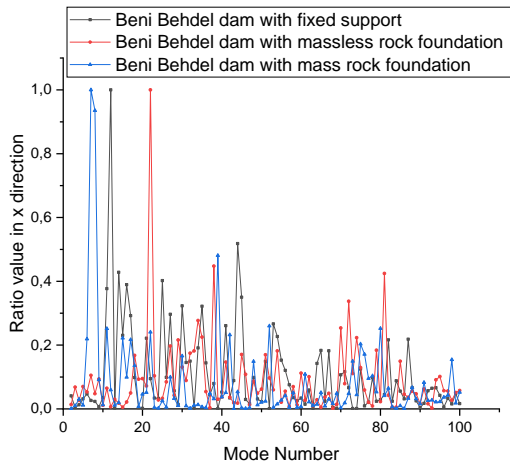


Fig. 9. Effect of Beni Behdel arch dam–rock foundation interaction modeling on the ratio value in x direction

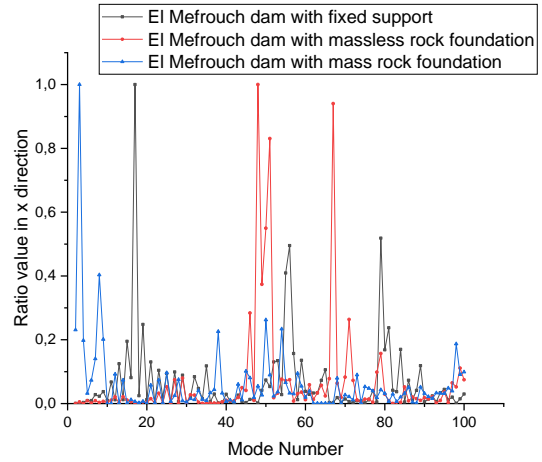


Fig. 12. Effect of El Mefrouch multi-arch rock foundation interaction modeling on the ratio value in x direction

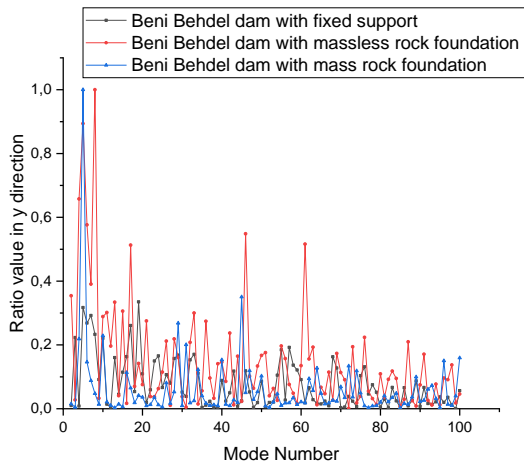


Fig. 10. Effect of Beni Behdel arch dam–rock foundation interaction modeling on the ratio value in y direction

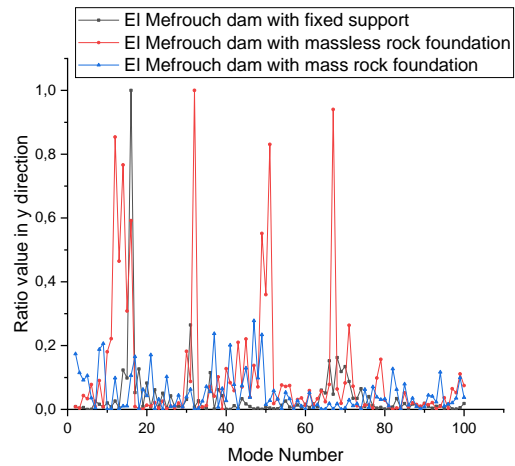


Fig. 13. Effect of El Mefrouch multi-arch rock foundation interaction modeling on the ratio value in y direction

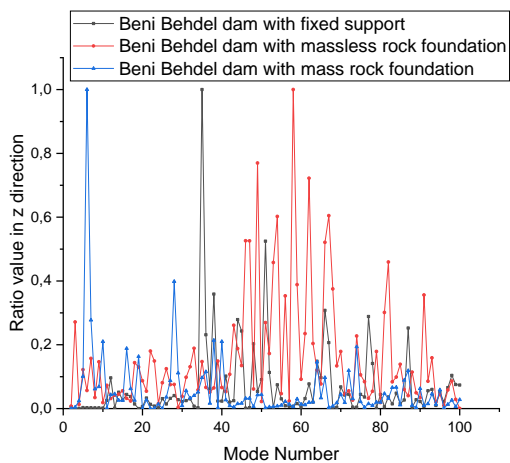


Fig. 11. Effect of Beni Behdel arch dam–rock foundation interaction modeling on the ratio value in z direction

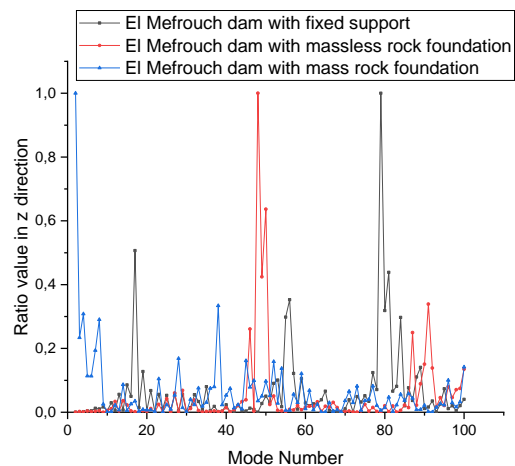
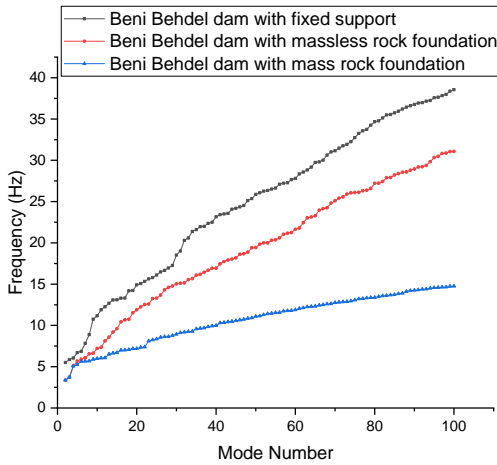


Fig. 14. Effect of El Mefrouch multi-arch rock foundation interaction modeling on the ratio value in z direction

Recall that the ratio value is the division of participation factor of mode “i” by the maximum participation factor. The rock foundation modeling has an impact on this ratio value-related quantity,

It is concluded that for the two researched arch dams, the studied direction and the interaction phenomenon modeling have an impact on the modal participation factor and, as a result, the ratio-related quantity value.

The effects of the rock–foundation interaction phenomenon on the modal frequencies of Beni Behdel and El Mefrouch multi-arch dams are depicted in Figs. 15 and 16, respectively.



**Fig. 15.** Dam–rock foundation interaction modeling effect on the modal frequencies of Beni Behdel multi-arch dam

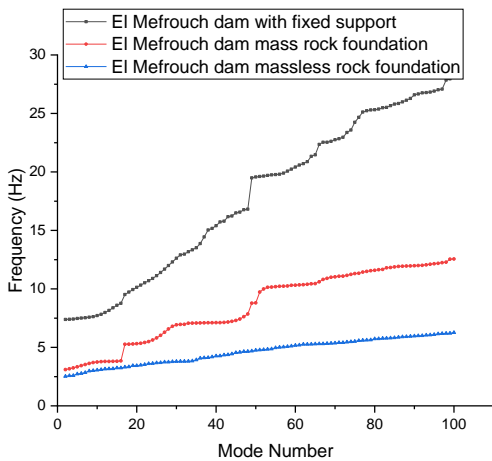


**Fig. 16.** Dam–rock foundation interaction modeling effect on the modal frequencies of El Mefrouch multi-arch dam

Figs. 15 and 16 make it very evident that adding in the foundation rock reduces system frequencies, especially if the rock is modeled as a mass rock foundation. Both the Oued Taht dam [16] and the Brezina concrete arch dam [3] yield the same results. The system becomes more flexible as a result of the addition of foundation, which also increases the system’s mass and, as a result, its period.

The interaction modeling-induced changes in natural frequencies have an impact on the resonance bandwidth, which has an impact on the resonance phenomena prediction.

It is deemed more acceptable to take into account the foundation presence in the modeling since changing the natural frequency values as a result of interaction modeling affects the dam’s dynamic response (transient response).

#### 4. CONCLUSIONS

To explore the modal behavior of the multi-arch dams Beni Behdel and El Mefrouch and to account for their interaction with

the rock–foundation medium, the present work models the dams using the 3D finite element code ANSYS. The output of a modal analysis is presented as frequencies and related quantities (participation factor, ratio, and effective mass). The following was discovered through this investigation:


- The ANSYS finite element code can provide the analyzed system’s modal characteristics in three directions (x, y, and z).
- Due to the varied inertia in the three directions, the two examined arch dams’ modal behavior in terms of participation factor, and consequently ratio and effective mass, differs for each direction.
- Rock foundation–dam interaction modeling affects the behavior of the dam in terms of frequency which is a curial dynamic characteristic to take into consideration for several analysis types (spectrum analysis, transient analysis).
- Rock foundation modeling modifies the fundamental mode’s position as well as frequency values (knowing that the fundamental mode is the mode which takes the maximum of mass).
- The interaction modeling-induced changes in natural frequencies have an impact on the resonance bandwidth, which has an impact on the resonance phenomena prediction.
- It is thought to be more acceptable to take into account the foundation presence in the modeling because changing the values of the natural frequencies as a result of interaction modeling changes the dynamic response of the dam (transient response).
- The fundamental mode must be taken carefully as a dynamic attribute in order to prevent resonance phenomenon.
- According to modal analyses, the upstream–downstream direction is not already the most unfavorable direction for dams because, for example, the two previous studied dams are more sensitive in both the transverse and upstream–downstream directions. Rather, it is required to examine these studied dams’s dynamic behavior as a result of excitation in both the transverse and upstream–downstream directions (x and y).

#### REFERENCES


1. ANSYS. ANSYS User’s Manual, ANSYS Theory Manual, vol. version 1
2. Azam MS, Malik AH, Irshad A, Iqbal M, Ahmad I. Elastic Parameter Measurement by Comparison of Modal Analysis Using ANSYS Workbench and Pulsed Laser Impulse Excited Frequency Response of Fully Clamped Thin Square Soda Lime Glass. *J Vibration Eng Technol.* 2022;1-10.
3. Berrabah AT, Belharizi M, Laulusa A, Bekkouche A. Three-Dimensional Modal Analysis of Brezina Concrete Arch Dam, Algeria. *Earth Sci Res.* 2012;1(2):55. DOI: 10.5539/esr.v1n2p55.
4. Berrabah T. Modal behavior of dam reservoir foundation system. *Electron J Geotech Eng.* 2011;16.
5. Chen D, Hou C, Wang F. Influences on the seismic response of the gravity dam-foundation-reservoir system with different boundary and input models. *Shock Vibration.* 2021. DOI: 10.1155/2021/6660145.
6. Chopra AK. Earthquake analysis of arch dams: factors to be considered. *J Struct Eng.* 2012;138(3):205-214.
7. Clough RW, Raphael JM, Mojtahedi S. ADAP: A computer program for static and dynamic analysis of arch dams. Earthquake Engineering Research Center, University of California; 1973.
8. Copen MD, Legas J, Lindholm EA, Tarbox GS, Reed FD. Design of gravity dams. a water resources technical publication. Final report. Denver, CO (United States): Bureau of Reclamation; 1976.

9. Doronin FL. Stress-Strain State of Intersection Joints of Concrete Dams under Dynamic Impacts. *Power Technol Eng*. 2021;55(4):549552. DOI: 10.1007/s10749-021-01395-z.
10. Ferdousi A. Nonlinear seismic response of arch dams considering joint opening effects and boundary conditions of discontinuous foundation. *J Numer Methods Civil Eng*. 2021;5(3):56-66.
11. Fok K, Hall JF, Chopra AK. EACD-3D: a computer program for three-dimensional earthquake analysis of concrete dams. Earthquake Engineering Research Center, University of California Berkeley, CA; 1986.
12. Fenves GL, R.B.R. S.M. ADAP-88: a computer program for nonlinear earthquake analysis of concrete arch dams. Tech. Rep. Berkeley, CA, USA: Earthquake Engineering Research Center, University of California at Berkeley; 1989.
13. Gorai S, Maity D. Seismic Performance Evaluation of Concrete Gravity Dams in Finite-Element Framework. *Pract Period Struct Des Constr*. 2022;27(1):04021072.
14. Karabulut M. Earthquake response of roller compacted concrete dams including galleries. *Struct Eng Mech*. 2019;72(2):141-153.
15. Maeso O, Domínguez J. Earthquake analysis of arch dams. I: Dam-foundation interaction. *J Eng Mech*. 1993;119(3):496-512.
16. Nasreddine K, Amina TB, Youcef H, Mohamed B, Mohamed M, el Amine MM. Soil-fluid-structure interaction applied to the Oued Taht dam (taking into account the membrane effect). *MATEC Web of Conferences*. 2022;vol. 149:2037.
17. Rea D, Liaw C, Chopra AK. Mathematical models for the dynamic analysis of concrete gravity dams. *Earthq Eng Struct Dyn*. 1974;3(3):249-258.
18. Tidke AR, Adhikary S, Farsangi EN. On the seismic performance evaluation of dam-foundation-reservoir system for the effect of frequency content and foundation flexibility. *Ocean Eng*. 2022;247:110586.
19. US Army. Corps of engineers, engineering and design-time-history dynamic analysis of concrete hydraulic structures. Tech. Rep. Washington, DC, USA: Department of the Army; 2003.
20. Wang C, Zhang H, Zhang Y, Guo L, Wang Y, Thira Htun TT. Influences on the seismic response of a gravity dam with different foundation and reservoir modeling assumptions. *Water (Basel)*. 2021;13(21):3072.
21. Yesane PM, Ghugal YM, Wankhade RL. Study on soil-structure interaction: a review. *Int J Eng Res*. 2016;5(3):737-741.
22. Pan JW, Song CM, Zhang CH. Simple model for gravity dam response considering radiation damping effects. *J Hydraul Eng*. 2010;41:493-498.
23. Ghaedi K, Hejazi F, Ibrahim Z, Khanzai P. Flexible foundation effect on seismic analysis of roller compacted concrete (RCC) dams using finite element method. *KSCE J Civ Eng*. 2017;22:1275-1287.
24. Bayraktar A, Hañer E, Akköse M. Influence of base-rock characteristics on the stochastic dynamic response of dam-reservoir-foundation systems. *Eng Struct*. 2005;27:1498-1508.
25. Stucky A. Le barrage des Beni-bahdel: ouvrage en béton armé à voutes de 20 m de portée. [Internet]. 1937.
26. Geometrical and geotechnical report of El Mefrouche multi-arch dam. [Old paper document].
27. Geometrical and geotechnical report of Beni-bahdel multi-arch dam. [Paper document].

Amina Tahar Berrabah:  <https://orcid.org/0000-0003-2904-8342>

Amina ATTIA:  <https://orcid.org/0009-0006-5599-0461>

Daoudi Mohammed Habib:  <https://orcid.org/0000-0003-1464-9831>

Djamel Ouzandja:  <https://orcid.org/0000-0002-6152-8461>



This work is licensed under the Creative Commons BY-NC-ND 4.0 license.

## NUMERICAL STUDY OF THE MECHANICAL BEHAVIOUR AND DAMAGE OF FGM BENT PIPES UNDER INTERNAL PRESSURE AND COMBINED BENDING MOMENT

Amin HOUARI<sup>\*✉</sup>, Kouider MADANI<sup>\*\*✉</sup>, Salah AMROUNE<sup>\*\*\*✉</sup>  
 Leila ZOUAMBI<sup>\*\*✉</sup>, Mohamed ELAJRAMI<sup>\*\*✉</sup>

<sup>\*</sup>Faculty of Technology, Department of Mechanical Engineering, University of M'hamed Bougara, Boumerdes 35000, Algeria

<sup>\*\*</sup>Faculty of Technology, Department of Mechanical Engineering, University of Djilali Liabes SBA, Sidi Bel Abess, 22000, Algeria

<sup>\*\*\*</sup>Faculty of Technology, Department of Mechanical Engineering, University of Mohamed Boudiaf-M'Sila, M'sila, 28000, Algeria

[a.houari@univ-boumerdes.dz](mailto:a.houari@univ-boumerdes.dz), [koumad10@yahoo.fr](mailto:koumad10@yahoo.fr), [salah.amroune@univ-msila.dz](mailto:salah.amroune@univ-msila.dz)  
[zouambileila@yahoo.com](mailto:zouambileila@yahoo.com), [eladjrami\\_mohamed@yahoo.fr](mailto:eladjrami_mohamed@yahoo.fr)

*received 15 February 2023, revised 25 April 2023, accepted 4 May 2023*

**Abstract:** The main objective of this work is the numerical prediction of the mechanical behaviour up to the damage of the bends of the functionally graded material (FGM) type ceramic/metal pipes. Firstly, the effective elastoplastic properties of bent FGM pipes were determined using the homogenisation law by the Mori–Tanaka models for the elastic part and TTO (Tamura-Tomota-Ozawa) for the plastic part based on a rule of mixtures per function in the form of a power law. Our work also aims at the use of a meshing method (UMM) to predict the behaviour of the FGM by finite element in the mesh of the model. The analysis was performed using the UMM technique for different loading cases and volume fraction distribution. Two stages are necessary for the analysis of the damage: the first is the model of initiation of the damage established by the criterion of maximum deformation named MAXPE and the second is criterion of the energy of the rupture according to the theory Hillerborg used to determine damage evolution. Both stages involve a 3D finite element method analysis. However, for damage, the XFEM technique was used in our UMM method to predict crack initiation and propagation in FGM pipe bends. The results of the numerical analysis concerning the mechanical behavior showed, that if the nature of the bent pipes is in FGM, a good reduction of the various stresses compared to those where the nature of the pipe is metallic material. The results were presented in the form of a force–displacement curve. The validation of the proposed numerical methodology is highlighted by comparisons of current results with results from the literature, which showed good agreement. The analysis took into account the effect of the main parameters in a bent FGM pipe under internal pressure and bending moment on the variation of the force–strain curves.

**Key words:** FGM, ceramic/metal, elbow pipe, internal pressure, bending moment, MMU technique

### 1. INTRODUCTION

Hollow cylinders and thick-walled cylindrical shells are common components used in structural applications and device systems involving aerospace structures and civil engineering structures, machinery, pipes, probes and petrochemical structures (1). These structures, mainly consisting of straight pipes and elbows, are subjected to mechanical stresses at their own weight, connection effects; the pipe elbow is a pipe connection. Regardless of the type of machinery, equipment and pipeline used, most of them are mainly used in oil transportation, gas transportation and bridge construction. Therefore, the effective boundary load analysis has attracted the attention of many researchers. In the study of Joong-Hyok et al. (2), limit load solutions for pipe bends under combined bending and torsional moment are given. Studies by Marie et al. (3) analysed elastic stress solutions for 90° pipe bends under plane bending with a mean radius-to-thickness ratio of up to 50. Li et al. (4) investigated the load interaction behaviour of smooth pipe elbows with long straight pipes with defect by using a finite element method and then established the yield interaction behaviour when an elbow is subjected to a load combination in-plane bending, torsion and internal pressure. Karamanos et al. (5) analysed the nonlinear elastic–plastic response of 90 degree pipe bends under internal pressure under in-plane and out-of-plane bending. Cui et al. (6), investigated the influence of

torque and bending moment on the limiting internal pressure of bends with local wall thinning defects. Peng and Changyu (7) considered in their analysis the effect of local wall thinning (LWT) of the pipe subjected to different loads; pressure, bending moment and combined loads. They analysed the resistance of the pipe experimentally and numerically by the finite element method. The results showed that the influence of depth and circumferential length of LWT on the limit load is more evident compared to that of the axial length when an elbow is under pressure, bending moment or torque. Elbows are used in piping systems as they provide flexibility in response to thermal expansion and other loads that impose large displacements on the system. As with most piping considerations, understanding the ideal uses of the elbow pipe in the application areas is essential for good design and for proper operation of the finished system. Therefore, there is a need to move towards new materials exhibiting high strength and thermal resistance when undergoing severe thermomechanical loads. To meet these requirements, the process of choosing and producing such materials must be improved. This is achieved by replacing existing conventional materials with such new generation materials. For this purpose, functional gradient materials are studied (8).

In recent years, functionally graded materials (FGMs) have attracted a lot of attention due to their many benefits. Functionally graded materials is an emerging field of research. FGMs with



brittle and ductile materials presented a rather important advantage in the application of the structures of high precision as well as those under mechanical loading. Therefore, current research is mainly centred on the discovery of the nature complex fracture mechanics due to the inhomogeneity of materials. From recently published work (9) a detailed analysis of functional gradient pipe bends under a bending moment was carried out using a finite element analysis of a numerical model. Dai et al. (10) presented the effect of the volumetric ratio of constituents and porosity on magnetoelastic stresses and perturbation of magnetic field vector and to design the optimum FGM cylindrical and spherical vessels. Yavar et al. (11) developed stress analysis of a functionally graded hyperplastic thick spherical shell subjected to internal and external pressures whose hyperplastic behaviour is modelled by using the modified neo-Hookean strain energy function with variable material parameters. Benslimane et al. (1) presented an analytical formulation to find displacements and stress components in thick-walled cylinder FGM subjected to internal and external pressures. Almasi et al. (12) developed an FGM cylindrical tube model for elastic limit domain assessment using an analytical solution. This tube undergoes internal pressure and temperature difference with superimposed heat generation. Nejad et al. (13) investigated the time-dependent thermoplastic creep response for isotropically rotating thick-walled cylindrical pressure vessels made of a functional gradient material (FGM), taking into account the creep behaviour of FGM pressure vessels. Using finite element analysis, damage problems of FGM structures have been widely studied in the literature. Lee and Toi (14) analysed the elastoplastic behaviour of FGMs subjected to thermal loading by using the finite element method using continuum damage mechanics (CDM). They used the Lemaitre damage model to analyse the damage behaviour of an FGM disk. They discussed the effect of FGM on thermal damage by some numerical examples for industrial materials. Thamburaj and Johnson (15) used a finite element model (LS-DYNA) to develop FGMs. The Johnson-Holmquist damage model (JH2 model) is used to predict and measure damage propagation in materials. Houari et al. (16) established a simple and efficient method using Matlab-UMM to model an FGM (Ti/TiB) according to several types of hardware designs and to compare the results to the classical ABAQUS method using UMAT (User Material). The meshing method (UMM) has been found efficient in the analysis of the elastic-plastic behaviour and damage of an FGM structure in the presence of a central circular notch. In another work, Houari et al. (17) authors analysed, by using the finite element method and the code of ABAQUS, the variation of the circular, radial and axial forces in a tubular structure in FGMs; it is assumed that that the used material is isotropic and heterogeneous, solicits only under the internal pressure. In our work, we proposed a multifunctional material graduated in 3D (which is new), that is to say the definition of the properties of the material by element molecular language, for the purpose of defining a resolution of a design produced by the Additive manufacturing method. To facilitate their use in various fields of specific application. Numerical studies on optimal vibration control of power law FGM (P-FGM) pipes subjected to a high-temperature environment are presented for different volume fraction indices of FGM.

## 2. MODEL GEOMETRIC

A bent pipe with an outside diameter of  $D = 185.4$  mm is considered in this study, with the value of angle of curvature (devia-

tion) equal to 90. The thickness of the pipe is equal to 23.4 mm, corresponding to a diameter-to-thickness ratio ( $D/e$ ) equal to 7.9. The radius-to-diameter ratio of the elbow ( $R/D$ ) is equal to 1.34. The vertical system pipe of length  $L = 727.5$  mm is embedded in a floor (Fig. 1). The pressure pipes are simulated, with an internal pressure equal to  $P = 7$  MPa (70 bar), and the horizontal pipe part of length  $l = 160$  mm was produced with a force of  $F = 480$  N and a bending moment to  $M_f = 200$  N. mm. The presence of a bend aims to concentrate the stresses and locate a plastification, which will act a source of initiation of damage.

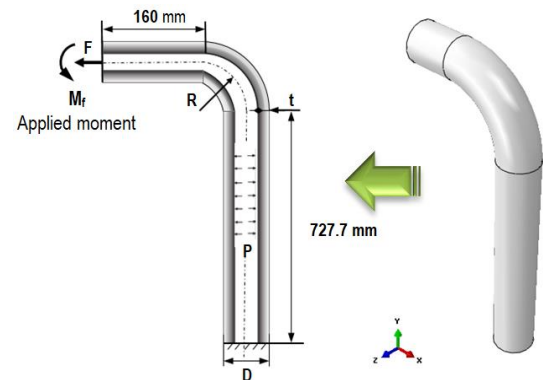


Fig. 1. Geometric model of a mass FGM cylinder

## 3. MATERIALS WITH PROPERTY GRADIENT (FGM Ti-TiB)

Metal/ceramic FGMs are becoming more and more important in modern technology; they are used to meet industrial requirements because they combine the properties of metals (ductility and high electrical and thermal conductivity) and the properties of ceramics (high hardness, resistance to corrosion and temperature). In addition, the presence of notches within the FGM constitutes not only a geometric discontinuity but also a source of crack initiation and stress concentration, which can damage the material with a property gradient with a brittle or ductile fracture. We used an FGM material (Ti titanium/TiB titanium monoborder). The FGM elbow pipe material is composed of two ductile/brittle materials (Ti/TiB); their material properties are defined in Table1.

Tab. 1. Material property [19]

Property	Metal Ti	Ceramic TiB
Young's modulus E	107,000 MPa	375,000 MPa
Poisson's ratio $\nu$	0.34	0.14
Yield stress $\sigma_Y$	450 MPa	-
Ultimate tensile strength $\sigma_{UTS}$	552 MPa	1,400
Fracture energy $G_{Ic}$	24 KJ/m <sup>2</sup>	0.11 KJ/m <sup>2</sup>
Ratio of stress to strain transfer "q"	4,500 MPa	

## 4. ANALYTICAL FORMULATION

Most articles in the literature on FGMs use the simple mixing rule to obtain effective material properties. Regarding volume fraction distribution functions, the equivalent material properties of FGMs could be determined by various functions in power law FGM (P-FGM), sigmoid law FGM (S-FGM) or exponential law FGM (E-FGM) form. There are several types of homogenisation

methods. For example, the Voigt method, which is frequently applied in FGM analysis, estimates the material properties of FGMs, and the Mori–Tanaka model estimates the effective shear G and isostatic modulus of elasticity K of the FGM, Y. It should be noted that the effective material properties given by the Hashin–Shtrikman lower bound are equivalent to the Mori–Tanaka micro-mechanical model, and the upper bound can also be obtained by interchanging the matrix and including in the formulation of the Mori–Tanaka model [20]. Tamura et al.[21] proposed a simple model to describe the stress–strain curves of composite materials. The model has been used to predict elastic and plastic constitutive responses for a range of representative multiphase materials. TTO formulation reduces to Voigt’s estimate for  $q_t = \pm\infty$  and the Reuss estimate for  $q_t = 0$ .

This part shows that the properties of FGM are continuously varied in their direction by row of finite elements according to the model used in this work – UMM, and this in accordance with the law of mixture. To determine the material properties of the elastic part of the FGMs, the Mori–Tanaka model was used to estimate the effective shear G and isostatic modulus of elasticity K of the FGM as follows:

$$K_{UMM}^k(r_i) = K_m + \frac{(K_c - K_m) \left(\frac{r_i - R_{in}}{R_{ex} - R_{in}}\right)^n}{1 + \left(1 - \left(\frac{r_i - R_{in}}{R_{ex} - R_{in}}\right)^n\right) \frac{3(K_c - K_m)}{3K_m + 4G_m}}$$

and

$$G_{UMM}^k(r_i) = G_m + \frac{(G_c - G_m) \left(\frac{r_i - R_{in}}{R_{ex} - R_{in}}\right)^n}{1 + \left(1 - \left(\frac{r_i - R_{in}}{R_{ex} - R_{in}}\right)^n\right) \frac{(G_c - G_m)}{G + f_1}} \quad (1)$$

$$f_1 = \frac{G_m(9K_m + 8G_m)}{6(K_m - 2G_m)} \quad (2)$$

Then, the effective value of Young’s modulus and Poisson’s ratio can be given as follows:

$$E_{UMM}^k(r_i) = \frac{9K_{UMM}^k(r_i)G_{UMM}^k(r_i)}{3K_{UMM}^k(r_i) + G_{UMM}^k(r_i)}$$

and

$$\nu_{UMM}^k(r_i) = \frac{3K_{UMM}^k(r_i) - 2G_{UMM}^k(r_i)}{2(3K_{UMM}^k(r_i) + G_{UMM}^k(r_i))} \quad (3)$$

where  $E_{UMM}^k(r_i)$  is effective Young’s modulus of FGM of row  $k$ ;  $i$  is the surface number; the subscript  $k$  denotes the location of a row of graduated elements; the subscripts  $c$  and  $m$  represent the ceramic and metallic phases, respectively;  $R_{in}$  denotes the inner radius of the cylinder;  $R_{ex}$  is the outside radius of the cylinder;  $r_i$  is the coordinate of each surface along the radius; and  $n$  is the exponent of the non-negative volume fraction. On the other hand, the TTO model homogenisation formulations are used in the UMM method to determine the properties of the plastic part. The TTO model equations are as follows:

$$H_{UMM}^k(r_i) = \left[ \left( H_m \frac{q + E_c}{q + H_m} - E_c \right) \left( \frac{r_i - R_{in}}{R_{ex} - R_{in}} \right)^n + E_c \right] / \left[ \frac{q + E_c}{q + H_m} \left( \frac{r_i - R_{in}}{R_{ex} - R_{in}} \right)^n + \left( 1 - \left( \frac{r_i - R_{in}}{R_{ex} - R_{in}} \right)^n \right) \right] \quad (4)$$

and

$$\sigma_{Y_0}^k(r_i) = \sigma_{Y_0m} \left[ \frac{q + E_m}{q + E_c} \frac{E_c}{E_m} \left( 1 - \left( \frac{r_i - R_{in}}{R_{ex} - R_{in}} \right)^n \right) + \left( \frac{r_i - R_{in}}{R_{ex} - R_{in}} \right)^n \right] \quad (5)$$

We propose

$$r_i = \Delta r_k (i - 1) + R_{in}$$

where  $\sigma_{Y_0}^k(r_i)$  is the row FGM yield strength and  $k \sigma_{Y_0m}$  is the yield strength of the metal and  $H_m$  tangent modulus of the metal.

The proposed criterion to predict FGM damage in our case of combined internal pressure and bending moment (Fig. 2). They rest on one or the other of the conditions of maximum deformation for initialisation of damage. The approach to predict the maximum deformation of FGM  $\varepsilon_{UTS}(r)$  is shown in the following equation:

$$\varepsilon_{UTS}(r_i) = \varepsilon_{UTSm} \cdot \left[ \frac{q + H_m}{q + E_c} \cdot (1 - V_m) + V_m \right] \quad (6)$$

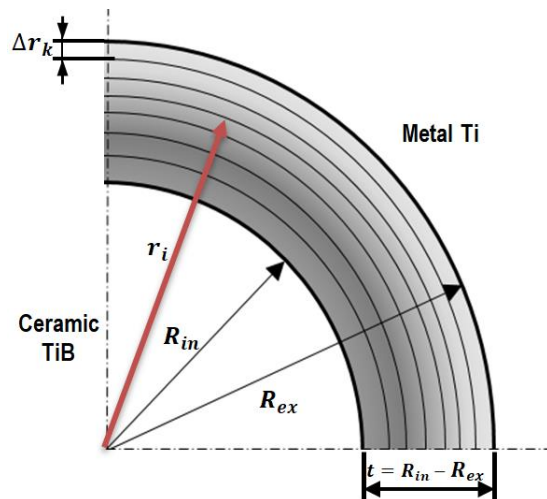


Fig. 2. Illustration of layers in an FGM (TiB/Ti) pipe

The MAXPS criterion as shown in the following equation:

$$w = \frac{\varepsilon_{eq}}{\text{Avg} \sum \varepsilon_{UTS}^k(r_i)} = 1 \quad (7)$$

where  $\varepsilon_{UTSm}$  denotes the maximum deformation of metal,  $H_m$  is the tangent modulus of metal,  $\Delta \varepsilon$  is the accumulated increment of the equivalent plastic strain of the FGM during an integration step,  $\varepsilon_f^{pl}$  is the equivalent strain of the FGM at failure and  $w$  is the damage parameter for failure initiation when it is equal to 1. The evolutions of the damage are defined by the energy condition to create new free surfaces (Eq. 2). The choice of the energy approach is often governed by the size of the finite elements.

$$G_f^k(r_i) = \int_{\varepsilon_f^{pl}}^{\varepsilon_f^{pl}} L \sigma_{Y_0}^k(r_i) d\varepsilon^{pl} \quad (8)$$

Thus, following the initiation of the damage, the variable of damage increases according to the following equation:

$$D = \frac{L d \varepsilon^{pl}}{\bar{u}_f^{pl}} \quad (9)$$

where  $\bar{u}_f^{pl}$  is the equivalent plastic displacement at failure of the FGM, which is calculated as in the following equation:

$$\bar{u}_f^{pl} = \frac{2 \cdot \text{Avg} \sum G_f^k(r_i)}{\text{Avg} \sum \sigma_{Y_0}^k(r_i)} \quad (10)$$

where  $\sigma_{Y_0}^k(r_i)$  is the elastic limit of the FGM,  $G_f^k(r_i)$  is the fracture energy of the FGM and  $L$  is the characteristic of the finite element.

5. FORMULATION OF FINITE ELEMENTS

The main feature of FGM is that it gradually changes inside the structure. This distribution of materials makes it possible to modify the properties inside the structure. Gradients of properties can thus be achieved at the mechanical, physical, chemical levels, etc. The main goal of the mechanics of materials is to predict the behaviour of materials. This requires estimating the effective mechanical properties of the two-phase composition, which is commonly referred to as homogenisation. Therefore, the analysis of FGM components involves two important aspects: the definition of the volume fraction at each point of the component and the evaluation of the effective composite properties at each point from the properties and volume fractions of each phase. In the numerical simulation, there are various possibilities of modelling the bent pipe in the ABAQUS/standard calculation code. In most studies in the literature, the pipe bend was also performed as part of the explicit calculation [5,7]. This method works, but it is relatively expensive. A much more efficient approach, which is simple in ABAQUS/standard and has been applied in this study, is the implicit–explicit coupling. The internal pressure is taken into account in a calculation step with ABAQUS/implicit, which takes only a few minutes, and then the model and the stress state are transferred to a calculation with ABAQUS/explicit for the bending moment.

We used a homogenization model (TTO) in the form of a

$$[C_{UMM}^k] = \begin{bmatrix} \lambda(r) + 2G(r) & \lambda(r) & \lambda(r) & 0 & 0 & 0 \\ \lambda(r) & \lambda(r) + 2G(r) & \lambda(r) & 0 & 0 & 0 \\ \lambda(r) & \lambda(r) & \lambda(r) + 2G(r) & 0 & 0 & 0 \\ 0 & 0 & 0 & G(r) & 0 & 0 \\ 0 & 0 & 0 & 0 & G(r) & 0 \\ 0 & 0 & 0 & 0 & 0 & G(r) \end{bmatrix} \quad (12)$$

For the UMM method, the MATLAB program was used to determine all the values of the mechanical properties of FGM for each row of finite elements according to its location and its gradation in the structure according to the TTO model. The purpose of this technique is to introduce the values of the mechanical properties of FGM directly into the ABAQUS computer code.

The UMM technique allows determining finite element stiffness equations by principle of virtual work, and the stresses for each row of finite elements can be given in the following form:

$$\sigma_{UMM}^k = [C_{UMM}^k][B]\{u_n\} \quad (13)$$

where  $\sigma_{UMM}^k$  is the constraint of each range,  $C_{UMM}^k$  is the elasticity matrix of each range  $k$  and  $u_n$  is the classic displacement field. For this purpose, Hooke's law is used to determine the stresses at the macroscopic levels:

$$\sigma_{UMM} = Avg \sum \{\sigma_{UMM}^k\} = Avg \sum [C_{UMM}^k][B]\{u_n\} \quad (14)$$

$$F_{UMM}^{FGM} = \int_V [B]\{\sigma_{UMM}\}dV \quad (15)$$

The technique of XFEM, which exists in the code ABAQUS, is compatible with the finite elements of the technique of mesh UMM in the structures out of materials with functionally graded (FGM). At the same time, the use of the method of XFEM to face a numerical difficulty that of the phenomenon of volumetric closure due to the incompressibility in plasticity.

$$u^h(x) = \sum_{i \in N} N_i(x)u_i + \sum_{i \in N_d} N_i(x)H(x)a_i + \sum_{i \in N_p} N_i(x) \left( \sum_{j=1}^4 F_j(x)b_i^j \right) \quad (16)$$

power law. The effective material properties of the FGM bent pipe are obtained for each volume fraction and have been determined by the Abaqus computer code using the UMM mesh method based on the size of the finite elements.. It should also be noted that the choice of elements for the discretisation of the structure is essential for the study of the damage of structure FGM.

The UMM technique is conditioned by the type of 3D solid finite element and the size of the finite elements in the direction of gradation. The structure is modelled by solid elements with eight nodes (C3D8R). So, all the FGM (ceramic/metal) models are analysed with the same type of the solid element C3D8R and with the same number of 100,000; the details are presented in Fig. 3. The UMM technique was used to determine the mechanical properties of FGM in element code finite ABAQUS, and the formulation of the approach is as follows:

$$P_{UMM}^k = \sum_{j=1}^m \sum_{i=1}^8 P_i^j N_i \quad (11)$$

where (i) represents number of nodes per element  $i = 1,8$  and  $P_{UMM}^k$  is the property of FGM of the row or «  $m$  » expresses the number of identical elements in each row (Fig. 2).

Afterwards, the formula of the UMM method can determine the two lame coefficients  $\lambda(r)$  and  $G(r)$ , which are expressed as a function of Young's modulus of composite  $E(x)$  and Poisson's ratio  $\nu(r)$ ; then the relation of tensions and stresses are deduced from the constitutive law using the 3D elasticity matrix from these equations:

where  $u_i$  is the classic displacement field at the node  $i$ ,  $N_i(x)$  is shape function,  $a$  and  $b$  are the corresponding degrees of freedom,  $H(x)$  is the heaviside type enrichment function and  $F_i(x)$  is the enrichment function. The final equation is as follows:

$$\sigma_{UMM} = Avg \sum \{\sigma_{UMM}^k\} = Avg \sum [C_{UMM}^k][B]\{u^h\} \quad (17)$$

6. RESULTS AND ANALYSES

6.1. Mesh sensitivity

This part aims to validate the numerical model chosen for the analysis by highlighting the effect of the density of mesh elements on the convergence of the results. Indeed the density of mesh must be appropriate to have good results compared to the practice or compared to the stability of the results. The choice of solid finite element type C3D8R in our study aims to create a row of the same type of element. Consequently, the UMM/USDFLD method consists in integrating the distribution of the mechanical properties of the different constituents of the FGM-type ceramic/metal by row of finite elements in all directions of the structure in 3D with a type of hexahedral element C3D8 (see Fig. 3.). Our choice was the type of hexahedral element C3D8R, which is widely used in the mesh of structures; however, the number of type of mesh elements has been varied (see Fig. 4.). We also used all the densities of mesh to determine their effects on the stability of the results

by the curves of traction in the form force\*–displacement. From the determined tensile curves, it was possible to demonstrate the effect of the mesh density in relation to the ultimate tensile force in the pipe elbow oriented at 90°.

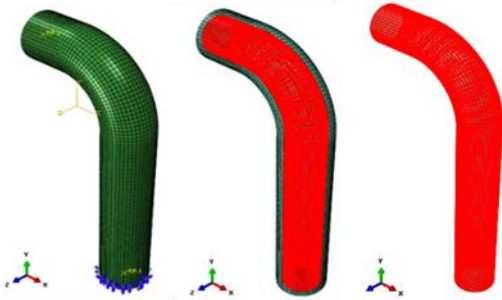


Fig. 3. Description of the mesh according to the material property variation of the FGM (TiB/Ti) per row

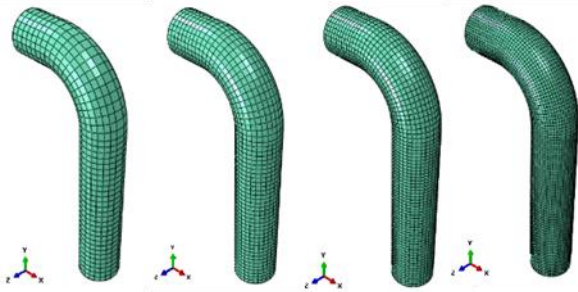


Fig. 4. Presentation of the mesh density in the 90° pipe bend: (a) 13,000 FE, (b) 22,500 FE, (c) 45,000 FE, (d) 100,000 FE

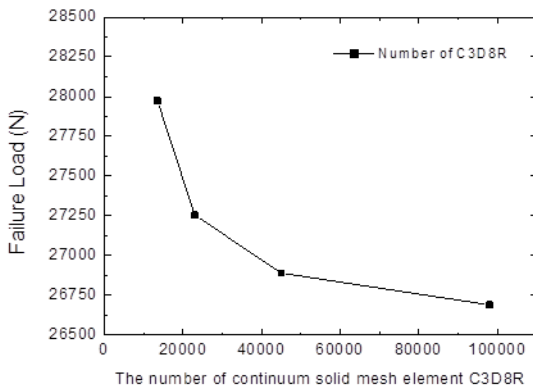


Fig. 5. Effect of the mesh element density on the response in the force–displacement tensile curve with respect to the pipe bend oriented at 90° under in-plane bending in metal Ti

Fig. 5 represents the tensile force–displacement curve of the 90° Ti metal pipe bend as a function of the different number of mesh elements. It can be noticed that compared to the elastic part, the density of elements does not have an influence on the variation of the curve force–displacement. On the other hand, the density of elements of mesh has an influence on the plastic part, or there can be a slight variation in the force according to the number of elements chosen for the mesh of the structure. From the tensile curves shown in Fig. 5, it was possible to represent the variation of the ultimate tensile force in the metal 90° pipe bend under in-plane bending as a function of mesh element density

(Fig. 6). The resistance of the bend on the metal part which has a plastic part clearly depends on the density of the mesh elements. It is preferable to have a structure discretised in a maximum number of elements (refined structure). The maximum value of the force determined numerically presents a value close to that found experimentally for the metal Ti (see Tab. 1 [19]).

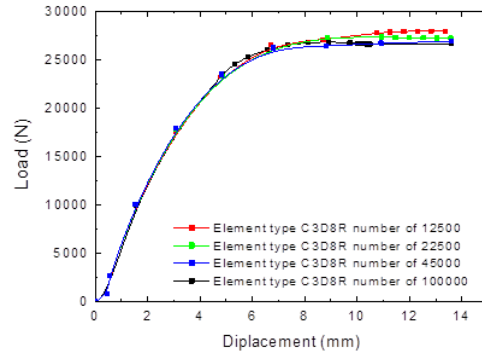


Fig. 6. Variation of maximum tensile strength of 90° pipe bend under in-plane bending in metal Ti as a function of mesh density

Another important parameter that was the subject of our sensitivity analysis is the number of surfaces introduced into the structure and the number of points of Gauss between these surfaces with the UMM technique. Our analysis of the effect of the density of mesh elements has no influence on the geometric approach to gradation but essentially on the behaviour to damage such as crack initiation and propagation. Element C3D8R has to demonstrate its performances in the comparison of the results with the experimental results; in the same way, this type of element is appropriate with the criterion of the evolution of damage and is known by these advantages with the use of XFEM [18].

## 6.2. The effect of gradation exponent on structural strength in FGM

In Fig. 7, we can notice if the structure is in rotation with respect to the axis  $xx$ , and that if  $n = 0.5$ , the pipe is rich in metal. The overall elongation of the bent pipe presents more plasticity with a maximum elongation. If the volume fraction exponent increases, the bent pipe becomes ceramic-rich and thus more strength and less ductility. An increase in the gradation exponent leads to an increase in the maximum force value of almost 4,500 N, which is beneficial for the structure.

If there is a rotation around the  $YY$  axis, the same phenomenon is observed, except that the value of the maximum force decreases considerably for an exponent of gradation equal to 2, where the structure is rich in ceramics. At this rotation, the structure has good resistance in terms of force and displacement for a balanced gradation coefficient equal to 1 and hence a linear distribution. If the elbow structure is rich in metal, the strength of the structure will be low.

If the structure is imposed on a rotation along the  $YY$  axis, the resistance of the elbow will be low and clearly lower than that when the rotation is imposed along the  $XX$  axis (Fig. 7). The effect of the gradation coefficient is important for the strength of the structure; if this coefficient has a low value (structure rich in metal), the structure has a very low resistance. However, if the structure is rich in ceramics, ie the gradation coefficient is high, it has good resistance but with low displacement.



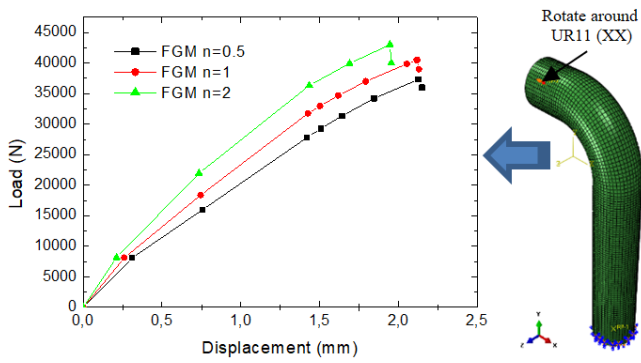


Fig. 7. Force–displacement of the pipe bent at 90 in FGM (TiB/Ti) with different exponents  $n = 0.5, 1$  and  $2$ , ratio condition ( $D/t = 7.9$ ) and rotate around UR11 (XX)

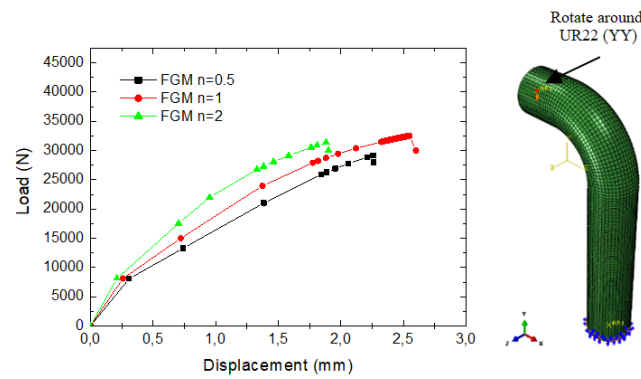


Fig. 8. Force–displacement of the pipe bent at 90 in FGM (TiB/Ti) with different exponents  $n = 0.5, 1$  and  $2$ , ratio condition ( $D/t = 7.9$ ) and rotate around UR22 (YY)

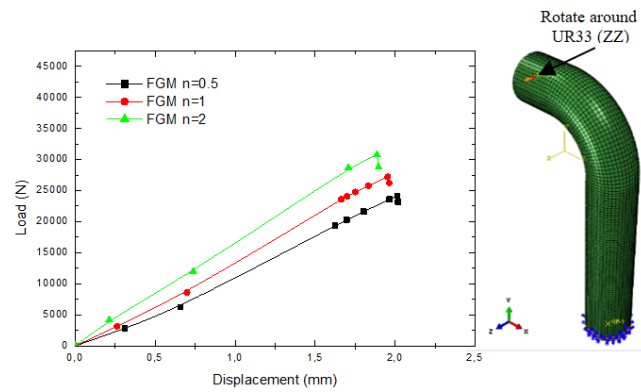


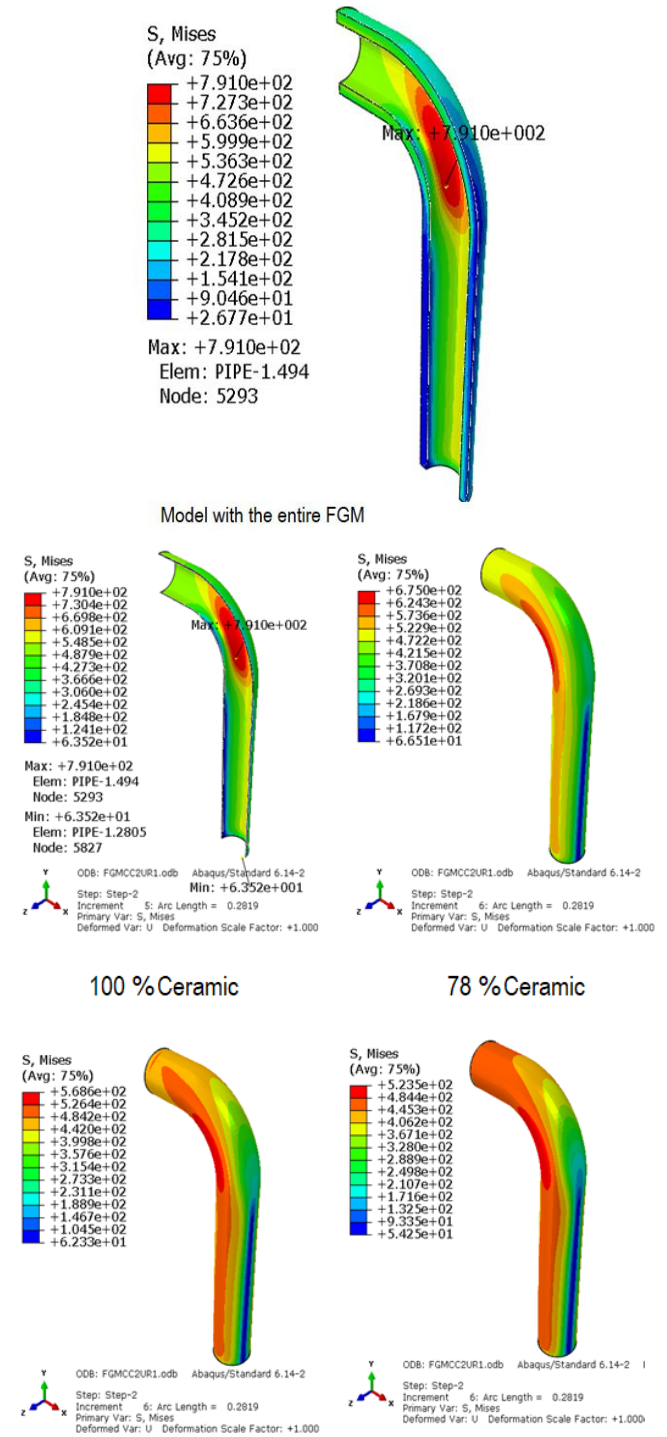
Fig. 9. Force–displacement of the pipe bent at 90 in FGM (TiB/Ti) with different exponents  $n = 0.5, 1$  and  $2$ , ratio condition ( $D/t = 7.9$ ) and rotate around UR33 (ZZ)

If one imposes a bending according to the axis ZZ, the structure presents one more weak resistance than when at the two other axes (Figs. 7 and 8). Similarly in Fig. 9, the effect of the gradation coefficient is importance for the resistance of the structure. The structure presents damage if a bending moment is imposed with respect to this direction.

### 6.3. Maximum stress analysis of bent pipe case $n = 2$ and moment around the axis (XX)

The analysis of the maximum stress level in the bent structure shows heterogeneity in the stress distribution at each layer of the

structure (Fig. 10). At the level of the internal radius where the ceramic-rich structure, it is clearly noticed that the maximum stress is at the level of the elbow on a very wide zone where the radius is minimal. Therefore, going outward from the bend, a significant concentration of stresses due to the simultaneous application of pressure and bending. Each layer of the FGM pipe has a different distribution depending on the % of each material. maximum stress is in the ceramic-rich part 791 MPa.. Towards the metal-rich part, there is more stress concentration zone but with lower stress values. For this load case, the stress in the metal part almost reaches the zone elastoplastic onset point of 454.2 MPa.



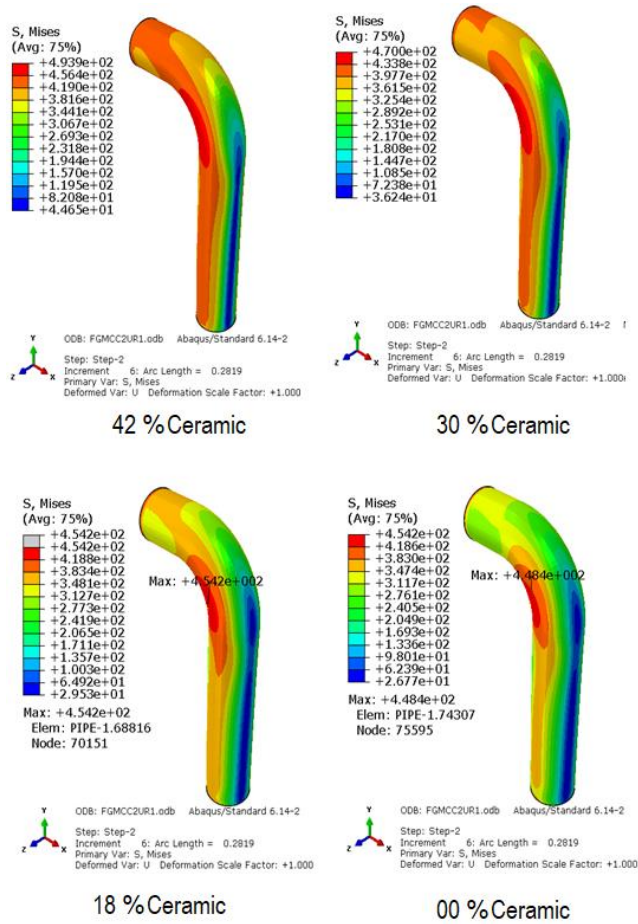


Fig. 10. Maximum stress analysis of bent pipe case exponent  $n = 2$  and moment around axis UR11 (XX)

6.4. Crack initiation case  $n = 2$  (rich ceramic) and moment around the axis (XX)

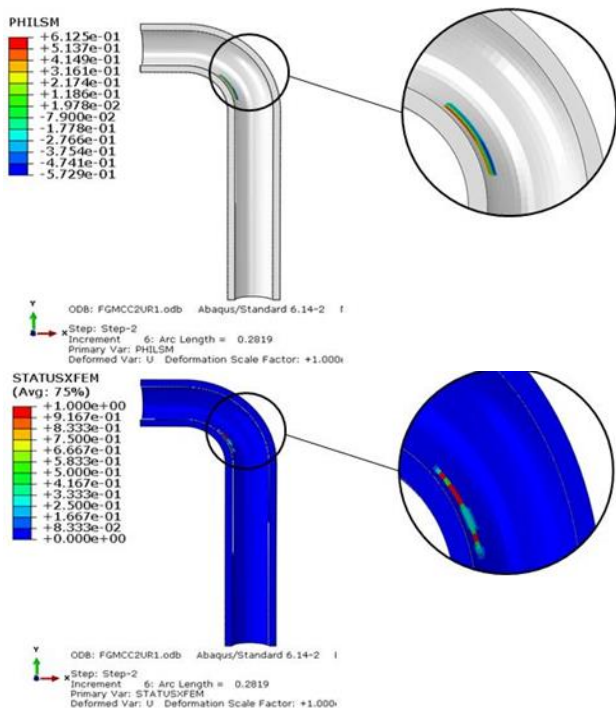


Fig. 11. Initiation of the crack case exponent  $n = 2$  (rich ceramic) and moment around the axis UR11 (XX)

Fig 11 shows the path of the crack. We notice at this part a force zone of stress concentration causing the initiation of the crack. For this value of gradation coefficient with a moment around the (XX) axis, it is better to optimise the distribution of the two materials according to a new design.

6.5. Deformation of the structure with the case  $n = 2$  (rich ceramic inside elbow) and moment around the axis (XX)

Fig. 12 shows the distorted circular shapes for elbows ( $D/t = 7.9$  and  $R/D = 1.34$ ) under in-plane bending around the XX axis of closing and opening.

It is clearly noted that for this rotation along the xx axis, the structure presents more deformation on the upper part of the elbow at the level of the metal face and slight concentration of stress at the level of the ceramic face, while the rest of the structure has good resistance.

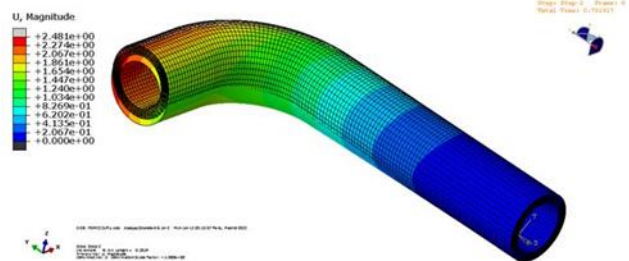
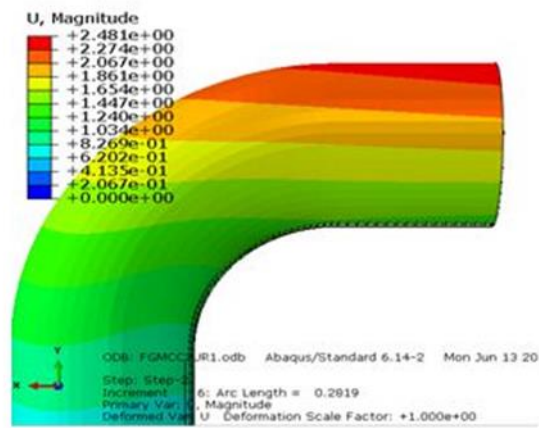
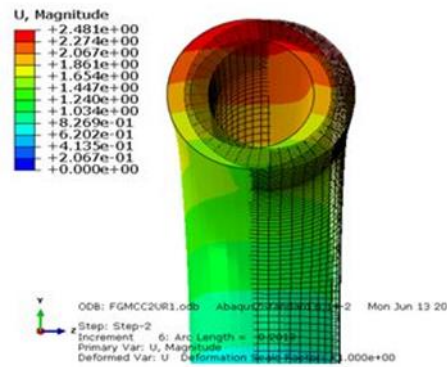


Fig. 12. Distorted circular shapes for elbows ( $D/t = 7.9$  and  $R/D = 1.34$ ) under in-plane bending around the XX axis of closing and opening

6.6. Moment effect around the axes

The determination of the variation of the bending moment as a function of the angle of rotation of the structure is essential to have an idea of the resistance of the elbow.

It is clearly noticed from Fig. 13 that regardless of the direction of rotation of the structure (according to XX or YY or ZZ) the value of the bending moment varies practically in the same way with the angle of rotation.

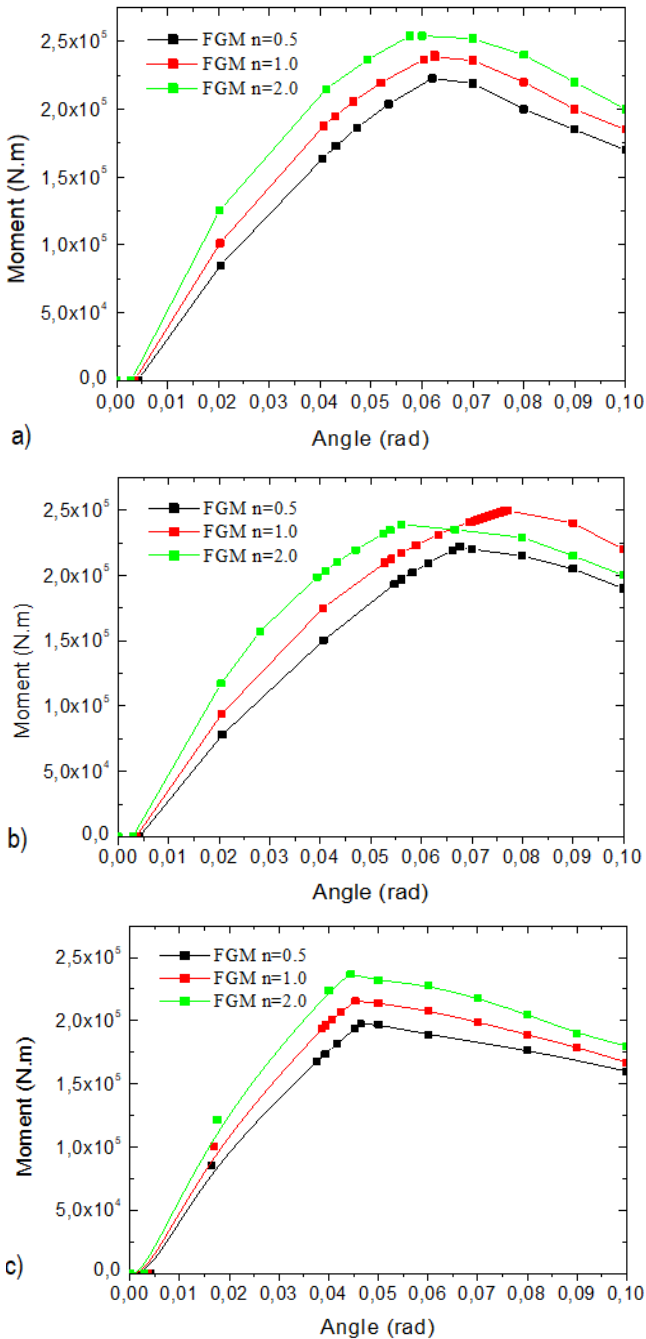


Fig. 13. Moment–rotation diagram of elbows under bending in the presence of external pressure, effect around the axes: (a) FGM-UR11, (b) FGM-UR22, (c) FGM-UR33

For the rotation along XX (Fig. 13a), the maximum value of the moment is reached for a rotation angle value equal to 0.06 rad and for the case where the structure is rich in ceramics. On the

other hand, if the rotation takes place along the YY axis (Fig. 13b), the maximum value of the moment is reached for an angle equal to 0.075 for the case where the gradation coefficient is equal to 1. Consequently, for the case where the rotation is the ZZ axis (Fig. 13c), the maximum value of the moment is reached quickly for an angle equal to 0.045 and for the case where the structure is rich in ceramics. If the structure is rich in metal, the value of the bending moment is low, and this applies for all cases of rotation along different axes.

7. CONCLUSION

Once a crack is initiated, the structure becomes weak in terms of strength, giving rise to a significant deformation of the structure at the most stressed area (i.e. elbow). The spatial and progressive variations of the properties of FGM make it possible to propose gradation concepts for innovative structures that can be exploited in many fields of application. The UMM technique gives us the advantage of varying more than two materials in the FGM. The present work has demonstrated the effectiveness of the numerical results with the proposed UMM technique with respect to the damage of a bent FGM pipe structure.


- The optimisation of the gradation coefficient provides better resistance to the structure.
- According to the direction of bending (rotation of the structure), the exponent of gradation presents an important factor in the structure in terms of force displacement.
- According to the rotation XX, for a gradation coefficient  $n = 2$ , the structure presents a better resistance. On the other hand, if the stress is along the YY axis, the gradation coefficient  $n = 1$  presents a better resistance of the structure in terms of force and elongation.


REFERENCES


1. Benslimane A, Bouzidi S, Methia M. Displacements and stresses in pressurized thick-walled FGM cylinders: Exact and numerical solutions. *Int. J. Press. Vessel.* 2018 December; 168: 219-224. <https://doi.org/10.1016/j.ijpvp.2018.10.019>.
2. An J, Hong P, Kim J, Budden J. Elastic stresses for 90° elbows under in-plane bending. *Int. J. Mech.* 2011;53(9): 762-776. <https://doi.org/10.1016/j.ijmecsci.2011.06.008>.
3. Marie S, Chapuliot S, Kayser Y, Lacire MH, Drubay B:BB, Triay M. French RSE-M and RCC-MR code appendices for flaw analysis: Presentation of the fracture parameters calculation—Part I: General overview. *Int. J. Press. Vessel.* 2007 October–November; 84(10–11): 590-600. <https://doi.org/10.1016/j.ijpvp.2007.10.008>.
4. Li Y, Gao B, Liu S, Ding J. Finite Element Analysis of the Limit Load of Straight Pipes with Local Wall-Thinning Defects under Complex Loads. *Appl. Sci.* 2022 Novembre; 12(10): 4850; <https://doi.org/10.3390/app12104850>.
5. Karamanos SA, Tsouvalas D, Gresnigt AM. Ultimate Bending Capacity and Buckling of Pressurized 90 deg Steel Elbows. *J. Press. Vessel Technol.* 2006; 128: 128–356..
6. Bao S, Liu Y, Mao J, Ge R, Li X. Numerical and experimental investigation on limit load of elbow with local thinning area. *International Journal of Pressure Vessels and Piping.* 2019 May; 172: 414-422. [doi:10.1016/j.ijpvp.2019.04.014](https://doi.org/10.1016/j.ijpvp.2019.04.014).



7. Peng C, Changyu Z. Limit Load Analysis of Elbow with Local Wall Thinning under Combined Loads. *Applied Mechanics and Materials*. 2015 April ; 750: 198-205.  
<https://doi.org/10.4028/www.scientific.net/AMM.750.198>.
8. Ansari S, Rahimi G, Citarella R, Shahbazi K, Sepe R, Esposito.. Analytical solutions for yield onset achievement in FGM thick walled cylindrical tubes undergoing thermomechanical loads. *Composites Part B: Engineering*. 2017 May; 116: 211-223.  
<https://doi.org/10.1016/j.compositesb.2017.02.023>.
9. Lee KH, Oh CS, Kim YJ, Yoon KB. Quantification of the yield strength-to-elastic modulus ratio effect on TES plastic loads from finite element limit analyses of elbows. *Engineering Fracture Mechanics*. 2009 May ; 76 (7): 856-875.
10. Dai HL, Fu YM, Dong Z. Exact solutions for functionally graded pressure vessels in a uniform magnetic field. *International Journal of Solids and Structures*. 2006 September; 43(18–19): 5570-5580.  
<https://doi.org/10.1016/j.ijsolstr.2005>.
11. Yavar A, Gholamhosein R.. Stress analysis of thick pressure vessel composed of functionally graded incompressible hyperelastic materials. *International Journal of Mechanical Sciences*. 2015 decembre ; 104 : 1-7. <https://doi.org/10.1016/j.ijmecs>.
12. Almasi A, Baghani M, Moallemi A. Thermomechanical analysis of hyperelastic thick-walled cylindrical pressure vessels, analytical solutions and FEM. *International Journal of Mechanical Sciences*. 2017 September ; 130: 426-436.<https://doi.org/10>.
13. Nejad Z, Kashkoli D. Time-dependent thermo-creep analysis of rotating FGM thick-walled cylindrical pressure vessels under heat flux. *International Journal of Engineering Science*. 2014 September ; Volume 82: 222-237.<https://doi.org/10.1016/j.ijengs>.
14. Lee M, Toi Y. Elasto-plastic damage analysis of functionally graded material disks subjected to thermal shock and thermal cycle. *Nippon Kikai Gakkai Ronbunshu, A Hen*. 2001 ; 67(655): 503-510.
15. Thamburaj P, Johnson W. Propagation of Damage in Functionally Graded Materials under Impact Loads. In 47th AIAA/ASME/ASCE/AHS/ASC Structures, Structural Dynamics, and Materials Conference 14th AIAA/ASME/AHS Adaptive Structures Conference 7th. 2012 Jun ;; <https://doi.org/10.2514/6.2006-2012>.
16. Houari A, Mokhtari M, Bouchikhi A, Polat A, Madani K. Using finite element analysis to predict the damage in FGM-3D notched plate under tensile load; Different geometric concept. *Engineering Structures*. 2021 15 June; 237: 112-160.  
<https://doi.org/10.1016/j.engstruct.2021.112160>.
17. Houari A, Mokhtari M, Bouchikhi A, Polat A, Madani K. Numerical analysis of the elastic-plastic behavior of a tubular structure in FGM under pressure and defect presence. *Frattura ed Integrità Strutturale*. 2022; 16(59): 212–231. doi: 10.3221/IGF-ESIS.59.1.
18. Jin Z, Paulino G, Dodds R. Cohesive fracture modeling of elastic–plastic crack growth in functionally graded materials. *Engineering Fracture Mechanics*. 2003 September; 70(14): 1885-1912.  
[https://doi.org/10.1016/S0013-7944\(03\)00130](https://doi.org/10.1016/S0013-7944(03)00130).
19. Mori T, Tanaka K. Average stress in matrix and average elastic energy of materials with misfitting inclusions. *Acta Metallurgica*. 1973 May ; 21(5): 571-574.[https://doi.org/10.1016/0001-6160\(73\)90064-3](https://doi.org/10.1016/0001-6160(73)90064-3).
20. Tamura Y, Tomota H, Ozawa.. Strength and Ductility of Iron-Nickel-Carbon Alloys Composed of Austenite and Martensite with Various Strength. *Proceedings of the 3rd International Conference on Strength of Metals and Alloys*, Cambridge. 1973 August ; 611.

 Amin Houari:  <https://orcid.org/0009-0004-2617-2182>

 Kouider Madani:  <https://orcid.org/0000-0003-3277-1187>

 Salah Amroune:  <https://orcid.org/0000-0002-9565-1935>

 Leila. Zouanbi:  <https://orcid.org/0000-0002-1732-5237>

 Mohamed Elajrami:  <https://orcid.org/0000-0003-0928-6124>


This work is licensed under the Creative Commons BY-NC-ND 4.0 license.



## MODELLING OF THE VISCOSITY EFFECT OF HEAVE PLATES FOR FLOATING WIND TURBINES BY HYDRODYNAMIC COEFFICIENTS

Ewelina CIBA\*, Paweł DYMARSKI\*\*

\*Faculty of Mechanical Engineering and Ship Technology, Gdansk University of Technology,  
ul. Narutowicza 11/12 8-233 Gdansk, Poland

[ewelina.ciba@pg.edu.pl](mailto:ewelina.ciba@pg.edu.pl), [pawdymar@pg.edu.pl](mailto:pawdymar@pg.edu.pl)

received 27 February 2023, revised 18 April 2023, accepted 24 April 2023

**Abstract:** One of the methods of modelling the movement of floating wind turbines is the use of the diffraction method. However, this method does not take into account the influence of viscosity; therefore, in many cases, it needs to be extended with a matrix of appropriate coefficients. The effect of viscosity causes both the added mass coefficient and the damping coefficient to increase. The determined coefficients were entered into the ANSYS AQWA program, and the calculation results of the transfer function determined with the use of linear and quadratic damping were presented. The results were compared with the results of the experiment, indicating greater convergence for the quadratic model.

**Key words:** spar platforms, heave plates, hydrodynamic coefficient, floating offshore wind turbines (FOWTs)

### 1. INTRODUCTION

The topic of floating offshore wind turbines (FOWTs) is becoming increasingly popular. There are many different platform concepts, with the most popular being various modifications of the Spar concept, such as the cell-Spar concept presented by Dymarski et al. [1].

For conceptual work, a very good method of simulating the platform in sea conditions is software based on the diffraction method, e.g. the commercial ANSYS AQWA program. Determination of wave forces on a stationary support structure for offshore wind turbines using the ANSYS AQWA program was demonstrated by Kraskowski and Marcinkowski [2], resulting in very high convergence as determined based on the results of the experiment. The use of this program was also presented by Motallebi et al. [3], who performed analyses of the DeepCwind semi-submersible FOWT platform with a nonlinear multi-segment catenary mooring line and intermediate buoy. The research carried out is very promising for this type of anchorage. It was concluded that by correctly selecting the buoy volume and position along the cable, the tension of the cable may be reduced by up to 45%.

ANSYS AQWA allows the user to quickly compare different concepts and check the impact of the applied modifications. However, the diffraction method on which it is based does not take into account the effect of viscosity, which may be of key importance in some cases; so, it should be supplemented by adding a matrix of additional coefficients. The paper presents the method of determining these coefficients for three different constructions: a smooth cylinder, a cylinder with a full heave plate and heave plates with holes, using forced oscillation tests carried out through the RANSE-CFD method. Initial considerations and results of model tests for heave plates and heave plates with holes were presented by Ciba et al. [4].

The issue of heave plates has been discussed many times in the literature. Extensive analyses of the damping plate effects were conducted by Subbullakshmi and Sundaravadivelu [5]. The authors examined various plate configurations, with reference to their diameter and position and double plates. They noticed, among other things, that the damping effect of the plate increases when its diameter is increased to 1.4 times the diameter of the platform, and thereafter, it begins to decrease. This is confirmed by the conclusions drawn by Tao and Cai [6]. They analysed vortex structures around a heave plate cylinder of different diameters. The research shows that the vortices flowing from the edge of the plate cannot be located too far from the cylinder surface, because then the damping is lower.

Medina-Manuel et al. [7] conducted model studies of a heave plate cylinder with a large plate diameter to cylinder diameter ratio ( $D_{hp}/D \sim 2.9$ ) in a wide range, changing both the motion amplitude and the excitation frequency. Using two methods, forced and free oscillations, they determined the values of the hydrodynamic coefficients of the tested plate. They presented the results on graphs depending on the number of Keulegan–Carpenter (KC) and  $\beta$ , giving the basis for estimating their size for other cases of interest to the reader.

Analyses presented by Ciba [8] showed that even residual heave plates significantly increase attenuation. This leads to the conclusion that the damping value is most influenced by the edge of the plate and not its surface. Hence, the concept of perforated plates was initiated.

Research for the circular porous plate itself was carried out by Tao and Dray [9]. They determined the hydrodynamic characteristics of an oscillating porous disk. The tests were carried out for forced oscillations. They noticed that the added mass coefficient is lower for the porous plate and that, with the low KC related to the amplitude of the displacements, there is an increase in damping for the porous plates.

Perforated square plates were examined by An and Faltinsen [10]. The tests were also carried out for an insulated plate by means of forced oscillations. They also noticed a reduction in added mass through perforation. They also pointed out that at low KC numbers, damping is mainly due to fluid flow through the holes. Similar studies were carried out by Tian et al. [11]. They examined the hydrodynamic coefficients of heave plates using the forced oscillation method. The influences of the thickness ratio, shape, edge corner radius, perforation ratio and hole size on the hydrodynamic coefficients of a single plate were analysed and presented. For the twin- and triplet-plate configurations, the spacing effects were also evaluated. The test results confirm that the holes allow us to reduce added mass in relation to the full plate. They also confirm the observation that for small KC numbers ( $KC < 0.6$ ), the damping coefficient of the plate with holes is greater than that of the solid plate. Mentzori and Kristiansen [12] presented interesting results of research and numerical simulations of hydrodynamic coefficients of two parallel perforated plates. They examined the influence of the distance between them on the nature of the flow and presented detailed visualisations of the tested cases. Based on the analyses, they indicate a tendency that a smaller distance between the plates gives greater attenuation. This is an interesting and promising concept, and further research in this area will be interesting. Molin [13] analysed perforated elements of various shapes, indicating potential applications in marine and offshore structures. In addition to heave plates, he also provided bilge keels, bodies that must be lifted down through the splash zone in a manner similar to mud mats and hatch covers. It confirms that porous structures are a good way to reduce inertial forces and slamming loads and to increase the damping of the resonant response.

For some time, the interest in the perforation of damping plates has been growing, which is a derivative of the growing interest in structures for offshore wind turbines. Mojtaba et al. [14] provided an extensive summary of damping plates. They noticed that the influence of the plates on the behaviour of the structure depends on the following parameters: the KC number, the frequency of oscillations, the ratio of perforations, the arrangement and size of cavitation, the thickness of the plate and its distance from the bottom and the free surface. They reported that at small numbers of KC, where the amplitude of the oscillations is limited, the viscous damping due to flow separation is proportional to the edge area. Hence, the addition of internal edges through perforation increases the viscous damping. So, they introduced an additional plate description factor: the ratio of the edge area to the plate area.

The method of determining the hydrodynamic coefficients by means of forced oscillations is slightly more troublesome than the method of free oscillations. However, it allows us to determine the value of the coefficients for different excitation frequencies, which is very important because in operating conditions the object will be exposed to waves of different frequencies. This was pointed out, among others, by Rao et al. [15]. They tested the coefficients of damping plates and compared the results with three different models of linear, quadratic and combined (quadratic with linear) damping, obtaining the best agreement for the linear model. This is contrary to the observations made by the authors further on within the present dissertation, but it may result from a greater number of KC of the analysed cases ( $KC \sim 2$ ), which is related to the amplitude of the movement and has a large impact on the character of the flow around.

Useful calculations for modelling heave plates were made by

Maron et al. [16]. They built one of the largest heave plate cylinder models ever studied to test the scale effect of this study. The conclusions from the conducted research are very useful for design, as they state that the hydrodynamic coefficients of heave plates depend mainly on the KC number, and the effect of the scale effect is small.

Experimental research and numerical analyses of the spar platform on a regular wave were carried out by Raed and Murali [17]. The calculations were made using the panel method with an additional damping matrix obtained using the free decay test. Against the backdrop of the results of the experiment, the aforementioned researchers compared the values and terms of the transfer function obtained for the model with only linear damping vis-à-vis those corresponding to quadratic damping, and observed that a better agreement was obtained in the case of the second of these. Determining the damping coefficients on the basis of forced oscillation tests would probably allow for even better agreement of results, although it is a more laborious method.

## 2. PURPOSE AND SCOPE OF THE RESEARCH

The present research aimed to compare a full heave plate and a heave plate with holes (Fig. 1), as an additional element for wind turbine platforms. For this purpose, the hydrodynamic coefficients for both structures were determined using the forced oscillation method (using RANSE-CFD calculations) and compared with each other. For comparison, coefficients for a smooth cylinder were also determined. Calculations were made for an excitation amplitude of  $z_a = 0.02$  m and periods equal to  $T = 0.6$  s,  $0.8$  s,  $1.0$  s,  $1.2$  s,  $1.4$  s,  $1.6$  s,  $1.8$  s and  $2.0$  s.

The determined coefficients were then introduced into the ANSYS AQWA program, thus supplementing the influence of viscosity, omitted in the diffraction method. Calculations of the behaviour of the structure on a regular wave were carried out using two methods: viscosity addition using the linear method and the quadratic method, using the Morison drag coefficient.

Based on the displacements of the structure in a regular wave, response amplitude operator functions were created and compared with the results of the experiment, and the results of the RANSE-CFD calculations are described by Ciba et al. [4].

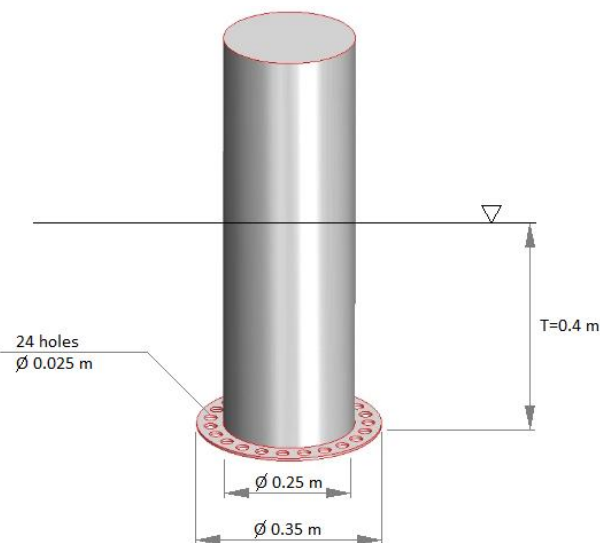


Fig. 1. Cylinder equipped with heave plates with holes

3. MATHEMATICAL DESCRIPTION OF ISSUE

The forced oscillation test is carried out by causing the object (Eq. [1]) to oscillate. The in-phase excitation force component is related to inertia and stiffness, while the out-of-phase component is related to damping. Integrating the equation of motion (Eq. [1]), we obtain the velocity (Eq. [2]) and acceleration (Eq. [3]) of the object:

$$z(t) = z_a \sin \omega t \tag{1}$$

where

$$\dot{z} = z_a \omega \cos \omega t \tag{2}$$

$$\ddot{z} = -z_a \omega^2 \sin \omega t \tag{3}$$

Hence, the equation of forced motion (Eq. [4]) can be written as follows (Eq. [5]):

$$(m + a)\ddot{z} + b\dot{z} + cz = F_a \sin(\omega t + \varepsilon_{F_z}) \tag{4}$$

$$z_a \{-(m + a)\omega^2 + c\} \sin \omega t + z_a b \omega \cos \omega t = F_a \cos \varepsilon_{F_z} \sin \omega t + F_a \sin \varepsilon_{F_z} \cos \omega t \tag{5}$$

Hence, the hydrodynamic coefficient can be determined from the following relations: added mass  $a$  (Eq. [6]), damping coefficient  $b$  (Eq. [7]) and restoring force coefficient  $c$  (Eq. [8]):

$$dla \ \omega t = \frac{\pi}{2}: a = \frac{c - \frac{F_a \cos \varepsilon_{F_z}}{z_a}}{\omega^2} - m \tag{6}$$

$$dla \ \omega t = 0: b = \frac{\frac{F_a \sin \varepsilon_{F_z}}{z_a}}{\omega} \tag{7}$$

$$\text{based on geometry: } c = \rho g A_w \tag{8}$$

The force components can be found by integrating the force over  $N$  number of cycles multiplied by  $\cos \omega t$  i  $\sin \omega t$ , respectively:

$$F_a \sin \varepsilon_{F_z} = \frac{2}{NT} \int_0^{NT} F(t) \cdot \cos \omega t \cdot dt \tag{9}$$

$$F_a \cos \varepsilon_{F_z} = \frac{2}{NT} \int_0^{NT} F(t) \cdot \sin \omega t \cdot dt \tag{10}$$

Morison's Eq. (11) assumes that we can separate the force acting on the body into an acceleration component – the inertia term and a velocity component – the drag term.

$$F(t) = \frac{1}{2} \rho C_D A_p |W - \dot{z}|(W - \dot{z}) + \rho V_b (1 + C_a) \left[ \frac{\partial W}{\partial t} + (U - \dot{z}) \frac{\partial W}{\partial z} \right] - \rho V_b C_a \ddot{z} \tag{11}$$

where  $F(t)$  [N] is the force acting on the structure,  $\rho$  [kg/m<sup>3</sup>] is water density,  $C_D$  [-] is Morison's drag coefficient,  $A_p$  [m<sup>2</sup>] is the cross-sectional area,  $W$  [m/s] is the water velocity,  $\dot{z}$  [m/s] is the speed of the structure,  $V_b$  [m<sup>3</sup>] is the volume of the submerged part,  $C_a$  [-] is the added mass coefficient and  $\ddot{z}$  [m/s<sup>2</sup>] is the acceleration of the structure.

4. RANSE-CFD CALCULATIONS

CFD calculations were made using STAR-CCM+. Non-stationary calculations were performed in the three-dimensional

domain, using the volume of fluid and K-epsilon turbulence models. By employing an overset mesh, it became possible to model cylinder displacements for a given motion trajectory. The computational domain measuring 4 m × 2 m × 2.25 m was prepared as indicated in Fig. 2.

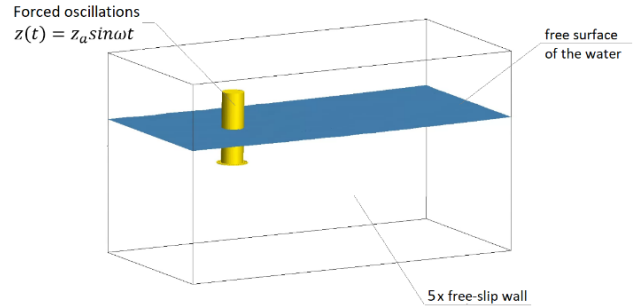


Fig. 2. Computational domain

The volume of water and air fractions for a plane wave was assumed as the initial condition. Slippery walls were placed on the walls of the field and on its bottom. From above, the domain was opened with the inlet condition with zero velocity by the volume of the air fraction.

An overset mesh was used (Fig. 3), consisting of a moving (green) and a fixed (black) part, allowing the simulation of the object's movement. The mesh was compacted near the free water surface, around the heave plate and in the area expected to move the cylinder. On the surface of the cylinder, an element size of 0.002 m from five prism layers with a total thickness of 0.002 m was applied. A mesh was obtained consisting of 1,281,102 cells in the movable portion and 1,282,998 in the fixed portion.

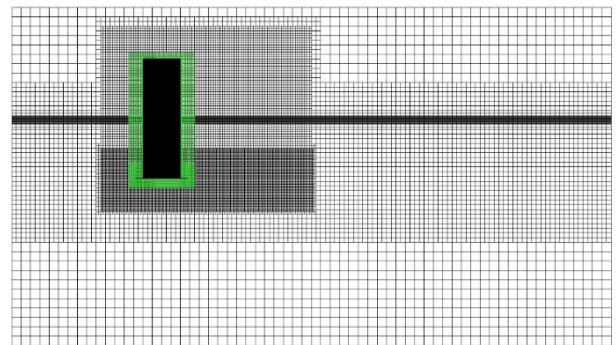


Fig. 3. Calculation grid in the symmetry plane divided into a movable (green) and a fixed (black) part

In order to ensure a thorough verification of the mesh, apart from the basic calculations performed in relation to the medium mesh characterised by 2,562,100 as the number of constituent elements, calculations were also performed on the coarse mesh (2,007,507) and the fine mesh (3,323,540); these calculations produced similar results, which are shown in Fig. 4, although these results do not count in terms of the ultimate conclusion gleaned from the present study.

Calculations were performed with time step  $t_k = 0.01$  s. The vertical force on the structure was measured.

The validity of the time step was ascertained by repeating the calculations with a smaller  $t_k = 0.005$  s and a larger  $t_k = 0.02$  s time steps. The comparison of the results is shown in Fig. 5.

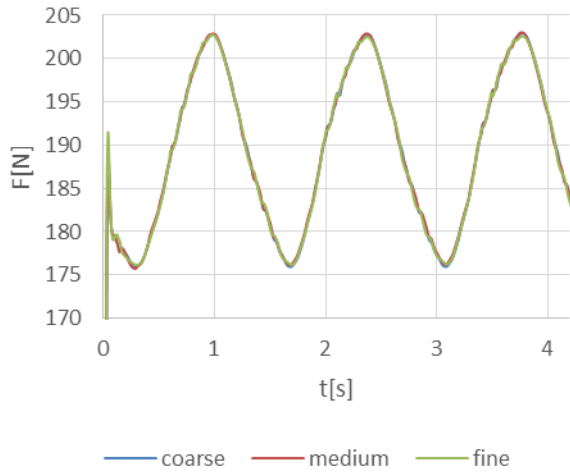


Fig. 4. Influence of the mesh density on the value of the calculated force

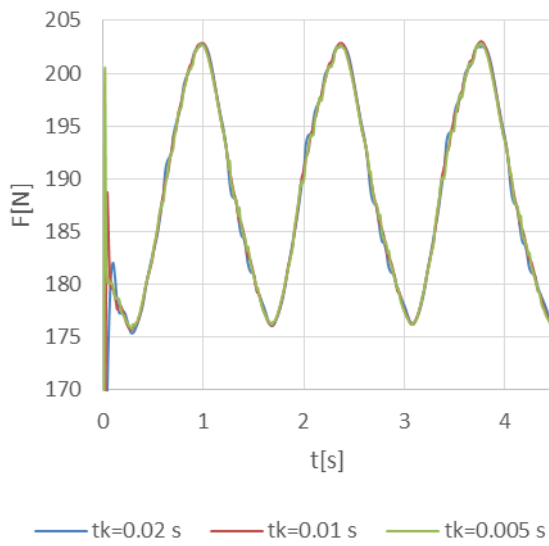


Fig. 5. The validity of the time step

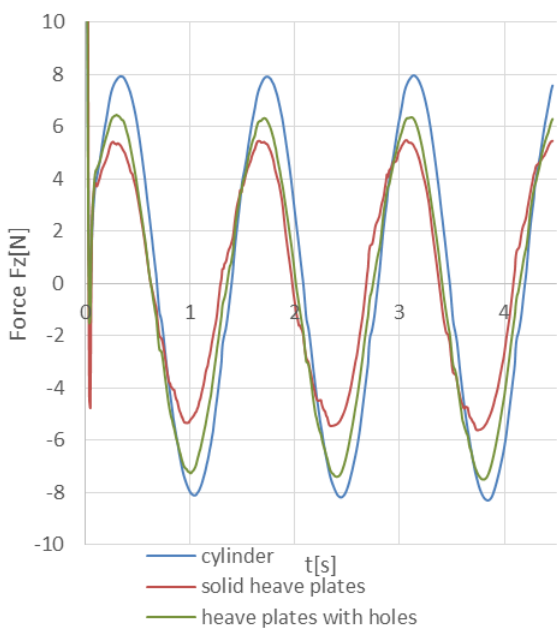


Fig. 6. Force on each of the three structures due to oscillatory excitation with period  $T = 1.4$  s

An exemplary course of forces for oscillations with a period of  $T = 1.4$  s for each of the three structures is shown in Fig. 6.

It may seem quite surprising that the largest force amplitude was obtained for a smooth cylinder. By way of offering an explanation for this, Fig. 7 shows the force distribution part related to inertia, damping and restoring force for a smooth cylinder.

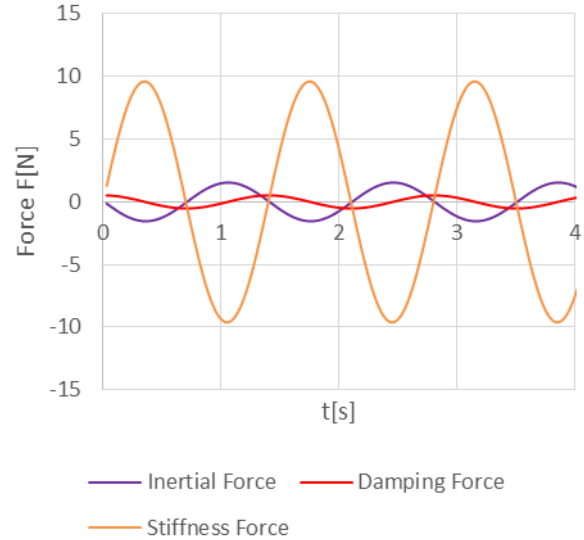


Fig. 7. Components of the force acting on a smooth cylinder

It can be seen from this that the stiffness force associated with the buoyancy of the structure has the largest share. The inertia force is in antiphase to it; hence, while the added mass of the smooth cylinder is the smallest, the net force acting on the cylinder will be the greatest.

In order to best analyse the properties of the structure, the waveforms of the inertia force (Fig. 8) and the damping forces (Fig. 9) for each of them have been shown. The course of the stiffness force is obviously the same because the waterline of each of them is the same.

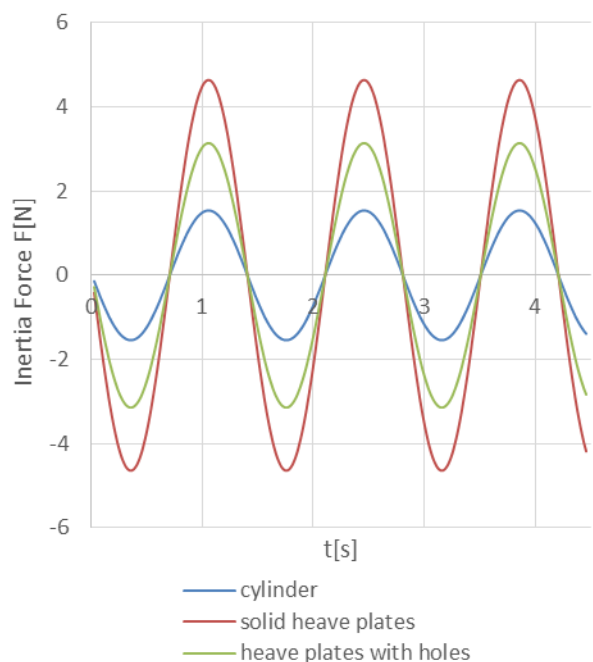


Fig. 8. Inertia force acting on the tested structures



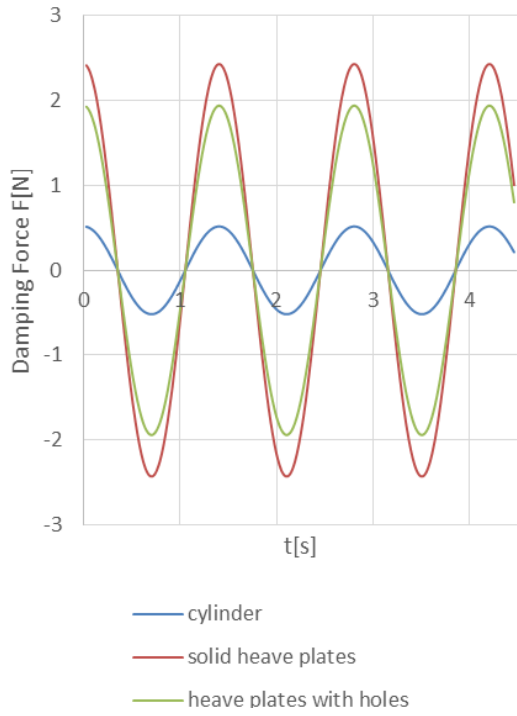


Fig. 9. The damping force acting on the tested structures

Analysing the data presented in the graphs, it is clear that the largest inertia force affects the structure with a solid damping plate, which is related to the largest added mass. The differences in the case of each of the three constructions are quite clear. In the case of the damping force, the differences between the solid plate and the plate with holes are not so large, although the force is clearly greater for the solid plate. From this, it can be concluded that the perforated plate causes quite a high damping without increasing the added mass as much as a solid plate, which in some cases can be very advantageous.

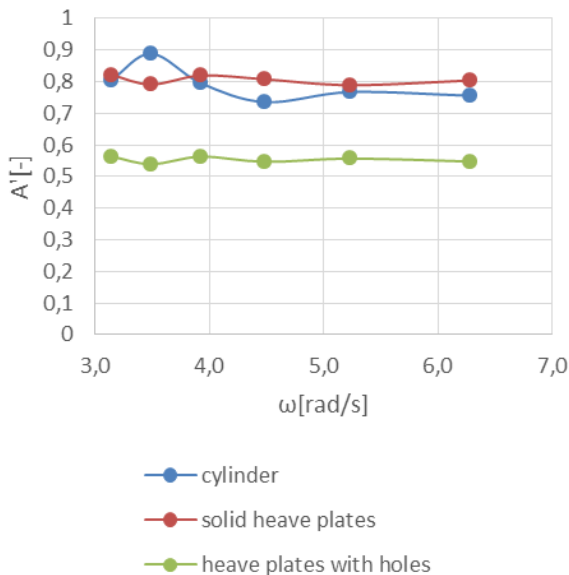


Fig. 10. Dimensionless added mass coefficient  $A' = a/m'$

On the basis of the performed simulations, the hydrodynamic coefficients of the linear equation, the added mass  $a$  and the damping coefficient  $b$  were determined. To facilitate the analysis, the obtained values are presented in a dimensionless form,

referring to the theoretical added mass for disc  $m' = 1/3\rho D^3$ , which is similar to the inference arrived at in the study of Tao and Dray [9], in which the following descriptions were given, that is to say,  $A' = a/m'$  (Fig. 10) and  $B' = b/2m'\omega$  (Fig. 11).

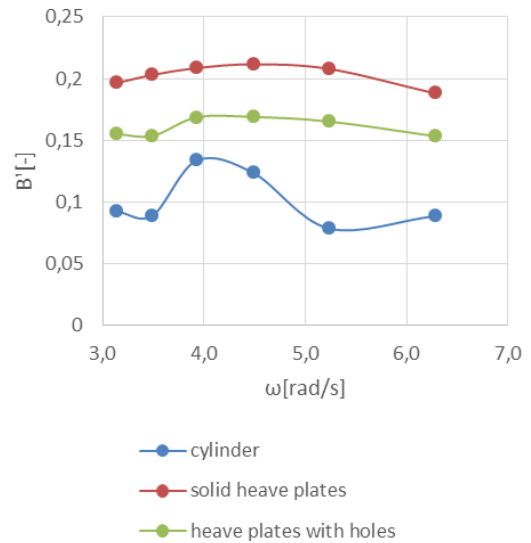


Fig. 11. Dimensionless damping coefficient  $B' = b/2m'\omega$

Based on the presented values, it is clear that a solid plate gives a greater added mass than a plate with holes. Also the damping coefficient is greater with a solid plate. Although this is not clearly visible after dimensioning, it should be emphasised that while the added mass does not change significantly depending on the oscillation period, in the case of the value of the damping coefficient, we observe a clear relationship: the longer the oscillation period, the lower the damping value.

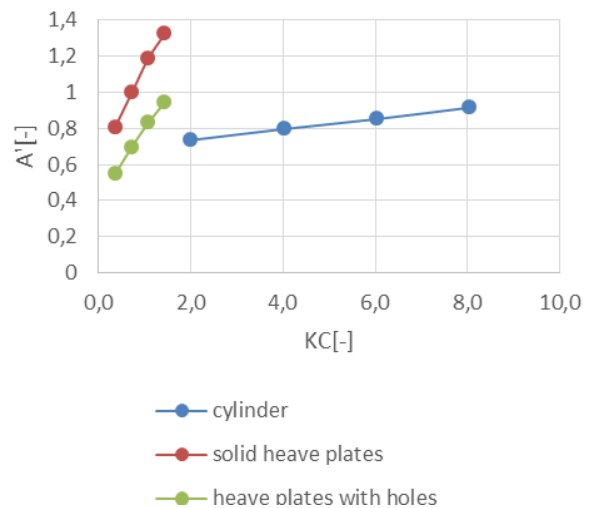


Fig. 12. Dimensionless added mass coefficient  $A' = a/m'$  dependent on KC. KC, Keulegan-Carpenter number

The assumption of linearity is actually a major simplification. It was therefore checked how the value of the determined coefficients changes depending on the amplitude of the movement. The results pertaining to the oscillation period  $T = 1.4$  s are shown in Fig. 12 for dimensionless added mass and Fig. 13 for dimensionless damping coefficient.

The obtained values of the dimensionless added mass coefficients and the damping coefficient for the solid plate are close to those presented in the literature, e.g. as reported by Medina-Manuel et al. [7].

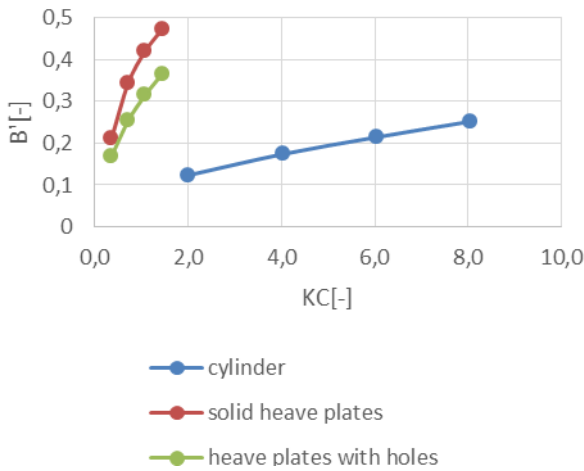


Fig. 13. Dimensionless damping coefficient  $B^* = b/2m\omega$  dependent on KC. KC, Keulegan–Carpenter number

Based on the presented values, it can be concluded that the greater the excitation amplitude, the greater the value of both the added mass and the damping coefficient. This is a very important observation, especially in the context of determining the transfer function. If we want to obtain a high compliance of the maximum value of the transfer function with reality, we should select the damping coefficient for the expected displacement amplitude. However, it may then turn out that we will receive underestimated values in the remaining wave range.

An example of calculations of the force course using a linear equation with determined coefficients (dashed line) and the force calculated in the program for a cylinder with a solid plate (solid line) oscillating with a period of  $T = 1.4$  s is shown in Fig. 14.

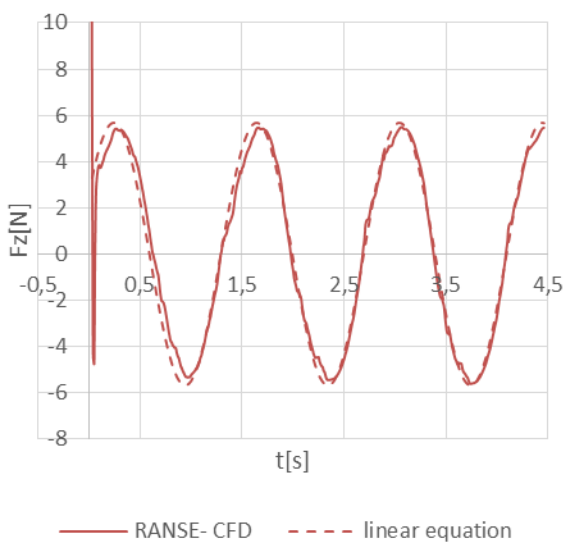


Fig. 14. Force on cylinder with solid heave plates

Using the method of least squares concomitant with employing the determined force values, the coefficients of the Morison

equation were also determined for the tested cases. Their values are shown in Fig. 15 – drag coefficient  $C_D$  and Fig. 16 – coefficient of added mass  $C_a$ . The values of the added mass coefficient were very similar to those determined on the basis of the added mass of the linear equation, which are marked on the graph with a dashed line.

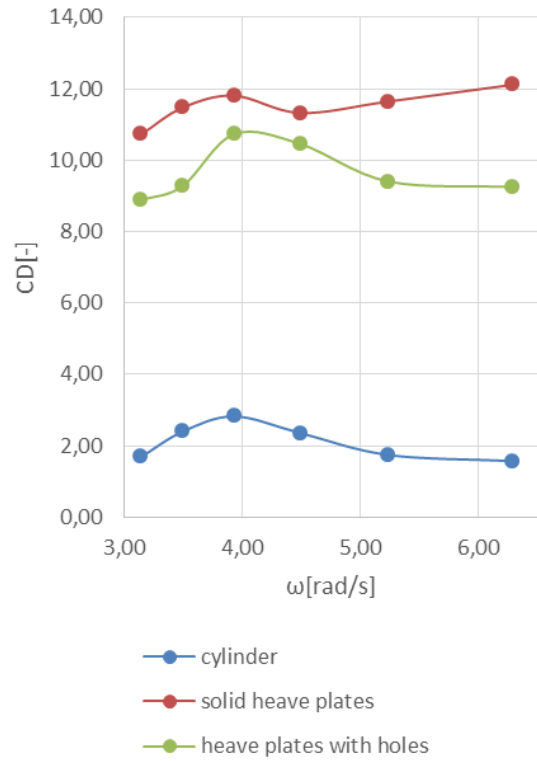


Fig. 15. Morison drag coefficient

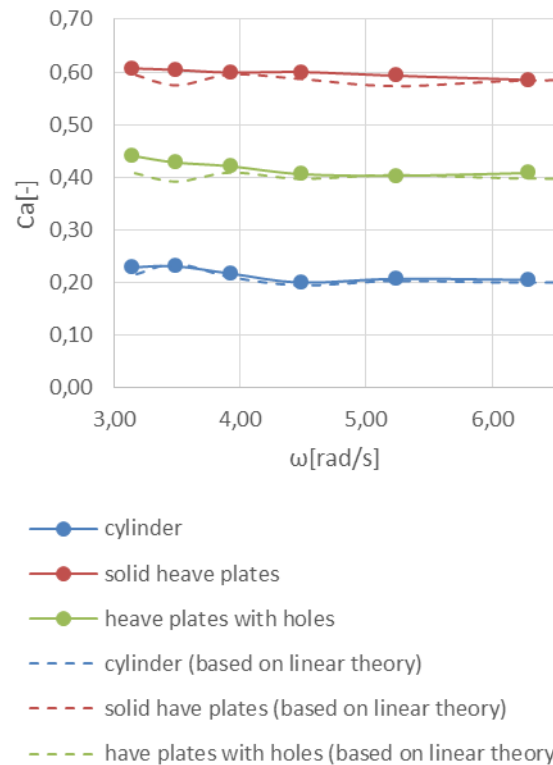


Fig. 16. Added mass coefficient

Based on the obtained results, the following conclusions can be drawn. Changes in the value of the drag coefficient depending on the oscillation period are not as large as in the case of the linear damping coefficient. This is very important from the point of view of viscosity modelling in the AQWA program because only a constant coefficient of additional drag is available there.

The values of the added mass coefficients determined by both methods are similar.

**5. CALCULATIONS OF RESPONSE AMPLITUDE OPERATORS**

In the case of analyses for floating objects, one of the key issues is to determine the transfer function, i.e. the response of the structure depending on the frequency of the excitation wave. It allows us to predict which waves pose the greatest threat to the safety of the structure, and by comparing it with the spectrum of an irregular wave, we can determine the expected actual displacement of the structure during its operation.

These functions for constructions with full heave plate and heave plate with holes were determined using various methods:

- an experiment;
- RANSE-CFD calculations;
- calculations using the diffraction method extended by linear drag coefficients (AQWA b); and
- calculations using the diffraction method extended by quadratic drag coefficients (AQWA CD).

The results, in the form of drawings, are presented in Fig. 17 for a solid plate and in Fig. 18 for a plate with holes.

It is clear that in the case of the diffraction method, much better results are obtained when the model is extended by quadratic rather than linear drag coefficients. This method gives results that are as good as, or even better than, those of the much more time-consuming RANSE-CFD method.

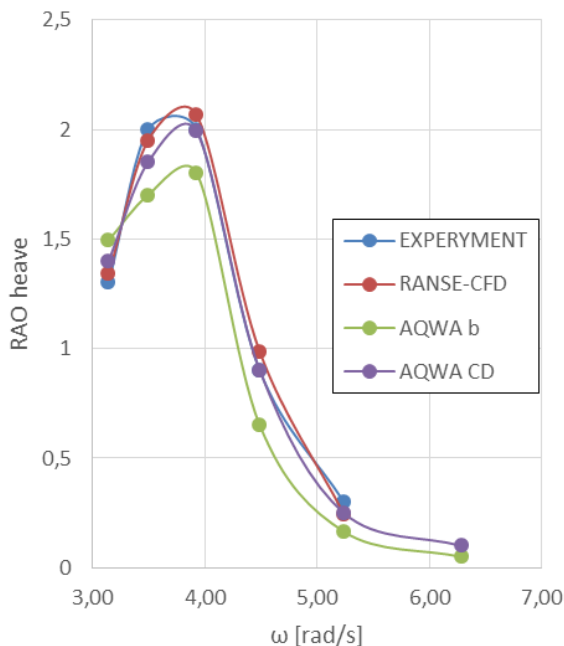


Fig. 17. Response amplitude operator for solid plates

Comparing the transfer functions obtained in the experiment for the structure with a solid plate vis-à-vis those for a plate with

holes (Fig. 19), we can see that the maximum displacement for a plate with holes is smaller than that for a solid plate. Cutting holes in the plate also transfers the maximum response towards higher wave frequencies.

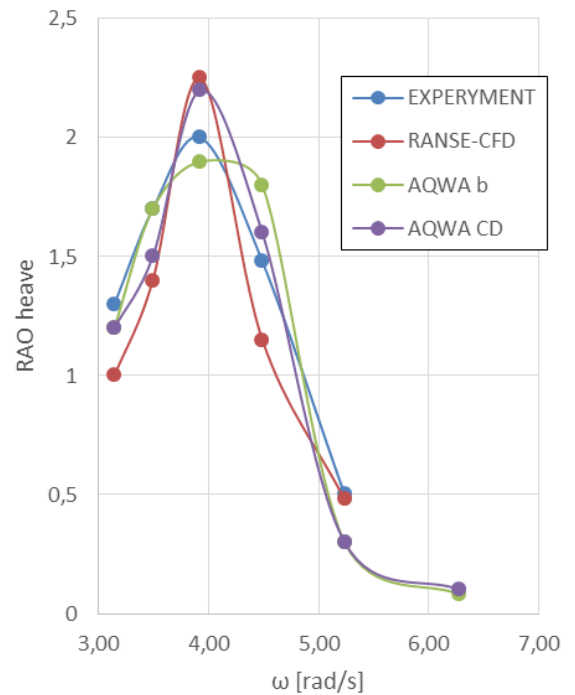


Fig. 18. Response amplitude operator for plates with holes

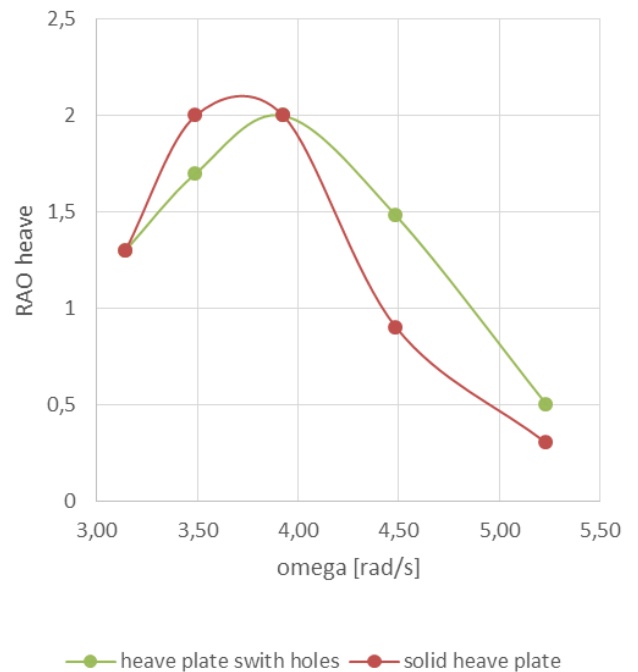


Fig. 19. Comparison of RAO for a solid and plate with holes

**6. CONCLUSIONS**

On the basis of the calculations carried out for the structure with a solid heave plate and a heave plate with holes, several conclusions can be drawn. The use of a heave plate results in an increase in both inertia and damping forces as compared with a


smooth cylinder. This is related to the increase in the added mass and the increase in the dissipation of energy flowing from the edge of the vortex plate. Cutting holes in the damping plate reduces the weight of the added mass in relation to the solid plate, while maintaining significant damping.

The hydrodynamic coefficients change both depending on the excitation frequency and the amplitude of the structure movement. In the case of the linear damping factor, these changes are much more pronounced than in the case of the quadratic damping factor. Therefore, when modelling the movement of the structure in a program based on the diffraction method, where the influence of viscosity is modelled with a constant linear or quadratic damping factor, a better solution is to choose a quadratic damping factor. The problem of modelling the value of the damping coefficient depending on the amplitude of the structure motion should be solved by determining its value at the expected maximum amplitude of the structure motion in operating conditions. It should be remembered that such a solution may result in underestimated displacements of the structure on waves in the remaining frequency range.

Performing a comparison between the transfer functions obtained for a structure with solid heave plates vis-à-vis those corresponding to heave plates with holes shows that cutting out the holes can reduce the maximum displacement of the structure in the wave. Cutting holes also shifts the transfer function towards higher wave frequencies. The use of a solid plate or a plate with holes for a specific structure should be decided after comparing the course of the transfer function with the expected spectrum of an irregular wave in the area of its operation.

## REFERENCES

- Dymarski P, Dymarski C, Ciba E. Stability Analysis of the Floating Offshore Wind Turbine Support Structure of Cell Spar Type During its Installation. *Polish Maritime Research* 2019, Vol. 26, 4(104), 109-116. DOI:10.2478/pomr-2019-0072.
- Kraskowski M, Marcinkowski T. Numerical and experimental analysis of the wave induced forces on the tripod support structure. *Laboratory study. Bulletin of Maritime Institute in Gdańsk* 2017 32(1):21-29. DOI 10.5604/12307424.1224269.
- Motallebi M, Ghassemi H, Shokouhian M. DeepCwind semi-submersible floating offshore wind turbine platform with a nonlinear multi-segment catenary mooring line and intermediate buoy. *Scientific Journals of the Maritime University of Szczecin* 2022, 69 (141). DOI: 10.17402/496.
- Ciba E, Dymarski P, Grygorowicz M. Heave Plates with Holes for Floating Offshore Wind Turbines. *Polish Maritime Research* 2022 vol 29 pp.26-33. DOI: 10.2478/pomr-2022-0003.
- Subbulakshmi A, Sundaravivelu R. Heave damping of spar platform for offshore wind turbine with heave plate. *Ocean Engineering* 2016 121, 24-36.
- Tao L, Cai S. Heave Motion Suppression of a Spar with a Heave Plate. *Ocean Engineering* 2004.
- Medina-Manuel A, Botia-Vera E, Saettone S, Calderon-Sanchez J, Bulian G, Souto-Iglesias. Hydrodynamic coefficients from forced and decay heave motion tests of a scaled model of a column of a floating wind turbine equipped with a heave plate. *Ocean Engineering* 2022,252. <https://doi.org/10.1016/j.oceaneng.2022.110985>.
- Ciba E. Heave Motion of a Vertical Cylinder with Heave Plates. *Polish Maritime Research* 2021, Vol. 28,iss. 1(109), s.42-47. <https://doi.org/10.2478/pomr-2021-0004>.
- Tao L, Dray D. Hydrodynamic performance of solid and porous heave plates. *Ocean Engineering* 2008. doi:10.1016/j.oceaneng.2008.03.003.
- An S, Faltinsen O.M. An experimental and numerical study of heave added mass and damping of horizontally submerged and perforated rectangular plates. *Journal of Fluids and Structures* 39 (2013) 87-101
- Tian X. et al. Hydrodynamic coefficients of oscillating flat plates at  $0.15 < KC < 3.15$ . *Journal of Mechanical Science and Technology* 2016. <https://doi.org/10.1016/j.apor.2019.102042>.
- Mentzoni F, Kristiansen T. Two-dimensional experimental and numerical investigations of parallel perforated plates in oscillating and orbital flows. *Applied Ocean Research*. 2020. 10.1016/j.apor.2019.102042.
- Molin B. On the added mass and damping of periodic Arrays of fully or partially porous disks. *Journal of Fluid and Structures* 2001, 15(2), 275-290. doi:10.1006/jfls.2000.0338.
- Mojtaba E, Tao L, Shabakhty N. Hydrodynamic damping of solid and perforated heave plates oscillating at low KC number based on experimental data: A review. *Ocean Engineering* 2022. DOI: 10.1016/j.oceaneng.2022.111247.
- Rao MJ, Nallayarasu S, Bhattacharyya SK. Numerical and experimental studies of heave damping and added mass of spar with heave plates using forced oscillation. *Applied Ocean Research* 2021, 111. <https://doi.org/10.1016/j.apor.2021.102667>.
- Maron A, Fernandez EM, Valea A, Lopez-Pavon C. Scale Effects on Heave Plates for Semi-Submersible Floating Offshore Wind Turbines. *Case Study With a Solid Plain Plate. Journal of Offshore Mechanics and Arctic Engineering* 2019. DOI: 10.1115/1.4045374.
- Raed K, Murali K, Experimental and numerical analysis of a spar platform subjected to regular waves, *Developments in Maritime Technology and Engineering – Guedes Soares & Santos (eds)* 2021. DOI: 10.1201/9781003216599-64.

Ewelina Ciba:  <https://orcid.org/0000-0002-9042-5234>

Paweł Dymarski:  <https://orcid.org/0000-0002-6033-0461>



This work is licensed under the Creative Commons BY-NC-ND 4.0 license.



## MATERIAL CHARACTERISTIC OF AN INNOVATIVE STENT FOR THE TREATMENT OF URETHRAL STENOSIS

Jagoda KUROWIAK\*, Agnieszka MACKIEWICZ\*, Tomasz KLEKIEL\*, Romuald BĘDZIŃSKI\*

\*Faculty of Mechanical Engineering, Department of Biomedical Engineering, University of Zielona Góra,  
 ul. Prof. Z. Szafrana 4, 65-516 Zielona Góra, Poland

[j.kurowiak@iimb.uz.zgora.pl](mailto:j.kurowiak@iimb.uz.zgora.pl), [a.mackiewicz@iimb.uz.zgora.pl](mailto:a.mackiewicz@iimb.uz.zgora.pl), [t.klekiel@iimb.uz.zgora.pl](mailto:t.klekiel@iimb.uz.zgora.pl), [r.bedzinski@iimb.uz.zgora.pl](mailto:r.bedzinski@iimb.uz.zgora.pl)

*received 24 February 2023, revised 3 May 2023, accepted 3 May 2023*

**Abstract:** The appropriate development and customisation of the stent to the urethral tissues requires the determination of many factors such as strength and degradation. Given the distinctive conditions of urethral tissues, it is important that the design of the stent be properly developed. The selection of a stent material requires knowing its material characteristics and verifying that they are suitable for the future implantation site. In the present study, the development of a polydioxanone (PDO)-based stent was undertaken. The PDO material was fabricated using an additive technique – 3D printing. Then, *in vitro* tests were performed to determine the degradation time of the material under conditions simulating an aggressive urinary environment. The changes in the parameters of mechanical properties before and after the degradation period were determined, and the changes in the structure of the material before and after degradation were observed. Numerical analysis was performed for the proposed stent design. The results showed that PDO has good mechanical properties, but its degradation time is too short to be used in a urethral stent. Among the innovations of the studies conducted are bending strength tests, which is not a frequently considered aspect so far.

**Key words:** polydioxanone, urethra, modelling, degradation, mechanical properties

### 1. INTRODUCTION

The urethra, bladder, kidneys and ureters are the anatomical components of the genitourinary system. This arrangement is a storage as well as a drainage system for urine and other toxins excreted from the body. The urogenital system monitors and controls electrolyte levels; regulates blood volume, pressure and pH; and, in case of men, is also responsible for reproductive functions. The structure of the urethra is formed by two main layers of cells: epithelium and smooth muscle cells. Each of these layers has a specific function. The epithelium of the lower urinary tract primarily constitutes a protective function. It protects the deeper layers of the urethra from the absorption of toxins expelled from the body. Smooth muscle cells, on the other hand, affect the elastic and flexible properties of the urethral tissues. There are also small blood vessels in the urethra, which serve the function of nourishing this tissues [1,2]. The literature indicates problems with the correct use of terminology to describe the anatomy of the urethra, mainly male urethra, which is much more likely to be diseased or damaged. As described by Verla et al. [3], male urethra consists of two main sections (from the bladder to the urethral outlet): posterior urethra and anterior urethra. The posterior urethra is divided into the prostatic and the membranous urethra, while the anterior urethra contains the bulbar and the penile urethra [3].

Currently, urological diseases are a major problem worldwide. Disorders related to urethral functioning not only lead to deterioration of the patients' quality of life and genital incapacity, especially in men, but also generate significant health-care expenses [1,2]. The main and most commonly diagnosed disorder of the urethra is urethral stricture. The clinical symptoms of urethral stricture include urinary problems such as increased micturition with less

urine output, lower urinary tract infections, discomfort and decreased quality of life, sepsis, bladder stone formation, kidney failure and, in the most serious cases, death. Urethral stricture occurs as a result of tissues fibrosis, which leads to a reduction in the urethral lumen that impedes the free flow of urine and other metabolic products [4–8]. All kinds of injuries to the epithelial and spongy parts are considered to be the cause of this pathology, which subsequently leads to changes in the cellular matrix of the urethral tissues. The primary activity of the epithelium at the site of injury at the time of malfunction is unable to replace the lost cells, which leads to fibrosis. This phenomenon is followed by the replacement of a healthy connective tissue by densely clustered fibroblasts in the stricture tissues. The ratio of type III collagen to type I collagen present in the tissues also decreases. In addition, dense collagen fibres replace smooth muscle cells, significantly impairing the elasticity of the entire system [1,9,10]. Due to specific physiological conditions of the urethra, which include pressure, flow and the interaction of adjacent structures, the urethral tissues must be properly adapted and sufficiently robust to cope with its normal function. Therefore, mechanical properties of the urethra depend on the structure and thickness of the connective tissue and muscle membrane. These tissues are anisotropic in structure and show a nonlinear stress–strain relationship. This is due to the presence of collagen and elastin fibres as well as biological fluids in the structure of the tissues. It provides the tissues with viscoelastic properties due to the presence of elastin, which is a highly elastic fibre that provides elasticity but low tensile strength, and due to the presence of collagen, which gives stiffness to the tissues [6].

The cause of male urethral stricture can vary. It can be caused by iatrogenic injuries, idiopathic causes, previous infectious disease or external trauma [3,9,11,12]. Mundy and Andrich

[12] indicated that for the strictures occurring in the penile area, iatrogenic trauma (40%) and conditions of inflammation (40%) are the most common causes, while the strictures involving the bladder could arise due to idiopathic (40%) and iatrogenic (35%) causes [12]. The literature is fairly explicit that endoscopic procedures performed to treat benign or neoplastic prostatic growths and bladder pathologies, as well as idiopathic causes of unknown origin and cause, are the most common causes of the urethral strictures.

The treatment and reconstruction of the urethral stricture is still a significant challenge for the urological community. There is still no indication concerning the best method of treating this condition; thus, various methods are used in an attempt to select them appropriately depending on the aetiology of the origin, location and length of the stricture [1]. The oldest method of treating the urethral stenosis is calibration, which aims to dilate the narrowed area using balloons, for example. Unfortunately, this method is only a maintenance and temporary treatment and does not counteract the causes of the tissue fibrosis. Long-term dilatation of the urethral wall can lead to frequent recurrence of the stricture. Another treatment that has been claimed to replace dilation is urethrotomy, which involves incision of the fibrotic tissues. The success of both the dilation and urethrotomy procedures mainly depends on the location and length of the stricture, and their main disadvantage is a high rate of the recurrent strictures. Their effectiveness decreases as the length of the stricture increases. Due to the low success rate of these procedures, their disadvantages and complications, the European Association of Urology (EAU) recommends that these procedures should not be used as a treatment when the length of the segment at which the stenosis occurs is  $>2$  cm [9,13–15].

There is the possibility of using the end-to-end method, which involves cutting out the stenosis and re-anastomosing the tissues. This method can be effective only if the length of the stenosis is  $<1$ – $2$  cm. Another treatment method is plastic reconstruction, or urethroplasty, which involves transplanting the tissue from the oral cavity or bowel mucosa [4,16]. Although urethroplasty shows better long-term success rates than dilation and urethrotomy, unfortunately, problems are still encountered. Bleeding, pain and swelling, contractures and scarring, and disruption of the salivary or gastrointestinal tract can occur at the donor site. On the other hand, complications such as fistula and infections can occur at the transplant site as the transplanted membrane flaps may not function properly in the urine environment [3,4,16].

Along with the high percentage of surgical failures and problems related to the availability of transplanted tissues, new alternative therapies based on the achievements of material engineering and additive technologies are being sought. The use of available biodegradable materials especially natural polymers (hydrogels, i.e., sodium alginate and chitosan), or synthetic polymers (poly(L-lactide [PLLA], poly-caprolactone [PCL], poly(D,L-lactide-co-glycolide) [PDLLA], poly(lactic-co-glycolic acid) [PLGA], polydioxanone [PDO]) along with 3D printing is a good approach for developing and manufacturing urological stents. Stenting is a good treatment option due to the availability of a wide range of biodegradable polymers. To properly select a material for a urological stent, it is necessary to determine the functional conditions of the stent [6–8,17], which allows determining of the requirements for the design including the selection of the mechanical properties of the material so as to match the mechanical characteristics of the stent appropriate to the deformability of the urethra. The key element that enables the design and fabrication of the

optimal biomimetic scaffolds for the urethra is to know the mechanical and material parameters of the urethral tissues [18].

One of the promising materials that can meet the demands of urological stents is PDO. PDO is a fully biodegradable synthetic polymer that has ester and ether groups in its structure. It is believed to have the potential to be a future material for biomedical applications [19–25] due to its good mechanical properties, biocompatibility, low inflammatory response and full metabolism by the body [26]. Adolffson et al. [25] developed innovative re-sorbable tourniquets for suspending vascular tissues during surgery. Bands made by the incremental methods with PDO have been tested in vitro in phosphate buffered saline (PBS) solution at  $37^{\circ}\text{C}$  for 10 days, 28 days and 140 days as well as in vivo – they were implanted subcutaneously in horses for the same period. While the fabrication of the bands was not a problem due to the good properties of the material, allowing 3D printing, a significant decrease in the mechanical strength of the in vivo implanted bands was observed as early as 28 days after implantation. Mechanical strength of the bands tested in vitro was significantly higher than that of the bands implanted in vivo. The results suggest that the in vivo environment is much more aggressive towards the tested implant; therefore, the implant degrades much faster in it [25]. Fathi et al., [27] fabricated composite intestinal splicing stents using pure PDO and its PCL composites at different mass ratios by 3D printing. The stents were tested in vitro in simulated intestinal fluid (SIF) and foetal bovine serum (FBS) solutions at  $37^{\circ}\text{C}$  for 3 days, 6 days, 10 days and 20 days, and in vivo by implanting the fabricated stents in the small intestine in pigs. In the in vitro tests, a predictable decrease in the weight of the implant samples associated with decomposition was observed. The maximum weight loss was about 80% after 20 days of the incubation in SIF solution. An in vivo test was conducted on two pigs by splicing the surgically cut intestine at the same locations. One of the pigs showed signs of inflammation and infection due to the rupture of the implant 14 h after implantation, so it was sedated. The other pig did not show similar symptoms, and dissection showed that the implant was accepted and remained tight after a longer period (2 weeks). Microscopic observation using a scanning electron microscope (SEM) showed that the layered design of the implants resulted in better cell adhesion to the implant, which positively affected the healing process [27].

Park et al. [28] investigated the inflammatory response in dogs to the implantation of a urological stent made of PDO wire by manual spinning. Each dog received two implants – a proximal and a distal urethral implant. The dogs were divided into three groups, which were dissected after 4 weeks, 8 weeks and 12 weeks. Implant weight reduction occurred sequentially by 54% after 4 weeks of implantation and by 84% after 8 weeks, and after 12 weeks, the stents were completely dissolved. The study showed a slight inflammatory reaction after the implantation and an increase in the granulation tissue formation with time, but no closure of the urethral lumen [28]. Stehlik et al. [29] implanted dilating tracheal stents made of PDO mono-wire in four patients with tracheal stenosis. All patients showed improvement immediately after the implantation and in the long term. The stents were completely absorbed after 7 months, with endoscopy showing residual traces of the stent implantation in the form of scarring and tissue granulation. The authors noted that due to the decreasing mechanical strength over time, resulting from the degradation of the stent made of PDO compared to, for example, classic stents made of NiTi alloy, recurrence of the tracheal lumen stenosis is possible. Nevertheless, the authors considered this type of im-

plant to be future-proof [29]. Zamiri et al. [30] studied the response to implantation of arterial stents made of various composites including PDO tested in vivo in pigs. The stents were implanted in the carotid arteries and left there for 30 days and 90 days. The animals were investigated for inflammation periodically against the disintegrating stents, and there was little or moderate inflammation in PDO. The authors also noted that the internal diameter of the stent made of PDO after 90 days of implantation in the artery was the smallest of all the tested ones. Considering all the composites and polymers tested, the authors concluded that resorbable materials are suitable for use as the stent materials in less than a year [30].

In the present study, the authors evaluated PDO. In vitro laboratory tests were performed for the requirements of urological stents. Strength requirements were determined by the numerical analysis. To evaluate the mechanical properties of PDO, mechanical tests were performed by static tensile testing and three-point bending. Material degradation tests were performed in an artificial urine environment reflecting the environmental conditions inside the coil including the effect of degradation on the mechanical properties. Fourier-transform infrared spectroscopy (FTIR) analysis and scanning electron microscope (SEM) surface morphology analysis were performed to describe the degradation-induced changes in the material structure.

2. MATERIALS AND METHODS

2.1. Stent deformability analysis

To determine the requirements for the stent, a numerical model, which was developed based the studies on the urethras of New Zealand rabbits, was used [6]. The diameter range of 0–15 mm depending on the pressure inside was assumed as the dimensions of the urethral canal [6]. Since the assumptions made considered that the stenosis covers about 2 cm of the length of the urethra, an implant of the shape, as shown in Fig. 1, was proposed.

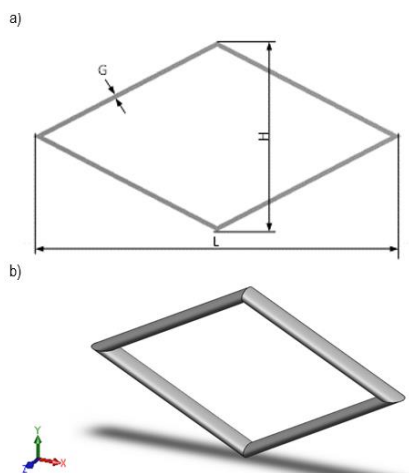


Fig. 1. Stent model: (a) dimensions L = 25 mm, H = 13 mm, G = 2 mm; (b) 3D model

The adopted shape of the stent was subjected to a numerical analysis to determine the values of the relative deformations occurring inside such a structure, resulting in the determination of

the limit at which changes caused by the material degradation will cause loss of the stent functionality. The pressure that occurs in the urethral canal of about 15 mBar was taken as the load of the stent [6].

2.2. Materials

In the research, RESOMER Filament X D1.75 Polydioxanone from Evonik (Alabama, USA) was used. The degradation process was carried out in an artificial urine solution, which was prepared according to a commonly used procedure presented in the works mentioned in Refs [7,17,31,32], among others. The solution consisted of urea (Sigma-Aldrich, Poznań, Poland), creatinine (Sigma-Aldrich, Poznań, Poland), sodium chloride NaCl (Sigma-Aldrich, Poznań, Poland), ammonium chloride NH<sub>4</sub>Cl (Chempur, Poland), sodium sulphate Na<sub>2</sub>SO<sub>4</sub> (Avantor Performance Materials Poland SA, Gliwice, Poland) and disodium phosphate (Avantor Performance Materials Poland SA, Gliwice, Poland). The artificial urine solution was prepared using ultrapure water.

2.3. Sample preparation – 3D printing

To manufacture the PDO specimens, 3D printing realised on a Flashforge Adventurer printer was used. The bending test was performed on perpendicular specimens prepared in accordance with ISO 178:2010 Plastics – Determination of bending properties. The tensile tests were performed on paddle specimens prepared in accordance with ISO 527:1998 Plastics. The determination of mechanical properties in static tension. The tests were carried out on specimens whose dimensions are specified by the mentioned standards.

Samples for bending tests: rectangular specimens were made on a scale of 1:3 (measuring length 26 mm, width 3.33 mm and thickness 1.33 mm).

Samples for tensile tests: paddle samples were made on a scale of 1:4 (measuring length 12.5 mm, width 2.5 mm and thickness 1.0 mm).

The PDO polymer printing parameters were chosen according to the manufacturer’s recommendations: nozzle temperature 150°C and table temperature 90°C. Other printing conditions to ensure that PDO specimens are ready for testing are as follows: fill density 100%, printing speed 30 mm/s, traverse speed 30 mm/s and printing accuracy is ± 0.2 mm. In Tab. 1, the nomenclature of the test samples is given.

Tab. 1. Name of the samples tested

Material	Incubation in a degrading environment [days]	Name of the sample
PDO	0	PDO_0d
	1	PDO_1d
	2	PDO_2d
	5	PDO_5d
	7	PDO_7d
	15	PDO_15d
	30	PDO_30d
	45	PDO_45d

PDO, polydioxanone

## 2.4. In vitro degradation

The degradation studies of PDO were carried out in artificial urine solution, and the mass change evaluation was determined after 0 day, 1 day, 2 days, 5 days, 7 days, 15 days, 30 days and 45 days. For each degradation period, the number of samples was  $n = 5$ . The obtained results were averaged. For the purpose of replicating the conditions as closely as possible, the degradation tests were carried out using an Avantgarde Line BD115 incubator (Binder GmbH, Tuttlingen, Germany) providing a constant temperature of 37°C. The samples were stored separately in sterile and tightly sealed polypropylene (PP) containers filled with 15 ml of the urine solution. The urine solution was replaced every 7 days. Change in the material weight due to degradation was calculated from relation (1):

$$\text{Weight change [\%]} = \left( \frac{M_{\text{wet}} - M_{\text{dry}}}{M_{\text{wet}}} \right) * 100\% \quad (1)$$

where  $M_{\text{wet}}$  is the initial mass of the sample and  $M_{\text{dry}}$  is the mass of the sample dried after immersion in the artificial urine solution.

## 2.5. Tensile strength

The tensile tests were performed on paddle specimens (Fig. 2) prepared in accordance with PN-EN ISO 527:1998 Plastics. The determination of mechanical properties in static tension. The tests were performed for PDO specimens after the process of manufacturing by 3D printing, until their destruction. Based on the tests, Young's modulus ( $E$ ), tensile strength ( $R_m$ ) and yield strength ( $R_e$ ) were determined. The number of test specimens was  $n = 5$ . The testing speed was 15 mm/min. The research conditions were as follows: temperature 23°C and air humidity 40%. During the degradation, the pH of the artificial urine solution was monitored using an Elmetron CPI-505 pH meter (Elmetron, Zabrze, Poland).

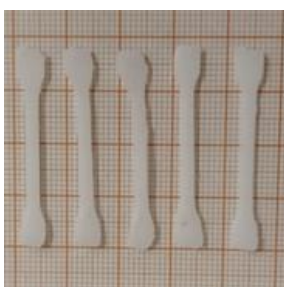


Fig. 2. PDO samples manufactured by 3D printing – for tensile strength testing. PDO, polydioxanone

## 2.6. Bending test

The strength tests determining the bending properties for the PDO material were performed on a Zwick Roell EPZ 005 testing machine (Zwick Roell, Ulm, Germany). The bending test was carried out in accordance with the requirements described in ISO 178:2010.

The perpendicular specimens (Fig. 3.) were made on a scale of 1:3: measurement length  $L = 26$  mm, width  $b = 3.33$  mm and thickness  $h = 1.33$  mm (dimensional accuracy due to the manufacturing technology was  $\pm 0.2$  mm).

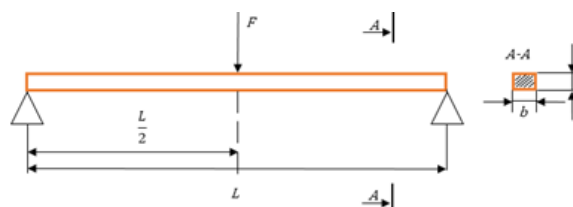


Fig. 3. Three-point bending test

The tests were conducted for the material before and after the specified degradation time (0 day, 1 day, 2 days, 5 days, 7 days, 15 days, 30 days and 45 days). After each degradation time, Young's modulus of the five specimens was determined with three replicates of each specimen ( $n = 15$ ). The test speed was 0.1 mm/s. The assumed deflection for each repetition was 1 mm. This is the parameter that allows performing of a non-destructive bending test. The tests made it possible to determine such parameters as the longitudinal elastic modulus – Young's modulus ( $E$ ), bending strength ( $\sigma_g$ ) and strain ( $\epsilon$ ). The material, after being drawn from the urine, was placed in the designed holder, and the bending process was started. The test conditions were as follows: temperature 23°C and humidity 40%.

The value of Young's modulus was determined according to the following steps:

- I. Measurement of the parameters of the test sample: width ( $b$ ), thickness ( $h$ ) and measurement length ( $L$ ).
- II. The deflection ( $s$ ) for the test specimen was determined, assuming  $s = 1$  mm.
- III. The plotting of force–displacement curves for a given deflection, reading the force ( $F$ ) for a deflection of 1 mm.
- IV. The calculation of the value of Young's modulus from relation (2):

$$E = \left( \frac{3FL^3}{8bh^3s} \right) \quad (2)$$

where  $F$  is the maximum force for deflection [N],  $L$  is the measurement length [mm],  $b$  is the specimen width [mm],  $h$  is the specimen height [mm] and  $s$  is the deflection.

Presentation of the obtained results of the calculated Young's modulus on a box plot.

## 2.7. FTIR-ATR analysis – Fourier-transform infrared spectrometry

The purpose of this research was to evaluate the chemical structure of the PDO material before and after incubation in an artificial urine solution. It was important to see if there are chemical changes in the material during the degradation process that could negatively affect the stent–tissue interactions. Infrared spectroscopy studies were performed using a Thermo Scientific Nicolet iS50 FTIR spectrometer (Thermo Fisher Scientific, Massachusetts, USA). FTIR spectra were measured in the range from  $500 \text{ cm}^{-1}$  to  $4,000 \text{ cm}^{-1}$ , using an ATR detector at a resolution of 16 scans per spectrum and an optical resolution of  $4 \text{ cm}^{-1}$ . The ATR crystal was thoroughly cleaned with an alcohol-soaked tissue paper before and after each measurement. Before a new measurement, the background spectrum was measured and collected. The analysis was carried out at ambient temperature. Before the analysis, the samples were air-dried for 24 h to get rid of water molecules that could distort the spectrum. The measurements were made in triplicate for each degradation time, which were then averaged.



### 2.8. SEM microscopy analysis

The surface of the PDO polymer was examined using a scanning electron microscope SEM (JEOL, JSM-7600F, Tokyo, Japan). The purpose of this study was to characterise changes in the morphology of the material occurring as a result of its degradation. Before the material was placed in the chamber and imaged, the samples were coated with a 9-nm-thick chromium conductive layer (QUORUM Q150TS). The structure of the material was observed at 1,500× magnification using a voltage of 15 kV.

### 3. RESULTS AND DISCUSSION

Numerical analysis for the assumed stent shape made it possible to determine how changes in the material properties affect the deformability of the adopted stent model. Fig. 4a shows the deformation of the stent at 15 mbar for the material in its original form, that is, before the degradation process. Reinforcement of the material due to degradation caused the strain in the radial direction to the coil channel to decrease by about 30% under the same loading conditions (Fig. 4b.).

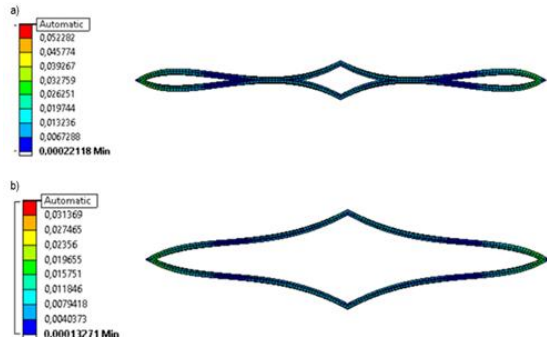


Fig. 4. Stent deformability under a circumferential pressure of 15 mBar for (a) material PDO before degradation test, (b) material PDO after 45 days degradation test. PDO, polydioxanone

The bending test was carried out on a degradable material and was a non-destructive test. It showed that during the degradation process of the stent made of PDO, its increased stiffness caused a decrease in the kinetics of the coil wall, which promotes both better micturition and generate problems related to the tissue fibrosis.

### 3.1. In vitro degradation

Degradation of the PDO material was evaluated by observing the change in its weight mass calculated from relation (1). Fig. 5 shows the results obtained. After 45 days of urine interaction simulating the conditions conducive to the degradation of this material, it was observed that for the first period of degradation (0–5 days), there was no significant weight change in the material (<1%). After 7 days, a slight decrease in the weight of the samples of about 2.5% was observed, while on the 45th day, the weight of the samples decreased by an average of about 15% from the initial weight. The measurement uncertainty was determined to be ±0.0021 g. This value is not statistically significant. The pH value of the urine solution was monitored during the degradation studies. The average pH value was 6.55, which is within the range of normal urine pH, that is, 4.5–8.0

It is widely accepted that the degradation time of PDO is <6 months [33–35]. From the degradation tests obtained in this study, a slight change in weight was observed, but the changes that occurred resulted in a decrease in the material strength.

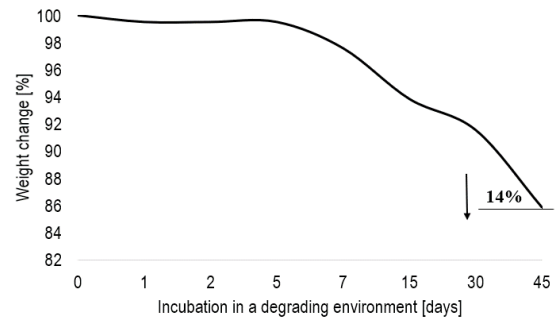


Fig. 4. Weight change of PDO material degraded in artificial urine solution. PDO, polydioxanone

### 3.2. Tensile strength

Strength tests for the static tensile test (Figs. 6 and 7) showed that Young’s modulus value was 450.68 MPa (418.75 MPa; 506.80 MPa), the tensile strength was 43.07 MPa (40.48 MPa; 45.11 MPa) and the yield strength was 9.79 MPa (9.04 MPa; 11.06 MPa). Bezrouk et al. [24] in their study on commercially available stents made of a PDO monofilament showed that their average Young’s modulus value was 958 MPa [24]. Similar results were obtained by Loskot et al. [20], where average Young’s modulus value for the specimens was 965 MPa.

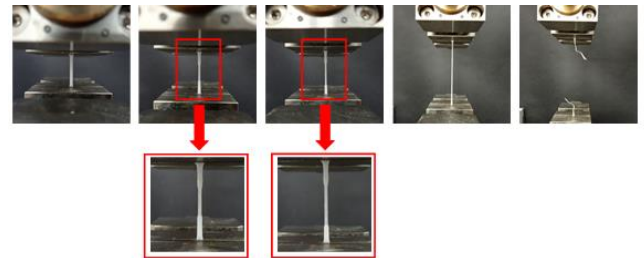


Fig. 5. Static tensile test of PDO – example photo of a sample. PDO, polydioxanone

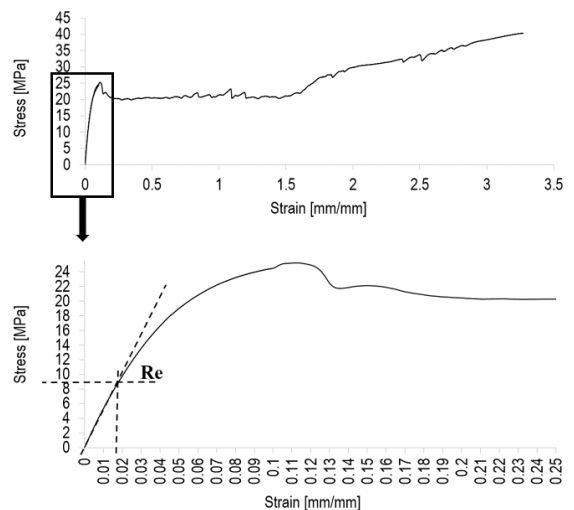
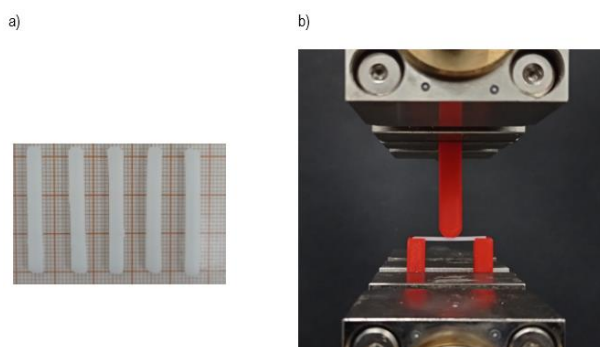


Fig. 6. Stress–strain curves for PDO static tensile testing. PDO, polydioxanone

### 3.3. Bending test

To evaluate the functionality of the stent, it was necessary to determine the mechanical properties of the material in question. In case of urological stents, it is desirable that the material used and the design of the stent allow high deformability. This high deformability should allow for large changes in the cross-sectional area of the urethra, which are naturally induced by the pressure changes and the activity of muscles acting in the urethra. This behaviour of the stent should be the stent's response to the urethral wall endeavour to close the channel. At the same time, this mechanical mismatch and low biocompatibility between the stent and the tissues can lead to restenosis or hyperplasia of the tissue structure.

The bending test performed (Fig. 8a,b.) for the printing PDO materials allowed the determination of Young's modulus (E) (Fig. 9). From the data obtained, it can be seen that the longer the degradation time in a fluid simulating urine, the higher the stiffness of the material. There was an increase in the maximum bending stress with a simultaneous increase in the value of the longitudinal modulus (E).



**Fig. 7.** PDO specimens produced by 3D printing technology (a), flexural strength test rig with a mounted specimen (b). PDO, polydioxanone

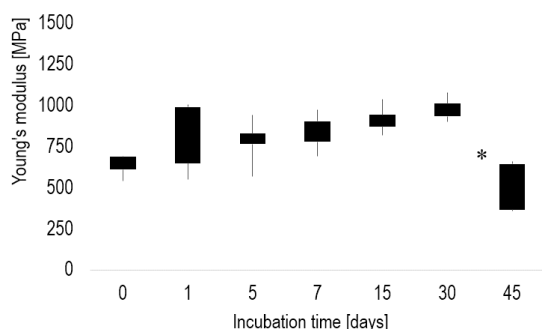


**Fig. 8.** Young's modulus of PDO material as a function of degradation time in urine. PDO, polydioxanone

Based on the results, it was also analysed how the average maximum force and Young's modulus (Tab. 2) changed during the deflection. The longer the incubation time in the urine environment, the higher the maximum force. This observation applies to studies involving up to 30 days of incubation. After the 45th day of the degradation, there was a sharp decrease in the maximum force along with a loss of mechanical properties of the PDO material. The material became brittle and much less strong, leading to failure at only 13.8% of the initial force. Lower values for Young's modulus obtained in this study are most likely due to the different

methods adopted for manufacturing of the samples and their different geometries. The higher the material Young's modulus, the higher its stiffness, and therefore, the less it deforms. Given the results analysed in relation to the urethral conditions, it is important to obtain the highest possible deformability, rather than stiffness, of the material.

**Tab. 2.** Summary of the average values of the action of maximum forces and the average values obtained for Young's modulus

	0 days deflection 1 mm	1 days deflection 1 mm	2 days deflection 1 mm	5 days deflection 1 mm	7 days deflection 1 mm	15 days deflection 1 mm	30 days deflection 1 mm	45 days* deflection 0.2 mm
Mean maximum strength [N]	0.94	1.14	1.15	1.16	1.22	1.35	1.46	<u>0.18</u>
Mean value of Young's Modulus [MPa=N/mm <sup>2</sup> ]	631.63	772.06	774.16	779.58	826.56	908.03	980.56	488.91

\* The loss of mechanical properties of the PDO material.

Conderman et al. [36] presented a mechanical analysis of a cartilage graft that was reinforced with a plate made of PDO. Young's modulus value in their study for PDO was  $692 \pm 37.4$  MPa. At the same time, it should be noted that in case of Conderman's study, the bending test for the PDO material was performed for the material using a different manufacturing procedure with no degradation process [36].

### 3.4. FTIR-ATR analysis – Fourier spectrometry in infrared

The characteristics of the FTIR spectra for the PDO material are presented in Fig. 10.

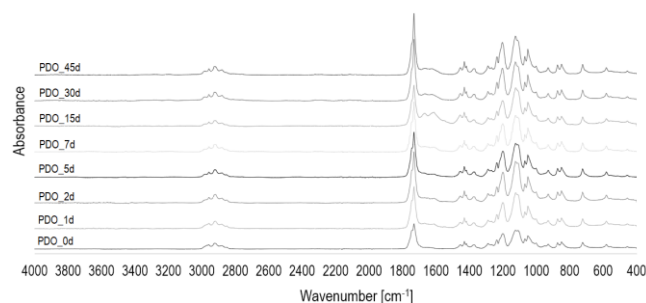


**Fig. 9.** FTIR spectra of the PDO material before and after a specified incubation time in artificial urine solution. FTIR, Fourier transform infrared; PDO, polydioxanone

The observed peaks correspond to and characterise the occurrence of individual functional groups. Peaks in the range from  $3,000 \text{ cm}^{-1}$  to  $2,800 \text{ cm}^{-1}$  are characteristic of symmetric and asymmetric vibrations of the C-H group of the aliphatic chain. A strong single peak corresponding to C=O stretching vibrations located in the ester carbonyl group for each of the degradation periods after averaging was recorded at  $1,731.95 \text{ cm}^{-1}$ . The peaks in the range from  $1,200 \text{ cm}^{-1}$  to  $1,000 \text{ cm}^{-1}$  are characteristic of asymmetric C-O stretching vibrations, while the peak near  $850 \text{ cm}^{-1}$  indicates the presence of symmetric C-O stretching vibrations. The peak observed near  $1,431 \text{ cm}^{-1}$  indicates the presence of bending vibrations of the C-H group. Deeper analysis of the different parts of the FTIR spectra did not reveal any deviations in the bands; therefore, it can be concluded that no new functional groups were formed during the degradation. This is

important from the point of view of the safety of using the PDO material in living organisms, especially if it stays in the body for >30 days. Li et al. [19] and Loskot et al. [37] obtained similar results, which may confirm that the degradation of the PDO material in fluids simulating the given environment is safe for the organism.

### 3.5. SEM microscopy analysis

Fig. 11 presents the obtained surface morphologies of the PDO material before and after temporary degradation at 1,500× magnification. The material before degradation (Fig. 11a) shows a smooth and homogeneous surface. The material shows deposited urine solution particles after 1 day, 2 days, 5 days, 7 days and 15 days of degradation, respectively (Fig. 11b–f.). However, after 30 days and 45 days of incubation in urine solution, cracks were observed on the material surface (Fig. 11g,h.). The number of cracks present after 30 days of degradation is quite large, and after 45 days, the number of cracks and deformation of the polymer fibres is even larger and more pronounced.

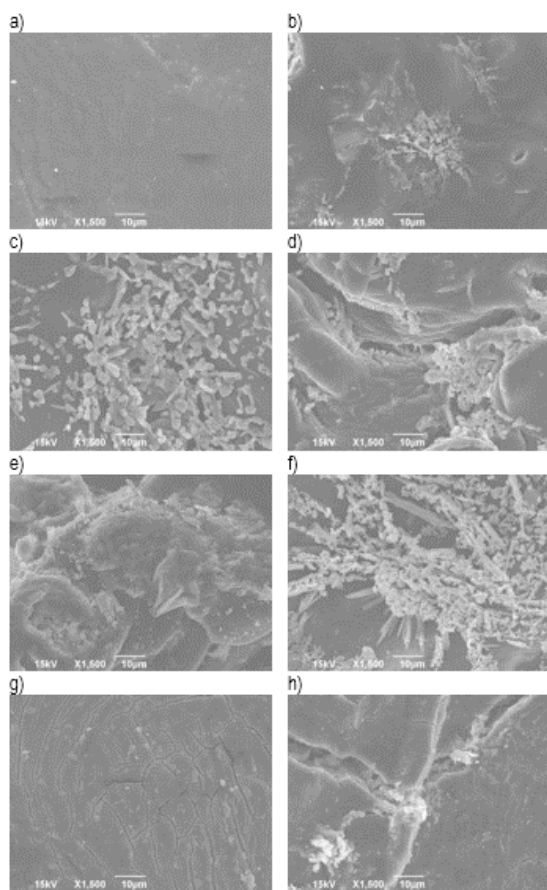


**Fig. 10.** Morphology of the PDO material surface before and after degradation: (a) before degradation, (b) after 1 day of incubation, (c) after 2 days of incubation, (d) after 5 days of incubation, (e) after 7 days of incubation, (f) after 15 days of incubation, (g) after 30 days of incubation, (h) after 45 days of incubation. PDO, polydioxanone

The characteristic arrangement of the cracks on the polymer surface indicates that the material is losing its elasticity and resilience, becoming a more brittle and vulnerable material. It can be assumed that the action of stimuli and external forces on such a

degraded material can cause serious damage and even prevent it from performing its function of decongesting the channel of the narrowed urethra. Microscopic observations of the material structure confirm the mechanical strength results that the material after 45 days of incubation in the urine environment is fully degraded, becomes brittle and loses its mechanical properties.

### 4. CONCLUSION

The analysis of the PDO material shows good mechanical properties, while the degradation time for the fabricated material is too short to be used as a urethral stent. Given the minimum of 60–90 days needed for the full regeneration of the urethral tissues, a change in the manufacturing method or an additive to the material produced by 3D printing should be considered to extend the degradation time. The success of the research is the testing of flexural strength, which is not a frequently considered aspect so far. With specific conditions in the urethra during the urine flow, it is important that the material used for the stent has high deformability. This is necessary due to the action of varying external forces on the urethra both from outside in the form of the muscle action and inside in the form of the urine pressure. During micturition, neighbouring muscles act on the urethra, which induces high stresses in the tissues. The research and results will serve as a prelude to further analysis for similar applications of PDO material in tissue engineering.

### REFERENCES

1. Tan Q, Le H, Tang C, Zhang M, Yang W, Hong Y, Wang X. Tailor-made natural and synthetic grafts for precise urethral reconstruction. *J. Nanobiotechnology*. 2022;20(392):1–23. <https://doi.org/10.1186/s12951-022-01599-z>
2. Xu K, Han Y, Huang Y, Wei P, Yin J, Jiang J. The application of 3D bioprinting in urological diseases. *Mater. Today Bio*. 2022;16(100388):1–17. doi: 10.1016/j.mtbio.2022.100388
3. Verla W, Oosterlinck W, Spinoit AF, Waterloos M. A Comprehensive Review Emphasizing Anatomy, Etiology, Diagnosis, and Treatment of Male Urethral Stricture Disease. *BioMed Res. Int*. 2019;2019:9046430:1–20. doi: 10.1155/2019/9046430
4. Lazzeri M, Sansalone S, Guazzoni G, Barbagli G. Incidence, Causes, and Complications of Urethral Stricture Disease. *Eur. Urol. Suppl*. 2016;15(1):2–6. doi: 10.1016/j.eursup.2015.10.002
5. Yao HJ, Wei ZW, Wan X, Tao YC, Zhang DC, Wang Z, Xie MK. Three new experimental models of anterior urethral stricture in rabbits. *Transl. Androl. Urol*. 2022;11(6):761–772. doi: 10.21037/tau-22-104
6. Klekiel T, Mackiewicz A, Kaczmarek-Pawelska A, Skonieczna J, Kurowiak J, Piasecki T, Noszczyk-Nowak A, Będziński R. Novel design of sodium alginate based absorbable stent for the use in urethral stricture disease. *J. Mater. Res. Technol*. 2020;9(4):9004–9015. <https://doi.org/10.1016/j.jmrt.2020.06.047>
7. Kurowiak J, Mackiewicz A, Klekiel T, Będziński R. Evaluation of Selected Properties of Sodium Alginate-Based Hydrogel Material-Mechanical Strength,  $\mu$ DIC Analysis and Degradation. *Materials*. 2022;15(3):1–15. <https://doi.org/10.3390/ma15031225>
8. Mackiewicz A, Klekiel T, Kurowiak J, Piasecki T, Będziński R. Determination of Stent Load Conditions in New Zealand White Rabbit Urethra. *J. Funct. Biomater*. 2020;11(4):1–9. <https://doi.org/10.3390/jfb11040070>
9. Farzamfar S, Elia E, Chabaud S, Naji M, Bolduc S. Prospects and Challenges of Electrospun Cell and Drug Delivery Vehicles to Correct Urethral Stricture. *Int. J. Mol. Sci*. 2022;23(18):1–37. <https://doi.org/10.3390/ijms231810519>

10. Basikn LS, Constantinescu SC, Howard PS, Mcaninch JW, Ewalt DH, Duckett JW, Snyder HM, Macarak EJ. Biomechanical characterization and quantitation of the collagenous components of urethral stricture tissue. *J. Urol.* 1993;150:642–647. 10.1016/s0022-5347(17)35572-6
11. Goel A, Goel A, Jain A, Singh BP. Management of panurethral strictures. *Indian J. Urol.* 2011;27(3):378–384. 10.4103/0970-1591.85443
12. Mundy AR, Andrich DE. Urethral strictures. *BJU International.* 2010;107(1):6–26. doi: 10.1111/j.1464-410X.2010.09800.x.
13. Engel O, Soave A, Rink M, Fisch M. Reconstructive Management with Urethroplasty. *European Association of Urology.* 2016;15(1):13–16. 10.1016/j.eursup.2015.10.004
14. Pudelko P. Rekonstrukcja cewki moczowej - urethroplastyka/Reconstruction of the urethroplasty. *Przegląd Urologiczny.* 2016;96.
15. Pastorek D, Culenova M, Csobonyeiova M, Skuciova V, Danisovic L, Ziaran S. Tissue Engineering of the Urethra: From Bench to Bedside. *Biomedicines.* 2021;9(12):1–12. 10.3390/biomedicines9121917
16. Cheng L, Li S, Wan Z, Huang B, Lin J. A brief review on anterior urethral strictures. *Asian J Uro.* 2018;5(2):88–93. 10.1016/j.ajur.2017.12.005
17. Kurowiak J, Kaczmarek-Pawelska A, Mackiewicz A, Będziński R. Analysis of the Degradation Process of Alginate-Based Hydrogels in Artificial Urine for Use as a Bioresorbable Material in the Treatment of Urethral Injuries. *Processes.* 2020;8(3):1–11. <https://doi.org/10.3390/pr8030304>
18. Cunnane EM, Davis N, Cunnane CV, Lorentz KL, Ryan AJ, Hess J, Weinbaum JS, Walsh MT, O'Brien FJ, Vorp DA. Mechanical, compositional and morphological characterisation of the human male urethra for the development of a biomimetic tissue engineered urethral scaffold. *Biomaterials.* 2021;269(120651):1–31. 10.1016/j.biomaterials.2021.120651
19. Li G, Li Y, Lan P, Li J, Zhao Z, He X, Zhang J, Hu H. Biodegradable weft-knitted intestinal stents: Fabrication and physical changes investigation in vitro degradation. *J. Biomed. Mater. Res. Part A.* 2014;102(4):982–990. <https://doi.org/10.1002/jbm.a.34759>
20. Loskot J, Jezbera D, Zmrhalová ZO, Nalezinková M, Alferi D, Lelkes A, Voda P, Andrýs R, Myslivcová-Fučíková A, Hosszú T, Bezrouk A. A Complex In Vitro Degradation Study on Polydioxanone Biliary Stents during a Clinically Relevant Period with the Focus on Raman Spectroscopy Validation. *Polymers.* 2022;14(5):1–19. <https://doi.org/10.3390/polym14050938>
21. Zilberman M, Eberhart RC. Drug-Eluting Bioresorbable Stents for Various Applications. *Annu. Rev. Biomed. Eng.* 2006;8:153–180. <https://doi.org/10.1146/annurev.bioeng.8.013106.151418>
22. Zhang W, Kanwal F, Fayyaz M, Rehman UR, Wan X. Efficacy of Biodegradable Polydioxanone and Polylactic Acid Braided Biodegradable Biliary Stents for the Management of Benign Biliary Strictures. *Turk J Gastroenterol.* 2021;32(8):651–660. 10.5152/tjg.2021.201174
23. Kwon C, Son JS, Kim KS, Moon JP, Park S, Jeon J, Kim G, Choi SH, Ko KH, Jeong S, Lee DH. Mechanical properties and degradation process of biliary self-expandable biodegradable stents. *Dig Endosc.* 2021;33(7):1158–1169. doi: 10.1111/den.13916
24. Bezrouk A, Hosszu T, Hromadko L, Olmrova-Zmrhalova Z, Kopecek M, Smutny M, Krulichova IS, Macak JM, Kremlacek J. Mechanical properties of a biodegradable self-expandable polydioxanone monofilament stent: In vitro force relaxation and its clinical relevance. *PLOS ONE.* 2020;15(7):1–16. <https://doi.org/10.1371/journal.pone.0235842>
25. Adolffson KH, Sjöberg I, Höglund OV, Wattle O, Hakkarainen M. In Vivo Versus In Vitro Degradation of a 3D Printed Resorbable Device for Ligation of Vascular Tissue in Horses. *Macromol. Biosci.* 2021;21(10):1–12. <https://doi.org/10.1002/mabi.202100164>
26. Saska S, Pilatti L, Santos de Sousa Silva E, Nagasawa MA, Câmara D, Lizier N, Inger E, Dyszkiewicz-Konwińska M, Kempisty B, Tunchel S, Blay A, Shibil JA. Polydioxanone-Based Membranes for Bone Regeneration. *Polymers.* 2021;13(11):1–16. <https://doi.org/10.3390/polym13111685>
27. Fathi P, Capron G, Tripathi I, Misra S, Ostadhossein F, Selmic L, Rowitz B, Pan D. Computed Tomography-Guided Additive Manufacturing of Personalized Absorbable Gastrointestinal Stents for Intestinal Fistulae and Perforations. *Biomaterials.* 2020;228(119542):1–36. doi: 10.1016/j.biomaterials.2019.119542
28. Park JH, Song HY, Shin JH, Kim JH, Jun EJ, Cho YC, Kim SH, Park J. Polydioxanone Biodegradable Stent Placement in a Canine Urethral Model: Analysis of Inflammatory Reaction and Biodegradation. *J Vasc Interv Radiol.* 2014;25(8):1257–1264. 10.1016/j.jvir.2014.03.023
29. Stehlik L, Hytych V, Letackova J, Kubena P, Vasakova M. Biodegradable polydioxanone stents in the treatment of adult patients with tracheal narrowing. *BMC Pulm. Med.* 2015;15(164):1–8. 10.1186/s12890-015-0160-6
30. Zamiri P, Kuang Y, Sharma U, Ng TF, Busold RH, Rago AP, Core LA, Palasis M. The biocompatibility of rapidly degrading polymeric stents in porcine carotid arteries. *Biomaterials.* 2010;31(31):7847–7855. 10.1016/j.biomaterials.2010.06.057
31. Kurowiak J, Kaczmarek-Pawelska A, Mackiewicz A, Baldy-Chudzik K, Mazurek-Popczyk J, Zaręba Ł, Klekiel T, Będziński R. Changes in the Mechanical Properties of Alginate-Gelatin Hydrogels with the Addition of Pygeum africanum with Potential Application in Urology. *Int. J. Mol. Sci.* 2022;23(18):1–16. <https://doi.org/10.3390/ijms231810324>
32. Chutipongtanate S, Thongboonkerd V. Systematic comparisons of artificial urine formulas for in vitro cellular study. *Anal. Biochem.* 2010;402(1):110–112. 10.1016/j.ab.2010.03.031
33. Gil-Castell O, Badia JD, Bou J, Ribes-Greus A. Performance of Polyester-Based Electrospun Scaffolds under In Vitro Hydrolytic Conditions: From Short-Term to Long-Term Applications. *Nanomaterials.* 2019;9(5):1–19. <https://doi.org/10.3390/nano9050786>
34. Zhao F, Sun J, Xue W, Wang F, King MW, Yu C, Jiao Y, Sun K, Wang L. Development of a polycaprolactone/poly(p-dioxanone) bioresorbable stent with mechanically self-reinforced structure for congenital heart disease treatment. *Bioact. Mater.* 2021;6(9):2969–2982. <https://doi.org/10.1016/j.bioactmat.2021.02.017>
35. Tian Y, Zhang J, Cheng J, Wu G, Zhang Y, Ni Z, Zhao G. A poly(L-lactic acid) monofilament with high mechanical properties for application in biodegradable biliary stents. *J. Appl. Polym. Sci.* 2020;138(2):1–8. <https://doi.org/10.1002/app.49656>
36. Conderman C, Kinzinger M, Manuel C, Protsenko D, Wong BJF. Mechanical analysis of cartilage graft reinforced with PDS plate. *Laryngoscope.* 2013;123(2):339–343. doi: 10.1002/lary.23571
37. Loskot J, Jezbera D, Bezrouk A, Doležal R, Andrýs R, Francová V, Miškář D, Myslivcová-Fučíková A. Raman Spectroscopy as a Novel Method for the Characterization of Polydioxanone Medical Stents Biodegradation. *Materials.* 2021;14(18):1–16. <https://doi.org/10.3390/ma14050938>

Acknowledgments: "The work has been accomplished under the research project No. DEC-2016/21/B/ST8/01972, funded by National Science Center, Poland".

Jagoda Kurowiak:  <https://orcid.org/0000-0003-2692-5311>

Agnieszka Mackiewicz:  <https://orcid.org/0000-0002-3956-8483>

Tomasz Klekiel:  <https://orcid.org/0000-0002-2699-3528>

Romuald Będziński:  <https://orcid.org/0000-0003-3611-2584>



This work is licensed under the Creative Commons BY-NC-ND 4.0 license.